europhysics
conference
abstracts

18th European Conference on

Controlled Fusion and Plasma Physics

Berlin, 3-7 June 1991
Editors: P. Bachmann, D.C. Robinson

Contributed Papers
Part III

Published by: European Physical Society

s Editor: Prof. K. Bethge, Frankfurt/M.

aging Editor: G. Thomas, Geneva

VOLUME
15 C
Part III

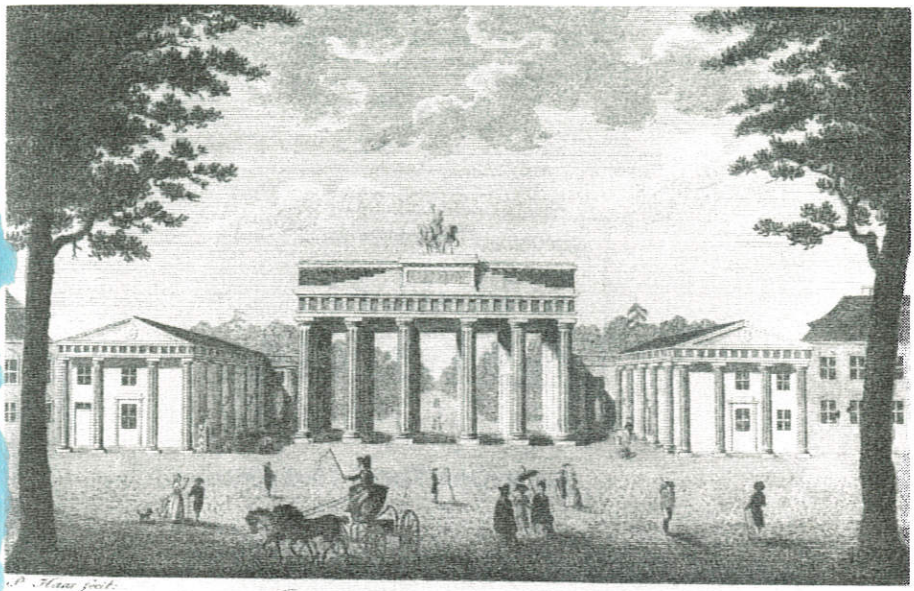

P. Haas fecit.

Das Brandenburger Thor zu Berlin.

18th
FUSION
BERLIN
1991

D
E

18th European Conference on

Controlled Fusion and Plasma Physics

Berlin, 3-7 June 1991
Editors: P. Bachmann, D.C. Robinson

Contributed Papers
Part III

PREFACE

The 18th European Conference on Controlled Fusion and Plasma Physics was held in Berlin, Germany, from 3th to 7th June 1991. The Conference has been organized by the Central Institute of Electron Physics (ZIE) on behalf of the Plasma Physics Division of the European Physical Society.

The programme, format and schedule of the Conference were determined by the International Programme Committee appointed by the Plasma Physics Division of the EPS. The programme included 14 invited lectures and 388 contributed papers from which 27 were selected for oral presentation.

This 4-volume publication is published in the European Conference Abstract Series and contains all accepted contributed papers received in due time by the organizers. The 4-page extended abstracts were reproduced photographically using the manuscript submitted by the authors. The invited papers will be published in a special issue of the journal "Plasma Physics and Controlled Fusion" and sent free of charge to each registered participant.

The editors would like to acknowledge the skilful and dedicated support given by colleagues in the Department of Plasma Wall Interactions of the ZIE, in preparing the manuscript for reproduction in these four volumes.

May 1991

The Editors

INTERNATIONAL PROGRAMME COMMITTEE

D. Robinson (Chairman), Culham Lab., UK
K. Appert, CRPP/EPFL, Switzerland
G. Briffod, CEN, France
M. Chatelier, CEN, France
V.A. Chuyanov, Kurchatov Institute, USSR
M. Keilhacker, JET, EC
U. Samm, KFA, Germany
F. Santini, EURATOM-ENEA, Italy
F.W. Sluijter, Tech.Univ.Eindhoven, NL
J. Lingertat, ZIE, Germany

LOCAL ORGANIZING COMMITTEE

J. Lingertat, Chairman
P. Bachmann, Scientific Secretary
M. Blaschke, Conference Secretary
D. Amonath
H. Gunkel
W. König
P. Pech
M. Wirsig

CONTENTS

PAPER IDENTIFICATION

All contributed papers are listed with their title and the name of the first authors. Each paper may be identified by its classification symbol which starts with a letter that indicates to which topic it belongs followed by a number.

T I T L E L I S T

A TOKAMAKS

A1 Tokamaks, General

A2 Transport and Modelling

A3 Turbulence, Waves

A5 Improved Confinement

A6 MHD Phenomena, Sawteeth

B STELLARATORS

C ALTERNATIVE CONFINEMENT SCHEMES

D PLASMA EDGE PHYSICS

E PLASMA HEATING AND CURRENT DRIVE

F GENERAL PLASMA THEORY

G DIAGNOSTICS

ONE-DIMENSIONAL MODEL FOR A DESCRIPTION OF TRANSITIONS OF A TOKAMAK EDGE PLASMA INTO A STRONGLY RADIATIVE STATE

M.Z.Tokar'

Institute for High Temperatures of the USSR Academy of Sciences,
Moscow, USSR

1.INTRODUCTION

The realization of a the tokamak edge plasma mode with strong radiation from light impurities is one of the perspective ways for the solution of the problem of plasma-wall interaction. In many devices discharges with so called "detached plasma" were obtained, in which more than 90% of the power transported to the periphery by charged particles are radiated uniformly onto the wall.

Up to now a large amount of experimental data has been accumulated concerning the transition into the "detached plasma" state [1,2]. The attempts for a theoretical description of the peripheral plasma with strong radiation are restricted so far to qualitative zero-dimensional models or to calculations of radiative losses for some "typical" profiles of plasma parameters [2,3]. But the experiments show [1,4] that these profiles suffer a qualitative modification with the transition into the state with strong radiation.

In the present paper an one-dimensional model is proposed for the self-consistent description of particle transport (hydrogen and impurities; neutral and charged) and of energy transport in the tokamak edge plasma inside the separatrix. Results from these model calculation and experimental data from TEXTOR are compared.

2. PHYSICAL MODEL AND BASIC EQUATIONS

We have restricted our consideration to the tokamak peripheral region inside the last closed magnetic surface (LCMS), touching the limiter, in which the processes of ionization of the recycling hydrogen atoms and the radiation form light impurities are important in the balance for particle and heat transport. The parameters averaged over the magnetic surfaces are considered and only the transport processes along the minor radius r are taking into account. The conditions under which such an averaging is applicable are discussed in Ref.[3]. It is assumed that the impurity atoms enter into the edge region across the LCMS with the velocity v_0 and the flux density j_0. For weakly ionized impurity ions the ionization is the dominating process resulting in a charge change, since estimates show that for these particles it is possible to neglect all kinds of recombination including charge-exchange with hydrogen atoms (the situation may be another one for the highly ionized particles, for example, C^{4+}, C^{6+}). In the stationary state the ionization compensates the particle transport across the magnetic surfaces and the continuity equations are

$$\frac{1}{r}\frac{d}{dr}(r n_0 v_0) = -k_i^0 n_0 n_e \qquad (1)$$

$$\frac{1}{r}\frac{d}{dr}(r\Gamma_z) = -k_i^z n_z n_e + k_i^{z-1} n_{z-1} n_e \qquad (2)$$

where $\Gamma_z = -D_\perp \, dn_z/dr + V_\perp n_z$ is the transversal flux density, n_z is the density, k_i^z is the constant of ionization, $D_\perp$ is the diffusivity, $V_\perp$ is the velocity of the convection of the impurity ions with charge z, n_e is the electron density.

For the hydrogen atoms coming into the edge region from the tokamak wall due to plasma recycling we use a diffusion approximation in which the atom trajectories are described as a random walk based on charge-exchanged collisions [5]:

$$\frac{1}{r}\frac{d}{dr}\left(-rD_a\frac{dn_a}{dr}\right) = k_i^a n_e n_a \qquad (3)$$

where n_a is the density, $D_a = V_i^2/(k_c n_i)$ is the diffusivity, k_i^a, k_c are the ionization and charge-exchange constants of the hydrogen atoms, n_i, $V_i=\sqrt{2T/m_i}$ are the density and thermal velocity of the hydrogen ions, T is the plasma temperature.

In a quasi-neutral plasma with the absence of charged particle sources in the discharge center the following conditions hold

$$n_e = n_i + \sum z n_z, \quad \Gamma_i = D_a \frac{dn_a}{dr} \tag{4}$$

where $\Gamma_i = D_\perp dn_i/dr$ is the flux density of the working gas ions. The equation of the plasma heat balance($T=T_e=T_i$ is assumed) has the form:

$$\frac{1}{r}\frac{d}{dr}(rq_\perp) = -k_i^a n_e n_a E_i - \sum L_z n_z n_e \tag{5}$$

Here $q_\perp=-\kappa_\perp dT/dr+\alpha\Gamma_i T$ is the transversal heat flux density, α=3-5, $\kappa_\perp$ is the heat conductivity of the plasma, $E_i\approx$25-30 eV is the energy loss on the ionization of the working gas atoms, $L_z(T) = \Sigma k_{ij}^z E_{ij}^z$ is the cooling rate of the ions with z charge, k_{ij}^z, E_{ij}^z are the constants of the excitation and energies of the main transitions.

The boundary conditions of Eqs(1)-(5) are posed at the LCMS

$$n_0 = j_0/v_0, \quad n_z = \Gamma_z/V_z^s, \quad n_i = \Gamma_i/V_i^s, \quad q_\perp = \gamma\Gamma_\perp T \tag{6}$$

where $V_{z,i}^s$ are determined by the transport processes in the scrape-off-layer (SOL), γ=5-10; at the conventional boundary between the edge and the central parts of the discharge($r=r_b$):

$$n_0 = n_z = 0, \quad n_e = n_m, \quad q_\perp = q_0 \tag{7}$$

where n_m is determined by the total number of the particles in the discharge, $q_\perp$ - by the total power launched into the plasma.

The system of Eqs(1)-(5) can be reduced to a very convenient form, from the computational point of view, if one takes the Alcator scaling for the coefficients of perpendicular transport : $D_\perp=A_D/n_e$, $\kappa_\perp=A_D/\varepsilon$; ε, A_D=const; $V_\perp=0$; assumes that the edge region thin one($a-r_b \ll a$); neglects the difference between n_e and n_i. These conditions hold as a rule in the discharges with pure ohmic heating.With introduction of new variables $u=\int\sigma_0 n\, dx$, $\eta_z=n_z v_0/j_0$, $\eta_a = n_a/n_a(0)$, $\eta=A_D\sigma_0 n/\Gamma_i(r=a)$, where $x=a-r$ is the distance from the LCMS, $\sigma_0=10^{-14}cm^2$ is the characteristic cross-section of the processes with the hydrogen atoms, Eqs(1)-(5) are reduced to

$$d\eta_0/du = \lambda_0\eta_0, \quad d^2\eta_z/du^2 = \lambda_z^2\eta_z - \lambda_{z-1}^2\eta_{z-1} \tag{8a}$$

$$d^2\eta_a/du^2 = \lambda_a^2\eta_a, \quad d\eta/du + \beta\, d\eta_a/du = 0 \tag{8b}$$

$$\frac{d}{du}\left(\frac{\eta}{\varepsilon}\frac{dT}{du} + (5T+E_i)\frac{d\eta}{du}\right) = \frac{S_I}{\sigma_0 v_0}\sum L_z(T(u))\eta_z \tag{9}$$

Here $S_I=j_0/\Gamma_i(r=a)$ is the effective erosion coefficient, $\lambda_0=k_i^0/(\sigma_0 v_0)$, $\lambda_z=\sqrt{k_i^z/A_D}/\sigma_0$, $\lambda_a=\sqrt{k_c k_i^a}/(V_i\sigma_0)$, $\beta=V_i\sigma_0/k_c$ are the coefficients depending only on the plasma temperature. The boundary conditions for this system are the following:

$$u=0: \quad \eta_0=1, \ \eta_z=\alpha_z^s d\eta_z/du, \ \eta=\alpha_i^s d\eta/du, \ \eta\, dT/du = \varepsilon(\gamma-\alpha)T d\eta/du \tag{10}$$

where the coefficients $\alpha_{z,i}^s=\sigma_0 A_D/V_{z,i}^s \ll 1$ depend on the particle transport processes in the SOL;

$$u=u_0 \gg 1: \quad \eta_a=\eta_z=0, \ \eta=\frac{A_D\sigma_0 n_m}{\Gamma_i(r=a)}, \ \frac{dT}{du}=\frac{q_0}{\kappa_\perp n_m \sigma_0} \tag{11}$$

The choice of u_0 for the numerical solution is determined by the condition that the increase of u_0 does not influence the results.

The formulation of the problem in the form of the Eqs(8),(9) and conditions (10),(11) allows to proceed for the more easily solved problem with initial conditions. Additionally, for (10) we take the temperature and the flux density of the charged particles on the LCMS: $T_s=T(r=a,u=0)$, $\Gamma_s=\Gamma_i(r=a,u=0)$ as parameters and after solving of Eqs(8),(9) determined from the conditions (11) the corresponding values of q_0 and n_m. It is important to note that the profiles of T(u), $\eta_0(u)$, $\eta_a(u)$, $\eta_z(u)$, $\eta(u)$ are determined only by the value of T_s.

After the first integration of Eq(9) one has the heat balance of the edge region:

$$q_0=(\gamma T_s+E_i)\Gamma_s+j_0E_A \tag{12}$$

where the first term in the right hand side gives the heat convective losses with the charged particles into the SOL, the second one - the energy radiative losses from the peripheral region, E_A is the radiative potential, introduced in Ref.[1]. For E_A we have obtained the following expression

$$E_A=\int_0^{u_0}\Sigma L_z(T(u))\eta_z(u)\frac{du}{v_0\sigma_0} \tag{13}$$

From the definition (13) it follows that except T_s, E_A depends only on the parameters A_D, ε, $\alpha_{z,i}^s$, S_I, v_0, which are external for the edge plasma model and are enough conservative for the ohmic discharges.

3. CALCULATION RESULTS, COMPARISON WITH THE EXPERIMENTAL DATA

The numerical solution of the Eqs(8),(9) has been obtained by an iteration method: with a given initial profile of T(u) the Eqs(8) are solved and then the new T(u) profile is calculated from the Eq.(9). The iteration process converges quickly - already the third iteration gives an error <5%.

The ionization constants of hydrogen and of the impurities are calculated according to the data from Ref.[6]. For computing the cooling rate the data of Ref.[7] have been used to obtain simple analytical approximative formulas for the L_z dependence on T : $L_z=A_z\sqrt{T}\exp(-E_z/T)/(1+B_z\sqrt{T}+C_zT)$. The magnitudes of the A_z, B_z, C_z and E_z parameters for the most intensively radiating impurity ions are presented in the following table.

element	z	$A_z(eV^{\cdot 5}cm^3/s)$	$B_z(eV^{-.5})$	$C_z(eV^{-1})$	$E_z(eV)$
carbon	1	$5.6\ 10^{-7}$	.213	.0143	7.76
	2	$7.27\ 10^{-7}$	.265	.023	7.59
	3	$7.54\ 10^{-7}$	.483	.565	5.48
oxygen	1	$1.07\ 10^{-7}$	.0	.025	6.23
	2	$1.59\ 10^{-7}$	.0	.0282	7.94
	3	$1.41\ 10^{-7}$	.0	.0095	7.61
	4	$2.7\ 10^{-7}$	.0	.0143	9.7
	5	$1.045\ 10^{-7}$	.0	.0134	4.13

The typical values for ohmic discharges were taken: $A_D=6\ 10^{16}$/cm/s, $\varepsilon=0.16$, $\alpha_{z,i}^s=0.15$, $S_I=.02$, $v_0=5\ 10^5$cm/s, but the variation of these parameters in a quite wide range does not influence the results qualitatively. The calculation of the dependence of the radiative potential on the plasma temperature at the LCMS is presented in Fig.2. The curve 1 corresponds to the case when only the carbon atoms enter into discharge; the curve 2 - when the ratio of the carbon and oxygen atom fluxes equals 2/1; the curve 3 shows the results of the radiative losses calculated for

n and T profiles in the edge plasma of TEXTOR typical for not a high averaged density $\bar{n} \leq 3\ 10^{13}$ cm^{-3} [1]. The measured data are presented by the crosses. Fig.3. demonstrates the dependence of the radiated part of the power launched into the discharge, α_r, on n_m. The calculations were carried out for ohmic discharges: the curve 1 corresponds to the plasma current I_p=260kA, the curve 2-I_p=340 kA; the loop voltage V_L equals 1V. It was assumed that 30% of the total power $I_p V_L$ is radiated from the discharge center with any n_m. The experimental points (diamonds and triangles) showing the dependence on the average density are also shown.

4. CONCLUSION

The one-dimensional model proposed for a self-consistent description of the particle and energy balances of the tokamak edge plasma taking into account the impurity transport and radiation is in good agreement with experimental data. This model gives a good basis for the examination of the controlled transition into a "detached plasma" with neon gas puffing under the condition of strong auxiliary heating [1].

REFERENCES

1) U. Samm U, "Radiating control in a limiter tokamak", KFA-Report Jül-2378 (1990)
2) Proc. of Sat.Workshop 'Relevance, realization and stability of a cold layer at the plasma edge for fusion reactors',DRFC/CAD report EUR-CEA-FC-1403(90).
3) A.V. Nedospasov, M.Z. Tokar', in "Problems of Plasma Theory" (Ed. B.B. Kadomtsev), Moscow (1990) 68
4) A. Grosman et.al., Plasma Physics Contr. Fusion 32 (1990) 101
5) B. Lehnert, Nucl. Fusion 8 (1968) 173
6) K.L. Bell et.al., Culham Report CLM-R216 (82)
7) Y. Itikawa et.al., Atomic Data Nucl. Data Tables 33 (1985) 150

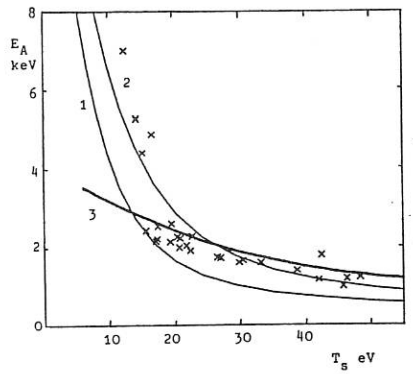

Fig.1. The dependences of the radiation potential on the electron temperature at the LCMS.

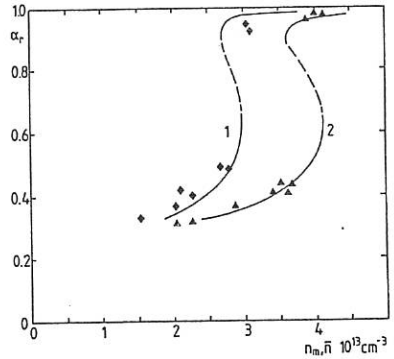

Fig.2. The dependences of the radiated part of the power launched into the TEXTOR ohmic discharges on the plasma density.

NEUTRAL TRANSPORT AND HYDROGEN RECYCLING IN EDGE REGION OF HL-1 TOKAMAK PLASMA

B.Q.Deng, X.R.Duan, H.Z.Li, L.L.Peng, C.J.Yuan,
S.K.Yang, S.X.Zhang, T.J.Huo, P.Zhang

Southwestern Institute of Physics, Chengdu,
P.O.Box 432, Sichuan, 610041, P.R. China

Introduction

A 1-D neutral transport code including molecular processes [1] and wall interactions [2] has been utilized to model the effect of molecular processes in edge region on neutral transport of HL-1 tokamak. The peak location and shape of neutral atom profile basically agree with the results derived from H_α measurements. The particle recycling in various wall and discharge conditions are studied. Two methods are used to improve particle confinement time and recycling. One is previous discharge cleaning with (H_2+Kr) instead of H_2; the other is to use pumping limiter.

Effect of Molecular Processes on Neutral Transport

The following molecular and atomic processes are involved:
dissociative excitation of H_2

$$H_2 + e^- \longrightarrow 2H^\circ + e^- \qquad (1)$$

ionization of H_2,

$$H_2 + e^- \longrightarrow H_2^+ + 2e^- \qquad (2)$$

dissociative ionization of H_2,

$$H_2 + e^- \longrightarrow H^\circ + H^+ + 2e^- \qquad (3)$$

dissociative excitation of H_2^+,

$$H_2^+ + e^- \longrightarrow H^+ + H^\circ + e^- \qquad (4)$$

and dissociative recombination of H_2^+,

$$H_2^+ + e^- \longrightarrow 2H^\circ \qquad (5)$$

The mesh points j, coordinates x and zones for calculations are shown in Fig.1. The internally born isotropic hydrogen atom source rate produced by molecular breakup of above processes is given by

$$S_{H^\circ}(x_j) \propto F_p^{in} \frac{n_e(x_j)}{\Delta_j} \cdot \left[E_3(\beta_j^\circ) - E_3(\beta_{j+1}^\circ) \right] \left\{ \frac{2\langle\sigma v\rangle_1 + \langle\sigma v\rangle_2 \cdot \left[\frac{\langle\sigma v\rangle_4 + 2\langle\sigma v\rangle_5}{\langle\sigma v\rangle_4 + \langle\sigma v\rangle_5} \right]}{\left[\langle\sigma v\rangle_1 + \langle\sigma v\rangle_2 \right] \cdot n_e(x_j)} \right\} \qquad (6)$$

which is treated in the same way as the neutral source due to charge exchange in original SPUDNUT code [3], the code is based on an integral equation for neutral transport. The hydrogen ion source rate is

$$S_{H^+}(x_j) \propto F_p^{in} \frac{\left[E_3(\beta_j^\circ) - E_3(\beta_{j+1}^\circ) \right] n_e(x_j)}{\Delta_j} \left\{ \frac{\langle\sigma v\rangle_2}{n_e(x_j)\left[\langle\sigma v\rangle_1 + \langle\sigma v\rangle_2\right]} \cdot \frac{\langle\sigma v\rangle_3}{\langle\sigma v\rangle_4 + \langle\sigma v\rangle_5} \right\} \qquad (7)$$

which contributes to plasma fueling. The F_p^{in} is initial flux introduced by low pressure gas puffing, the $\langle\sigma v\rangle$ is rate coefficients of above mentioned processes, E_3 is the exponential integral, Δj is the zone width.

The temperature and density profiles of edge plasma region(8cm slab) are fitted by Langmuir probe data and others. Assuming that the external (puffed or released form wall) initial neutral gas influx $F_p^{in} = 5.7 \times 10^{15}/s.cm^2$, the hydrogen atom density profile and hydrogen atom ionization rate profile

are obtained. Comparisons to the case where the neutrals are assumed to be incident on edge plasma as atoms are made (see Fig. 2-3). It is found that molecular processes have a strong effect on the neutral transport.

Figure 2 shows the neutral atom density profiles. The molecular case fairly agrees with the result of Hα measurment (see Fig. 4). For the same initial incident flux, the neutral density is lower in the molecular case. This is because the breakup of H_2 produces H° as well as H^+. In addition, the H° produced is isotropic as internal-born source and therefore has an equal probability of heading back to the wall as penetratimg deeper into the plasma . The peak is located a couple of centimeters from the limiter. This indicates that most of the incident molecules are broken up within this distance. It is obvious that in atomic case the density of H° peaked at the edge and declines monotonously.

The hydrogen ionization rate profiles are shown in Fig. 3. In case 2, the peak approaches the wall a little more as compared with atomic case 1. This is because the mean free paths of molecules are shorter than atom's at the same temperature . The atoms can penetrate farther, as a result, the profile is broadening.

Table 1 and 2 show the effects of molecular processes on particle flux and energy flux of hydrogen atoms respectively. The indices "in" and "out" denote entering and outgoing edge region; "col" and "hot" refer to cold and energetic atoms; "net" refers to net flux over the edge region. "ref" means reflected from wall.

Table 1. Particle fluxes of H°

10^{15}/s.cm^2	F^{in}_{p}	F^{out}_{col}	F^{in}_{col}	F^{out}_{hot}	F^{in}_{ref}	F^{out}_{in}	F_{net}
1	5.7	0	0	-0.703	0.495	-1.98	3.51
2	5.7	-1.4	0.572	-0.33	0.234	-0.732	4.04

Table 2. Energy fluxes of H°

mW/cm^2	E^{in}_{p}	E^{out}_{col}	E^{in}_{col}	E^{out}_{hot}	E^{in}_{ref}	E^{out}_{in}	E_{net}
1	4.56	0	0	-33.2	10.7	-39.2	-57.2
2	4.56	-1.12	0.458	-14.6	4.72	-16.5	-22.5

Experiment Studies

In our experiments, a multi-channel optical detecting system is used to measure absolute intensity of Hα emission. The system consists of fiber-optic cables, interference filter and photomultipliers. The neutral hydrogen density $n_H(r,t)$ is determined by

$$n_H(r,t)=\frac{4\pi N_v(r,t)}{n_e Q_{12} B} \qquad (8)$$

where, Nv(r,t), the number of photons, is obtained from measured absolute intensity of Hα.

The global particle confinement time τ_p is given by

$$\tau_p = 1/(n_H s_o - n_+ \alpha_+) \qquad (9)$$

where the coefficients So and α_+ are available[4].

1. Space-temperal Distribution of Neutral Hydrogen

The space-temperal distribution of neutral hydrogen measured by Hα

detectors under typical discharge conditions of HL-1 tokamak (B_t =2.2T, I_p =120KA, n_e=5.2×10^{13} cm^{-3}) also confirms the molecular effect in edge region. When limiter radius a= 20cm, the peak of n_{H^0} is about at r=18cm. While a= 18cm, it shifts to r=16cm (Fig. 4). As shown here, the neutral hydrogen density at r=16cm is about 100 times as high as that of plasma centre. The majority of H^0 atoms are in the neighbouring region of molecular mean free path.The experimental results also shows its toroidal ununiformity, n_{H^0} = 10^9-$10^{10}$$cm^{-3}$ near the limiter, and n = 10^8 - 10^9 cm^{-3} far apart from it.

2. The Effect of Previous (H_2+Kr) Discharge Cleaning

The global particle recycling coefficient is determined by

$$R = 1 - \frac{\tau_p}{\tau_p^*} \qquad (10)$$

where τ_p is obtained from the formula (8), and τ_p^* is the density decaying time constant. After discharge cleaning with (H_2+Kr) , the particle recycling coefficient R is obviously lower than that with H_2 cleaning. Figure 5 shows the global confinement time is improved; particle recycling R decreases by 0.2.

3. The Influence of Pumping Limiter

Figure 3 indicates the changes of τ_p and R with $\bar{n}_e$. It can be seen that pumping limiter is moved to r=18cm, the τ_p increases and recycling from plasma surface is reduced. From our experiments, we concluded that the τ_p increases by 17.7% , R decreases by 13.2%, hence, the particle and energy confinements are improved and the loss of energetic particles is reduced by using pumping limiter.

The authors would like to thank professor J.H.Haung for many helpful discussions.

References

[1] H. C. Howe, Jr., J. Nuc. Mater. 111 & 112, 424 (1982)
[2] O. S. Oen and M. T. Robinson, Nucl. Instrum. Methods 132 (1976), 647.
[3] K. Audenaerde, G. A. Emmert, and M. Gordinier, J. comp. Phys. 34, 268 (1980).
[4] L.C. Johnson and E.Hinnov, J. Quart. Spectr. Radiat. Transfer 13 333(1973).

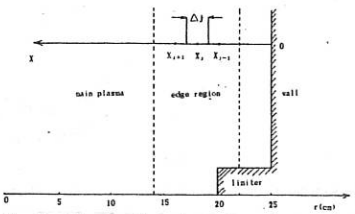

Fig.1 Scheme of meshpoints and zons for neutral transport calculation

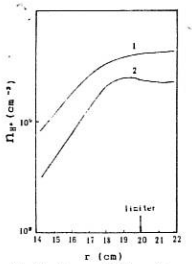

Fig.2 Radial profile of neutral atom density. 1--- atom case, 2--- molecular case.

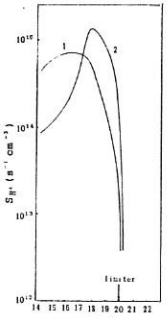

Fig.3 Radial profile of hydrogen atom ionization rate. 1--- atom case, 2---molecular case.

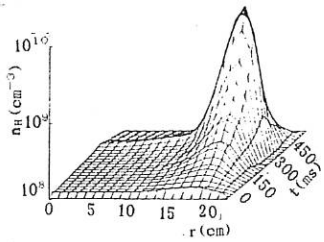

Fig.4 Space-temperal distribution of neutral hydrogen density.

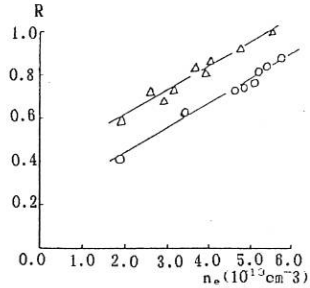

Fig.5 The relation of R to $\bar{n}_e$ after discharge cleaning with various gas. Δ-- H_2 AC(50Hz)-DC; o-- H_2+Kr AC(50Hz)-DC.

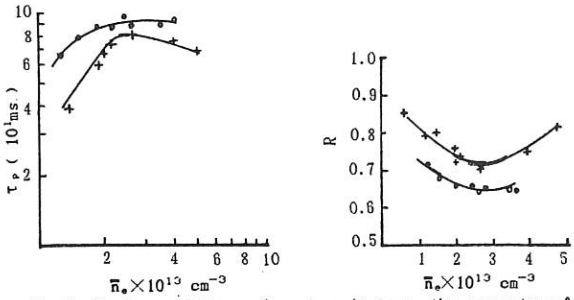

Fig.6 On the conditions of various limiers, the comparism of the relasions (a) τ_p to $\bar{n}_e$ and (b) R to $\bar{n}_e$. o --- a_{PL}=18cm, a_L=20cm. + --- a_L=18cm.

Analyses of a Scheme to Improve the SOL Transport Properties by Plasma Current Modulation

A. Nicolai
Forschungszentrum Jülich GmbH, Association EURATOM-KFA

1. Introduction

Ergodization of the plasma boundary by helical perturbation fields has been proposed and experimentally investigated as a means to improve the desired properties of the SOL for heat and particle exhaust /1,2/. It was shown that depending on the stochasticity parameter a chain of overlapping islands gives rise to a region with almost vanishing particle and energy confinement. Outer conductors are employed to generate the helically perturbing field.
This paper analyses another proposal /3/ to serve the same purpose; it is investigated how to excite tearing mode islands periodically by a modulation of the plasma current with a rise and a subsequent decay phase. The first phase is intended to generate radially hollow current density profiles and thus nonmonotonical q-profiles revealing maxima in the vicinity of the plasma boundary.The second phase is needed to retrieve the original q-profile just before the respective current rise phase.
The evolution of the q-profile is tracked by means the 1d-transport code TORUS I and its stability with respect to tearing modes is analysed by means of the RSF-code.

2. Three dimensional plasma simulation by the RSF-code /5/

This 3d-code tracks the time evolution of the vorticity function and of the poloidal flux function on the basis of Strauss' equations presupposing a large aspect ratio and a low total beta. These conditions are roughly fulfilled in case of ohmically heated TEXTOR discharges. The equations for the vorticity function U and the poloidal flux function Ψ read /4,5/

$$\left(\frac{\partial}{\partial t} + \vec{v}_\perp \nabla\right) \Psi = \eta J_\zeta - \frac{\partial \Phi}{\partial \zeta} - E_\zeta^w$$

$$\left(\frac{\partial}{\partial t} + \vec{v}_\perp \nabla\right) U = -S^2 \left(\vec{\zeta} \cdot (\nabla \Psi \times \nabla J_\zeta) + \frac{\partial J_\zeta}{\partial \zeta}\right) \qquad (1)$$

Here $\vec{v}$ is the fluid velocity $\perp$ denotes the direction perpendicular to the unit vector in the toroidal direction $\vec{\zeta}$. J_ζ is the toroidal component of the plasma current. E_ζ^w is the equilibrium toroidal electric field at the wall. In (1) lengths are normalized to the minor radius and the time is normalized to the resistive time. The parameter S is the ratio of the resistive time to the poloidal Alfvén transit time; S is in the range $10^5 \leq S \leq 10^8$. A Fourier-Fourier representation in the poloidal and the toroidal coordinate and radially a finite difference approximation is chosen. The Fourier representation implies a truncation of the discrete Fourier space.This is done by concentrating on those modes which are likely to occur. By increasing the number of modes under

investigation it may be checked if more modes significantly contribute to the solution. The initial state is a slightly perturbed plasma equilibrium. To this end a function which is similar to the linear eigenfunction of the respective problem is superimposed on the equilibrium flux function. Concerning the boundary conditions it is assumed that the radial component of the speed vector vanishes (rigid wall). This implies that the electric field is constant at the boundary.

3. Computation of the evolution of the q-profile by means of the 1d transport code TORUS I /6/

TORUS I tracks the time evolution of the discharge on the basis of the 1d-transport equations /6/ originally derived by neoclassical theory. It presupposes a set of nested circular and concentric flux surfaces and balances the flux surface averaged particle and energy loss terms for electrons and ions. Under similar assumptions it solves the diffusion equation of the poloidal magnetic field on the resistive time scale. Thus islands cannot occur. However, the confinement deterioration due to islands is roughly accounted for by using empirical transport coefficients.
The q-profiles emanating from the 1d-calculation are in principle checked by RSF with respect of their stability against the evolution of tearing mode islands. If islands occur, the discharge is assumed to be dominated by the tearing mode activity. On the basis of the island structure the new transport behaviour may be estimated. It is not attempted to achieve consistency between the 1d and 3d calculations because of the limited computational resources. Due to the large computer time needed for the 3d-calculations only these q profiles with the aforementioned nonmonotonical behaviour in the plasma boundary region and exceeding slightly the values $q_{max} = m/n = 4, ..., 7$ there, are checked. A four parametric fit for the profiles generated by TORUS I is made. This fit ensures that the main properties essential for the tearing mode region stay unchanged and that an irrelevant bumpiness of the profile is removed.

4. Results

The calculations are based on TEXTOR data: minor radius a = 45 cm, major radius R = 175 cm, toroidal field B_t = 2.4 T. The repetitive current rise is described by the rise time t_r = 100 ms, the current decay time t_d = 400 ms, the current swing ΔI_p = 300 kA and the mean current $\langle I_p \rangle$ = 250 kA.
Fig.1 shows the classical time evolution of the q-profile within four seconds ($0 \leq t \leq 4$ sec). Initially (t=0) the q-profile is given by a parabolic current density (I_p = 100 kA). The subsequent current rise leads to nonmonotonical q-profiles with maxima reaching the plasma interior. These maxima touch the planes with $4 \leq q \leq 9$ defined in the parameter space of Fig.1 so that a wide range of poloidal mode numbers is available for the double tearing mode. However, this is not investigated here in detail. During the subsequent evolution the q-value at the plasma center approaches 3.5. The relative maxima of the successive q-profiles touch the q=4 and q=5 planes in Fig.1 so that the m=4, n=1 and m=5, n=1 double tearing mode may evolve. In fact, the analysis with the RSF-code shows that the respective islands (m=4, n=1 in Fig.2) appear indeed.

These islands overlap radially and partly also poloidally so that a quasi-ergodized region develops. The width of this region is around 10 cm.
In case of the m=5, n=1 islands similar results are obtained. The excitation of the harmonics of the aforementioned islands is not checked because the present state of RSF does not allow this.
Since the aforementioned current rise rate is rather large, the question is investigated if smaller current increase rates may lead to hollow q profiles as well. Analogous calculations as those yielding Fig.1 show that already a small decrease of the just mentioned rate prevents the build up of nonmonotonical q-profiles. It follows that the current increase rate of delta $I_p/t_r = 3$ MA/sec is a minimum rate. One might reduce the decay time t_d so that the unloading via the tearing mode islands becomes more effective. However, analogous calculations show that such a reduction leads to an increase of the central q value, since the current distribution cannot contract anymore. On the other hand a more consistent description certainly entails a more rapid current penetration because of the enhanced transport via the tearing mode islands.

5. Conclusions

The excitation of tearing mode islands seems to be a way to be considered for a reduction of the edge power fluxes which otherwise impinge on the limiter or the divertor strike plate with much larger intensity. In combination with pellet injection and a pumped toroidal belt limiter a stationary state might be reached with a large exhaust efficiency and helium removal rate.
Due to the lack of consistency the calculations contain a considerable amount of uncertainty. In reality the relaxation of the current density is more rapid after the excitation of the tearing mode islands. However, before this excitation the aforementioned description should be accurate so that the condition for the current increase rate is realistic.

/1/ W. Feneberg, G. H. Wolf, Nucl. Fus. 21 (1981) 669
/2/ A. Nicolai, J. Nucl. Mater. 111 & 112 (1982) 428
/3/ G. H. Wolf, private communication (1990)
/4/ H. R. Strauss, Phys. of Fluids 19 (1976) 134
/5/ H. R. Hicks et al., J. Comput. Phys. 44 (1981) 46
/6/ A. Nicolai, P. Börner, J. Comput. Phys. 80 (1989) 98

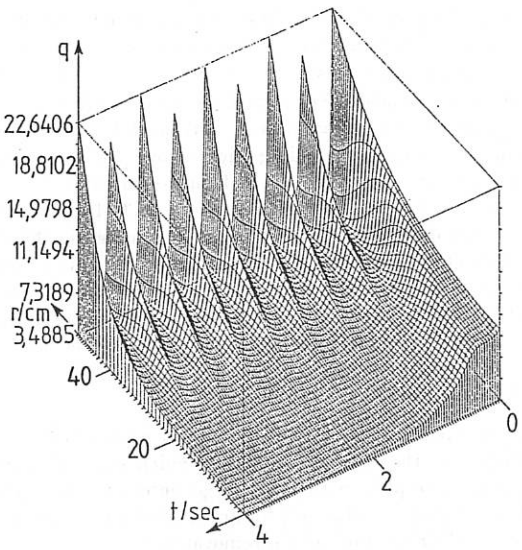

Fig.1
Time evolution of the q-profile. The repetitive current rise effects nonmonotonical q-profiles with maxima in the range ($4 \leq q \leq 5$).

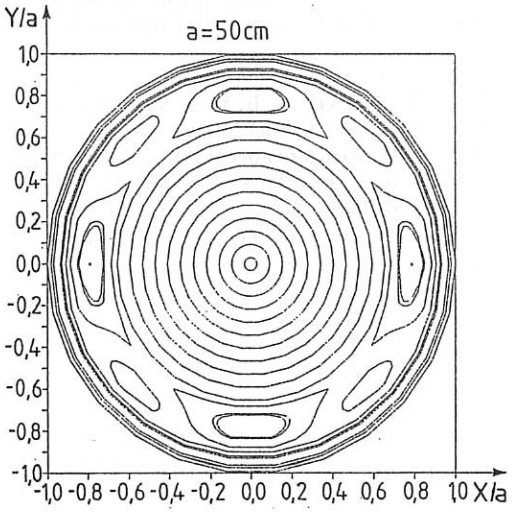

Fig.2
The m=4,n=1 double tearing mode evolves if q_{max} is slightly larger than 4. The width of the quasiergodized region is around 10 cm.

INFLUENCE OF LIMITER BIAS AND INTERCHANGE INSTABILITIES ON THE STRUCTURE OF THE TOKAMAK PLASMA EDGE

H. Gerhauser, H.A. Claaßen

Institut für Plasmaphysik, Forschungszentrum Jülich GmbH,
Association EURATOM-KFA, P.O. Box 1913, D-5170 Jülich, FRG

The Jülich 2d boundary layer code SOLXY has proved as a useful tool for investigating specific physical questions in the plasma edge of limiter tokamaks /1/. The present paper considers the above two different problems related to a toroidal belt limiter like the ALT-II of TEXTOR. We use the coordinates y radially and Θ poloidally (length elements $dy = R\, dr/R_0$, $dx = a\, d\Theta$) as indicated in Fig.1 and Pl.8, with the limiter at $\Theta = -45°$. The separatrix radius $y_s \approx 1.9$ cm corresponds to the minor radius $a = 46$ cm.

For the investigation of a limiter bias we subdivide the limiter radially into two parts, with the inner part $y < y_b$ put at a potential $\Phi_{lim} = \Phi_l < 0$ and the outer part $y > y_b$ at $\Phi_{lim} = \Phi_h > 0$, such that the bias potential step at the insulating break $y_b \approx 3.7$ cm becomes $\Phi_{bias} = \Phi_h - \Phi_l$. This creates a potential and transport barrier at the bias line $y = y_b$ poloidally around the scrape-off layer. The very steep gradient $\partial\Phi_p/\partial y$ of the plasma potential at $y \approx y_b$ cannot be realistic (and cannot be handled numerically). It must be smoothed out by the reaction of the sheath potential drop $\Delta\Phi = \Phi_p - \Phi_{lim}$ upon additional electric drift currents ($j_{b\Theta} = h_\Theta j_{b\parallel}$, $j_{by} < 0$) that leave the outer part of the limiter, penetrate the whole sol along $\vec{B}$, cross the bias line y_b and finally enter the inner part of the limiter. Clearly the anisotropy of the conductivity ($\sigma_\parallel$ very large, $\sigma_\perp$, σ_r very small) entails that these currents are localized radially near y_b and distributed poloidally quite uniformly. We construct reasonable "imprinted" bias currents $\vec{j}_b$ by an appropriate choice of $f_{lim}(y)$ with $f_{lim}(y_b) = 1$ and $f_{lim}(y) \to 0$ for increasing distance $|\, y - y_b\, |$, and set $e\Phi_{lim} f_{lim} = T_e \ln(1 \mp j_{b\Theta}/en\,|\,h_\Theta c_s\,|\,)$ with the upper (-) sign for the ion side and the lower (+) sign for the electron side; $en\,|\,h_\Theta c_s\,|$ is the projection of the ion saturation current. This defines an additional bias stream function ψ_b by $\mp\partial\psi_b/\partial y = \pm j_{b\Theta} = en\,|\,h_\Theta c_s\,|\,[1 - \exp(e\Phi_{lim} f_{lim}/T_e)]$ with the rhs > 0 for $y < y_b$ and < 0 for $y > y_b$. Linear interpolation between e-side and i-side yields $\psi_b(\Theta, y)$ for all Θ. The bias currents are sketched in Fig. 1. We find then that the plasma potential

$$\Phi_p = \Phi_{lim} f_{lim} + \Delta\Phi = \Phi_{lim} f_{lim} - \frac{1}{e} T_e \ln\left[\sqrt{\frac{2\pi m_e}{m_i}\,\frac{T_e + T_i}{T_e}}\left(1 \mp \frac{j_{p\Theta} + j_{b\Theta}}{en\,|h_\Theta c_s|}\right)\right]$$

is left continous near $y = y_b$ and almost unchanged by the introduction of Φ_{lim} and $j_{b\Theta}$, whereas the true plasma potential $\Phi = \Phi_{pb} = \Phi_{lim} + \Delta\Phi$ is still continuous, but strongly deformed, see Pl.5. Integration of Ohm's law along $\vec{B}$ yields $\Phi(\Theta, y)$ for all Θ. Note that the maximum of ψ_b occurs for $y = y_b$ at the e-side, the minimum at the i-side, and $\psi_{bmax} - \psi_{bmin}$ is the total imprinted bias current J_{bias} (per unit length toroidally) from the outer limiter part to the inner one. The reactions of the other plasma currents $\vec{j}_p$ and of all plasma parameters on the applied bias including recycling of neutrals and boundary conditions at the limiter are computed self-consistently. We plot results for $(\Phi_l, \Phi_h, \Phi_{bias}) = (-77, 35, 112)$ V and $(\psi_{bmin}, \psi_{bmax}, J_{bias}) = (-10, 9, 19)$ A/m. The total current density $j_y = Rj_r/R_0 = \partial\Psi/\partial x$, $j_\Theta = -\partial\Psi/\partial y$ is derived from the total stream function $\Psi = \psi_p + \psi_b$ and shown in Pl.6. The localized $j_{br} < 0$ leads to a similarly localized negative radial drift velocity $v_{rd} = (1/eBn)\,\partial p_e/\partial x - \partial\Phi/B\partial x + (j_{pr} + j_{br})/en$, see Pl.4. This counteracts radial diffusion near $y = y_b$, thus steepening there the density profile (Plots 1,9), and reduces $\Gamma_\parallel = nv_\parallel$ for

$y > y_b$ (Pl.2).The ions are collected predominantly by the inner part of the limiter, the electrons by the outer one. Furthermore the rotational drift $v_\perp = (1/enB)\, \partial p_i/\partial r + \partial\Phi/B\partial r$ is reversed locally by the radial potential barrier (Pl.3). This distorts also the v_Θ-profiles (Pl. 11). As a consequence the radial density profiles near the (bottom facing) i-side develop a pedestal-like deformation similar to the one observed experimentally /2/ with ICRH near the radius of the antenna protection limiters where the sheath rectification effect simulates positive bias. Because of the i-side pedestal the e-side density profile intersects twice the i-side profile. The temperature gradients $\partial T_e/\partial x$, $\partial T_i/\partial x$ are adapted along the bias line to sustain the local j_{by}, see Pl.13 for T_e. As an application we propose an electrically biased pump limiter (Fig.2) in such a way that a potential ditch is created channelling the particles (D,T- ions and impurities) into the limiter scoops while reducing the particle load and material sputtering at the neighbouring parts of the limiter, i.e. the leading edge of the blade and the side faces of the pumping duct.

Fig.1

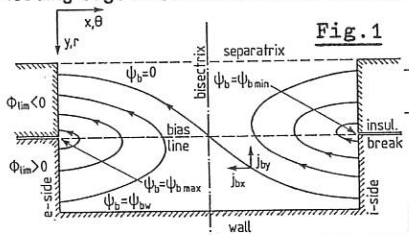

Fig.2

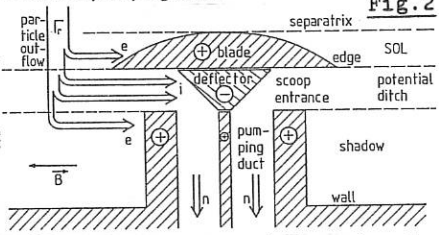

For the investigation of interchange instabilities we perform a numerical experiment by triggering and cultivating unstable short wave length modes in the boundary layer. We just switch off part of the numerical smoothing described in ref./3/. It has been predicted theoretically /4,5/ that the anomalous transport in the plasma edge is due to the destabilizing action of interfering material surfaces (limiter or divertor targets) on parallel electric currents along the open field lines. A major candidate for inducing microturbulence are interchange instabilities (flutes) in regions of unfavourable curvature with growth rates γ scaling as k_Θ^2. We find indeed an instability of this kind growing predominantly near the outboard midplane and close to the separatrix with the shortest numerically possible wave length of 6 poloidal grid spacings or $k_\Theta = 1/2.28$ cm (Plots 10,12 for n, v_Θ). The usual time relaxation leads here to a purely exponential growth. The time evolution for $\delta\Phi(t) = \Phi(t)-\Phi(0)$ is displayed by Pl.7. The numerically determined growth rate near ($\Theta = 0°$, $y = y_s$) is $\gamma = 1/35.5$ μsec. We estimate /4/ the turbulent diffusion coefficient to be represented by $D_\perp = \gamma/k_\Theta^2 \approx$ 14.6 m^2/sec. The same value can be derived by a suitable application of eq. (13) in ref. /5/. Because of the small k_Θ it simplifies to $2\gamma/k_\Theta^2\rho_i^2 v_i$ - $[H(\Theta_2)-H(\Theta_1)]\, q/L_N = 0$ with $H(\Theta) = 3\sin\Theta - 2\Theta\cos\Theta$ and $\Theta_2 = -45°$, $\Theta_1 = 315°$. For T_i = 45 eV, B= 2T, q=3 and p_e-decay length $L_N = 2$ cm we get $\gamma/k_\Theta^2 \approx$ 14.5 m^2/sec. A nice pattern of current convective cells develops near ($0°$,y_s), see Pl.8, which produces locally a strong viscosity heating of ions. The calculation stopped at $T_{imax} = 100$ eV (Pl. 14). The most unstable physical k_Θ is certainly much larger than the numerical one and $\sim 0.1/\rho_i$, but $D_\perp$ is independent of k_Θ. Experimental observations at TEXTOR show that T_i is always significantly larger than T_e near $y = y_s$, and the usually very flat n-profiles in the outboard midplane should also be caused by this locally enhanced anomalous diffusion.

/1/ H. Gerhauser and H.A. Claaßen, J. of Nucl. Mater. 176 (1990), in print
/2/ G. van Oost et al., Fusion Engineering and Design 12 (1990) 149-170
/3/ H. Gerhauser and H.A. Claaßen, Contrib. Plasma Phys. 30 (1990) 89
/4/ A. V. Nedospasov, Sov. J. Plasma Phys. 15 (1989) 659-661
/5/ X. Garbet et al., A model for the turbulence, Report EUR-CEA-FC-1398 (June 1990)

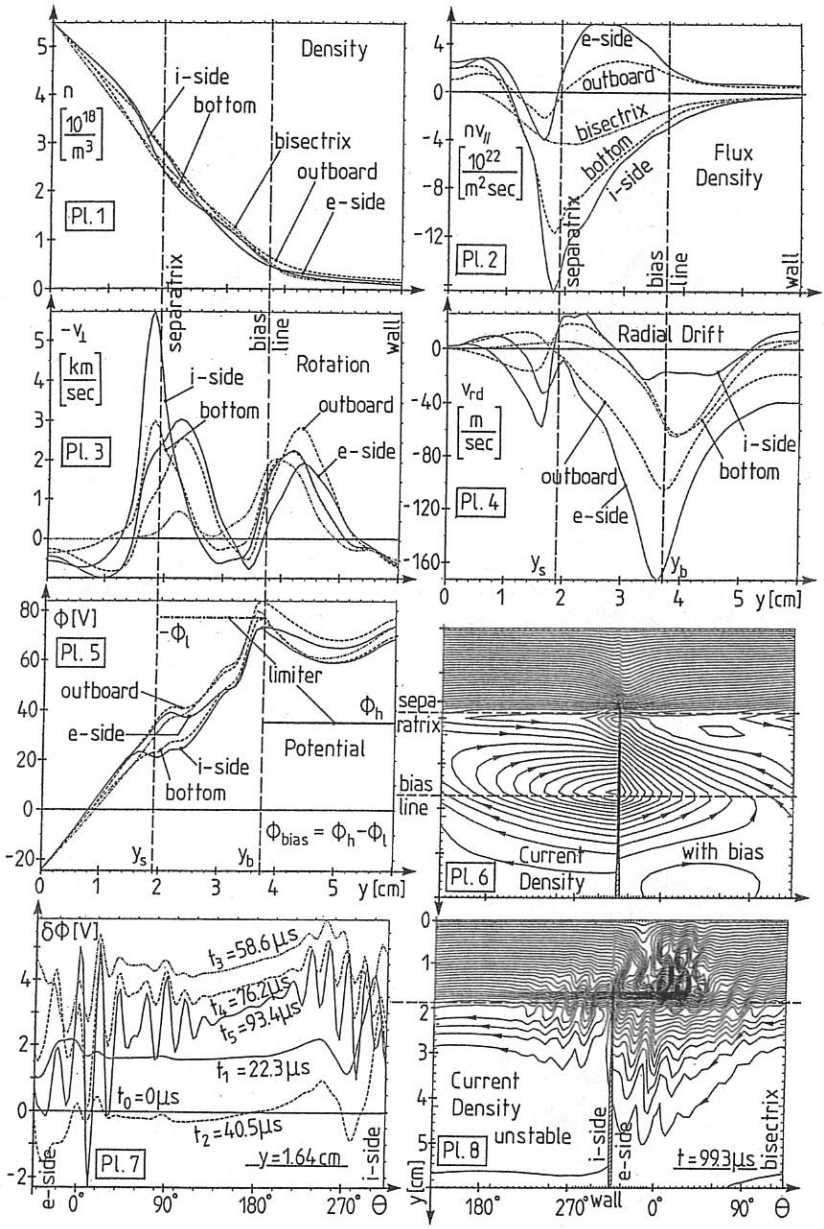
Density
n
[10^18 / m^3]
i-side
bottom
bisectrix
outboard
e-side
Pl. 1
separatrix
bias line
wall
e-side
outboard
bisectrix
bottom
i-side
nv//
[10^22 / m^2 sec]
Flux Density
Pl. 2
-v1
[km / sec]
Rotation
i-side
bottom
outboard
e-side
Pl. 3
Radial Drift
vrd
[m / sec]
outboard
e-side
i-side
bottom
Pl. 4
ys
yb
y [cm]
Φ [V]
-Φl
limiter
Φh
outboard
e-side
i-side
bottom
Potential
Φbias = Φh-Φl
Pl. 5
separatrix
bias line
Current Density
with bias
Pl. 6
δΦ [V]
t3 = 58.6 µs
t4 = 76.2 µs
t5 = 93.4 µs
t1 = 22.3 µs
t0 = 0 µs
t2 = 40.5 µs
y = 1.64 cm
i-side
e-side
Pl. 7
Current Density
unstable
i-side
e-side
t = 99.3 µs
bisectrix
wall
Pl. 8
y [cm]
Θ

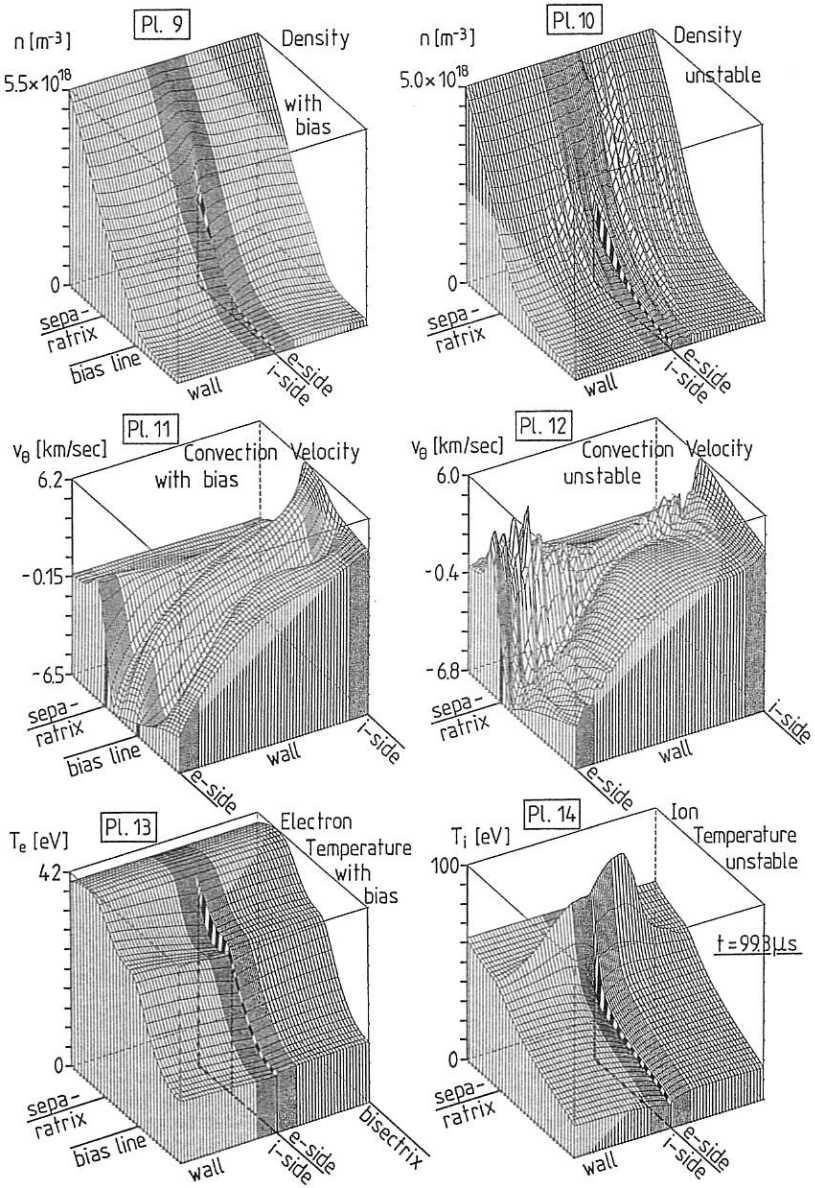
Pl. 9
n [m⁻³]
Density
5.5×10¹⁸
with
bias
0
sepa-
ratrix
bias line
wall
e-side
i-side
Pl. 10
n [m⁻³]
Density
5.0×10¹⁸
unstable
0
sepa-
ratrix
wall
e-side
i-side
Pl. 11
vθ [km/sec]
Convection Velocity
with bias
6.2
-0.15
-6.5
sepa-
ratrix
bias line
wall
i-side
e-side
Pl. 12
vθ [km/sec]
Convection Velocity
unstable
6.0
-0.4
-6.8
sepa-
ratrix
wall
i-side
e-side
Pl. 13
Te [eV]
Electron
Temperature
with
bias
4.2
0
sepa-
ratrix
bias line
wall
e-side
i-side
bisectrix
Pl. 14
Ti [eV]
Ion
Temperature
unstable
100
t=99.3μs
0
sepa-
ratrix
wall
e-side
i-side

EXCITATION OF AN INSTABILITY BY NEUTRAL PARTICLE IONIZATION INDUCED FLUXES IN THE TOKAMAK EDGE PLASMA

P. Bachmann (a), D. Kh. Morozov (b), D. Sunder (a)

(a) Central Institute of Electron Physics, O-1086 Berlin, FRG
(b) I.V. Kurchatov Institute of Atomic Energy, Moscow, USSR

1. Introduction

Strong density and potential fluctuations in the edge plasma of toroidal nuclear fusion devices can lead to anomalously fast particle and energy transport. There are some reasons to assume the level of these fluctuations to be connected with neutral particles which enter the plasma by gas puffing or recycling processes. The influence of neutral particles on the behaviour of electrostatic drift modes is investigated in [1-3]. Using the balloning transformation the excitation of dissipative drift waves in tokamaks is studied taking ionization and charge exchange into consideration in [1]. Ionization driven drift wave turbulence is analyzed in [2,3].

The higher the neutral particle density is the more important the plasma-wall interaction and the less important the action of the limiter becomes. Instabilities localized in the edge plasma and far from the limiter can be one of the reasons of such a phenomenon. In the present paper we show that such an instability may exist. Usually the neutral particle density is large in the vicinity of the limiter and decreases rapidly with the distance from it. Plasma particles generated by ionization of these neutrals outside the limiter shadow, move along the magnetic field lines into a region without neutrals and diffuse slowly across the magnetic field. We solve the stability problem for modes with a perpendicular wave length that is much larger than the ion Larmor radius with electron temperature, and much smaller than the minor plasma radius. The excitation of such modes localized far from the limiter is investigated. An one-dimensional differential equation is derived in the cold ion approximation without taking shear and toroidal effects into consideration. In the case of low flow velocities a nearly aperiodic instability is found analytically. Its growth rate is proportional to the equilibrium plasma velocity at the boundary of the neutral particle's free region and to the inverse of the extension of this zone. This mode is localized in the edge plasma far from the limiter and cannot be suppressed by anomalous particle diffusion. The case of an arbitrary flow velocity is studied numerically.

2. Basic Equations

We consider the following simplified slab-model. The magnetic field $\vec{B}_o$ is assumed to be oriented along the z-axis, the toroidal geometry is taken into consideration by assuming all quantities to be periodically with respect to L_T. The neutral particles localized in the vicinity of the limiters ($z_L = \pm L_T/2$) in a region $l_N/2$ ($l_N \ll L_T$ - toroidal extent) are ionized and leave this region along the field lines diffusing across the field in x-direction. We consider only the particles generated above the limiter and assume the particle diffusion to be anomalously large and the ions to be colder than the electrons ($T_i \ll T_e = \text{const}$).

Under the conditions $\rho_e/L_\perp \ll 1$ and $\partial/\partial t \ll \Omega_i$, ν_{ei} we obtain neglecting viscose effects the following equations

$$\vec{v}_{e\perp} = v_e \rho_e [\vec{b}, \vec{\nabla}(\Phi - \ln n_e)] - D_e \vec{\nabla}_\perp \ln n_e \tag{1}$$

$$\vec{v}_{i\perp} = v_e \rho_e \{[\vec{b}, \vec{\nabla}\Phi] - (\partial/\partial t)\vec{\nabla}_\perp \Phi/\Omega_i\} - D_i \vec{\nabla}_\perp \ln n_i \tag{2}$$

$$v_e^2 \nabla_\parallel (\Phi - \ln n_e) - \nu_{ie}(v_{e\parallel} - v_{i\parallel}) = 0 \tag{3}$$

$$(\partial/\partial t)v_{i\parallel} + (v_i\nabla)v_{i\parallel} = -v_e^2 \nabla_\parallel \Phi - \nu_{ie}(v_{i\parallel} - v_{e\parallel}) - \nu_{cx} v_{i\parallel} \tag{4}$$

$$(\partial/\partial t)n_\alpha + \operatorname{div}(n_\alpha \vec{v}_\alpha) = Q_\alpha \tag{5}$$

where $L_\perp$ is the characteristic scale length perpendicular to $\vec{B}_o$, $\Omega_i = e_i B_o/m_i c$, $\vec{b} = \vec{B}_o/B_o$, $\nu_{ei} = (m_i/m_e)\nu_{ie}$ is the electron-ion collision frequency, $v_e = (T_e/m_i)^{1/2}$, $\rho_e = v_e/\Omega_i$, $\Phi = e\phi/T_e$, D_α is the anomalous diffusion coefficient and $Q = n_e \nu_{ion}$ is the particle source term, $\nu_{cx} = k_{cx}N$ and $\nu_{ion} = k_{ion} N$; k_{cx}, k_{ion} are the rate coefficients for charge exchange and ionization, respectively, N is the neutral particle density.

For the equilibrium state we obtain in the region without neutrals $|z| < L/2$ assuming $n_{eo} = n_{io} = n_o$, $\nabla\Phi = 0$, $D_{eo} = D_{io} = D_o$, $v_{io\parallel} = v_{eo\parallel} = v_{o\parallel}$ the equations

$$n_o = n_{oo}(x)\exp(-M^2/2) \tag{6}$$

$$M(1 - M^2/3) = -\xi\,(L/2n_{oo}v_e)(\partial/\partial x)D_o(\partial n_{oo}/\partial x) \tag{7}$$

with $M = v_{o\parallel}(\xi)/v_e$, $\xi = 2z/L$, $L = L_T - l_N \simeq L_T$. Eq. (7) must be solved with the boundary condition

$$M(\xi = \pm 1) = \mp M_o \tag{8}$$

where $M_o = v_o/v_e$; v_o is the velocity of the plasma particles entering the region $|z| \leq L/2$:

$$v_o = N_o k_{ion} l_N \tag{9}$$

Then we obtain with the condition $M(\xi = 0) = 0$ the solution

$$M = -2\sin\{\arcsin(3\eta\xi/2)/3\},\quad \eta = M_o(1 - M_o^2/3), \tag{10}$$

which reduces for $M_o \ll 1$ to

$$M = -\xi M_o(1 - M_o^2(1 - \xi^2)/3). \tag{11}$$

The perturbative treatment of Eqs. (1) - (5) leads with the ansatz $\delta A = \exp(-i\omega t + i \vec{k}_\perp \vec{r}_\perp) A(\xi)$ for the perturbative quantities to the following equation for the potential Φ:

$$(\partial^2/\partial\xi^2 + g_1 \partial/\partial\xi + g_0)\,\Phi = 0 \tag{12}$$

with

$$g_0 = \hat{\omega}(\bar{\omega} + 2iM' - iM f'/f)/(1-M^2),\ g_1 = iM(\hat{\omega} + \bar{\omega} + 4iM')/(1-M^2) + f'/f$$

$$\hat{\omega} = \bar{\omega} + i\delta - \bar{\omega}_*,\quad f = \bar{\omega} + iM'(1+M),\quad \bar{\omega} = \omega/\omega_s,\quad \delta = D_0 k_\perp^2/\omega_s, \tag{13}$$

$$\bar{\omega} = k_y v_*/\omega_s,\ v_* = v_s \rho_s |\partial \ln n_0/\partial x|,\ \omega_s = 2v_s/L,$$ where the prime denotes the derivative with respect to ξ.

3. Results

For the case $M_0 \ll 1$ we get with (11) the solution

$$\Phi = 2^{q/2} \exp\{-(h_1 + \sigma^{1/2})\xi^2/2\}\, H_q(\sigma^{1/4}\xi) \tag{14}$$

with

$$q = (E/\sigma^{1/2} - 1)/2,\ E = h_0 - h_1,\ \sigma = h_1^2 - h_2,\ h_0 = \hat{\omega}(\bar{\omega} - 2iM_0),$$
$$h_1 = -(iM_0/2)[\hat{\omega} + \bar{\omega} - 4iM_0\bar{\omega}/(\bar{\omega} - iM_0)], \tag{15}$$
$$h_2 = M_0^2\{\hat{\omega}[\bar{\omega} - 4iM_0\bar{\omega}/(\bar{\omega} - iM_0)] + 2iM_0[\hat{\omega} + \bar{\omega} - 7iM_0 + M_0^2(5\bar{\omega} + iM_0)/(\bar{\omega} - iM_0)^2]\}$$

and H_q - Hermite function.

For the lowest order mode solution with $q = 0$ we obtain the dispersion equation

$$E^2 = \sigma \tag{16}$$

and the normalized field

$$\chi = |\Phi(\xi)|/|\Phi(0)| = \exp(-s\xi^2),\ s = \mathrm{Re}(h_0)/2 \tag{17}$$

The analytical solutions $\bar{\omega} = \bar{\omega}_r + i\bar{\omega}_i$ of Eq. (16) for the case $|\hat{\omega}| > 1$ and $s > 0$ are given by

$$\bar{\omega}_{1,2} = iM_0(1 \pm A),\ A = [8M_0/(\delta + i\bar{\omega}_*)]^{1/2} \tag{18}$$

where especially the second mode is strongly localized far from the limiter at $\xi = 0$ if the condition $\delta M_0 > 1$ is fulfilled.
For T-10 parameters $R \simeq 2\ 10^2$cm, $q \simeq 3$, $v_s \simeq 6\ 10^5$cm/s, $D_0 \simeq (1 \div 10)\ 10^2$cm^2/s and $k_\perp \simeq 10$/cm δ is estimated to $3 \div 30$. The numerical solutions of Eq. (16) together with the corresponding s value is displayed in Fig. 1 for $\delta = 10$, 20 which are in reasonable agreement with the analytical estimation ($\omega \simeq \omega_2$). The eigenfunctions and eigenvalues for $M_0 > 3$ calculated numerically from Eq. (12) are shown in Fig. 2.

References

[1] D.Kh. Morozov, N.N. Morozov, D. Sünder, Int. Workshop on Plasma Edge Theory in Fusion Devices, Augustusburg 1989 Contrib. Plasma Phys. 30 (1990) 31; IAEA-CN-52/D-4-3 (Washington 1990).
[2] A.S. Ware, P.H. Diamond, D.R. Thayer, B.A. Carreras, J.N. Leboeuf, 1990 Sherwood Theory Conference, Williamsburg, Paper 1C13.
[3] CH.P. Ritz et al., IAEA-CN-53/C-3-4 (Washington 1990).

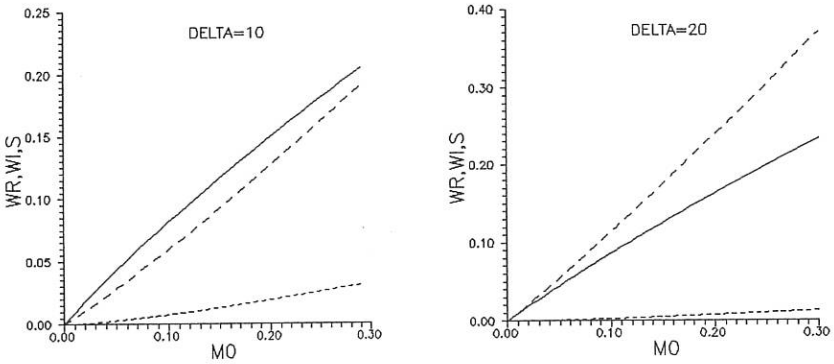

Fig. 1 Normalized eigenvalues $w_r = -10\bar{\omega}_r$ (----) , $w_i = \bar{\omega}_i$ (———) and S = 0.1s (– – –) as functions of M_o for $\bar{\omega}_* = 1$, $\delta = 10$ and $\delta = 20$.

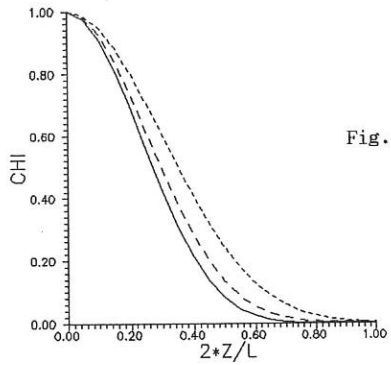

Fig. 2 Eigenfunctions for $\delta = 20$, $\bar{\omega}_* = 1$ and
$M_o = 0.4$ ($\bar{\omega}_r$=-0.004, $\bar{\omega}_i = 0.206$) (----)
$M_o = 0.6$ ($\bar{\omega}_r$=-0.006, $\bar{\omega}_i = 0.282$) (– – –)
$M_o = 0.8$ ($\bar{\omega}_r$=-0.007, $\bar{\omega}_i = 0.330$) (———)

ION VELOCITY DISTRIBUTIONS AT THE TOKAMAK EDGE

R. A. Pitts

AEA Fusion, Culham Laboratory, UKAEA/Euratom Fusion Association, OXON, U. K.

1. INTRODUCTION

Although the problem of modelling plasma flow along the magnetic field to the tokamak limiter or divertor plate has been the subject of much theoretical work, experimental tests of the theories have been limited. Because the flow is unimpeded by the field, the situation is inherently one-dimensional and may be approached from a kinetic or fluid point of view, neglecting the magnetic field. Whilst both the kinetic and fluid approaches often lead to similar estimates for quantities of important practical interest [1], unlike the fluid treatments, kinetic models can also be used to compute the form of the ion velocity distribution at any point in the flow. In particular, they provide the form of the distribution parallel to **B** at a solid surface, $f_w(v_{||})$. Knowledge of the latter is important for accurate characterization of the ion-surface interaction. It is also significant in the sense that it can be directly measured and hence used to compare experiment and theory. This paper describes the first attmept at such a comparison using experimental data from a Retarding Field Analyser (RFA) operated in the DITE tokamak.

2. KINETIC MODELLING

The most appropriate kinetic models are those in which the source ions are allowed to have finite temperature, T_s, since the ion and electron temperatures in the tokamak edge are known to be comparable [2]. Of these, the collisionless treatments of Emmert et al. [3], and Bissel and Johnson [4] contain convenient analytic forms for the ion velocity distribution function at the sheath edge, $f_{se}(v_{||})$.

They are also interesting in that a different, but similar source function is chosen by each to represent the birth of ions in the SOL. Emmert et al. [3] consider a source of the form

$$S_p(x, v_{||})dv_{||} = H(x)\frac{m_i v_{||}}{2kT_s} exp\left[-\frac{m_i v_{||}^2}{2kT_s}\right] dv_{||} \quad (2)$$

where $H(x)$ is the spatial variation of the source strength, singly charged ions are assumed and the plasma is taken to have zero net drift velocity. Bissel and Johnson assume a slightly different form

$$S_p(x, v_{||})dv_{||} = H(x)\frac{m_i}{2kT_s} exp\left[-\frac{m_i v_{||}^2}{2kT_s}\right] dv_{||} \quad (3)$$

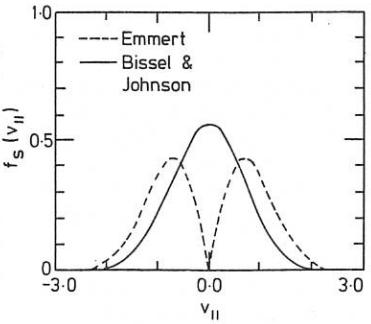

Fig.1 *The normalized source terms described by Eqns.(1) and (2).*

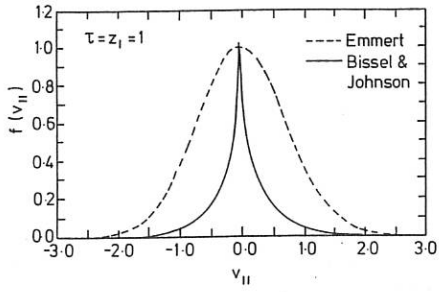

Fig.2 *Normalized forms of* $f(v_{||})$ *at* $x = \phi_p = 0$

The source functions are plotted in Fig.1 whilst Fig.2 shows the velocity distributions arising from them at the point $x = \phi_p = 0$, where ϕ_p is the plasma potential. Eqn.(1) is in the form of a flux and describes a source which, in the absence of electric fields in the plasma, would give rise to a Maxwellian velocity distribution. Physically, the source achieves this through the velocity weighting factor in Eqn.(1) which means that the faster particles are produced at a faster rate to compensate for the loss to the walls. In contrast, the Bissel [4] source represents, for example, that which would arise from the velocity independent ionization of a Maxwellian distribution of neutrals at temperature T_s. The source is Maxwellian but, as shown in Fig.2, leads to a clearly non–Maxwellian distribution at $x = 0$, having fewer fast and more slower ions.

For these collisionless models, once the source function is specified, the ion density may be obtained from a solution to the kinetic equation for the conservation of particles. Assuming the electron density in the presheath electric field to be described by a Boltzmann relation, an equation for ϕ_p may be established and the ion distribution function evaluated explicitly at any point up to the plasma/sheath boundary for a given value of $\tau = T_s/T_e$ and ion charge state, Z_i. For comparison with data from the RFA, however, the form of the distribution at the wall, $f_w(v_{||})$, is required. This is obtained by applying conservation of energy

$$\frac{1}{2}m_i v_w^2 = \frac{1}{2}m_i v_{se}^2 + Z_i k T_e(\psi_w - \psi_{se}) \qquad (3)$$

under the assumption of a sheath sufficiently thin that the source may be neglected there. This criterion is easily satisfied in the tokamak SOL where the Debye length, λ_D, is typically $\sim 25 \rightarrow 50\mu$m compared with a presheath dimension of several metres [2]. In Eqn.(3), the subscripts se and w refer to sheath edge and wall respectively and ψ is the normalized plasma potential (eg. $\psi_p = e\phi_p/kT_e$). Eqn.(3) and the analytic forms of $f_{se}(v_{||})$ given in refs.[3,4] have been used to generate the curves in Fig.3 which illustrates both f_{se}^E, f_{se}^{BJ} and the accelerated distributions, f_w^E, f_w^{BJ} for the case $\tau = Z_i = 1$. Each distribution has been normalized to unity and the same sheath acceleration has been used in both cases for comparative purposes (the actual sheath potential fall, $V_s = \phi_{se} - \phi_w$, predicted by each model is slightly different). Fig.3 shows clearly how the distributions become bunched in velocity

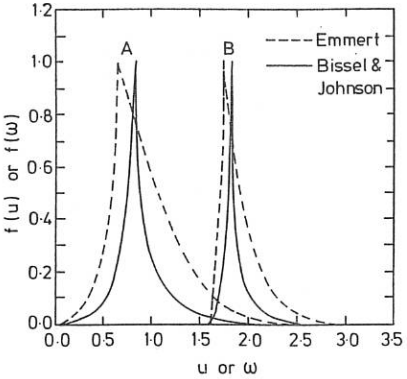

Fig.3 *Normalized* $f(v_{||})$ *at the sheath edge (A) and at the wall (B) vs. normalized velocity* $(u^2 = m_i v_{||}^2/2kT_s, w^2 = m_i v_{||}^2/2kT_e)$.

space as they are accelerated through the sheath and presheath, but still retain the essential features evident at $x = 0$. The shape of the regions encompassing all velocities up to the peak in the distributions – corresponding to the presheath – is also different in each case due to the differing source terms.

3. EXPERIMENT

The RFA provides a simple means of measuring the the ion velocity distribution at the tokamak edge [2]. Ions enter the device through a small slit (width $\sim \lambda_D$) and experience a retarding field due to a positive voltage applied to a grid electrode. By aligning the analyser normal to the tokamak magnetic field and ramping this ion repeller voltage from zero to some large positive value, the current measured at a collector behind the grid gives the *integral* of $f_w(v_\parallel)$. Two example I–V characteristics from the DITE edge are shown in Fig.4. Both were obtained at different times in the same, rising density, ohmic helium discharge with $I_p = 115$kA and $B_T = 1.8$T. The curves show a clear saturated region at low voltages – identified as due to the sheath and presheath fields – and an approximate exponential decrease at higher grid voltages. The full lines in Fig.4 are the result of a non–linear least squares fit assuming $f(v_\parallel)$ to be a 1–D Maxwellian beyond a voltage corresponding to the maximum enery gained in falling through the sheath and presheath potentials ie. $I_c = I_o exp(Z_i V_g / kT_{exp})$, where I_c is the collector current, V_g the grid voltage and T_{exp} the 'experimental' ion temperature. As $\overline{n}_e$ increases the ratio T_{exp}/T_e decreases, as does the magnitude of the fitted sheath potential.

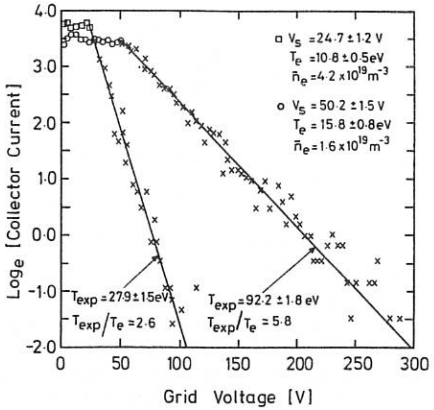

Fig.4 *Experimental integral distributions from the DITE RFA at two values of* $\overline{n}_e$.

4. COMPARISON WITH THEORY

Owing to the relatively high experimental noise level, direct comparison of the theoretical distributions of Fig.3 with the characteristics of Fig.4 is only possible by reconstructing, from $f_w(v_\parallel)$, the expected RFA characteristics for each model. This has been performed for the Emmert and Bissel distributions by numerical integration of the analytic expressions for $f_w(v_\parallel)$. The results are shown in Fig.5a,b where the ordinate is actually the integral $\int uf(u)$ or $\int wf(w)$ since the RFA collector current really represents an ion flux. In both cases $T_e = 15$eV has been arbitrarily assumed and the current at $V_g = 0$ chosen to be similar for comparative purposes. In all cases the region of the characteristic due to ion acceleration in the presheath has been highlighted. The curves for $\tau = 1, 2, 3$ and $Z_i = 1$ only are shown and the magnitude of the sheath energy gain has been calculated from each model. Since secondary electron emission is not considered in these kinetic models, the calculated values of the sheath potential will not generally coincide with experimental observation [2]. The integral distributions illustrate the difficulty of extracting information regarding the presheath from experimental RFA characteristics. With the exception of the Bissel curve at $\tau = 1$,

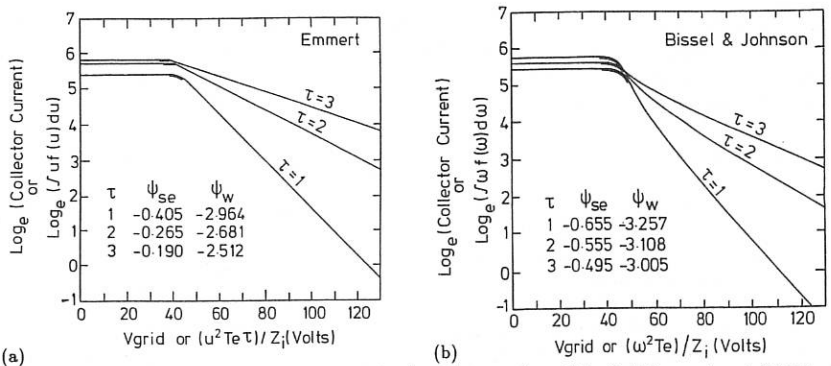

Fig.5 *Theoretical RFA characteristics arising from integration of the (a) Emmert and (b) Bissel expressions for* $f_w(v_{||})$.

there is very little curvature or 'rounding off' of the characteristic before the current begins to decrease rapidly. As shown by the experimental curves in Fig.4, the normal level of scatter in the data is sufficient to mask these small effects. At higher values of τ, Fig.5 shows that any effect would be difficult to detect, particularly if Emmert's model were more appropriate. It is true, however, that in the presence of strong secondary electron emission, the sheath potential can fall dramatically [2] whilst the presheath voltage drop remains unchanged. In practice, the presheath is ignored during the fitting process. Although differences in the theoretical integral distributions are evident, firm conclusions regarding the validity of either model cannot be drawn from the data in Fig.4. Whilst the curves appear to decrease exponentially at high V_g, there is, at least in the characteristic for which $T_{exp}/T_e = 5.8$, some slight curvature away from a pure straight line decrease. Such effects can actually be attributed to a high impurity concentration in the analysed flux [2], but would not produce the kind of dependence in the presheath region predicted by Bissel (Fig.5b). In fact, despite the relatively high noise level, strong evidence for the kind of behaviour predicted for the Bissel source, has not been detected in any of the DITE RFA characteristics. However, for the purposes of modelling ion interaction with surfaces in the tokamak, it is clear from Fig.4 that *assuming a one-dimensional, accelerated Maxwellian distribution will not invoke large error in any calculation.*

It should be possible to obtain more conclusive results using the RFA by restricting the grid voltage scan to the presheath region of the characteristic and increasing the sampling rate. Noise levels could be minimized by averaging a large number sweeps during steady state plasma conditions, or even by modulating V_g and using a lock-in amplifier detection system. Impurity effects should be reduced by operating in edge plasmas with low Z_{eff}. This may be achieved at high density when, in addition, τ is lowest [2] and the presheath becomes more important.

REFERENCES

[1] R. C. Bissel, P. C. Johnson, P. C. Stangeby, Phys. Fluids **1** (1989) 1133
[2] R. A. Pitts, Phd Thesis, University of London (1991)
[3] G. A. Emmert, R. M. Wieland, A. T. Mense, J. N. Davidson, Phys. Fluids **23** (1980) 803
[4] R. C. Bissel, P. C. Johnson, Phys. Fluids **30** (1987) 779

EXPERIMENTAL VERIFICATION OF SIMPLE SCALING RELATIONS FOR THE EDGE-PLASMA DENSITY IN TOKAMAKS

K.F. Alexander, K. Günther, M. Laux

Zentralinstitut für Elektronenphysik, O-1086 Berlin, FRG

In large fusion devices with gas fuelling the recycling takes place in the plasma edge because neutral atoms cannot penetrate into the central region before being ionized (Lehnert's impermeability criterion [1]). In this case the scaling of bulk and scrape-off densities, n and n_s (at the last closed flux surface) can easily be derived from the balance of neutral and plasma particle fluxes in the edge region inside the LCFS [2,3]:

$$\Gamma_N + \Gamma_p = 0 \qquad \Gamma_N = -v_N N. \qquad (1a,b)$$

Eq. (1b) is nothing but a formal definition of an effective radial penetration velocity, v_N, of the neutral atoms which may depend on r.

If slab geometry is used, the plasma ion balance reads

$$\frac{d\Gamma_p}{dx} = \xi_i n N = \frac{\xi_i}{v_N}\Gamma_p n \qquad \Gamma_p = -D_\perp \frac{dn}{dx}, \qquad (2a,b)$$

where ξ_i is the ionization rate coefficient. In these equations the absolute value of the anomalous diffusion coefficient $D_\perp$ does not matter, and it drops out completely if $D_\perp = const$. In this case, the resulting equation

$$\frac{d^2n}{dx^2} = \frac{\xi_i}{v_N} n \frac{dn}{dx} \qquad (3)$$

can be integrated if the ratio ξ_i/v_N is treated approximately as constant. This is a crude assumption if a constant v_N based on the idea that the influx of neutrals can be modelled by a "beam" of atoms that undergo nothing but ionization [3] is used and, moreover, v_N is an unknown parameter then. By contrast, the diffusion model for the neutrals (see below) yields, first of all, an unambiguous

$$v_N = \sqrt{\frac{\xi_i}{\xi_{cx}+\xi_i}\frac{T_i}{m_i}} \qquad (4)$$

which, in addition, has the advantage that its temperature dependence makes the ratio

$$\Sigma = \frac{\xi_i}{v_N} = \sqrt{\xi_i(\xi_{cx}+\xi_i)\frac{m_i}{T_i}} \qquad (5)$$

fairly constant in the temperature region typical for the plasma edge [2] (see fig.1). Thus, from (3):

$$\frac{dn}{dx} = \frac{1}{2}\Sigma\,(n^2 - n_\infty^2)\,. \qquad (6)$$

Evaluation of (6) at the LCFS ($x = x_s$) by introducing the local decay length λ_s according to $dn/dx = -n_s/\lambda_s$ yields the scaling equation

$$n_s = \frac{1}{2} \Sigma \lambda_s (n_{-\infty}^2 - n_s^2) . \qquad (7)$$

This rather general relation includes the special quadratic scaling of n_s with the line average density $\bar{n}$,

$$n_s \propto \bar{n}^2 , \qquad (8)$$

if the following conditions are fulfilled:

(i) $n_{-\infty} \approx \bar{n}$

(ii) $n_s^2 \ll \bar{n}^2$

(iii) λ_s invariable with respect to $\bar{n}$

(iv) $D_\perp$ independent of x in the edge region (fuelling region).

The approximate equality (i) is a reasonable assumption, considering that the actual density profile will show some central peaking due to pinch effects, and (ii) holds in any case. As for condition (iii), however, the scrape-off thickness λ_s may not be constant. It should be looked upon as an experimental parameter which makes the scaling law (7) more general than the special case (8). Likewise, an x-dependent $D_\perp$ may also invalidate the simple relation (8).

In fig.2 we have collected recent experimental data from TEXTOR [4], JET [5], and FT [6] where values for λ_s are available, together with our earlier results from T-10 [2]. The scaling relation (7) is satisfied fairly well, and the mean value of $\Sigma = 7 \times 10^{-19} m^2$ derived from the experimental fit agrees with the theoretical expectation for deuterium gas (fig. 1) despite the large range of geometrical dimensions and operational conditions of the different devices. Except for T-10, the scaling proves to be substantially influenced by a systematically varying λ_s which decreases with increasing $\bar{n}$. The scatter of experimental points probably reflects experimental uncertainties in the determination of λ_s and the precise location of the LCFS. Furthermore, λ_s may vary appreciably in dependence on the position where it was measured (poloidal asymmetries, distance to limiters, etc.), whereas the simple scaling relation is based on an 1-D description. In particular, the systematic deviation of the JET data points is understandable [7] because the small outboard values of λ have been used. The approximate validity of (7) suggests that radial variations of $D_\perp$ and density-dependent variations of profile-shaping pinch fluxes are of minor importance.

Relation (7) contains no "free" parameters because the refuelling process is assumed to be dominated by a diffusive penetration of fast neutral atoms which acquire the temperature of the ions through multiple charge exchange processes. The model of quasi-diffusive transport of neutrals owing to charge exchange reads [2]:

$$\Gamma_N = - \frac{T_i}{(\xi_{cx} + \xi_i) m_i} \frac{1}{n} \frac{dN}{dr} , \qquad (9)$$

where ξ_{cx} and ξ_i are the rate coefficients for charge exchange and ionization, respectively. The question whether $T_i dN/dr$ should be replaced with $d(T_i N)/dr$ is unimportant due to the relatively large radial gradient length of $T_i(r)$. The same argument allows a general integration of the neutral particle balance in slab geometry (x instead of r):

$$\frac{d\Gamma_N}{dx} = -\xi_i n N . \qquad (10)$$

After multiplication by eq. (9), integration yields

$$\Gamma_N^2 = \frac{\xi_i}{\xi_{cx}+\xi_i}\,\frac{T_i}{m_i}\,N^2 . \qquad (11)$$

This relation defines the effective velocity v_N according to eqs. (1b) and(4).

It is interesting to note that the effective diffusion velocity so obtained is completely independent of the particular plasma density profile; it depends on r only via the electron and ion temperatures. This allows a simple calculation of the neutral flux profile $\Gamma_N(x)$ for a given plasma density profile $n(x)$ by integration of the local neutral particle balance:

$$\frac{d\Gamma_N}{dx} = -\xi_i n N = \Sigma n \Gamma_N \qquad \Gamma_N(x) = \Gamma_{N,S}\exp\left[-\int_x^{x_s}\Sigma(x')\,n(x')\,dx'\right], \qquad (12)$$

where $\Gamma_{N,S}$ is the neutral flux at LCFS.

Simonini et al. [8,9] have dealt with the same problem by using a Monte-Carlo procedure to calculate $\Gamma_N(r)$ for given JET profiles $n(r)$. The results in terms of an effective neutral particle penetration depth $\lambda_{1/2}$ defined by flux attenuation to one half have been summarized by

$$\lambda_{1/2} = a/\bar{n} \qquad a = 0.46\times10^{19}\,m^{-2} . \qquad (13)$$

According to the diffusion model result (12), this quantity $\lambda_{1/2}$ is given by

$$\exp\left[-\int_{x_s-\lambda_{1/2}}^{x_s}\Sigma n\,dx\right] \approx \exp\left[-\Sigma\int_{x_s-\lambda_{1/2}}^{x_s} n\,dx\right] = \frac{1}{2} . \qquad (14)$$

The essentially linear behaviour of $n(x)$ in the edge region gives rise to the estimate $\lambda_{1/2}\,n(x_s-\lambda_{1/2})/2$ for the integral, and the estimation $n(x_s-\lambda_{1/2}) \approx \bar{n}/2$ can be justified by the fact that half of the neutral particles penetrate beyond $\lambda_{1/2}$ by definition. In this way eq. (14) leads to the same relation (13) with $a = 4\ln 2/\Sigma$. Thus, the quite realistic value $\Sigma = 6\times10^{-19}m^2$ yields complete correspondence of the two results, which demonstrates again the relevance of the diffusion model.

So far we have treated the "diffusion cross-section" Σ as constant. For the global scaling relations (7) and (14) this is tolerable because they involve integrations over the entire refuelling region. However, in order to calculate the profiles of flux, $\Gamma_N(x)$, and density, $N(x) = \Gamma_N(x)/v_N(x)$, of the neutrals according to eq. (12) it is recommendable to take account of the x-dependence of Σ and v_N by using appropriate temperature profiles if available. First attempts have shown good agreement with much more laborious calculations.

References

[1] Lehnert, B., Nucl. Fusion **8** (1968) 173, and Nucl. Fusion **23** (1983) 1327.
[2] Alexander, K.F., et al., Nucl. Fusion **26** (1986) 1575.
[3] Stangeby, P.C., J. Nucl. Mater. **145-147** (1987) 105.
[4] Laux, M., et al., *this conference, paper E-49.*
[5] Tagle, J.A., et al., Proc. 14th Europ. Conf. on Contr. Fusion and Plasma Phys., Madrid 1987, Vol. 2, p. 662.
[6] Pericoli-Rudolfini, V., Nucl. Fusion **31** (1991) 127.
[7] Stangeby, P.C., et al., Plasma Phys. Contr. Fusion **30** (1988) 1747.
[8] Simonini, R., et al., Contrib. Plasma Phys. **28** (1988) 459.
[9] Simonini, R., et al., Plasma Phys. Contr. Fusion, *in print.*

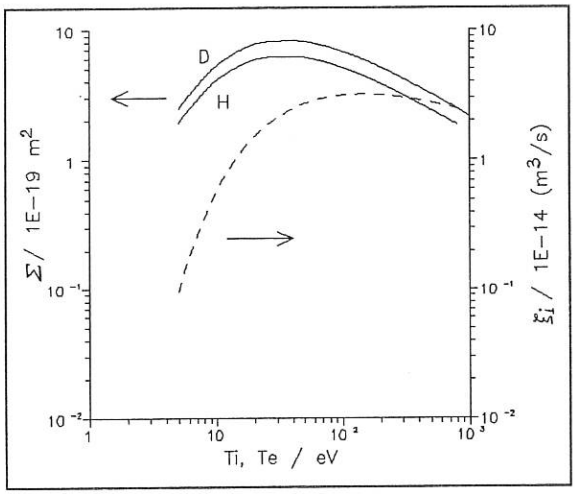

Figure 1 Σ and ξ_i versus ion or electron temperature

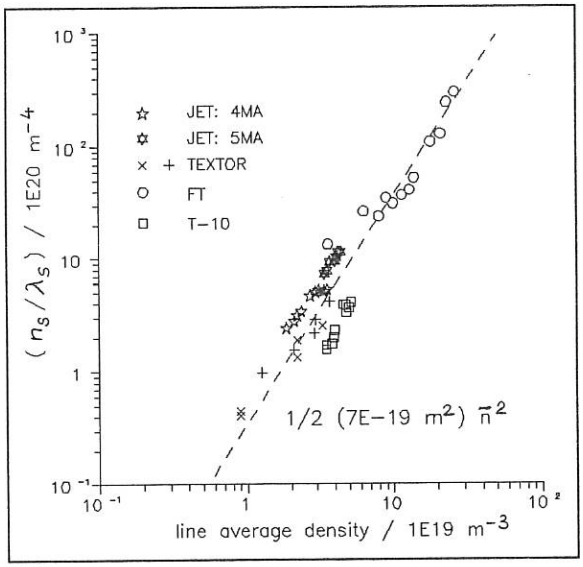

Figure 2 n_s/λ_s versus line average density for different tokamaks

2-D Modelling of the Edge Plasma with Arbitrary High Level of Impurity Concentration.

Igitkhanov Yu.L, Pozharov V.A.

I.V.Kurchatov Institut of Atomic Energy.

The 2-D - multifluid hydrodinamical Double Divertor Impurity Code (DDIC-90) was developed to simulate the divertor and the SOL plasma parameters including Carbon impurities originated from the divertor plate due to sputtering and selfsputtering. The transport model based on the electron-ion fluid equations for DT plasma and impurity ions of all charge states.The 27-moment Grad approximation was used to describe heat and momentum fluxes along the m. f. lines [1]. Such an approach permits one to simulate the plasma parameters in a wide range of impurity concentration changes from a practically pure plasma to the completely impure one.

In this paper the first preliminary results, obtained in the frame of rectangular geometry of the SOL and the divertor volume are presented. All input parameters and geometrical scales ware chosen for ITER [2]. The corresponding heat fluxes at the separatrix and total hydrogen particle number in the region are preset. Neutrals are simulated within the framework of a hydrodinamical equation. The continuity of particle, energy and parallel momentum fluxes are chosen as boundary conditions at the divertor plate. Incident back onto the plate or reaching the wall surface, the impurity ions are neutralized and enter the plasma as neutrals of carbon. The different value of impurity reflection coefficient (C recycling at the plate) is chosen. At the separatrix we assume the outgoing carbon fluxes to be zero. The transversal impurity fluxes are represented as a diffusion one, similar to the DT ions with anomalous constant coefficients: $\chi_e = 2\ m^2/s$, $\chi_i = D = 2/3\ m^2/s$. The symmetric boundary conditions are assumed at the midplane in the private divertor region.

Two regimes (A & B) corresponding to the different impurity reflection coefficients at the divertor plate are presented below. As calculations show in the case of low impurity recycling (A1 & A2), when reflection coefficient < 1 the distribution of plasma parameters remains to be almost the same as in the case of pure plasma, except the region nearest to the plate, where impurity ions of all charge states are localized and Z_{eff} achieves $\simeq 3$ (see Figs.3,4). In case A2 the divertor plate is considered to be perpendicular to the m. f. lines, whereas in case A1 inclined at the angle 15^0. This fact decreases the effective recycling and plays a decisive role on the value of plasma temperature at the plate. High impurity recycling case (B) corresponds to the refflection coefficient equal one. The comparison is presented below:

TABLE	Case A1	Case A2	Case B
Power into SOL (all), MW	90	90	75
C Radiated Power , %	14	70	98
Power Load q_e/q_i , MW/m^2	8/3.4	1.7/1.3	≤ 0.1
T_e / T_i midplane , eV	140/210	125/244	85/170
T_e / T_i plate , eV	35/15	6.3/7.4	≤ 1
Density at midplane , $10^{19}m^2$	3.2	3	3.6
Z_{eff} max near the plate	2.7	3.1	4.2
Plate inclination ,	15^0	90^0	15^0
Net Erosion , m/burn year	3.2	0.1	negligible

One should note that both modes of operation are not quite stationary. In the case "A" the oscillations are localized in the vicinity to the divertor plate. These relaxational oscillations (with the characteristic time ~ 2-3 ms) are provided by an ambiguity of a thermal balance in the presence of radiation losses due to carbonic impurities. An analysis shows that the heat removal to the plate can be realized in three stationary modes of operation, differing from each other by the plasma temperature in the divertor. Two of them are stable and correspond to a different temperature divertor modes [3]. An intermediate mode is unstable and related with an inverse dependence of the power of radiation losses for a carbonic ion on temperature under non-corona equilibrium conditions. A deviation from the corona distribution of impurities is related with a finite ion residence time, being typical under divertor plasma conditions. A low temperature mode is of great interest, when a noticeable part of energy can be radiated by carbon. For the physical stage of ITER operation up to 50% of power can be radiated in this mode (T ≤ 30 eV), when the plasma flux to the plate $\geq 3 \times 10^{24}$ 1/s [3]. An analysis shows that the oscillation can be treated as a transition between two stationary branches. A strong sputtering results in the impurity concentration growth and in the plasma cooling due to radiation. This, in its turn, reduces the temperature in the vicinity of the plate and reduces the plate erosion. With reduction in the impurity concentration the energy flux delivered by particles to the plate is increased that results in the growth of sputtering. In Fig.5,6,7 the oscillations of plasma parameters are shown. A linear analysis shows that the characteristic time of oscillations is about 2-3 ms and is in a good agreement with the numericle result. Such a state corresponds to a stable focus of the system under rather strong recycling and at the finite resident time of impurities.

The B-mode of operation, when almost the whole power is radiated with impurities, is of greatest interest. The ther-

mal loading by particles to the plate is negligible. The temperature and concentration distributions along the separatrix from a midplane to a plate for the most typical ion C is shown in Fig.2. The impurity remains to be localized in the divertor ($Z \geq 30$ m), where the zone of cold and dense plasma blanket is being formed. Z_{eff} equals $\cong 4$ in a wide range of divertor domain, electron density attains its maximal value, $\sim 10^{15} cm^{3}$. At such a density the impurities are gathered in a potential well, and their good retention in the divertor volume is explained by this fact. The B-mode is a quasi-stationary one. A hot front burns out the cold zone for the time of the order of 5 milliseconds and reaches the plate. The temperature nearby the plate rises up and an intense sputtering starts. The impurity entry into the divertor results in the plasma cooling and the backward plasma cooling wave emerges in the vicinity to the plate. The characteristic times of this process are determined by the time of transversal impurity escape and by the time of their scattering from the potential well due to collisions.

Conclusion:

1. The preliminary calculations with DDIC show that both the impurity transport and the divertor plasma parameters can differ much from the test model predictions, when $Z_{eff} > 1.4$.

2. Under ITER divertor plasma conditions, P ~ 90 MW, relaxational oscillations of the divertor plasma parameters take place. These oscillations with the characteristic time ~ 2 ms assist in the reduction of a peak power loading on the plate.

3. Quasi-stationary modes of operation with a practically-complete energy radiation by carbonic impurities have been obtained. A cool (a few eV) dense ($> 4 \times 10^{14} cm^{-3}$) plasma is localized in the divertor volume and balanced by a great gradient > 100 eV/m, in the divertor throat. Practically all impurities are trapped in the divertor, being retained in the potential well. The time of existence for such a phase ≥ 5 ms.

References

1.Igitkhanov Yu.et al.USSR Contribution to the Phase IIA Part 3 of the INTOR Workshop.Brussels,1986.Group A,- P.52
2.ITER Conceptual Design: Interim Report,Vienna,1990.
3.Igitkhanov Yu.,et al.in 9th Int.Conference,Bournemouth,1990

Figures captions

Fig.1 $T_{e,i}$ profiles along the m.f.lines (separatrix);solid lines correspond to case A2, dashed - case A1).
Fig.2 $T_{e,i}$ & the most representative C_2 ions profiles (case B)
Fig.3 C - ions profiles along the separatrix (cases A1).
Fig.4 The same across the m f.lines at the plate.
Fig.5 Oscillation of $T_{e,i}$ at the plate; (case A1).
Fig.6 Oscillation of the particle flux onto the plate.
Fig.7 The same for the flux of carbon atoms from the plate.
Fig 8 Power distribution across the plate (case A2).

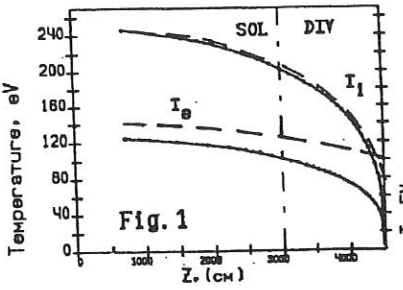

Fig. 1

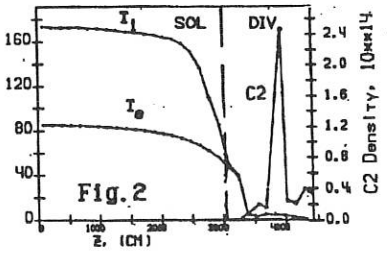

Fig. 2

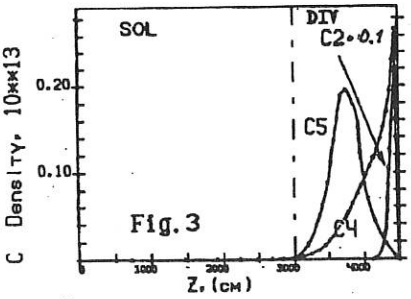

Fig. 3

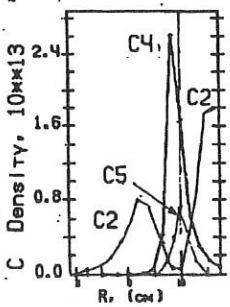

Fig. 4

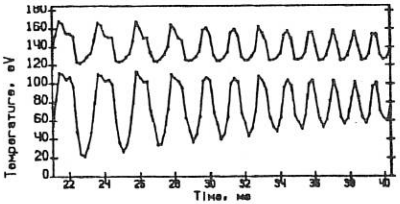

Fig. 5

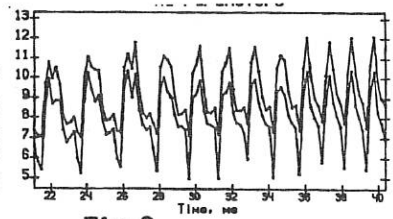

Fig. 6

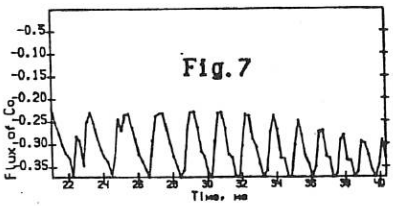

Fig. 7

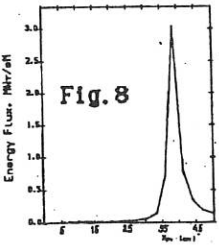

Fig. 8

EDGE PLASMA TRANSPORT IN GRAD APPROACH

Marek Rabiński

Institute for Nuclear Studies
05–400 Otwock–Swierk, Poland

Introduction

Modelling of a tokamak scrape–off plasma in the framework of the fluid approach is satisfactory as long as the mean free path of electrons is small in comparison with a temperature gradient length. Meanwhile, one can observe a discrepancy between experimental data and computational results for temperatures and concentration in the SOL midplane. As it is known, this effect is caused by overestimating the thermal conductivities and viscosity value in a region where validity of the hydrodynamic approach is violated. In this case heat fluxes are not determined by the local temperature gradients but they depend nonlocally on temperature profiles.

Several approaches had been applied to obtain a more realistic description of transport coefficients. Usually the nonlocal electron heat flux formulation, as proposed by Luciani *et al.* [3], had been implemented. Otherwise, the BOUND1D package of one–dimensional computational codes, that was developed for analysis of tokamak edge plasma, has been improved by introducing a more sophisticated model of nonlocal transport with heat fluxes and viscous stresses in the Grad approach [4]. A set of time independent differential equations for the transport coefficients have been taken according to the Igitkhanov & Yushmanov paper [2]. However, computational studies have showed that the applied description of nonlocal coefficients leads to irrationally large values, which destabilize subsequent calculations [4].

A critical analysis of the results obtained made possible to find several unmotivated simplifications preceding the time independent equations proposed by Igitkhanov & Yushmanov. First of all, it was justified to assume that the steady state formulation of the transport coefficients is improper for the simulation of plasma dynamics. In the presented paper a new, improved model for nonlocal heat fluxes and viscous stresses is given.

Plasma transport model

Plasma behaviour is described by a one–dimensional two–fluid model, based on the Braginskii equations, with viscous stresses and heat fluxes treated as independent variables

$$\frac{\partial n}{\partial t} + \frac{\partial}{\partial s}(nv) = S_n \qquad (1)$$

$$\frac{\partial}{\partial t}(m_i nv) + \frac{\partial}{\partial s}\left\{m_i nv^2 + n\varkappa(T_e+T_i) - \pi_i - \pi_e\right\} = S_p \qquad (2)$$

$$\frac{\partial}{\partial t}\left\{\frac{3}{2}n\varkappa T_e\right\} + \frac{\partial}{\partial s}\left\{\frac{5}{2}\varkappa T_e nv + q_e\right\} = v\frac{\partial}{\partial s}(n\varkappa T_e) - Q_{ei} + W_e \qquad (3)$$

$$\frac{\partial}{\partial t}\left\{\frac{3}{2}n\varkappa T_i + \frac{1}{2}m_i nv^2\right\} + \frac{\partial}{\partial s}\left\{(\frac{5}{2}\varkappa T_i + \frac{1}{2}m_i v^2)nv + q_i\right\} - \pi_i(\frac{\partial v}{\partial s}) =$$

$$= - v\frac{\partial}{\partial s}(n\varkappa T_e) + Q_{ei} + W_i \qquad (4)$$

where

s – coordinate along the direction of magnetic field line,
n – plasma concentration,
v – plasma flow velocity along the field line,
$\varkappa$ – Boltzmann constant,
T_e, T_i – electron and ion temperatures,
π_e, π_i – longitudinal viscous stresses for electrons and ions,
q_e, q_i – heat fluxes for electrons and ions,
Q_{ei} – the electron–ion energy equilibration term connected with the Coulomb collisions,
S_n, S_p, W_e, W_i – the density, momentum, electron and ion energy source terms taken from the iteraction with recycled neutrals and induced by a plasma flow across the separatrix,
m_e, m_i – electron and ion masses, respectively.

Nonlocal transport coefficients

Equations describing the nonlocal heat fluxes and viscous stresses have been derived within the framework of the 21 moment Grad approach, on the basis of general formulae given by Zhdanov for a multicomponent plasma [5]. For consistency with the dynamic model of plasma transport, the time derivatives have not been neglected. Hence, the following set of partial differential equations has been obtained for each of the plasma components (subscript $k = e,i$ denotes electrons and ions, respectively)

$$\frac{dq_k}{dt} - \frac{\partial}{\partial s}\left\{\sigma_k + \frac{\pi_k}{\gamma_k}\right\} + \frac{5}{2}\frac{P_k}{m_k}\frac{\partial}{\partial s}(\varkappa T_k) = [- a^k_{11}q_k + a^k_{12}\gamma_k r_k] / \tau_{kk} \qquad (5)$$

$$\frac{dr}{dt}^k - 2\frac{\partial}{\partial s}\left\{\frac{\sigma}{\gamma}^k\right\} = [a^k_{21}\frac{q}{\gamma}^k - a^k_{22}r_k] / \tau_{kk} \qquad (6)$$

$$\frac{d\pi}{dt}^k + \frac{4}{5}\frac{\partial q}{\partial s}^k = [- a^k_{31}\pi_k + a^k_{32}\gamma_k \sigma_k] / \tau_{kk} \qquad (7)$$

$$\frac{d\sigma}{dt}^k + \frac{7}{5}\frac{\partial}{\partial s}\left\{\frac{q}{\gamma}^k\right\} + \frac{2}{5}\frac{\partial r}{\partial s}^k = [a^k_{41}\frac{\pi}{\gamma}^k - a^k_{42}\sigma_k] / \tau_{kk} \qquad (8)$$

where: $\frac{d}{dt}^k = \frac{\partial}{\partial s}^k + v_k \frac{\partial}{\partial s}^k$ denotes the convective derivative;
$\gamma_k = m_k/(\varkappa T_k)$; $P_k = n_k \varkappa T_k$; τ_{kk} is the relaxation time;
σ_k and r_k are the additional variables (higher order moments) introduced by the Grad method. Coefficients in equation set (5–8) have the following values for ions:

$$a^i_{11} = \frac{13}{10}; \quad a^i_{12} = \frac{69}{140}; \quad a^i_{21} = \frac{69}{20}; \quad a^i_{22} = \frac{433}{280};$$

$$a^i_{31} = \frac{6}{5}; \quad a^i_{32} = \frac{9}{35}; \quad a^i_{41} = \frac{9}{5}; \quad a^i_{42} = \frac{51}{35}; \qquad (9)$$

and for electrons:

$$a^e_j = a^i_j \sqrt{2} + b^e_j \; ; \qquad (10)$$

$$b^e_{11} = \frac{2}{5}; \quad b^e_{12} = \frac{3}{35}; \quad b^e_{21} = \frac{3}{5}; \quad b^e_{22} = \frac{9}{14};$$

$$b^e_{31} = \frac{3}{5}; \quad b^e_{32} = \frac{9}{140}; \quad b^e_{41} = \frac{9}{20}; \quad b^e_{42} = \frac{41}{56} . \qquad (11)$$

Models of neutral gas and impurities

Three alternative models of neutrals has been introduced into the BOUND1D package: a hydrodynamic model, a steady state diffusion and commonly used analytical formulae describing neutral gas parameters.

The only influence of impurities on the plasma transport consists in radiational losses. For the presented application this phenomenon was simulated in a very simplified manner by defining the proportion of impurities in comparison with local plasma concentration.

Numerical solution

The partial differential equations describing the model in question have been solved on a nonuniform staggered mesh. An implicit method [1] developed for the quasilinear parabolic equations has been employed, while the convective terms have been discretized according to the upstream scheme of the donor cell type. For nonlinear terms, the first order Taylor expansion has been used to accelerate the convergence. The applied numerical method is linear according to the i–th approximation of the variable at a new time step, therefore the obtained tridiagonal matrix equations could be solved succesively by the highly efficient Gauss technique.

Concluding remarks

The first computational results, as obtained from the improved theoretical model described above, show that the previously reported [4] unphysical solutions disappear. It seems to be proved that the use of the time independent description of nonlocal transport coefficients was the reason of these difficulties. The steady state model given in [2] can be quite useful for obtaining analytical solutions of extremely simplified cases, but its implementation as a part of plasma dynamic codes is practically impossible. Inadequacy of this combination can be better understood when the mathematico–physical implications of above described connection are more deeply analysed. One can find a strict analogy between unapplicability of the steady state diffusion model of a neutral gas and those of the time independent description of transport coefficients.

At the time, some studies are carried out to develop a consistent system of boundary conditions, both for plasma model and nonlocal transport coefficients. The inclusion of additional variables σ_k and r_k introduced by the Grad method make it a more complex problem. As it was found during the preliminary calculations, the requirement that at the divertor plate the hydrodynamic moments are equal to the kinetic ones does not establish solution.

Acknowledgement

The author wishes to thank Dr. Yu.Igitkhanov from the Kurchatov Institute for his sugestion of the coupling a plasma code with the description of transport coefficients in the Grad approach.

References

[1] Dnestrovskii Yu. and D. Kostomarov: Numerical Simulation of Plasmas, Springer–Verlag, Heidelberg 1985.

[2] Igitkhanov Yu. and P.Yushmanov: Non–Local Transport in the Scrape–Off Tokamak Plasma, Contrib. Plasma Phys. **28** (1988) 4/5, 341–344.

[3] Luciani J., P.Mora and J.Virmont: Nonlocal Heat Transport Due to Steep Temperature Gradients, Phys. Rev. Lett. **51** (1983) 18, 1664–1667.

[4] Rabiński M.: One–Dimensional Modelling of Tokamak Edge Plasma Transport in Grad Approximation, Contrib. Plasma Phys. **30** (1990) 1, 121–126.

[5] Zhdanov V.: Transport Phenomena in Multicomponent Plasma *(in Russian)*, Energoizdat, Moscow 1982.

INSTABILITIES OF PLASMA-COLLECTOR INTERACTION IN IMITATION EXPERIMENTS.

I.V.Vizgalov, S.K.Dimitrov, V.A.Kurnaev, Yu.V.Chernyatjev.

Moscow Engineering Physics Institute, Moscow, USSR.

Abstract

A highly nonequilibrium long-thin plasma with widely varied parameters n = 10^{15} - 10^{19} m^{-3}; T=5-30 eV; T=1-5eV is generated by means of electron beam driven discharge in magnetic field to achieve physical modelling of principal edge plasma features. The nozzle is used to obtain subsonic plasma flows towards the collector plate. In dense plasma interacting with different materials there are observed strong instabilities revealed as plasma column sweeping over collector surface and intense high frequency oscillations. Mechanisms responsible for instabilities and HF oscillations are discussed. The possible one is abnormaly high ion-electron emission from the cold solid surface evoking negative differential resistance of plasma-collector system.

Introduction

Electron beam-plasma discharge in magnetic field (BPD) permits to generate a long-thin plasma. Its main properties and parameters (density, energy and space distributions, level of the turbulence, mass- and charge compositions of impurities) can be varied in wide ranges and approached to those inherent in the edge plasma (more exactly in its scrape-off layer - SOL) of present day tokamaks. Particle, energy, impulse source and sink rates in both cases are determined by charged particles interaction with hydrogen and impurities as well as by nonclassical cross field transport. Boundary conditions both in BPD and SOL concerning the details of plasma interaction with material surfaces can be made similar too. BPD thus is capable of reproducing the principal SOL features and presents unique opportunities not only for complex testing of candidate edge materials and devices but also for direct physical modelling of edge plasma-surface interaction.

The main emphasis of our experiments is made on the behaviour of the plasma flowing along magnetic field onto the solid surface under variable potential. This aspect is of particular interest in connection with now being discussed problem of edge plasma control by means of biased limiters[1].

Experimental set-up.

The experimental facility is shown in fig.1. It includes

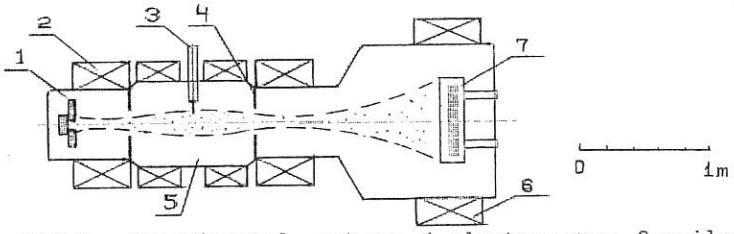

Fig.1. Experimental set-up: 1-electron gun; 2-coils; 3-probe; 4-fused silica diafragms; 5-gas puff chamber; 6-correction coil; 7-collector plate.

a vacuum vessel with magnetic system of a mirror machine type, electron gun, special target devices. The imitation complex is also provided with plasma and collector plate diagnostics including probes movable in parallel and radial directions, mass- and energy spectrometers, gauges of thermal and impulse flows, thermometry. A vacuum sluice-way is used to introduce different plates or probes into the plasma flow. Plasma parameters can be programmly varied in wide ranges: $n_e=10^{15}-10^{19}$ m^{-3}, T_e =5-30 eV with saturation ion current density up to j_i =1A/cm^2. Collector section is also equipped with coils allowing to bend the magnetic tube axis or to form magnetic nozzle configurations in front of the collector. Water cooled collector plate is insulated and its potential can be varied.

Experimental results.

The overall character of the BPD generated plasma column behaviour observed in our experiments with biased plates is analogous to that observed in edge experiments with biased limiter plates [1]: negative collector potential increases the plasma column density, positive potential leads to opposite result.

We observed rather strong hydrodynamical instabilities revealing in the form of plasma column radial broadening or straightening (for the curved magnetic axis). In our experiments with auxilliary plasma acceleration due to nozzle the effect took place even for small magnetic tube curvatures (1/R=0.2m) and for grounded and highly conductive (copper) plates. Damped periodic development and stabilization of these instabilities accompanying by auto-oscillations of gas and plasma longitudinal density distributions are identified as radial pulsing (by a factor of 2) and transverse sweeping of curved plasma column (with amplitude of 0.01m) at rather low frequencies (not higher than 1 kHz).

We also observed generation of powerful HF auto-oscillations of collector current and plasma potential influencing the properties of the column at its full length.

Fig.2 shows typical current versus voltage characteristics (CVC) obtained for the collector plate immersed into the plasma flow. Without any magnetic nozzle

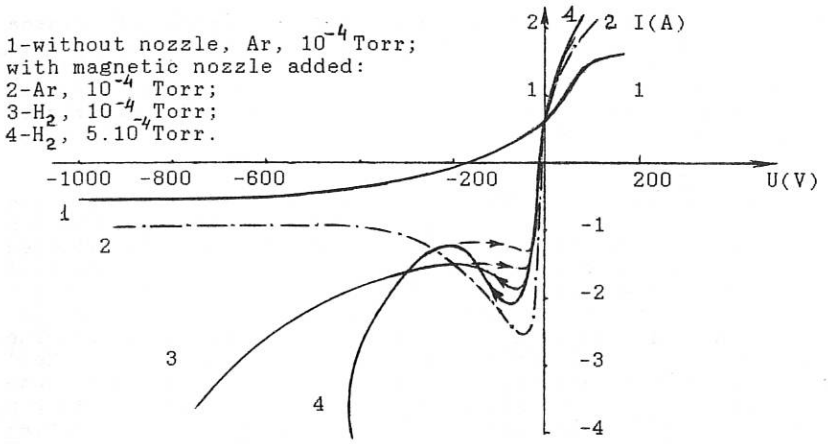

Fig.2. Current vs voltage characteristics of beam-plasma discharge with cooled aluminum collector plate.

CVC1 qualitatively is analogous to the probe characteristic measured behind a small orifice in the grounded collector plate (some faint differences between them are connected with unsuppressed secondary emission and BPD perturbations). CVCs for different combinations of working gases and collector plate materials are similar in general, and their differences in details can be explained by the peculiarities of elementary processes for every pair of collector material and gas used.

When a nonisothermal magnetic nozzle is applied in front of a collector plate ion current considerably increases and the CVCs modify drasticly: floating potential decreases, CVC obtains N-form (CVC2) with strongly marked hysteresis in some cases (CVC3-CVC4). For collector materials with a low work of electron exit (an aluminum for example) ion current increase is more pronounced. An analysis of experimentally measured mass/charge and energy spectra, as well as data on thermal and impulse flows onto the plate show that maximum of ion current coincides with the maximum effective value of the secondary ion-electron emission coefficient (γ = 0,5-1,5), the latter being much higher than that for corresponding elementary process. CVC4 shows the transition to a self-maintained discharge: electron gun can be switched off and grounded, power injection into the plasma column is accomplished by secondary electrons from cooled and biased collector plate operating as the only discharge cathode. Its emission current density achieves 1A/cm^2. It is pertinent to note that electron energy spectra measured in plasmas generated by both self-maintained discharge and normal BPD are similar.

In the voltage range where γ decreases, the system consisting of the plasma flow and collector plate has a very

unstable character, shows much greater level of plasma potential oscillations, turbulence and radial diffusion than in the range with γ increase. The CVC fall off (negative differential resistance) permits to induce powerful (up to 1kW) electromagnetic oscillations in the outer LC-contour with frequencies up to 100MHz.

Discussion.

We do not know exactly the origin of enhanced electron emission from the cold solid surface under intensive ion bombardment. Exiting of powerful HF oscillations excludes possible explanations based on such relatively inertial processes as dielectric layers formation, unipolar arcs or gas recycling on the plate surface, though these effects can take place in some regimes and affect discharge dynamics. The possible explanation of abnormal emission (now being checked) is a nonlinear increase of an ion-acoustic wave amplitude generated in a collisionless nozzle by energetic electron component and successive modification of an ion space charge wave in double-layer in front of the plate. The coincidence of the wave front overturning with its arrival to the plate surface instantaneously increases the ion space charge, current density and E-field up to the values sufficient for collective exitation of electron gas or its zone structure alteration in the solid surface layer and so induces an autoemission of electrons. Excessive ion acceleration at higher voltage bias according to supposed mechanism transforms the ion grouped front into broadening multyvelocity ensemble, weakens the ion cumulation and then destroies it completely lowering collector current to its normal value (CVC2).

In our opinion effects observed in BPD can take place under some conditions in edge plasmas too. For example, in plasma-limiter regime accompanied by abnormal electron emission limiter voltage bias corresponding to increasing of γ might stabilize plasma potential fluctuations, decrease floating potential and so reduce collector sputtering (with some increase of the thermal load). On the contrary, voltage bias with decreasing γ might stimulate HF plasma potential oscillations and SOL turbulent broadening. This unstable state can arise for a biased plate as well as for a floating or even grounded plate. In the latter case electromagnetic oscillations can be generated in virtual LC-circuits involving SOL, plate and maybe vessel walls, energy being consumed from the internal edge layers with unteared magnetic lines. This effect can be used for the turbulent blanket concept [2] provided no additional plasma contamination (due to sputtering) occurs.

References.

1.P.C.Stangeby, G.M.McCracken. Nucl.Fusion 30 (1990), 1225.
2.N.N.Vasilyev, A.V.Nedospasov, V.G.Petrov, M.Z.Tokar.Proc. 8th Europ. Conf.on Controlled Fusion and Plasma Physics. Prague (1977) V1, p.164.

MAIN CHARACTERISTICS OF A HIGH-POWER FULL-SCALE QUASI-STATIONARY PLASMA ACCELERATOR QSPA-Kh-50 AND SOME RESULTS OF PRELIMINARY EXPERIMENTS

N.V.Kulik, V.S.Manojlo, V.A.Malikov, O.S.Pavlichenko, D.G.Solyakov, V.V.Stal'tsov, V.I.Tereshin, Yu.I.Tashchev, S.A.Trubchaninov, B.Yu.Tsupko, V.V.Chebotaryov,

Kharkov Institute of Physics & Technology, 310108 Kharkov, USSR

and A.I.Morozov

I.V.Kurchatov Institute of Atomic Energy, 123182 Moscow, USSR

The solution in principle of the problem of quasi-stationary acceleration of plasma opens prospects for generating plasma streams with a sufficiently great energycontent at high ion energies. Such streams can be used to simulate the processes occurring on the first wall and the divertor plates of a reactor-tokamak, and in some other applications. The studies made so far on different model accelerators [1-3] as well as the theoretical analysis [4,5] have demonstrated that the objectives can be successfully achieved if a quasi-stationary plasma accelerator (QSPA) satisfies special requirements. In particular, the acceleration should be accomplished in two stages, and in this case, the first stage ensures plasma creation and preacceleration. To avoid considerable jumps in potential in the vicinity of the electrodes of the main accelerating channel and to ensure against cathode erosion, it is essential that the discharge current should be carried by ions, i.e., ions or atoms should be supplied from the anode side, and the electrode elements should be magnetically screened. So, the electrodes of the main accelerating channel of the QSPA are complicated functional units, the so-called anode and cathode transformers. All these considerations were laid in the basis of the full-scale accelerator QSPA Kh-50 constructed at the Kharkov Institute. Its block diagram is shown in Fig. 1.

The first stage of the QSPA consists of five individual input ionization chambers, where plasma streams with a density of 2 to 5 10^{15} cm^{-3} and an average velocity of 3 to 5 10^{6} cm/s are generated during a 300 μs pulse. The main accelerating channel is a set of coaxial active electrodes-transformers. The z-type anode transformer has a complicated cylindrical surface with the operation zone, 50 cm in diameter. A three-row system of current-carrying conductors laid along the surface of the anode transformer provides for the formation of the magnetic emitting surface (MES) - separatrix,

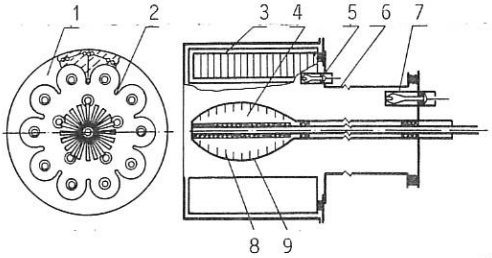

Fig. 1. Block diagram of the QSPA Kh-50. 1: Anode transformer, 2: anode collector, 3: anode transformer current windings, 4: cathode transformer, 5: anode ionization chamber, 6: drift chamber, 7: input ionization chamber, 8: cathode transformer rods, 9: needle-type cathode emitters.

extending along the axis of the system, with 10 periods in azimuth. A cold plasma, serving as an emitter of "current-carrying" ions in the accelerating channel, is injected along 10 zero lines of the MES. The cathode transformer is a multirod electrode of an ellipsoid shape with a maximum diameter of 32 cm. The current ensuring magnetic screening of 20 rods is supplied by an individual capacitor bank. The discharge current takes the path through needle-type electron emitters placed between the rods in the internal region of the cathode transformer.

The plasma streams generated by the QSPA are injected into a vacuum chamber, 10 m long and 1.5 m in diameter. The total energy content of the main-discharge capacitor bank is 2.2 MJ (at U_c=25 kV), and that of the capacitor banks supplying the rest of the QSPA units is 1.1 MJ.

So far, the experiments have been carried out at a voltage of the main-discharge capacitor bank of 12 kV ($U_c \approx 400$ kJ), the total consumption of gas (hydrogen) admitted through the input ionization chambers and the anode ionization chambers up to 1.5 l per pulse, the amplitude and time duration of the discharge current being up to 340 kA and 300 μs, respectively.

Among most important QSPA performance characteristics are the current-voltage curves which determine the relationship between the electrode voltage in the main accelerating channel U_d and the discharge current I_d. The experiments performed at different initial conditions have shown that this relationship is described by the exponential function $U_d \sim I_d^{\alpha}$. Under certain conditions of matching the two stages, when the plasma density

at the input of the main accelerating channel grows from the anode to the cathode, and with the switched-on magnetic systems of the anode and the cathode transformers, the exponent α reaches the value between 2.5 and 2.7, this being close to the calculated α=3.

The plasma stream velocity was determined from the time-of-flight measurements between two electrical probes. It has been indicated previously [2] that the velocity values so obtained are in good agreement with independent measurements based on the Doppler shift of atomic hydrogen and impurity ion spectroscopic lines, and also with proton energy spectrum measurements. The plasma velocity values obtained under different modes of QSPA operation are depicted in Fig. 2 as functions of the total current I_c flowing through the cathode transformer elements, and of the main discharge

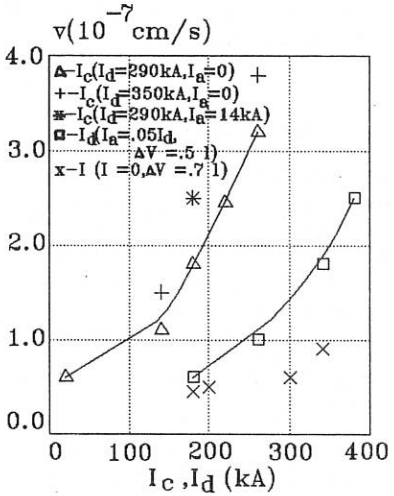

Fig. 2. Plasma velocity versus cathode (I_c) and discharge (I_d) currents.

current I_d. It is seen from the figure, that the plasma stream velocity sharply increases with the discharge current I_d and the gas influx into the anode transformer ΔV_a. The plasma velocity also increases with the increasing I_c, attaining its peak value when all QSPA units are in operation. The highest plasma stream velocity value was measured at U_c=10 kV to be 3.8×10^7 cm/s (~800 eV).

Fig. 3 shows the radial distributions of the energy flux density q_w measured by a calorimeter at a distance of 3m from the accelerator.

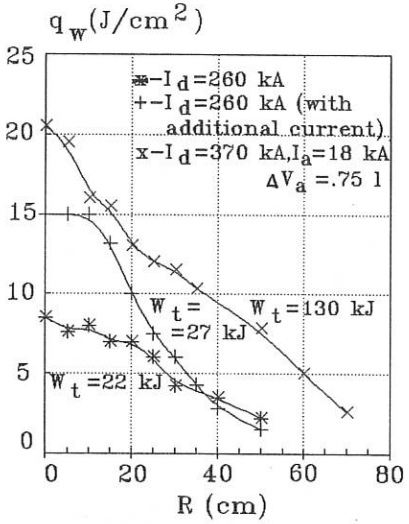

Fig. 3. Radial energy density distribution.

The q_w value and the total energy content in the plasma stream W_t appreciably increase with an improved matching of the two stages due to an additional discharge current in the first stage. Apart from the increasing q_w, as the capacitor bank voltage grows, there occurs a sharp broadening of the radial energy profile, so that the mean plasma stream radius reaches 40 cm, and the total energy content in the stream is as great as 130 kJ (U_c=10 kV, $W_c \approx$360 kJ). The energy flux density measured at 1.5 m from the accelerator was greater than 100 J/cm^2, and recalculated with the 0.5 m distance was found to be above 0.5 kJ/cm^2. So, the preliminary results obtained give evidence for a highly efficient operation of the full-scale QSPA. The plasma stream power of $\gtrsim$ 5 MW/cm^2 attained for the quasi-stationary phase duration of $\sim$100 μs correspond, to a certain extent, to the conditions which may appear on the first wall during current disruptions in the reactor-tokamak.

[1] Vinogradova, A.K., Morozov, A.I., In: "Fizika i primenenie plazmennykh uskoritelej", Minsk, Nauka i Tekh. publ., 1974, 103-141.
[2] Voloshko, A.Yu., et al., Fiz. Plazmy 2 (1990) 158.
[3] Belan, V.G. et al., Fiz. Plazmy 2 (1990) 176.
[4] Morozov, A.I., Fiz. Plazmy 2 (1990) 131.
[5] Brushlinskij, K.V. et al., Fiz. Plazmy 2 (1990) 147.

IMPURITY DEPOSITION ON SURFACE PROBES DURING DIFFERENT OPERATION MODES AT EXTRAP T1.

I. Gudowska, H. Bergsåker, G. Hellblom*

Manne Siegbahn Inst. of Phys., Ass. EURATOM-NFR, S-10405 Stockholm, Sweden
* Alfven Laboratory, The Royal Institute of Technology, S-100 44 Stockholm, Sweden

Introduction. Surface probes were used in the impurity control program during initial operation of the EXTRAP T1 device. The EXTRAP concept, design and operation characteristics are given elsewhere [1,3]. The dimensions of the device are R/a = 0.5m/0.06m. Four different modes of operation were studied: pure EXTRAP, mixed EXTRAP, RFP and ULQ. Details are discussed by Hellblom et al.[4] and Brunsell et al. [3]. Briefly, all four are toroidal plasma discharges, with poloidal magnetic field due to the toroidal plasma current. In the ULQ case, a relatively strong external toroidal magnetic field is applied. In the RFP, and in the mixed mode, an external toroidal field is applied early in the discharge, and the plasma subsequently relaxes into a state with self-generated toroidal field. In the EXTRAP and mixed EXTRAP modes, an additional strong external octupole field is applied, breaking the poloidal symmetry. Throughout the initial period of operation of the device, the plasma performance was largely dominated by impurities, in particular fluorine, which was present due to an accidental contamination of the vessel. Probes have been exposed in wall/liner position, and the objective has been to measure erosion and deposition and try to identify which mechanisms are mainly responsible for impurity production.

Experimental. Figure 1 shows a poloidal cross section of EXTRAP T1. The vacuum vessel consists of six SS 316L bellows with inner diameter 57 mm, intersected by port sections with inner diameter 55 mm. Schematically indicated are the toroidal plasma current I_p, the toroidal field B_Φ and the eight external conductors which carry a current I_{oct}, creating an octupole field in the EXTRAP and mixed EXTRAP modes. Without octupole field, the field configuration is poloidally symmetric, taking into account the large aspect ratio. With the octupole field applied, the poloidal symmetry is broken, and the plasma surface interaction can be expected to be more localised than for the other modes. Some discharge parameters for the different modes of operation are given in table 1: plasma current, average toroidal field $< B_\Phi >$, poloidal field $B_\theta(a_w)$ at wall radius, pinch parameter $\Theta = B_\theta(a_w)/< B_\Phi >$ and the ratio I_{oct}/I_p, which is a measure of the poloidal field asymmetry. All discharges except the ULQ ones were in helium, and were initiated at 1.5-3 mtorr filling pressure. The electron density estimated from the pressure to be in the range $0.3-1\cdot10^{14}$ cm^{-3}. The ULQ discharges were in hydrogen, at 1 - 10 mtorr. Loop voltages were typically 700 V, so that the ohmic input power was 7 - 35 MW. The electron temperature has been estimated from langmuir probes and VUV spectroscopy to be 10 - 30 eV. Discharge durations were typically 0.5 ms.

Probes were mounted on a movable rod and inserted radially at the position indicated in figure 1. Most probes were exposed at wall radius $a_w = 55$ mm, level with the wall surface. Graphite probes and single crystal silicon probes have been exposed with the intention of collecting metals, fluorine and hydrogen. Nickel foils of 6 μm thickness

mounted on a stainless steel support were exposed in order to collect carbon, fluorine and helium. The nickel foil samples were exposed at minor radius $r = 56$ mm and $r = 66$ mm in an attempt to discriminate between ions and neutrals. To measure possible erosion, graphite probes were prepared with a boron marker at the surface. These samples were covered with $\sim 3 \cdot 10^{14}$ B/cm^2 prior to exposure in EXTRAP by sputter deposition from a target with composition $\sim BC$. Each probe was exposed to 10 - 100 plasma discharges, giving total exposure times of 3 - 53 ms.

After exposure, the probes were transported in air to the analysis station, and the surface was investigated with optical microscope, SEM, Rutherford Backscattering (RBS), Proton Induced X-ray Emission (PIXE) and Nuclear Reaction Analysis (NRA). The areal density of fluorine on all exposed samples was determined with NRA using the ^{19}F(p,α)^{16}O nuclear reaction with 1350 keV protons. The amount of helium on the thin foil samples was estimated using enhanced elastic backscattering of 2.5 MeV p, and carbon on the nickel and silicon probes was measured with enhanced elastic proton backscattering with 1735 keV p. The areal density of boron on the erosion probes was determined before and after exposure by NRA, detecting α_1 from the ^{11}B(p,α)^{8}Be nuclear reaction and using 650 keV protons.

Since the probe exposures were without time resolution, it is not possible to know if the observed deposition took place continously throughout the plasma shots, or if it happened at certain instants. In what follows it will be implicitly assumed that all processes were continous, and deposition will be given as rates.

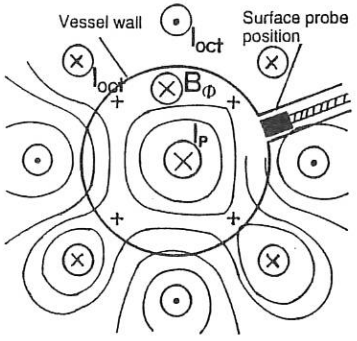

Fig.1 A poloidal cross-section of EXTRAP showing position of the surface probe.

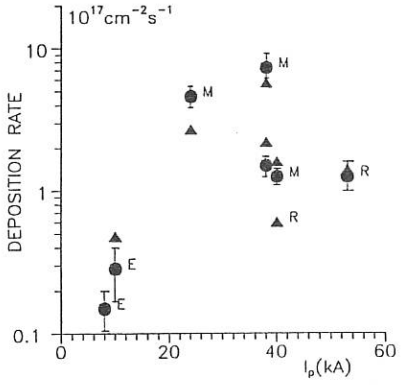

Fig.2 Metal (Cr+Fe+Ni) (●) and fluorine (▲) impurity deposition rate. Operation modes: E - EXTRAP, M - mixed, R - RFP.

Results. One graphite probe with boron marker was exposed to 13 RFP discharges with $I_p = 50$ kA, making a total exposure time of 4 ms. Three probes with boron marker were exposed to similar series of discharges in mixed mode with $I_p = 24$ and 40 kA. In all cases it can be concluded that less than $6 \cdot 10^{13}$ B/cm^2 was eroded. Taking into account that the surface composition on these samples was originally $\sim BC$, it follows that the erosion rate was less than $3 \cdot 10^{16}$ at. cm^{-2} s^{-1}.

One nickel foil probe was exposed at $r = 56$ mm to 108 RFP shots with $I_p = 40$ kA , and another at $r = 66$ mm to 60 discharges in mixed mode, with the intention to discriminate between neutrals and ions. The aperture towards the plasma was 17 mm

wide, and larmor radii of He- ions can be estimated to be of the order 5 - 10 mm, if $T_i \approx T_e$. Carbon impurities collected on nickel foil during the RFP mode shows that the carbon deposition rate was about $2.0 \cdot 10^{18}$ cm^{-2} s^{-1}. Spot-like deposition was observed, where the carbon concentration varied by a factor 10 on a mm scale. No significant carbon deposition was observed on the foil exposed at $r = 66$ mm. On both foils, the helium trapping was less than 10^{15} He/cm^2, indicating a trapping rate smaller than $\sim 2 \cdot 10^{16}$ He cm^{-2} s^{-1}. Fluorine was deposited on both foils, in the range $0.6 - 1.3 \cdot 10^{17}$ at F cm^{-2} s^{-1}.

Fig.2 shows the relation between the metal and fluorine deposition rate and plasma current for different modes of operation. The metal impurity deposition rate was in the range $1.1 - 9.0 \cdot 10^{17}$ cm^{-2} s^{-1} for the mixed EXTRAP and RFP modes. PIXE and RBS show that the composition of the metals is mainly Fe, Cr and Ni. A small amount of molybdenum was measured on probes exposed in the mixed mode. Molybdenum was deposited in the rate of about $0.3 \cdot 10^{16}$ cm^{-2} s^{-1}. In the case of EXTRAP and plasma current about 10 kA, the metal impurity deposition rate was 10 times lower. A similar relation as for metals shows also in the fluorine deposition rate. For the discharges with high plasma current, some decrease in fluorine deposition rate with the operation time is observed as the vessel became more clean. Table I presents the relation between the metal and fluorine deposition rate and some discharge parameters. Note that the results for the ULQ mode may not compare easily to the others, as they were in hydrogen and at different pressures.

The surface of the graphite probes was investigated by SEM and optical microscopy and some surface damage was observed which was interpreted as traces from electrical arcs. These tracs are observed only on the samples exposed in mixed mode whereas probes exposed in RFP mode with similar plasma current do not show this kind of damage. The deposition of steel components appears to be uniform, since no droplets or other aggregates with steel composition and a size larger than 0.3 μm could be detected with SEM. Particles containing V and Ti were observed, but could be attributed to the machining process and did not contribute significantly to the PIXE and RBS analysis.

TABLE I.

EXTRAP Mode I_p(kA)	Exp. Time (ms)	$\langle B_\phi \rangle$ (mT)	B_θ (mT)	Θ	$\frac{I_{oct}}{I_p}$	Metal Dep.rate 10^{17}cm^{-2}s^{-1}	Fluorine Dep.rate 10^{17}cm^{-2}s^{-1}
EXTRAP 10	23	~0	35	>4	0.8	0.2	0.5
Mixed EXTRAP 40	4	80	140	1.75	0.05	1.3*	2.0
RFP 50	3	89	175	1.96	0	1.0*	1.3
ULQ ~30	80	200	105	0.52	0	4.0	2.0

* – graphite samples with boron erosion rate less than $3 \cdot 10^{16}$ at cm^{-2}s^{-1}

Discussion and conclusions. The origin of the fluorine is an accidental contamination while the vessel was being assembled. Flanges and other parts of the original vessel have been investigated with NRA and microscopically, and they carried con-

taminants with $\sim 10^{18}$ F/cm^2, largely in the shape of ~ 10 μm particles. Parts of the vessel have been removed and cleaned during the period when these experiments were performed, which explains an observed decrease with time of the fluorine deposition on probes. Most of the vessel was eventually entirely replaced, and this is expected to solve the fluorine problem completely. From the result with the retracted collector it seems likely that fluorine was deposited in neutral state, e.g. due to evaporation.
The composition of the metal impurities which were deposited on the probe, mainly Fe but also a few % Mo, makes it likely that they originate from the SS 316L liner and bellows. Possible ejection mechanisms are sputtering and evaporation.
It is difficult to make an apriori estimate of the sputtering rate at the steel liner, since neither the impact ion energy nor the flux is known. Firstly, the ion temperature is not known. Secondly, the magnetic field is at grazing angle to the surfaces and ion gyro radii are likely to be large, so that a complicated electrostatic sheath structure can be expected. Finally the particle flux escaping from the plasma is not known. The energy confinement time can be estimated from the plasma density, electron temperature and input power, and is of the order $\tau_E \approx 0.5$ μs. However, this energy loss is more likely due to radiation than to particle loss. The retention of He in the nickel foils gives an indication. The incident He flux has to be less than $2 \cdot 10^{16}/\alpha$ cm^{-2} s^{-1}, where α is the probability of trapping. In the upper 10 eV and 100 eV energy range, the trapping probability of He in Ni is ~ 0.3. If in the present case $\alpha > 0.1$, then the incident flux density Φ_{He} of He at the wall was less than $2 \cdot 10^{17}$ cm^{-2} s^{-1}. Provided, furthermore, that the plasma ions were mainly He^{++}, then the particle confinement time $\tau_p \approx n_e a_w / 4\Phi_{He} > 0.3$ ms.
Consider the RFP case, which is poloidally symmetric and where it may be justified to assume that erosion and deposition are uniformly distributed. If this is so, the measured net deposition rate 10^{17} at. cm^{-2} s^{-1} of metals on the probes is also a lower limit for the erosion rate at the wall. But the erosion of the boron marker probes was less than $3 \cdot 10^{16}$ cm^{-2} s^{-1}, and the sputtering rate of boron and carbon according to Bohdanskys formula for low energy sputtering [5] is typically at least a factor two higher than that of iron, for He, C, or F ions in the 10 - 100 eV range. It follows that uniform physical sputtering can not be the main source of metal impurities. Sputtering can not be excluded as a major source of impurities if it is strongly localized. The average power load on the wall is ~ 2.5 kW/cm^2. With 0.5 ms discharge time, the power is deposited within a diffusion length ~ 0.2 mm at the steel surfaces, which would lead to a temperature rise of only ~ 20 K if the power is distributed uniformly. For evaporation of metals to take place, the powerload needs to be strongly localised. The presence of arc spots on the probes themselves suggests that evaporation in arcs may be the major source of metal impurities, although no droplets could be found. The surface damage on the probes was moreover observed only in the mixed mode of operation, and this is also when the largest metal deposition took place, as shown in figure 2. Arcing would also explain the release of other impurities. It is known that arcing can be avoided by appropriate surface conditioning and by avoiding sharp edges in the design.

References

[1] B. Lehnert, Nucl.Inst.Meth. 207(1983)223.
[2] M. Tendler, Nucl.Inst.Meth. 207(1983)233.
[3] P. Brunsell et al. Royal Institute of Technology, Stockholm, TRITA-PFU-91-02.
[4] G. Hellblom, P. Brunsell and J. Drake, these proc.
[5] J. Bohdansky, Nucl.Inst.Meth. B2(1984)587.

ANALYSIS OF HYDROGEN AND IMPURITY OUTGASSING UNDER CARBON,BORON AND BERYLLIUM FIRST WALL CONDITIONS

V.Philipps, J.Ehrenberg*, H.G.Esser, M.Erdweg, E.Vietzke,

Institut für Plasmaphysik,Forschungszentrum Jülich,Ass Euratom-KFA,
*Jet Joint Undertaking,Abingdon,Oxon,OX14,3EA,UK

ABSTRACT: Hydrogen and impurity outgassing has been analysed after discharges in TEXTOR with carbon and boron/carbon walls and in JET with beryllium walls by mass spectroscopy. It has been found that the temporal behaviour of hydrogenic outgassing is characterized by a uniform power law t^{-n} with $n = 0.7 \pm 0.1$ independent of the wall situation. With carbon walls the chemical reactivity between the carbon and hydrogen or oxygen leads to large amounts of hydrocarbon and CO outgassing increasing with increasing wall temperature. Boronization of TEXTOR has decreased the hydrocarbon and CO outgassing by factors of around 2 and 3 respectively. Under beryllium wall conditions in JET the CO outgassing has nearly completely disappeared.

1. INTRODUCTION. Analysis of the hydrogen outgassing process after plasma discharges is one important tool to investigate hydrogen recyling at the walls and to analyse the long term hydrogen retention in the walls of tokamaks which is important for meassuring the tritium inventory. With carbon or carbonized surfaces facing the plasma the hydrogen recycling and retention is dominated by the built-up of a hydrogen saturated near surface layer (by implantation or redepostion) with a ratio of H/C of about 0.4 (at R.T.). Trapping of hydrogen and desorption can yield reycyling coefficients >1 and lead to uncontrolled plasma density rises. The addition of boron to the carbon has decreased the recycling coefficient enabling good density control even under strong auxiliary heating. Even stronger improvement of hydrogen wall pumping has been achieved with beryllium walls /1/. The enhanced wall pumping is achieved via an enhanced dynamical retention of hydrogen:compared with pure carbon walls about a factor of 4 more hydrogen gas is needed to achieve the same electron density and hydrogen outgassing after the discharge is increased by a similar factor /2/.

The use of boron and beryllium have both decreased the impurity contamination of the plasmas significantly. In JET, the oxygen impurities have practically disappeared,also leading to smaller carbon impurity levels and,as a consequence,the plasma dilution is reduced significantly /3 /.

It has been demonstrated now in different tokamaks that the main benefit of boron as plasma facing component is a reduction of oxygen impurities.

This report presents an anylysis of the characteristic temporal behaviour of the hydrogen outgassing under different wall conditions and results on the relative amounts of outgassing impurities are being compared.

2. HYDROGENIC OUTGASSING: Hydrogenic and impurity outgassing have been measured for 15 min after discharges in JET and for 4 min after TEXTOR discharges using conventional quadrupol mass-spectrometers. From the measured partial pressures the outgassing rates have been calculated according to :

$$Q(t) = dp(t)/dt \cdot V + p \cdot S \cdot 273/T_W$$

where p(t) is the respective partial pressure, V is the torus volume,S the effective pumping speed and T_W the temperature of the walls surrounding the mass-spectrometer. The main result of interest for the hydrogen outgassing is shown in fig 1 where the hydrogen outgassing rate is shown as a function of time in a log-log plot after a TEXTOR discharge under boron/carbon walls and for JET with beryllium walls. Wall temperatures in TEXTOR were 150

°C and in JET 150 °C. The temporal behaviour,measured here over 1000 sec in JET and 240 sec in TEXTOR,is identical and follows an uniform power law t^{-n} with $n=0.7\pm0.1$. The same power law has been obtained in TEXTOR under carbon wall conditions. The temporal behaviour shown in Fig 1 does not change with wall temperature (in TEXTOR rising from 150°C to 350°C)nor with changing plasma operation conditions such as density, external heating,limiter or X-point configuration (JET) as long as the discharges have a soft landing behaviour during current ramp down.
The physics behind this power law and its implications on the hydrogen transport,recycling and retention mechanism in plasma facing components will be discussed in a separate paper. Here we state that the assumption of a single hydrogen transport process,determined either by diffusion,recombination or trapping taking place within a semi-infinite solid fails to decribe this release behaviour. Instead it appears that recycling and outgassing takes place in a layer structure such that any particle transport in the bulk is prevented.

3. IMPURITY OUTGASSING: Under the wall conditions mentioned above impurity outgassing consists nearly totally of hydrocarbon and CO outgassing with a minor contribution from CO_2. Under carbon wall conditions in TEXTOR the methan outgassing amounts to about 4-10 % of the deuterium outgassing and C_2-type hydrocarbons are 20-25% of the methan. The temporal behaviour of the hydrocarbon release rate is similar to that of the hydrogen. Fig 2 shows the ratio of methan to the deuterium pressure as a function of the wall temperature between 150 °C and 400 °C. The relative amount of hydrocarbon outgassing increases from about 4% to 8 %. It is interesting to note that during the discharge the same ratio of the methan pressure to the deuterium pressure is measured with a similar temperature dependence. Similar results are obtained in beam or plasma simulation experiments with hydrogen impinging on a carbon target /4/. From this result it is evident that the analysis of the hydrocarbon outgassing can be used to obtain information on hydrocarbon formation on the tokamak walls during plasma operation.
Under boronized wall conditions in TEXTOR (deposition of an amorphous boron/carbon layer with B/C 1:1) hydrocarbon outgassing has decreased roughly by a factor of 2 compared with the all carbon situation. This behaviour is demonstrated in Fig3 where the ratio of the CD_4 to D_2 measured 12 sec after the discharge is plotted as a function of shot number during the changeover from carbon to boron/carbon wall conditions. These data are obtained from discharges of three successing days with wall temperature of 150°C.
Hydrocarbon outgassing in JET under beryllium wall conditions has been measured to be between 0.3 and 1.2 % of the deuterium. A similar value (1%) has been obtained using gas chromatography of the exhaust gas compared with 3% under carbon wall conditions. Thus hydrocarbon outgassing under beryllium wall conditions in JET seems to have decreased by a similar factor then under boron wall conditions in TEXTOR. It is interesting to note that the hydrocarbon outgassing does not increase in JET when X-point plasmas are run on the carbon X-point tiles instead a limiter plasma running on the solid beryllium tiles. This suggests that the hydrocarbon outgassing(and probably the hydrocarbon formation during plasma operation) is effectively reduced by small amounts of beryllium being deposited on the carbon tiles.
The behaviour of CO outgassing during changeover from carbon to boron/carbon wall conditions in TEXTOR is shown in Fig4. It shows the ratio of CO/D_2 at $t=12$ sec for the same sequence of discharges as before. The CO outgassing decreases by a factor of 2-3 with a clear tendency towards a continous decrease with increasing operational time under the new boron/carbon wall conditions. The oxygen fluxes measured spectroscopically in front of the TEXTOR limiters have decreased during this changeover by a factor of about three wheras the reduction of oxygen line radiation from higher oxygen ionisation states was even more pronounced/5/. Thus the reduction of the oxygen impurity contamination is consistent with the reduction of the CO outgassing showing that CO outgassing is clearly connected with oxygen impurities appearing during plasma operation.

CO outgassing in JET under beryllium conditions has been found to be below the detection limit of the mass-spectroscopic detection. This can be seen from FIG 5 which shows after a JET discharge a typical ion spectrum of masses between 22-30. The fig shows also a fit of the mass-distribution assuming the production of C_2D_2, C_2D_4 and C_2D_6 using their known cracking patterns at an electron energy of 100eV. As can be seen no CO release is needed to explain the signal of mass 28. The integrated amount of outgassing at mass 28 corresponds to about 10^{-4} of the D_2 outgassing.This represents therefore un upper limit of CO outgassing under these conditions in JET. This result has to be compared with a relative CO outgassing of $1\text{-}8x10^{-1}$ measured during the carbon phase using gas chromatography. This value is in good agreement with TEXTOR results under carbon walls. Thus the suppression of CO outgassing in JET with beryllium walls is very effective. This is in line with the observed reduction of oxygen measured by spectroscopy .There a reduction by a factor of 100 has been reported.

4.SUMMARY: The temporal behaviour of the hydrogen outgassing after plasma discharges under carbon,boron/carbon and beryllium wall conditions is identical and follows a uniform power law t^{-n} with $n=0.7\pm0.1$.

With carbon walls hydrocarbon and CO outgassing amount to ratios between 4-10% and 1-10% of the deuterium outgassing depending on wall temperature (hydrocarbons) and oxygen impurity contamination of the plasma (CO). Boronization in TEXTOR has decreased the hydrocarbon outgassing by a factor of about 2. A similar reduction is observed in JET after using beryllium as first wall material. CO outgassing in TEXTOR has decreased after boronisation by a factor of about 3 whereas in JET the CO outgassing has practically disappeared with beryllium walls.

1 J.Ehrenberg,V.Philipps,L.De Kock et al,J.Nucl Mat. 176&177, (1991),226
2.R.Satori,G.Saibene,D.H.J.Goodall et al,J.Nucl.Mat.176&177,(1991) 624
3.P.Thomas and the JET team,J.Nucl.Mat. 176&177,(1991) 3
4.E.Vietzke,V.Philipps,Fusion Techn.Vol15,(1988) 108
5.J.Winter,H.G.Esser,L.Könen et al,J.Nucl Mat 162-164, (1989) 713

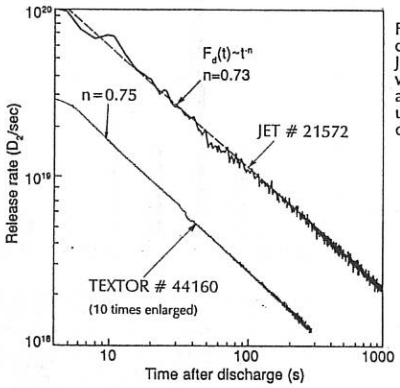

Fig1: Log-log plot of the deuterium outgassing rate after a JET discharge under beryllium wall conditions (300°C wall) and after a TEXTOR discharge under boron/carbon wall conditions(150°C wall).

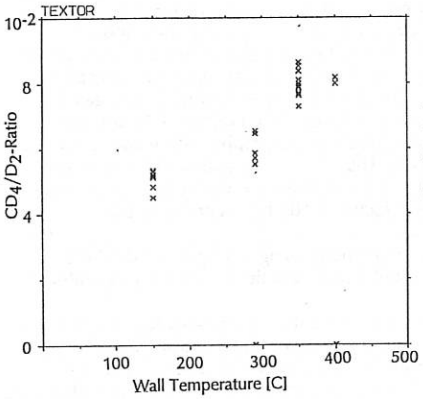

Fig2:Ratio of CD_4 to D_2 pressure measured 12 sec after the discharge for a serie of equal discharges as a function of the wall temperature in TEXTOR (Liner)

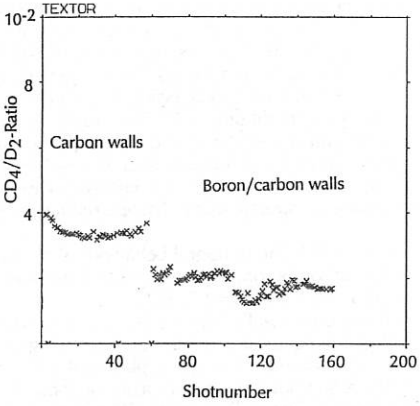

Fig3:Evolution of the ratio of CD_4 to D_2 pressure measured 12 sec after the discharge during changeover from carbon to boron/carbon walls

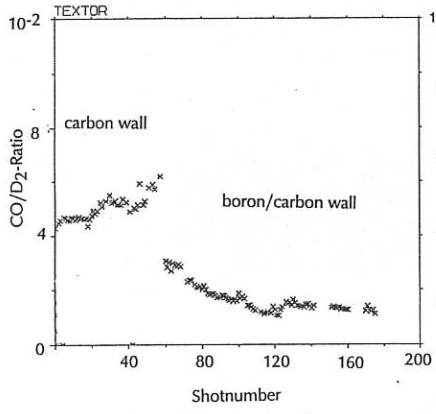

Fig4: Evolution of the ratio of CO/D_2 pressure measured 12 sec after the discharge during changeover from carbon to boron carbon wall conditions in TEXTOR

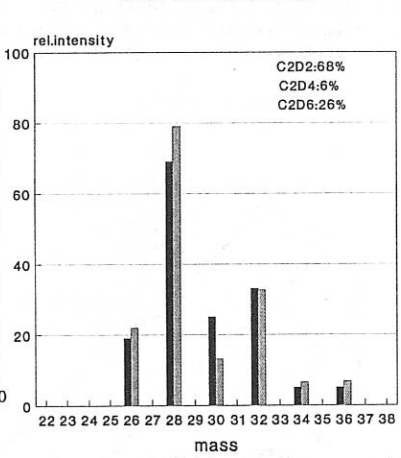

Fig5: Mass 26-36 ion-mass spectrum measured 120 sec after a JET discharge under beryllium wall conditions (■). Also shown is an attempt to fit the spectrum assuming the production of C_2D_2(68%),C_2D_4(6%) and C_2D_6(26%) using known chracking pattern taking from literatur(▨).

SPUTTERING AND REDEPOSITION OF IMPURITIES IN T15 STUDIED BY COLLECTOR PROBES

A.Herrmann, D. Hildebrandt, H.Wolff, WASA-Team ZIE, Berlin, FRG
S.Grashin, G.Igonkina, A.Terebkov, A.Vertiporokh IAE, Moscow, USSR
V.Alimov, A.Gorodetsky, R.Zalavutdinov, A.Zacharov IPCh, Moscow, USSR

Collecting probes in the tokamak scrape-off layer (SOL) are able to give information on sputtering, transport and redeposition of impurities in the SOL and on the erosion inside the tokamak vessel [1,2,3]. Two types of collector probes were used for the investigation of sputtering and redeposition during the first working period of the tokamak T-15 (XI.1989-III.1990). Long term probes made from silicon (Si) and stainless steel (SS) were located at eighteen different toroidal and poloidal positions (Fig.1) at a radius r=77cm (wall radius r_w=80cm) for the whole working period. The transfer and diagnostic station WASA-II [4] was used for simultaneous exposure (0,1 to 10 hours) of a SS and a tantalum collector probe and there in-situ analysis. Their surface concentration of impurities on the WASA probes were analyzed by AES, that on the long term collecting probes by EPMA, AES, SIMS, PES and PIXE methods. Additionally, the residual gas composition was monitored. After the end of the working period, when T-15 was open to air, a visual inspection of the first wall was carried out.

The working period of T-15 [5] included an extensive cleaning procedure: baking out up to a liner temperature of T=250°C followed by several cycles of glow discharge cleaning (GD) in argon, hydrogen and helium with varying parameters (see table 1), and about 100 ohmic discharges ($I_p \leq 10.7$MA, $B_t \leq 12.7$ T, $t_d \leq 1.2$ sec). The vacuum vessel of T-15 is made from stainless steel, two ring and a rail limiter (Fig.1) are made from graphite.

The surface analysis has shown that the long term probes were covered by a film having a thickness of 10-20 nm. It contains mainly carbon and oxygen. Usually the Fe,Cr,Ni content does not exceed 20% (see table 2). The variation of the C- and O-concentration over all probes is in the order of the measured variation across a single sample. We can conclude that there is no proof of a clear inhomogeneity in the toroidal and poloidal distribution of the deposited impurities even for carbon which definitely stems from local sources (limiters).

Typical depth profiles observed on long term probes by AES and SIMS are shown in Fig. 2. The elements are homogeneously distributed in the layer. The high oxygen content in the films (table 1) is contributed mainly by the SiO_2 interface and the adsorption due to probe transfer on air. The slower decay of the Fe,Cr,Ni - signals inside the bulk material compared to the C and O signals might be explained by diffusion into Si at baking temperatures ($T \leq 200$°C).

As always the same collecting probes (SS, Ta) were exposed during all GD cycles (the exposure was interrupted only during the in-situ analysis) we may assume that its surface composition is the same as for the wall. The surface concentration of various elements on the SS and Ta probes measured after each GD cycle is shown in fig.3. At the end of the cleaning procedure the composition of the deposited layer on the WASA probe was qualitatively the same as on the long term probes after the end of the whole working period. It seems, that the films were deposited mainly during GD. This is confirmed by

the fact that erosion traces typical for GD are predominating the typical erosion traces of ohmic discharges and that SIMS depth profiles shows a nearly homogeneous distribution of the GD anode material (Titanium) in the layer on the long term probes.

The WASA-II transfer and analysis station was used to monitor the temporal evolution of impurity deposition. These measurements demonstrate that sputtering and redeposition of iron (Fe,Cr,Ni) occurred continuously during the cleaning procedure, wheras the iron concentration is higher in a Helium GD than in a Hydrogen GD (see fig.3, discharge V-X). This difference corresponds to a higher physical sputtering yield of SS under Helium irradiation compared with Hydrogen. For carbon sputtering there is no significant difference between helium and hydrogen GD because physical sputtering rises in helium but chemical effects became negligible.

Intensive carbon sputtering occurred at the beginning of the cleaning procedure, especially during the GD in Ar. Analysis of the temporal variation of the carbon concentration during each GD cycle revealed that carbon sputtering was much more intensive at high wall temperatures (100-140°C) than at low temperatures (-80-0°C). This is confirmed by the corresponding RGA data and explained by a rise of chemical sputtering.

A combination of the data from the collector probes and the residual gas analysis allowed us to estimate the total amount of carbon and iron sputtered during the operation period of T-15. This amount is about 0.5-1.0 g for iron and about 3.0-5.0 g for carbon. The sputtered iron is uniformly redeposited around the vessel. About 50% of the sputtered carbon formed gaseous compositions (CO, CH_4, C_2H_4, ...) - and were pumped away from the vessel.

CONCLUSIONS:

1. The collector probes around the vessel were covered with a thin film (≤20nm thickness) consisting of carbon (≥40%), oxygen and SS-components.
2. The film is the result of a low net deposition rate (1-2 Å/sec) and hinders the GD to remove the iron oxide layer from the liner.
3. The impurities sputtered during the GD cleaning are redeposited homogeneously around the vessel although at least the carbon source is a locale one.
4. Sputtering of iron in a helium GD is about 3 times higher than in hydrogen. This difference is negligible for carbon. With the hot vessel (100-140°C) carbon is sputtered several times more intensive than with the cool one (-80-0°C).
5. During 90 hours of GD cleaning 0.5-1.0 g iron and 3-5 g carbon were redeposited.

REFERENCES

/1/ P.C.Stangeby,G.M.McCracken, Nucl. Fusion, 30 (1990) 1225.
/2/ E.Taglauer, J.Nucl.Mater., 128&129 (1984) 141
/3/ P.Wienhold, et al., Proc. 16th EPS Conf., Venice 1989, Vol.III, p.999
/4/ M.Behnke et al., Vacuum, 37 (1987) 145-147
/5/ N.N.Britousov,A.N.Vertiporokh et al., 16th Symposium on Fusion Technol., London 1990, Abstracts, p.76

Table 1: Parameters of the Glow discharge in the tokamak T-15

GD Nr.	Working gas	Duration /h	Wall temp. /°C	Pressure /mtorr	Current. /A
I	Ar	3.5	80	1-5	8-12
II	H_2	5.0	90	2-4	8-12
III	H_2	6.5	100	4	10
IV	H_2	7.5	115	4	10
V	H_2	10.0	10	3-4	4-8
VI	H_2	4.0	-80	4	12
VII	He	6.0	-70	2.5-3.5	12
VIII	He	28.0	140- 170	2.5-3.5	12
IX	He	8.0	40-(-10)	4	12
X	H_2	11.0	-30-(-60)	4	12

Table 2: Impurity concentration on the surface of the long term Si-probes measured by EPMA (C,O) and PES,PIXE (Fe,Cr,Ni)

Probe Nr.	C 10^{16}	O 10^{16}	Fe 10^{15} at/cm^2	Cr 10^{15}	Ni 10^{15}
1	4.3	5.6	13.2	4.1	3.3
2	3.2	2.1			
3	3.9	2.0	9.2	2.5	2.0
4	2.8	1.5			
5	3.4	2.8	4.4	1.3	1.2
6	5.1	5.0			
7	7.1	2.7	26.6	9.1	5.0
8	4.3	3.4			
9	2.7	2.5	4.9	1.1	0.9
10	4.7	6.1			
11	3.9	4.0	6.3	1.3	1.3
13	2.7	2.8	8.8	2.5	2.0
14	6.2	5.0			
15	4.4	3.9	3.5	0.5	0.4
16	5.6	4.6			
17	4.9	6.0			
18	5.7	3.7			

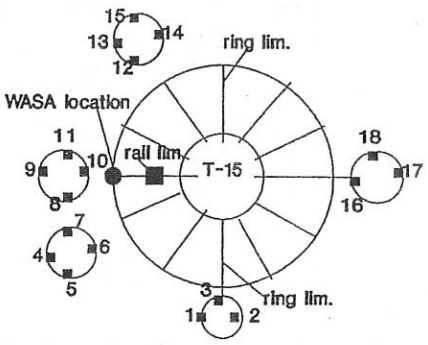

Fig.1: Location of the long term probes, the WASA-II probe and the graphite limiters inside the T-15

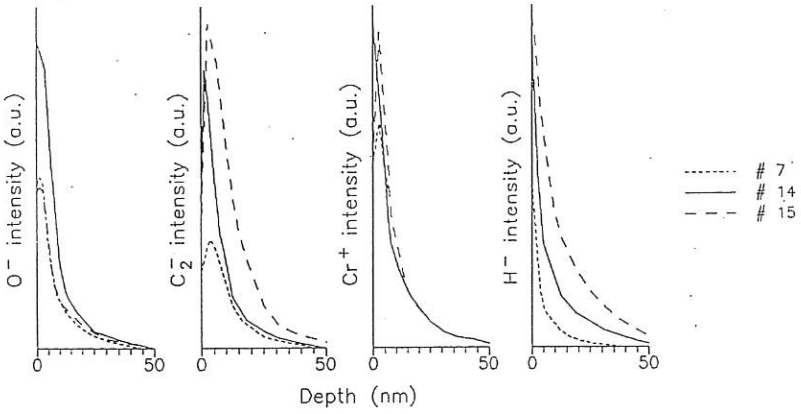

Fig. 2: Depth distribution of impurities in the films deposited on Si long term probes. **(a)** SIMS measurements, 7th, 14th and 15th positions.

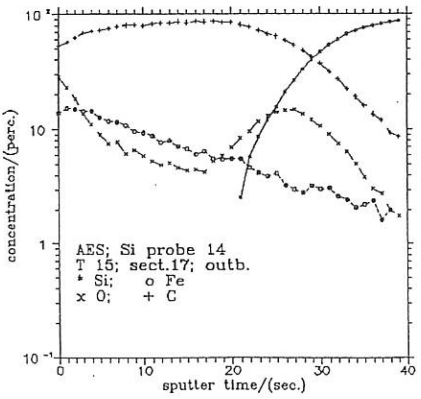

Fig. 2b: Sputter-AES measurements, 14th position.

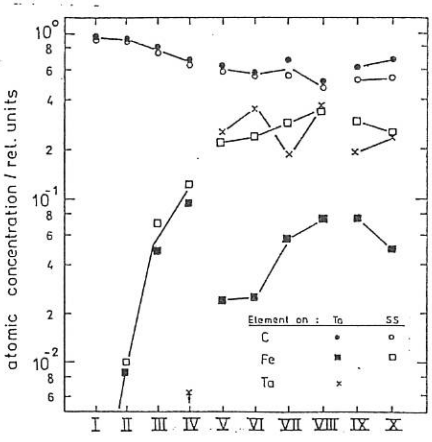

Fig.3. Atomic concentration of various elements on the surface of the WASA-II probes at the end of the given GD.

CHARACTERIZATION OF THE WALL RECYCLING PROPERTIES AND BULK PARTICLE LIFE TIME IN TORE SUPRA

C. Grisolia, T. Hutter, B. Pégourié

Association EURATOM-CEA sur la Fusion Contrôlée
Centre d'Etudes Nucléaires de Cadarache, B.P. n°1
F-13108 Saint-Paul-lez-Durance

One of the major goals of TORE SUPRA is the study of very long plasma pulses for which the density control is of crucial importance. For quasi steady-state conditions (recycling coefficient R≈1, sources and sinks equal), only three parameters are sufficient to describe the total particle balance:

-*i*- the number of particles present in the inner wall and "available" to refuel the plasma : N_W,

-*ii*- the R≈1 equilibrium plasma density : n_e^{∞},

-*iii*- the particle confinement time : τ_p.

The analysis of long series of successive shots (up to 30) which only differ from one another by the wall saturation state allows to estimate N_W and n_e^{∞}. The experimental procedure is the following : before the beginning of a series of shots, the whole vacuum vessel (≈90m^2) is cleaned by 60 hours of He glow discharges (≈4.7 10^{23} particles removed (870 Pa.m^3), i.e. about 5.2 10^{21} particles per m^2 of graphite coated wall). During the first part of the experiment, the inner wall (≈10m^2 in direct interaction with the plasma) is filled up with a series of identical D_2 ohmic shots (Figure 1) : the discharge is initiated on the outer limiter; a gas puff (between 0.5 and 1.2 Pa.m^3/s during 3 to 4s) begins ≈0.75s after the plasma start up and, 2s after the end of the puff, the plasma is moved onto the inner wall. The behaviour of the plasma density just after the plasma motion is a good indicator of the wall saturation state (see [1] for similar results). Once the wall is completely saturated, several He discharges are used to remove most of the particles present in the inner wall. When the pumping rate after the plasma displacement recovered its initial value, a series analogous to that described above begins. During the whole series, the balance of the gas injected or pumped and the isotopic ratio $\rho_p=n_H/(n_H+n_D)$ of the plasma and of the pumped gas are recorded.

The particle confinement time τ_p is estimated from the evolution of the plasma isotopic ratio ρ_p (measured by fast neutral analysis) during pellet injection experiments.

WALL PARTICLE CONTENT

The basic hypothesis is that the particle confinement time and the recycling coefficient are equal for both hydrogen and deuterium. In these conditions, once a wall-plasma equilibrium is reached, ρ_p is identical to the wall isotopic ratio ρ_W. Let us define, for the i^{th} shot :

- N_H^i and N_D^i : the total number of H and D atoms present in the inner wall after the shot;
- Q_D^i : the total number of D atoms injected during the shot;

- QP_H^i and QP_D^i: the total number of H and D atoms extracted by the turbomolecular pumps after the shot;
- q_H : a constant H flux coming from the bulk graphite and refilling the outer layers of the inner wall;
- $\delta t(i,i-1)$: the time interval between shots n° i and i-1.

N_H^i and N_D^i are then governed by the two equations :

$$N_H^i = N_H^{i-1} + q_H \cdot \delta t(i,i-1) - QP_H^{i-1}$$

$$N_D^i = N_D^{i-1} + QI_D^i - QP_D^{i-1}$$

Since QP_H^i is negligible in these experiments, one obtains:

$$\rho_p^i = \left(N_H^o + q_H \sum_{j=1}^{i} \delta t(j,j-1)\right) / \left(N_H^o / \rho_W^o + q_H \sum_{j=1}^{i} \delta t(j,j-1) + QI_D^i + \sum_{j=1}^{i-1} [QI_D^j - QP_D^j]\right)$$

Only three quantities are unknown in the above expression : q_H, N_H^o and ρ_W^o. The latter is taken equal to ρ_p^1 (this is not a critical choice).The others are then adjusted to best fit the experimental ρ_p^i's. An example is given Figure 2 for a series of 16 D_2 shots. The corresponding values for the wall H flux and initial content are : $q_H = (3.5 \pm 0.25)\ 10^{16}$ atoms/s/m^2 and $N_W^o = N_H^o / \rho_W^o \approx 3.6\ 10^{21}$ atoms. During this experiment, N_W increases from $3.6\ 10^{21}$ (shot TS 5066) to $N_H^M = 5\ 10^{22}$ atoms (shot TS 5085), this last value corresponding to a complete saturation of the wall (more generally, this maximum value N_H^M can vary from 5 to $8.5\ 10^{22}$ atoms ; i.e. 5 to $8.5\ 10^{21}$ atoms per m^2).

The inner wall is then cleaned by ≈5 He plasma discharges before another series of D2 shots. The comparison between two successive series of D2 shots gives an estimation of the number ΔN_W of particles removed from the inner wall by the cleaning procedure. Since, in every case, one has :

$$\Delta N_W >> \sum_{He} (QP_D + QP_H - q_H\, \delta t)$$

a part αN_W of the inner wall content must be more uniformly spread on the whole vessel surface during the He discharges. A good agreement is found for $0.05 < \alpha < 0.15$.

EQUILIBRIUM AVERAGE DENSITY

The effective particle confinement time, τ_p^*, is defined by $\tau_p^* = N_e/(\Gamma - dN_e/dt)$, where N_e is the total number of electrons in the plasma. When the gas puff intensity Γ is varied during the current plateau of D_2 limiter discharges, τ_p^* is shown to be proportional to $1/\Gamma$. An example of such a behaviour is shown Figure 3 for shot TS 3626. This implies that, for long times, N_e tends towards an asymptotical value $N_e^\infty = \Gamma \tau_p^*$. It is therefore not possible to change significantly the plasma density on a time interval much larger than τ_p^* : the wall pumps or outgasses according as N_e/N_e^∞ is larger or smaller than 1. This prominent part taken by the wall in the discharge particle balance is not restricted to the case described above. A similar behaviour is observed during pumped limiter experiments [2] : most of the flux which enters the limiter throats (≈8% of the parallel flux in the SOL) is due to the wall outgassing whereas the plasma core is only weakly affected by the pumping ($\Delta R \approx 9$‰).

The equilibrium density $n_e^\infty = N_e^\infty / V_p$ (where V_p is the plasma volume) was measured for various wall saturation states and values of the ohmic power P_Ω. It is given, with a good accuracy, by the following scaling (for $0.8 < P_\Omega < 1.15$MW):

$$n_e^\infty \approx n_{sl} = 9.5\ 10^{14}.\ N_w^{1/5}\ .\ P_\Omega^{3/4}$$

An example of comparison between a series of experimental data and the values given by the above scaling law is shown Figure 4.

PARTICLE CONFINEMENT TIME

The Figure 5 shows ρ_p, Ne and the plasma current Ip for the shot TS 3174. It is a H_2 plasma discharge and each gap in Ne corresponds to the injection of a D2 pellet. During the current plateau, there is no gas puff and the plasma is maintained on the inner wall. At each pellet injection, ρ_p decreases almost instantaneously, in a time shorter than the CX diagnostic time resolution (a few ms), and then recovers its preceding equilibrium value with an exponential like evolution of characteristic time τ_m. During this transient phase, the hypothesis $\rho_p = \rho_W$ is no longer verified and the time history of the total numbers of H and D in the plasma (N_H and N_D) is governed by the two equations:

$$dN_H/dt = - N_H/\tau_p + R.\rho_w.\ (N_H+N_D)/\tau_p$$

$$dN_D/dt = - N_D/\tau_p + R.(1-\rho_w).(N_H+N_D)/\tau_p$$

from which one obtains : $d\rho_p/dt = -(\rho_p-\rho_w)/\tau_m$ (with $\tau_m = \tau_p/R$).

The value of τ_p^* is deduced from the Ne decay during the first 1/2s after the pellet injection. Since $R = 1-\tau_p/\tau_p^*$, one obtains : $\tau_p = \tau_m.\tau_p^*/(\tau_p^*+\tau_m) \approx \tau_m/(1-\tau_m/\tau_p^*)$. From the data displayed fig.5, one has $0.1 < \tau_p < 0.17$.

CONCLUSION

In this paper, it is shown that the steady-state plasma equilibrium density n_e^∞ is strongly dependent on the inner wall saturation state (i.e. N_W). The relation between these two quantities is quantatively established for 1.2 to 1.5MA ohmic discharges in TORE SUPRA. The wall-plasma equilibrium mainly depends on three parameters : the wall saturation (N_W), the input power in the discharge (P_Ω, for the experiments discussed in this paper) and the particle confinement time (τ_p). This last quantity is determined by the analysis of the time evolution of the plasma isotopic ratio ρ_p during pellet fuelled discharges, leading to the four main parameters (N_W, P_Ω, τ_p and n_e^∞), characterizing, at the lowest level, the discharge global particle balance. Since any change in the plasma or in the wall changes the wall-plasma interactions, this study is only relevant for ohmic discharges. Particularly, a modification of the plasma edge (during ergodic divertor operations, for instance) or input power (additional heating or current drive) can modify these quantities.

REFERENCES:

[1] H.F.Dylla, P.H.LaMarche, M. Ulrickson *et al.*, Nucl. Fus. **27** (1987) 1221

[2] C.C. Klepper, P. Bonnel, J.L. Bruneau *et al.*, J. of Nucl. Mat. **176 & 177** (1990) 798

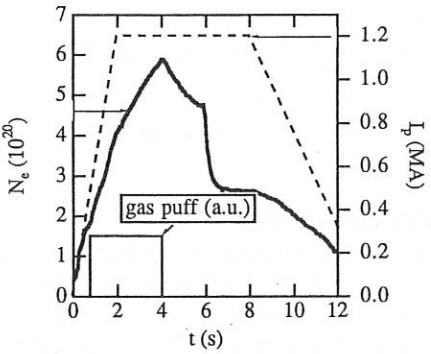

Figure 1: Time history of I_p, N_e and gas puff Γ for shot TS 5068.

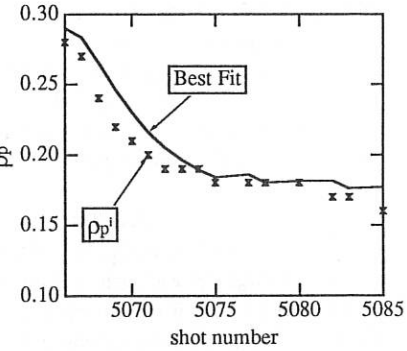

Figure 2: comparison between the experimental and calculated ρ_p^i's for a series of 16 shots.

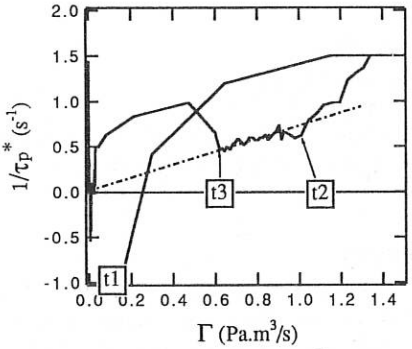

Figure 3: Evolution of $1/\tau_p^*$ with Γ.
t1= beginning of the shot;
t2 = current plateau;
t3 = end of the gas puff.

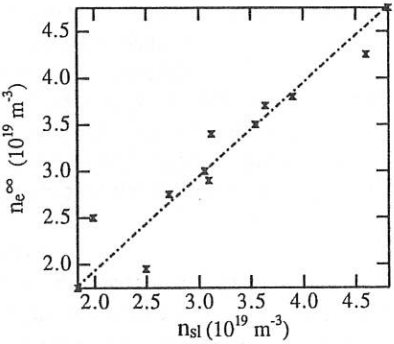

Figure 4: Comparison between n_e^∞ and n_{sl}.

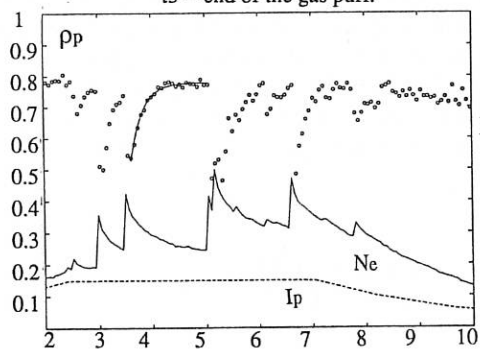

Figure 5: Time history of ρ_p, N_e and I_p for the pellet shot TS 3174. I_p=1.5MA during the current plateau; the maximum value of N_e is 7.7 10^{20}.

SCALING PROPERTIES FOR THE EDGE TURBULENCE IN THE ATF TORSATRON

C. Hidalgo*, M. A. Meier#, T. Uckan, Ch.P. Ritz#, J.H. Harris, A.J. Wootton#, T.L. Rhodes#

Oak Ridge National Laboratory, Oak Ridge, TN 37831, USA
**Asociación EURATOM-CIEMAT, 28040 Madrid, Spain*
#Fusion Research Center, University of Texas, Austin, TX 78712, USA

Introduction

Much effort is being done to understand the connection between electromagnetic turbulence and anomalous transport. There is experimental evidence showing that the induced turbulent transport can account for most of the particle transport in the edge region of the plasma in tokamaks and stellarators (1,2). Although our understanding of the plasma turbulence has been improved during the last few years, the nature of the instabilities responsible for the turbulence have not been identified yet (3).

Due to the accessibility of the plasma edge, the experimental study of the scaling properties of fluctuations and transport can best be done in this plasma region, thus providing experimental criteria to test theoretical models for edge turbulence. Studies of this type have been carried out in the outer region of the plasma ($r/a_{shear} > 0.98$) in the TEXT tokamak (4), where a_{shear} denotes the plasma region where the phase velocity of the fluctuations reverses direction (shear layer). However, it has been recently shown that the shear layer location determines a characteristic plasma region with different drives for the turbulence in the edge ($r/a_{shear} > 1$) and in the scrape-off layer ($r/a_{shear} > 1$) region (3,5).

In this paper the scaling properties of the edge fluctuations and transport have been studied in the plasma edge region ($r/a_{shear} = 0.8$-0.9) in the Advanced Toroidal Facility (ATF).

Experimental

ATF is a l = 2, M = 12 field period torsatron with $R_0 = 2.10$ and $\bar{a} = 0.27$ m. In the present experiments plasmas were achieved using electron-cyclotron heating (ECH).

Discharges with $P_{ECH} \approx$ (200-400) kW, $\bar{n}_e \approx$ (2-6) 10^{12} cm^{-3}, stored energy $S_E \approx$ (1-2) kJ, and magnetic field B = 1 T have been studied.

Plasma edge turbulence has been characterized by means of Langmuir probes using the experimental methods described elsewhere (1).

Influence of local electron temperature on edge turbulence

When the line average density is changed in the range (4-6) 10^{12} cm^{-3}, the edge electron density and the radial electric field ($E_r \approx$ (1-2) V/cm) profiles remain basically constant whereas the local electron temperature decreases from 40 to 10 eV. Figure 1 shows the influence of the edge electron temperature on the poloidal phase velocity of the fluctuations (v_{ph}) as well as on the velocity due to the radial electric field ($v_{ExB} = E_r / B$). The phase velocity is in the electron diamagnetic drift direction with a value in the range (0.5 - 2) x 10^5 cm/s and is considerably larger than v_{ErxB} ($\approx$ 0.2 x 10^5 cm/s). It has to be noted that v_{ph} increases with increasing electron temperature. In this plasma region the phase velocity is comparable to the electron diamagnetic drift velocity ($v_{ph} \approx T_e / B\, L_n$) and shows a similar scaling with temperature. This situation is completely different to what happens in the shear layer region, where v_{ph} is controlled by the v_{ExB} velocity (6).

The influence of local electron temperature on the spectral width of the k-spectra (σ_k) and σ_k/k is shown in Figure 2; σ_k is inversely proportional to the poloidal correlation length and σ_k/k is the ratio of the mean wavelength to the correlation length. In the studied temperature range, the spectral width decreases with temperature whereas σ_k/k is basically independent of temperature. The product $k\rho_s$, where ρ_s is the ion gyroradius at the electron temperature, is about $\approx$ 0.05 - 0.1, and is temperature independent. In the studied temperature range $\tilde{\phi}_{fl}/T_e$ as well as T_e/T_e (measured by means of the triple probe method) are systematically larger than $\tilde{n}/n$ (5).

The influence of local temperature on density fluctuation levels has been studied in plasmas with different line average density. Figure 4 shows density, temperature and density fluctuation profiles measured in plasmas with $\bar{n}_e \approx 4 \times 10^{12}$ cm^{-3} and $\bar{n}_e \approx 6 \times 10^{12}$ cm^{-3}. The electron temperature in the edge decreases with increasing the average electron density, while the edge radial density profiles are not much affected. The modification in the local temperature in the range (10 - 50) eV, keeping unchanged the density profile, does not have any significant influence on the density fluctuation levels (i.e. $\tilde{n}/n \approx T_e^0$). Density gradient driven turbulence models by Terry-Diamond and Waltz-Dominguez (7,8) predicts $\tilde{n}/n \approx T_e^{0.5}$. So far, no dependence of $\tilde{n}/n$ with L_{Te} has been observed.

Density gradient drives

Density fluctuation levels increase with decreasing density scale length (L_n) (Fig.4). This is in agreement with the basic prediction of density gradient driven turbulence models. However, it has to be noted that a dependence $\tilde{n}/n \approx 1/L_n$ is also expected in other turbulence models such as impurity radiation (9) and resistive gradient driven turbulence (10). Besides density fluctuation levels is well described by the mixing length level, $\tilde{n}/n \approx (0.5\text{-}1)/(kL_n)$, where k is the perpendicular wave number.

Particle fluxes

The particles fluxes increases with decreasing σ_k/k (Fig.5). This is consistent with the expectation that a transport barrier is formed when the correlation length becomes as small as the mean wave length of the fluctuations.

Particle fluxes inferred from electrostatic fluctuations scale as, $\Gamma \approx n\,\tilde{n}$.

References

(1) Ch.P. Ritz, L. Hin, T.L. Rhodes and A.J. Wootton, *Phys. Rev. Letters* **65**, 2543 (1990).

(2) T. Uckan, C. Hidalgo, J.D. Bell, et al., *Physics of Fluids B* (1991, in press)

(3) Ch.P. Ritz , T.L. Rhodes, H. Lin, et al., *Proc. 13th Int. Conf. on Plasma Physics and Controlled Nuclear Fusion Research, Washington, 1990 (IAEA, Vienna, 1991)* (in press).

(4) T.L. Rhodes, FRCR #352 (1989)

(5) C. Hidalgo, J. Harris, T. Uckan, et al., *Nuclear Fusion*, (1991, in press)

(6) Ch.P. Ritz, R.D. Bengtson, S.J. Levinson and E.J. Powers, *Physics of Fluids* **27**, 2956 (1984).

(7) P.W. Terry and P.H. Diamond, *Physics of Fluids* **28**, 1419 (1985)

(8) R.E. Waltz and R.R. Dominguez, *Physics of Fluids* **26**, 3338 (1983)

(9) D.R. Thayer and P.H. Diamond, *Physics of Fluids* **30**, 3724 (1987).

(10) T.S. Hahm, P.H. Diamond, P.W. Terry, L. García and B.A. Carreras, *Physics of Fluids* **30**, 1452 (1987).

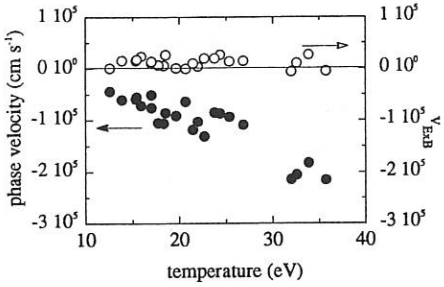

Fig. 1 Phase velocity of the fluctuations and the velocity due to the radial electric field as a function of the local electron density.

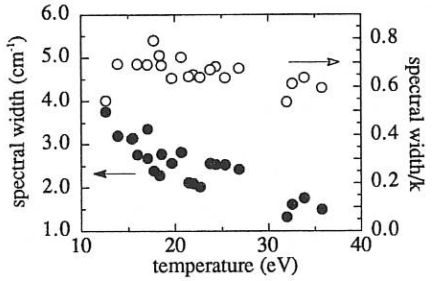

Fig. 2 Spectral width of the k-spectra (σ_k) and σ_k/k versus the electron temperature.

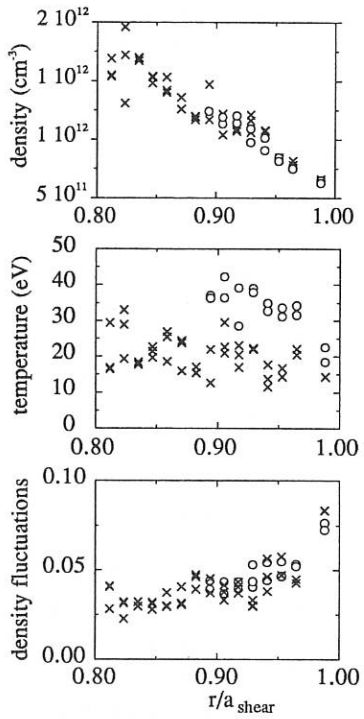

Fig. 3 Radial profiles for density, temperature and density fluctuation levels measured in plasmas with $\bar{n}_e \approx 4 \times 10^{12}$ cm^{-3} (o) and $\bar{n}_e \approx 6 \times 10^{12}$ cm^{-3} (x).

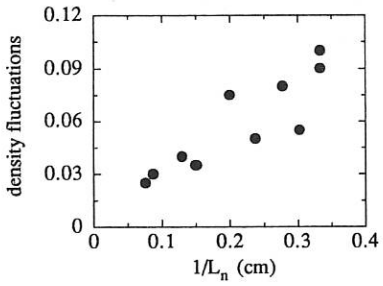

Fig. 4 Density fluctuations versus $1/L_n$.

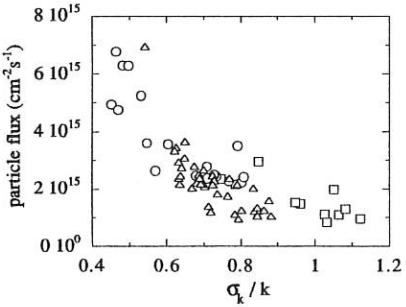

Fig. 5 Particle flux versus σ_k/k.

EXPERIMENTAL STUDY ON EDGE ELECTRIC FIELD IN HELIOTRON-E CURRENTLESS PLASMA

T.Mizuuchi, H.Matsuura*, K.Kondo, S.Sudo, F.Sano, H.Zushi, S.Besshou, H.Okada, K.Miyake, T.Obiki and Heliotron Group

Plasma Physics Laboratory, Kyoto University,
Gokasho, Uji, 611 JAPAN
*College of Engineering, University of Osaka Prefecture,
Mozuume-machi, Sakai, 591 JAPAN

1. Introduction

Heliotron-E is a stellarator/heliotron device with l=2/m=19 helical coil. In this magnetic configuration, edge plasma flows to the wall in distinct flux bundles[1,2]. This situation is similar to an open divertor in tokamaks. In contrast to tokamaks, however, the field line in the edge region of the stellarator/heliotron device moves stochastically. In order to construct a divertor system by using this flux bundles, uniformity of particle flux and heat load on the wall (divertor plates) is one of important key issues. On the other hand, as the flux bundles are terminated at the metal surface, it is not required the ambipolarity in the plasma flow in a local area. The edge plasma transport might be affected by the electric field due to this non-ambipoler flow in the edge region.

Besides the heat load on the wall, the ion saturation current and the floating potential to the wall are measured with poloidal calorimeter arrays of thin metal plates located at four different cross sections in one helical pitch of the torus (Fig.1).

2. Plasma distribution near the wall

Figure 2 shows an example of the distributions of the heat load, the ion saturation current, Is, and the floating potential, Vf, for an ECH plasma. The line averaged electron density was $(1.2-1.5)\times10^{19}m^{-3}$. In this case, the magnetic configuration parameters[3], α^* and β^*, are 0.05 and -0.192, respectively (an experimentally optimized configuration). As in the next section, the edge density suddenly jumps up to a high value during RF pulse. Is and Vf at two different times, before (filled symbols) and after (open symbols) the jump-up of the edge density, are plotted. As for the heat load, the integrated value during a discharge is plotted.

The localization of the ion saturation current and the wall heat load on the divertor trace[2] in one poloidal cross section is reported in [4]. The same localized distribution

was confirmed for other three poloidal sections. The variation in the peak value of the ion saturation current among these sections is kept within a factor of three except the sections #9.5-O and #8.5-B. Especially, a very high current was observed at #8.5-B, where large spikes in the floating potential at the density clamping were observed.

Not only the absolute value but also the polarity of the floating potential is varied in poloidal and toroidal directions. This suggests that the ambipolarity of the plasma flow is broken in a local area. Since it was observed that the polarity of the floating potential of many plates was consistent with the direction of ∇·B drift and was reversed by the change of the helical field direction, it is considered that ∇·B drift has an important part in this non-ambipoler flow.

3. Floating potential at the density clamping

For ECH plasma, the density clamping is usually observed in Heliotron-E and this prevents controlling the plasma density. Figure 3 shows an example of the time dependence of the line averaged electron density in the standard configuration ($\alpha^* = 0$, $\beta^* = -0.185$). Time traces of H_α-emission, the ion saturation current of a Langmuir probe at the divertor trace and the floating potential of #17 plate (#8.5-B section) are also plotted. As in this figure, the intensity of ion saturation current and H_α-emission suddenly increase during RF pulse. At almost the same time, the line averaged density starts to decrease. Once this has happened, it is hard to recover or increase the density by gas puffing.

The way of change in the floating potential at the density clamping is not the same for each plate. The most interesting is a spike in potential observed at some positions (Fig. 3). Both of negative and positive spikes were observed depending on the positions, but the largest one is negative spikes ($Vf \lesssim -80$ V) at #8.5-B. Taking account that the typical electron temperature is about 20 eV near the wall at the steady-state phase (no data at this transient phase at present), this large negative spike suggests the possibility of the burst of high energy electrons. Since these abrupt change of the edge plasma is not observed when a carbon limiter was deeply inserted into the core region ($< r/a > \sim$ 0.7), it is considered that this is an edge relating phenomenon. On the other hand, the uncontrollable density decay can be reduced by superimposing toroidal field ($\alpha^* > 0$) even without the limiter. However, the burst of edge plasma is still observed here. In this case, the outer plasma edge might contact with bumper limiters or other materials at the high field side. This suggests that not the gas puffing at the low field side but the increase of gas feed due to change of recycling or fueling efficiency caused by contact with materials at the high field side improves the situation.

Recently, a new clamping-free mode was observed even in the standard magnetic limiter configuration. In this mode, not only the density was kept high but also the rapid increase of H_α-emission and the ion saturation current was not observed. The large negative spike in the floating potential also disappeared. Up to now, this mode is out of our control but it seems that the key parameter is a little change of the filling pressure (or

the recycling condition) just before RF pulse or the pre-ionization condition. Since the electron temperature of the core plasma was almost the same as that in the low density case with clamping, the internal energy of the confined plasma increased in this mode.

4. Conclusion

In order to study the distribution and the characteristics of the particle/heat flow to the wall, the ion saturation current and the floating potential near the wall were measured for ECH plasma.

- Localization of the flux expected from the field configuration was experimentally confirmed.
- The non-uniformity of the floating potential in poloidal and toroidal directions suggests that the ambipolarity of the plasma flow is broken in a local area. $\nabla \cdot B$ drift seems to take an important part in the particle flow.
- Relating to the abrupt increase of ion saturation current at the density clamping, a large negative spike in the floating potential is observed.
- The new ECH discharge mode without rapid increase of the ion saturation current and a large negative spike in the floating potential was observed. In this mode, the internal energy of the core plasma was increased compared with that in the clamping mode.

Acknowledgment

We are grateful to all the collaborators for their excellent experiments and useful discussions.

Reference

[1] T.Mizuuchi, et al., J.Nucl.Mater., 121 (1984) 3.
[2] T.Obiki, et al., Plasma Phys. Controlled Nucl. Fusion Research 1988, Vol.2 (IAEA,Vienna,1989) 337.
[3] T.Obiki, et al., Fusion Tech., 17 (1990) 101.
[4] T.Mizuuchi and Heliotron Group, J.Nucl.Mater., 162-164 (1989) 105.

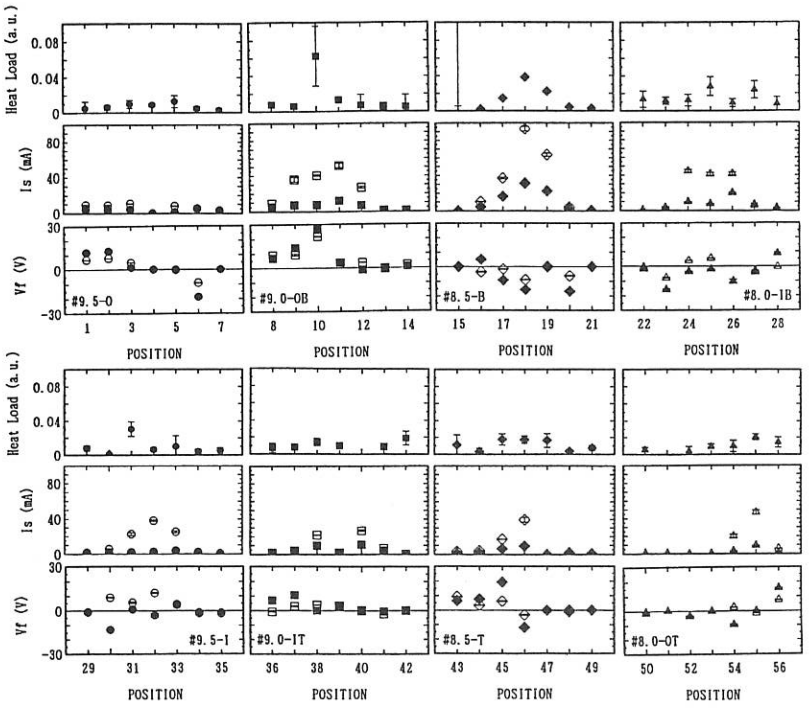

Fig.2 Distributions of wall heat load, ion saturation current and floating potential for different positions (see Fig.1) before (filled symbols) and after (open symbols) density clamping. ($\alpha^* = 0.05$, $\beta^* = -0.195$)

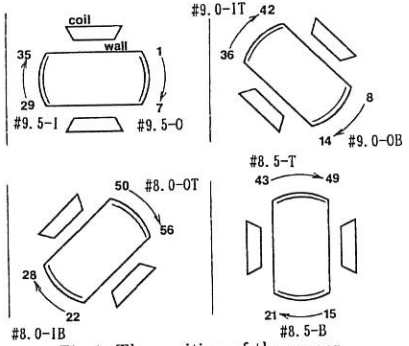

Fig.1 The position of the sensor plates (#1 – #52) at four poloidal cross sections.

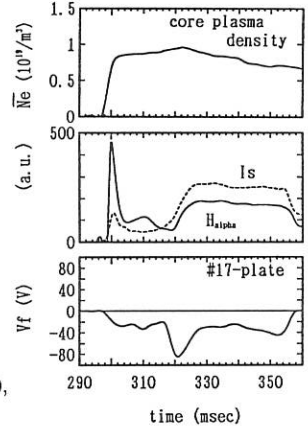

Fig.3 Time trace of an ECH discharge with the density clamping. ($\alpha^* = 0$, $\beta^* = -0.185$)

EFFECTS OF ENERGETIC ELECTRONS ON THE EDGE PROPERTIES OF THE ETA BETA II REVERSED FIELD PINCH

V.Antoni, M.Bagatin, D. Desideri, E. Martines^, Y. Yagi*

Istituto Gas Ionizzati del CNR
EURATOM-ENEA-CNR Association
Padova (ITALY)

^ Scuola Normale Superiore, Pisa, Italy
* Electrotechnical Laboratory, 1-1-4 Umezono, Tsukuba-shi, Ibaraki, Japan

INTRODUCTION

It is commonly observed in Reversed Field Pinch (RFP) experiments that the power transport in the edge flows asymmetrically [1-4]. This asymmetry has been interpreted in terms of current carried by hot electrons generated in the core plasma [5], which have been suggested to be responsible for the anomalous resistivity, commonly observed in RFP's [6]. Combined measurements of heat and particle fluxes by means of calorimeter Langmuir probe and electron energy analyzer in ZT-40M [3], as well as by X-ray emission of targets inserted in the boundary plasma of TPE-1RM15 [7], have been performed to determine the flux and energy spectrum of fast electrons.

EXPERIMENTAL SET UP

On ETA BETA II (R=0.65m, a=0.125m), to investigate the edge plasma with a fine spatial resolution , a small calorimeter Langmuir probe has been developed. The equipment is shown in fig. 1: the electrode (shaped as a half cylinder 1.5 mm wide and 3.5 mm long) is made of tungsten and is supported by an alumina insulator tube, both protected by a graphite cylinder shaped so as to expose the electrode for a collection surface of 1.2 mm^2. The other end is welded to a chromel-alumel thermocouple junction and to a conductor wire. The experimental set up consists of three identical probes with the collector surfaces oriented toward opposite sides (fig.1). The probes can be inserted, through a vertical port, by means of a linear translator, operated by a rack and pinion system, allowing also a rotation around its axis [8]. During the present campaign one electrode was operated as a single Langmuir probe and two electrodes as calorimeters detecting simultaneously the heat fluxes on opposite sides. The probe orientation is defined by the angle α between the normal to the collector surface and the poloidal magnetic field direction. The edge parameters have been investigated in different magnetic configurations obtained varying the pinch ratio Θ ($\Theta = B_\theta(a)/\langle B_\Phi \rangle$) and the reversal parameter F ($F = B_\Phi(a)/\langle B_\Phi \rangle$). The experiment has been

operated at toroidal current I≈150 kA and electron density $n_e \approx 5*10^{19}$ m^{-3} almost constant at normal Θ and slightly decreasing at higher Θ. To avoid other effects, during this operation the density has been varied so as to keep approximately the same I/N ratio (N is the electron line density). All of the data have been taken keeping the probe behind the bellows inner convolution (r=0.125 m). With this probe insertion, global confinement properties such as loop voltage, V_{loop}, toroidal current I, discharge duration, and electron density, n_e, did not show any change with the insertion depth within shot to shot deviations.

EXPERIMENTAL RESULTS AND DISCUSSION

The exposure of the collection area of the probes toward the magnetic field has been varied from normal to tangential incidence. The heat fluxes have been derived from the temperature increment measured by thermocouples, assuming thermal isolation. The heat flux q, incident on the exposed surface, exhibits a strong angular dependence, confirming the behaviour previously found on ETA BETA II [4]. A q shallow minimum found when the surface is parallel to the magnetic field, can be attributed to the partial screening of the incident fluxes by the up stream probe. From the current flow the electron drift side has been distinguished from the ion drift side [4]. The heat flux is maximum on the electron drift side at $\alpha \sim 170^o$ (fig.2), corresponding to the local pitch of the magnetic field lines at the edge as derived by the F/Θ ratio . The heat flux reaches, at r~0.13 m, q~200MW/m^2 on the electron drift side and q~40MW/m^2 on the ion drift side, resulting in an asymmetric heat flux deposition between the opposite sides of ≈ 5.

Varying the insertion of the probes the spatial dependence of the heat flux has been investigated. In fig.3 the heat flux collected on the ion and electron drift side at normal incidence is shown as a function of the insertion parameter $X=r_w-r$ where r_w is the effective radius of the wall. The heat flux on the electron drift side exhibits a discontinuity at r=13.2 ∓ 0.1cm, and this position has been assumed for the effective radius of the wall r_w. The discontinuity of the heat flux on the electron drift side at r_w is a common feature, independent on Θ, and it can be explained by the presence of fast electrons intercepted by the probe when protruded beyond the port hole. The ratio of the heat deposition between opposite sides changes suddenly from a value around or less than 1 for X<0, up to 7-3, depending on Θ, and almost constant for X>0. An e-folding characteristic scale length for the radial dependence of the heat flux, in the ion drift side has been estimated to be $\lambda_{qi} \approx 5$ mm, comparable with that found in TPE-1RM15 $\lambda_{qi} \approx 7$ mm [2].

The parameters of the background cold plasma at the edge measured by Langmuir probes at low Θ are $n_o \sim 10^{19}$ m^{-3}, and $T_o \sim 10$ eV [8]. If the distribution function of the hot electron component is expressed by a half Maxwellian with temperature T_h [3], thus current density j_h and particle density n_h can be plotted as a function of T_h keeping the heat

flux constant (fig.4). In the case of ETA BETA II, a heat flux q = 300 MW/m^2 at r~ 0.125 m, and an estimated edge current density j = 0.5 MA/m^2 , assuming 100% of the current density at the edge carried by the hot electrons, give a minimum estimate for T_h of 280 eV and a maximum estimate for n_h of $5.6*10^{17}$ m^{-3}. In the case of TPE-1RM15 where q = 500-600 MW/m^2 and j = 0.5 MA/m^2, it results T_h > 480-580 eV and n_h < $3.8\text{-}4.3*10^{17}$ m^{-3} [7]. It is worth noting that these minimum estimates for T_h, assuming a half Maxwellian distribution, are roughly comparable to the electron temperature of the core plasma in both machines (200-250 eV in ETA BETA II and 450-650 eV in TPE-1RM15).

In fig.5 the heat flux collected on the ion and electron drift side is shown at different values of Θ. The data refer to X~2mm, and since the F/Θ ratio did not change significantly, the exposure angle has been kept constant at normal incidence. It appears that the heat flux on the electron drift side is strongly affected, whereas on the ion drift side is almost constant. The asymmetry thus decreases from 7 to 3 moving towards higher Θ. In the present context the balance between total input power and heat flux on the probes is not discussed since it would require to consider also the change of the connection lenght due to the change of the magnetic field line pitch. However the heat flux decrease at higher Θ on the electron drift side is suggested to be accounted by a corresponding reduction in the fast electron energy.

Since fast electrons at the edge have been suggested to be directly related to the degree of stochasticity of the plasma, and the magnetic field diffusion coefficient D_m is related to the normalized magnetic fluctuation amplitude b/B, thus the heat flux has been investigated as a function of b/B. Magnetic fluctuation amplitude has been changed by varying the pinch parameter, Θ, while keeping I/N almost constant. In fig.6 the heat flux deposition on the electron drift side is shown as a function of the magnetic fluctuation amplitude. The heat flux in the electron drift side decreses with b/B , and a simple fit shows a dependence as $(b/B)^{-0.8}$, confirming a relationship between fast electron energy and magnetic fluctuations.

ACKNOWLEDGMENTS

The authors would like to acknowledge E. Baseggio and I. Molon for the technical assistance.

REFERENCES

[1] J. N. Downing et al.,J. Nucl. Mater. 128 (1984) 517.
[2] Y. Yagi et al., J. Nucl. Mater. 162-164 (1989) 702.
[3] J.C.Ingraham et.al., Phys.Fluids B2 1 (1990) 143
[4] V. Antoni, M. Bagatin, D. Desideri, Int. Conf. on Plasma Physics (New Delhi, 1989), Vol. I, 141.
[5] A.R. Jacobson and R.W. Moses, Phys. Rev. A 29 (1984) 3335.
[6] R.W.Moses, K.F. Schoenberg, D.A. Baker, Phys. Fluids 31 (1988) 3152.
[7] Y.Yagi et. al.,17th Eur. Conf. on Contr. Fusion and Plasma Phys.(Amsterdam, 1990) Vol.II 545.
[8] V. Antoni et al. , J. Nucl. Mater. 176-177 (1990) 1076.

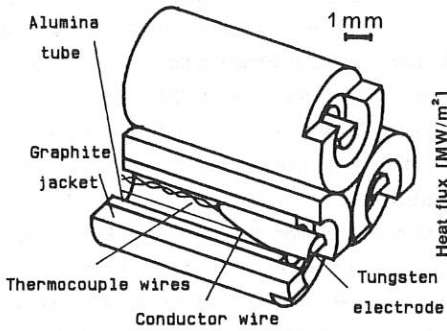

Fig.1

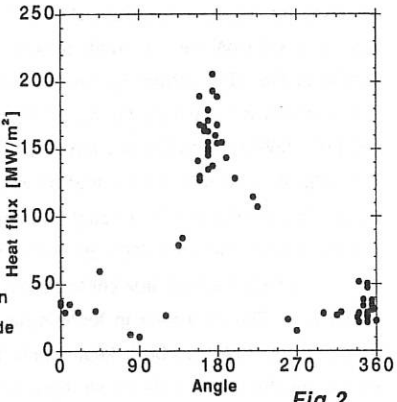

Fig.2

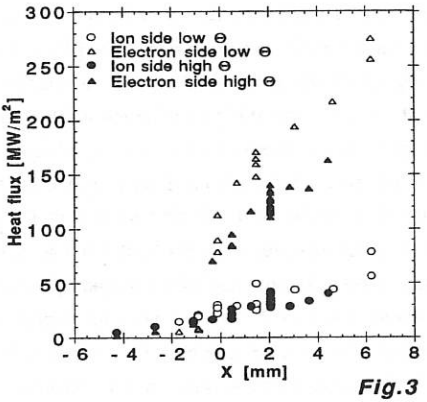

Fig.3

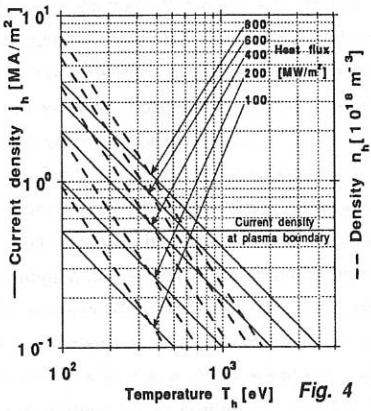

Fig. 4

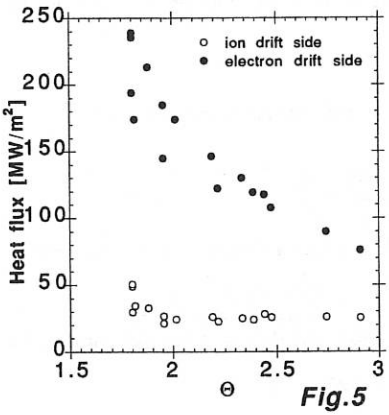

Fig.5

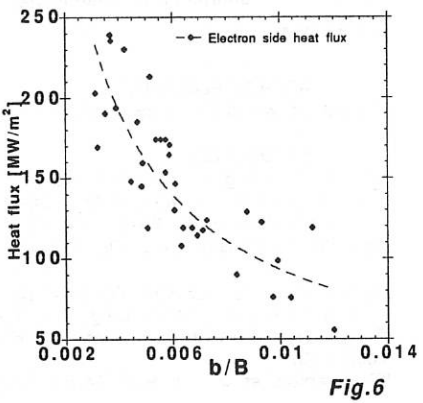

Fig.6

BORONIZATION, RECYCLING AND ISOTOPE RATIO CONTROL EXPERIMENTS ON COMPASS

S.J.Fielding, K.B.Axon, P.G.Carolan, F.V.Chernyshev, M.Dunstan, R.Durst, H.G.Esser+, T.Edlington, S.D.Hanks, I.Jenkins, P.C.Johnson, A.I.Kislyakov*, S.Ya.Petrov*, S.J.Manhood, A.W.Morris, P.Nicholson, B.A.Parham, K.Stammers, T.N.Todd, D.L.Trotman, M.Valovič@, J.Winter+*

AEA Fusion, Culham Laboratory, UKAEA/Euratom Fusion Association, OXON, UK.
+Institut fur Plasmaphysik, Kernforschungsanlage Jülich, Gmbh,
Association Euratom KFA, D–5170 Jülich,Germany
* A. F. Ioffe Physico–Technical Institute,
Academy of Sciences of the USSR, Leningrad, USSR
@I. P. P. Czechoslovakia Academy of Science, Prague, Czechoslovakia

1. INTRODUCTION

Boronization of COMPASS has been carried out using trimethyl boron ($B(CH_3)_3$), a less hazardous alternative to diborane used to boronize other machines [1,2,3,4]. $B(CH_3)_3$ has previously been used on TEXTOR with good results [5], but residues from earlier boronizations using diborane may have influenced the wall conditioning. The data presented here, therefore, correspond to the first use of $B(CH_3)_3$ boronization in a tokamak with no previous surface conditioning by any thin film deposition. This has resulted in excellent, long-term impurity control but with a significant change to the hydrogen recycling characteristics.

In a fusion reactor the relative densities of deuterium and tritium should be controlled at an optimal level. Mass analysis of the emitted atomic fluxes has been proposed as a method to monitor the hydrogen isotope ratio. To test this concept a calibrated neutral particle analyser (ACORD-12) has been developed by the Ioffe Institute capable of making simultaneous measurements of energy spectra and neutral particle fluxes of hydrogen and deuterium. We report here the results of the first experiments on isotope ratio control in COMPASS using a system based around the ACORD-12.

2. BORONIZATION OF COMPASS

Prior to boronization COMPASS wall conditioning was by means of RF assisted glow discharge cleaning (GDC) in hydrogen or helium at room temperature. Moderate vessel baking to 120°C was used only after a major vacuum opening and not simultaneously with GDC. The resulting tokamak discharges did not meet the requirements for ECRH $2\omega_{ce}$ experiments of clean, low density ($\leq 10^{19}\mathrm{m}^{-3}$) low loop-voltage plasmas with no significant runaway/slide-away component. Table 1 gives diagnostic data from well-conditioned standard shots in hydrogen before boronization (machine parameters: R=0.557m, a_L=.196m, 316 stainless steel vacuum vessel, graphite full poloidal limiter, plasma parameters: B_T=1.1T, I_p= 100kA, $\overline{n_e} \sim 1.7\times10^{19}\mathrm{m}^{-3}$). The Z_{eff} value of 2.9 was derived from the measured loop-voltage, Te(0) assuming a parabolic squared temperature profile, Spitzer resistivity and including neo-classical corrections, and indicates a significant impurity content.

The initial COMPASS boronization was made by ~ 15 minutes GDC (unstable, fluctuating 200 – 400V, 15mA – 1A) in pure $B(CH_3)_3$, at a pressure of $\sim 10^{-1}$ mb. This operating pressure was considerably higher than that intended, but the glow self-extinguished at lower values. The deposited layer was estimated to be ~ 55nm thickness, with a B/C ratio of ~0.2.

Wall	UB	B1	B1	B1	B1	B2	B2
Gas	H_2	H_2	He	H_2	H_2	H_2	D_2
Shot No.	2823	2875	3225	4215	4338	4874	5757
B_t(T)	+1.1	+1.1	+1.1	-1.1	+1.1	+1.1	+1.1
Current(kA)	100	105	100	100	95	100	100
Loop Volts(V)	2.4	1.3	1.75	1.65	1.75	1.5	1.4
T_e(eV)	730	690	646	600	600	n/a	750
(SiLi)	±20	±30	±23	± 20	± 50	–	±50
T_i(eV)	190	250	210	110	130	–	155
	±10	±15	±25	±10	±10	–	±15
n_e ($10^{19}m^{-3}$)	1.7	1.6	1.6	1.6	1.4	1.75	1.8
Wall CII (a.u.)	580	120	300	150	205	80	80
Wall OII (a.u.)	270	<4	40	50	54	5	10
Wall CrI (a.u.)	150	<4	90	12	21	<4	<4
Wall H_7 (a.u.)	300	650	40	270	430	400	180
BIV		3000	2900	900	n/a	3000	3000
P_{rad} (kwatts)	180	40	87	n/a	n/a	–	–
P_{rad}/P_{ohmic}	0.75	0.3	0.5	n/a	n/a	–	–
X-ray Anom (SBD Array)	75.6	2.1	n/a	14.1	26.6	–	–
Z_{eff}	2.9	1.1	1.5	1.3	1.4	–	1.6

UB: Unboronized; B1,B2: first and second boronizations.

Table 1 COMPASS Standard Discharges

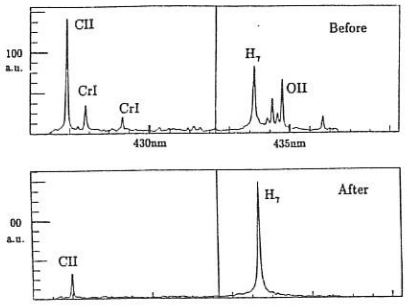

Fig 1 Impurity line emission before and after boronization.

Standard tokamak discharges in hydrogen after boronization display and a dramatic improvement in impurity content. The line emission spectra in fig 1 show that there is a virtual absence of oxygen, chromium and iron influxes and a considerable reduction in carbon($\times 1/5$). Other comparison diagnostic data is given in table 1. As a result of the reduced impurity influx Z_{eff} falls from 2.9 to 1.1. The loop voltage decreases from 2.4V to 1.3V with corresponding reduction in ohmic power input, but with little change in electron temperature, corresponding to $\sim 2\times$ increase in electron energy confinement. Hard X-ray (E>250 keV) emission in these discharges was unmeasurable, in contrast to pre-boronization plasmas which at low density had a substantial runaway content.

In contrast to the impurity behaviour, the hydrogen influx is observed to increase after boronization. This is consistent with the associated increased proton content after boronization with no change in particle confinement.

Initial attempts to run tokamaks after boronization met with considerable difficulty in achieving good density control, a series of low density slide-away discharges being followed abruptly by discharges with uncontrollably rising density. GDC in He to remove hydrogen from the walls led to a repeat of this behaviour. Only after the working gas was changed to helium was good density control obtained.

Table 1 shows that standard helium discharges exhibited a substantial increase in impurity influxes (but still considerably lower than in pre-boronized discharges), presumably due to increased sputtering, but the Z_{eff} value indicates that that the plasma resistance is dominated by the working gas, with significant hydrogen pollution.

Following ~400 discharges in helium, hydrogen was again used as the working gas and good density control was retained.

A gradual deterioration in discharge quality with shot number was apparent and after a total

of ~1500 discharges following boronisation significant increases were apparent in all impurity influxes (table 1). The torus was then reboronized using an admixture of 5%$B(CH_3)_3$ and 95%He, the He buffer allowing operation at low pressure (9×10^{-3}mb), for 120 minutes (stable GDC at 375V, 400mA) and resulting in a 1700nm thick layer of higher B/C, 0.4.
The initial performance of the tokamak closely duplicated that following the first boronization in terms of the low impurity influxes. When the working gas was changed to deuterium no significant increase in impurity levels was observed.

Strongly pumping or strongly hydrogen emitting walls, depending on He GDC, again prevented the required densities from being reproducibly achieved. Controlled-density tokamak operation in hydrogen or deuterium was only obtained after the implementation of a closed-loop density feedback system and regular He GDC.
The observed density behaviour after boronization points to the presence of a large reservoir of hydrogen in the deposited films not accessible to depletion by GDC. This has significant influence on the species content of the plasma when the working gas is changed. After the second boronization, tokamak discharges in helium had an uncontrollable rise indensity due to the emission of hydrogen from the wall. In deuterium the density was better controlled but measurements of the D/H ratio ratio several tens of discharges after the species change-over showed that hydrogen still dominated the discharge (n_D/n_H <0.5). The D/H ratio was observed to increase after He GDC and then decrease shot-by-shot. Fig 2 shows this behaviour in a sequence of D_2 discharges some 160 shots after the change-over from H_2, where it can be seen that n_D/n_H is still low ~1. It is planned to use $B(CD_3)_3$ in the next boronization of COMPASS (after installation of the D-vessel) when significantly isotopically-purer deuterium plasmas are expected to result, but a solution to avoid the high gas retention in the wall is required.

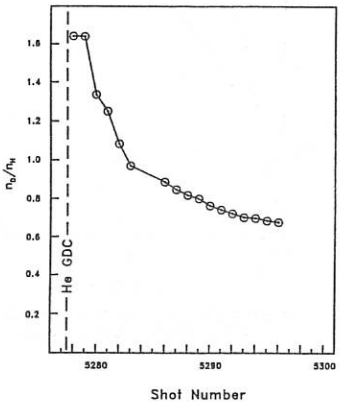

Fig 2 Sequence of deuterium discharges following He GDC ~ 160 shots after changeover from hydrogen gas fill.

ISOTOPE RATIO CONTROL EXPERIMENTS

The isotope control feedback system is shown schematically in fig 3. Analyser channels detecting hydrogen and deuterium atoms of approximately equal energy are electronically processed to generate a difference signal. This difference signal is calibrated in terms of a D/H plasma density ratio by the inclusion of an escape-probability correction factor, generated by a neutral transport simulation code. The D/H flux ratio correction factor has a rather weak dependence on the plasma parameters examined and can be assumed constant (within ±10 %) and equal to 1.42 ($E_{D,H}$=500eV) for the experiments described.

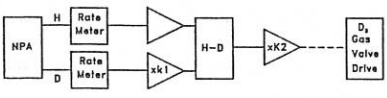

Fig 3 Schematic of isotope control feedback-loop system.

The calibrated difference signal was used to drive the deuterium gas-puff valve, providing closed loop feedback of the D/H density ratio in the plasma core. The demand D/H ratio was set by appropriate choice of amplifier gain k_1.

Initial experiments were undertaken prior to boronization. Plasma conditions were I_p=100kA, B_ϕ=1.1T with hydrogen prefill. NPA energy spectra showed that for all discharges the protons and deuterons were in thermal equilibrium.
H_α/D_α spectroscopy was used to monitor the recycling neutral particle influx. A time delay of $\sim$ 5ms was observed between the demand voltage being applied to the deuterium gas valve and any D_α increase, and an additional $\sim$ 10ms before the deuterium efflux showed a rise. This resulted in a phase delay in the feedback loop and contributed to the observed oscillatory behaviour in the n_D/n_H ratio at high loop gains. The n_D/n_H ratio in the plasma for different demand ratios has been measured in a sequence of discharges and is shown in fig 4. The demand and measured n_D/n_H ratios were similar at low demand values, but deviated very significantly at high n_D/n_H due to increased hydrogen recycling from the walls resulting from the increased D_2 gas puff, and the finite through-put of the D_2 gas valve.

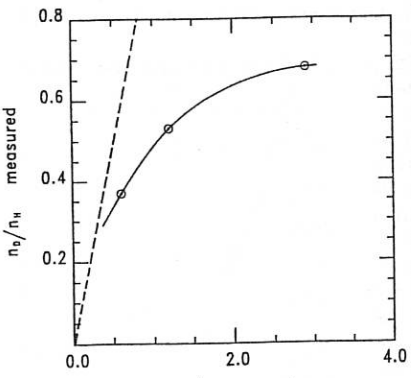

Fig 4 Measured n_D/n_H ratio for different demand n_D/n_H values in H_2 pre-fill discharges, feed-back controlled D_2 gas-puff.

When these experiments were repeated after boronization the hydrogen recycling influx from the wall dominated the discharge constituents. Little deviation from the ambient ratio was possible (n_D/n_H 0.8$\rightarrow$1.1), despite using the maximum available gas puff (30 mbl/s of D_2), before a density limit disruption was produced.

ACKNOWLEDGEMENTS

We are grateful to Dr D.C.Robinson for advice and encouragement, and to the COMPASS Technical and Engineering Sections for machine operations.

REFERENCES

[1] J. Winter, H. G. Esser, L. Könen et al, J. Nucl Mater 162–164, 713(1989).
[2] U. Schneider, W. Poschenrieder et al, J. Nucl Mater 176–177, 350(1990).
[3] C. Hollenstein et al, J. Nucl Mater 176–177, 343 (1990).
[4] T. Dudok de Wit et al, 17th EPS Conf on Contr Fus and Plasma Htg, Amsterdam, 1990.
[5] J. Winter, H. G. Esser, J. Nucl Mater 176–177, 486(1990).

EXPERIMENTAL DETERMINATION OF THE HELIUM PUMPING BY BERYLLIUM

G Saibene, S Clement, J Ehrenberg, A Peacock, V Philipps*, R Sartori

JET Joint Undertaking, Abingdon, Oxon, OX14 3EA, U.K.
*Institut fur Plasmaphysik, KFA Julich, D-5170 Julich, Germany

Introduction: In 1989 the plasma facing material in JET was changed from graphite to beryllium. This change has dramatically affected the global recycling behaviour of the plasma /1/.
An experiment devoted to the measurement of the pumping/release characteristics of He in Be has been carried out in a test bed at JET. The results obtained are compared with global recycling data deduced for He fuelled discharges in JET.
The interest of such a study lies in the assesment of the passive pumping capability of Be for He, which could be important for ash removal in a next step device.

Test bed experiment: The ability of Be to pump He has been measured in a test bed in JET. The experimental rig, originally built to test the Be evaporators, is described in detail in /2/ and /3/. A Be evaporator can be inserted in the chamber and provides an in-situ coating of the internal surfaces. The repeated operation of the evaporator resulted in the chamber walls being coated by a Be layer several hundred of μm thick. The vacuum chamber is equipped with a glow discharge apparatus (RF and DC), with an inlet gas system, regulated by a flowmeter, and with a fast, high precision vacuum gauge interfaced with a digital data acquisition system .
A fresh Be layer a few μm thick was deposited before each measurement, to ensure the reproducibility of the wall conditions. The method used to load the walls with He is essentially the same as that described in /3/ for H and D recycling measurements on Be. The inlet of neutral He gas is adjusted until a stationary pressure is established in the test chamber. A RF assisted DC discharge is then ignited (pumping phase), the total current (i.e. the ion flux) being kept constant. The total pressure evolution is measured . The He pumping experiment was carried out at 3 temperatures : 100, 200 and 290 °C . The energy of the ions was typically around 300 eV and the incident flux ϕ_i was of the order of 0.9 to 2×10^{18} [$m^{-2} s^{-1}$] . The experiment was repeated twice at each temperature, to check for possible "memory effects" of the Be layer.

Results: Fig. 1A shows the typical time evolution of the total pressure p(t) in the test chamber during an experimental run. The graph is divided in 4 zones, corresponding to the 4 phases of the experiment. Fig. 1B shows, for comparison, the analogous p(t) vs. t trace recorded during an earlier experiment /3/, where H was used as the working gas. The two measurements were carried out at the same wall temperature; the initial He ion flux was a factor of 2 to 3 lower than the H flux and the average He ion energy was a factor of 2 higher than for H.
The gross structure of the time behaviour of p(t) during the He experiments is similar to that found in earlier measurements with H. The DC on phase is characterised by a net pumping, with p(t) first decreasing rapidly and then increasing to a stationary value ; when the DC is switched off a release phase is triggered. In addition, the He curve shows some extra features: two fast peaks at the beginning and at the end of the DC phase, and oscillations of p(t), then going to a stationary value higher then its initial one. The superposition of He pumping and desorption of bulk dissolved H could qualitatively explain the p(t) behaviour, as briefly outlined later.

1. *Pumping phase.* The voltage drop across the chamber accelerates the He ions (a mixture of He^+ and He^{++}) to the Be coated walls ; the fast decrease of the total pressure is the measure of the He pumping by the walls: the slope of p(t) evaluated at t = 0 gives the initial ion influx ϕ_1 (maximum wall pumping). The time evolution of p(t) is then determined, at any time, by the balance between the incoming flux and the reemitted flux.
   To characterise the He transient pumping in Be one can define (by analogy to H pumping studies) a characteristic time τ_{He} as the time required for the outcoming flux to reach 1/2 of the value of the incident flux. τ_{He} is linked to the material properties and to the incident flux via the relation $\tau_{He} = T_p/\phi_1$, where T_p is a phenomenological constant which embodies all material-related parameters characterising the He retention and reemission. τ_{He} and ϕ_1 are determined from the pumping curve, for each temperature; the calculated T_p is plotted in fig. 2 , for the 3 temperatures investigated (2 measurements for each temperature). In the same graph, for comparison, we have plotted the best fit curve for H and D pumping in Be /3/. Clearly T_p does not depend on the Be temperature, in the range investigated, and its value is reasonably constant at fixed temperature, indicating a good level of reproducibility in the experiments. At test vessel wall temperature of 300 °C (the temperature at which the JET tokamak is routinely operated) $T_p(He)$ is a factor of 2 to 3 lower than $T_p(H)$. This indicates that, for the same incoming ion flux, one expects Be to pump less He than H.

2. *Release phase.* Shown in the last part of fig. 1 is the He release that occurs when the DC discharge is switched off. The release rate is very similar at all temperatures (it varies between 0.8 and 1 $\times 10^{18}$ [$m^{-2} s^{-1}$]); p(t) reaches a stationary value (e.g. the outgassing flux becomes negligible) faster for He than for H. A comparison of the areas below the pumping and release curves shows that the absolute amount of gas released in the DC off phase does not account for all the He pumped; this could indicate that there is some long term trapping effect . These results contrast with what was observed for H : a high fraction of the implanted H ($\simeq$ 50%) is released within few hundred seconds from the end of the implantation phase and a long tail in the outgassing curve accounts for most of the remaining H. This is in good agreement with the wall outgassing measurements after JET plasma discharges /4/.

3. *Additional features.* Superimposed to the dominant implantation/reemission patterns, there are additional phenomena contributing to the total pressure behaviour. Ion induced desorption of H absorbed in the near-surface layers of Be is a likely candidate to explain the observed peak at the beginning of the implantation, since it would cause a step-like influx of H in the chamber ; the p(t) value at equilibrium at the end of the pumping phase and the fast transient decrease of p(t) measured when the ion flux is switched off are also consistent with this explanation. The oscillations of the pressure could be caused by the superposition of phenomena having different time constants. Trapping and thermal detrapping of He in Be, as well as the presence of any BeO could also influence the transient retention of the implanted He ions. More detailed measurements of the discharge parameters (such as the H and H^+ content) as well as of the material characteristics, in particular the diffusion coefficient of He in Be and BeO, are needed to understand the detailed structure of p(t).

Tokamak discharge data: At any time, the plasma particle content is determined by the balance of the external fuelling, the plasma losses and the release flux from the plasma facing surfaces . To compare the recycling behaviour of He and D during a plasma discharge it is useful to define global discharge parameters /5/ that quantify the dynamical sharing of particles between the plasma and the material surfaces. In particular, we looked at the integrated fuelling efficiency F(t), defined as the ratio between the plasma ion content and the time integrated fuelling. The number of He (or D) ions in

the plasma is obtained from the electron density profile measurements, Z_{eff} data and spectroscopic data of the ionic composition of the plasma.
At constant plasma parameters, one expects the global plasma particle balance to depend on the gas species and on the plasma-facing material; we have analysed He fuelled ohmic limiter discharges (plasma current of 3 MA, toroidal field of 2.1 - 2.2 T) , in the C and Be phases of JET, and D fuelled discharges in the Be phase. All the quoted figures have been calculated 2 s after the start of the current flat-top. The results are summarised in table 1.
In the C phase, the He fuelling efficiency is $\simeq 1$, indicating that there is almost no He pumping by C. This is consisitent with the well known disruptive behaviour of He discharges during the current ramp-down, when the discharge reaches the density limit. The He fuelling efficiency does not depend on wall conditioning, in contrast to what was observed for D /1/.
In the Be phase, net He pumping is observed, with F typically varying between 0.2 and 0.4 . The calculated pumping rate (that is the net loss of He ions from the plasma) is of the order of $10^{20}\ s^{-1}$, and the effective He containement time ($\tau_{He}^{*} = \tau_p/(1 - R)$, where τ_p is the particle confinement time and R is the global recycling coefficient) is of the order of 10 s . With the same wall conditions, the D fuelling efficiency is about 0.1 or less, and τ_D^{*} varies from 1 to 4 s.
Detailed measurements have been done in a series of 5 dedicated He fuelled plasma shots (limiter configuration, ohmic, 3 MA, 2.8 T), with different but constant fuelling rates. Net pumping is observed for all the duration of the discharge ($\simeq$ 10 s), at a rate up to $3 \times 10^{20}\ s^{-1}$, and the integrated net losses are up to 3×10^{21} He atoms; no saturation effect is observed from shot to shot.
A possible explaination of the He pumping during plasma discharges is codeposition of He and Be. To check this hypotesis we calculated for each discharge the total Be flux in the scrape-off layer (SOL), using the density and temperature data measured with Langmuir probes situated at the limiters. It is assumed that the Be production process is physical sputtering /6/ and that all the Be produced is in the charge state 2+ and available for self-sputtering. The results show that there is no clear correlation between the total sputtering rate and the pumping rate. In particular the number of sputtered Be atoms is constant from shot to shot (within $\simeq$ 10%), while the net pumping varies by a factor of 3 to 4.

Conclusions: The test bed measurements and tha data from JET discharges both show that He is pumped by Be and that, for the same wall conditions, the pumping is lower for He than for D. The outgassing observed after implantation indicates the presence of a mobile He population in Be. This is also confirmed by post-pulse outgassing measurements carried out at JET.
The characteristic pumping time τ_{He} calculated from the test bed measurements is consistent with the observed He pumping during a JET discharge, taking into account the areas and fluxes involved in each case.
The detailed mechanism causing the net retention of He in Be to take place is not clear, but it appears that more than one process is responsible for the pumping/release pattern observed.

References

/1/ P R Thomas and the JET Team, J. Nucl. Materials, 176-177 (1990) 3.
/2/ A T Peacock et al., JET rep. JET-R-(90)02.
/3/ G Saibene et al., J. Nucl. Materials 176-177, (1990) 618.
/3/ R Sartori et al., as above, p.624.
/5/ J Ehrenberg and the JET Team, Bull. Am. Phys. Soc., 34 n.9 (1989) 2056.
/6/ J Bodansky, Nucl. Fus. Special Supplement 1984 (1984) 61.

Gas - Wall Material	$\overline{N_e}$ [x 10^{21}]	$\overline{N_i}$ [x 10^{21}]	$\overline{F}$	$\overline{P}$ [x 10^{19} s^{-1}]	$\overline{\tau^*}$ [s]
He → C	4.2	1.3	0.9 -1	1.4	> 50
He → Be	2.3	0.7	0.2 - 0.4	10	10
D → Be	2.3	2	0.1 - 0.2	90	1 - 4

Table 1 : Comparison of He and D recycling in Ohmic limiter discharges, in the C and Be phases of JET. Data averaged over 5 shots.

$\overline{N_e}$:average electron content
$\overline{N_i}$: average plasma ion content (He or D)
$\overline{F}$: average fuelling efficiency
$\overline{P}$: average net pumping
$\overline{\tau^*}$: average effective particle containement time

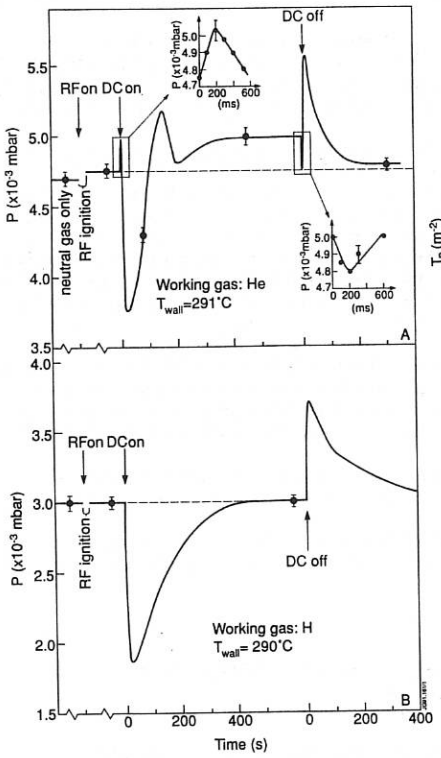

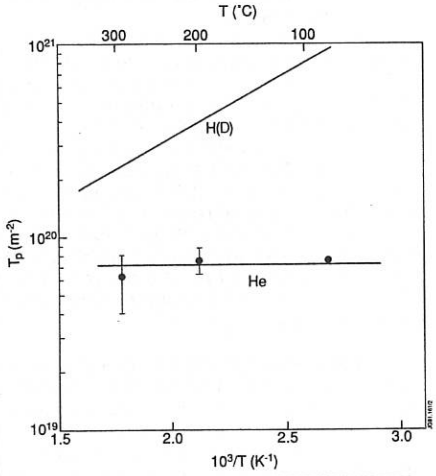

↑ **Fig. 2 :** T_p as a function of the Be temperature (He and H/D data) .

← **Fig. 1 :** Time evolution of the total pressure in the test vessel (He and H data) at 300 °C vessel wall temperature .

DEUTERIUM AND TRITIUM RELEASE ON VENTING THE JET TORUS TO AIR AFTER THE BERYLLIUM PHASE

J P Coad, A. Gibson, A D Haigh, G Kaveney and J Orchard

JET Joint Undertaking, Abingdon, Oxon, OX14 3EA, UK

INTRODUCTION

During plasma operations in tokamaks impurities which enter the plasma are redeposited in the scrape-off layer (SOL). Hydrogen isotopes from the plasma are trapped in these deposits by co-deposition, and are found by subsequent analysis to be at atomic concentrations of up to 30% of the layer [1]. In JET the principal gas used to fuel the plasma is deuterium, so this is the main isotope present in the deposits, with a total inventory in the torus of ~10^{24} atoms. However, small amounts of tritium are also produced in the plasma as a result of (d,d) fusion reactions which can produce either a triton plus a proton, or helium 3 plus a neutron with approximately equal probability. Thus equal numbers of tritons and neutrons result from (d,d) reactions. The tritons (initially of 1 MeV) may be thermalised within the plasma by collisions, in which case they behave in the same way as the deuterium with respect to incorporation in the deposits or exhaust from the torus [2], or they may be implanted at high energy into the surfaces surrounding the plasma: tritium is found to penetrate up to 25μm into the surface [3]. Gas balance measurements [2] suggest about half the tritium is thermalised.

When the torus is vented to air after a period of plasma operations some of the hydrogen isotopes are released from interior surfaces of the vessel, presumably by isotopic exchange with water vapour in the air. During the all-carbon phase of JET the amount of deuterium released was ~1.3 x 10^{23} atoms [4] and of the order of 10^{16} atoms of tritium were released. The amount of tritium released varies with the number of tritons produced in the preceeding operations, so the release can be conveniently expressed as a percentage of the tritons [neutrons] produced in the previous period of plasma operations. For a simple venting to air in the all-carbon phase the tritium release was ~ 6.7% of the tritium produced in the 300 discharges prior to venting, whilst the deuterium release was equivalent to 10% of the fuelling for the 300 discharges and is a significant contribution to the balance between the gas fuelling of the discharges and the long-term retention in the walls of the machine. The quantity of tritium released from JET is very small, since the (d,d) reaction rate is low: the number of tritons produced in a pulse is typically about seven orders of magnitude less than the number of deuterons fuelling the pulse. However, if a tokamak is fuelled with a deuterium - tritium mixture, then the amount of tritium retained in the walls, and the release on venting would be similar to the present D release. Such a tritium release would require careful radiological control.

The retention within, and release of hydrogen isotopes from, tokamaks may be expected to depend strongly on the materials of the first wall. Since Be was introduced into JET, the gas fuelling required to maintain plasma density is greatly increased. However, the fraction of deuterium exhausted at the end of a pulse has also increased, and the nett retention of deuterium per pulse is similar to the all-carbon phase [2]. Deuterium in the torus appears to behave more stably with a Be rather than a carbon environment, in that with Be there is no need to deplete the walls periodically to prevent start-up problems due to uncontrolled density surges, and the density limit behaviour is rather different [5]. This paper compares the hydrogen isotope release on venting in the two cases, presents data on the long-term release characteristics, and describes methods by which the release can be reduced.

EXPERIMENTAL

As soon as JET is vented to air, through a needle valve located in Oct V of the torus, sampling of the atmosphere in the vessel commences. Gas is drawn out of the torus using Charles-Austin pumps via manifolds either from the pumping box in Oct V or from under Oct IV (Figure 1). In the present beryllium operations the gas is passed through an "absolute" filter to prevent Be dust contaminating the equipment. Air is either pumped through two bubblers filled with distilled water so that isotopic exchange can take place, or through a liquid nitrogen trap which collects water vapour from the torus air as it passes through. From a knowledge of the volume of air pumped through the bubblers, or the humidity (ie total water content) in the vessel, respectively, the total tritium content in the torus atmosphere can be determined by each method. The deuterium release can also be determined from the sample collected by the second method, provided the level exceeds the naturally-occurring deuterium content of the moisture in the venting air, but this natural abundance swamps the level of deuterium isotopically exchanged in the bubblers. Sampling is typically for periods of 1-2 hours. Once the Torus Access Cabin (TAC) is in position the tritium level is monitored on a long-term basis by passing air from the torus through bubblers situated in the TAC. (All the air flow through the torus exhausts via the TAC).

RESULTS

The tritium level in the Oct V bubblers following the initial venting corresponds to 5.8 x 10^{15} atoms released into the 200m^3 vessel volume, which is 1% of the number of neutrons observed from the last 300 pulses of the campaign (5.9 x 10^{17}). The tritium level determined from the water collected in the liquid-nitrogen cooled trap was 7.7 x 10^{15} atoms (at a humidity of 38%). However, the deuterium content in the torus derived from the same sample was 2.4 x 10^{23} atoms, i.e. about a factor of two higher than all-carbon phase results.

The long-term (chronic) tritium release from the vessel is plotted in Figures 2a and 2b. The concentration of tritium (as HTO) in the TAC bubblers is shown in Figure 2a. The concentration has then been multiplied by the ratio of the volume sampled to the volume of air passing through the vessel per day, to give the number of tritium atoms released from the in-vessel surfaces per day (Figure 2b). The concentration measurements show a sharp drop after 28 November when the air flow rate was increased from 1.5 x 10^3 m^3 day^{-1} to 2.7 x 10^4 m^3 day^{-1} but the total evolution shown in Figure 2b during this period indicates there is a genuine source within the vessel which has reached an approximately constant release rate by 20 November. The release on the first day (on venting) is included on the graph as this is also a release from the surfaces. The average evolution 2-5 days later was ~40 times lower, and decreased a further factor of 10 over the next 12 days. This is consistent with measurements during the all-carbon phase which typically showed an order of magnitude lower in-vessel tritium concentration on the day after venting and opening access ports .

Experiments have been conducted at JET prior to the beryllium phase on ways of reducing the release of D and T into the vessel. Coating the in-vessel surfaces with carbon by glow-discharge carbonisation reduced the deuterium and tritium by factors of 5 and 4.5 from those expected without carbonisation, respectively. Bleeding nitrogen into the torus at 1 mbar for 12 hours before venting (as the vessel cooled from 300°C to near room temperature) resulted in a subsequent release of D and T factors of 2 and 3 lower (respectively), while venting the vessel to air for 2 hours (without removing any ports) then re-evacuating and re-venting the next day resulted in a tritium level lower by a factor of ten after the second venting.

DISCUSSION

Although the rate of deuterium accumulation in the JET vessel is probably unchanged since Be was introduced, the improved stability of the retained inventory with respect to start-up and density limit behaviour might have led to an expectation of reduced release on venting. Clearly isotope exchange is not affected in the same way as plasma desorption.

At first sight there is a conflict between the results indicating greater deuterium release but reduced tritium release from JET following the introduction of Be. However, the amount of (deuterium) fuelling required per discharge is much greater in the Be phases. The average deuterium fuelling for the last 300 pulses of 1990 operations was 3.26×10^{22} atoms, compared with 4.36×10^{21} for the last pulses in the carbon phase of 1988, i.e. a factor of 7.4 greater. On the other hand the tritons are borne in the plasma, and their number is unaffected by the changed fuelling rate. As the amount of long-term D retention per pulse is similar for Be- and C-phases[2] but there was 7.4 times more deuterium input per pulse in 1990, then the probability of a deuteron being retained in the vessel in 1990 was reduced by a factor of ~7.4: the same reduction would be expected for thermalised tritons. Furthermore, the number of neutrons observed in the Be-phase includes a number of neutrons produced by (^{3}He, Be) fusion reactions during high power RF-heated discharges which are not accompanied by tritium generation. It is difficult to establish precisely the contribution to the neutron inventory from this source, but it may reach 25% in the latter stages of the 1990 campaign. Together these effects could explain why the tritium release has not increased in 1990 relative to 1988 in an analogous way to deuterium.

The decay in the in-vessel tritium level in the first few days ventilation is much slower than expected from the exhaust of the initial release if there is perfect mixing of the venting air within the torus atmosphere, suggesting some further release from the near-surface inventory. The long term tritium levels in the machine, which have remained sensibly constant over the 4 months observed so far, certainly suggest another source coming from more firmly bound tritium.

If the source of the chronic release comes from the high energy implanted tritium, then in a D-T phase the release would be ~200 times greater, in line with the greater fusion yields. However, it is perhaps more likely to come from the near-surface reservoir of trapped thermalized tritium. In this case the chronic release, as the prompt release, will be a factor of 10^7 greater, which is the increase to be expected in the tritium inventory in the vessel if tritium becomes a fuelling gas in a D-T phase. Thus, assuming similar air flows in the vessel, a chronic activity level of ~10 MBq/m^3 may be anticipated for a long time after venting following D-T operations. This is many times greater than the Derived Air Concentration (DAC) of 0.8MBq m^{-3}, and would impose severe restrictions on personnel working within the machine (eg full pressurised suits). The prompt release on venting can be reduced by about an order of magnitude by taking simple palliative measures when venting. Whether these measures also reduce the chronic release is unknown, since these are the first careful measurements to have been made. However if a reduction of about two orders of magnitude could be made by controlling the build-up of the inventory, reducing the release rate, or increased ventilation, then it may be possible to maintain an in-vessel tritium content below the DAC. This would reduce the restrictions under which in-vessel work would be permitted.

CONCLUSIONS

A slightly greater amount of deuterium is released from JET on venting since beryllium has been added as a first wall material. Prompt tritium release is reduced by a factor of about 6.7, but this may reflect a reduced probability of tritium retention in the vessel due to greater gas fuelling and an overestimate of triton production from neutron data..

A chronic tritium release, likely to persist for years, results in a current in-vessel activity of ~1 Bqm^{-3}. In a D-T phase tritium releases are expected to be ~10^7 greater, which if uncontrolled would then result in a long-term activity level ~100 times above the DAC.

Prompt releases can be reduced by more than an order of magnitude in the all-carbon machine, and it may also be possible to limit the build-up of the hydrogenic in-vessel inventory. It would be instructive to determine whether the chronic release is similarly reduced (and to check that the reductions still occur since Be has been introduced)

REFERENCES
1. J P Coad et al, J. Nuclear Materials 162-164 (1989) 533
2. R Sartori et al, J. Nuclear Materials 176&177(1990)624
3. D H J Goodall et al, J. Nuclear Materials 162-164 (1989) 1059
4. J P Coad et al, J. Nuclear Materials 160 (1988) 95
5. The JET team (presented by P R Thomas), J. Nuclear Materials 176&177(1990)3

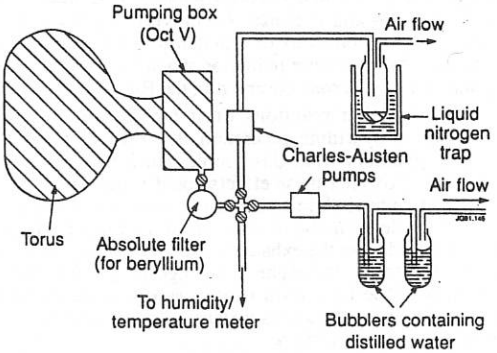

FIGURE 1
Experimental arrangement for measuring D and T concentrations in the torus atmosphere

FIGURE 2 (a) T activity in the air collected in bubblers in the TAC. (b) Calculated total release of T from the JET vessel per day. (Errors in vertical scale ± 25% for (a) and (b))

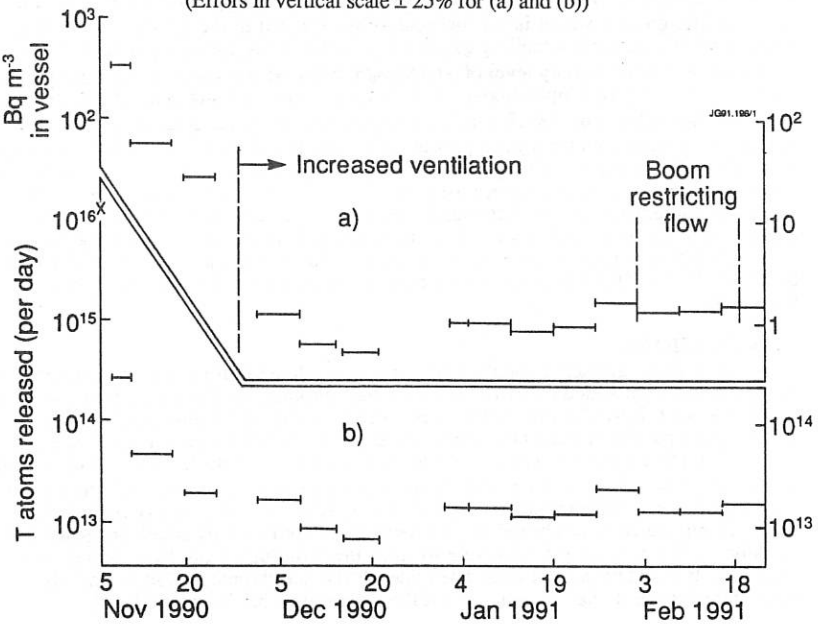

TURBULENCE STUDIES IN THE PROXIMITY OF THE VELOCITY SHEAR LAYER IN THE TJ-I TOKAMAK

C. Hidalgo, M.A. Pedrosa, I. García, E. de la Luna, T. Estrada, R. Balbín, B. Brañas, J. Sánchez, J. Harris# , Ch.P. Ritz*, J. Vega, J. Sentíes** and A.P. Navarro

Asociación EURATOM-CIEMAT, 28040 Madrid, Spain
 # Oak Ridge National Laboratory, Oak Ridge, TN 37381, USA
** Fusion Research Center, University of Texas, TX 78712, USA*
*** Universidad de Cantabria, Santander, Spain*

1.-Introduction

Search for effects of the radial electric field on confinement in different devices has been conducted during the last years. Particular interest has been devoted to studying the role of the radial electric field in the transition to the H-mode (1).

A reversal in the phase velocity of the fluctuations (shear layer), due to gradients in the radial electric field, has been observed in the edge region of devices with different magnetic configuration (2,3). The shear layer can substantially modify the structure of the edge turbulence (4). On the other hand turbulence may play an important role in the generation of poloidal flows (5,6).

To go deeper in the clarification of the mechanism for stabilization of turbulence by the generation of poloidal sheared flows, as well as in the influence of turbulence in the generation of poloidal flows, requires a detailed study of the structure of the electromagnetic turbulence in the shear layer region.

2.-Experimental

Density, floating potential and magnetic fluctuations have been characterized in the proximity of the shear layer location in the TJ-I tokamak (R =0.30 m, $\bar{a}$ =0.10 m) by means of Langmuir and magnetic probes using the experimental method described elsewhere (7).

In addition, density fluctuations have been monitored from the plasma bulk to the edge region by means of a two-frequency microwave reflectometer (8). With this diagnostic we have measured fluctuations in the cosine of the phase ($\tilde{\phi}$), where $\tilde{\phi}$ is related with radial density fluctuations ($\tilde{\phi} \approx \tilde{n}$).

Temperature fluctuations have been measured using a fast swept (≈ 150 kHz) single Langmuir probe. From the current-voltage (I-V) characteristic we have deduced the electron temperature, in a time scale that is small compared with the relevant times of the turbulence.

Measurements were carried out in plasmas with chord average density $\bar{n}_e \approx (1 - 2)\ 10^{13}$ cm^{-3}, plasma current $I_p \approx 20 - 35$ kA, and toroidal magnetic field B = (0.8 - 1.4) T.

3.-The velocity shear layer

In TJ-I, as in other devices, the poloidal phase velocity of the fluctuations (v_{ph}) has been observed to change sign in the vicinity of the limiter radius (a_s); for $r<a_s$ fluctuations propagate in the electron diamagnetic drift direction ($v_{ph} \approx (1\text{-}2)\ 10^5$ cm s^{-1}) and for $r>a_s$, the fluctuations propagate in the ion diamagnetic direction.

4.-Density and potential fluctuations

Relative density fluctuation levels decrease systematically inside the plasma with $\tilde{n}/n \approx 0.50$ at the shear layer location. Floating potential fluctuations (ϕ_{rms}) reach a minimum in the proximity of the shear layer (Fig. 1). This reduction is due to the quenching of the higher frequency components (Fig. 2).

The reflectometry results show a sharp collapse of the high frequency components of the radial turbulence when the reflecting layer approaches the shear layer position (Figure 2).The mean frequency of the fluctuations is affected by the frame of reference (Doppler shift). However, the usual Doppler shifted poloidal rotation does not affect the dynamic of the turbulence (i.e. fluctuation levels) and should not have influence in the radially varying density fluctuations.

The coherence between two probes, measuring the floating potential and poloidally separated 0.3 cm, decreases at the shear location as shown in Fig. 3. This result show the existence of a spatial decorrelation of the fluctuations in the shear layer region of the TJ-I tokamak. Similar results have been recently reported on TEXT (4).

The parallel observation, in the shear layer region, of a reduction in the rms values with a decrease of the higher frequency fluctuating components and the spatial decorrelation of the fluctuations is an indication of turbulence characteristics modified by sheared poloidal flows.

5.-Magnetic fluctuations

Figure 4 shows a radial profile for the radial and poloidal magnetic fluctuations in the edge plasma region. It should be noted the substantial increase in the magnetic fluctuations inside the plasma ($r/a_{shear} <1$), whereas in the outer region ($r/a_{shear} >1$) $\tilde{b}_r$ and $\tilde{b}_p$ are rather constant.

Measurements taken in plasmas with low MHD activity have revealed the existence of asymmetries in the structure of the magnetic fluctuations in a poloidal plane, perpendicular to the toroidal magnetic field, with $\tilde{b}_r < \tilde{b}_p$ inside the plasma ($r/a_{shear} <1$) and $\tilde{b}_r \approx \tilde{b}_p$ outside the plasma ($r/a_{shear} >1$). This result could be an indication of radial gradients in the coupling of the radial and poloidal turbulence, which have implications in the mechanisms responsible for the shear generation (5,6), but may also be a sign of a change in the magnetic structure when we go through the shear layer location. Actually, a direct coupling between shear layer location and the last closed flux surface (i.e. magnetic configuration) has been observed in ATF (3).

On the other hand, the radial profile of magnetic fluctuations appears to be linked to the shear layer position (i.e. magnetic fluctuation levels move with the shear position). This result is very consistent with previous measurements in ATF, where the levels of radial density fluctuations were observed to be determined by the shear layer location (9).

6.-Temperature fluctuations

Figure 5 shows the I - V characteristic for a single Langmuir probe measured at 150 kHz sweeping rate in the plasma edge region. Although the dominant frequencies of the fluctuations are well below 200 kHz, changes in the structure of the I-V characteristic are still observed in the time scale of the swept probe (Fig. 5). This fact, together with the errors accumulated in the estimation for the electron temperature from the linear fitting of $\ln(I_e)$ versus the applied potential (V), implies that the measured temperature fluctuations are only an upper bound for $\tilde{T}_e/T_e$.

Preliminary results show the possibility for substantial temperature fluctuations ($\tilde{T}_e/T_e \approx \tilde{n}/n$) in the shear layer location of TJ-I. This result, which is consistent with measurements in ATF (3), may have important consequences in the current picture for edge turbulence models (9). Further experiments are in progress to quantify temperature and density fluctuation in the edge plasma and outside the shear region.

7.-Correlation lengths

In the edge plasma ($r/a_{shear} < 1$) the spectral width of the k-distribution in the poloidal direction (σ_p), which is inversely proportional to the poloidal correlation length ($\approx 1/L_p$), was observed to increase with q(a).

The spectral width for radially varying fluctuations (σ_r), measured by reflectometry, increases with increasing frequency (fig.6).

References

(1) R. J. Groebner, K.H. Burrel and R.P. Seraydarian, *Phys. Rev. Lett.* 64, 3015, (1990).
(2) Ch. P. Ritz, R. D. Bengton et al., *Phys. Fluids* 27, 2956, (1984).
(3) C. Hidalgo, T. Uckan et al. *in Controlled Fusion and Plasma Physics (Proc. 17th Eur. Conf. Amsterdam, 1990)* voll. III, pag. 1353.
(4) Ch. P. Ritz, L. Hin et al.*Phys. Rev. Letters*, 65, 2543, (1990).
(5) P. Diamond and Y. B. Kim, *Physics of fluids B*, (1991, to be published)
(6) B. Carreras, V. Lynch and L. García, *Physics of fluids B*, (1991, to be published)
(7) C. Hidalgo, M.A. Pedrosa et al. *Nuclear Fusion* , 30, 717, (1990)
(8) T. Estrada, J. Sánchez et al. *Rev. Sci. Instrum.* 61, 3034,(1990).
(9) Ch. P. Ritz , T.L. Rhodes et al., *Proc. 13th Int. Conf. on Plasma Physics and Controlled Nuclear Fusion Research, Washington, 1990 (IAEA, Vienna, 1991)*, Paper IAEA-CN-53/C-3-4 (in press).

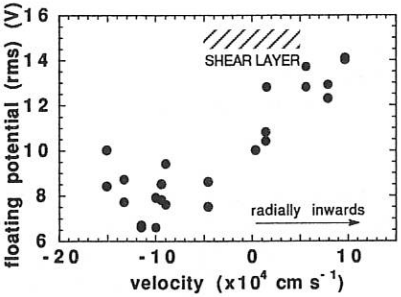

Fig.1.-Floating potential (rms) versus the phase velocity of the fluctuations in the vicinity of the shear layer.

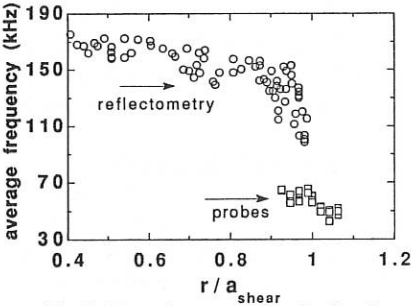

Fig.2.-Mean frequency for the floating potential fluctuations and for the cosine of the phase as a function of the normalized radial location.

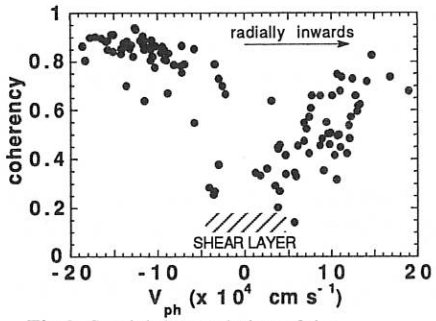

Fig.3.-Spatial decorrelation of the fluctuations in the proximity of the shear region in TJ-I.

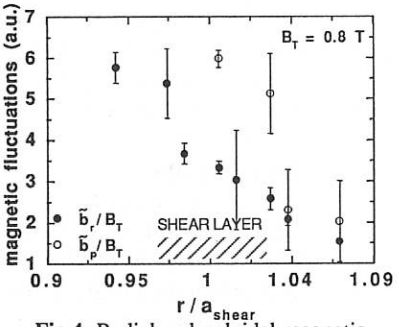

Fig.4.-Radial and poloidal magnetic fluctuations in the edge region of TJ-I.

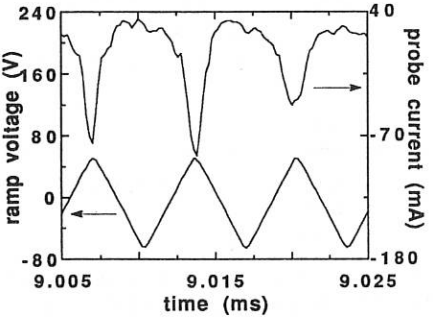

Fig.5.-Probe current-voltage characteristic in TJ-I.

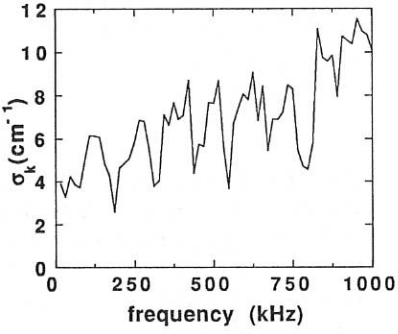

Fig.6.-Frequency resolved σ_r, measured by reflectometry.

OHMIC AND H-MODE PARTICLE TRANSPORT IN THE CCT TOKAMAK EDGE PLASMA

G.R. Tynan, R.W. Conn, R. Doerner, R. Lehmer, L. Schmitz

Institute for Plasma and Fusion Research
University of California, Los Angeles 90024 USA *

ABSTRACT

Measurements of equilibrium and turbulent plasma parameters in the far edge and scrape-off layer region of CCT H-mode discharges are presented. The results indicate a large reduction in cross-field particle transport rates during the transition from Ohmic to H-mode confinement. The reduced transport is due in part to changes in saturated fluctuation amplitudes as well as changes in the nature of the edge turbulence. In H-mode, the peak cross-field particle flux is reduced by a factor of 3-6 over the flux in an Ohmic discharge. These changes in edge transport rates are similar to changes in global particle confinement time. Analysis of the radial profiles indicates that poloidal and/or toroidal variations in transport play an important role in the overall particle transport.

This paper presents measurements of equilibrium and fluctuating plasma parameters made during a CCT H-mode transition. In these experiments, an Ohmic discharge was initiated and brought to equilibrium. The plasma current was 38 kA, the toroidal magnetic field was 2500 G, line averaged density $2x10^{12}$ cm^{-3} (Ohmic confinement), plasma major/minor radii were 148 and 35 cm respectively, Z_{eff} was less than 2, and the working gas was hydrogen. The walls of the tokamak were coated with a titanium gettering surface to eliminate hydrogen recycling and reduce impurity levels. The flux surfaces were circular, and the plasma column was displaced such that the limiter was formed by the toroidally symmetric inside midplane vessel wall. This limiter configuration results in the formation of a scrape-off layer region on the outside midplane where the data presented in this paper were taken. To induce an H-mode transition, a slow (15 ms) voltage ramp (floating to -300 V) was applied to an electron emitter located on a closed magnetic flux surface. The electron emitter was located 105 deg away toroidally from the Langmuir probe and was inserted to a normalized plasma radius r/a=0.75. This applied bias results in the injection of a net electron current into the plasma. Over a 10 ms period the injected current was increased to a peak value of 25 amps, at which time a bifurcation to the H-mode regime occurred as discussed previously [1]. At the bifurcation, a radially thin (<1 cm) region with strong (-100 V/cm) inward radial electric field developed at the limiter radius, the line-averaged plasma density increased by a factor of 3-6 with a constant gas fueling rate, and a steep density gradient formed at the plasma edge. Langmuir probes located at the outside midplane of the tokamak were then used to study the transition to the H-mode regime.

Measurements of the edge plasma equilibrium density, electron temperature, and plasma potential at the outside midplane are shown in Fig. 1a-c. In the scrape-off layer region (r>35cm) the plasma density has a peak at 38 cm at t=0 ms before the start of current injection. As the injected current is increased, the peak in the density profile is reduced and

finally disappears after the bifurcation to the H-mode regime occurs. The electron temperature profile in Fig. 1b appears relatively unchanged during the transition. The plasma potential profile has a peak inside of the limiter radius at 0 ms. As the electron current is increased, the central plasma potential begins to decrease and the peak in the plasma potential profile moves outwards slightly towards the limiter radius. After the bifurcation, the plasma potential profile forms a strong radially inward electric field inside the limiter radius.

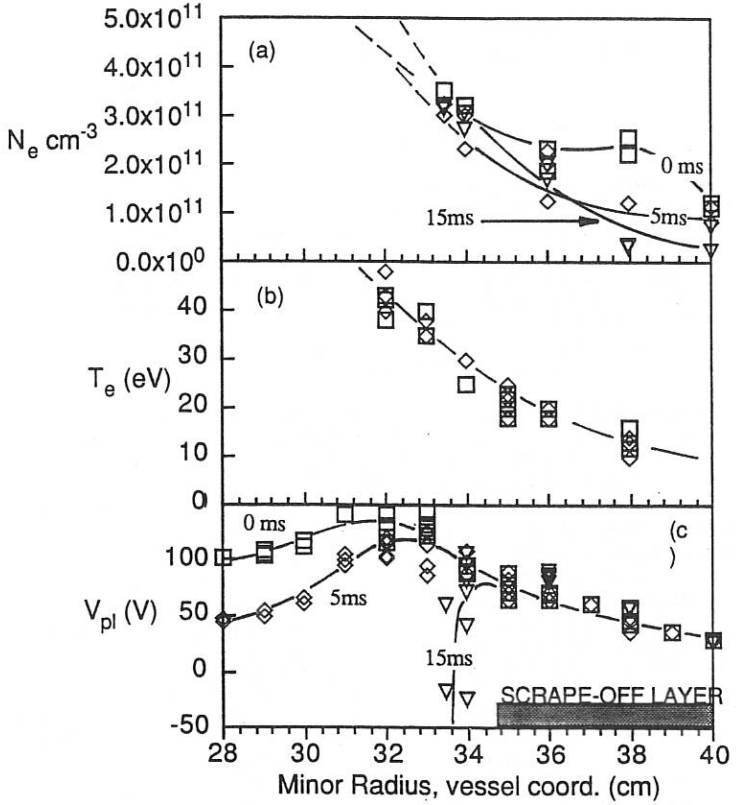

Figure 1: Evolution of equilibrium plasma profiles during the CCT H-mode transition. (a) Equilibrium plasma density (b) Equilibrium electron temperature (c) Equilibrium plasma potential v. minor radius. The peak in the plasma density in the scrape-off layer is eliminated during the transition to H-mode confinement and the plasma density gradient steepens near the limiter radius. The electron temperature profile is relatively unchanged in the transition. The plasma potential profile is peaked inside the limiter radius before the start of the transition (□ 0 ms). As the electron current is increased (◇ (5ms) to ○ (10 ms)) the peak moves out towards the limiter radius and the central plasma potential falls. After bifurcation (▽ 15ms) the plasma potential profile inside the limiter radius collapses to form a strong radial electric field over a narrow region.

The edge Langmuir probes were also used to study the evolution of the edge plasma turbulence during the CCT H-mode transition . In the scrape-off layer region ($r > 35$ cm), the density fluctuation levels are not significantly changed (Fig 2a), while the floating potential fluctuation levels are reduced substantially (Fig 2b) as the rotation rate is increased. The radial particle flux induced by the electrostatic turbulence [2] was reduced in the edge region by factors of 3-6 as the rotation rate increased (Fig 2c) . Assuming toroidal and poloidal symmetry, the radial particle flux at the limiter radius implies a global particle confinement time of 5-8 ms during Ohmic discharges and 20-40 ms during the CCT H-mode, consistent with measurements of the global particle confinement [1] made by termination of the neutral gas fueling.

This reduction in radial particle flux would suggest that turbulent driven transport accounts for the particle transport in the edge region of CCT in Ohmic discharges in agreement with previous experiments [3] and that reductions in turbulence are responsible for the increased particle confinement in the H-mode. However, in the CCT H-mode the "transport barrier" appears to be located 1-2 cm inside the limiter radius during the H-mode, concomitant with the increased density gradient and strong radial electric fields and currents. Furthermore, consideration of the continuity equation suggests that if turbulence was the sole mechanism for cross-field particle transport in CCT, the radial particle flux should then peak at the limiter radius (35 cm) and decrease in the scrape-off layer since ionization sources are small in the measurement region. In the H-mode this peaked flux profile would then simply decrease in amplitude. The data discussed above suggest a more complex picture of transport in the edge plasma region.

In CCT the turbulent-driven particle flux peaks well into the scrape-off layer region during Ohmic discharges. Furthermore, prior to the H-mode transition, the equilibrium density profile has a peak in the scrape-off layer indicating that a simple one-dimensional radial diffusion model of transport is inadequate. Upon the transition to the H-mode confinement regime, the peaked equilibrium density and fluctuation-induced particle flux profiles are modified over the entire region being considered in this paper. These observations suggest that particle transport in CCT Ohmic and H-mode plasmas is not merely a one dimensional diffusion process. Instead, the turbulent-driven transport is poloidally asymmetric and time-stationary plasma convection plays an important role in particle transport. Hence a complete physical picture of particle transport in Ohmic and H-mode plasmas must include these effects. Experiments are underway to explore the radial and poloidal distribution of turbulent and convective transport mechanisms in CCT and results will be reported in future work.

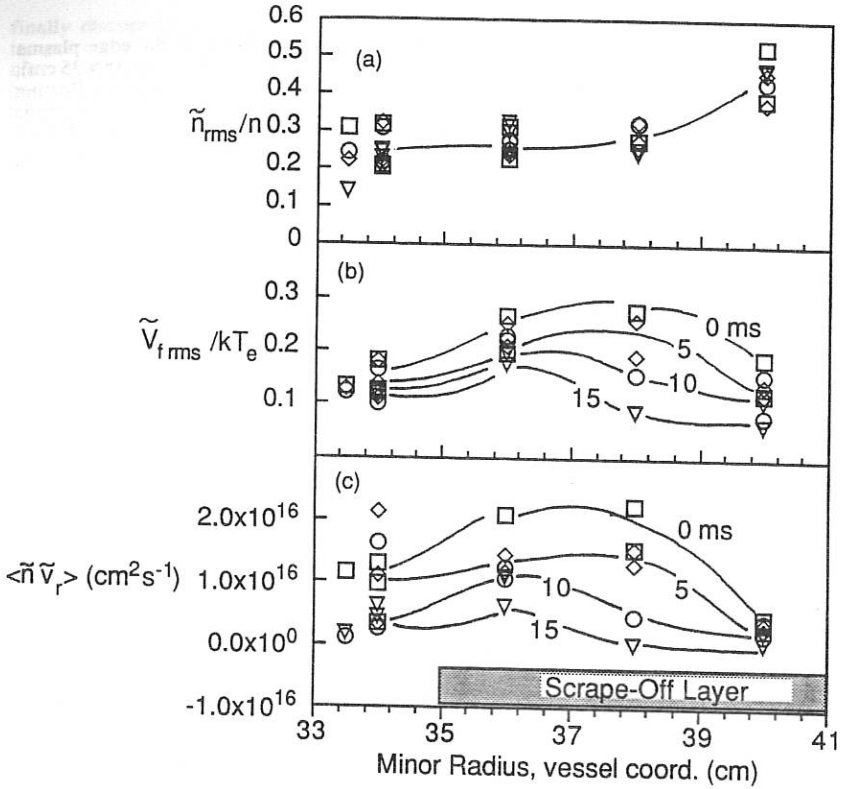

Figure 2: Evolution of edge turbulence during H-mode transition (a) Ion density fluctuations level (b) Floating potential fluctuation level (c) Turbulent-driven particle flux. The potential fluctuation and turbulence driven fluxes are reduced in the scrape-off layer region during the H-mode transition.

ACKNOWLEDGEMENTS: One of us (GRT) thanks R.J. Taylor for many useful discussion related to this work. The invaluable contributions of the CCT Tokamak laboratory technical staff are also gratefully acknowledged.

* Work supported by the U.S. Department of Energy under contract #DE-FG03-86ER52134

REFERENCES:

[1] R.J. Taylor et.al., Physical Review Letters **63**, 2365 (1989)
[2] E.J. Powers, Nuclear Fusion **14**, 749 (1974)
[3] W.L.Rowan et.al., Nuclear Fusion **27**, 1105 (1987)

EDGE RADIAL PROFILES AND TRANSPORT IN JET X-POINT PLASMAS

J A Tagle, M Bures, D Campbell, S Clement, L de Kock, S K Erents*, P J Harbour, A Loarte, and C Lowry

JET Joint Undertaking, Abingdon, Oxon, OX14 3EA, UK
* AEA Technology, Culham Laboratory, Abingdon, Oxon, UK

1. INTRODUCTION

Profiles of local plasma parameters were measured along the X-point target plates (by means of a poloidal array of up to 8 Langmuir probes mounted in the apex of the tiles) and in the scrape-off layer (SOL) of JET (half way between divertor plates and the upper belt limiter) by a fast scanning probe (stroke 10 cm in 200 ms) often crossing the separatrix [1]. The SOL data presented here contain profile information mainly for discharges at $I_p = 3$ MA in single (SN) and double (DN) null configuration with neutral beam and/or ion cyclotron frequency heating (monopole or dipole phasing of the rf antennae); for different magnetic fields ($B_t = 2.2$ - 3.4T) and different directions of the ion ∇B drift; and for various distances of the X-point to the target plates ($\Delta x \approx$ 0-13 cm). Frequently a comparison is available between ohmic, L and H mode confinement regimes. Data are for the probe on the ion drift side.

Although the data presented do not constitute a complete set of scalings with the independent parameters they illustrate the dramatic differences that can be observed between the different discharge conditions used. Profile information will be interpreted in terms of transport coefficients using simple models.

2. TARGET PROFILES IN SINGLE AND DOUBLE NULL PLASMAS

Profiles of the ion flux and electron temperature for a DN X-point discharge ($I_p = 3.1$ MA, $B_T = 3.4$ T) with ion ∇B drift towards the upper target with ohmic and combined heating (NBI + ICRF) are shown in figure 1. In this typical example the power deposited in the inner strike zone is higher than in the outer one, in contrast to the observation in a SNX discharge [2], where it is the opposite. In the outer strike zone the effects of the three confinement regimes can be observed. L-mode shows the flattest profile ($\lambda = 80$ mm, meaured locally along the tiles) as compared to $\lambda = 72$ mm in ohmic and $\lambda = 35$mm in H-mode. In the inner strike zone these changes are usually visible to a lesser degree. In this example they are hardly visible.

The asymmetry in the power deposition on the two strike zones, as deduceable from Fig 1, is also present in SNX discharges with the ion ∇B drift towards the target, but the power deposited at the outer strike-zone is higher, as has been reported previously. This gives rise to an early onset of the "carbon bloom" during high power additional heating. A reversal of the toroidal field in the SNX discharge (ion ∇B drift away from the target) makes the power deposition more symmetric. Fig 2 shows the two H-mode cases for the SNX discharges with the DNX (H-mode) discharge for comparison. A more detailed picture of the redistribution of the power deposition has been obtained from CCD camera observations [3], conforming the trend of fig 2, which suffers from large uncertainties (as indicated by error bars and broken lines), and depends on the assumption $T_i = T_e$.

In reverse field, where the power loading is higher at the inner strike zone, the target probe data shows that the power deposition becomes more symmetric when the separation between the X-point and the target plate is increased. This effect is not clear from CCD Camera observations where the scatter in the data does not allow to draw firm conclusions. However, the CCD cameras provide good evidence that increasing particle flux on the target,

as shown to be well correlated to D_α intensity in the private flux region, leads to a shift of the relative power deposition to the outer strike zone [3]. Both effects can be used to make the power loading more symmetric leading to a longer delay in the onset of the carbon bloom at similar power levels [4].

3 SCRAPE-OFF LAYER PROFILES AND RADIAL DIFFUSION (FROM FAST SCANNING PROBE)

Detailed measurements of decay lengths of edge parameters up to the last closed magnetic surface (LCFS) have been made for different magnetic fields (B_t = 2.2 - 3.4T), direction of the toroidal field (forward/reversed), plasma regimes (ohmic, L, H phase) and additional heating methods (NBI, ICRF dipole and monopole phasing).
Fig 3 shows the profiles of I_{sat} for ohmic, H-mode (NB, ICRH monopole, ICRH dipole). These and other radial profiles are used to derive local transport coefficients using the simple non-collisional uniform model ($D_\perp = \lambda_\Gamma \lambda_n C_s/2L$, $\chi_\perp = \delta\lambda_T\lambda_P C_s/2L$), where λ_Γ, λ_n, λ_T, λ_P are the decay lengths for flux, density, temperature and power respectively; C_s the sound speed, L the connection length and δ the sheath transmission factor. Some of the profile information is summarised in Table I. Only the values of $D_\perp$ are given here since $\chi_\perp$ has very large uncertainties. Although the absolute values are model dependent, their relative values are reasonably reliable. From the Table and Figure 3 we observe:

- For a given toroidal field the profiles flatten during the transition from ohmic to L-mode and become very steep in the H-mode. As can be seen in figure 3 the steepening of profiles in the H-mode occurs only in a localized region very near (~ 2 cm) the separatrix, while the rest of the SOL profiles are as in the L-mode.
- The changes of the radial profiles between L are H-mode do not depend directly on the type of heating applied. However, the value for $\Gamma(a)$ for the DNX discharge with ICRH in monopole phasing is anomalously high. This is confirmed by probes in the X-point target, and is probably related to the fuelling with 2.7 mm pellets at 2 Hz during these discharges with monopolar phasing. It is not confirmed, however, by observations with the CCD Camera.
- The e-folding lengths of the saturation current near the LCFS are similar for H-mode with NBI and ICRH with dipole antenna phasing. With ICRH in monopole phasing the e-folding length is longer. This is consistent with the observation that in the first case the quality of the H-mode is the same and in the second case degraded.

4. RADIAL ELECTRIC FIELD IN THE SOL

The fast scanning probe can cross the separatrix and from the measured floating potential V_f and electron temperature the plasma potential V_p (versus vessel) and radial electric field E(r) can be calculated [5]. In Fig 4a the clearest example is shown with the change of V_p in ohmic (or L mode) and H-mode. For the same data E(r) is shown in Fig 4b. Uncertainties originate from the accumulated errors in the basic data and the position of the LCFS as given by the magnetic interpretation codes. Taking these caveats the radial electric field E(r) changes sign from ohmic (or L-mode) to the H-mode in a region close to the LCFS (slightly inside or outside).

5. CONCLUSIONS

- DN discharges reverse the power deposition asymmetry observed on the upper X-point tiles during SN forward field discharges (ion ∇B drift towards the target).
- The symmetry of the power deposition on inner and outer strike zones is improved when the X-point is pushed further inside the vessel.

- The edge transport coefficient decreases by ~ 60% during H-mode transition in a region of ≈ 2 cms outside the last close flux surfaces. This a valid for NBI and ICRH with dipole phasing of the antennae. The decrease is less for monopole phasing, but may be affected by pellet fuelling during monopole operation.
- Qualitatively the behaviour of the SOL is the same for H-modes with NBI and ICRH in monopole or dipole phasing of the antennae. Quantitatively there are differences in he absolute value of the particle flux (unexplained) and in the λ's. These might partly be explained by the pellet fuelling and partly by the fact that ICRH heating requires a DN configuration, whereas the other observations are in SN.
- A preliminary observation of the changes of the radial field E(r) at the L-H mode transition shows a change in E(r) from slightly negative to positive just inside the LCFS.

REFERENCES

[1] J A Tagle et al, J. Nucl. Materials 162-164(1989)282-287
[2] P J Harbour et al, J. Nucl. Materials 162-164(1989)236-244
[3] R Reichle et al, this Conference.
[4] D Stork et al, this Conference
[5] J A Tagle et al, Fusion Engineering and Design 12(1990)217-222

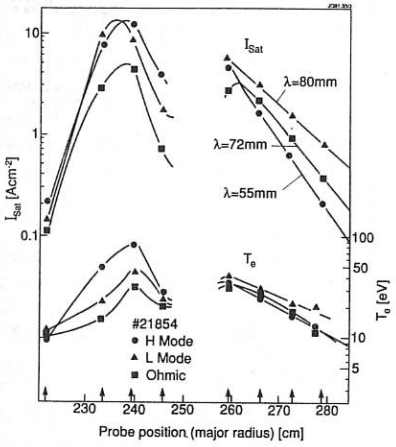

Fig 1: Profiles of I_{sat} as measured poloidally across the target. Arrows indicate the probe positions. Double null X-point discharge at I = 3MA, B_T = 3.4T and ion ∇B drift towards the upper target.

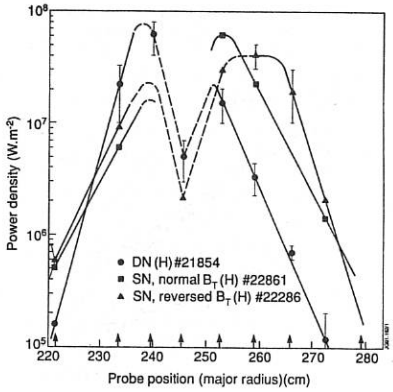

Fig 2: Profiles of I_{sat} as measured poloidally across the target for discharges in DN, SN with ion ∇B drift up/down.

TYPE OF DISCHARGE		$\Gamma(a)$ (A cm^{-2}) Ω	L	H	λ_Γ (mm) Ω	L	H	T_e (a) (eV) Ω	L	H	λ_T (mm) Ω	L	H	$D_\perp$ (m^{2}s^{-1}) Ω	L	H
3.1/3.4	SNX NBI	3.35	-	1.19	35	-	14	41	-	45	59	-	62	1.33	-	0.15
3.1/2.8	SNX NBI	4.1	0.54		27	44		48	50		59	84		0.75	1.81	
3.1/2.2	SNX NBI	1.9		3.0	34		6	38		58	64		16	1.07		0.04
3.1/2.0	DNX RF-Dip	-	3.9	3.5	-	33	11	-	46	-	-	76	-	-	1.12	-
3.1/2.8	DNX RF Mon	-	5.9	25	-	38	15	-	61	82	-	66	53	-	2.49	0.68
3.1/-3.4	SNX NBI	-	3.64	-	-	31	-	-	40	-	-	65	-	-	0.76	-
3.1/-2.8	SNX NBI	-	-	1.64	-	-	28	-	-	27	-	-	84	-	-	0.53

TABLE 1:Overview of profile information obtained by means of the fast scanning probe.

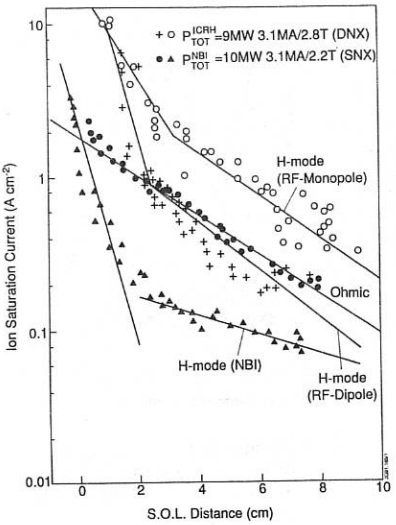

Fig 3: Profiles of I_{sat} as a function of radius (⊥ to LCFS) measured by means of the fast scanning probe. Discharges in ohmic, H-mode (NBI,ICRH dipole ICRH monopole) are compared. Absolute values depend on discharge conditions.

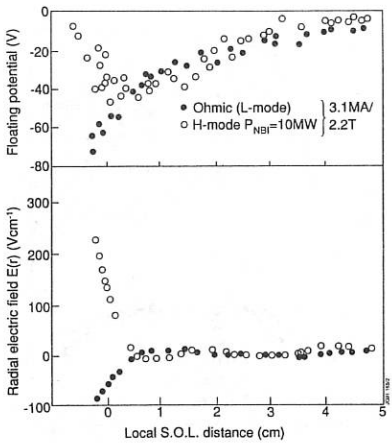

Fig 4: One example of the radial profile of the floating potential V_f and the calculated E(r) in a discharge with an clear L and H-mode phase.

DEPENDENCE OF HE RETENTION ON X-POINT PLASMA PARAMETERS IN JET

G. Janeschitz, N. Gottardi, H. Jaeckel, J.P. Coulon, B. Denne, R. Giannella, G. Haas, K. Lawson, T. Tagle

JET Joint Undertaking, Abingdon, OXON, OX14 3EA, UK

Introduction:

In future ignition devices, three equally important key parameters (τ_p^{He}, τ_D^{He}, τ_{pump}^{He}) will determine the efficiency for the removal of He ash from the plasma. The first parameter is the global confinement time for He (τ_p^{He}) in the core plasma. This parameter is discussed in ref. /1/ considering also the effects of a He source inside the closed flux surfaces. In our paper we describe the dependence of the second parameter, namely the divertor- retention capability for He, on the X-point plasma conditions. For the present purposes the use of a characteristic time constant (τ_D^{He}) /2,3/ to represent the retention capability is a simplified but adequate description. In order to obtain this time constant from the temporal behaviour of line intensities measured in the main plasma /2,5/, the third parameter, namely the overall pumping time constant for the impurity gas concerned (He: τ_{pump}^{He}, Ar: τ_{pump}^{Ar}), must be known /3/. In JET X-point discharges performed on the carbon target plates, this pumping time constants are practically infinite compared with the discharge duration. Therefore the temporal behaviour of e.g. the He II line intensity in those discharges, is solely dependent on the two time constants τ_D^{He} and τ_p^{He}. The method to obtain τ_D^{He} from this temporal behaviour is therefore the same as the one described in ref. /2,5/. In steady state conditions τ_D^{He} determines the major part of the He source term at the plasma edge (scrape off), while the ratio τ_D^{He}/τ_p^{He} yields the fraction of the total content of He in the machine, which is accessible to pumping in the divertor area.

Experiments to measure the He retention capability of divertor configurations have been undertaken to date in ASDEX /2,4/ as well as in JET. The JET results described in reference /5/ are based on ohmic double null X- point discharges, which revealed a rather poor retention of He and Ar. During the 1990 operation campaign of JET a more detailed investigation of the dependence of τ_D^{He} on the X-point plasma parameters as well as on the X-point to target plate distance has been performed.

Experiments and discussion:

For the above mentioned investigation, two series of single null X- point discharges were run. Each series consists of three similar discharges but with different distances of the X- point to the target plate (see table 1, Δx = positive means the X-point is inside the vessel). In all plasma shots of these series the X- point configuration is formed at 12 sec into the discharge and lasts until 20 sec. A He gas puff, similar to the one described in ref. /5/ is applied at 13 sec. Except for one discharge (6MW heating power) the plasma is heated with 10 MW neutral beam injection from 16 sec to 19 sec. The first series of discharges was performed with a reversed toroidal field (Ion-grad B drift away from the X- point), while the second set of discharges has a normal toroidal field. Beside the difference in the toroidal field direction, the latter series of plasmas was accidentally contaminated with a small amount of Xe gas.

The Xe gas seems to radiate strongly in the scrape off layer and in the X- point region, where it is compressed by the same mechanism as the He (retention). This radiation cools the scrape off

layer and the divertor plasma significantly. It results in a detachment of the plasma from the target plate during the Ohmic heating phase. This detachment can be best seen by the Langmuir probes, which are built into the target plates. During the Ohmic heating phase of the Xe contaminated discharges, no density and temperature can be obtained from these probes in contrast to the uncontaminated discharges. When the NBI is switched on at 16 sec the plasma is re-attached to the target plate. This is demonstrated by a sudden appearance of Langmuir probe density and temperature signals. However, in the X-point region as well as in the scrape off layer, the electron and the ion temperature can be assumed to be substantially different from the uncontaminated case. This is supported by the increased radiation levels seen by the bolometer arrays from these regions compared to the uncontaminated shots.

In the Ohmic phase of the Xe contaminated discharges a significantly higher retention than in the uncontaminated shots is found for all X- point distances. This higher retention is characterised by the more pronounced overshoot of the He II signal after the gas puff (Fig. 1 lower curves, Fig. 3b) and subsequent by a bigger τ_D^{He} (see table 1), compared to the uncontaminated shots (Fig. 1 upper curves, Fig. 3a).

TABLE 1 (OH-PHASE)	Δx = -3 cm	Δx = +10 cm	Δx = +17 cm
Xe contaminated plasma	τ_D^{He} = 0.70 sec	τ_D^{He} = 0.40 sec	τ_D^{He} = 0.40 sec
Uncontaminated plasma	τ_D^{He} = 0.25 sec	τ_D^{He} = 0.15 sec	τ_D^{He} = 0.15 sec

The difference in the retention capability between Xe contaminated and uncontaminated discharges, can be understood by the strong dependence of the characteristic decay length λ_{par} of the impurity density along fieldlines on T_i /4/. This decay length is the ratio of the classical diffusion coefficient along field lines to the velocity of the background plasma $V_{par} = MV_{sound}$, which streams towards the target plates.

$$\lambda_{par} = \frac{D_{par}}{V_{par}} = \frac{8.84 \times 10^{12}}{(1+m_i/m_z)\,\ln\Lambda} \frac{T_i^2}{M\,Z^2\,n_i[cm^{-3}]}\ [cm] \qquad (1)$$

As can be seen from equation (1), the impurity decay length λ_{par} has a square dependence on T_i. Therefore variations of the ion temperature in the scrape off layer and particularly in the X-point region should change λ_{par} substantially. We can further assume that impurity ions, which travel along fieldlines from the divertor beyond the X-point into the main plasma scrape off layer, have a high probability to enter the closed flux surfaces. Therefore τ_D^{He} is determined by the ratio of n_z^{div} to n_z^{scra} and thus depends strongly on λ_{par}. Due to the open divertor configuration in JET, the exact position in the scrape off layer, where n_z^{scra} should be obtained, is difficult to define. However, it can be assumed to be somewhat beyond the X-point location towards the plasma. The connection length from this position to the target or to a point in the divertor, where the impurities are ionized (He), is the effective connection length L_{par}. The probability P for divertor impurities to reach the above described position in the main plasma scrape off layer can then be expressed by equation (2).

$$P = e^{-<L_{par}/\lambda_{par}>} = e^{-\text{const}\,L_{par}\,<M\,Z^2\,n_i/T_i^2>} \qquad (2)$$

Equation (1) and (2) represent only the most simple analytical expression for the retention capability of a divertor configuration. In reality other parameters such as thermal drag forces, which are dependent on the gradient of T_i along field lines have to be taken into account. The above simple equations, however, should help to understand the different importance of the various scrape off layer parameters for the retention of impurities in a X-point configuration.

In contrast to the expectation from equation (2) both, the Xe contaminated and uncontaminated discharges display the highest divertor time constants when the X- point is slightly behind the target plate (Δx=-3 cm) (see table 1). In this case L_{par} should be very short and the probability for the impurities to reach the main plasma scrape off should be substantial. The observed reversed dependence on the connection length can be explained by the lack of poloidal baffling in JET. Plasmas with X-points slightly behind the target plates fill the JET vessel more effectively than plasmas with bigger X-point to target distances. In the latter cases the He atoms can travel further as neutral particles before they are ionized and such the effective connection length is probably shorter than in the case where the X-point is on the target.

Particularly during neutral beam heating the strong dependence of the retention on T_i in the scrape off layer can be inferred. In the Xe contaminated plasmas a significant deterioration of the retention was observed during neutral beam heated L- mode phases. As shown in Fig. 3b the He II intensity increases substantially when the beams are switched on indicating an additional influx of He from the divertor. In contrast to this behaviour the He II signal is predicted to drop (Fig. 3b lower broken line) due to the increased temperature (radiating shell at bigger radius) when keeping τ_D^{He} constant at 0.4 sec. In order to simulate the measured He II signal, τ_D^{He} must be reduced to 0.15 sec at the onset of the beams. Later during the L-mode τ_D^{He} increases again to 0.3 sec (at 17 sec) reaching 0.4 sec at 18 sec into the discharge. This behaviour is in line with the observed X-point-area radiation, which increases slowly from 16 to 18 sec and such reduces the power flow into the divertor.

Discharges, which switch into the H- mode shortly after the onset of the NBI, or L-mode discharges heated with low power (6 MW), do not display such a deterioration of τ_D^{He} (Fig. 1: , 3a). This behaviour is consistent with the different amount of energy, which is conducted into the scrape off layer and subsequent into the divertor plasma compared to high power (10 MW) L-mode discharges. Again the sensitivity of the retention time (τ_D^{He}) towards T_i is demonstrated.

Conclusion:

In the cases of a moderate power flow into the scrape off layer (H- mode, low heating power, high radiation in the divertor/ scrape off) a moderate T_i so that a reasonable collisionality is maintained (eq. 1,2) and a high enough friction force is sustained in order to retain the He in the X- point region. However, as already mentioned in the introduction a high τ_D^{He} on its own is not enough to obtain a reasonable exhaust efficiency in a future device with burning plasma. Fig. 2 and Fig. 3c show the calculated particle balance between the divertor and the plasma for the above described discharges. Fig.2 compares a L-mode discharge having a low τ_D^{He} (0.25 sec) with a H-mode discharge (Xe contaminated) having a 3 times higher τ_D^{He} (0.7sec). Regardless of the high τ_D^{He}, the H-mode discharge displays an unfavourable particle balance during the heating phase compared with the L-mode shot due to the increase of τ_p^{He} in the core plasma. This is even more true for the discharges shown in Fig. 3c, where the H-mode has no ELM's. Here the particle content of the divertor falls below that of the main plasma, which is a disaster for the ability to pump He. In all of the above described experiments τ_p^{He} in the plasma does not account for sources of He inside the closed flux surfaces. This would make τ_p^{He} even bigger and such result in a less favourable particle balance.

/1/ T. Jones, M.v. Hellermann, et al. see proceedings of this Conference
/2/ G. Janeschitz, G. Fussmann, P.B. Kotze et. al. Nucl. Fus. Vol. 26, No. 12, (1986)

/3/ J. Neuhauser, R. Aratari, M. Bessenrodt-Weberpals, et.al., IAEA-CN-53/A-5-52, Wash. 1990
/4/ G. Fussmann, European Tokamak Workshop, Gut Ising (1989)
/5/ G. Janeschitz, R. Giannella, H.J. Jaeckel, et. al., 17 th EPS conference Amsterdam (1990)

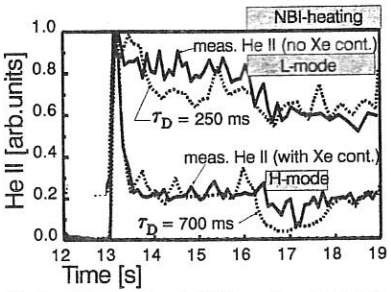

Fig.1: Measured (solid) and simulated (broken) He II signals following a He gas puff into the OH-phase of single null X-point discharges with the X-point positioned on the target plate.
Lower pair of curves: He II signal after puffing into a Xe contaminated discharge;
upper pair of curves: He II signals in the case of a not contaminated discharge. The pronounced difference in τ_D is shown.
No Xe cont.: L-mode during the heating phase (only 6 MW NBI),
Xe cont.: brief ELMy H-mode.

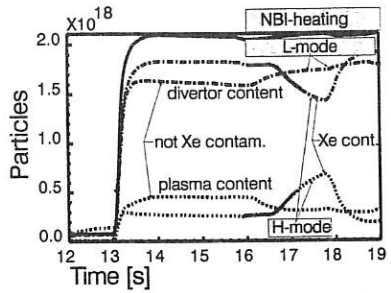

Fig.2: Calculated He particle content in the divertor (upper pair of broken lines) and in the plasma (lower pair of broken lines) for the same discharges as in Fig.1. The pronounced change of these particle contents due to the improved τ_p during the H-mode (Xe contaminated) is demonstrated.

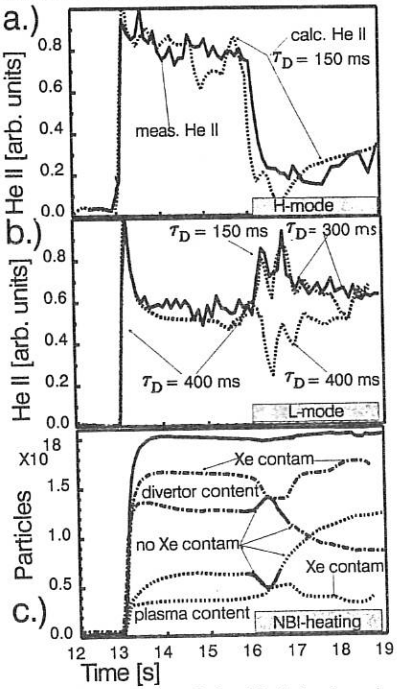

Fig.3: Comparison of the He behaviour in Xe and not Xe contaminated single null X-point discharges with the X-point 10 cm inside the vessel.
a.) no Xe contamination: ELM- free H-mode during the NBI phase.
b.) Xe contamination: L-mode during the heating Phase; displays a breakdown of τ_D when the heating is switched on (increase of He II signal).
c.) Behaviour of the calculated He particle content in the divertor (upper broken lines) as well as in the plasma (lower broken lines). The extreme change of these particle contents due to the improved τ_p during the ELM-free H-mode is shown (no Xe).

THE BEHAVIOUR OF NEUTRAL PARTICLES IN THE PRIVATE REGION OF X-POINT DISCHARGES IN JET

G.Haas*, D.Düchs, J.Ehrenberg, M.Lesourd, A.Montvai, R.Reichle, D.Summers

JET Joint Undertaking, Abingdon, Oxon OX14 3EA, UK
* Max-Planck-Institut für Plasmaphysik, D-8046 Garching, Germany

Abstract

During JET divertor discharges measurements were made of the Dα photon flux and the flux of neutral deuterium onto the wall in the private plasma region. The photon efficiency derived from these signals gives a lower limit for the electron density in the interaction zone between neutrals and plasma, which can be as high as 10^{20} m^{-3}. A rapid decrease of the flux at the onset of NBI indicates a concentration of the recycling in the strike zones. The flux from successive shots shows a memory effect depending on the particle inventory of the X-point region. The measurements are compared with results of a multi-fluid model for the plasma and the neutrals.

Introduction

In divertor tokamaks the recycling flux of neutrals in the x-point region is usually much higher than the external gas puff. The behaviour of the neutrals near the wall in this region determines the density control, i.e. refuelling and pumping. For the boundary of the main plasma the neutral particle flux can be derived from the Dα-photon flux, since the ratio S of ionization events per Dα-photon is rather constant for the plasma parameters typical for that region /1/. However, this is not the case for the region of colder, more dense plasma in the X-point region where S becomes a strong function of T_e and n_e. Therefore a flux measurement independent of Dα is required. If, however, the ionization rate and the Dα-photon flux are measured independently of each other, one can determine limits for the plasma parameters in the zone where neutral gas and plasma interact. We report measurements made during JET X-point discharges of the deuterium particle flux ϕ_{D2} reaching the wall in the region between the strike zones (private region) and the Dα-photon flux $\phi_{D\alpha}$ from the same poloidal position.

Discharge parameters and experimental arrangement

Plasma configuration	:	single upper X-point
Toroidal field	:	B_{tor} = 2.2 and 2.8 Tesla
		Ion ∇B drift downwards ("reverse B_{tor}" see e.g./2/)
Volume averaged plasma density <ne>x10^{19}m-3	:	ohmic phase: (2.2±0.4)
		NBI phase: (2.9±0.6)
Plasma current	:	$I_{pl} \sim 3.0$ MA
Heating power	:	$P_{OH} \leq 3$ MW, $P_{NBI} \leq 12$ MW
X-point position	:	Major radius 2.48 ≤ Rx ≤ 2.55 m
X-point-tile distance	:	-4.2cm ≤ δx ≤ 17.2 cm

ϕ_{D2} was measured with an encased ASDEX-type pressure gauge /3/. It was installed at a position between bands of target tiles at R=2.45 m, and at a distance of 2.6 cm behind the apex of the X-point tiles. It was calibrated against the gas-

puff within 50%. For $\phi_{D\alpha}$ the intensity integrated along a line of sight from the outer mid plane to a position corresponding to that of the pressure gauge has been used. The main contribution to $\phi_{D\alpha}$ is expected from the private region. It was observed by a CCD camera which was absolutely calibrated within ±30%.

Results and Discussion

Within the same discharge ϕ_{D2} and $\phi_{D\alpha}$ behave rather similarly: (Fig.1) both decrease immediately after the onset of NBI. In contrast the Dα-intensity measured outside the private region initially increases, before it also falls. All shots with NBI heating show this behaviour. Of the neutrals produced at the strike zone by neutralization of the impinging plasma apparently a smaller fraction can escape and contribute to the neutral gas in the private region, if the plasma is heated by NBI. This indicates, that the X-point plasma in JET is in a high recycling state even for rather low NBI power ($P_{NBI} \geq 2.7MW$) and low $\langle n_e \rangle$. Similar behaviour has been observed on DIII-D in shots which had an unusually high neutral flux in the private region before NBI and a small separation between X-point and the target. Normally in DIII-D the neutral flux in the private region increases at the onset of the NBI and remains higher than during the ohmic phase. Reasons for the different behaviour in JET might be related to the larger dimensions of the divertor plasma and the short distance from X-point to the tiles. The latter assumption is supported by the fact, that ϕ_{D2} and $\phi_{D\alpha}$ increase for shorter δx.

Despite the rather small range of discharge parameters such as B_{tor}, I_{pl} and $\langle n_e \rangle$ within the data set, ϕ_{D2} and $\phi_{D\alpha}$ vary by factors of 30 and 8, respectively. ϕ_{D2} and $\phi_{D\alpha}$ are closely correlated, but not proportional to each other. The ratio $\phi_{D2}/\phi_{D\alpha}$ varies between 20 and 120 D_2/D_α-photon depending on the flux. (Fig.2) A statistical analysis shows, that most of the scatter in the correlation may be attributed to changes in Rx and δx. Comparing these values with those calculated allows an estimate of the magnitude of plasma parameters in the interaction zone between neutral gas and plasma.

For determining the experimental ionization to excitation ratio S_{exp} from the pressure gauge signal, ϕ_{D2}, and the Dα-photon flux, $\phi_{D\alpha}$, the rate, ϕ_D, of D atoms ionized inside the plasma must be estimated using ϕ_{D2}. The surface between the strike zones is assumed to recycle >90% of all impinging deuterium atoms, molecules or ions. Due to the low power density most of them leave the wall as thermal D2 with wall temperature (600K). In the plasma they undergo one of the following two processes:

$$D2+e^- \Rightarrow D2^+ + 2e^- \Rightarrow D + D^+ + 2e^- \quad (1a)$$

$$D2+e^- \Rightarrow 2D + e^- \quad (1b)$$

The relative probabilities are f for (1a) and (1-f) for (1b). The value of f rises with increasing Te from 0 to 1 (e.g. f(20ev)=0.6)/4/. All D atoms are created as Franck-Condon neutrals. Half of them escape from the plasma. The others penetrate into the plasma and are ionized. Charge exchange with D^+ is neglected for this empirical analysis, because it produces another slightly faster D atom.

Finally we get: $\phi_D/\phi_{D2} = (1-f/2)$ (2)

and $\phi_{D2}/\phi_{D\alpha} = \phi_D/(1-f/2)\phi_{D\alpha} = S_{exp}/(1-f/2) = S'_{ex}$ (3)

Expected values for S' can be calculated, since S and f are known functions of ne and Te. As long as the same Te is used for S and f, the result may be too high by

a factor of ≤2 , because excitation and ionization of the atoms will take place further from the surface than the dissociation or ionization of the D_2, where T_e will be higher and f larger. $\phi_{D2}/\phi_{D\alpha}$= 20, the lowest value found, is compatible with rather moderate plasma parameters (T_e=10 to 20eV, $n_e \approx 10^{19} m^{-3}$) or with a very cold dense plasma (T_e=2 to 3 eV, $n_e \approx 10^{20} m^{-3}$). The highest value $\phi_{D2}/\phi_{D\alpha}$=120 would require $n_e \geq 10^{20} m^{-3}$ for any T_e. In addition, there must be a density gradient length $n_e/\nabla n_e \leq 1cm$ in accordance with the penetration depth of the D atoms.

These results can be understood on the basis of a multi-fluid model. A thin neutral gas in contact with a cool dense plasma can be described by such a model, if polarisation effects in the elastic collision cross-sections between D^+ and D_2 or D are taken into account./5/ The neutral pressure gradients are balanced by friction predominantly with the outstreaming plasma ions. These equilibrium fluxes are then used in the continuity equations, together with sources and sinks, to determine density profiles. According to such a model, densities of deuterium molecules and atoms depend strongly on the plasma temperatures (and density) in the private region. For temperatures ~10eV and electron densities near to $10^{20} m^{-3}$ the measured neutral flux densities could be reproduced. Deeper in the X-point plasma, where the relative velocity of ions and neutrals (predominantly FC-neutrals) is larger, polarisation effects become less important. Kinetic (Monte-Carlo) computations for this situation have not yet been performed.

During similar discharges ϕ_{D2} and $\phi_{D\alpha}$ change from shot to shot with a parameter which describes the particle content of the wall in the X-point region

$$\mathfrak{M}(N,t) = Q_{xp}(N,t) + \sum Q_{xp}(\nu)\, D(t_{\nu,N}) \qquad (4)$$

N and ν are sequence numbers of shots: N refers to the shot under investigation and ν to previous shots. t denotes the time during shot N, when ϕ_{D2} is measured. $Q_{xp}(\nu)$ and $Q_{xp}(N,t)$ are the amounts of gas puffed-in during the X-point phases of shots ν and N, but in the case of shot N only until the time slice t. $D(t_{\nu,N})$ is a decay factor, which depends only on the elapsed time $t_{\nu,N}$ between shot ν and shot N. The sum runs over all shots prior to shot N. Reasonable correlation with ϕ_{D2} was achieved with $D(t_{\nu,N}) = e^{-t_{\nu,N}/\tau}$ ($\tau \approx 2$ hours) and with $D(t_{\nu,N}) = 1/(t_{\nu,N})^{0.7}$. (Fig.3) There is no influence on the decay factor by the discharges themselves. This can be understood, since the gas liberated from the wall during a discharge is redeposited afterwards again. The strongest effects were seen on ϕ_{D2} and $\phi_{D\alpha}$ (factors up to 6 and 2, resp.), but other signals were also modulated, e.g. the plasma density despite feedback stabilisation.

Conclusion

The effects studied in this paper have positive or negative impacts on the performance of a divertor depending on whether the energy-or particle-removal capability is considered. For the former the high plasma density is advantageous, since it raises the radiative power losses and reduces the power load on the collector plates. In addition, it improves the impurity retention capability of the X-point plasma. For these beneficial effects high recycling is essential, and it can be shown, that even for a small additional heating power the plasma near the target is in the high recycling state. For the latter a high neutral pressure is essential which we have found only during the ohmic phase. With the onset of additional heating the pressure decreases by up to 75% even during the L-phase, followed, in some shots, by a further drastic drop at the L to H transition.

References

/1/ L.C.Johnson and E.Hinnov, J.Quant.Spectr.& Rad.Trans. 13 (1973) 333

C.Mahn and V.Welge, MPI fur Plasmaphysik IPP Report 2/239 (1978)
R.M.Kulsrud, H.P.Furth et al., Phys.Rev.Lett. 49 (1982) 1248
M.Greenwald, D.Gwinn et al.,Phys.Rev.Lett. 53 (1984) 352
/2/ R.Reichle, S.Clement et al., this conference
/3/ G.Haas, J.Gernhardt et al., J.Nucl.Mat. 121 (1984) 151
/4/ D.E.Post, D.B.Heifetz et al., J.Nucl.Mat. 111&112 (1982) 383
/5/ D.Düchs, NRL-Report 7340 (1972)

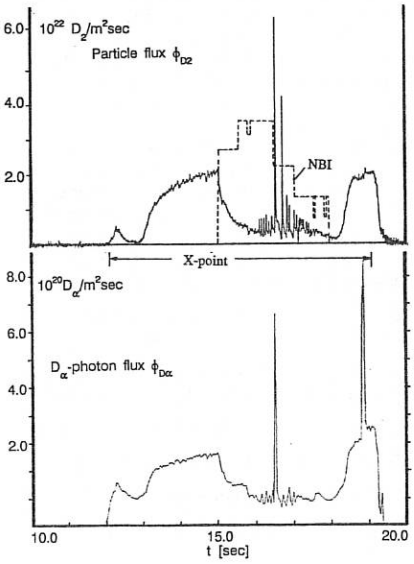

Fig.1 Dα-intensity and particle flux measured in the private region during a typical shot

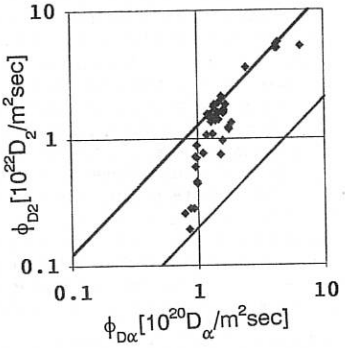

Fig.2 Correlation of ϕ_{D2} with $\phi_{D\alpha}$ The lines represent $\phi_{D2}/\phi_{D\alpha}$=20 and 120 resp.

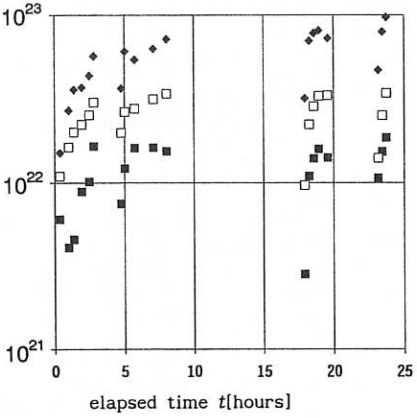

Fig.3 ϕ_{D2} (■) from a series of similar shots compared with two versions of the memory parameter:
(□) exponential decay, (◆) decay ~ $t^{-0.7}$

POWER LOADING AND RADIATION DISTRIBUTION AT THE X-POINT TARGET IN JET FOR NORMAL AND REVERSED TOROIDAL FIELD

R Reichle, S Clement, N Gottardi, H J Jaeckel, M Lesourd, D D R Summers

Jet Joint Undertaking, Abingdon, Oxon OX14 3EA, UK

1. Introduction

It has been observed that the power threshold for transitions from L- to H-mode is lower when the ion ∇B drift is towards the target tiles than for the opposite direction [1]. This was also found in JET [2] where the orientation of the toroidal field with the lower threshold is normally used (hence "normal field"). However In JET the highest neutron yields were recently achieved in discharges with the ion ∇B drift away from the target tiles (reversed field). As high performance discharges in JET were usually terminated by strong carbon influxes, presumably released by thermal sublimation from hot target zones [3], the question arose whether reversed field discharges have a better distribution of the heat load that might delay the onset of such overheating. The heat load was investigated with thermography of the carbon target tiles and the different processes i.e. sputtering or sublimation were interpreted using VUV spectroscopy of the carbon fluxes near the target. Although many plasma properties near the target changed position relative to the radius of the X-point when the ion ∇B drift was reversed a particular group of observations affecting the asymmetry of the power loading between inner and outer strike zone were found to be unaffected by the field reversal.

2. Experiments

The discharges used for this investigation were single null upper X-point discharges of 3MA plasma current with toroidal fields from 2.2T to 3.4T in both directions (mostly 2.2T). The X-point to wall distances δx varied from δx=-10cm (X-point 10cm outside the vessel) to δx=15cm (X-point inside the vessel) with a majority of discharges at a distance of δx=7cm. Neutral beam heating from 7MW to 16MW was applied. The upper X-point target structure and the technique used to measure temperature and calculate the deposited power were as described in [3]. Differences in detail were that the deposited power was calculated from measurements at about 200 points at the target tiles instead of only the hottest points on each strike zone and temperatures up to 3000C were directly measured depending on the attenuation of the filters used, i.e. no extrapolations of the high temperatures were necessary. But the low temperature part of the temperature curves was interpolated from the beginning of the power flux to the X-point tiles until the measurements rose above noise level. The other camera mentioned in [3] which is equipped with a filter changer was in most discharges used for H-α intensity measurements above the private flux region. The radiation distribution of CII and CIV lines near the X-point was measured with a VUV spectrometer [4]. These measurements were compared with results from the bolometer and Langmuir probes.

3. Results

Typical time traces of the power onto the outer and the inner strike zones for normal and reversed field are shown in figure 1. With normal field there is a strong asymmetry and more loading on the outer side; in reversed field there is almost equal loading on both sides. The beginning of the power traces commences at the onset of the additional heating, the end coincides with the disappearance of the stored magnetic energy. Big radiation spikes on the bolometer are associated with deep dips in the deposited power (see 1a), sawtooth crashes are correlated with spikes on the power traces. Individual bands of tiles receive quite different heat loads probably due to misalignment. The band of tiles under observation receives for example up to 3 time more power than its equal share for small X-point to target separations. With larger separation the relative overloading decreases as might be expected with misaligned tiles.

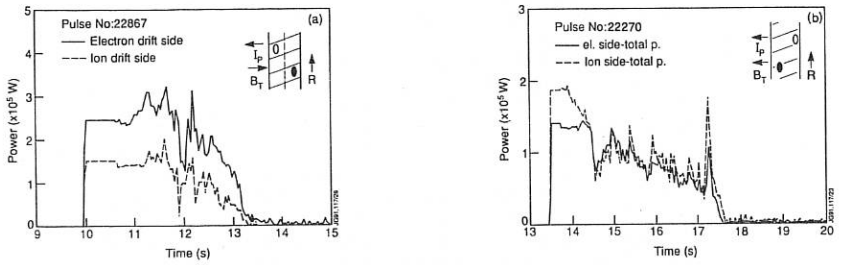

Fig. 1: Temporal evolution of the power deposited on the inner and outer strike zones (see inset patterns) in normal(a) and reversed(b) field .

Typical results of the carbon radiation are shown in fig. 2 as time traces of CIV lines of the radiation at the outer and inner strike zones. In ohmic discharges the maximum of the radiation in normal field is on the inner strike zone (fig. 2a) and in reversed field (fig. 2b) on the outer strike zone (except for a few unexplained cases where the maxima change position in the middle of an ohmic discharge). With additional heating at first the same pattern is observed as in ohmic discharges but as the target surface reaches high temperatures (≈2300C) the carbon signal increases rapidly especially on the more heavily loaded side which is in normal field the outer strike zone (fig 2c).

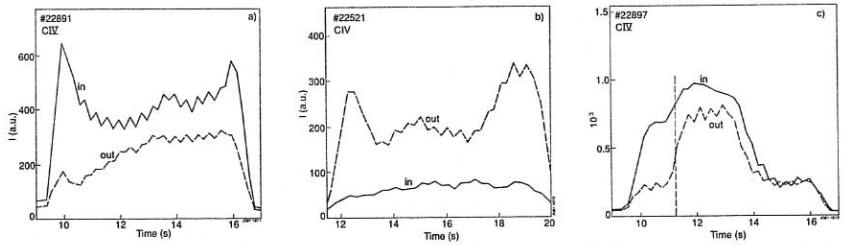

Fig. 2: CIV intensity at the inner and outer strike zones for ohmic discharges in normal (a) and reversed (b) field and for a normal field discharge with NBI heating starting at 10secs (c). Indicated in (c) is the end of the H-mode when the target temperature rapidly rises above 2300C.

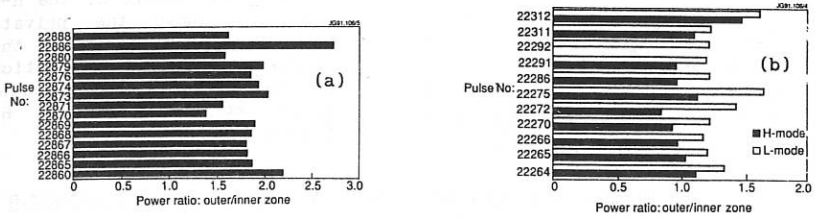

Fig. 3: P_{out}/P_{inn} ratios for normal(a) and reversed(b) field.

Two sets of measurements of P_{out}/P_{inn}, the ratio of the loading on the outer strike zone to that on the inner strike zone, are compared in fig. 3. An average value of ≈ 1.7 is found for P_{out}/P_{inn} during H-modes in normal field, whereas in reversed field the value is ≈ 1.0 for H-Modes and ≈ 1.2 for L-Modes. P_{out}/P_{inn} in normal field was also found to be larger in L- than in H-mode. The target tiles in JET are not equally spaced toroidally. Taking this into account and neglecting probably stronger effects due to misalignments the measured values of P_{out}/P_{inn} would be multiplied by 1.4 for normal field direction, and divided by the same factor for the reversed field case to calculate the power flow in the plasma. For both field directions unusually high P_{out}/P_{inn} ratios in fig. 3 were accompanied with high recycling rates.

The observations of changes with the reversal of the toroidal field are summarised in table 1. They include electron temperature and density from Langmuir probe measurements in single null discharges. The observation of the deposited power from Langmuir probes and CCD camera agree qualitatively [5] (as well for double null discharges not discussed here).

Table 1: Position of maxima of plasma properties in both field directions

Plasma property (Maximum)	Normal field (strike zone)	Reversed field (strike zone)
Deposited power	outer	more equal (inner)
Carbon radiation		
- in ohmic discharges	inner	outer
- with add. heating	variable	variable
Electron temperature	outer	more equal
Electron density	inner	outer

When looking for correlations between variations of P_{out}/P_{inn} and other changes (table 2) it was found that not everything reverses with the toroidal field as table 1 might suggest. It was generally observed (fig. 3) that high recycling occurs with relatively high loading on the outer strike zone. An effect that was observed to be stronger on the inner strike zone was that heavy gas puffing suppressed the loading [6] whereas hot ion mode discharges with high edge ion temperatures [7] increased it. It was observed for both field directions that at the L- to H- transition the power loading ratio changes in the same way: In L-mode, where the recycling is higher relatively more load goes to the outer strike zones than in H-mode (compare with figure 3). For the reversed field in which the L-mode phase could be better observed the change of the P_{out}/P_{inn} ratio at the L- to H-transition and the change of the recycling rate (fig.4) were very similar once more emphasising the link between power loading and recycling.

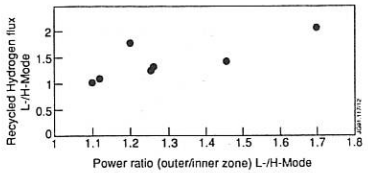

Fig. 4: The change of the H-α intensity above the private flux region (indicating the recycling rate) as a function of the change of the Pout/Pinn ratio at the L- to H-transition.

Table 2: Observations of factors affecting Pout/Pinn

Factor	accompanied by bigger Pout/Pin	accompanied by smaller Pout/Pin	observed in (tor. field)
Edge ion temperature	low	high	normal
Recycling rate	high	low	both
Discharge mode	L	H	both
Gas puff	heavy	-	both

4. Discussion

The observations in table 1 concerning heat flux and radiation are consistent with each other if one interprets the radiation pattern in ohmic discharges as caused by sputtered carbon and during additional heating as dominated by thermally released carbon. The finding that in normal field the plasma on the inner strike zone is denser and cooler with less heat deposited there than on the outer strike zone and that these positions reverse with reversal of the toroidal field is in agreement with observations from other tokamaks and the description of Hinton and Staebler [1]. The observation about the position of the maximum of the heat flux is also explainable by ion orbit calculations [8]. The more equal heat load distribution found in reversed field may well explain, probably together with a better peaking due to 120 keV beams, that in this configuration better high performance discharges were achieved than in normal field.

The observations summarised in table 2 of effects which don't change sides on toroidal field reversal are linked by the recycling rate: increased recycling is accompanied by relatively more load on the inner strike zone. If one assumes that the anomalous flow is, in both field directions, strongest at the outer midplane [1] one might interpret these effects as the result of changes of that flow. The observations about the change of Pout/Pinn with the edge ion temperature are another hint and deserve special attention in coming investigations.

The existence of a component of the power loading which does not change sides when reversing the toroidal field may explain why the loading ratio does not completely reverse and is less asymmetric in reversed field.

We thank P J Harbour for pointing out the geometrical factor of 1.4.

[1] F.L. Hinton, G.M. Staebler, Nucl. Fusion **29** (1989) 405.
[2] D. Ward, et al.this conference.
[3] R. Reichle, et al. J. Nucl. Mater. **176** & **177** (1990) 375.
[4] P. Chabert, et al. Contributed paper to the 16th European Conference on Controlled Fusion and Plasma Physics (EPS) Venice March 13-17 1989, 1505.
[5] T. Tagle et al. this conference.
[6] D. Stork et al. J. Nucl. Mater. **176** & **177** (1990) 409.
[7] H. Weisen et al., Bull. Am. Phys. Soc. **35**,9 (1990) 1999.
[8] D.D.R. Summers, et al., this conference

RESULTS FROM EDGE SPECTROSCOPY IN JET

K D Lawson*, R Barnsley, B Denne-Hinnov, R Giannella, N Gottardi,
N C Hawkes*, P D Morgan, T K Patel, N J Peacock* and M F Stamp

JET Joint Undertaking, Abingdon, Oxon, OX14 3EA, UK
*Culham Laboratory, UKAEA/Euratom Fusion Association, Oxon, OX14 3DB.

1. INTRODUCTION

An understanding of the edge region of a tokamak plasma is crucial in determining the behaviour of the impurities since the plasma edge conditions regulate the impurity release into the scrape-off-layer and the screening of the impurity ions from the bulk plasma. Spectroscopic data on high density or high power limiter operation and a series of X-point experiments have been recorded during the experimental campaign of 1990 and are analysed in this paper.

Edge spectroscopy is used for a wide range of diagnostic purposes, from which a few interesting topics have been selected. The reduction in the D influx in the L- to H-mode transition of X-point discharges is illustrated and a comparison is made between the influxes and ion temperatures of two high-power limiter pulses.

For the 1990 experimental campaign the Ni, ICRH Faraday shields were replaced by Be shields, these complementing the existing Be belt limiters. Consequently, the Ni radiation was reduced to background levels. Throughout the operations with Be, O has been suppressed by gettering, so that the dominant low Z impurities were Be and C. Significant radiation from the Cl impurity in JET has been observed during the campaign. Factors affecting its release are discussed.

2. HIGH POWER BE-LIMITER PULSES

The visible spectrum is monitored routinely on JET, by relaying the radiation from the torus to detectors outside the biological shield using quartz optical fibres [1,2]. One fibre views the region in front of ~ 25 cm length of the upper Be belt limiter and by use of a survey spectrometer fuel and impurity influx measurements and local ion temperatures and electron densities can be measured [3]. During the 1990 campaign the main limiter influxes observed were of Be and the fuel, D.

The use of a multi-Gaussian line fitting routine enabled ion temperatures to be determined from the Doppler-broadened profile of the D_α, 6561Å spectral line. After the removal of weak components due to residual H, "warm" and "cold" D_α components can be isolated. The "cold" component is emitted by the D atoms resulting from the break-up of the D_2 molecules that enter the plasma. There is insufficient time for these atoms to thermalise before being ionised by electron impact or involved in charge-exchange collisions and the measured temperature reflects the Frank-Condon energies associated with the molecular break-up. The charge-exchange cross-section is similar to that of electron impact ionisation and the "warm" component is a result of charge-exchange collisions to already thermalised D nuclei, this component being indicative of the near-edge plasma conditions.

Figure 1 illustrates the ion temperature measured from the "warm" D_α component for two JET pulses, 22948 and 22958. The former has 10.5 MW of additional heating (7.5 MW ICRH and 3MW NBI) and the latter ~ 16MW of ICRH. The ohmic value of 120eV is in agreement with

previous measurements [3], the line average densities for these pulses being ~ 2.5 x 10^{19} m^{-3}. With the onset of additional heating at 8 s, the ion temperatures are seen to rise sharply, peaking at ~ 350 eV. However, it should be noted that the precise radial location of the emitting region is unknown and could change during the heating phase. As in the ohmic case [3], strong D_2 gas puffing from 8.7 to 10s in pulse 22958 reduces the measured ion temperature. This may be due to cooling of the edge or a result of the increased density reducing the penetration of the D atoms.

The ion temperature of the "cold" component for these pulses is ~ 9 eV which is consistent with the molecular break-up energies. That for neutral Be, which is derived from the Doppler width of the 4407 Å line, is ~ 7 eV and this confirms that physical sputtering is the dominant release mechanism of Be.

The D and Be influxes, measured from the D_α and BeII, 4361 Å spectral lines, are shown in figures 2 and 3, respectively, for the same pulses. The strong gas puffing in pulse 22958 leads to an increased D influx and there is clear evidence that the high additional heating power in this pulse has resulted in the Be limiter melting in a region neighbouring that viewed. The ratio of the Be to D influxes gives an approximate measure of the effective Be sputtering yield. The presented influx data imply that the yield reaches values well in excess of 1.0 for pulse 22958. The effect of the gas puffing is discussed by Gondhalekar et al.

3. THE L-H MODE TRANSITION

An important aspect of the X-point programme has been to study and optimise H-mode plasmas. As would be expected, the characteristic high-confinement of these plasmas is reflected in their edge behaviour.

A comparison of the fuel influx as measured by the D_α, 6561 Å spectral line from a horizontal view of the inner wall and a vertical line into the private region of the X-point shows a marked difference in behaviour. Previous measurements using a poloidal array viewing the vessel walls have demonstrated a reproducibility of the influx from different lines-of-sight to within ~ 20% and hence the inner wall signal can be adjusted to represent the total wall flux, as is shown for pulse 21801 in figure 4. The wall influx is seen to increase somewhat from the ohmic X-point level when additional heating is applied and subsequently to fall by a factor ~5 at the L- to H-mode transition.

In contrast, only a small decrease or no change in the influx is observed in the X-point private region at an L- to H-mode transition, this depending on the extent to which the line-of-sight includes the X-point interaction zones. This difference emphasises the separate behaviour of the plasma within the X-point private region.

4. FACTORS AFFECTING THE RELEASE OF Cl

The Cl impurity in the JET plasma has accounted for a significant fraction of the radiation throughout the 1990 experimental campaign and is, therefore, detrimental to plasma performance. This elemental component can range, typically, from 20 to 75% of the total radiated power and is even higher at high densities, Cl radiating over 90% of the power as the density limit is approached [5]. In most cases the presence of Cl determines the density limit.

The chemical nature of the release mechanism is evident from two observations. Firstly, a marked reduction in the Cl content of the plasma is observed when the D plasma gas is replaced by He, as is shown in figure 5 by the Cl radiated power components of ^4He pulses following the D pulse 20591. This suggests that DCl will be involved in the chemical desorption process. Secondly, a SF_6 leak from the lower hybrid launcher after pulse 22930 resulted in an order of magnitude increase in the Cl content. This can be seen in figure 6 which plots the Cl component and total radiated power at 4s against JET pulse number. This change in the Cl levels is attributed to the presence of F in the vessel, since the time development of the Cl and F spectral line intensities during a pulse and from pulse-to-pulse are closely correlated. It is expected that the more chemically reactive F substitutes for Cl, thereby releasing the heavier element into the plasma.

Another significant decrease in the Cl content appears to be correlated with a reduction in the vessel temperature from 300° to 210°C. Although needing confirmation, this can be understood in terms of the dependence of the chemical reaction rate on temperature and implicates the walls as the main source of Cl.

A number of other factors which might affect the Cl release have been investigated, such as magnetic configuration, additional heating type, plasma position, the presence of other impurities and a range of plasma parameters. Generally those events which lead to some disturbance of the vessel, for example a plasma disruption or a period of machine maintenance or the plasma coming into contact with fresh wall areas, as occurs when the plasma current is increased, can lead to increased levels of Cl in the plasma.

5. CONCLUSIONS

Ion temperatures have been measured from the spectra emitted by Be and D limiter influxes during additional heating. They confirm that the main release mechanism of Be is physical sputtering and indicate edge ion temperatures of up to 350eV, although the precise radial location is unknown. Be influx measurements indicate that surface melting of the Be limiter during high power additional heating is commonly observed.

A difference is noted between D influxes from the X-point private region and D wall influxes during the L- to H-mode transition. The latter is typically reduced by a factor of 5, whereas little change occurs in the private region.

Evidence is presented indicating chemical desorption involving D as the main release mechanism of Cl. The presence of F in the vessel led to a significant rise in the Cl levels.

REFERENCES

[1] P D Morgan et al., Rev. Sci. Instrum., 1985, vol 56, p 862.

[2] M F Stamp et al., J. Nucl. Mat. 1989, vol 162-4, p 404.

[3] M F Stamp and H P Summers, Proc. 17th EPS Conference, Amsterdam, 1990, vol 3, p 1377.

[4] A Gondhalekar et al., these proceedings.

[5] K D Lawson et al., Proc. 17th EPS Conference, Amsterdam 1990, vol 3, p 1413.

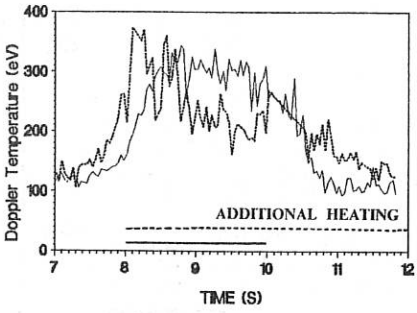

Figure 1. Edge ion temperatures measured from "warm" D_α component for pulses 22948 — and 22958.....

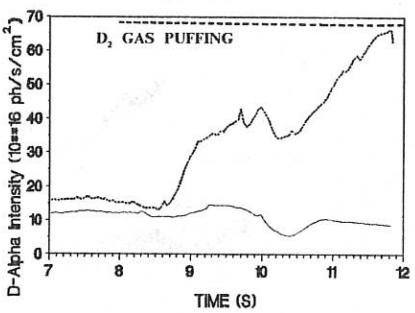

Figure 2. D_α spectral line intensities which are a measure of the D influx, for pulses 22948 — and 22958.....

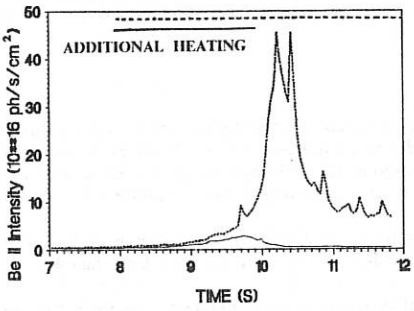

Figure 3. Be II spectral line intensities, which are a measure of the Be influx, for pulses 22948 — and 22958.....

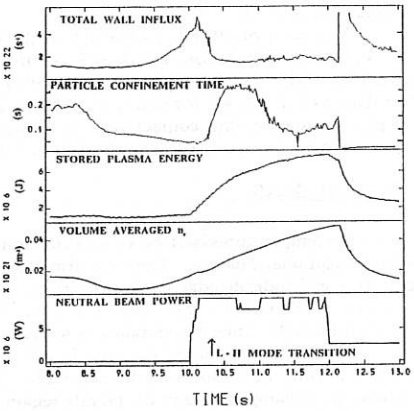

Figure 4. Total wall influx, particle confinement time, stored energy, volume averaged n_e and neutral beam heating power for the H-mode pulse 21801.

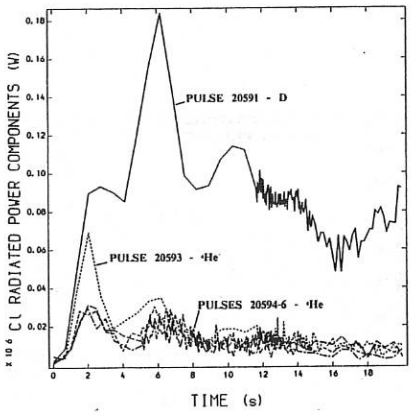

Figure 5. Power radiated by Cl in D and ^{4}He plasmas.

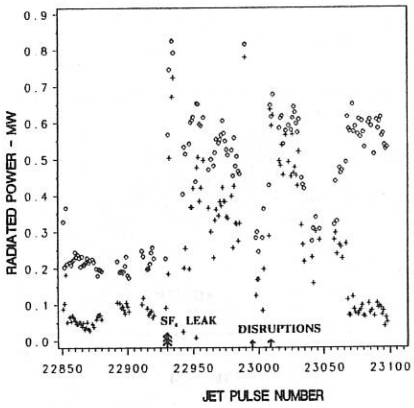

Figure 6. Cl component, +, and total radiated powers,◊, measured at 4s versus pulse number before and after the SF_6 leak at pulse 22930.

MEASUREMENT OF THE RADIAL ELECTRIC FIELD AT THE PERIPHERY OF ASDEX PLASMAS

A. R. FIELD, G. FUSSMANN, J. V. HOFMANN

Max-Planck-Institut für Plasmaphysik
D-8046, Garching, FRG

1. Introduction: From spectroscopic measurements of the drift velocities of BIV impurity ions we infer that a strong negative radial electric field ($|E_r| \approx 25$ kV/m) develops during the H-mode just within the separatrix. This result supports those of similar investigations on DIII-D and JFT-2M. (We have investigated the principle of such measurements in detail.) Such changes in E_r and v_θ (or their gradients) have been proposed by several authors to offer a theoretical explaination of the sudden confinement improvement occuring at the L→H-mode transition. Our results indicate that the origin of E_r and $v_{i\perp}$ ($\perp\vec{B}$) may be related to edge ion temperature and pressure gradients. We compare our results with neo-classical predictions for the BIV ion and deuteron poloidal velocities. For a detailed discussion and references refer to our paper [1] and report [2].

2. Measurement Technique: The basic relation between the perpendicular ($\perp\vec{B}$) fluid velocity of a particle species $v_{i\perp}$ and E_r is the radial force balance:

$$e Z_i n_i [E_r - v_{i\perp} B] = \frac{\partial p_i}{\partial r} \quad (1)$$

where eZ_i, n_i and p_i are the charge, density and pressure of the species. $v_{i\perp}$ is tangiential to the magnetic surfaces and nearly in the poloidal direction. From Equ. (1) $v_{i\perp}$ is given by:

$$v_{i\perp} = -\frac{1}{e Z_i n_i B}\frac{\partial p_i}{\partial r} + \frac{E_r}{B} = v_{dia} + v_{ExB} \quad (2)$$

where the component v_{dia} depends upon the charge and arises from the gyration of the particles and the component v_{ExB} arises from the ExB drift and is independent of the charge. In general v_{dia} has to be taken into account when inferring E_r from $v_{i\perp}$.

An appropriate measurement of the Doppler shift of a spectral line does not provide a direct measurement of $v_{i\perp}$ as observed photons are emitted from excited ions who's gradients, over distances of the order of the gyro-radius, will not reflect those of the ground state ions unless their lifetimes τ_k are short compared with the recipricoal gyro-frequency $1/\omega_i$ ($\omega_i\tau_k << 1$). Considering this effect in detail we find that the perpendicular velocity $v_{i\perp}^*$ inferred from the (locally) measured Doppler shift is given by:

$$v_{i\perp}^* = -\frac{1}{eZ_i n_i B}\frac{\partial p_i}{\partial r} - \frac{T_i \Gamma}{eZ_i B}\left[\frac{\frac{\partial}{\partial r}(\zeta_k)}{\zeta_k}\right] + \frac{E_r}{B} = v_{dia} + v_{pseudo} + v_{ExB} \quad (3)$$

$$\Gamma = \frac{(\omega_i\tau_k)^2}{1 + (\omega_i\tau_k)^2} \quad (4)$$

The component v_{pseudo} arises solely from the gradient of the excitation probability ζ_k and is not a component of the fluid velocity. With $(\omega_i\tau_k)^2 << 1$, Equ. (3) reduces to Equ. (2) and with $(\omega_i\tau_k)^2 >> 1$ the terms v_{dia} and v_{pseudo} may be combined into a single term $T_i\partial(\ln(\varepsilon T_i))/\partial r/eZ_iB$ where ε is the emissivity. Both ε and T_i can be measured spectroscopically.

We have concentrated our measurements on the BIV(2823Å) and CIII(4649Å) triplet lines as these are emitted with sufficient intensity from narrow shells near separatrix (r_{sep} = 40 cm). Light from a single line of sight is collimated into a 1m Czerny Turner spectrometer (fitted with a 3600 l/mm grating and a 1024 channel detector providing spectra at 20 ms intervals) by a rotatable mirror at the entrance to a port at the horizontal mid-plane and a lens. Observations can be made along opposing toroidal, poloidal or $\perp\vec{B}$ directions (via upper and lower fixed edge mirrors) during successive shots. Radial emissivity profiles (measured by oscillating the mirror, moving the plasma or from shot-to-shot) show that, in the OH-phase, the BIV(2823Å) emissivity has a maximum at 2±1 cm inside the separatrix (FWHM ~3 cm) and that of CIII(4649Å) a maximum at the separatrix (±1 cm, FWHM ~4 cm) and that these shells move outward by ~1 cm at the OH→L- transition and a further ~1 cm at the L→H-transition.

Measured radial profiles of ε of the BIV(2823Å) line and T_i (BIV) inferred from the Doppler broadenning are used to calculate $v_{i\perp}$* from Equ. (3) with Γ= 0.58. These values are used to calculate the drift velocity $v_{i\perp m}$* which would be inferred from the Doppler shift of the centroid of the integrated emissivity along a line-of-sight (LoS) orientated at an angle γ to the poloidal plane and at an impact radius r_o for various cases. From these simulations we conclude that, with the LoS aligned $\perp\vec{B}$ and observing along chords with 35cm < r_o < 40cm ($r(\varepsilon_{max})$ = 40cm), E_r can be inferred directly from $v_{i\perp m}$* without making corrections for diamagnetic drifts or radial excitation probability gradients, even in the prescence of high velocities $\|\vec{B}$. Both from a measurement and from the statistical uncertainties in the data evaluation procedure we have determined that the accuracy of our drift velocity measurements is better than ±1.0 km/s.

3. Results: Results of the analysis of the BIV(2823Å) triplet spectra (measured along chords of r_o = 38±2 cm) show that, at the L→H-transition, $v_{i\perp}$(BIV) begins to increase from the small values observed in the OH- and L-phases ($|v_{i\perp}(BIV)| \leq 2.0$ km/s) to high values ($|v_{i\perp}(BIV)| \leq 20.0$ km/s) in the electron diamagnetic drift ($-\vec{B}\times\nabla p$) direction during the H*(ELM-free)-phase. The direction of $v_{i\perp}$(BIV) reverses on reversal of B_t (and I_p). The temporal evolution of $v_{i\perp}$(BIV) is shown in fig.1 along with the Hα divertor intensity, T_i(BIV) (determined from Doppler broadening) and ∇p_e at the edge (from Thomson scattering). There is a clear similarity between the temporal dependence of $v_{i\perp}$(BIV), T_i(BIV) and ∇p_e. These results are consistent with the presence of a strong negative radial E-field ($|E_r| \leq$ 25kV/m) just within the separatrix in the H*-phase.

Results of the analysis of the CIII(4649Å) triplet spectra, emitted from radii at or just outside the separatrix, showed that $v_{i\perp}$(CIII) is small under all conditions (OH-, L- and H*-phases) and thus $|E_r| \leq 3.0$ kV/m at these radii. Together with the results from BIV this indicates that, in the H*-phase, there must be strong positive gradients of E_r just within the separatrix.

Fig. 2 (a, b) shows vector diagrams of $\vec{v}$ (BIV) constructed from the measured values of $v_{i\perp}$ and $v_{i\phi}$ determined from the differential Doppler shift observed along opposing directions during successive shots (2.0 MW Co-NBI, B_t = 1.74 T, I_p = 280 kA, r_o = 36 cm). In the L-phase $|v_{i\perp}| \leq$ 2.0 km/s ($<< v_{i\phi}$) whereas in the H*-phase $|v_{i\perp}| \leq$ 15.0 km/s ($\approx v_{i\phi}$) and is in the $-\vec{B}\times\nabla p$ direction. This implies that E_r has increased in magnitude, from $|E_r| \leq$ 3.0kV/m in the L-phase, to about -20 kV/m in the H*-phase.

In the H*-phase $|E_r|$ increases with Co-NBI power (at constant B_t= 1.74 T and I_p= 280 kA) from -16kV/m at P_{NI} = 1.6 MW to -22 kV/m at P_{NI} = 2.3 MW. $|v_{i\perp}|$ and $|E_r|$ are similar in cases with Co- and Ctr-NBI directions in the H*-phases; with 2.3 MW Co-NBI E_r = -22 kV/m and with

2.0 MW Ctr-NBI E_r = -18 kV/m. On increasing B_t and I_p together ($q_a \approx 3$, Ctr-NBI 2.0 MW) $v_{i\perp}$ remains largely unaltered in the H*-phase implying that $|E_r|$ has increased from 22 kV/m at B_t= 1.74 T (and I_p= 280 kA) to 36 kV/m at B_t= 2.8 T (and I_p= 460 kA).

4. Discussion and Conclusions: The temporal and parametric dependencies of $v_{i\perp}$(BIV) and E_r suggest that their origin may be related to the edge ion temperature and pressure gradients. With respect to the interpretation it is essential to realize that the observed impurity velocities can differ substantially from those of the background ions. Recently, the neoclassical theory has been extended to cover these questions [3].The expressions derived for the poloidal velocities of impurities (I) and background ions (i) are:

$$v_\theta^i = \frac{1}{2}\, v_{th,i}\rho_i \left\langle K_1 L_{T_i}^{-1} \right\rangle \frac{B^2}{\langle B^2 \rangle} \qquad (5)$$

$$v_\theta^I = \frac{1}{2}\, v_{th,i}\rho_i \left\langle \left(K_1 + \frac{3}{2}K_2\right) L_{T_i}^{-1} - L_{p_i}^{-1} + \frac{Z_i T_I}{Z_I T_i}\, L_{p_I}^{-1} \right\rangle \frac{B^2}{\langle B^2 \rangle} \qquad (6)$$

where $L_{T_i}^{-1} \equiv \partial(\ln T_i)/\partial r$ etc., $v_{th,i} \equiv$ ion thermal velocity, $\rho_i \equiv$ ion gyro-radius, $p_i \equiv$ ion pressure and $K_{1,2}$ are coefficients of O(1) which dependent mainly upon the collisionality of the background ions ν_i^* and the impurity strength $\alpha = Z^2 n_I / n_i$. For the BIV experimental conditions ($T_i \approx 200$ eV , $n_i \approx 1{\cdot}10^{19}$ m^{-3}) we have $\nu_i^* \approx 1.2$ and $\alpha \approx 1$ resulting in $K_1 = 0.27$ and $K_2 = 0.59$. This leads to a very weak dependence of v_θ^I on the temperature gradient (note that the last term in eq. (6) can be neglected because of $L_{pI}^{-1} \approx 0$). With $L_{ni} \approx L_{ne} \approx 1.2$ cm (from Li-beam measurements) we estimate finally $v_\theta^i = 2.5{\cdot}10^3$ m/s and $v_\theta^I = -3.9{\cdot}10^3$ m/s. This neoclassical impurity velocity is in the right direction but about a factor of five too small in magnitude.

Because of the smallness of the neoclassical velocities we have been searching for other physical mechanisms that could yield an appropriate poloidal torque. Due to the 1/R dependence of B_t such a torque could for instance be produced by a divergence-free current flowing between the inside and the outside of the minor cross-section of the plasma (at smaller minor radii this current could be force free by flowing parallel to $\vec{B}$ on the magnetic surfaces). The same current, however, would also produce a rather large vertical force which would be compensated for by the equilibrium control system by a change in the radial equilibrium field $B_{r,eq}$. We indeed observe a temporary (10 ms) change in $B_{r,eq}$ at the L→H-mode transition (and at ELM events) which, if due to such a radial current flowing in a sheet at the mid-plane, could provide sufficient torque to accelerate the plasma to the measured poloidal velocities. On the other hand, such a momentary torque is unlikely to maintain the poloidal rotation, which is observed throughout the H*-phase, against damping forces. The origin of the observed large poloidal velocities is thus still unclear.

5. References:

[1] Field, A.R., Fussmann, G., Hofmann, J.V.,"Measurement of the Radial Electric Field in the ASDEX Tokamak", submitted to Nuclear Fusion.

[2] Field, A.R., Fussmann, G., Hofmann, J.V., IPP Report, IPP-III/165, December 1990.

[3] Kim, Y.B., Diamond, P.H., Groebner, R.J.," Neoclassical Poloidal and Toroidal Rotation in Tokamaks.", private communication.

[4] Hazeltine, R.D., Phys. Fluids, 17, 5 (1974) 961.

6. Figures:

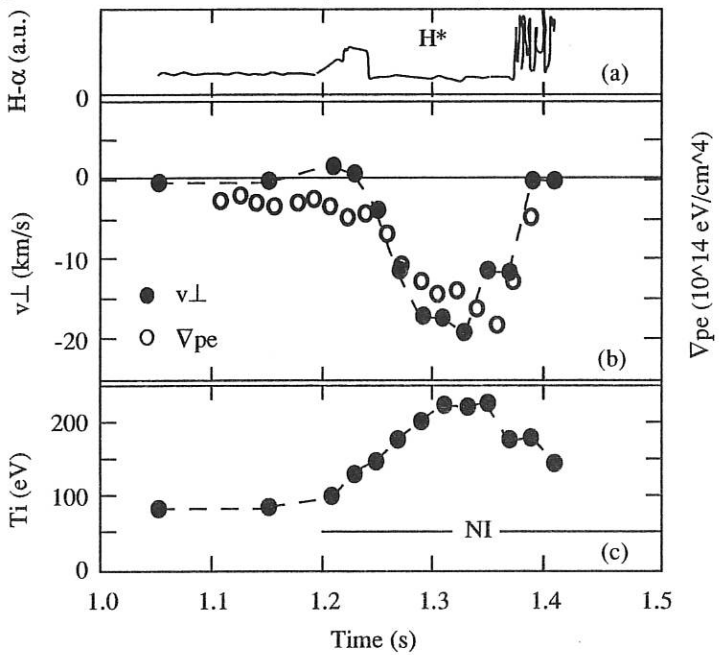

Fig. 1 The time evolution of the Hα divertor intensity; the measured $v_{i\perp}$ of the BIV ions; T_i (BIV) from Doppler broadening; and the edge ∇p_e determined from Thomson scattering data. (Co-NBI, 2.3MW, B_t = 1.74 T, I_p = 280 kA).

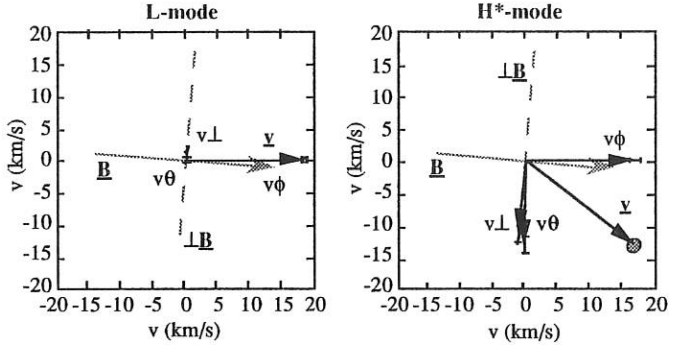

Fig. 2 Vector diagrams showing the BIV drift velocity $\underline{v}$ constructed from components $v_\perp$ and v_ϕ measured in the L-phase (Co-NBI, 1.0 MW) and in the H*-phase (Co-NBI, 1.6 MW). In both cases B_t = 1.74 T, I_p = 280 kA, $q_a \approx 3$.

ION TEMPERATURE NEAR THE SEPARATRIX AT ASDEX

R. Schneider, H. Verbeek, D. Reiter (*), J. Neuhauser, and the ASDEX team

Max-Planck-Institut für Plasmaphysik, EURATOM Association
W-8046 Garching/München, Boltzmannstr.2, FRG
(*) Forschungszentrum Jülich (KFA)
Institut für Plasmaphysik, EURATOM-KFA Association
W-5170 Jülich, P.O.B. 1913, FRG

1. Introduction

The ion temperature profile near the separatrix and in the scrape-off layer of a tokamak is a crucial quantity for the transport of energy and particles in this region, but is mostly unknown in present tokamaks. Typical relaxation times as well as edge plasma simulations indicate the possibility of strongly different electron and ion temperatures [1], at least in cases of low edge densities. Indirect experimental evidence for that has been reported from several tokamaks, e.g. ASDEX [2] and JET [3].

2. Method

Charge exchange (CX) neutral spectroscopy combined with numerical models for neutral hydrogen gas transport is a standard procedure to determine bulk ion temperatures in tokamak plasmas. It has proven to be a fairly robust method even in cases in which the model assumptions at the plasma edge are quite uncertain [4]. This valuable insensitivity against less well known parameters as surface interaction models and other typical plasma edge effects vanishes if the low energy (neutral energies less then 1000 eV) neutral particle spectra are considered as required to determine edge ion temperatures. At ASDEX this spectral range was routineously measured by a time-of-flight system (LENA) [5], but hitherto the information contained has not been fully exploited. Only moments of the measured spectra have been used, e.g. mean energy, power or wall sputter yield [6]. In this energy range neutral gas models are more sensitive now to geometrical effects, spatial source distribution and assumptions on recycling. This complexity has left Monte Carlo methods as the only means for numerical assistance in data interpretation. Therefore, we used the fully 3D Monte Carlo neutral particle code EIRENE [4] to calculate the low-energy charge exchange spectra for energies below 1000 eV and to analyse their information with respect to ion temperature profiles.

The input plasma profiles for the simulation of ion density and electron temperature are taken from YAG laser scattering, continuum radiation and lithium-beam diagnostic. The result of a CX-spectrum simulation for typical ASDEX ohmic conditions is shown in Fig. 1 as full line compared with the measured spectrum (open symbols). Obviously, the simulation is able to reproduce the measurement. The spatial origins of the detected particles with energies E are shown as diamonds in the upper

part of Fig.1, the variances of this distribution function are shown as vertical bars. This clearly demonstrates that the information of the low-energy spectra is in fact restricted to the region close to the separatrix, because most of the particles seen by the time-of-flight analyser originate from this region.
By varying the ion temperature profile in the simulation and optimising the results of the simulation compared to the experimental CX-spectra, the ion temperature profile can be determined [7] in the radial range from which the particles in the spectrum originate, that means in our case from the region near the separatrix.

3. Results

We analysed the time-dependence of the ion temperature profile for three ASDEX shots (# 33474: a density limit shot; # 24703: an ohmic shot with SOC-IOC transition; # 33144: a shot with neutral beam heating and L-H-H* transition).
For all three shots and for all times we get very low ion temperatures (less than or equal 40 eV) at the separatrix and for larger radii. This reflects the monotonic increase of the neutral flux to low energies in the measured spectra (see Fig. 1) and agrees well with spectroscopic results of ion temperatures from C III measurements at approximately the separatrix position [8]. A strong variation of the ion temperature profile occurs in the region just inside the separatrix (radius less than 40 cm, see Fig. 2). The density limit shot (# 33474) exhibits for low densities in the region between 30 cm and 36 cm much higher ion temperatures (by a factor of about 2-4) than electron temperatures. With increasing density both profiles approach each other as expected from relaxation times.
No significant difference between SOC and IOC could be found for the edge ion temperature profiles (ohmic shot # 24703) in agreement with previous results of center ion profiles derived from active and passive CX analysis at higher energies. [9].
Neutral injection drastically increases the ion temperatures in the region inside the separatrix (shot # 33144). The L-H-H* transition is characterised by the change of the ion temperature profile in this region from a steep one (L) to flat profiles (H,H*). The ELM'y H-phase shows a high ion temperature gradient near the separatrix. In the ELM-free H*-phase the ion temperature profile has the same form as in the ELM'y H-phase, but the ion temperatures are significantly lowered [10].

4. Discussion

Ion temperature profiles determined by our analysis assume Maxwellian distribution functions $f(E_i)$. However, the distribution function of the ions is not necessarily Maxwellian in the scrape-off layer: particle confinement time in this region with high gradients in the ion temperature is comparable to ion-ion relaxation time for tail ions, at least for lower densities. Therefore, ion distribution functions are expected to have non-Maxwellian tails. Experimental evidence for this is given by high-energy CX-measurements of reflected particles in the divertor [11], which gave ion temperatures of about 150 eV. To check this in the simulation we used a two Maxwellian distribution, one Maxwellian for the spatially varying bulk ion temperature (majority) with weight 0.9 and one with weight 0.1 for the 150-eV-minority assumed spatially con-

stant (see insert Fig. 3). In Fig. 3 the result of such a calculation is shown as a full line. Using only the Maxwellian for the majority ions (open symbols in Fig. 3) results in a small increase of the ion temperature close to the separatrix and a reduction in the region between 35 cm and 38 cm compared to the 2-Maxwellian result.
The procedure for determination of the ion temperature profile as described above give quite detailed results, but is very time-consuming. Inverting the problem is much more efficient: varying all input profiles and using function parametrisation methods only one time a set of spectra covering the whole parameter range must be calculated and then the experimentally unknown ion temperature profiles parameters - and therefore the ion temperature profile itself - can be calculated by multivariate regression very fast for every measured neutral spectrum, using the spectrum and the experimentally known profiles as input values.
This alternative approach has been tested in some detail with the following result: statistical analysis allows the determination of the separatrix ion temperature with an error of about 30 eV and the derivative of the ion temperature profile expressed as a decay length with an error of about 1.5 cm. A crucial point for practical application is the limitation of the number of profile parameters due to calculation-time problems. Significant progress may be expected by introducing a generalized coordinate (essentially the line integrated density up to the spatial point r). This is forseen for ASDEX-Upgrade, where also YAG profiles at the edge will be available with much better resolution.

5. Conclusions

Simulation of measured low-energy CX-spectra by a Monte Carlo neutral gas code allows determination of ion temperatures in the region close to the separatrix. In ASDEX we get rather low temperatures (less equal than 40 eV) at the separatrix with strong increase just inside it. A hot ion minority expected from simple estimates slightly changes the majority temperature profile, but cannot determined quantitatively on the basis of present data. A fast method for ion temperature profile determination has been tested, but still needs improvement.

6. References

[1] J. Neuhauser et al., Plasma Phys. Contr. Fusion 31 (1989) 1551
[2] J. Neuhauser et al., IAEA-CN-53/A-5-2
[3] S. K. Erents et al., Europhys. Conf. Abstr. 14B (1990) 1385
[4] D. Reiter, JUEL report 1947 (Jülich, 1984)
[5] H. Verbeek, J. Phys. E19, 964 (1986)
[6] V. Dose, H. Verbeek, Appl. Phys. Lett. 51 (1987) 229
[7] D. N. Rucic, D. B. Heifetz, and S. A. Cohen, J. Nucl. Mater. 145-147 (1987) 527
[8] A. R. Field, G. Fussmann, J. V.Hofmann, IPP report III/165 (Garching, 1990)
[9] U. Stroth et al., Nucl. Fusion 29 (1989) 761
[10] ASDEX-Team, Nucl. Fusion 29 (1989) 1959
[11] F. Wagner, Nucl. Fusion 25 (1985) 525

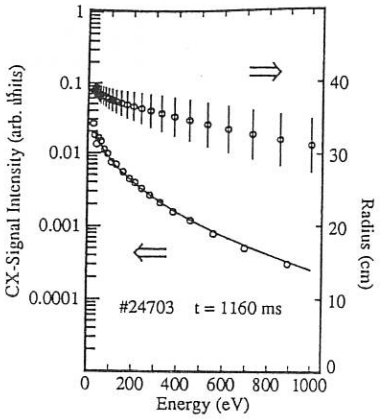

Fig.1: Calculated CX-signal intensity as a function of energy (full line) for typical ASDEX ohmic conditions plasma input profiles.

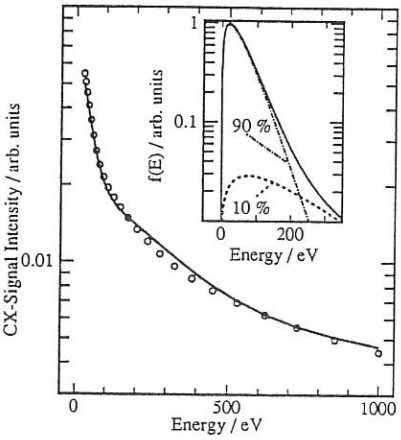

Fig.3: Result of a CX-simulation with a two Maxwellian ion distribution function $f(E_i)$: one Maxwellian for the spatially varying bulk ion temperature with weight 0.9 and one with weight 0.1 for the 150-eV-minority (see insert). The result of the two Maxwellian calculation (full line) can be reproduced by using only the Maxwellian for the bulk ions (open symbols) with small changes in the majority ion temperature profile.

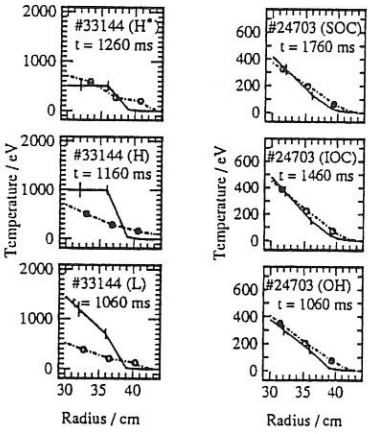

Fig.2: Radial profiles of ion temperatures (full line) for different regimes at ASDEX as determined by simulation of measured CX-spectra. Vertical bars indicate the errors in ion temperatures. For comparison, electron temperature profiles measured by YAG laser scattering (open symbols) are shown as dash-dotted lines.

EXPERIMENTAL INVESTIGATION OF E×B TRANSPORT DURING THE TRANSITION FROM ATTACHED TO DETACHED PLASMAS IN TEXTOR

D. Bora[1], *G. Fuchs* ,*R.S. Ivanov*[2], *U. Samm, G. Van Oost*[3]

Institut für Plasmaphysik KFA Jülich GmbH, Ass. EURATOM-KFA
[1]Institute for Plasma Research, Bhat, Gandhinagar-382424, India
[2]Institute for High Temperatures, Academy of Sciences, Moscow
[3]Laboratoire de Physique des Plasmas-Laboratorium voor Plasmafysica, Association EURATOM-Etat Belge-Associatie EURATOM-Belgische Staat, Ecole Royale Militaire-Koninklijke Militaire School, B-1040 Brussels

Abstract

A movable multi-element Langmuir probe was implemented in TEXTOR in order to study properties of the edge and scrape-off plasma. The investigations have been focused on the variations of plasma boundary properties in plasmas with pure ohmic heating. Special attention has been paid to the change of transport properties during the transition to a detached plasma, which occurs if the plasma density exceeds a critical value. In particular, a substantial reduction of the poloidal rotation velocity at the limiter edge and a profound change of the edge turbulence spectra and amplitudes have been observed for detached plasmas.

Introduction

The transport of energy and particles across the magnetic field near the boundary of tokamaks is still poorly understood. However, a possible explanation for the anomalously large losses is plasma turbulence [1, 2], but more experimental evidence is needed in order to understand the physical origin of such turbulence. An experimental program, devoted to investigate turbulence induced transport, has been started and – in collaboration with the Institute for High Temperatures (IVTAN) in Moscow – a multi-electrode Langmuir probe has been developed and implemented in TEXTOR.
This probe simultaneously provides data on electric potentials, electric fields in radial, poloidal and toroidal direction, plasma density and electron temperature. Both time-averaged and fluctuating quantities have been considered in order to evaluate the DC and turbulence-driven cross-field particle fluxes. The spectral analysis of the fluctuating floating potentials at spatially separated probe pins allows to determine the velocity associated with the rotation of the boundary plasma.

Experimental Setup and Data Processing

The array of probes is inserted on the midplane at the low field side of TEXTOR. It can be moved radially on a shot to shot basis and positioned in space relatively to within 1 mm and 3 mm absolutely. Because of the thermal expansion of the liner holding the limiters the probe position with respect to the separatrix is known to within 5 mm only. The multi–pin probe arrangement, mounted on a graphite shield, is shown in fig.1. The graphite pins are 2 mm in diameter, 2 mm long and separated by 1 cm. One of them sticks 2 mm further out from the baseplate and is partly shielded by a boron–nitride cylinder. Three of the pins have been used to measure the radial and poloidal electric fields from the difference in floating potential, the other two measure the plasma density together with its fluctuations from the ion saturation current and the electron temperature.
To determine the electron temperature we use one of the pins and employ an oscillatory technique [3] based on the overlay of sinusoidal wave packets obtained by gating a sine wave of 500 kHz with a square wave of 1 kHz. Because of the curvature of the probe characteristic the floating potential is increased by $\Delta\Phi = T_e \times ln[I_0(\tilde{U}/T_e)]$, where I_0 is the modified Bessel function and $\tilde{U}$ is the amplitude of the sine wave applied. In this way T_e can be calculated from the amplitude of the 1 kHz oscillation on the floating potential, thus limiting the time resolution on T_e to 1 ms.
The fluctuation frequency spectra usually peak in the range 10–100 kHz. For such large frequencies the cross–field particle transport may be divided into a DC part $\vec{\Gamma}_0$ and a fluctuation induced part $\vec{\Gamma}_{fl}$. For the latter we use [4]

$$\vec{\Gamma}_{fl} = \frac{1}{T}\int_0^T \frac{\tilde{n}(t)\tilde{E}}{B}dt, \tag{1}$$

where T is an averaging time period, $\tilde{E}$ the fluctuating electric– and B the magnetic–field. From the fluctuations measured on different probes we may calculate the wave speed as well as the direction of propagation, provided the spectrum is sufficiently broadband and within the range of our sampling frequency (500 kHz). From the pick up signals $f(t)$ we calculated the Fourier transform $f(\omega)$ and subsequently the spectral correlation function

$$S_{ij}(\omega,\phi) = \sum f_i f_j \frac{\sin((\omega-\omega_i)\Delta t)\sin(2\pi(\phi-\phi_j)/\Delta\phi)}{(\omega-\omega_i)\Delta t \times 2\pi(\phi-\phi_j)/\Delta\phi}, \tag{2}$$

where the terms $sin(x)/x$ are the Fourier transforms of the sampling pulse and we assumed that we can adopt equal spacing in Φ direction as well. The phase difference $\Delta\Phi$ is related to the wave number k by $\Delta\Phi = k \times d$, where d is the distance between the probe tips. The speed and direction of the wave propagation can be obtained whenever a pronounced ridge is observed on the function $S(\omega,\Phi)$, giving along that ridge the phase– and group–velocities as $d\omega/dk$ and ω/k respectively[1]. A flat spectral function indicates that the fluctuations on the signals are random noise. This method does, however, not tell the difference between a standing wave in a moving plasma and a moving wave in a standing plasma.

[1] $S(\omega,\Phi)$ is hard to visualize in black and white contouring, see [5] for an example in color

Experimental Results

Based on the experimental technique described before, the following parameters have been measured: the time–average of the floating potential $\langle V_f \rangle$, the ion saturation current $\langle I^+ \rangle$, the local plasma density n, the electron temperature T_e, the poloidal and the radial electric field E_p and E_r respectively, the fluctuation levels of E_p and E_r (root–mean–square, rms), the relative density fluctuation level $\tilde{n}/n$, the DC convective flux Γ_0 and the particle fluxes driven by turbulence, the maximum values of cross–correlation functions C_0 and the fluctuation phase velocities v_{ph} (fig.2).
For ohmic discharges and plasmas, which are attached to the limiter, the plasma parameters found in TEXTOR [5] are similar to what has been observed in other machines [3]. From both methods, the measurement of the electric field E_r as well as the calculation of the speed of rotation from the spectral function we obtain a strong shear of the plasma rotation near the separatrix. The plasma in the scrape–off layer rotates with a speed of about 2 km/s in the ion diamagnetic direction whereas the plasma inside the separatrix rotates with about the same speed in the other direction. Slight discrepancies between the results of the rotation speed as observed with the two methods might be due to secondary electron emission from the probe causing a shift of the floating potential [6].
The plasma parameters near the plasma edge change slowly with increasing density. However, when the plasma density is increased to a level, where the plasma detaches from the limiters, there is a drastic change. The plasma density, the floating potential and the plasma rotation are reduced, the latter almost to zero. The fluctuation spectra, which are broadband in the attached state are shifted to lower frequencies and exhibit lines (see fig.3). The k–spektra show longer wavelengths in the detached state. The radial flux is increased, which is found to be due to an increase of correlations. Due to the reduction of shear, the large radial transport in the detached state might be caused by an increase of the size of the convective cells and a change from chaotic to laminar flow as suggested by the change of the fluctuation spectra.

References

[1] P.S. Liewer, Nucl. Fusion, 25, 543, (1985)

[2] A.J. Wootton, J. Nucl. Mat. 176–177, 77 (1990).

[3] A.V. Nedospasov, V.G. Petrov, G.N. Fieldman, Nucl. Fusion, 25, 21, (1985).

[4] S.J. Zweben, P.C. Liewer, R.W. Gould, J. Nucl. Mat., 111–112, 39, (1982).

[5] R.S. Ivanov, D. Bora, G. Fuchs, K. Höthker, R.A. Moyer, U. Samm, R. Van Nieuwenhove, G. Van Oost; Jül–Report No.2432 (1991).

[6] G. Fuchs, B. Schlarbaum et al., J. Nucl. Mat., 145–147, 268, (1987) (1987). (see also H. Amemiya and G. Fuchs, to appear.)

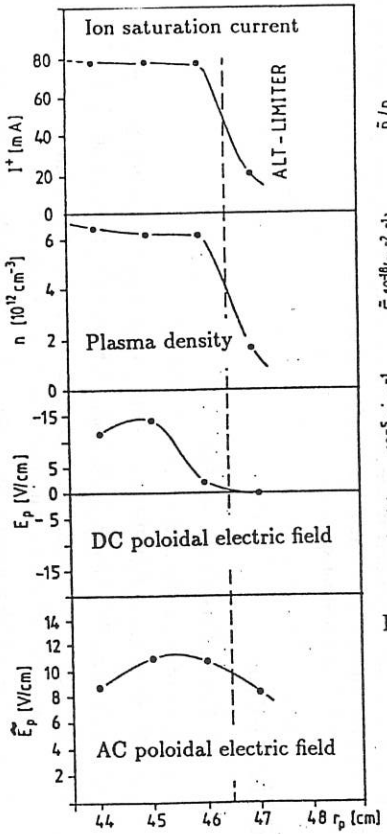

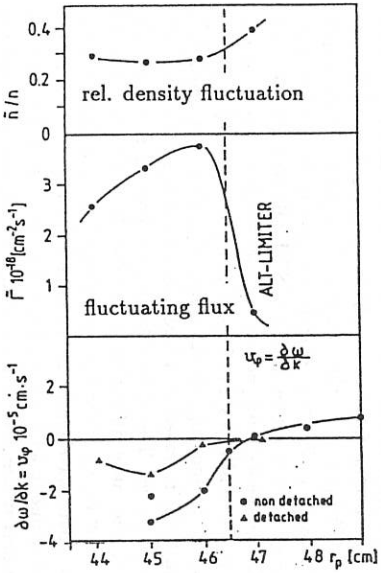

Fig.2 Radial profiles of plasma parameters near the limiter edge for the case of a detached Plasma.

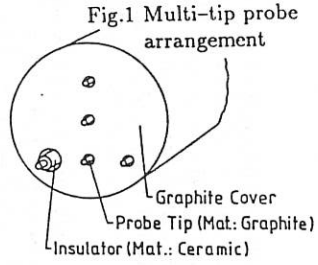

Fig.1 Multi-tip probe arrangement

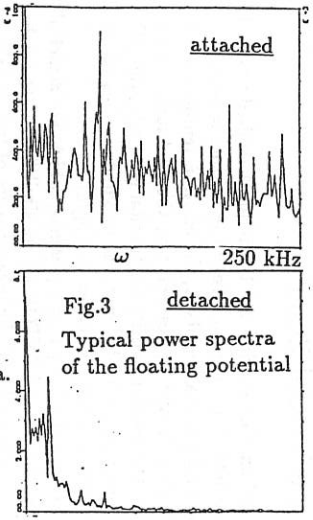

Fig.3 detached
Typical power spectra of the floating potential

TEMPERATURE PROFILES OF C^{6+}-IONS IN THE TEXTOR EDGE PLASMA - MEASURED WITH LITHIUM-BEAM ACTIVATED CHARGE-EXCHANGE SPECTROSCOPY

R.P. Schorn, H.A. Claaßen, E. Hintz, D. Rusbüldt, and E. Unterreiter*

Institut für Plasmaphysik, KFA Jülich GmbH, Association EURATOM/KFA
Postfach 1913, D-5170 Jülich, Germany
* Institut für allgemeine Physik, Technische Universität Wien
Wiedner Hauptstraße 8-10, A-1040 Wien, Austria

1. Introduction

We employ a new method to obtain the temperatures of highly charged carbon ions in the boundary layer of tokamak discharges. The lithium-beam activated charge-exchange spectroscopy ("Li-CXS", [1]) is used to measure spectral profiles of lines in the visible region excited by electron transfer between impurity ions and a fast neutral lithium diagnostic beam. Assuming a Maxwellian velocity distribution of the ions, temperatures are deduced by fitting a Gaussian profile to the Doppler broadened emission lines. Additional non-thermal line broadening due to magnetic fields (→ Zeeman-effect) and due to a collisional ℓ-level-mixing of the upper electronic state, which may both give rise to several overlapping transitions of slightly different wavelengths, has been taken into account. The method does not depend on the presence of NI-heating beams and therefore is capable of investigating different heating scenarios, including ohmic discharges, beam-heated and high-frequency-heated plasmas, as well as combinations thereof. Furthermore, the relatively high cross-section of charge-exchange between neutral lithium and carbon ions allows the use of a narrow beam diameter and a low current density, so that strictly local measurements of ion temperatures can be performed without changing plasma conditions by the diagnostic experiment itself. In this paper, we present radial temperature profiles of the fully stripped C^{6+}, which have been obtained with and without additional NI-beam-heating in the outmost 20 cm of TEXTOR plasmas, for the first time using the neutral lithium diagnostic beam. The method itself is based on ref. [2] and details will be published in ref. [3].

2. Experimental

A high current fast lithium beam injector is installed at TEXTOR. The device is based on a metal vapor ion source and can produce a neutral lithium beam of 20 keV energy, 5 to 10 mA total equivalent current, and 40 mm diameter at the plasma boundary. The Li^0-beam is located

in the equatorial plane of the torus and penetrates the plasma edge in radial direction. To separate Li-CXS-photons from radiation originating from the same C VI-transition, but being caused by charge exchange with neutral atomic hydrogen or deuterium in the scrape-off layer and by collisions of C VI with plasma particles, the arc voltage of the ion source's discharge chamber is pulsed with frequencies up to 500 Hz, and a chopped Li^0-beam is generated. As a result, a charge-exchange modulation is superimposed onto the more or less continuous background radiation. The beam shows a mean penetration depth of typically 25 cm into ohmically heated TEXTOR plasmas and roughly 15 to 20 cm into additionally heated discharges, depending on the plasma parameters. A more detailed description of the injector's properties and technical features, as well as of the experimental setup at TEXTOR, is given in refs. [1,4].

We make use of the charge-exchange reaction $C^{6+} + Li^0 \rightarrow (C^{5+} + h\nu) + Li^+$, and observe the optical CX-radiation $h\nu$ between the 8th and the 7th principle electronic shell of C VI at a wavelength of 529 nm. The light is detected spectrally, spatially, and temporally resolved by means of a large aperture (1:5.5) spectrometer with a focal length of 800 mm, which is located outside the TEXTOR-bunker and coupled to the plasma with a fibre-optical light-guide. It employs a grating of 1200 lines/mm being blazed at 2700 nm. A spectral scan is achieved by shifting the spectrum across the exit slit of the instrument by means of a galvo-driven thick glass plate being tilted by a maximal amount of ±15°. During the experiments discussed in this paper, the entrance slit was adjusted to a size of 0.1×10 mm. The apparatus width of the device was measured to be 0.042 nm at the wavelength of 529 nm, allowing the determination of ion temperatures down to about 30 eV. A complete spectral scan is performed within 100 ms. To improve the signal-to-noise ratio, several spectra are integrated during the stationary phases of TEXTOR discharges. Radial scans are performed by means of a galvo-driven tilting mirror.

3. Results

Fig. 1:

Radial ion temperature profile of C^{6+} during the flat top phase of an ohmically heated TEXTOR D_2-discharge in comparison with the electron temperature T_e. The line-averaged N_e was $3\times10^{13}/cm^3$ in the plasma center.

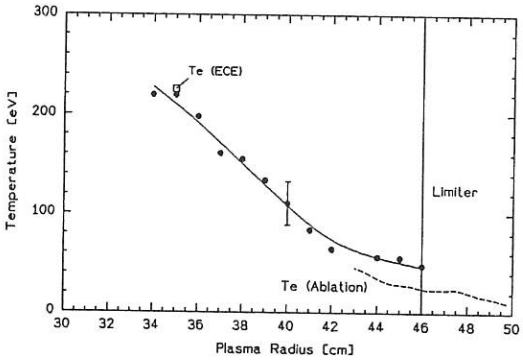

Fig. 2:

Radial ion temperature profiles of C^{6+} during heating beam injection of 1.7 MW hydrogen into H_2- and D_2-plasmas, the line-averaged central N_e being $2.5\times10^{13}/cm^3$. For comparison, also the electron density is shown in the scrape-off layer for D_2.

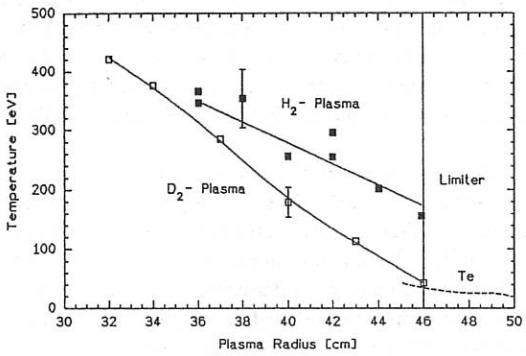

4. Discussion

In figs. 1 and 2 radial profiles of the C^{6+}-ion temperature, which have been measured with Li-CXS, are displayed for different plasma regimes in order to demonstrate the capabilities of the method. Each profile has been obtained by means of a series of reproducible TEXTOR-discharges, as at the moment only a single radial location can be recorded during one shot. Common features of all discharges under investigation are a plasma current of 340 kA, and a toroidal magnetic field of 2.25 Tesla. Only the ALT II-limiter, positioned at a minor radius of 46 cm, was activated, the main poloidal limiters being withdrawn.

Fig. 1 shows a temperature profile of C^{6+} for a "standard ohmic" discharge with a long flat-top phase of more than two seconds. The CX-line profiles were integrated over the entire stationary plateau. The line-averaged electron density was $3\times10^{13}/cm^3$ in the plasma center. For comparison, also the electron temperature, obtained from ECE [5] and by means of another atomic beam method, the laser-ablation of multilayer-targets [6], is plotted. Well inside the limiter position, i.e. at r = 35 cm, the electron temperature matches the C^{6+}-temperature quite well, while near the limiters T_{C6+} exceeds T_e by roughly 60% for r > 42 cm.

Additional heating by hydrogenic NI-beams has also been studied. We made use of co-injection at a power of 1.7 MW into deuterium and hydrogen plasmas with a central electron density of $2.5\times10^{13}/cm^3$. Different gases have been used to study the appearance of the isotopic effect in impurity ion temperatures. Fig. 2 shows T_{C6+}-profiles for the NI-phase of these discharges. Near the limiters, both kinds of plasmas show almost no difference in temperature between the additional heating and the ohmic pre-phase, which is very similar to the pure OH-profile shown in fig. 1 for D_2 and therefore not depicted in fig. 2. Inside a minor radius of 38 cm, however, carbon temperatures rise during NI-heating by more than a factor of 2 with respect to OH. This behavior can be explained by an elevated electron density at the edge

during NI and by an enhanced carbon concentration. In both heating phases, C^{6+}-temperatures measured in hydrogen discharges are elevated by a factor of up to 4 near the limiters, compared to deuterium shots. Inside r = 38 cm, however, no major difference between H_2 and D_2 can be seen. The same behavior has been found previously for the electron temperature [7]. The impurity ion temperatures match the electron temperatures also during NI-beam heating at least for deuterium plasmas in the very boundary, see fig. 2.

Some conclusions may be drawn from these early measurements. First, the time of equipartition [8], i.e. the time necessary to equilibrate the temperatures of two different ion species by collisions, is calculated to be always less than 0.1 ms for D^+ and C^{6+} at densities below $10^{13}/cm^3$ and temperatures below 500 eV. The particle confinement time, however, is estimated to be roughly 1 ms for typical TEXTOR boundary layer plasmas. Thus, the measured carbon ion-temperatures should be equal to the deuterium- resp. hydrogen-ion temperatures, which according to our results do not deviate much from the electron temperatures in the TEXTOR edge plasma. Secondly, the relatively high values of T_e = 30 eV and T_{C6+} = 50 eV for shots in D_2 at the limiter radius together with C^{6+}-densities of $5\times10^{10}/cm^3$ in the ohmic case [1] and even higher densities in the NI-case lead to an acceleration of the carbon ions by a sheath potential of $6\times3kT_e$ = 540 eV. As a result, a C^{6+}-flux of more than $4.7\times10^{17}/cm^2s$ should lead to a relatively high level of carbon self-sputtering at the limiter surfaces, as corresponding sputtering yields [9] are 0.3 for a perpendicular incidence (0°) and 0.8 for an angle of 70°.

5. References

[1] R.P. Schorn, E. Hintz, D. Rusbüldt, F. Aumayr, M. Schneider, E. Unterreiter, H. Winter: Appl. Phys. B **52** (1991) 71.

[2] R.J. Fonck, D.S. Darrow, K.P. Jaehnig: Phys. Rev. A **29** (1984) 3288.

[3] R.P. Schorn, E. Hintz, D. Rusbüldt, E. Unterreiter: to be published.

[4] H.L. Bay, E. Dullni, P. Leismann: KFA-Report Jül-2062 of May 1986.

[5] G. Waidmann: private communication.

[6] A. Pospieszczyk, G.G. Ross: Rev. Sci. Instrum. **59** (1988) 605.

[7] U. Samm et al.: Europhys. Conf. Abstracts **13B/III** (1989) 995 (16th European Conference on Controlled Fusion and Plasma Physics, Venice, 1989).

[8] L. Spitzer, Jr.: "Physics of fully ionized Gases", second edition, page 135, Interscience Publishers, New York 1967.

[9] J. Roth, J. Bohdansky, W. Ottenberger: J. Nucl. Mater. **165** (1989) 193.

FLUX AND ENERGY OF NEUTRAL DEUTERIUM AND RADIAL FLUX OF NEUTRAL BORON IN TEXTOR.

H. Bergsåker, B. Emmoth and P. Wienhold*

Manne Siegbahn Institute of Physics, S-104 05 Stockholm, Sweden.
* Institut für Plasmaphysik, KFA, POB 1913, D-5170 Jülich, FRG.

Introduction. Graphite probes have been exposed in TEXTOR in order to collect neutral deuterium and neutral impurities which escape radially from the plasma. The first objective was to investigate the possibility of estimating neutral flux and ion temperature from retention versus fluence behaviour of deuterium in graphite, following [1]. The comparison of how this scheme works at TEXTOR with other diagnostics is a reference case for future experiments on a smaller device [2]. Secondly, collector probes have recently been used in experiments where the impurity ion temperature is determined from Larmor radius effects. In such experiments the deposition of neutrals constitutes a background and a possible source of error; the present investigation provides a basis for estimating and eliminating that difficulty. Furthermore, probes exposed far away from the plasma provide information on erosion and deposition at the liner/wall. Erosion and deposition at the liner is relatively weak but may still be of importance due to the large area of the liner. Finally it was an aim to explore the possibilities in collecting neutral particles as a general tool to investigate the structure of the scrape-off plasma.

Experimental. Figure 1 shows the geometry of the experiment. Circular graphite disks are exposed through the slit aperture of a graphite shield. The collecting surfaces are at 65 cm minor radius, i.e. in a porthole 10 cm outside liner radius. The viewing angle is limited by a circular opening in the liner. The probe is obviously not exposed to plasma ions and it does not have free line of sight to any surface exposed to the plasma. The probe enters horisontally at the midplane of TEXTOR. The disks are rotated either between plasma shots to expose selected areas to one or more complete tokamak disharges, or rotated during shots for time resolution. After exposure the disks were removed and transported in air to the surface analysis station, and the areal densities of deuterium and boron were determined by Nuclear Reaction Analysis. The front plate of the shield is also removed after exposure and analysed on the front side to provide a data point with long exposure time, and on the back side to give information on reflection and erosion at the disk surface. Two series of exposures have been made, the first in Dec. 1989 (shots 39733-39806), and the second in March 1990 (shots 40986-41145). The first series was made two and a half months after the third boronisation of TEXTOR, which had been performed on 23 Sept. 1989. The second series was made immediately following the boronisation on 26/3 1990. The confined plasma was limited mainly by the toroidal ALT limiter at 46 cm minor radius.

Results and discussion. Figure 2 shows the collected areal densities of deuterium and boron in a region of an exposed disk. The peak at 40° is in an area which has been exposed to 25 complete discharges (shots 41001-41025). The area from 78° to 138° has been exposed to 27 overlayed discharges (41032-45, 41051-62), each time rotating the disk uniformly 60 degrees in four seconds. The corresponding time scale

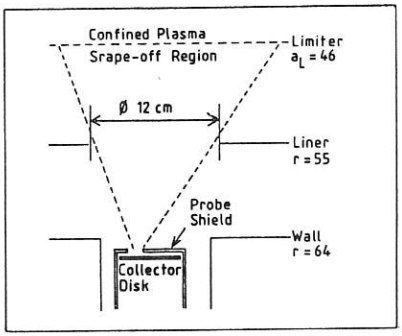

Figure 1.

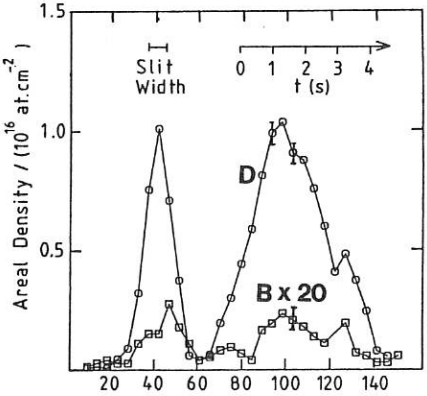

Figure 2.

is indicated in the figure. The fact that deposition is extended over the whole exposed area shows that it occurs throughout the discharge, rather than coming e.g. all at the end. Figure 3 shows the deuterium retention and the areal density of boron as a function of exposure time. The exposures with time resolution have been plotted with half the peak areal density in order to make an average over the discharge time. The D-retention increases linearly with exposure time up to at least 10^{17} D/cm^2, indicating a temperature of at least 400 eV [1], which is reasonable for charge exchange neutrals. The exposure time has not been sufficient to give an upper limit for T_i. Since retention is still in the linear regime, an incident flux of deuterium can immediately be derived, $\Gamma_D \approx 2.2 \cdot 10^{14}$ D^0 cm^{-2} s^{-1}, if reflection is neglected. This number is in agreement with what may be expected from other diagnostics [3]. The areal density of boron also appears to increase linearly with exposure time, with deposition rate $\Gamma_B \approx 1.3 \cdot 10^{12}$ B cm^{-2} s^{-1} in the first series of exposures, with an old boronisation, and $\Gamma_B \approx 3.7 \cdot 10^{12}$ B cm^{-2} s^{-1} after a fresh boronisation. In the former case there is a slight tendency to saturation, a behaviour which if verified could be attributed to erosion which is proportional to the areal density, such as sputtering. At the back side of the shield deuterium and boron were found at levels suggesting $\sim$ 15 % probability of reflection for both species. This particular point has been discussed more in detail elsewhere [4]. It is striking that boron is collected at a rate of several percent of that of deuterium. If the collected neutrals are created by neutralisation of singly charged boron ions, then the source is only a thin layer of the edge plasma where singly charged boron is abundant, whereas the source of charge exchange neutral deuterium is in principle the whole plasma. To quantify this, some model calculations have been made to estimate the radial distribution of B^+. The model is one dimensional, for radial transport. The electron density and temperature profiles $n_e(r)$ and $T_e(r)$ are assumed to be given as parabolic inside limiter radius $a_L = 46$ cm, and exponential in the scrape-off region $a_L \leq r < a_w$, where $a_w = 55$ cm is liner radius. Boron ions of all charge states are assumed to diffuse radially with diffusion constant $D = 0.5$ m^2/s. Transitions between charge states are taken to proceed according to the rate coefficients of refs. [5,6]. The recombination rate coefficients are obtained by extrapolating the fitting parameters of [6] along isoelecronic sequences. For example, at $T_e = 20$ eV the

dielectronic recombination rate coefficient for neutralisation of B^+ which has been used was $1.0 \cdot 10^{-11}$ cm^3/s and radiative recombination is negligible. In the scrape-off region ions are assumed to be lost by parallel flow to the limiters with a time constant $\tau_{\|} = L/(0.5 \cdot c_s)$, where $c_s = \sqrt{2 \cdot T_e(r)/m_D}$ is the ion sound speed of the main plasma ions and with connection length $L = 50$ m. The limiter and liner surfaces are assumed to be absorbing walls. Figure 4 shows three examples of primary sources of singly charged ions which have been used. The calculations are for typical TEXTOR parameters: $n_e(0) = 2.5 \cdot 10^{13}$ cm^{-3}, $T_e(0) = 1$ keV, $n_e(a_L) = 2 \cdot 10^{12} cm^{-3}$, $T_e(a_L) = 30$ eV and scrape-off widths $\lambda_n = 1.5$ cm and $\lambda_T = 2.5$ cm. Case A is meant to be characteristic of physical sputtering. Neutrals are thought of as being introduced at a rate $n_e c_s Y_p/L$ in the region $a_L \leq r < a_w$ with $Y_p(E)$ derived from [7] and $E = 4.5 \cdot T_e$. Furthermore, they are assumed to be ejected at 2.9 eV with cosine angular distribution from a surface tangential to the density gradient. From the model calculations with this source a central boron concentration of 0.17 % results. The model also yields parallel boron flux in the scrape-off layer of a few times 10^{15} B cm^{-2} s^{-1} and ~ 2.5 cm scrape-off width for boron, roughly in agreement with [4]. Case B is meant to be characteristic of chemical erosion, neutrals are created at a rate $n_e c_s Y_c/L$, with $Y_c = 0.012$ adjusted to give the same central boron concentration as in case A. The neutrals in case B are injected in the same way as in case A, but with thermal velocity. Case C is a constant source $3.9 \cdot 10^{13}$ cm^{-3} s^{-1} of B^+ over one cm inside limiter radius, also adjusted to give the same central concentration as case A. Figure 5 shows the resulting steady state density distributions of B^+. The contributions of neutral boron flux at the collector due to dielectronic recombination has been estimated by numerical integration over the distributions shown in figure 5 and are 2.5, 6.1 and 1.2 $\cdot 10^9$ at. cm^{-2} s^{-1} respectively, for the cases A,B and C. This is about three orders of magnitude less than the measured deposition rates. The discrepancy is significant, even allowing for, say, an order of magnitude higher impurity production rate and a factor five higher recombination rate. Hence it is necessary to conclude that impurity transport at the edge is significantly different from the assumptions. A possiblility is that the neutral density in the vicinity of the limiter is high enough for charge exchange processes to dominate. Another possibility is that molecular transport is responsible for buildup of boron deposits at the wall surface.

Conlusions. A flux of neutral deuterium $\Gamma_D \approx 2 \cdot 10^{14}$ D^0 cm^{-2} s^{-1} at wall radius with typical energy in excess of ~ 400 eV can be inferred from retention in graphite. The corresponding deposition rate of boron was $\Gamma_B \approx 3.7 \cdot 10^{12}$ B^0 cm^{-2} s^{-1} in conditions with fresh boronisation and a third of that with old boronisation. This is at least two orders of magnitude more than what is expected from a simple model of radial impurity transport which takes into account diffusion, electron impact ionisation and recombination, and parallel flow in the scrape-off layer. The large impurity deposition may have implications for the interpretation of collector probe experiments inferring ion temperatures from larmor radius effects.

References.

[1.] W.R. Wampler et al. J.Nucl.Mater. 103-104(1981)304.
[2.] I. Gudowska, H. Bergsåker and G. Hellblom, these proc.
[3.] W.T. Shmayda, N. Kherani et al., J.Nucl.Mater. 162-164(1989)582.
[4.] I. Gudowska, H. Bergsåker, B. Emmoth et al. J.Nucl.Mater. in press.
[5.] M.A. Lennon et al., CLM-R.270, Culham lab. 1986.
[6.] S.M.V. Aldrovandi and D. Pequinot, Astron.Astrophys. 25(1973)137.
[7.] J. Bohdansky, Nucl.Ins.Meth. B2(1984)587.

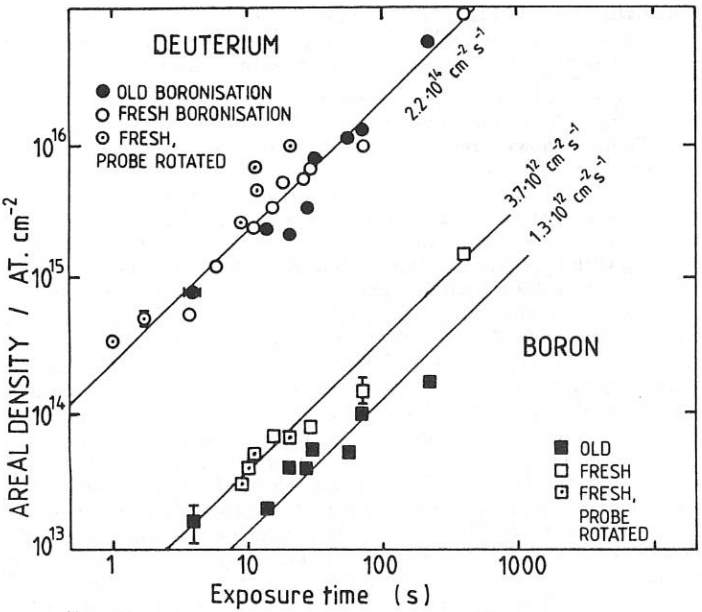

Figure 3.

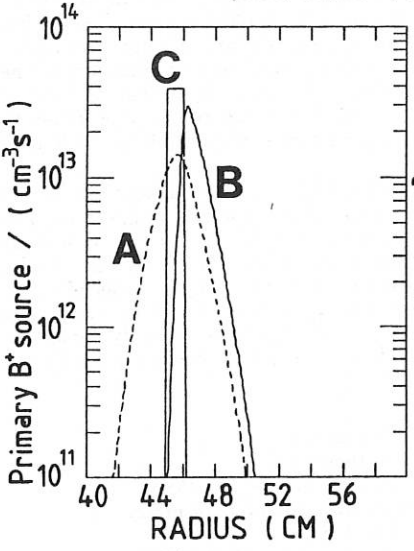

Figure 4.

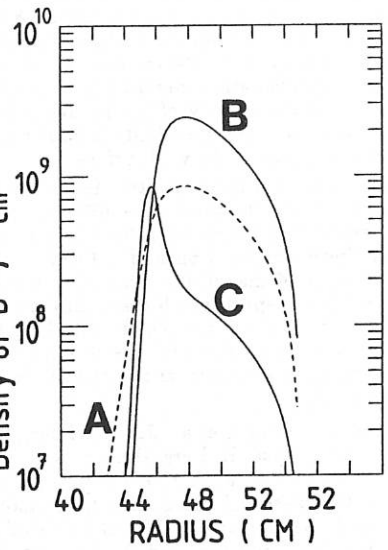

Figure 5.

DENSITY PROFILE AND DC ELECTRIC FIELD MEASUREMENTS IN THE TEXTOR BOUNDARY FOR OHMIC AND ICRF-HEATED DISCHARGES

M. Laux[1], H. Bergsaker[2], B. Emmoth[2], K. Günther[1], K. Höthker, Y.T. Lie, R.A. Moyer[3], A. Pospieszczyk, U. Samm, B. Schweer, R. Van Nieuwenhove[4], G. Van Oost[4], P. Wienhold

Institut für Plasmaphysik, KFA Jülich GmbH, Ass.Euratom-KFA
[1] Zentralinstitut für Elektronenphysik, Berlin
[2] Research Institute of Physics, Ass.Euratom-NF3, Stockholm
[3] Institute of Plasma and Fusion Research and Mechanical, Aerospace, and Nuclear Engineering Department, UCLA, Los Angeles
[4] Laboratoire de Physique des Plasmas - Laboratorium voor Plasmafysica, Association "Euratom-Etat belge" - Associatie "Euratom-Belgische Staat", Ecole Royale Militaire - B 1040 Brussels - Koninklijke Militaire School

Introduction

TEXTOR is a medium size tokamak with circular cross-section equiped with the ALT II toroidal pumped limiter [1]. The major and minor radii are 1.75 m and 0.46 m, respectively, and ALT II, consisting of eight movable graphite blades, is situated at the outside about 45° below the equatorial plane. Two antenna pairs extending poloidally from 15° below the outer midplane to 7.5° from the top of the machine are installed for auxiliary heating in the ion cyclotron frequency range [2]. TEXTOR is dedicated to plasma wall interaction studies towards a better understanding of the scrape-off layer (SOL) and the plasma at the limiter edge.

TEXTOR is equiped with active and passive diagnostics for the SOL/edge region such as continuous thermal Li-beam spectroscopy (T=550°C, 2×10^{14} particles/sec, 128 Si-diode array), laser ablation technique (LiF/C target, 1 J ruby laser, E<10 eV, $n=10^{16}m^{-3}$, same type of camera), a reciprocating Langmuir probe (150 voltage sweeps per probe plunge, 500 Hz, total transit time for 30 cm of 0.3 s), a rotating Langmuir double probe (rotation frequency 2 Hz, 200 voltage sweeps per rotation), and a collector probe head instrumented with four flush mounted Langmuir double probes (two at each toroidal side, one voltage sweep every 5 ms).

At a toroidal field of 2.25 T and with ALT at 0.46 m as the leading limiter, a density scan ($\bar{n}$=0.9 to 3.3 10^{19} m^{-3}) and a current scan (I_p=220 to 475 kA) were carried out using about 45 discharges in D shortly after boronization of the TEXTOR walls. A 700 kW ICRH pulse at 32.5 MHz was applied to most discharges from t=1.5 s on using antenna pair 2 in π-phasing [2]. The antenna protection limiters (PL) of both pairs as well as the poloidal and bumper limiters were radially situated at 0.49 m, thereby creating a second scrape-off zone with much shorter connection length (6 m) for the locations of most edge diagnostics, compared to the long flux tubes (45 m) in the foremost layer defined by ALT.

Results and discussion

The first part concentrates on the ohmic phase of the discharges. The radial density profiles observed in the near-LCFS layer by both the Li-beam and the instrumentation double probes show the same exponential behaviour (fig.1a) described by an e-folding length λ of 0.0145 m. The transition to the much steeper profile ($\lambda = 0.0062$ m) in the adjacent region with short connection between ALT and antenna is well marked because the front layer is deep enough ($\Delta r \approx 2\lambda$) to be well developed, even if flux continuity at the interface is taken into account. Taking a mean value of 25 eV for the near-LCFS layer measured by the same double probe (somewhat questionable because obtained in the shadow of a large limiter-like probe head) and the reduction factor from [3] a diffusion coefficient of 0.1 m^2/s is obtained. The ratio 2.3 of the e-folding lengths for the two SOL parts is somewhat smaller than expected from the square root of the connection lengths ratio (2.7) because in the near-LCFS layer the position of measurement was relatively close to the limiter, which leads to a diminished λ [3], whereas in the remote layer the observation was almost at the stagnation point.

From the series of shots with varying central line average density $\bar{n}$ the scaling of n_{SOL} and λ at the plasma edge (LCFS, r = 0.46 m) is obtained. Li-beam values at 0.46 m and Langmuir probe results extrapolated to that radius agree satisfactorily and give an n_{SOL} that rises supralinearly with $\bar{n}$, whereas λ is, approximately, inversely proportional to its square root (fig. 2). Similar dependences were observed on different tokamaks [4] and can be explained by a simple one-dimensional model of plasma transport which includes neutrals diffusing radially inwards [5]. The model calculation results in $n_{SOL} = \frac{1}{2}\Sigma\lambda\bar{n}^2$, where Σ depends on the rate coefficients of ionisation and charge exchange for the neutrals and λ is treated as an experimental parameter. The expression demonstrates that in the case of a decreasing λ the scaling of n_{SOL} with $\bar{n}$ is less than quadratic.

The ratio of minimum saturation currents to the tips of a rotating double probe [6] allows the evaluation of the Mach numbers characterizing the streaming of SOL plasma along magnetic field lines [7]. Measurements in the different radial zones of the SOL reveal that in the near-LCFS layer the plasma streams with Mach 0.2 onto ALT as expected [8], but at radial positions outside 0.49 m a fast flow (Mach -0.5) in the direction of the ICRH protection limiter (PL) was found (fig. 1b). The latter was measured near midpoint of the flux tube between ALT and PL (somewhat closer to PL). The relatively high Mach number, however, is likely to be caused by an asymmetry of velocities at the toroidally oriented ALT surface and the poloidally oriented PL surface if a poloidal plasma rotation at TEXTOR is taken into account [8].

In the following the interest is focused on the ICRH phase of the discharge. An ICRH pulse influences the SOL density at least in two ways. An overall density rise is observed [2] and the radial profile is completely changed loosing its exponential character and developing an undulating structure [9] (fig. 3a). Two effects can account for those changes: radial electric fields strong enough to interrupt the parallel transport [10] or strong changes of the radial transport itself depending on the radius [11]. During the ICRH phases of the shots of our experimental series the reciprocating probe was used to identify large poloidal electric DC-fields in the SOL [12] as was also done at JET [13]. Those fields exhibit a pronounced radial dependence even changing sign at certain positions. However, the precise

structure of the field profile was found to depend on the distance to the active antenna [12]. Such a field introduces a radial drift velocity of at least the same order of magnitude as the diffusive one. Using the formula for the ExB drift and the radial particle flux

$$v_{drift} = \frac{E_p \times B}{B^2} \qquad \Gamma_\perp = -D_\perp \frac{dn}{dr} + v_{drift} n$$

together with particle conservation

$$\frac{d\Gamma_\perp}{dr} = -\frac{c_s}{L_\parallel} n$$

leads to

$$E_p = B D_\perp \left[\frac{d\ln n}{dr} + \frac{1}{n}\int_r^\infty dr' \frac{1}{\lambda_0^2} n(r')\right] \qquad \lambda_0 = \sqrt{\frac{L_\parallel D_\perp}{c_s}} = \textit{ohmic decay length.}$$

Now the experimental density profile observed (Li-beam) during ICRH and the e-folding length of the corresponding ohmic case can be used to calculate the poloidal electric DC-field that can account for the observed density profile in this simple model. Fig. 3b shows qualitative agreement with the measured DC-field. The differences can be attributed to different toroidal positions of the reciprocating probe and the Li-beam with respect to the active antenna. The influence of a radial electric field, which does exist according to our observations [12], can also account for departures, particularly in the outer SOL layer.

Acknowledgements

Valuable discussions with H. Gerhauser and H.A. Claassen are thankfully acknowledged.

References

[1] D.M. Goebel et al., J. Nucl. Mat. **162-164** (1989) 115.
[2] G. Van Oost et al., Fusion Eng. Des. **12** (1990) 149.
[3] U. Samm et al., J. Nucl. Mat. **162-164** (1989) 24.
[4] K.F. Alexander et al., *this conference*.
[5] K.F. Alexander et al., Nuclear Fusion **12** (1986) 1575.
[6] K. Hoethker et al., Rev. Sci. Instr. **61** (1990) 114.
[7] K. Hoethker et al., Proc. 15th Europ. Conf. Plasma Phys. and Contr. Fusion, Amsterdam, 1990, p. 1568.
[8] H. Gehrhauser and H.A. Claassen, Contrib. Plasma Phys. **30** (1990) 89.
[9] R. Van Nieuwenhove and G. Van Oost, J. Nucl. Mat. **162-164** (1989) 288.
[10] B. La Bombard et al., Plasma Phys. Contr. Fusion 7 (1990) 483.
[11] M. Laux et al., Fusion Eng. Des. **12** (1990) 223.
[12] R. Moyer et al., J. Nucl. Mat. **176 & 177** (1990) 293.
[13] J.A. Tagle et al., Fusion Eng. Des. **12** (1990) 217.

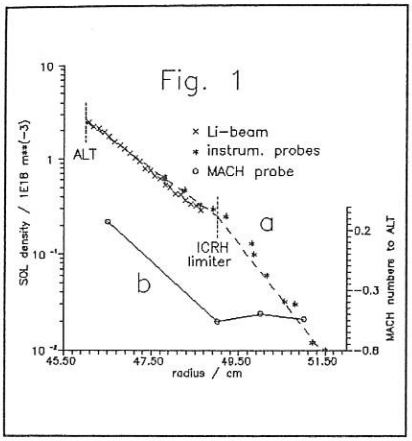

Figure 1 radial profiles of SOL density (a) and Mach number (b) in the ohmic phase

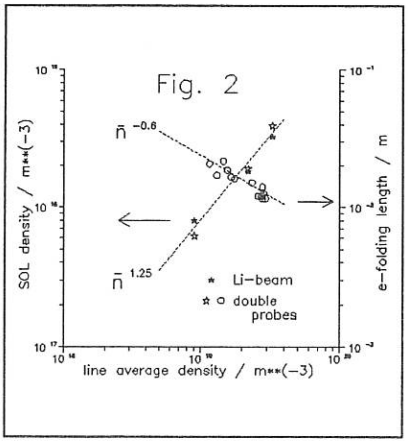

Figure 2 density and e-folding length at the edge versus line average density

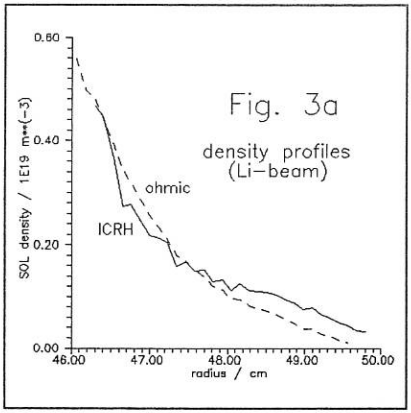

Figure 3a SOL density profile during ICRH compared to ohmic

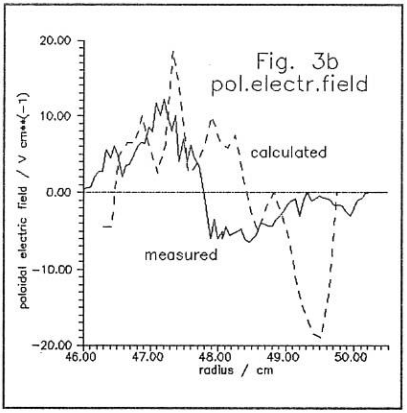

Figure 3b poloidal electric DC-field during ICRH

SUPPRESSION OF MARFES BY PLASMA POSITION FEEDBACK CONTROL BASED ON INTERFEROMETRIC MEASUREMENTS

U. Samm, H.R. Koslowski, H. Soltwisch

Institut für Plasmaphysik, Forschungszentrum Jülich, FRG, Ass. EURATOM-KFA

1. Introduction

When rising the average electron density $\bar{n}_e$ in a tokamak plasma and approaching the density limit, regions of strong radiation may develop at the plasma boundary. The plasma in the radiating layer has low electron temperature ($T_e \approx 10eV$) and enhanced electron density n_e compared to plasmas with lower $\bar{n}_e$. The plasma is called detached in case the radiating zone is poloidally symmetric [1]. Very often poloidally asymmetric radiation, predominantly located at the high field side, is observed in tokamaks. These radiating zones, which extend to about 10%-30% of the poloidal circumference are called MARFEs [2]. There is general agreement that both phenomena, detachment and MARFEs, are based on the specific radiation characteristics of impurities at the plasma boundary [2]. In most cases the MARFE formation precedes a major disruption, whereas detached plasmas can be quasi-stationary. In order to use the advantages of a detached plasma one would like to avoid MARFE formation.

In TEXTOR for many years only detached plasmas and no MARFEs have been observed. But when, due to technical reasons, the measurement of the horizontal plasma position for the feedback control has been switched from interferometric to magnetic methods also in TEXTOR MARFEs have been detected frequently [3]. We use the possibility available on TEXTOR to apply from shot to shot the magnetic or interferometric measurements alternatingly for position control in order to show evidence that the interferometric method is a means for suppressing MARFEs.

2. Experiment

For the results presented in this paper we refer to the standard TEXTOR conditions : major radius R=175cm, minor radius r=46cm defined by the poloidal limiter segments and by the toroidal pump limiter ALT-II, plasma current I_p=340kA. The limiters are made of graphite and all plasma facing components are boronized [4]. We concentrate on cases in which the MARFE formation is pronounced, namely in neutral beam heated discharges in deuterium with a small admixture of neon (<1%). Neon is used in addition to the intrinsic impurities carbon and oxygen for increasing the radiation from the boundary [5]. During a discharge a sufficiently high radiation level necessary for MARFE formation is provided by either increasing the amount of neon or by rising $\bar{n}_e$.

The relevant diagnostics for MARFE detection are the following. A D_α CCD-camera observing a full poloidal cross-section at the location of the poloidal limiters. A 9-channel interferometer/polarimeter [6] providing information on $\bar{n}_e$ along vertical chords from r=-31cm (inside) to r=47.5 cm (outside). A bolometer detects the total radiation.

The interferometric horizontal plasma position is defined as $R-R_0=c(\Delta\varphi(r=30cm)-\Delta\varphi(r=-31cm))$, where $\Delta\varphi$ is the phase shift and c is proportional to $1/(\Delta\varphi(r=20cm)-\Delta\varphi(r=40cm))$. The term c allows to obtain a position signal which is, to a certain degree, independent of the absolute value of $\bar{n}_e$ [7]. The magnetic plasma position is derived from the poloidal magnetic field measured outside of the plasma [8]. The latter method, used in practically all tokamaks, essentially provides information about the position of the plasma current. For the vertical plasma position only magnetic measurements are used.

3. Results

Position control based on magnetic measurements

Most clearly, a MARFE can be seen in the emission of D_α light measured with a CCD-camera. A rather small zone of intense D_α-light (enhanced by a factor 20-60 compared to the MARFE-free case, see Fig.3) is observed at the high field side located mostly about 45° below the horizontal midplane, having a peak radiation at r=44-45cm and extending in poloidal direction by 10-15cm and in radial direction by 5-10cm (Fig.1). The integral intensity of D_α is about proportional to the flow of deuterium [9]. Thus, as is obvious from Fig.1, the deuterium flow in the MARFE is as strong as the recycling flow at one of the main poloidal limiter segments; this flow amounts to about $10^{20}s^{-1}$. Normally, the location of the MARFE rotates poloidally (counter-clockwise in Fig.1=direction of poloidal magnetic field=direction of $B\times\nabla B$) and reaches typically after 100ms the upper limiter. Then either a major disruption occurs or the MARFE disappears and a new MARFE starts again in the lower part.

The interferometer channel at r=-31cm is lost in the presence of a MARFE due to refraction of the laser beam in the zone of high dn_e/dl. On the other hand, the high sensitivity of the interferometer unveils a pre-MARFE phase in which already a significant increase of n_e is detectable, whereas the D_α signal is only slightly enhanced (factor 2) compared to the MARFE-free case. In Fig.2 the phase shift profile measured during this phase exhibits a pronounced shoulder on the inner side due to an increase of the phase shift on the channel at r=-31cm. The corresponding enhancement of $\bar{n}_e$(r=-31cm) along a chord of 80 cm is 0.8 $10^{13}cm^{-3}$. Assuming that this enhancement is caused by a pre-MARFE zone extending over 10-20 cm we obtain an increase of n_e in the pre-MARFE region of 3.2-6.4 $10^{13}cm^{-3}$. The pre-MARFE phase may last for several 100ms then converts within 10-50ms into the main MARFE phase as is shown in Fig.3. It is important to note, that the interferometric method of determining the plasma position, based on the channels at r≈±30cm and assuming symmetric profiles, interprets a profile with a shoulder as shown in Fig.2 as a very pronounced plasma shift (>4cm) *inwards*. The magnetic position remains constant for all phases of the discharge.

Position control based on interferometric measurements

The development of a main MARFE as shown in Fig.1 never has been observed when the interferometric method for positioning is applied. Only the initial stage of the plasma to convert into the pre-MARFE phase is detected and it can be demonstrated how the reaction of the feed-back system for plasma positioning suppresses any further development of the MARFE. As an example a discharge with a density ramp is presented (Fig.5c). Fig.4 shows the phase-shift traces for all interferometer channels. The time at which the transition into the pre-MARFE phase starts is indicated by a sudden increase of the phase-shift at r=-31cm. The corresponding interferometric plasma position signal, as shown in Fig.5a, exhibits an inward shift of 2.5cm. The feed-back system reacts by shifting the plasma column *outwards* until the phase-shifts in both channels, at r≈±30cm, are symmetric again. The phase-shift profiles before and after this event are shown in Fig.2. The density profile becomes broader, in particular in the boundary zone, and develops a shoulder on the high field side. The location of the density peak is shifted by 1.2cm outwards. This value agrees with the variation of the magnetic plasma position, shown in Fig.5b, as is expected from the coincidence of peak density, peak T_e and peak current. The MARFE formation remains suppressed for the whole density rise during which a detached plasma develops and finally a major disruption occurs at the radiation limit $P_{rad}/P_{heat}\approx 1$. The density limit is about 20% higher compared to a similar discharge but with MARFEs occurring.

4. Discussion and Conclusions

Due to the definition of the interferometric plasma position based on the assumption of

symmetric density profiles, any small asymmetric increase of n_e at the plasma boundary produces a large variation of the position signal. The interferometric system is extremely sensitive to such asymmetries and therefore reacts by shifts of the plasma column in a very early phase of MARFE development.

The fact that plasma shifts have influence on MARFE formation manifests the direct influence of the recycling flux of deuterium at the inner bumper limiter in a region close to the MARFE on the evolution of the MARFE itself. The flux in a main MARFE is as high as at a main limiter segment. Such a flux can recycle from the bumper limiter, 2.5cm outside the separatrix, if there is a compensation for the decrease of n_e and T_e inside the scrape-off layer (SOL) in the MARFE region. This can be a significant increase of n_e at the separatrix and in addition an enhanced particle transport resulting in a larger e-folding length λ_n and λ_T. Assuming that the SOL thickness does not change and that T_e remains constant at the separatrix, we conclude that at the separatrix close to a MARFE n_e is enhanced by a factor of 20-40; thus yielding electron densities of $>10^{14}cm^{-3}$. This figure is consistent with estimates obtained from the interferometer data. In view of this large factor it is remarkable that for the suppression of MARFEs the distance between separatrix and inner wall has to be increased only by about 1cm, i.e. about one e-folding length. This indicates that the recycling flux has important influence in the initial stage of MARFE development.

We conclude that a system for horizontal plasma positioning which forces the electron density profile at the plasma boundary to be symmetric is a means for suppressing MARFE formation and allows to reach quasi-stationary plasmas close to the density limit with a poloidally symmetric radiating belt and, at least in certain cases, leads to an enhanced density limit.

In theories describing the MARFE phenomenon the basic mechanism is a thermal instability developing when the radiation term L has a T_e-dependence with $\partial L/\partial T_e<0$ and dominates over the variation of parallel heat conduction [2][10]. The radiation characteristics of light impurities, like C, O or Ne, can provide such a behaviour [5]. Our results demonstrate that a strong coupling between a plasma zone with such an instability and the recycling flux of deuterium and impurities close to it can be essential for the dynamics of MARFE development. This coupling should been considered in all MARFE theories, e.g. the approach made in [11].

References

[1] U. Samm, "Properties of detached plasmas", KFA-Report Jül-2123 (1987)
[2] B. Lipschultz, J. Nucl. Mater., 145-147 (1989) 15
[3] U. Samm, "Radiation control in a limiter tokamak", KFA-Report Jül-2378 (1990)
[4] J. Winter et.al., J. Nucl. Mater., 162-164 (1989) 713
[5] U. Samm et.al., "Radiation cooling with intrinsic and injected impurities in the plasma boundary of a limiter tokamak", this conference
[6] H. Soltwisch, "Combined interferometric and polarimetric diagnostics for TEXTOR", KFA-Report Jül-1638 (1980)
[7] H. Soltwisch, Nucl. Fusion Vol.23, No.12 (1983)
[8] G. Waidmann, KFA-Report Jül-1579 (1979)
[9] P. Bogen, E. Hintz, in "Physics of Plasma-Wall Interactions in Controlled Fusion", Eds. D.E. Post and R. Behrisch (Plenum New York 1986)
[10] J. Neuhauser et.al., Nucl. Fus. Vol.26, No.12 (1986)
[11] A.V. Nedospasov et.al., , Contrib. to Plasma Physics, Vol.28, No.4/5 (1988) 453

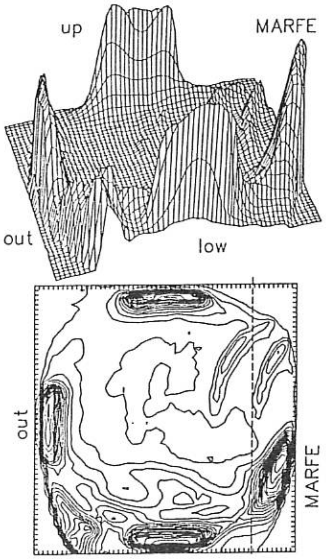

Fig.1 3-D and contour-plot of D_α light emission from cross-section with poloidal limiters (up,down,out); dashed line=chord at r=-31cm

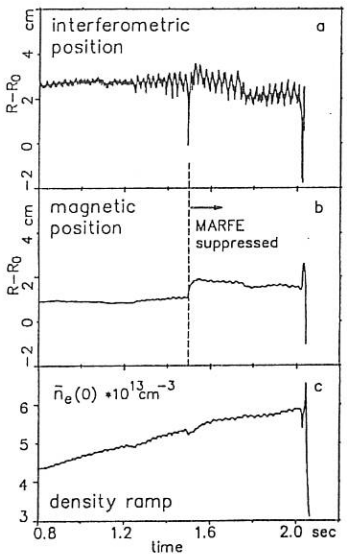

Fig.5 Suppression of a MARFE at the initial stage

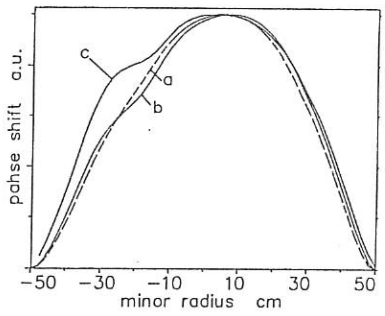

Fig.2 Phase-shift profiles from HCN-interferometer for the MARFE-free (a), suppressed MARFE (b) and pre-MARFE (c) phases

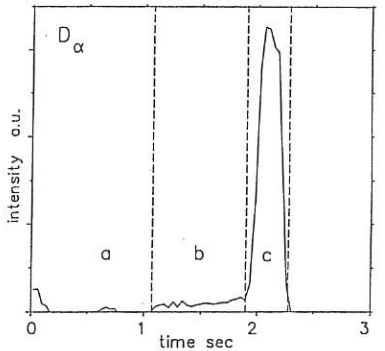

Fig.3 The three phases of D_α light emission from the MARFE zone until disruption: MARFE-free (a), pre-MARFE (b) and main MARFE (c)

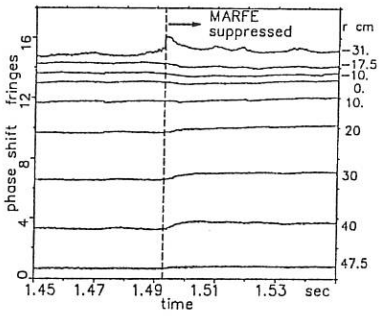

Fig.4 Phase-shift traces from HCN-interferometer for MARFE suppression at the initial stage

WALL CONDITIONING BY LITHIUM PELLET INJECTION ON TFTR

J. A. Snipes, J. L. Terry, E. S. Marmar
MIT Plasma Fusion Center
K. W. Hill, D. L. Jassby, D. K. Mansfield, D. M. Meade, H. K. Park,
A. T. Ramsey, J. D. Strachan, E. J. Synakowski,
and the TFTR Group
Princeton Plasma Physics Laboratory

Introduction Many wall conditioning techniques have been used on TFTR to remove adsorbed gases from the C/C composite limiter and reduce the electron density[1] to improve plasma performance in auxiliary heated discharges.[2] In addition to boronization, which has greatly reduced the oxygen levels in the plasma,[3] and standard 'He-conditioning', which reduces the C and D influxes, a new wall conditioning technique using lithium pellet injection has been discovered that further enhances the plasma performance. This new technique was used in the discharge with a record neutron rate ($S_n = 5\times10^{16}$ n/s), as well as in many of the discharges having the highest values of Q_{dd} ($1.5\times10^{-3} < Q_{dd} < 1.8\times10^{-3}$) for TFTR. By injecting Li pellets into a series of He conditioning discharges, the pre-pellet electron density and carbon content of the plasma were reduced at a much higher rate than with He conditioning alone. Single Li pellets injected into supershot discharges about 1 sec before neutral beam injection (NBI) reduced the carbon content during the supershots and increased the maximum neutron rates by 8 - 16% over similar discharges without Li pellets. Cumulative effects were also observed on the second discharge of a 2 shot sequence whereby a Li pellet was injected $\sim$ 0.5 s after NBI on the first shot and on the following shot a Li pellet was injected $\sim$ 1 s before NBI. This sequence produced 16 - 22% higher maximum neutron rates. Enhancements were also observed in the plasma stored energy, beta poloidal, energy confinement time, and central ion temperature.

Li Pellet Injection into He-Conditioning Discharges While standard helium plasmas (I_p=1.4 MA, B_T=4 T) are normally used to reduce C and D recycling at the limiter and lower the plasma electron density, it was discovered that the addition of Li pellets into such He conditioning discharges enhances the rate of reduction of the plasma electron density and carbon content. Figure 1 shows the chord averaged central electron density and the C^{+1} emission measured at 3.0 s as a function of shot number throughout a series of He conditioning discharges. There is a clear change in slope of the electron density and C^{+1} emission versus shot number for the discharges in which Li pellets have been injected. The change in slope indicates that the rate of reduction of the central electron density and carbon content is more than an order of magnitude greater with Li pellets than without. Thus, the wall conditioning process is greatly accelerated by adding a single Li pellet to every discharge.

Figure 1 also shows the intensity of the n=2 to 1 transition in Li^{+2} measured just before the pellet injection time. It indicates that the amount of background Li increases (from zero) over this sequence of discharges. Detailed calculations based on spectroscopic measurements show that the concentration of background Li remains small, such that, at the end of this series of discharges $n_{Li}/n_C \approx 0.03$. Since the remainder of the plasma is almost entirely C (based on the measured Z_{eff}), the total number of Li ions in the plasma is $N_{Li} \lesssim 1.5\times10^{18}$, while the total number of C ions has decreased from the beginning to the end of this series of discharges by $\approx5\times10^{18}$. Note that the number of Li atoms in a single pellet ($\sim3\times10^{20}$) is much larger than the number of Li ions in the plasma even after 23 successive discharges, each with a Li pellet. The number of atoms in a single pellet is calculated to cover 1 - 2 monolayers of the active surface of

the inboard bumper limiter. These data suggest that layers of Li atoms are accumulating on the limiter throughout the sequence of discharges with Li pellets and that this covering reduces the sputtered influx of carbon from the limiter, which in turn results in lower electron densities and lower carbon recycling.

Characteristics of Supershots with Li Pellets Careful comparison of similar supershots, one with a Li pellet injected about 1 s before NBI ('Li pre-injection') and one without pellet injection has led to the characterization of the effects of Li pre-injection on supershots. These effects include reduced edge electron density and reduced C^{+1} emission just before and during NBI, as well as reduced D_α emission during NBI. The typical effects are shown in Fig. 2, which compares a supershot with Li pre-injection and a similar supershot without pellet injection. The Li pellet was injected at 2 s and NBI was on from 3 to 4 s at 20 MW. The electron temperature 5 cm inside the plasma boundary is nearly the same just before and during the first 0.15 s of NBI, but, after about 0.4 s of NBI, becomes about 10% higher in the discharge with Li pre-injection. Thus, the observed decreases in carbon influx with Li pre-injection are not the result of changes in the edge electron temperature, but are probably due to decreased sputtering brought about by the lower edge density, the lower initial carbon content, and the smaller charge and mass of the Li ions compared to C ions.

Characteristic changes in global and central plasma parameters during NBI are also observed following Li pre-injection. These changes include a higher peak neutron rate (8-16%), plasma stored energy (5-10%), energy confinement time (5-14%), and central ion temperature (8-13%) relative to similar no-pellet supershots. Figure 3 shows the differences in the neutron rate, plasma stored energy, energy confinement time, and central ion temperature for a series of similar supershots with and without Li pre-injection. Note that the MHD activity in this series of discharges remained low up to the time of the peak neutron rate in both pellet and no-pellet discharges. Thus, MHD activity is not responsible for the differences shown in Fig. 3. Just after the neutron rate peaks, however, a large burst of MHD activity (predominantly m=2, n=1 at the wall) arises in the Li pre-injection discharges and the neutron rate subsequently collapses. There is little difference in the central electron temperature between pellet and no-pellet supershots, though the profile becomes slightly broader (FWHM increases by 4 to 8%) in the discharges with a Li pellet. The maximum density profile peakedness during the supershot is on the average about 8% larger in the discharges with a Li pellet. To determine for how many discharges the Li effects would persist, several similar supershots were run without Li pellets after a series of 25 supershots with Li pellets. Plasma performance was only slightly reduced in the first no-pellet discharge, but then degraded over the next three no-pellet discharges to a level only slightly above that achieved before any Li pellets had been injected. All of these results are consistent with previous observations about supershots[4] that changes in the plasma wall interaction physics, which in this case are due to a thin layer of Li atoms on the limiter, can also strongly affect the central plasma parameters.

Further experiments were performed to determine if increasing the amount of Li in the plasma would further improve supershot performance. While the pellet injector was only capable of injecting one Li pellet per discharge, it was thought that additional Li deposition could be achieved by injecting a Li pellet near the end of one discharge, and then injecting another Li pellet 1 s before NBI in the following discharge. The idea was that the Li atoms from the first pellet would coat the limiter and not be buried nor burned away before the Li atoms from the pellet in the second discharge added another coat. Further enhancements in the peak neutron rate, plasma stored energy, and energy confinement time were observed in the discharges with a 'double' Li pellet coating compared to discharges with only a 'single' Li pellet coating. In

particular, the discharge that produced the highest neutron rate achieved to date in TFTR (5×10^{16} n/s) had such a 'double' Li pellet coating. These results suggest that additional deposition of Li may further improve plasma performance.

Transport Analysis The SNAP[5] code has been used to analyze the differences between similar supershots with and without Li pre-injection. The results of comparing several such pairs of supershots indicate that the shots with a Li pellet exhibit small increases in the central absorbed beam power (4-6%), somewhat larger increases in the central pressure (5-10%), and substantial decreases in the ion thermal conductivity (50-150%) in the off-axis region $0.25<r/a<0.5$. Note that the ion temperature profile was measured only for $r/a<0.5$, and was assumed to fall linearly to the edge from there. Figure 4 shows the measured ion temperature profiles at 3.32 s comparing two similar supershots with (dashed line) and without (solid line) Li pre-injection. at 2.0 s. These large differences in the ion temperature profile clearly indicate an improvement in confinement and thermal ion heating in the discharge with Li pre-injection.

Consistent with the measurements, the calculated fusion reaction rates and stored energies were also enhanced in the discharges with Li pellets, with most of the enhancement coming from the thermal ion population. The increase in the thermal component of the fusion reaction rate accounted for $\approx$40% of the total enhancement, while the beam-thermal component accounted for $\approx$60% and the beam-beam component remained unchanged, on the average. Similarly, for the stored energy, the increase in the ion thermal energy accounted for $\approx$50% of the total enhancement, while the enhancement in the electron energy accounted for 25%, and the enhancement in the beam energy accounted for 25%, on the average. This analysis indicates that most of the improvement in plasma performance due to Li pellets has come about through improved confinement and heating of the thermal ions.

Conclusions Reproducible improvements in heating effectiveness and confinement result from the injection of Li pellets $\approx$1 s before NBI into supershot plasmas in TFTR. Small reductions in the edge electron density and in the carbon and deuterium recycling lead to appreciable increases in the central ion temperature, total plasma stored energy, and peak neutron rate. These changes in edge conditions are apparently due to a thin Li coating deposited on the limiter that makes it then more resistant to plasma bombardment. Such impurity influx suppression is qualitatively similar to that observed after Be evaporation in JET[6] and after boronization in TEXTOR[7] and ASDEX[8]. Transport analyses of similar supershot discharges with and without a Li pellet indicate that the improvements in plasma performance observed in the Li pre-injection discharges are due to large decreases in the ion thermal conductivity and to small increases in the central absorbed neutral beam heating power. These experiments also clearly demonstrate the importance of the plasma edge in connection with core plasma confinement.

Supported by the United States Department of Energy.

References

[1] M. Ulrickson, et al., 12th Int. Conf. IAEA, Nice 1988, Vol. 3 (1989) 419.
[2] R. J. Hawryluk, et al., 11th Int. Conf. IAEA, Kyoto 1986, Vol. 1 (1987) 51.
[3] H. F. Dylla, et al.,9th PSI Conf. Bournemouth 1990, to be pub. in J. Nucl. Mater.
[4] H. F. Dylla, et al., J. Nucl. Mater. **162/164** (1989) 128.
[5] H. Towner and R. Goldston, Bul Am Phys Soc **29** (1984) 1305.
[6] JET Team, 13th Int. Conf. IAEA, Washington D.C. 1990, paper A-6-2.
[7] J. Winter et al., J. Nucl. Mater. **162/164** (1989) 713.
[8] U. Schneider, et al., 9th PSI Conf. Bournemouth 1990, to be pub. in J. Nucl. Mater.

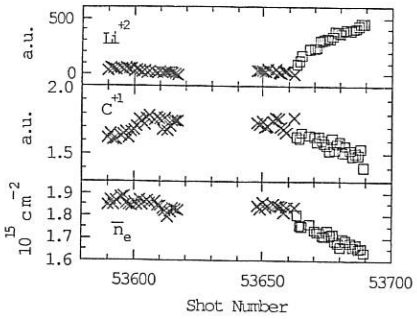

Fig. 1. *The intensity of a Li^{+2} line, the edge carbon emission C^{+1}, and the central chord averaged electron density measured at 3.0 s in a series of ohmic He conditioning discharges. (Squares indicate those discharges that were preceded by a discharge in which a Li pellet was injected at 3.2 s.)*

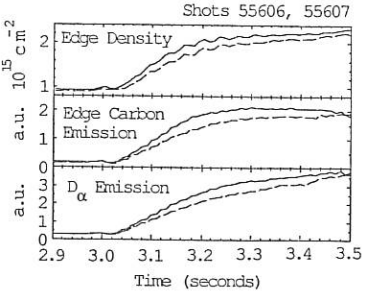

Fig. 2. *Inboard edge chord averaged electron density, C^{+1}, and D_α emission versus time just before and during NBI for a pair of nearly identical supershots, one with a Li pellet injected at 2.0 s (dashed line) and the other without a pellet (solid line).*

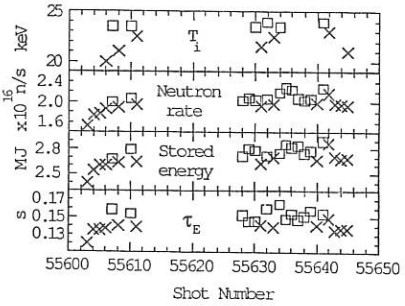

Fig. 3. *Central ion temperature, neutron rate, plasma stored energy, and energy confinement time taken at the time of maxiumum neutron rate for a series of supershots. (Squares indicate discharges with Li pellet pre-injection.)*

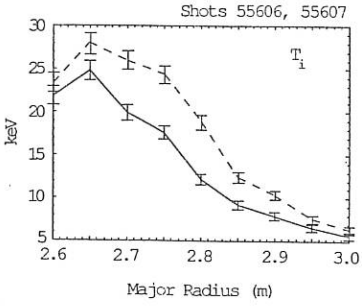

Fig. 4. *Charge exchange ion temperature profiles at 3.32 s comparing similar supershots with (dashed line) and without (solid line) Li pellet pre-injection at 2 s.*

THE EFFECT OF DENSITY ON BOUNDARY PLASMA BEHAVIOUR IN TFTR

C S Pitcher*, P C Stangeby**, R V Budny, C E Bush, J D Elder**, K W Hill,
S J Kilpatrick, D M Manos, S S Medley, A T Ramsey, J F Schivell and M Ulrickson
Princeton Plasma Physics Laboratory, Princeton, NJ 08543, USA

* Canadian Fusion Fuels Technology Project, Toronto, Canada

** University of Toronto Institute for Aerospace Studies, Canada

1 Introduction

The dependence of the plasma boundary conditions on central density has been investigated both experimentally and theoretically in a controlled sequence of Ohmic deuterium discharges in TFTR. The purpose of this work was to produce a wide range of well-diagnosed boundary plasma conditions which could be used to validate models of the plasma boundary. The models that are compared with experiment in this paper include: a Monte Carlo impurity production and transport code called LIM [1] (Sec. 3) and a simple zero-dimensional analytic model (Sec. 4).

2 Experimental Results

The boundary plasma diagnostics on TFTR include: a fast reciprocating Langmuir probe, used to obtain full radial profiles of plasma density n_e and electron temperature T_e throughout the scrape-off layer (SOL), poloidal visible spectroscopy arrays which are used to obtain the influxes of deuterium (from D_α) and carbon (from C II), and bolometer arrays to give the spatial distribution of radiated power.

Detailed boundary plasma measurements were made across a range of plasma densities from $< n_e >= 1x10^{19}\, m^{-3}$ to $< n_e >= 4x10^{19}\, m^{-3}$ in discharges with $I_p = 1.4\, MA$, $B_T = 4\, T$, $R_0/a = 2.45\, m / 0.80\, m$ and with constant Ohmic input power $P_{tot} \sim P_\Omega \sim 1\, MW$. The experimental results from the density scan appear in Fig. 1, from the top, the edge density $n_e(a)$ and electron temperature $T_e(a)$, e-folding distances in the SOL for density λ_n and electron temperature λ_T, the deuterium Γ_D and carbon Γ_C influxes, the central Z_{eff} and the radiated power fraction P_{rad}/P_{tot}.

As found in previous studies [2], the edge temperature is high at low density $T_e(a) \sim 60\, eV$ and decreases to $T_e(a) \sim 25\, eV$ at high density. The edge density scales linearly with average density, $n_e(a) \sim < n_e > /3$. The e-folding distances, λ_n and λ_T, are approximately equal at low density $\lambda_n, \lambda_T \sim 6\, cm$, but diverge at higher densities with λ_n decreasing slightly and λ_T increasing to ~ 15 cm.

The carbon influx Γ_C is approximately constant with density while the deuterium influx Γ_D becomes very small at low density and rises somewhat faster than linear with increasing density. At the lowest density, the discharge is supplied with electrons primarily by the carbon impurity influx with only a small fraction contributed by deuterium. Such conditions are only achieved after extensive helium conditioning discharges [3], which purge the limiter surface of deuterium and enable the Supershot regime to be accessed. The high carbon concentration at low density is indicated by the high $Z_{eff} \sim 5$, which decreases monotonicly towards unity with increasing density.

The radiated power fraction is approximately constant over the density scan at a level of $P_{rad}/P_{tot} \sim 0.5$, except at the highest density where there is an abrupt transition to a MARFE [4], at which point $P_{rad}/P_{tot} \sim 1$. The abrupt increase in P_{rad} clearly demonstrates the thermal-instability nature of the MARFE.

3 LIM Impurity Code

The impurity production and transport in these discharges have been modelled with the Monte Carlo impurity code LIM [1]. The code uses as input the background plasma conditions as determined by the probe and other diagnostics. The code launches physically sputtered carbon atoms into a plasma grid, and follows the carbon ions within the plasma until they redeposit on the limiter surface. Both deuteron sputtering and carbon self-sputtering are taken into account using sputtering yields from the literature. Parallel-field transport is assumed to be classical, while cross-field transport includes diffusion $D \sim 1\, m^2 s^{-1}$ and an inward pinch velocity $v = -2Dr/a^2$. The limiter and plasma poloidal shapes are approximated as circles. Results from the code appear in Fig. 2, appearing from the top, the effective sputtering yield on the limiter $Y_{eff} \equiv \Gamma_C/\Gamma_D$, the required sputtering yield enhancment factor η needed to fit the experimental Y_{eff}, the energy radiated per carbon atom entering the plasma E_{rad}, the carbon ion particle confinement time τ_p, and the central Z_{eff} of the discharge.

The experimental Y_{eff} in Fig. 2 varies from $Y_{eff} \sim 1$ at low density, where $T_e(a)$ is high, to $Y_{eff} \sim 10^{-2}$ at high density where the edge temperature is reduced. The edge temperature, through its effect on the incident ion energies striking the limiter, directly controls the sputtering yield on the limiter. The LIM code is able to reproduce the yield at moderate to high density but fails at low density. LIM can reproduce the whole data set if a fitting factor η is used to increase both the deuteron and carbon sputtering yields at normal incidence. η approaches a value of 2 to 3 at low density, Fig. 2. Under such conditions, the discharge density is maintained almost entirely by the carbon influx, which is predominantly produced by carbon self-sputtering as the self-sputtering yield ηY_C approaches unity. An enhancement of the sputtering yields at low density may be explained by an increase in the average angle of ion impact on the limiter surface which may occur when the edge ion temperature $T_i(a)$ becomes larger than the edge electron temperature $T_e(a)$. Another possibility is that the deuterium-depleted graphite surface at low density may possess higher sputtering yields compared with deuterium-saturated graphite [5].

The calculated energy radiated per carbon atom entering the plasma is approximately constant with plasma density at $E_{rad} \sim 2\, keV$, whereas the experimental value is $E_{rad} \sim 6\, keV$, Fig. 2. The discrepancy may be due to the presence of neutral hydrogen in the plasma which can significantly increase the rate of power radiated due to the effect of charge exchange [6].

The LIM carbon particle confinement time, derived by averaging the trajectories of the injected carbon ions within the plasma, decreases with density as $\tau_p \propto < n_e >^{-1}$ in reasonable agreement with experiment, although the absolute times differ by a factor of ~ 2. The decrease with density demonstrates the ability of a densified boundary plasma to screen impurities from the central discharge. These confinement times, along with the experimental carbon influx, are used to derive the central Z_{eff} in Fig. 2 using $< n_C > = \Gamma_C \tau_p / V$, where V is the plasma volume.

4 Analytic Comparison

A relation between $n_e(a)$ and $< n_e >$ for a pure deuterium plasma has been given in [7],

$$n_e(a) = 1.7x10^{-19} < \lambda_T > < n_e >^2$$

where $< \lambda_T >$ is the average particle flux e-folding distance in the SOL. The $n_e(a)$ predictions using this expression are shown in Fig. 1 and are in reasonable agreement with experiment, particularly for high $< n_e >$ where the plasma is cleaner.

In the case of the effective yield Y_{eff} given in Fig. 2, we have from [8],

$$Y_{eff} \equiv \frac{\Gamma_C}{\Gamma_D} = \frac{\eta Y_D}{1 - \eta Y_C}$$

where the D^+ ions striking the limiter are assumed to have an energy of $5T_e(a)$ ($2T_e$ thermal energy + $3T_e$ sheath potential) and a sputtering yield Y_D, and the carbon ions are assumed to have a charge of four (C^{+4}), an energy of $14T_e(a)$ and a sputtering yield Y_C. As with the LIM simulation, a similar discrepancy in Y_{eff} is found at low density which can be explained by an enhancement in the physical sputtering yields. To obtain the central Z_{eff}, the central dilution is determined from [8],

$$\frac{< n_C >}{< n_D >} = \left[\frac{\Gamma_C}{\Gamma_D}\right]\left[\frac{\lambda_C}{\lambda_D}\right]$$

where the experimental yield is used for $\Gamma_C/\Gamma_D = Y_{eff}$ and λ_C/λ_D is the ratio of effective penetration distances for carbon and deuterium (assumed constant ~1/2, ie the transport of carbon relative to deuterium is constant). The good agreement with experiment for the analytic Z_{eff} suggests that carbon transport relative to deuterium transport is indeed constant and that the central Z_{eff} is determined primarily by the sputtering yield at the limiter.

5 Conclusions

Detailed boundary plasma measurements have been made over a range of densities in Ohmic deuterium discharges in TFTR. The resulting edge conditions vary significantly from a low edge density with a high temperature to a high edge density with a low temperature. The comparison between theory and experiment confirms the following: (1) physical sputtering is the dominant impurity release mechanism in these discharges, with carbon self-sputtering dominating at low density (2) sputtering yields are enhanced at low density above those associated with normal incidence (3) the energy radiated per carbon atom is constant with density and elevated probably due to the presence of atomic hydrogen charge-exchange (4) the carbon particle confinement time τ_p decreases with density, demonstrating the increased screening of the plasma boundary as density increases (5) the central Z_{eff} is controlled to a large extent by the effective sputtering yield at the limiter Y_{eff} (6) simple zero-dimensional modelling can give reasonable agreement with experiment in these cases.

This work was supported by US DOE Contract Nos. DE-AC02-76-CHO-3073, DE-AC04-76DO00789 and DE-FG05-90ER54091.

References

(1) P C Stangeby et al, Nucl Fus 28 (1988) 1945.
(2) S K Erents et al, Nucl Fus 28 (1988) 1209.
(3) H F Dylla et al, Nucl Fus 27 (1987) 1221.
(4) B Lipschultz, J Nucl Mat 145-147 (1987) 15.
(5) J N Brooks et al, J Nucl Mat 162-164 (1989) 363.
(6) P G Carolan et al, Plas Phys 25 (1983) 1065.
(7) P C Stangeby, J Nucl Mat 145-147 (1987) 105.
(8) C S Pitcher, Fus Eng Design 12 (1990) 63.

Fig.1 Experimental results: edge electron density $n_e(a)$ and temperature $T_e(a)$, density λ_n and temperature λ_T e-folding distances in the SOL obtained by the reciprocating Langmuir probe at the outside mid-plane, global carbon Γ_C and deuterium Γ_D influxes obtained by the poloidal spectroscopy array, central Z_{eff} obtained by visible bremsstrahlung and radiated power fraction P_{rad}/P_{tot} from the bolometer arrays. Also shown is a comparison between the experimental $n_e(a)$ and values determined using the analytic expression of Sec. 4 (+).

Fig.2 Comparison between experiment and modelling using LIM and the analytic expressions of Sec. 4: effective sputtering yield on the limiter $Y_{eff} \equiv \Gamma_C/\Gamma_D$ assuming no enhancement, the enhancement η in the normal-incidence sputtering yields required to fit the experimental Y_{eff}, the energy radiated per carbon atom influx E_{rad} experimentally determined using the radiated power P_{rad} and the carbon influx rate Γ_C and determined with LIM using radiation rate coefficients, carbon particle confinement time τ_p and central Z_{eff}.

Fig. 1

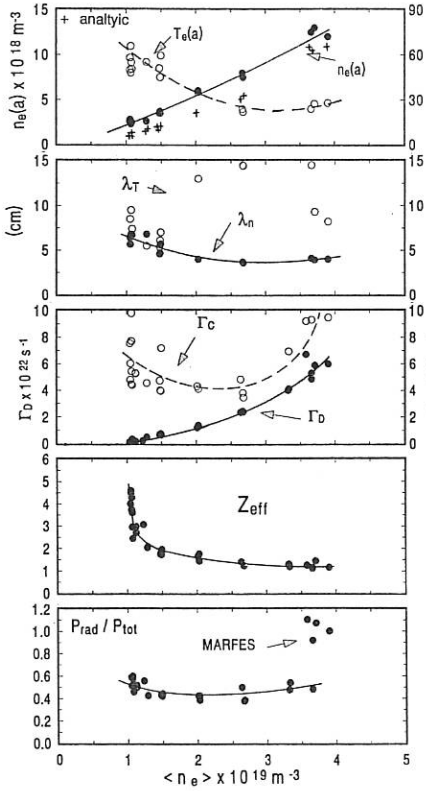

Fig. 2

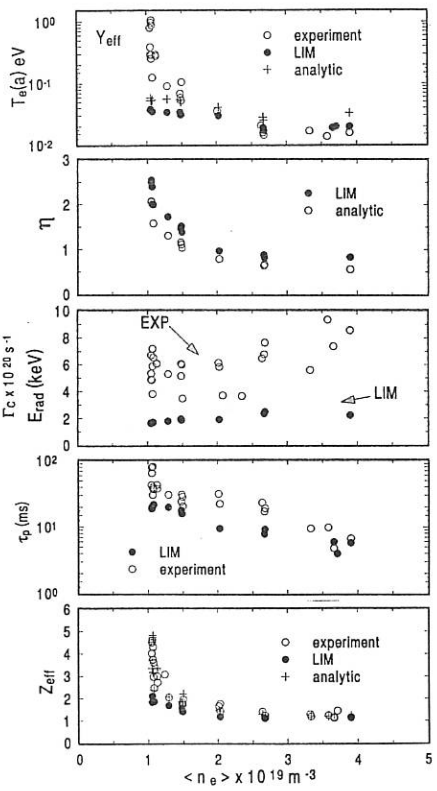

POWER FLOW THICKNESS AND EDGE TEMPERATURE AND DENSITY SCALING IN THE SCRAPE-OFF LAYER OF JET WITH Be LIMITERS

J A Tagle, S Clement, S K Erents*, P J Harbour, L de Kock, A Loarte, and S D Richards**

JET Joint Undertaking, Abingdon, Oxon, OX14 3EA, U.K.
*AEA Technology, Culham Laboratory, Abingdon, Oxon OX14 3DB, U.K.
**Imperial College, London SW7 2BZ, U.K.

INTRODUCTION:

We describe the parametric scaling of the power flow decay length (λ_P) for the scrape-off layer (SOL) in JET, and the edge temperature $T_e(a)$ and density $n_e(a)$ in terms of the main (core) plasma parameters. The scaling is given for ohmically heated limiter-bound plasmas with volume averaged density $0.6 \leq < \overline{n_e} > \leq 6x10^{19} m^{-3}$, plasma current $1 \leq I_p \leq 7MA$ and toroidal field $1.9 \leq B_t \leq 2.4T$. The measurements of the edge parameters were made by using Langmuir probes built into the beryllium toroidal limiter tiles, and located at different toroidal/poloidal (upper/lower belt) positions. These fixed probes are radially separated allowing an estimate of SOL thickness of the edge parameters in nearly every discharge, assuming exponential decay of the density and temperature from the last closed flux surface (LCFS) to the wall. Justification for this assumption has been obtained from a complete radial profile measured by using a fast movable reciprocating probe in the JET SOL /1/.

The scaling presented is for the so called 'Steady state SOL' conditions, which in the case of Be limiters were very difficult to obtain due to the strong pumping of the Hydrogen isotopes by the Be covered walls. The measurements were taken during the plasma current flat top, when the relative fraction of the radiated power was constant (in practice the loop voltage was also constant). Despite the careful selection of the quasi steady state conditions there is a large scatter in the data with Be limiters. A preliminary attempt has been made to scale, by linear regression, the edge parameters with I_p, $< \overline{n_e} >$, the safety factor q and the power conducted to the edge P_c (total input power P_{tot} minus the radiated power).

POWER SOL THICKNESS:

The power flux density ($W\,m^{-2}$) in the SOL is calculated from the measurements of the ion flux to the probe I_{sat} ($A\,cm^{-2}$) and the electron temperature T_e (eV) using the experimentally determined sheath transmission factor $\gamma(T_e)$ /1/. The power decay length λ_P is calculated from the power measured by the two probes, radially apart, and assuming exponential decay of the power in the SOL.

Figure.1 shows the variation of λ_P with the safety factor q_{cyl} for different plasma currents. The individual measurements show a large scatter; however it has to be noted that the core plasma density varies by a factor of 10 and the current increases by a factor of 7. It is found that:

- λ_P is typically less than 1 cm, in agreement with predictive models of the edge plasma for large Tokamaks /2,3/, leading to large peak power loads to the limiters (or divertor plates).

- λ_P increases with the safety factor q_{cyl}. This is more noticeable by comparing discharges at fixed current with different toroidal fields (typically the series at 3.0 MA).

- Preliminary scaling gives a weak dependence of λ_P with $< \overline{n_e} >$ and I_p (constant q), in agreement with model predictions for regimes with edge densities $n_e(a) < 10^{19}\ m^{-3}$ /2,3/.

- The previously reported dependence of λ_P on I_p^{-1}, obtained with discrete graphite limiters in JET /4/ is not found with full toroidal Be limiters.

- Analysis of high power additionally heated discharges ($P_{tot} < 30$ MW, NBI and ICRF heating) indicates a stronger dependence of λ_P on $< \overline{n_e} >$ ($\lambda_P \sim < \overline{n_e} >^{\xi}$ with $\xi \simeq 0.13\text{-}0.30$), mainly due to an increase of the conducted power P_c and $n_e(a)$ at higher input powers and also in agreement with model predictions /2/.

EDGE DENSITY AND TEMPERATURE:

The edge electron temperature and density extrapolated to the separatrix (LCFS) are shown in Figs.2 and 3, from which we can draw the following conclusions:

- There is a broad relationship between the edge density and the bulk (volume averaged) density (Fig.2). The rather wide spread in the data is associated with the variation in fuelling rate which affects the density profile /4/.

- The gradient of the relation between edge and core density lies between those previously reported, either linear /5/ or square-law scaling /6/, but the variation in fuelling rates provides at least one hidden variable which makes any regression fitting of the data inconclusive. Regression analysis gives a relation $n_e(a) \sim < \overline{n_e} >^{1.4}$, whereas a simple model predicts $n_e(a) \sim < \overline{n_e} >^{2.0}$ /6-7/.

- The edge temperature $T_e(a)$ is a strong function of the edge electron density $n_e(a)$, decreasing $\sim n_e(a)^{-x}$ with $x \simeq 0.6\text{-}0.8$, but flatter at low $n_e(a)$ and steeper at high $n_e(a)$. Also $T_e(a)$ is weakly dependent on plasma current I_p, which for the selected ohmic discharges is proportional to P_c.

- Simple power balance models predict that if P_c is not a function of $n_e(a)$ then $x = 2/3$ (for constant λ_P) or 0.8 (if λ_P varies as in /2/). Thus our data are consistent with constant P_c over a range of density, but do not suggest that the power in the electron channel in the SOL increases linearly with P_c as predicted.

- The departure from constant P_c behaviour at low density may be due to an increase in the ratio T_i/T_e at these low densities, as reported previously /8/. The steepening of the curves in Fig.3 at high densities is believed to be caused by local radiation near the limiters, not seen by the bolometers in JET /9/.

- The values of $T_e(a)$ shown in Fig.3 are similar to if a litle lower than previous measurements in the JET SOL with graphite limiters /5/. However there are two main differences: with graphite the curve at fixed I_p is much steeper ($T_e(a)$ was measured over a very limited range of $n_e(a)$) and the sensitivity to I_p (hence to P_c) is greater than with Be limiters. The reasons of these differences are not yet understood, but may perhaps be associated with the different radiation characteristics of Be and C, alternatively with higher secondary electron emission in Be. The first results reported with Be limiters in JET for $T_e(a)$ /8/, showed an apparent saturation of $T_e(a)$ at low densities, but those results are included here and the saturation is no longer in evidence. One reason why $T_e(a)$ was higher in 1990 at low $n_e(a)$ than in 1989 might be that the sheath transmission coefficient decreased with aging of the Be limiters, perhaps due to contamination eg. with a.CH, which reduces the secondary electron emission coefficient.

TRANSPORT IN THE SOL:

The measurements of λ_P ,$T_e(a)$ and $n_e(a)$ in ohmic discharges have been analysed in a number of ways. Any method of analysis is affected by the rather large scatter of the data. Some of this scatter is inherent in the measurements, especially since most of them were made "parasitically" in the course of other experiments. Some of it is associated with hidden variables, not included in our analysis. Using linear regression, it was found that the uncertainties in the interpretation were too large to draw many quantitative conclusions. Instead we have compared the measured λ_P to the value predicted by eq.10 of ref/2/. This equation suggest that λ_P plotted against $q^{0.5}T_e(a)^{-0.25}$ should give a straight line with gradient proportional to $\chi_\perp^{0.5}$. No such trend was found, but to obtain reasonable agreement between model and experiment, $\chi_\perp$ must nevertheless lie in the range $0.3 < \chi_\perp < 1.0 m^2 s^{-1}$

A second comparison was made using eq.9 of ref/2/, in the present notation: $n_e(a) = 2n_t = (\lambda_P P_c)/(4\chi_\perp T_e(a)\pi^2 R a_s)$. Writing $\lambda_P P_c/T_e(a) = n_{sc}$ as an edge density scale factor, gives the correlation between $n_e(a)$ and n_{sc} shown in Fig.4. The general trend of the data is linear and, despite the scatter, n_{sc} is a satisfactory scaling parameter. However a quantitative comparison with the model requires $\chi_\perp \approx 10 m^2 s^{-1}$, which is inconsistent with the above value, $\chi_\perp \sim 1.0 m^2 s^{-1}$. Furthermore, combining eq.10 of ref /2/ with eq.9, rewritten as above, gives $n_e(a) \sim q^{0.5} P_c T_e(a)^{-1.25}$ and this scaling parameter requires $\chi_\perp \sim 10^2 m^2 s^{-1}$ for quantitative agreement. Obviously something is wrong. There is good reason to believe the measured I_{sat} because it agrees to better than a factor of two with the total influx determined by H_α intensity. There is no reason to doubt the $T_e(a)$ greatly unless the electrons are non-Maxwellian. Even if the sheath transmission factors are wrong they are unlikely to be wrong by as much as a factor of two. Basically our problem is that the value of λ_P is too small to allow $\chi_\perp$ to be large and yet the power flowing into the SOL of JET is, in conjuntion with other measurements, too large to be reasonable unless $\chi_\perp$ is much larger.The situation can only be resolved in terms of the simple SOL model if we chose eg $\chi_\perp = 1 m^2 s^{-1}$, with $P_c = 0.2 P_c$(measured) and $T_i/T_e = 3$. Alternative choices are also possible,eg with P_c and T_i/T_e larger. One factor not considered in any detail is that there are two belt limiters in JET and there are some uncertanties in the balance between them.

SUMMARY: The experimental scaling of edge parameters in JET for ohmic heated plasmas has been tested with simple predictive models of the edge plasmas.The experiments are in qualitatively good agreement with model predictions. Quantitative scaling leads to re-examination of the input parameters and input data to the model.

References

/1/ S K Erents et al.., J. Nucl. Materials, 162-164 (1989)226-230.
/2/ P J Harbour Nuclear Fusion 24(1984)1211.
/3/ ITER Team, ITER Concept definition, Vol.2 (IAEA 1989) 48-58.
/4/ S Clement et al.., J.Nuclear Mater. 176-177(1990)432.
/5/ J A Tagle et al., 14th EPS Conf. Cont. Fus. (Madrid 1987). Vol 11D,part II,p 662
/6/ K F Alexander et al.., Nuclear Fusion 26(1986)1575.
/7/ P C Stangeby J. Nucl Materials 145-147(1987)105-116.
/8/ S K Erents et al.., 17th EPS Conf. on Contr. Fus. (Amsterdam 1990) Vol.14B, Part III,p 1385.
/9/ A Loarte (private communication).

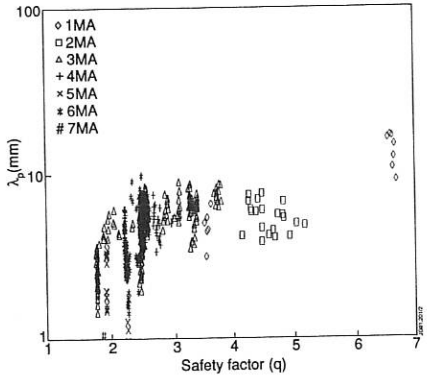

Fig.1 Power flow thickness as a function of the safety factor (q) for different plasma currents (Ip = 1-7 MA), toroidal fields (Bt = 1.8-3.4 T) and .br volume averaged densities (0.6-6.0 $10^{19} m^{-3}$).

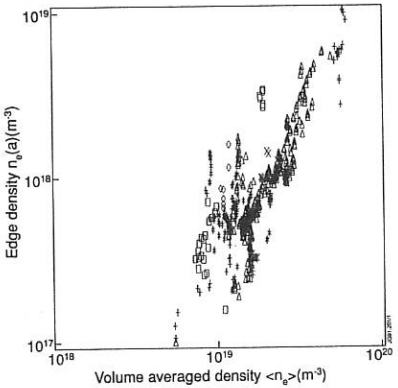

Fig.2 Edge electron density versus volume averaged density (symbols as in Fig.1).

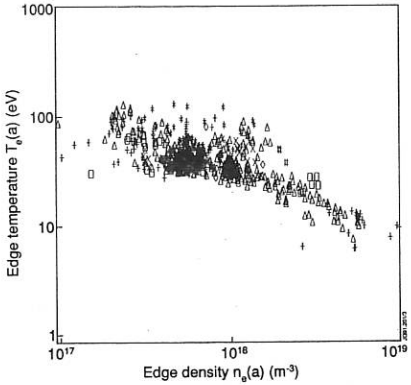

Fig.3 Edge electron temperature versus edge electron density (symbols as in Fig.1).

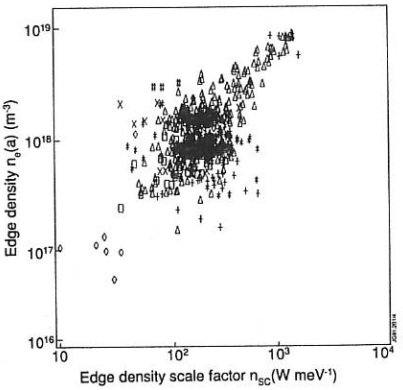

Fig.4 Scaling of the edge density with the edge density scale factor $n_{sc} = \lambda_p P_c / T_e(a)$ (symbols as in Fig.1).

DEUTERIUM DEPTH PROFILES AND IMPURITIES ON THE BE COATED CARBON BELT LIMITER IN JET

A.P. Martinelli[+], I. Hughes[*)1], R. Behrisch[+], A.T. Peacock

JET Joint Undertaking, Abingdon, Oxfordshire, U.K.

[+] Max-Planck-Institut für Plasmaphysik, EURATOM Association, D-8046 Garching, Germany

INTRODUCTION

In plasma experiments with magnetic confinement, such as Tokamaks, the limiter surfaces are subjected to the most intense particle and energy bombardment causing erosion, deposition, implantation, release, and surface heating. This changes the surface properties of the limiter and affects the plasma parameters and performance and will determine the tritium inventory in a future fusion reactor. In this work a Carbon tile of the JET belt limiter has been analysed in detail with respect to D-retention and depth profile as well as with respect to the impurity content in the surface layers.

EXPERIMENTS AND RESULTS

The carbon belt limiters were installed in July 1987 and subjected to about 7500 JET discharges during the 1987/1988 experimental campaign. After installing the Be evaporators in May 1989 about 350 further JET discharges were performed without Be evaporation /1-3/. Be evaporation started in mid 1989 and about 1250 JET discharges were performed. The carbon limiter tiles, onto which a Be layer of total thickness about 5μm had been evaporated, were removed in July 1989 and replaced by solid Be tiles /2,3/.

Several pieces were cut from the plasma exposed side of a carbon tile from octant 8 of the top belt limiter which had been in use for the JET discharges from 1987 to 1989. They were analyzed on a line along the poloidal direction for the deposition of impurities with Z > 20 within a surface layer of about 5μm by PIXE (H^+, 1.5 MeV) and within a surface layer of about 1 μm by RBS (^4He, 1.5 MeV). NRA [$D(^3He, p)^4He$] was applied at 0.79 MeV for measuring the D in a layer of about 0.7 μm /4,5/ and at energies in the range of 0.3-2.4 MeV in a resonance like technique to determine the depth profile and the total D quantity in the surface layers up to 8 μm /4/.

The results for Cr, Fe, Ni, and D deposition are shown in Fig.1. There is a broad maximum of both the metal and the D deposition on the area around the tangency point (pos.320) and mimima on both sides (pos 245 and 400), followed by a second maximum and a decrease to the very sides furthest away from the last closed magnetic surface.

---

1) DAAD Stipend from the Queens University of Belfast

The deuterium depth profiles for the positions 245 and 295 are shown in Fig.2. The total amount of trapped D is a factor of 2 to 10 larger than the D measured in the depth <1μm.

The Rutherford backscattering analysis at several points of the belt limiter tile showed that the depositions were nearly uniformly distributed up to depths <0.5μm with a tendency for the Ni,Cr,Fe to peak near the surface. The concentrations determined for the different elements in the surface layer are summarised in table.1.

	Pos.245	Pos.295
	at.%	at.%
Ni,Cr,Fe	0.41	0.33
	($4\ 10^{16}$ cm^{-2})	($1\ 10^{17}$ cm^{-2})
O	12	20
C	67	30
Be	15	42
D	6	8
	($1.5\ 10^{18}$ cm^{-2})	($4\ 10^{18}$ cm^{-2})

Table 1. Concentrations of different elements in the surface layers of a JET carbon tile from the top belt limiter as measured with RBS (depth about 1μm). For Ni,Cr,Fe and D also the total amounts in the surface layer of about 1μm and 8 μm, respectively, are given in parentesis.

DISCUSSION

The deposition and the distributions measured on the limiter tile are the result of a large number of JET discharges, of venting the vessel and finally of Be evaporations during the last experimental campaign. Each discharge has different phases such as start up, flat top, sometimes with additional heating by NI and/or ICRH and the ramp down phase. Furthermore the plasma shape and position was changed for different JET discharges and even during single JET discharges. The distributions measured on the plasma exposed limiter surface represent the integral effect of all these discharges, discharge phases and plasma positions/1-3/.

Only one belt limiter tile was analysed in detail. Langmuir probe measurements showed reasonable toroidal symmetry in JET /5/. Though the ripple of the toroidal magnetic field and local additional heating may introduce asymetries, the general form of the measured distributions are expected to be representative of the majority of the tiles within the belt limiters.

The majority of the discharges were performed in the first experimental campaign with bare carbon limiters and only in the second experimental campaign Be was regularily evaporated. During the non Be discharge period, Ni,Cr,Fe, eroded from the inconel vessel walls and also from the antenna were deposited on the limiters. In addition carbon together with the small amount of Ni,Cr,Fe were eroded and redeposited on the limiter tiles along with D from the discharge gas during this phase.

The general shape of the metal distribution measured in this work is in reasonable agreement with the distributions of erosion and

redeposition of carbon measured previously by the change of the geometrical shape of JET belt limiter tiles /7/. These distributions agreed in shape and magnitude with calculated curves assuming erosion by sputtering, ionisation in the SOL plasma and bombardment back on the divertor tiles /7/. For the Ni,Cr,Fe deposition measured in this work the best agreement is found for an e-folding length of 15 mm for particle flux and ion temperature in the SOL. This is in agreement with the values measured with Langmuir probes at the belt limiters /5/. It shows that the distributions are essentially determined by erosion and redeposition processes rather than by deposition alone.

At the erosion dominated area, such as pos.245, the total Ni,Cr,Fe deposition as measured with PIXE in a layer of about 5 μm is lower than at the deposition dominated area, such as pos.295. The volume concentrations of Ni,Cr,Fe in a layer of about 1μm, as determined by RBS, show the opposite behaviour. For Be the volume concentration is much larger at the deposition dominated area than at the erosion dominated area (table 1). This indicates a preferential erosion of Be at the erosion dominated area, i.e. the Be which was deposited by evaporation is quickly eroded and partly deposited at the deposition dominated area. The Ni,Cr,Fe deposited on the carbon during the "pre Be" discharge campaign is partly uncovered resulting in the large concentrations of C and Ni,Cr,Fe at the erosion dominated area. At the deposition dominated area we have also Ni,Cr,Fe deposition resulting in the larger total amount than at the erosion dominated area. However, the volume concentration is low due to the simultaneous large Be deposition. This means that erosion and deposition are different for different elements.

Finally, the relatively large oxygen concentration measured on the limiter tile is in agreement with the good oxygen gettering of the Be deposits and the low oxygen concentration measured in the plasma /1,2/.

CONCLUSIONS

Detailed surface layer analysis of the JET belt limiter tile shows erosion and deposition dominated areas with differences for different elements. The general feature is found to be in good agreement with the results of a previous analysis of erosion and deposition on belt limiter and divertor tiles /6,7/.The total D inventory on the limiter is about 3 times larger than the D contents detected with NRA at 0.79 MeV. This large D quantity in a 5-8μm depth contributes to the D inventory but it is unlikely to contribute to recycling during a discharge except perhaps if the limiters get very hot during extended high power discharges.

REFERENCES

/1/ The JET Team, P. Stott, J. Nucl. Mat. 162-164 (1989) 3
/2/ The JET Team, P.R. Thomas, J. Nucl. Mat. 176-177 (1990) 3
/3/ A.T. Peacock, J.P. Coad et al. J.Nucl.Mat. 176-177 (1990) 326
/4/ I. Hughes et.al. to be publ. Nucl. Instr. Meth. Phys. Res. (1991)
/5/ S. Clement A. Tagle et al.J. Nucl. Mat: 176-177 (1990) 432
/6/ G.M.McCracken,R.Behrisch et al. 16th EPS Conf. Venice (1989)
/7/ A.P. Martinelli, R.Behrisch et al. 16th EPS Conf. Venice (1989)

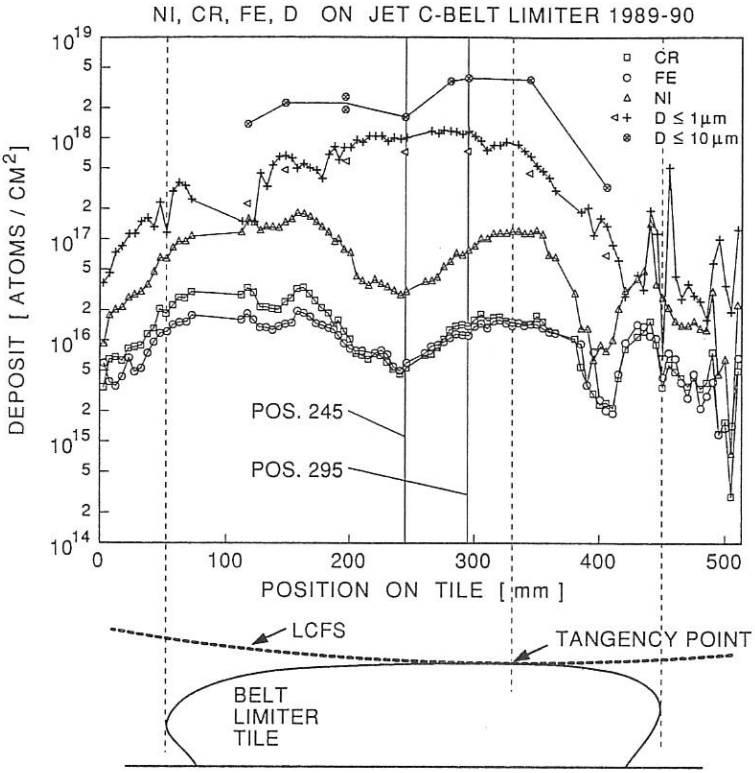

FIG. 1. Distributions of Ni, Cr, Fe, and D (within different depths) on the plasma exposed side of a JET belt limiter tile after the 1989/90 experimental period.

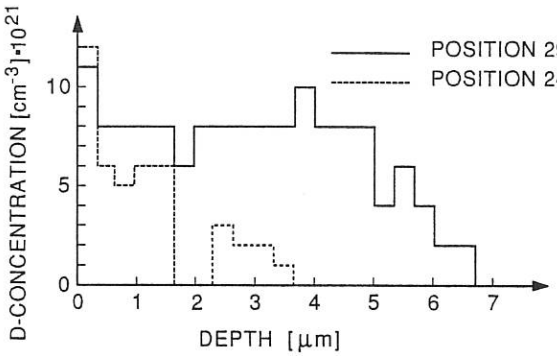

FIG. 2. Depth profiles of the trapped D on the JET belt limiter tile at the positions 245 and 295 mm.

RADIATION COOLING WITH INTRINSIC AND INJECTED IMPURITIES IN THE PLASMA BOUNDARY OF A LIMITER TOKAMAK

U. Samm, G. Bertschinger, P. Bogen, H.A. Claaßen, H. Gerhauser, E. Graffmann, E. Hintz, L. Könen, Y.T. Lie, A. Pospieszczyk, D. Rusbüldt, J. Schlüter, R.P. Schorn, B. Schweer

Institut für Plasmaphysik, Forschungszentrum Jülich, FRG, Ass. EURATOM-KFA

1. Introduction

Line radiation from impurities in the boundary of a tokamak plasma is the main means for distributing the power flux uniformly onto the wall. Thereby, critical power loads to the limiter edge or the divertor plate can be avoided. The objective is to find the appropriate impurity species, which allow to radiate on a high power level and at the same time fulfill the principal requirements for radiation cooling in a fusion plasma : a) restriction of the radiation to the boundary zone, b) impurity concentration in the centre below a critical value (fuel dilution, bremsstrahlung) and c) thermal stability.

The study of plasmas with various levels of radiation ($\gamma=P_{rad}/P_{heat}$) is a subject of ongoing research on TEXTOR. In particular, emphasis has been put on investigating the properties of plasmas with a cold radiative edge close to the density limit (detached plasma) [1]. These studies have first been concentrated on the case of pure ohmic heating, but recently have been extended to discharges with strong auxiliary heating. A quasi-stationary high radiation level (γ close to 100%) has been achieved by injecting Ne into the plasma. In the present paper we summarize these results, discuss the radiation characteristics and check the data with respect to the requirements for radiation cooling in a fusion plasma.

2. Experiment

The plasma facing components in TEXTOR consist mainly of low z-materials : the limiters (poloidal limiter, toroidal pump limiter ALT-II) are made of graphite and the wall is carbonized or boronized. The data in this paper refer to the standard TEXTOR operation parameters: major radius R=175cm, minor radius r=46cm, plasma current I_p=340kA, magnetic field B=2.25Tesla, gas filling D_2. In case of auxiliary heating we refer to neutral beam co-injection (NBI) of H. Comprehensive plasma edge diagnostics is available on TEXTOR. With the help of emission spectroscopy the particle fluxes at limiter and wall (e.g. H/D, C, O, Ne) are measured. Various atomic probing beams (thermal Li, 30kV Li, 10 eV Li/C, thermal He) provide information e.g. on electron density $n_e(r)$ and electron temperature $T_e(r)$ at the plasma boundary [2][3]. The total radiation is measured by a bolometer. The concentration of impurities in the plasma centre can be derived from the plasma conductivity on axis, from cx-spectroscopy or from soft-x-ray measurements.

A unique plasma positioning system based on interferometric measurements (HCN-interferometer [4]), in contrast to the magnetic method generally used in tokamaks, is available on TEXTOR. This system derives the horizontal plasma position from the electron density profile and assures symmetry in n_e in the boundary region. It is found, that this method suppresses poloidally asymmetric radiation (MARFEs) [5] and allows to obtain quasi-stationary discharges at the highest radiation levels.

3. Results

Intrinsic impurities C, O

Ever since carbonization and graphite limiters have been introduced in TEXTOR the

dominating impurities are carbon and oxygen. These impurities are released from limiter and wall mainly due to sputtering and chemical erosion. For a given impurity level, mainly determined by wall conditioning, the radiation level can be increased by rising the electron density $\bar{n}_e$, thereby decreasing $T_e(a)$. The impurities C and O fulfill the requirements for radiation cooling in a fusion device : the radiation is located at the edge close to the separatrix, stable and quasi-stationary discharges with γ=1 are possible (detached plasma), and the concentration in the plasma centre remains below a critical level (<3% n_i/n_e). For the low-z impurity ions the recombination time at the plasma boundary is much longer than the confinement time, thus the ions are not in coronal equilibrium, and the ionization distribution is dominated by transport processes. Under these conditions it is appropriate to express the radiation in terms of impurity fluxes rather than impurity densities. This is done by introducing the *radiation potential* [6] $E_A=P_{rad}/\Gamma_i$, where Γ_i is the total impurity flux. E_A represents the average energy being radiated per impurity particle during its dwell time in the plasma. E_A has been determined experimentally [6] e.g.by measuring P_{rad} and Γ_i and by theoretical modelling [7][8]. O radiates about a factor 3 more than C. For a given impurity species the most important parameter for E_A is T_e. For similar T_e-profiles $T_e(a)$ at the separatrix is a reasonable parameter. Generally E_A increases with decreasing $T_e(a)$. As an example experimental data are shown in Fig.1 for a given impurity mixture of C:O=2:1. Note that the bolometer measurements cannot distinguish between radiation from C and O. For comparison the results from a semi-analytical model [8] are also shown. It is remarkable, that E_A may rise by a factor of 5 during edge cooling. This dependence on T_e allows to increase P_{rad} significantly without increasing the impurity flux Γ_i according to $P_{rad}=E_A\Gamma_i$. Auxiliary heating leads to a rise of $T_e(a)$ and therefore normally reduces E_A (e.g. factor 2 with NBI [9]). On the other hand, all particle fluxes increase (confinement deterioration) and the rise of Γ_i by a factor 4-5 overcompensates the decrease in E_A, but not enough to reach the level of heating power (factor 10). Additional impurities are necessary to obtain a high radiation level.

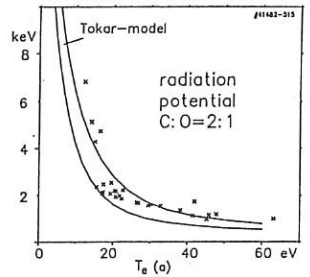

Fig.1 *Radiation potential derived from measured P_{rad}/Γ_i (x) and model calculations for pure C (lower curve) and a mixture of C and O (upper curve)*

Injected neon

By using an inert gas we expect not to destroy or alter the first wall conditioning. Furthermore, due to the relative high z of neon compared to C and O we expect an enhanced E_A. In a first attempt of neon injection it turned out that a stationary neon level is difficult to obtain, in particular, close to γ=1. Therefore, an automatic control system for neon puffing has been developed and applied on TEXTOR. Elements of the control system are : a fast piezo-valve for gas injection, the pump limiter ALT-II as a sink and a NeVIII line as the control variable. An example of the controller action is given in Fig.2. Evidently the NeVIII line follows the double-step function of the set-value rather fast (<100ms). The slowest element in the control system is the pump limiter (time constant ≈0.5s). Fig.2 exhibits also the concomitant increase of the total radiation, its constant value during the flat phase of the set-value, and the cooling effect at the plasma boundary manifested by the drop of T_e at the separatrix. In this example $\gamma\approx$0.7 is reached. The full range of γ-values, from 20-96%, obtained for quasi-stationary (>1sec) discharges ($P_{heat}\approx$1.8MW) is given in Fig.3a. The corresponding variation of the heat load to the limiters, deduced from the relation $P_{conv}=P_{heat}(1-\gamma)$, shown in Fig.3b demonstrates impressively how radiation can protect the limiters from high heat loads : the heat flux can be reduced by more than a factor of 20 down to negligible values. That the radiation is limited to the boundary region is shown in Fig.4. for a discharge with γ=0.95. The radiation peaks at r≈40cm (limiter at r=46cm); inside of r<15-20cm nearly no radiation occurs. The locations at which the radiation from Ne^{7+} and Ne^{8+} is expected to peak are indicated in Fig.4. We conclude that the radiation is mainly provided by the lithium-like neon Ne^{7+}, radiating at about $T_e\approx$140eV. The maximum decrease of

the convective heat flux, as shown in Fig.3, is linked to a decrease of n_e and T_e (factor 1.6 and 5.4 respectively) at the separatrix (Fig.5). It is remarkable, that with this strong drop of T_e at the boundary, the central T_e value does not change, provided $\bar{n}_e$ is kept constant and strong detachment is avoided, as it is the case for the data shown in Fig.5. Also the energy confinement time τ_E remains constant; in this case 40ms obtained from measurements of diamagnetism. Only in case of strong detachment τ_E deteriorates; a typical value for a detached case is τ_E=35 ms.

The radiation potential can be deduced from P_{rad} and the total neon flux derived from the measurement of NeI. For the different T_e values at the boundary (80-10eV) we obtain E_A=5-30keV. This is about 2-3 times higher than the corresponding values for oxygen and shows about the same dependence on T_e (factor 5).

An example of the neon contamination in the plasma centre is displayed in Fig.2. Z_{eff}, derived from conductivity measurements on axis, assuming q=0.8, is shown as a function of time for a double step increase of neon. For a level of about 1MW radiation we obtain a ΔZ_{eff} of 0.3, thus the neon concentration is $n_{Ne}/n_e \approx 0.3\%$. If we extrapolate this result to a heating power density typical for the largest tokamaks (3MW in TEXTOR corresponds to 0.35MW/m^3 or a wall load of 0.1MW/m^2) then the neon concentration in the centre still remains below 1%. These values would still be tolerable for a fusion plasma.

4. Conclusions

In discharges with pure ohmic heating (ca.0.035MW/m^3) and a carbonized or boronized first wall the intrinsic impurities carbon and oxygen provide good edge cooling. In particular, close to the density limit stable and quasi-stationary discharges with $\gamma \approx 1$ are possible. With strong auxiliary heating (ca.0.35MW/m^3) the injection of neon as an additional impurity allows to obtain good edge cooling up to $\gamma \approx 1$. With the help of a neon feed-back system also quasi-stationary conditions are possible. Neon fulfills all the requirements for radiation cooling in a fusion plasma, in particular, radiation from edge and n_{Ne}/n_e<1% in centre. The radiation potential of Ne varies with T_e at the boundary in the range of 5-30keV. The negative derivative $\partial E_A/\partial T_e$ causes a significant amplification of the cooling rate, in particular in edge plasmas with low T_e (10-20eV), without leading to an unstable situation. In this respect, a plasma position control which suppresses asymmetric radiation (MARFEs) can be essential.

Acknowledgement

The TEXTOR team is gratefully acknowledged for providing excellent experimental conditions. We wish to thank W. Brocke and P. Hüttemann for the help in setting up the electronics of the feed-back system for neon injection.

References

[1] U. Samm et.al., "Properties of detached plasmas", Report KFA Jülich Jül-2123 (1987)
[2] A. Pospieszczyk et.al., J. Nucl. Mater. 162-164 (1989) 574
[3] B. Schweer et.al., "Measurement of T_e-profiles in the boundary layer of TEXTOR by means of spectroscopical observation of a thermal helium-beam", this conference
[4] H. Soltwisch, Nucl. Fus., Vol.23, no.12 (1983)
[5] U. Samm et.al., "Suppression of MARFEs by a plasma position feed-back control based on interferometric measurements", this conference
[6] U. Samm et.el., J. of Nucl. Mater. 176&177 (1990) 273
[7] H. Claaßen and G. Gerhauser, Contrib. to Plasma Phys. 30 (1990) 83
[8] M. Tokar', "One-dimensional model for a description of transitions of a tokamak edge plasma into a strongly radiative state", this conference
[9] U. Samm et.al., Proceedings of the 16th Europ. Conf. on Plasma Physics and Controlled Fusion, Venice 1985, Vol.III, p.991

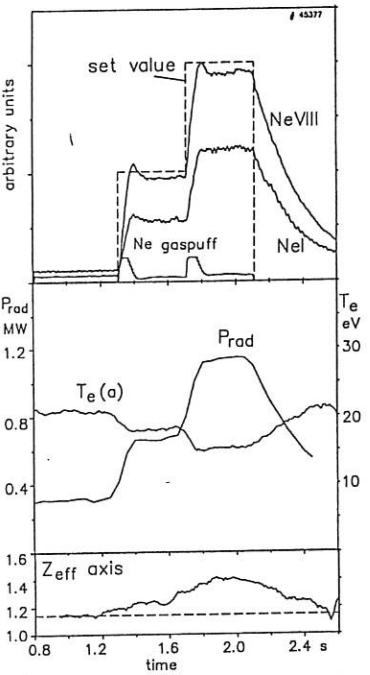

Fig.2 *Variation of neon line emission, total radiation, T_e at the separatrix and Z_{eff} on axis (q=0.8) for a double-step function of neon injection*

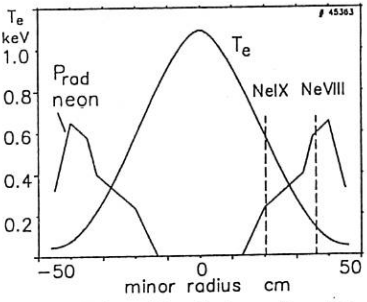

Fig.4 *Radial profile of the total radiation (bolometer) and of the electron temperature (Thomson scattering)*

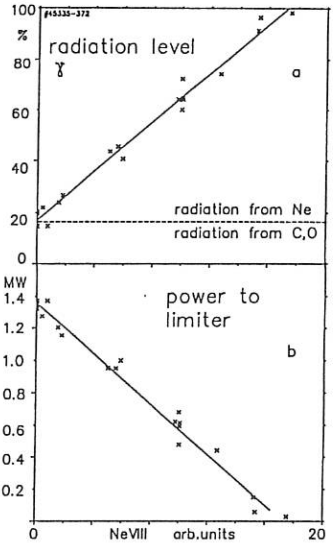

Fig.3 *Dependence of the radiation level $\gamma=P_{rad}/P_{heat}$ and the convective power to the limiter $=P_{heat}-P_{rad}$ on the neon line emission (amount of neon injected)*

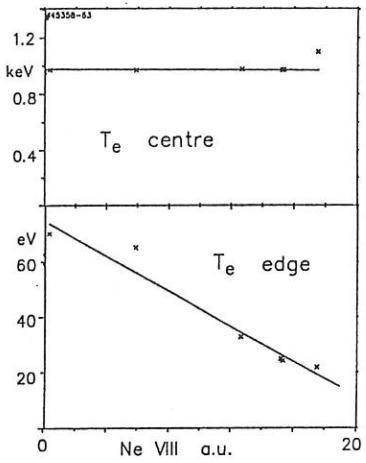

Fig.5 *Variation of T_e close to separatrix (r=44cm) and in centre (Thomson scatt., ECE)*

A MODEL FOR LIMITER HEAT FLUX PROTECTION BY LOCAL IMPURITY RADIATION

M.Z.Tokar', A.V.Nedospasov, U.Samm*

Institute for High Temperatures of the USSR Academy of Sciences, Moscow, USSR
*Institut für Plasmaphysik, Forschungszentrum Jülich, Ass.EURATOM-KFA, FRG

1.Introduction

On the largest tokamaks (JET, TFTR, JT-60) the level of power launched into the discharge has reached tens of MWs. This has created a qualitatively new situation for the interaction of the edge plasma with material surfaces like limiters or divertor plates. In particular, the phenomenon of "carbon blooms" has been discovered [1,2], characterized by a sudden increase of carbon particles being released into the discharge and a subsequent strong growth of energy losses by radiation. These "carbon blooms" are localized at hot spots on the wall with a surface temperature of more than 3000 K. The processes causing such "carbon blooms" are a serious obstacle for further progress towards controlled fusion. Therefore, a study of this phenomenon, both from the experimental and theoretical point of view, and the search of ways to overcome this problem is of great importance.

The analysis of experimental data on "carbon blooms" [2][3] found evidence that hot spots and the strong increase of carbon release may be linked to the mechanism of radiation enhanced sublimation (RES) [4]. The fact, that an enhanced impurity release leads also to an increase of impurity ion flow in the scrape-off-layer (SOL), thereby increasing the heat flow by transfer of ionization energy to the surface, may be a reason for the rapid growth of "hot spots" [3]. On the other hand, rising impurity radiation from the plasma in the vicinity of the limiter may cause a reduction of heat flow due to cooling of the electrons. Experimental data from TEXTOR indicate, that this cooling mechanism may play an essential role for limiting the heat flow towards a strongly heated surface [5]. With the help of strong auxiliary heating by neutral beam injection the heat load to the poloidal graphite limiter reached values of 2-3 kW/cm^2. A pronounced rise of the limiter surface temperature proportional to $\sqrt{t}$ is observed, as can be expected for a constant heat flux (Fig.4). The limiter surface temperature increase slows down when RES sets on and the temperature saturates at about 2000°C; thus the convective energy flow towards this hot limiter surface must be reduced significantly, although the total energy loss via convection in the SOL remains almost constant.

In the present paper an attempt is made to model theoretically the thermal balance of the plasma at the limiter by considering a cloud of radiating impurities in the vicinity of a hot limiter surface protecting the limiter surface from overheating.

2. Physical model and basic equations for plasma and impurities

The geometry of the SOL with a poloidal limiter, typical for TEXTOR, is presented schematically in Fig.1. The carbon atoms coming from the limiter surface are partly ionized in the SOL near the surface. Under the condition for the angle of inclination $\varepsilon \ll 1$ the impurity atom balance equation is the following

$$\partial(n_I^z v_o)/\partial x = -k_I^z n_e n_I^z \quad (1)$$

where n_I^z is the density of the impurity with charge z, v_o is the carbon atom velocity which is determined by the mechanism of impurity release ($v_o \approx 1.\ 10^5$cm/s for thermal particles and $v_o \approx 5.\ 10^5$cm/s for sputtered particles), k_I^z is the constant of impurity particle ionization, n_e is the electron density.

In the situation under consideration the impurity ion densities near the limiter can exceed considerably the density of the working gas ions (deuterons) n_i. In contrast, the relation for the corresponding ion temperatures is $T_z \ll T_i$. In such a case the coulomb collisions couple effectively the differently charged impurity ions and their dynamics can be described in the hydrodynamic approximation by introducing the total impurity ion density $n_I = \Sigma n_I^z$, the average charge $\overline{z} = \Sigma z n_I^z / n_i$ and the mass velocity along the magnetic field V_I [6].

The equations of continuity and motion along the magnetic field B of the impurity ions have the form

$$\frac{\partial n_I}{\partial t} + \frac{\partial}{\partial x}\left(-D_I \frac{\partial n_I}{\partial x}\right) + \frac{\partial}{\partial l}(n_I v_I) = k_I^o n_e n_I^o \quad (2)$$

$$\frac{\partial}{\partial t}(n_I v_I) + \frac{\partial}{\partial l}(n_I v_I^2) + \frac{\partial}{\partial x}\left(-D_I \frac{\partial n_I}{\partial x} v_I\right) = \frac{n_I}{\tau_I}(v_i - v_I) + e n_I \overline{z} \frac{E_{//}}{m_I} \quad (3)$$

where D_I is the diffusivity across B, τ_I is the time of the momentum transfer between the impurity ions and deuterons, V_i is the longitudinal velocity of the deuterons, $E_{//}$ is the electric field. The force balance of the non-inertial electrons

$$\partial(n_e T_e)/\partial l = -e n_e E_{//}. \quad (4)$$

Beyond the Debye layer near the surface the plasma is quasi-neutral

$$n_e = n_i + \overline{z}\, n_I. \quad (5)$$

In the electron energy balance the conductive and convective transport along B and the losses on the impurity ion excitation are taken into account by

$$\frac{\partial}{\partial t}\left(\frac{3}{2} n_e T_e\right) = \frac{\partial}{\partial l}\left(\kappa_{//}^e \frac{\partial T_e}{\partial l}\right) - \frac{\partial}{\partial l}\left(\frac{5}{2}\Gamma_e T_e\right) - \sum_z L_z n_e n_I^z \quad (6)$$

where $\Gamma_e = n_i V_i + \overline{z}\, V_I\, n_I$ is the electron current density, $L_z = \Sigma k_{ij} E_{ij}$, k_{ij} and E_{ij} are the excitation constants and energies of the main carbon ion transitions. For the present model a simple analytical formula has been used, based on data from ref.[7], for describing the T_e-dependence of the cooling rate L_z.

The level of the longitudinal electron heat flux dissipation in the carbon ion cloud surrounding the limiter is determined by the cloud dimension L_I along B and the relative concentrations C_z of the particles with different z. The analysis of equ.2-5 shows, that the impurity dynamics in the cloud is strongly coupled to the electric field $E_{//}$. If $E_{//}$ were absent the impurity ions would be localized in the region of ionization near the limiter due to friction with the deuterons streaming towards the limiter. But the strong gradient of the impurity ion density at the boundary of the cloud leads to a strong gradient of electron pressure and according to equ.4 to a large electric field, which forces the impurities to move away from the limiter (see Fig.2). Such a picture is analogous to one proposed in ref.[8] for the kinetic description of a mixture of cold and hot hydrogen ions in a divertor plasma. In our case the spreading of the impurity cloud along B is limited by the ion diffusion perpendicular to the magnetic field. In order to estimate

the value of L_I we follow equ.4 and take $E_{//}\approx T_e/(eL_I)$ and assume that the friction force balances the electric force (equ.3). This gives $L_I\approx z\ T_e\tau_I/(m_I V_i)$ and for the typical parameters of the TEXTOR SOL plasma ($T_i\approx T_e\approx 50$eV, $\Gamma_I=n_i V_i=10^{20}$cm^2/s, $n_i\approx 10^{13}$cm^3, $z\approx 3$) we obtain $L_I\approx 40$ cm. This value is much larger than the extent of the region of impurity ionization near the limiter (~1cm). The change of the impurity ion concentration $C_s=n_I^s/n_I$ with l is described by the equation $V_I\partial C_s/\partial l=-C_s k_i^s n_e+C_{s-1}k_i^{s-1}n_e$ with the boundary conditions $C_1(l=0)=1$ and $C_{s>1}(l=0)=0$.

3. Heat transport inside the limiter

The coefficient of the radiation enhanced sublimation R_{RES} is a very strong function of the surface temperature T_W. Based on data given in ref.[5] this dependence can be approximated by the formula $R_{RES}\approx 306\ \exp(-15900/T_W)$ (T_W in K). Under the real experimental conditions the limiter has not enough time to be heated up as a whole during a discharge. Therefore, non-stationary heat transport in the limiter bulk has to be considered. In the approximation of a semi-infinite body with a constant heat conductivity κ_W and heat capacity C_W the time evolution of the limiter surface temperature is given by the expression

$$T_W(t)=\int_0^t q_s(T_W(\tau))d\tau/\sqrt{\pi\kappa_W C_W(t-\tau)} \qquad (7)$$

where $q_s=q_{ps}-q_{cs}$, q_{ps} is the heat flux density directed from the plasma towards the surface, and q_{cs} is the heat lost from the surface by thermal radiation and particle sublimation.

4. Results

In the present paper the solutions of equ.1-6 have been obtained in a zero-dimensional approximation by using the characteristic values and dimensions of the changes of e.g. n_e, n_I, T_e in the impurity cloud, assuming $\partial/\partial x=1/\delta$, $\partial/\partial l=1/L_I$, where δ is the characteristic length of the parameter change across the SOL. For the deuteron temperature and its flux along B we take the typical values [5] : T_i=50 eV, $\Gamma_i=10^{20}$cm^2/s, $D_I=1$ m^2/s, δ=0.8 cm. The heat flux density $q_{//}^{\circ}=-\kappa_{//}^{i}\partial T_e/\partial l+5/2\Gamma_i(T_e+T_i)$ at the outer boundary of the impurity cloud ($l>L_I$) corresponds to the heat flux perpendicular to the limiter surface of 2.75 Kw/cm^2.

Fig.3 shows the calculated heat flux density at the limiter $q_{ps}=(q_{//}^{\circ}-\int\Sigma L_s n_e n_I^s dl)\sin\varepsilon$ as a function of the surface temperature for the stationary state. The sharp increase of the carbon particle flux from the limiter at T≈2000°C when R_{RES} exceeds 0.1 leads to the significant drop of q_{ps} at $T_W=T_W^c\approx 2100$°C. In the non-steady state, described by equ.7, the drop of q_{ps} is less pronounced. But when T_W becomes smaller than T_W^c then q_{ps} increases again; thus oscillations of T_W near T_W^c may occur. The period and amplitude of these oscillations are determined by the impurity transport in the cloud. From the calculation we obtained for the period a value of the order of the diffusion time $t_D=\delta^2/D_I$ and the relative amplitude was <1%. Fig.4 shows the measured [5] and calculated time evolution of the limiter surface temperature (t≈0.8s corresponds to the beginning of the neutral beam injection). The variation of the fraction of $q_{//}^{\circ}$ being radiated by the impurity ions $\alpha_r=1-q_{ps}/(q_{//}^{\circ}\sin\varepsilon)$ is also presented in this figure. A good agreement between experimental and calculated data is obtained. Returning to the problem of the hot spots it is necessary to emphasize that our results show that the energy being radiated from the SOL plasma due to the entrance of one carbon atom, E_A, is much more than the energy transferred to the limiter by the impurity ion, including the ionization potentials, E_i. E_A changes from 400eV with T_W=800°C to 1.2keV with 2100°C, whereas E_i is significantly smaller for the ions which circulate near the limiter. This means that the additional energy transported to the limiter by the impurity ions cannot compensate the decrease of the heat flux due to radiation. Therefore, the mechanism of the hot spots formation proposed in ref.[3] is questionable.

5. Conclusions

The dynamics of the impurity particles coming into the SOL plasma from the limiter is strongly coupled with the selfconsistent electric field generated due to the presence of the impurity ions themselves. The length of the radiating cloud of charged impurities in the SOL near the limiter can be much more than the extent of the region of atom ionization. When the limiter surface temperature exceeds the critical value $T_W^c \approx 2100°C$ the impurity radiation in the SOL near the limiter increases strongly. This stabilizes T_W on the level of T_W^c. This theoretical result is in good agreement with experimental data from TEXTOR.

References

1) Pitcher C.S., et.al.,in Proc. of 16th Eur. Conf. on Controlled Fusion and Plasma Physics, Venice 1989, Vol.III p.879
2) Ulrickson M., J. of Nucl. Mater. 176&177 (1990) 44
3) Pitcher C.S., et.al., Topical Meeting on High Temper. Erosion of Graphite in Plasmas, Princeton 1989
4) Philipps V., et.al., J.Nucl.Mater. 111-112 (1982) 781
5) Pospieszczyk A., et.al., J. of Nucl. Mater. 176&177 (1990) 180
6) Igitkhanov Yu.L., Contrib. to Plasma Physics 28 (1988) 477
7) Itikawa Y., et.al., Atom. Data Nucl. Data Table 33 (1985) 150
8) Bailey A.W., Emmert G.A., Nucl.Fusion 24 (1984) 1439

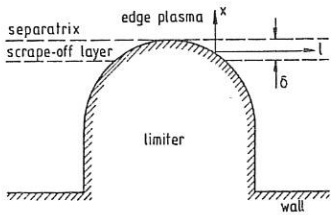

Fig.1. Geometry of the SOL with poloidal limiter.

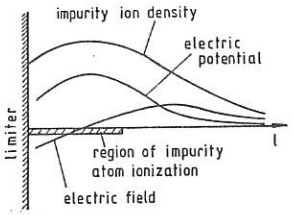

Fig.2. Qualitative view of the longitudinal profiles of the electric potential, the electric field and the impurity ion density near the limiter.

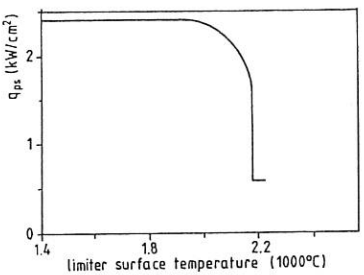

Fig.3. Heat flux to the limiter by charged particles as a function of the limiter surface temperature.

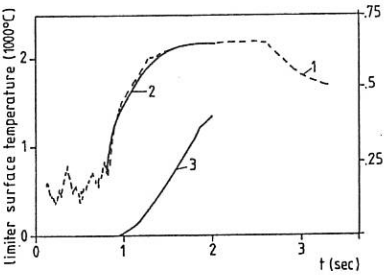

Fig.4. Measured (1) and calculated (2) temporal evolution of the TEXTOR limiter surface temperature and the relative fraction of radiation in the plasma energy balance (3) near the limiter.

OXYGEN COLLECTION IN THE LIMITER SHADOW OF TEXTOR DEPENDING ON WALL CONDITIONING WITH BORON

P. Wienhold[1], M. Rubel[2], J. v. Seggern[1], H. Künzli[3], I. Gudowska[2]

[1]IPP-KFA Jülich GmbH, Ass. EURATOM/KFA, D-5170 Jülich, FRG
[2]MSI, Ass. EURATOM/NFR, S-10405 Stockholm, Sweden
[3]Inst. of Physics, Univ. of Basel, CH-4056 Basel, Switzerland

I. Introduction

One of the major consequences of the boronization of TEXTOR compared to the carbonized machine was the further and remaining decrease of the oxygen contamination of the plasma. This has lowered also the carbon chemical sputtering by a factor of two in spite of higher radiative power loads to the graphite limiters /1/ and made auxiliary heating up to 6 MW possible /2/. The fact, that oxygen did not reoccur as it happened during operation with carbonized walls caused the suggestion of gettering by the formation of a stable bond to the boron /3/. Therefore, a period (may/june 89) where different conditioning treatments with boron were applied to TEXTOR gave ideal circumstances for collection experiments in the SOL and the subsequent analysis of the deposits aiming at the understanding of this hypothesis.

2. Experiments and analysis

Beginning with freshly carbonized walls TEXTOR was first operated for 50 discharges before it was in a second step flushed for 1.5 hours with a mixture of B_2H_6 (10 %), CH_4 (10 %) and He molecular gas (10^{-2} mbar). 100 discharges later TEXTOR became boronized (third step) by a RG discharge in the diborane containing mixture /4/ and operated with no further conditioning until the last collector probe experiment. Collection was made on graphite samples in the SOL by means of the Stockholm-TEXTOR probe in an equatorial position in section 5/6. The targets were oriented on electron and ion drift side perpendicular to the toroidal direction and exposed over 4 successive discharges soon after each of the conditioning steps (see following table). Only the fourth exposure was made 200 discharges after the boronization.

date	step of	conditioning	discharges delayed	total exposure time
18.5.89	I	carbonized	10	12.6s
23.5.89	II	B_2H_6 flushed	11	13.8s
30.5.89	III	boronized	15	14.4s
07.6.89	IV	boronized	200	12.4s

During all exposures the discharge conditions were the same (I_p = 340 kA, B_T = 2.25 T, n_e = 2.8 x 10^{13} cm^{-3}, filling gas D_2) except a slight density increase in case IV (3.2 x 10^{13} cm^{-3}). The plasma radius was fixed at a = 46 cm by the toroidal limiter system (ALT II), other limiters were withdrawn to r = 50 cm in the SOL which ends at the liner (r = 55 cm, T_L = 150 °C).

After exposure the targets were dismounted. The deposits which consist mainly of amorphous carbon (a-C:D) has grown up to 50 nm on the graphite. They were analyzed over the full radial distances by nuclear reaction for the collected amounts of B and D and by RBS technique for O and Fe+Cr+Ni. Few depth profiles were established at selected radii by means of sputter AES, and XPS was applied to part of the specimen in order to detect the possible oxidic bonds.

3. Results and discussion

The selected results shown in the figure can't be complete, but are representative and summarize the major findings. Most plausible is the evolution of the collected B depending on conditioning and given as rates in the upper left at r = 48.5 cm (e-drift side). The roman figures refer to the situations given in the table. After the carbonization (I) little boron is collected which had been remained from TEXTOR's first boronization about one year earlier (march 88). But, the level increased after the treatment with B_2H_6 gas (II) which indicates that B from the molecules flushed through was bound to the carbonized surfaces and liberated by the succeeding discharges. After the boronization (III), we measure with 2.8 x 10^{15} B $cm^{-2}s^{-2}$ a rate which is comparable to values found after the first boronization (2.1 x 10^{15} $cm^{-2}s^{-1}$ after ~ 200 discharges). 200 discharges after the boronization made here (IV) the maximum value had decreased accordingly.

Oxygen, given for the same target position in the upper right of the figure (thick line) shows similar to B an increasing trend when going from carbonized (I) to boron conditioned (III) walls, but remains constant after boronization. This behaviour of O is in full contradiction to the OI-light emission which is measured in the vicinity of the upper and withdrawn (r = 50 cm) poloidal graphite limiter (see sketch) where oxygen ions become neutralized and remitted as atoms. This light is integrated in two dimensions and can serve as a measure for the oxygen influx. As the electron temperature at 50 cm as almost equal (~ 5 eV) for all discharges used we can straightforward convert the light emission into fluxes /5/. Although the drastic decrease (down to 1/20) of the flux, i.e. the amount of oxygen ions which can stick on the surface we collect about twice as much O as in the carbonized machine (I).

It is near at hand to relate the increased O collection yield to the increased amount of codeposited B, i.e. to suppose oxygen being gettered by boron as an additional collecting mechanism. It might be linearly related to B via a coefficient G. The lowering of the contribution G x B as expected for the transition from case III to case IV can be balanced then by an according increase of the sticking term which is assumed as S x OI in a first approximation. But, also O absorption from air has to be taken into account which is proportional to the thickness of the deposit and hence to the codeposited amount of deuterium: A x D. Values between 6 and 12 % of D can be concluded from /6/. When the model equation for the oxygen deposition rate

$$O(r) = S(r) \times OI\ (50\ cm) + G \times B(r) + A \times D(r) \qquad (1)$$

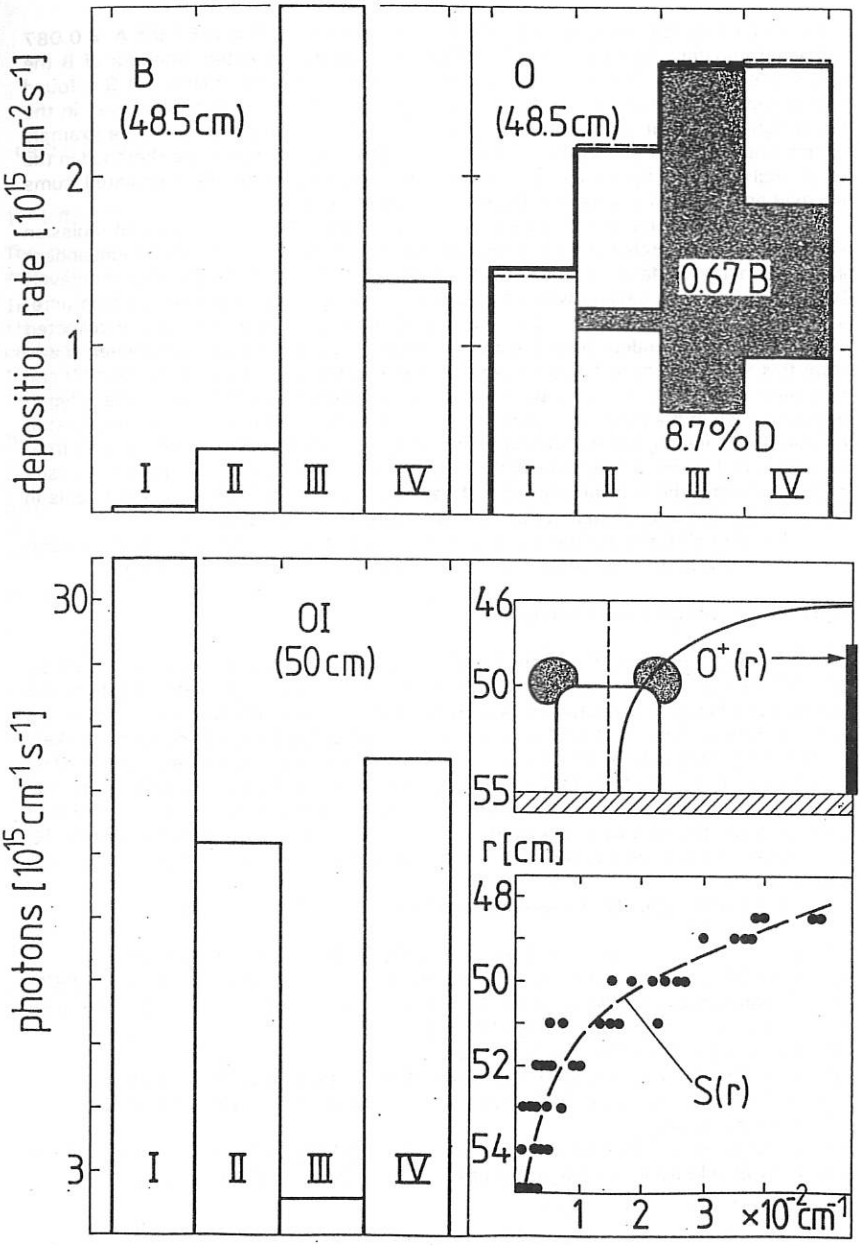
B
(48.5cm)
O
(48.5cm)
0.67 B
8.7% D
deposition rate [10^{15} cm^{-2}s^{-1}]
2
1
I
II
III
IV
OI
(50 cm)
photons [10^{15} cm^{-1}s^{-1}]
30
3
46
50
55
O^+(r)
r [cm]
48
50
52
54
S(r)
1
2
3
$\times 10^{-2}$ cm^{-1}

was proven it turned out to our surprise that the coefficients G = 0.67 and A = 0.087 remained constant (within ± 10 %) independent on the collected amounts of B the target orientation (e^-, ion drift side) or the position r in SOL. The coefficient S is found radius dependent because it weights the OI emission at r = 50 cm. S is given in the lower right of the figure as an average from all individual values (dots). As one example for the application of eq. (1) the different contributions of the terms are sketched in the upper right of the figure. It demonstrates the coincidence of the calculated sums (dashed line) with the measured deposition rates for oxygen.

The appearance of a distinct term which is proportional to the OI light emission suggests its direct relation to the oxygen ion flux in the SOL and their independent sticking on the surface of the growing deposit. The yield must be small however, because even in the case III where the flux is low, enough oxygen is left to feed unrestricted the getter mechanism. 2/3 O atoms (G = 0.67) in the average are collected additionally to any codeposited B atom which suggests an oxidic bond between O and B for this fraction. This is likely because of the energetic deposition of the ions /7/ and has been proven by XPS /8/. Because of the stability of such a bond, the oxygen contamination of the plasma remains decreased after the boronization. It is accumulated (gettered) in deposited layers as long as free boron is available. The oxygen uptake from air was found to be 8.7 % related to the amount of D for boron containing deposits only. It seems to be negligible in boron free deposits (case I). Probably, larger voids in boron containing amorphous carbon /9/ may cause the difference.

Eq. (1) holds also for the oxygen rates measured earlier /10/ after the first boronization of TEXTOR were the comparison was made to an old carbonization.

4. Summary, conclusions, references

A model equation is found empirically from collector probe experiments in the SOL of TEXTOR which relates the collected amounts of oxygen on graphite targets to the codeposited boron and deuterium rates and to the OI light emission measured in the SOL. Gettering, absorption and sticking, respectively could be identified as most likely contributing mechanisms. The oxygen contamination in the plasma remains low after boronization because of the formation of stable oxides due to the energetic ion deposition. The dependence of one of the terms on the OI light intensity in the SOL should allow to study the relation to the oxygen ion flux. We suggest, however the use of ^{18}O as a tracer in such an experiment in order to avoid the uncertainties with oxygen absorbed from air.

The authors greatly acknowledged advice from A. Pospieszczyk.

/1/ J. Winter, H.G. Esser, L. Könen et al., J. Nucl. Mat. 162-164(1989)713
/2/ A.M. Messiaen, H. Conrads, et al., Plasma Phys. and Contr. Fus. 32, II(1990) 889
/3/ F. Waelbroeck, J. Winter, et al., Plasma Phys. and Contr. Fus., 31, 2(1989) 185
/4/ J. Winter, J. Nucl. Mat., 176+177(1990)14
/5/ Equipe TFR, Nucl. Fusion (1975) 1053
/6/ M. Rubel, F. Waelbroeck, H. Bergsåker et al., J. Nucl. Mat. 161(1989)153
/7/ R. Zehringer, H. Künzli, P. Oelhafen et al., J. Nucl. Mat., 176+177(1990)370
/8/ to be published
/9/ G. Kögel, et al., Phys. Rev. Letters, 60, 15(1988)1550 and private communication
/10/ P. Wienhold et al., H. Bergsåker et al., J. Nucl. Mat., 176+177(1990)150

H_α- DIAGNOSTICS OF THE LIMITER SURROUNDING IN T-15 USING A CCD-CAMERA

H. Kastelewicz, A. Pigarov

Central Institute of Electron Physics, Berlin; Kurchatov Institute, Moscow

1. INTRODUCTION

The presented calculations refer to a theoretical reference model for measurements of H_α radiation which are intended for the limiter surrounding in T-15. The CCD-camera is installed poloidally opposit to the limiter, thus looking through the whole plasma column. The aim of this work is to calculate the radiation intensity received by each pixel of the detector and to relate it to the neutral hydrogen density and the neutral hydrogen influxes from limiter and wall.

The theoretical calculations are based on a simplified version of the Monte-Carlo model developed at the Moscow Kurchatov Institute. The calculation refers to the geometry and the expected plasma conditions of T-15. The radiaton of each neutral received by the detector is obtained from usual optics. This problem is simplified by the fact that radiation absorption by the (thin) plasma as well as radiation reflection from the wall can be neglected.

2. OPTICAL ARRANGEMENT

The arrangement of limiter and CCD-camera is schematically shown in Fig.1a. The geometrical model of the tokamak is a straight cylinder. The limiter consists of two inclined level planes located at the bottom of the cylinder. It is assumed that the CCD-camera is focussed on the horizontal plane through the edge of the limiter and the field of view is limited by a circle with diameter $d_{obj} \approx 71$cm. The limiter and its projection upon the CCD-detector by the optical system is shown in Fig. 1b (50cm $\rightarrow N_y \times L_y$).

Actually, the CCD-detector consists of $N_x \times N_y = 512 \times 576$ separate pixels as shown in Fig. 2. (We consider here, however, the case of 51×57 pixels only.) Each pixel is composed of a sensitive area (shaded region in Fig. 2) and a larger not sensitive part. A radiating atom being located in the focussed plane is imaged as a point on the detector while an atom at other places in the observable volume of the torus is out of focus and will approximately yield a small circle on the detector where the light intensity is nearly homogeneously distributed. The radius of this circle depends on the deviation from the focussed plane. Two such circles are shown in Fig. 2. The light intensity received by the individual pixels is given by the ratio of the sensitive area covered by the circle and the total area of the circle.

3. NEUTRAL ATOMS AND RADIATION

To describe the neutral hydrogen atoms we use a time independent Monte-Carlo model based on the pseudocollisional formalism [1]. Instead of single particles each test flight describes a whole packet of particles which is statistically weighted by a function G. At the beginning of the flight this function is given by $G = \Phi_o/N$, where Φ_o is the total particle flux

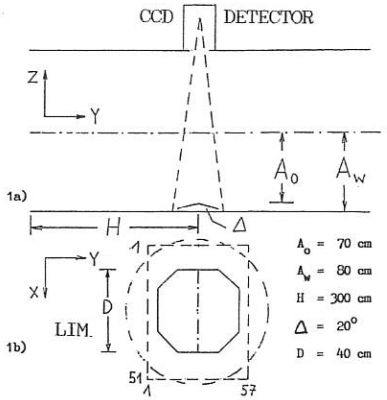

Fig. 1 Optical arrangement

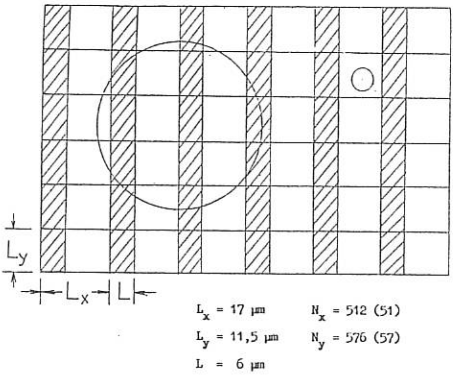

Fig. 2 Structure of the CCD matrix

(particles per second) released from the surface of limiter or wall and N is the total number of test flights. At each real collision with the plasma the weight is diminished due to ionization by the factor $P_{cx} = \lambda_{tot}/\lambda_{cx} \cdot \lambda_{tot}$ is the local mean free path length and λ_{cx} is the mean free path length due to charge exchange only.

The radial density and temperature profiles of the background plasma are assumed as follows:

$0 \le r \le a_o$:

$$T(r) = T(a_o) + [T(0) - T(a_o)] \cdot [1 - (r/a_o)^2]^3, \quad (1)$$

$$n(r) = n(a_o) + [n(0) - n(a_o)] \cdot [1 - (r/a_o)^2]^2, \quad \text{where} \quad (2)$$

$T(a_o) = 20$ eV, $T(0) = 10$ keV, $n(a_o) = 0.5 \cdot 10^{13}$ cm^{-3}, $n(0) = 3 \cdot 10^{13}$ cm^{-3}.

$a_o \le r \le a_w$:

$$T(r) = T(a_o)\, e^{-(r-a_o)/\lambda}, \qquad n(r) = n(a_o)\, e^{-(r-a_o)/\lambda} \quad (3)$$

where $a_o = 70$ cm, $a_w = 80$ cm, $\lambda = 2$ cm.

The hydrogen atoms are initially emitted from the surface of the limiter (or the wall) according to a cosine distribution with fixed energy $E_o = 10$eV. The source intensity at the limiter is assumed to be proportional to the incident ion flux, i.e., $\Phi(r,\varphi) \propto r\, e^{-r/\lambda}\, dr\, d\varphi$ (r = radial co-ordinate, φ = azimuthal angle). The source distribution at the wall is assumed to be homogeneous.

Within the plasma the atoms may be scattered with the local ion temperature via charge exchange collisions or be ionized by electron impact. In the latter case they are removed from the packet. Atoms that impinge on the surfaces of limiter or wall with the energy E are reflected according to a cosine distribution with the same energy. The energy emitted per second by the particle packet via H_α radiation along the path length element ds is :

$$dW = \frac{ds}{v} \cdot G \cdot I_\alpha \cdot n_e \,. \quad (4)$$

The dependence of the H_α emission rate I_α on the electron temperature and density is tabulated in Ref.[2] and is shown in Fig. 3 for $n_e = 10^{13}\,cm^{-3}$.

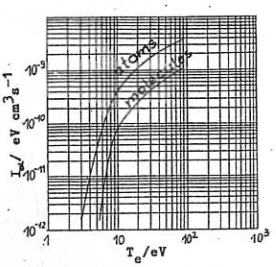

Fig.3 H_α emission rate

The fraction of the emitted energy that reaches the detector is $dW_{in} = (\Delta\Omega/4\pi) \times dW$, where $\Delta\Omega$ is the solid angle of the area of the optical diaphragm as seen from the emission point of the particle. dW_{in} is distributed over the different pixels as discussed above and has to be integrated along that part of the whole particle path between successive collisions that is imaged on the detector.

Finally, to obtain in addition the neutral atom density one can compare the energy emitted per volume element and per second,

$$\eta = I_\alpha \cdot n_e \cdot n_o \qquad (5)$$

with the respective path integral of (4) within the volume elements of the specified grid. Here, the base of the grid is defined by optically projecting the detector pixels on the horizontal plane through the limiter edge and parallel planes to the latter one in distances of $\Delta z = 2$ cm. The other dimensions of the grid are in this case according to the parameters given above: $\Delta x = 1.296$ cm and $\Delta y = 0.877$ cm.

4. RESULTS

Some results of the calculation are shown in Figs. 4-7. The total neutral atom fluxes emitted from the limiter and the wall are $\Phi_L = 5 \cdot 10^{20}\,s^{-1}$ and $\Phi_W = 10^{21}\,s^{-1}$, respectively. Two main features are to be stressed:

i) There is a good correspondence between the observed H_α intensity (Fig.4) and the mean atom density in the near vicinity of the limiter as a result of the short mean free path length of the neutrals. This can also be seen from Fig.6 which is obtained by subtracting the normalized mean atom density between the limiter edge plane and the plane 2cm above the latter one (Fig.5b) for each volume cell from the normalized H_α intensity for each corresponding pixel. The deviation never exceeds 20% but is usually smaller.

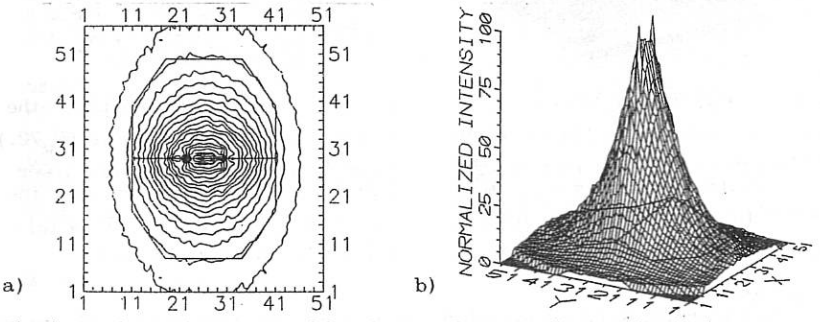

Fig.4 H_α intensity received by the CCD detector due to the limiter sources

a) Contour plot

b) Normalized intensity (maximum intensity $I_{max} = 5.9 \cdot 10^9$ eV/s is normalized to 100)

The difference results mainly from the atoms below the limiter edge plane where, however, the H_α emission rate strongly drops.

ii) There is an almost homogeneous background contribution of the wall sources to the observed H_α intensity which amounts to about 6% of the total limiter source contribution. It may be neglected when observing the limiter.

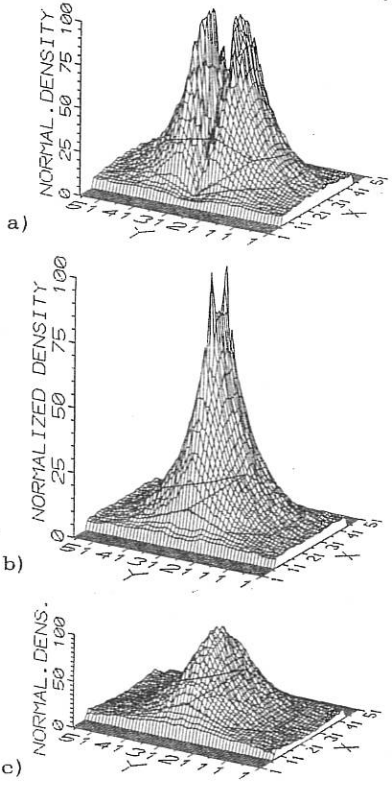

Fig.5a-c Mean H atom density at the planes 1cm below (a), 1cm above (b) and 3cm above (c) the limiter edge plane (maximum densities n_{max}/cm^3 = $5.5 \cdot 10^{11}$(a), $8.6 \cdot 10^{11}$(b), $3.0 \cdot 10^{11}$(c) are normalized to 100)

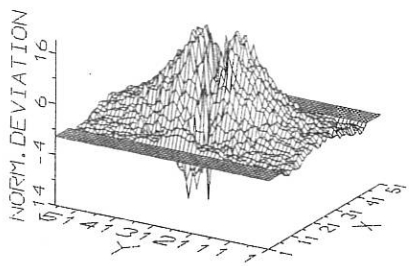

Fig.6 Deviation between H_α radiation and neutral H_α density near the limiter edge

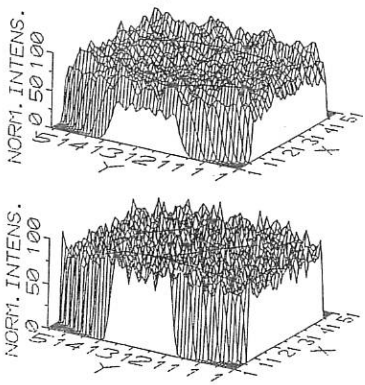

Fig.7 H_α intensity received by the detector due to wall sources ($\Phi_w/2.$) from the upper halfe (a) and lower halfe (b) of the cylinder (max. intensities $I_{max}/eV\ s^{-1} = 3.7 \cdot 10^7$(a), $4.5 \cdot 10^7$(b) are norm. to 100)

REFERENCES

[1] A.S.Kukushkin, V.I.Pistunovich, S.V.Putvinski, IAEA-CN-35/B4, Plasma Physics and Contr. Nuclear Fusion Research, IAEA, Vienna, Austria, 1977

[2] V.A.Abramov, A.Vainstein, A.Yu.Pigarov, Recommended data for hydrogen and helium plasmas, INDC(CCP)-286?GA, IAEA, Vienna, 1988

TEST OF A CARBONIZED MOLYBDENUM LIMITER IN TEXTOR

J. Winter, P. Wienhold, H.G. Esser, L. Könen, U. Samm
U. Littmark[1], E. Kny[2], W. Grasserbauer[3]

IPP, [1]IGV, Forschungszentrum Jülich GmbH, Ass. EURATOM/KFA, D-5170 Jülich, FRG
[2]Österreichisches Forschungszentrum Seibersdorf, A-2444 Seibersdorf, Österreich
[3]Inst. f. Analytische Chemie der Technischen Universität Wien, A-1060 Wien, Österreich

I. Introduction

Molybdenum is an attractive material for wall components in fusion devices due to its good heat conduction and the high melting point (2617 °C), which make it well suited for actively cooled structures. The main problem associated with the use of unprotected Mo is plasma impurity generation by sputtering. The maximum tolerable concentration is about $10^{-4} \times n_e$. In particular self sputtering may become a serious problem /1/. For this reason, a low-Z coating of the surface is advisable. Mo components to which graphite is brazed /2/ are being suggested for NET and ITER /3/. In the case of failure of the carbon attachment deposition of thin films is a potential in situ repair technique. It is thus important, to study the behaviour of thin carbon layers on molybdenum under plasma exposure.

2. Experimental

A limiter head was machined of molybdenum (115 x 60 x 84 mm). Its top contour was circular (r = 67 mm) formed by four removable slabs in the central part. The head was coated in a test vessel with an a-C:H layer of about 150 nm thickness. The limiter was introduced into TEXTOR from the bottom (sector 11/12) and oriented toroidally. The surface temperature was observed via IR radiation by a CCD camera. Mo impurities have been monitored by optical spectroscopy and particle collection in the SOL by the Stockholm-TEXTOR probe system.

The Inconel liner and the graphite poloidal limiters (PL), had been carbonized three days prior the experiment and baked to 350 °C followed by a RG discharge in pure D_2. For the experiment all temperatures were reduced to 150 °C. All discharges were made in D_2 and ohmically heated (I_p = 340 kA, B_T = 2T). Gas puffing was made until 600 ms into the discharge; thereafter the density developed according to the global recycling. n_e decreased from its maximum value (3×10^{13} cm^{-3}) by 15 - 20 %, giving rise to a slight increase of T_e. The similar decrease of n_e measured at 40 cm indicates constant shapes of the density profiles during the plateau phase.

3. Results and discussion

The intensity of the C IV line radiation at 800 ms is shown in fig. 1a as a func-

tion of the discharge number. With the Mo limiter withdrawn (r = 50 cm) and the poloidal limiters in use (PL = 46 cm), the C IV emission shows constant values. This base line level may be correlated with a carbon impurity concentration of about 3 % as deduced from the enhancement factor of the soft x-ray continuum. But, if the limiter is positioned at 46 cm (# 804) with all other limiters withdrawn C IV increases abruptly by about 30 %. The increase may be interpreted as an additional carbon concentration in the plasma of about 1 %. This is reasonable since removing less then 1/10 of the a-C:H layer by plasma erosion would be sufficient. As will be shown below the limiter surface became very hot when it was positioned at r = 44 cm (# 810 - 816) and almost complete erosion of the layer was observed. Thus, a further progressive enhancement of the C IV signal is unlikely. But, Mo is now released from the highly loaded areas.

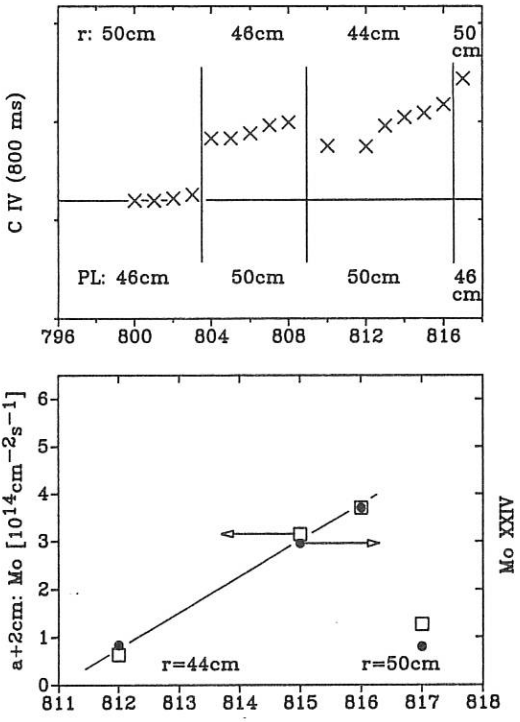

Figure: 1a, 1b

Fig. 1b shows on the right hand scale (a.u.) the maximum shot to shot increase of the Mo XXIV radiation from the core plasma for these discharges compared to the unsignificant variation found with the limiter at r = 46 cm. This may be interpreted as a growth of areas where unprotected Mo is exposed and released to the plasma. The Mo deposition rates 2 cm into the SOL /4/ have been plotted as open squares in fig. 1b (left hand scale) and the Mo XXIV intensity is normalized for # 816. The good correlation indicates, that the collected amount of Mo has been diffusing out of the main plasma. Using the characteristic length $\lambda \sim 2$ cm of the rates, the amount of Mo deposited on the poloidal limiter at r = 50 cm is evaluated to about 0.5 monolayers. It is probably part of these Mo atoms which are observed in the plasma and on the collector probe when the Mo limiter is withdrawn and the poloidal limiters are used (# 817) again. The total amount of Mo is still small compared to metals (Fe, Cr, Ni) released from other sources. There is however evidence, that prolonged use will lead to substantial Mo distribution around the machine.

After the experiment, the limiter was dismounted and a plot of the thickness contours of the remaining a-C:H film was deduced from the interference colours /5/

(fig. 2a). Significant erosion is observed at areas 2,4. Surface temperatures up to ~ 1150 °C were /inferred from the IR observations. Fig. 2b gives as example the temperature distribution at 2.4s into the discharge 812. The pattern is expected for a power flux increasing exponentially into the plasma (λ ~ 1 cm) as measured previously /6/, and the curvature of the limiter surface. The temperatures on the electron and ion drift side indicate that no other obstacles were shadowing the power flux. The temperature at the tangency point did not exceed 600 °C.

SIMS depth profiles of C, Mo, H and D were taken from the samples at positions 1-5 (fig. 3). Carbide was measured by the yield of mass 110 (MoC). The thickness scale was deduced from the interference colours and the sputter ion dose. On the highly exposed areas 2,4 the original a-C:H film is completely eroded. Little carbon is present in the form of molybdenum carbide. This may be a bombardment induced

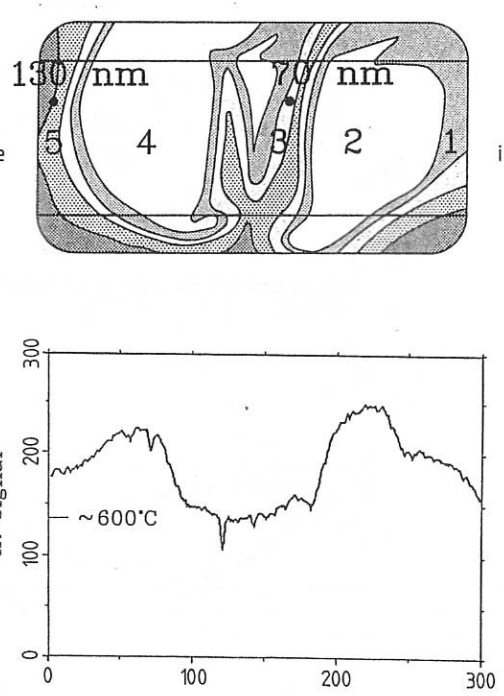

Firgure: 2a, 2b

effect, however thermal processes play an important role in addition. At 1100 °C, one evaluates the formation of 40 nm Mo_2C during 1s. The original film is essentially preserved (~ 130 nm) on position 5 (and 1). A well defined peak of MoC is observed at the interfaces to the Mo substrate which is due to the original film preparation. The sample taken from the tangency point (3) shows an intact layer, but reduced in thickness (70 nm). The Mo on the surface has not diffused from the bulk, but more likely deposited by plasma transport as it had been rendered by spectroscopy and impurity collection. The presence of H shows that temperatures did not exceed 700 °C were it would be released by thermal desorption. D (about 15 nm below the surface) originates from implantation of plasma ions. No deuterium was present in the original films. The distribution may be affected by recoil mixing during the SIMS analysis. D is detected also in these zones 2,4 (not shown), pointing to trapping at radiation induced or structural defects in Mo.

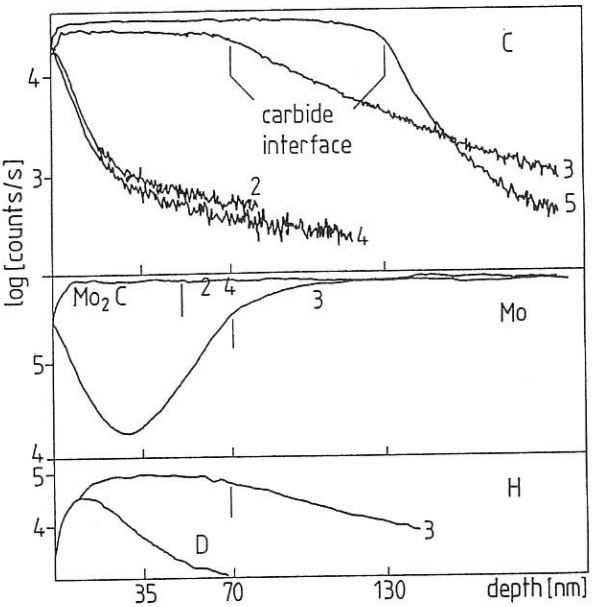

Figure: 3

4. Conclusions and references

An a-C:H coated Mo limiter was exposed in TEXTOR to 11 ohmic tokamak discharges. Complete erosion of the carbon film is observed at areas of largest heat flux (1100 °C). This leads to an increase of the carbon concentration in the plasma. Mo is released progressively and led to the contamination of the carbon limiters positioned in the SOL. It is liberated from there when the limiters are later exposed and shows the proliferation of Mo onto all wall areas. This may be prohibit the use of unprotected Mo wall components. The formation of Mo_2C on the limiter surface is emphasized. Retention of hydrogen from the tokamak plasma in the carbon layers and the eroded limiter may be an important process, in particular when T operation is aimed at.

/1/ M. Saidoh, K. Sone, Jap. J. Appl. Phys. 22 (1983) 1361
/2/ I. Smid, E. Kny, K. Koizlik et al., Fus. Techn. 1988, 1071
/3/ G. Vieider, M. Akiba, A. Antipenkov et al., IAEA-CN-53/F-3-12, 1990
/4/ M. Rubel, H. Bergsåker et al., 17th EPS Contr. Fusion, 14 B 110(1990)1401
/5/ P. Wienhold, U. Littmark, E-MRS Symp. Proc., Vol XVII(1987)441
/6/ U. Samm, P. Bogen, H. Hartwig et al., J. Nucl. Mat., 162-164 (1989), 24
/7/ U. Littmark et al., Plasma Surf. Eng., Garmisch-Partenkirchen, 2 (1989) 1101

THE PRELIMINARY STUDIES OF HL-1 PLASMA WITH PUMP LIMITER

L. B. Ran G. D. Li S. Q. Sum L. H. Yao
C. J. Yuan K. H. Li Z. C. Deng J. L. Luo
M. L. Shi G. Y. Diao C. Chao and HL-1 group

Southwestern Institute of Physics
P.O.Box 15, Leshan, Sichuan, China

1. INTRODUCTION

Reduction of the impurity and control of the density are very important task in the present tokamak research. Some experiments showed that the pamp limiter is effective to improve impurity and density control[1] [2] [3].

A small-scale pump limiter has been installed on HL-1 Tokamak in 1990 and the experiment has been carried out firstly with hydrogen ohmic discharge. In this paper we would present the improvements of the plasma properties as the pump limiter was main limiter and the movable limiter was auxiliary limiter.

2. DESCRIPTION OF PUMP LIMITER AND DIAGNOSTICS IN HL-1 TOKAMAK

The pump limiter in HL-1 Tokamak and it's diagnostics are shown in Fig.1. This pump limiter is consisted of a single-throat head, a slot, a nentralizer plate and a chamber. The single-throat head is made of stainess steel and covered by graphite titles, it's shape is arc and it's curvature radius is 20cm. The slot is opend on the ion drift side and it's width can be changed within 1-2.5cm. The neatralizer plate also is made of stainless steel. The chamber is connected by a turbomolecular pump with the pumping speed of 1500l/s. A Langmuir probe was inserted in the pump limiter throat to measure density, temperature and influx of particle to enter the slot. A visible monitor was installed near by the meatralizer plate to measure $H\alpha$, HeI and CIII emissions. Another probe was installed on the head to measure plasma edge density and temperature near the pump limiter.

The pump limiter was located in the outer midplane of the torus and the movable limiter was installed at the bottom. Another visible monitor was located opposite the pump limiter in the torus to measure $H\alpha$ emission near the wall. A VUV spectrometer and a movable Langmuir probe were installed on the turos to measure the impurity emissions and the plasma edge density and temperature near the wall. The electron density was measured by HCN interferometer, the electron temperature was measured by soft x-ray PHA, the plasma radiation loss was measured by bolometer.

During the pump limiter experiment the operation perameters were Ip=100-130KA, Bt=1.8-2.2T, H2 discharge. The plasma position was controlled by the position displacement feed back control system. The gas puff was controlled by the program control system or the density feed back control system, according to the reqirement of the experiment.

3. THE PLASMA PROPERTIES WITH PUMP LIMITER

The plasma properties were apparently changed with pump limiter in HL-1 Tokamak.

When the pump limiter was main limiter and the movable limiter was auxiliary limiter, namely a(pl)<a(ml), using the program gas puff to keep the evolation of gas puff was same in every discharge , and the plasma current Ip and the toroidal magnetic field Bt were same, the density ne behaviors were observed with different pump limiter radius a(pl) as typically shown in Fig.2. In shot 9582, a(pl)=18.5cm, first ne rose slowly, then a flat-top ne(max)=2.47×10 /cm was arrived at 200ms and a duration of~150ms was kept. In shot 9586, a(pl)=19cm, first ne rose slowly, a step ne~2×10 /cm was arrived, and then continued to rise again to arrived the maximum of the density, ne(max)= 2.89×10 /cm, no flat-top. In shot 9589, a(pl)=19.5cm, ne rose continuelly, no flat-top, almostly no step, and ne(mex)=3.28×10 /cm. Shot 9582—9590 were a series of discharges with different radius of pump limiter and same gas puff. The dependence of ne(max) to be possible to achieve on a(pl) in these discharges is shown in Fig.3 in which the shot 9583 is expelled because of disruption and it is clear that the maximum density ne(max) in this case is decreased with decreasing the pump limiter radius a(pl) . This behavior is contrary to the one with movable limiter only, in that case the maximum density ne(max) is increased with decreasing the radius of movable limiter a(ml) as same gas puff was used in those discharges.

The improvement of the plasma properties have been observed with different pump limiter radius a(pl), and with gas puff feed back control to keep the density to be not variated, and with position displacement feed back control to keep the plasma position to be not variated. The typtical shots are shown in Fig.4. The Fig.4 shows that as a(pl) is changed from 19cm to 18.5cm, the Hα intensity (OF8) measured by the visible monitor in the pump limiter chanber is enhanced, however the Hα intensity near the wall measured by the visible monitor located opposite the pump limiter in the torus is weakened, the OVI intensity measured by VUV spetrometer is decreased, and the plasma radiation loss Pr measured by the bolometer is reduced too. In Fig.5, the Hα intansity near the wall with a(pl)=18.5cm and 19cm is plotted against the ne/Ip. Fig.4 and Fig.5 show that the neutral hydrogen atoms at the plasma edge are decreased, illustrating the recycling is decreased, with decreasing the pump limiter radius a(pl) . In Fig.6, the OVI intensity with a(pl)=18.5cm and 19cm is plotted against the ne/Ip. It is shown in Fig.4 and Fig.6 that the oxygen impurity in the plasma is decreasing with the decrease of the pump limiter radius a(pl).

A series of discharges were carried out for comparing the role of the pump limiter and the movable limiter. In these discharges the radii of pump limiter radius a(pl) and movable limiter radius a(ml) were changed from a(pl)=18cm and a(ml)=20cm to a(pl) =20cm and a(ml)=18cm, and the Hα intensity , the OVI intensity and the plasma radiation loss are compared in Fig.7 and Fig.8. It can be found in Fig.7 and Fig.8 that when the pump limiter is main limiter (a(pl)=18cm,

a(ml)=20cm) the Hα intensity, the OVI intensity and the radiation loss Pr are less than the case in which the movable limiter is main limiter (a(pl) =20cm, a(ml)=18cm), illustrating that the pump limiter is effective to reduce the neutral hydrogen atoms at the plasma edge, the oxygen inpurity in the plasma and the plasma radiation loss.

The intensities of Hα and OVI illustrate the concentration of the neutral hydrogen atoms at the plasma edgl and the concentration of the oxygen impurity in the plasma, but these concentration were strongly influenced by the wall conditioning before the experiment, therefore the data in Fig. 4,5,6,7,8 are taken from the shots discharged in the same day respectively. Only like this the wall condition is same, and the improvements of the plasma properties are the effects of the pump limiter.

4. CONCLUSIONS

The preliminary experiment of pump limiter in HL-1 Tokamak has shown that the pump limiter is effective to control the plasma density, and reduce the neutral hydrogen atoms at the plasma edge, the oxygen impurity in the plasma and the radiation of the plasma.

REFERENCES

[1] MIODUSZEWSKI, P., Joural of Nucl. Mater. 111&112 (1982)253-267
[2] The TFR Group, Joural of Nucl. Mater. 145-147 (1987)819-824
[3] SENGOKU, S. et al., proc. 8th PSI conf. (1988)192

Figure captions

Fig.1 Schimatic of pump limiter in HL-1 Tokamak (1) movable limiter; (2) TiC title; (3) slot; (4) Langmuir probes; (5) Hα monitor; (6) pump limiter chamber.

Fig.2 Time elolution of ne with different radius of pump limiter a(pl)=18.5, 19.0, 19.5cm, Ip=107,101,103KA respectively.

Fig.3 Decrease of maximum ne with decreasing pump limiter radius as gas puff was same in these discharges.

Fig.4 Comparision of the plasma properties with a(pl) =18.5cm and 19.0cm, in the two discharges the ne(max) and Ip were almost same, the plasma position was controlled by position displacement feed back control system.

Fig.5 Dependence of Hα intensity on ne/Ip with a(pl)=18.5cm, 19.0cm.

Fig.6 Dependence of OVI intensity on ne/Ip with a(pl)=18.5cm, 19.0cm.

Fig.7 Dependence of Hα intensity on ne/Ip as exchanging the radius of pump limiter and the radius of movable limiter
Δ a(pl)=18cm a(ml)=20cm
\+ a(pl)=20cm a(ml)=18cm

Fig.8 Dependence of OVI intensity and radiation loss on ne/Ip as exchanging the radius of pump limiter and the radius of movable limiter.
Δ intensity of OVI as a(pl)=18cm, a(ml)=20cm
\+ intensity of OVI as a(pl)=20cm, a(ml)=18cm
0 radiation loss as a(pl)=18cm, a(ml)=20cm
* radiation loss as a(pl)=20cm, a(ml)=18cm

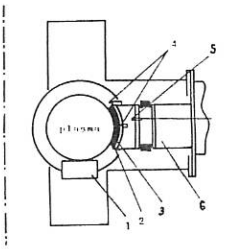

Fig.1

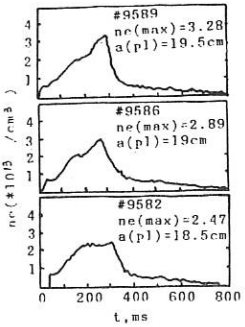

Fig.2

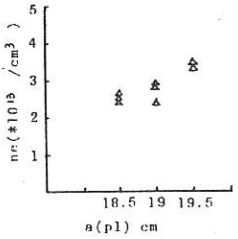

Fig.3

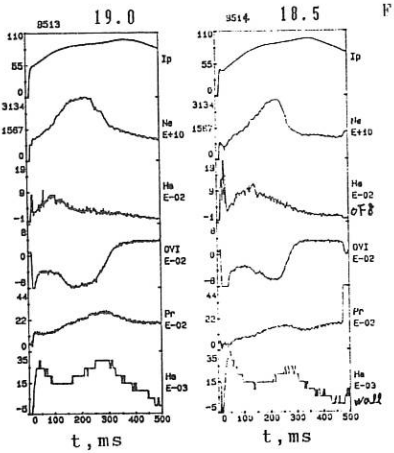

Fig.4

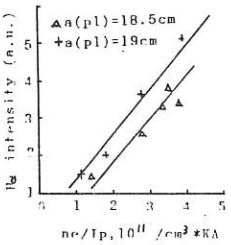

Fig.5

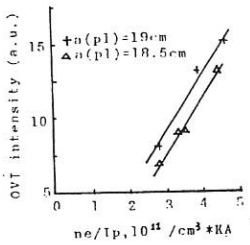

Fig.6

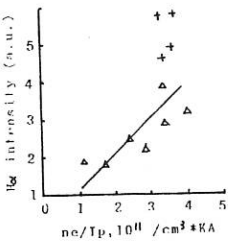

Fig.7

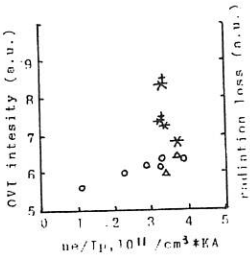

Fig.8

CHANGES IN THE LIMITER SHADOW OF T-10 DURING CURRENT AND/OR FIELD REVERSAL

M. Laux, H.-D. Reiner, P. Pech
Zentralinstitut für Elektronenphysik, O-1086 Berlin, FRG

A. V. Chankin, S. A. Grashin, A. V. Sushkov, V. A. Vershkov
Institute of Atomic Energy "I. V. Kurchatov", Moscow, USSR

Introduction

Two Mach-probes (bidirectional Langmuir probes) were introduced into the scrape-off layer (SOL) of the T-10 tokamak (major radius R = 1.50 m , minor radius a = 0.39 m) from the top and the bottom of the vessel, respectively. Both probes were situated in the same poloidal cross-section a quarter toroidal circumference away from the poloidal aperture limiter (fig. 1) that determines the SOL. The two directed tips of each Mach probe (fig. 2) have been operated as Langmuir single probes applying a -200...+200 volts ramp and recording probe characteristics using a four channel Langmuir electronics. At a constant radial position (r_p = 0.35 m) the probes were employed to monitor principal changes occuring in the SOL after reversal of plasma current I_p or toroidal magnetic field B_t. In the standard case both are directed counterclockwise looking from above the machine.

Experimental

The investigated series of shots was carried out in D_2 at B_t = 1.5 T, I_p = 220 kA, and an average plasma density of $n = 2 \times 10^{19}$ m^{-3}. The exclusive operation of the poloidal limiter ring made all flux tubes approximately the same length and, therefore, avoided any additional structuring of the SOL. Consequently, field or current reversal could only displace the fairly long flux tubes related to the probe tips from the poloidal outside to the inside or vice versa in dependence on whether the probe considered is located at the top or the bottom of the vessel.

General discharge parameters like central density, position of the column, ohmic power input, limiter radius, and absolute values of field and current were kept almost constant. Moreover, wall conditions and recycling are believed to be constant too, because all shots belong to the same operations day and the series was interrupted neither by discharges with different parameters nor by disruptions.

The measured single probe characteristics have been used to obtain the ion saturation current I_s, floating potential V_f, and, from the slope of the characteristic at the floating point, the electron temperature T_e. Thereupon, the SOL plasma density n_{SOL}, the pressure nT_e and, assuming the sheath potential to be 3 T_e,

the plasma potential V_p have been determined .

Results and Discussion

Results are discussed in terms of averages ($\overline{nT}$, $\overline{V_p}$) over pairs of values obtained by the two tips of the same probe pointing in opposite directions (thereby simulating the outcome of a fictitious isotropic measurement) as well as of differences (ΔV_p) or ratios of the paired values. From the ratio of saturation currents of corresponding tips the Mach number is derived following Hutchinson [1].

At standard orientations of current and field the average ("isotropic") plasma potential at the top probe was roughly two times the potential found at the bottom (both probes nominally at the same radius r_p = 0.35 m) and the average pressure was even about eight times as high (fig. 3). If either the current or the field is reversed the average values obtained at top and bottom simply interchange (cf. 3). Now the bottom probe shows high potential and pressure, whereas the values at the top approach former bottom results. Fig. 3 suggests also that simultaneous reversal of current and magnetic field obviously makes potential as well as pressure to remain nearly unchanged. The fact that both, current and field reversal cause the same reaction demonstrates that it is the poloidal position of essential parts of the flux tubes that matters: a probe sees high potential and pressure if the related flux tube extends mainly along the outer (low-field) region, otherwise the measured isotropic values are substantially lower. Such an asymmetry is well known from the literature [2,3,4] and may be attributed to stronger sources in the low-field region due to enhanced transport of particles and energy to the outside. The effect can be enlarged in the presence of modes of ballooning type [5] also favouring the outside.

Unfortunately, the behaviour of the observed directed quantities (like plasma potential differences between tips of the same probe or ratios of saturation currents expressed as Mach numbers) during field or current reversal is not all that simple. To begin with, top and bottom probe give essentially different Mach numbers for distinct exemplars of shots at normal orientations of current and field (fig. 4). At the top a substantial streaming onto the nearby aperture limiter is indicated, whereas at the bottom, rather unexpected, a slow streaming away from the limiter was found or no streaming at all (cf. 4). A remarkable potential difference of about -7 Volts was observed for both probes at normal orientations. A field or current reversal drives the Mach number at the bottom to the value of the top probe, which itself was found to remain more or less unchanged (cf. 4). During current reversal the potential differences changed sign for both probes, whereas during field reversal only the bottom probe shows this behaviour and the top probe's result remains unchanged. The conclusion is that as far as directed quantities are concerned top and bottom probe behave

remarkably different. A convenient explanation is not at hand but it can be speculated there might be a transport of momentum from the edge region plasma column (just inside the limiter radius) into the SOL. For T-10 it is known from measurements of the radial electric field [6] that the edge plasma must carry large momentum. If the transport of momentum takes place predominantly in the direction of the $B\times\nabla B$ drift of the electrons the bottom probe should be strongly influenced at standard orientation of the field and will react to a current reversal that is expected to imply a reversal of the momentum direction in the column. A reversal of the magnetic field disconnects the bottom probe from the additional momentum. Now the top probe is expected to show the effect in contrast to the experimental observation.

In summary it can be concluded from the results of experiments in a very simple SOL governed by a single circular aperture limiter alone, that isotropicly measured parameters of the SOL plasma (like density, plasma pressure or plasma potential) suffer an in/out (high-field/low-field) asymmetry, whereas directional quantities (like plasma potential differences or plasma flow velocities) are obviously affected by directed influences originating from the plasma column and, afterwards, transported into the SOL by an up/down asymmetric process.

Acknowledgement

The technical assistance of the T-10 operational staff is greatly acknowledged.

References

[1] I.H.Hutchinson, Phys. Fluids 30 (1987) 3777.
[2] B.LaBombard and B.Lipschultz, Nucl. Fusion 27 (1987) 81.
[3] A.N.Hill, Nucl. Fusion 28 (1988) 902.
[4] V.A.Vershkov et al., J. Nucl. Mater. 162-164 (1989) 195.
[5] A.V.Chankin and V.A.Vershkov, J. Nucl. Mater. 162-164 (1989) 208.
[6] Yu.A.Sokolov, private communication.

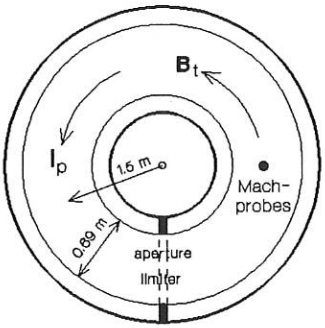

Figure 1 schematic top view of T-10

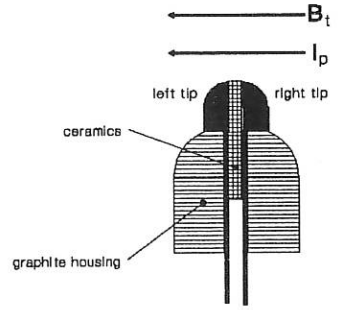

Figure 2 schematic drawing of a Mach probe head

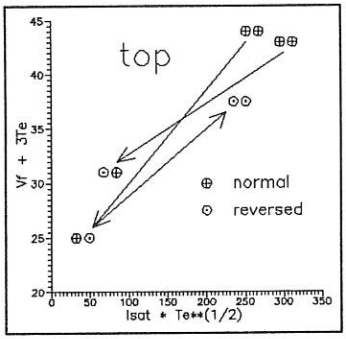

Figure 3a av. plasma potential versus av. pressure for top probe (left symbol: current, right symbol: field)

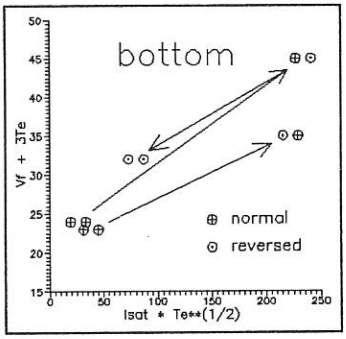

Figure 3b same as Fig. 3a but for bottom probe

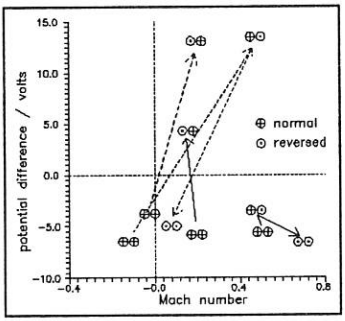

Figure 4 potential difference ΔV_p versus Mach number (solid line: top probe, dashed line: bottom probe)

A SHEATH MODEL OF ASYMMETRIC HEAT FLOW TO A POLOIDAL LIMITER

M.G. Haines

Blackett Laboratory, Imperial College, London SW7 2BZ.

Introduction

Experimental results on JET and other tokamaks with poloidal limiters have shown that there is typically a 50% difference in heat flow to the two sides of a poloidal limiter. Defining the 'ion' side of a poloidal limiter as that which would receive a toroidal ion current in the same direction as the induced toroidal current of the tokamak, and the 'electron' side as the other side, it is estimated from experimental data by Lowry[1] that the energy flux received by the 'electron' side is typically half of that on the 'ion' side. The recent review of the scrape-off layer by Stangeby and McCracken[2] also contains evidence to support this, even suggesting a factor of 10 in asymmetry of density. Lowry has suggested that this asymmetry can arise through the preferential arrival of ions into the outer scrape-off layer with toroidal angular momentum in the J_φ direction. This arises from a consideration of ion drift orbits in the banana neo-classical regime; at the plasma edge parts of phase space of the ion distribution function are depleted, because the orbits of these ions would originate at an earlier time from further away from the minor axis. Such a mechanism would also lead to a steady exchange of toroidal angular momentum between the plasma and the limiter. The effect would be reversed on a poloidal limiter on the inside of the torus as compared to one on the outside. In this paper a completely different model is developed which is based on an extension of Child-Langmuir sheath theory.

The model

We assume for simplicity that the poloidal limiter is non-emitting. The plasma in the scrape-off layer experiences the same applied toroidal electric field, $E_\varphi = -\partial A_\varphi/\partial t$, as in the neighbouring magnetically confined plasma. A toroidal current density, J_φ, can therefore flow in the scrape-off layer. This means that at the electron side of the (periodic) poloidal limiter more electrons than ions should arrive in unit time, while at the ion side more ions than electrons should arrive. The limiter will receive equal numbers of ions and electrons when counting up both sides. It is assumed that the limiter is made of good conducting material so that the J_φ current density flows through the limiter with negligible voltage drop. There will be Child-Langmuir sheaths on each side of the poloidal limiter in order to reduce the electron flow. These sheaths are a few Debye lengths in thickness. There will also be pre-sheath regions in which electric fields exist in quasi-neutral plasmas to accelerate the ion species to the ion sound speed, $c_s \equiv (k_B/T_e/m_i)^{\frac{1}{2}}$. This is called the Bohm condition. The number density at the interface of the sheath and pre-sheath is n_1 at the electron side and n_2 at the ion side.

All the ions that arrive at the pre-sheath-sheath interface will also arrive at the limiter, having been accelerated through the Child-Langmuir potential. The ion current density in the φ direction at the 'electron' side of the limiter is therefore $-en_1c_s$ and the 'ion' side will be $+ en_2c_s$. Taking the sheath potential at the 'electron' side to be Φ_1 and at the 'ion' side to be Φ_2 and defining the dimensionless potentials to be $\eta_1 \equiv -e\Phi_1/k_B T_e$ and

$\eta_2 = -\Phi_2/k_BT_e$ respectively, the electron current density arriving at the 'electron' side will be $\frac{1}{4}\, en_1c_e \exp(-\eta_1)$ where c_e is the electron mean thermal speed, i.e. $c_e = (8k_BT_e/\pi m_e)^{\frac{1}{2}}$ [3]. Again, measuring the currents as positive in the $+\varphi$ direction, the electron current density at the 'ion' side will be $-\frac{1}{4}\, en_2c_e \exp(-\eta_2)$. It is a reasonable assumption because of parallel thermal conduction to keep the electron temperature along the flux tube in the scrape-off layer constant. The current density on the 'electron' and 'ion' sides of the limiter will be equal so that no net charge is lost from the plasma. We can therefore write

$$J_\varphi = \tfrac{1}{4}\, en_1c_e \exp(-\eta_1) - en_1c_s \qquad (1)$$

$$= -\tfrac{1}{4}\, en_2c_e \exp(-\eta_2) + en_2c_s \qquad (2)$$

(Readers familiar with the standard zero current Child-Langmuir sheath [3] will see that Eqs.(1) and (2) would both yield for $J_\varphi = 0$ the result that the dimensionless wall potential η_w would be given by $\ell n\,(c_e/4c_s) = \frac{1}{2}\,\ell n\,(m_i/2\pi\, m_e) > 0$). With $J_\varphi \neq 0$, the inequalities $\eta_1 \neq \eta_e$ and $n_1 \neq n_2$ follow. Indeed we will find that for $J_\varphi > 0$ we have $n_2 > n_1$ and $\eta_2 > \eta_1$.

In the quasi-neutral plasma region between the two Child-Langmuir and including the pre-sheath regions an Ohm's law of the form

$$E_\varphi = -\frac{\partial A_\varphi}{\partial t} = -\frac{\nabla_{||} P_e}{n_e e} + \frac{J_\varphi}{\sigma} \qquad (3)$$

holds. The integral $\int E_\varphi . d\underline{\ell}$, connecting the two adjacent poloidal diverter separated by a distance L and including the sheaths and pre-sheath regions, gives

$$E_\varphi L = -\frac{\partial A_\varphi}{\partial t} L = -\frac{kT_e}{e}\eta_1 - \frac{k_BT_e}{e}\ell n\frac{n_2}{n_1} + \frac{J_\varphi L}{\sigma} + \frac{k_BT_e}{e}\eta_2 \qquad (4)$$

where the second term on the right hand side arises from the $\nabla p_e/n_e e$ term in Eq.(3). This term dominates the pre-sheath regions. To eq.(4) can also be added the potential difference across the poloidal limiter itself, e.g. graphite. If we assume that the current density J_φ in the adjacent confined plasma and scrape-off layers are equal, then $-\partial A_\varphi/\partial t = J_\varphi/\sigma$ and Eq.(4) simplifies to give the relationship,

$$n_1 \exp(-\eta_1) = n_2 \exp(-\eta_2) \qquad (5)$$

We will find that our results are insensitive to this assumption because the terms in J_φ/σ and E_φ are of order $L/\lambda_{mfp}\,(m_e/m_i)^{\frac{1}{2}}$ compared to the other terms, i.e. $\sim 10^{-4}$ times the others. λ_{mfp} is the electron mean-free-path. Equations (1) and (2) can be written as

$$\frac{J_\varphi}{\frac{1}{4}ec_e} = n_1 \exp(-\eta_1) - n_1\left[\frac{2\pi m_e}{m_i}\right]^{\frac{1}{2}} = n_2\left[\frac{2\pi m_e}{m_i}\right]^{\frac{1}{2}} - n_2 \exp(-\eta_2) \qquad (6)$$

which, with Eq.(5) gives

$$n_1 \exp(-\eta_1) = \frac{n_1+n_2}{2}\left[\frac{2\pi m_e}{m_i}\right]^{\frac{1}{2}} \qquad (7)$$

and

$$\frac{J_\varphi}{\frac{1}{4}ec_e} = \frac{n_2-n_1}{2}\left[\frac{2\pi m_e}{m_i}\right]^{\frac{1}{2}} \qquad (8)$$

It therefore can be seen that the presence of a current density J_φ leads to a *difference* in number density (n_2-n_1) between the 'ion' and 'electron' side of the limiter, measured just outside the respective Child–Langmuir sheaths. This asymmetry will be shown to lead to a large asymmetry in enthalpy flux. But first we note that Eq.(8), which can alternatively be written as

$$n_2 - n_1 = 2\frac{J_\varphi}{e}\left[\frac{m_i}{k_B T_e}\right]^{\frac{1}{2}} = \frac{2J_\varphi}{ec_s} \qquad (9)$$

demonstrates that there is a *maximum* current density in the scrape–off layer which occurs when n_1 tends to zero. The measured current density in JET is close to this value, e.g. $J_\varphi \sim 5 \times 10^3$ A m^{-2}, for $T_e = 50$eV and $n = 10^{18}$ m^{-3} in deuterium. (In practice the current density in the confined plasma adjacent to the scrape–off layer could be higher because it is driven not only by the applied electric field but also by the outward plasma diffusion across the magnetic field lines).

Heat flux

The enthalpy flux by ions and electrons to the 'electron' side of the limiter, q_1 , is

$$q_1 = n_1 c_s \left[\frac{1}{2} m_i c_s^2 + k_B T_i \left(\frac{5}{2} + \eta_1\right)\right] + \frac{m_e}{2\pi^{\frac{1}{2}}}\left[\frac{2k_B T_e}{m_e}\right]^{3/2} n_1 \exp(-\eta_1) \qquad (10)$$

and to the 'ion' side q_2 is

$$q_2 = n_2 c_s \left[\frac{1}{2} m_i c_s^2 + k_B T_i \left(\frac{5}{2} + \eta_2\right)\right] + \frac{m_e}{2\pi^{\frac{1}{2}}}\left[\frac{2k_B T_e}{m_e}\right]^{3/2} n_2 \exp(-\eta_2) \qquad (11)$$

Because of Eq.(5) the electron contributions to the enthalpy flow are the same but there is a marked asymmetry in the ion enthalpy flow because n_2 is greater than n_1, as a result of the toroidal current flow, J_φ, as shown in Eq.(8). The terms in η_1 and η_2 in the ion contribution play only a weak though additional role because $\eta_2 - \eta_1$ depends only logarithmically on n_2/n_1 (Eq.(5)). Therefore a significant heat flux asymmetry especially if T_i is greater than T_e[4] in favour of the 'ion' side can be explained by this theory. It is interesting to note that this asymmetry is in the opposite direction to that of a Z–pinch which has emitting electrodes[4].

Momentum flux

Turning to momentum flux, or toroidal force on the poloidal divertors, we note that in a one−dimensional sheath and plasma in steady state we have

$$\frac{d}{dx}\left[n_i m_i v_{ix}^2 + p_i + p_e - \frac{1}{2}\epsilon_o E_x^2 \right] = 0 \qquad (12)$$

where the last term arises from the electrostatic force per unit volume on a non−neutral plasma,

$$e (n_i - n_e) E_x = \epsilon_o E_x \frac{dE_x}{dx} = \frac{d}{dx}\left[\frac{1}{2}\epsilon_o E_x^2 \right] \qquad (13)$$

and where the x direction is taken to be of the magnetic flux tube connecting the two poloidal limiters. It immediately follows that if there is no net momentum flux in the toroidal direction in the plasma diffusing into the scrape−off layer, there will be no net momentum flux to the limiters. There is however a net *particle* momentum flux, i.e. an asymmetry in the terms $(n_i m_i v_{ix}^2 + p_i + p_e)$ due to $n_1 \neq n_2$ but this is exactly compensated by the difference in the electrostatic force per unit area, $\frac{1}{2}\sigma_s E_x$ caused by the difference in surface charge density σ_s on the two sides of the limiter. Therefore it is possible to have a large asymmetry in enthalpy flow with no asymmetry in momentum flow.

Conclusion

In conclusion we have shown that the presence of a toroidal current density in the scrape−off layer between non−emitting poloidal limiters leads to an asymmetry in the Child−Langmuir sheaths so that the 'ion' side receives more in unit time ions than electrons, while the 'electron' side receives more electrons than ions. This leads to a higher density at the sheath boundary on the 'ion' side and to a significantly higher ion enthalpy flux. But there is no asymmetric transfer of toroidal angular momentum by this effect. The theory also predicts an upper limit to the toroidal current density in the scrape−off layer of $\frac{1}{2}n_2 e c_s$. These effects could also be relevant to ion thruster behaviour.

Acknowledgements

The author acknowledges useful discussions with C. Lowry, R. Pitts, J. Connor and R. Fitzpatrick. He also thanks Culham Laboratory for support.

References

(1) C.G. Lowry (1990) private communication.
(2) P.C. Stangeby and G.M. McCracken, Nuclear Fusion 30 1225 (1990).
(3) See for example, R.N. Franklin, Plasma Phenomena In Gas Discharges (1976) (Clarendon Press, Oxford).
(4) Recent measurements on JET have indicated that T_i is significantly higher than T_e, and this has been employed by S.K. Erants to correct the particle energy flux calculations.
(5) M.G. Haines, Proc. Phys. Soc. 77, 643 (1961).

HELIUM AND CARBON IONS FLOW IN A PUMP LIMITER CHANNEL

N.N.Brevnov, S.B.Stepanov, L.N.Khimchenko

I.V.Kurchatov Institute of Atomic Energy, Moscow, USSR

Comprehension of the mechanism of an impurity flow in a divertor channel plays an important role in modelling of processes in a vicinity to the neutralization plates. Great expectations are related with the enhanced particle recycling, as a method for locking impurities in a divertor. Outflow of the particles ionized in a divertor into a main plasma will result in both a reduction in the divertor plates self-sputtering and a contamination of the plasma column with impurities. Numerical modelling, using 2-D plasma code [1], shows, that immediately in front of the plates the plasma flow directed towards the plates, but a short distance further out, it is reversed for regions near the separatrix. To test this result at the TVD tokamak [2] **He** and CO_2 gases were puffed into the pump limiter volume and the degree of an impurity recycling was determined from the particle balance model.

The pump limiter channel was 6cm long; ≃ 1.5cm wide. A control over the plasma parameters was realized along and accross the channel [$n_i \simeq (0.5 \div 2.0)10^{12} cm^{-3}$, $T_e \simeq 20 \div 40 eV$]. The particle flux to the neutralization plates was $j \leq 0.5 A/cm^2$; the pressure of puffed neutral particles inside the pump limiter volume was $p \simeq 10^{-3}$ torr. The optical lines H_α, **CI, CII, CIII, HeI, HeII** were registrated from the zone in the vicinity to the neutralization plates. The piezovalve allowed one to increase the gas pressure for 1ms at the facility pulse

duration ≃ 20ms. The experiments were done with a hydrogen plasma.

The relative plasma flow velosity to the neutralization plates, $A_{\parallel np} = v_{np}/c_s = I_{np}/n_i c_s S_\perp$, where I_{np} is the ion current to the neutralization plates , c_s is the sound speed, $S_\perp$ is the transverse area of the neutralization plates, indicates a degree of a hydrogen plasma recycling. With a rise in the plasma temperature from 20 to 40eV the magnitude of $A_{\parallel np}$ is reduced from 0.5 to 0.1 (Fig.1). The ion current to the neutralization plates under the hydrogen gas puffing inside the pump limiter till pressure ≃ 10^{-3}torr hasn't being changed. This, probably, shows, that a greater part of the particles ionized in the channel gets out to SOL, not to the neutralization plates.

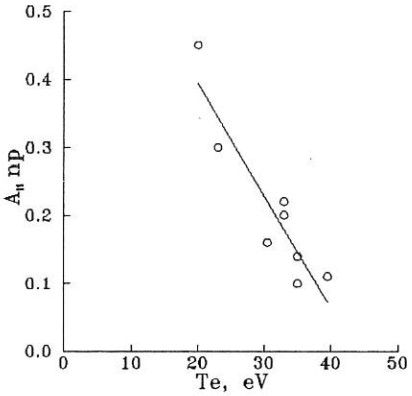

Fig.1.

A powerfool gas puffing (equivalent flux ≃ 60A) into the pump limiter volume was realized to study the recycling of helium. Quantitative estimates of particle fluxes in the channel were done for the moment of switching the gas puffing off. Knowing the atomic helium flux entering the channels at the

pressure decay stage and calculating the ionization rate of helium atoms, one can find the fluxes of helium atoms F^{o}_{out} and ions F^{i}_{out}, leaving the channel. The fraction of ions in the sum of these fluxes $B_{\parallel out} = F^{i}_{out} / (F^{i}_{out}+F^{o}_{out})$ rises from 0.2 to 1.0 with increase in plasma temperature within the channel from 20 to 40eV (Fig.2). In this case the fraction of helium ions entering the neutralization plates, proportional to $I^{He}_{np} / (F^{i}_{out} + F^{o}_{iout})$ is rather small ($\leq$ 0.1). Knowing the helium ion flux F^{i}_{out} and the helium ion density n_{He^+}, one can estimate the velocity of helium ions, leaving the channel $v_{\parallel out} = F^{i}_{out}/S_{\perp}\, n_{He^+}$ (Fig.3). It turns out that the value of $v_{\parallel out}$ linearly depends on temperature. In this case the energy of those helium ions attained 80 eV at $T_e \simeq$ 40eV.

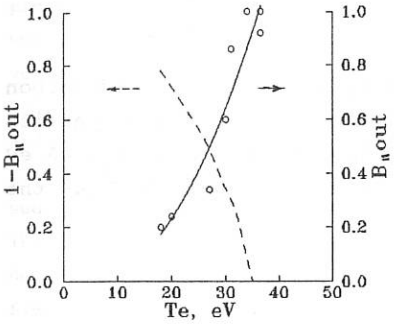

Fig.2.

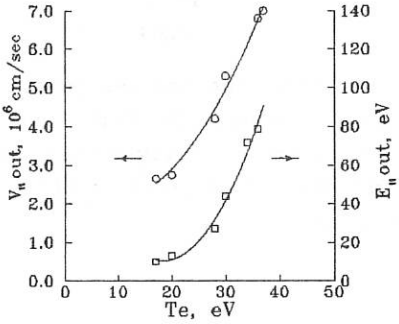

Fig.3

A similar data on the outflow of carbon were obtained under the CO_2 puffing into the pump limiter volume. From the spectroscopy of optical lines the temperature dependence of relative carbon concentration at various ionization stages was singled out (Fig.4). The velocity of C^+ ions leaving the zone in the vicinity to the plates was calculated from the particle balance [3]. One can see, that the velocity these C^+ ions linearly rises with the plasma temperature T_e rise simi-

lar to the case with helium (Fig.5). At the CO_2 gas puffing the neutralization plate current is not changed that probably speens about the C^+ outflow from the pump limiter channel.

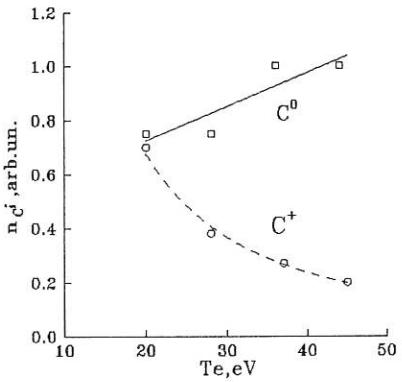

Fig.4

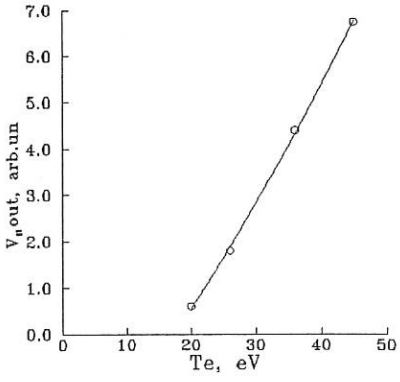

Fig.5

Thus, the process general for hydrogen, helium and carbon ions in a pump limiter channel is a weak recycling of particles in the vicinity to the neutralization plates at $T_e \simeq 40$ eV and the significant outflow of ionized particles from the channel.

1. B.J.Braams, P.J.Harbour, M.F.A.Harrison, et al., J.Nucl.Mater. 121. (1984). 75.
2. A.V.Bortnikov, et al., Preprint IAE-4554/8, Moscow, 1988.
3. V.A.Abramov, N.N.Brevnov, V.I.Pistunovich, et al., In Controlled Fusion and Plasma Physics (Proc. 18 Eur. Conf. Berlin., 1991.).

MAGNETIC SHIELDING OF A LIMITER

N.N.Brevnov, S.B.Stepanov, L.N.Khimchenko, G.F.Matthews*, D.H.J.Goodal*

I.V.Kurchatov Institute of Atomic Energy, Moscow, USSR

*) Culham Laboratory, Abingdon, OX14 3DB, UK

Localization of plasma interaction with material surfaces in a separate chamber, from where the escape of impurirties is hardly realized, i.e. application of magnetic divertors or pump limiters, is the main technique for reduction of the impurity content in a plasma. In this case, the production ofa divertor configuration requires a considerable power consumption and results in a less effective utilization of the magnetic field volume. Utilization of a pump limiter, for example the ICL-type (Fig.1a) [1], under tokamak-reactor conditions would result in the extremely high and forbidden local heat loadings onto the limiter surface.

Moreover, the magnetically-shielded pump limiter (MSL) [2] was proposed to combine positive properties of the divertor and the pump limiter. The idea of magnetic shielding is to locate the winding with current inside the limiter head so that the field lines of the resultant magnetic field does not intercept the limiter surface (Fig.1b). In this case the plasma flows aroundthe limiter leading edges and penetrates into the the space under the limiter. The shielding magnetic field can be directed either counter the toroidal field or counter the poloidal one of a tokamak, dependent on the concrete diagram of the device [3].

Such a limiter has a number of advantages:

- opportunity to control over the particle and impurity recycling without practical influence upon the plasma column geometry,
- perturbation of a plasma column magnetic configuration from the side of such a limiter is less than that from the side of the divertor coils.

The main deficiency is the necessity to locate active windings inside the discharge chamber.

The MSL mock-up was tested at the TVD-facility [4]. The limiter head, inside which a solenoid was located, had the following dimensions: 15cm long, 8cm high, 1.5cm thick. The proper magnetic field of of the solenoid was directed against the toroidal field of the tokamak (1T value). The discharge duration was 20ms. The magnetic shielding was switched on at a quasi-stationary phase of the discharge, ≃ 10ms long; the current through the solenoid attained 3.8kA, the linear current density through the solenoid was ≃ 15kA/cm^2. H_α- radiation in the vicinity to the limiter surface, within an input channel of the pump limiter, as well as close to the neutralization plates, was registered in the experiment. A CCD TV camera supplied with replaceable interferential filters imaged the light of single spectral lines from the zonenear the limiter surface and from the limiter duct having containing the diagnostic probes. The signals were recorded with a video recorder. The video records were processed by a video analyser to obtain the intensity profiles of individual spectral lines along the chosen directions that allowed us to make visible a location of the most intensive interaction between the plasma and the limiter and, as a result about the efficiency of the applied protection technique.

In the experiment the limiter surface was located either parallel to the toroidal magnetic field or slightly inclined to it. When the limiter surface was in parallel to B_{tor}, the H_α -radiation was symmetrically distributed along the limiter surface (Fig.3a). In this case the switching of the limiter magnetic field on reduced the H_α -line in the vicinity to the limiter surface and increased it within the limiter duct (Fig.2) in a few times. The current of charged particles to the neutralizing plates was also increased by 1.5 times. It is probably connected with a reduction in the flux of particles to the limiter surface and with the plasma penetration inside the limiter channel. The mock-up experiments with an electron beam confirm this conclusion.

A small inclination of the limiter axis ($tg\alpha \simeq 0.05$) towards the toroidal magnetic field (Fig.3b) results in an asymmetry in the visible light intensity distribution along the limiter surface. In this case, the characteristic intensity decay length in the radial direction is correlated with the plasma density decay towards the plasma edge. Switching the magnetic shielding on results in a redistribution of radiation intensity

and a shift of the peak intensity towards the limiter edge. Assuming this occurs due to the redistribution of the field lines and the plasma density in the vicinity of the limiter surface, from the change in the visible light glow, the relative displacement of the magnetic field lines was calculated. This is in a good agreement with the relative displacement of magnetic field lines, obtained from the simulation of the magnetic configuration.

So, the experiments show effective limiter shielding with proper magnetic field.

Opportunities for application of such a magnetic shielding are rather wide. For example, for the initial stage of ITER discharge ($t < 40s$) the toroidal limiter modification with a magnetic shielding (poloidal divertor analogue) was calculated [5]. The calculation shows that the serviceable protective configuration can be produced, using the acceptable current densities ($j \leq 30$ A/mm^2).

The TVD experiments have shown it is possible to magnetically protect the limiter surface effectively and to shape the magnetic field lines around the limiter surface. The plasma-limiter interaction results give some initial data on the possibility of sweeping the separatrix position across the neutralizing plates (and, thus to reduce local heat loadings upon the neutralization plates of ITER), using the solenoids located below them and modulating a feeding current. In this case, the magnetic field of a solenoid acts over a distance of the order of the solenoid width, at greater distances the effect on the equilibrium magnetic plasma shape is negligible. The calculation for ITER shows that it is possible to design a solenoid capable of shifting the separatrix along the neutralizing plates by 10cm at the average current density in the turns $j \leq 12$A/cm^2.

1. G.F.Matthews , S.J.Fielding , G.M.McCracken , et al.,
Nucl. Fusion 28 (1988) 2209.

2. S.B.Stepanov, L.N.Khimchenko License SU-1400341 A1. 1989.

3. A.N.Mel'dianov, S.B.Stepanov, L.N.Khimchenko
Novosti Atomnoj Nauki i Techniki (ser. Termojad. synt.) 2, 1990.

4. A.V.Bortnikov , N.N.Brevnov et al.
Preprint IAE-4554/8, Moscow,1988.

5. N.N.Brevnov, A.N.Mel'dianov, S.B.Stepanov, L.N.Khimchenko
ITER-IL-PH-13-9-5-17.

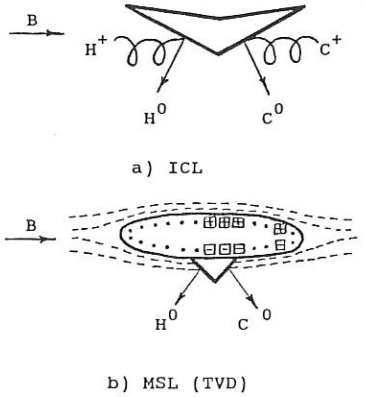

Fig.1 Limiter design:
a) Impurity control limiter
b) Magnetically shielded limiter

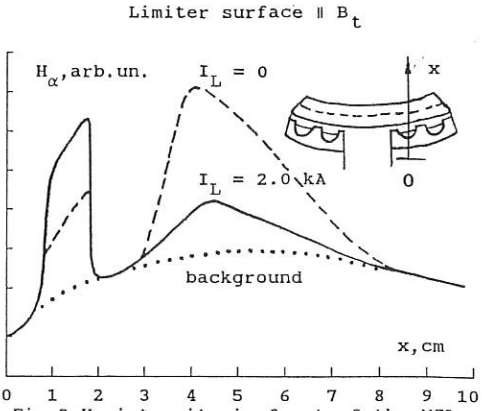

Fig.2 H_α intensity in front of the MSL and in the duct with and without a solenoid current

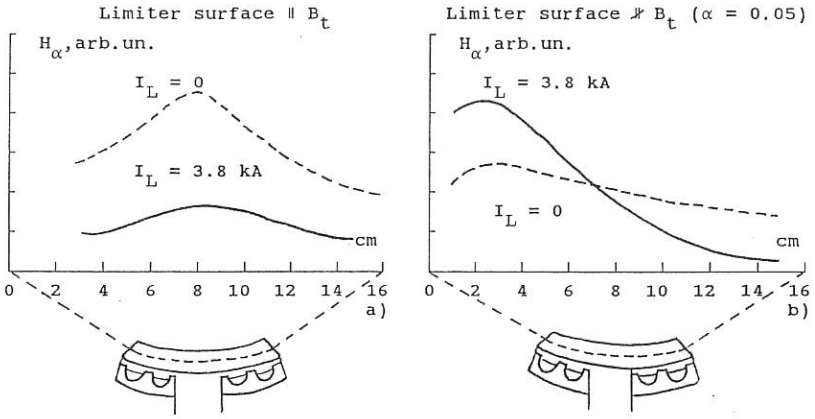

Fig.3 The H_α intensity distribution along the limiter surface with:
a) Limiter surface ∥ B b) Limiter surface ⊁ B (α = 0.05)

TOWARDS FULLY AUTHENTIC MODELLING OF ITER DIVERTOR PLASMAS

G P Maddison, E S Hotston
AEA Fusion, Culham Laboratory, Abingdon, Oxon OX14 3DB, UK
(Euratom/UKAEA Fusion Association)

D Reiter, P Börner
IPP, KFA Jülich GmbH, P O B 1913, D-5170 Jülich, BRD
(Association Euratom/KFA)

T Baelmans
Catholic University of Leuven, Celestijnenlaan 300B, B-3030 Heverlee, Belgium

1 Introduction

Ignited next step tokamaks such as NET or ITER are expected to use a poloidal magnetic divertor to facilitate exhaust of plasma particles and energy. We report a development coupling together detailed computational models for both plasma and recycled neutral particle transport processes, to produce highly detailed and consistent design solutions. A particular aspect is involvement of an accurate specification of edge magnetic geometries, determined by an original equilibrium discretisation code, named LINDA. Initial results for a prototypical 22MA ITER double-null configuration are presented. Uncertainties in such modelling are considered, especially with regard to intrinsic physical scale lengths. Similar results produced with a simpler, analytical treatment of recycling are also compared. Finally, a further extension allowing true oblique target sections is anticipated.

2 Accurate discrete geometries

Realistic simulations of proposed divertors require an accurate representation of their actual magnetic structure, common to both plasma and recycled neutral particle transport models. An original discretisation code, designated LINDA (**L**inearly **I**nterpolated **N**umerical **D**ivertor **A**rchitecture)[1], has been developed, capable of producing arbitrary orthogonal discretisations of either single- or double-null axisymmetric configurations from prepared equilibrium data. Outputs are tailored specifically to the discrete metric function requirements and organisation of the BRAAMS two-dimensional steady-state edge plasma transport code[2,3], both in its along-field[2] and poloidal cross-section[3] co-ordinate frame versions. In addition, matching discrete cell co-ordinates are provided for Monte Carlo neutral gas transport simulators such as EIRENE[4], NIMBUS[5], or DEGAS[6].

These numerical representations are constructed using only geometric methods, on a basis of piecewise linear interpolation through-out[1]. Fundamentally, ordered piecewise linear flux and orthogonal surfaces are identified according to an isosceles construction

between intersecting segments. Cotangent of field line pitch $\tau \equiv (B_p/B_t)$ is similarly interpolated, giving an elementary magnetic connection length $ds_x^F = \int_{s_{xA}^P}^{s_{xB}^P} (\sqrt{1+\tau^2}/\tau) ds_x^P$ between positions s_{xA}^P; s_{xB}^P on a poloidal flux surface :-

$$ds_x^F = \frac{s_{xB}^P - s_{xA}^P}{\tau_B - \tau_A} \left\{ \sqrt{1+\tau_B^2} + \frac{1}{2} \ln\left(\frac{\sqrt{1+\tau_B^2}-1}{\sqrt{1+\tau_B^2}+1} \right) - \sqrt{1+\tau_A^2} - \frac{1}{2} \ln\left(\frac{\sqrt{1+\tau_A^2}-1}{\sqrt{1+\tau_A^2}+1} \right) \right\}.$$

An average cosine of field line pitch is inferred correspondingly from $(\widetilde{B_p/B}) = ds_x^P (1/ds_x^F)$. Thus full magnetic sheer through-out the system is incorporated.

Our calculations include also a thin annulus of closed flux surfaces interior to the separatrix, in order to impose inner boundary conditions at a position of more certain poloidal symmetry. Conditions at the separatrix are then determined by the transport model itself. If transport of plasma energy across this closed region is wholly **diffusive**, ie $\mathbf{q}_\perp = -n\chi_\perp \nabla T - (5/2) D_\perp T \nabla n$, with coefficients which further depend only on flux (ψ) surface quantities, then $\mathbf{q}_\perp \equiv \mathcal{F}(\psi)\nabla\psi$. Ignoring effects of poloidal drifts and any induced gradients on closed surfaces, the asymmetry in total power effluxes to inside and outside SOL's of a double-null arrangement hence becomes a ratio of purely geometric integrals :-

$$\left\{ \int_{S_\psi^{\rm OUT}} \mathbf{q}_\perp \cdot \mathbf{dS} \right\} \Big/ \left\{ \int_{S_\psi^{\rm IN}} \mathbf{q}_\perp \cdot \mathbf{dS} \right\} = \left\{ \int_{S_\psi^{\rm OUT}} |\nabla\psi| \, dS \right\} \Big/ \left\{ \int_{S_\psi^{\rm IN}} |\nabla\psi| \, dS \right\}. \qquad (1)$$

Discretisation of an early, illustrative ITER double-null configuration for the 22MA ignited phase is shown in Fig.1. Null to strike point depths for inside & outside targets are respectively 0.5m & 1.2m, while equatorial widths of both SOL branches are 0.1m. Spatial resolutions are discussed below. Variation in magnetic sheer in each SOL is depicted in Fig.2. Shallower field line pitch produces larger connection lengths on the inside, despite its smaller major radius. Also shown is the diffusive ratio of power effluxes from (1), implying almost 4.5 times as much power to the outside SOL as to the inside. Thus geometry alone here might account for the expected imbalance.

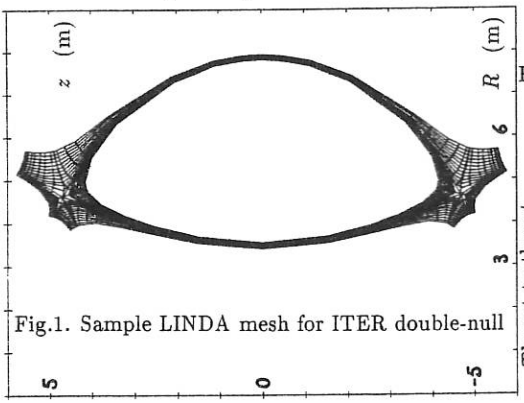

Fig.1. Sample LINDA mesh for ITER double-null

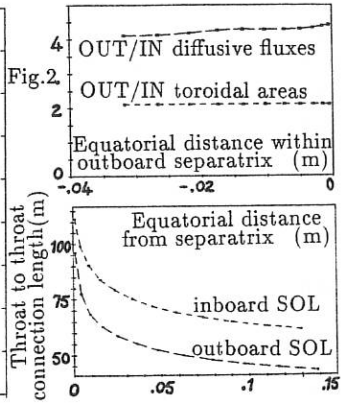

Fig.2.

3 Coupled transport calculations

The latest poloidal cross-section version of BRAAMS[3] was coupled in the orthogonal full four target ITER geometry with EIRENE[4] Monte Carlo simulation of recycling. A full EIRENE re-evaluation of instantaneous sources was executed after every ~200 internal BRAAMS iterations. In between, sources were adjusted implicitly by rescaling neutral particle densities with instantaneous target fluxes, then recomputing plasma interactions with the EIRENE rate coefficients. This technique promotes stability. A number of outer cycles were conducted to seek overall convergence.

A single ion species of $A_i = 2.5$ and $Z_i = 1$ was prescribed. Cross-field transport coefficients in BRAAMS were set $D_\perp = 1\mathrm{m}^2\mathrm{s}^{-1}$; $\chi_{\perp e} = 3\mathrm{m}^2\mathrm{s}^{-1}$; $\chi_{\perp i} = 1\mathrm{m}^2\mathrm{s}^{-1}$. Parallel coefficients are classical, except that Spitzer-Härm electron conduction was flux limited[3] according to $K^e_\parallel = K^e_{\parallel\mathrm{SH}}/(1-\{K^e_{\parallel\mathrm{SH}}\nabla_\parallel T_e\}/\{\alpha n_e T_e\sqrt{T_e/(2m_e)}\})$, with a strong parameter value[3] of $\alpha = 0.1$. Chodura sheaths[7] were defined at each target, which are assumed to be carbon and all 100% recycling. Pumping thus occurs only via a **neutral particle albedo** over the **duct opening** in the **outside lower divertor**. Zero plasma particle flux was imposed on all outer boundaries. Total power efflux is 111MW, in ratios of 5:1 between electrons & ions, and here 3:1 between outside & inside SOL's. Note also that inside and outside portions of the plasma are separated by **insulating** grid cuts[1].

Evolution through the cycles is depicted in Fig.3. Although convergence is not complete, conditions are settling to a very high recycling regime (total flux amplification ratio $\gamma \approx 1300$), as expected for the realistic asymmetric pumping. Coincident peak plasma properties before the outside lower plate indicate that crucial conditions here are substantially relaxed. Immediately striking are the **very low temperatures** of $\hat{T}^{\mathrm{TOL}}_{e,i} \approx 3 \rightarrow 4$ eV only, with a peak density of $\hat{n}^{\mathrm{TOL}}_e \approx 1.3 \times 10^{21}\mathrm{m}^{-3}$. Strong radiation of power occurs, even without impurities. Separatrix density at the outboard equatorial plane is similarly steady around $n^{\mathrm{SEP}}_{e\mathrm{EQ}} \approx 3.4 \times 10^{19}\mathrm{m}^{-3}$.

Closely equivalent calculations substituted the simpler Hotston analytical treat-

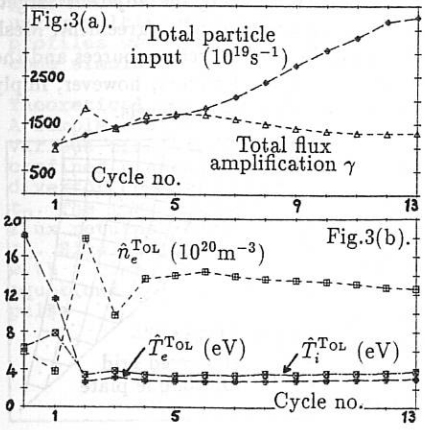

Fig.4. Values across $\mathrm{T_{OL}}$ after cycle 13

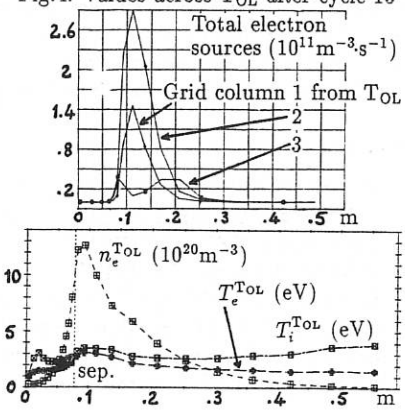

ment of recycling[8] for EIRENE. Pumping was by a fractional recycling coefficient on every target, while neutral particle ranges were artificially extended along each flux tube crudely to anticipate plate inclinations of 45° inside & 20° outside to the separatrix. Allowing for this, values when $\alpha = 0.1$ of $\hat{T}_{e,i}^{\text{TOL}} \approx 5 \rightarrow 6$ eV; $\hat{n}_e^{\text{TOL}} \approx 7.5 \times 10^{20}\text{m}^{-3}$; $\gamma \approx 690$ and $n_{e\text{EQ}}^{\text{SEP}} \approx 3.5 \times 10^{19}\text{m}^{-3}$ were still in agreement. Moreover, a recent fully automated linkage of BRAAMS and EIRENE, which cycles whenever sources alter by more than some tolerance, again tends to similar cool target plasmas.

Cross-section resolutions of cells up to each outside strike point are $ds_x^P \approx 8.25$mm; 2.5mm; 0.5mm, correspondingly $ds_x^F \approx 94$mm; 28.4mm; 5.9mm along the field. For $n_e = 1.2 \times 10^{21}\text{m}^{-3}$; $T_e = 3$eV, abundant thermal molecules from carbon plates have commensurate mfp's of $\lambda_{\text{mol}} \approx 0.8$mm. Resolution of EIRENE source terms on the mesh is demonstrated in Fig.4. Simultaneously, electron-electron mfp's are $\lambda_{ee} \approx 0.2$mm, so the essential fluid approximation of BRAAMS is also vitally supported. In contrast, eg $n_e \approx 5 \times 10^{20}\text{m}^{-3}$; $T_e \approx 20$eV would imply $\lambda_{\text{mol}} \approx 0.12$mm; $\lambda_{ee} \approx 14$mm, so cells matching source scales **could not** also conform to a BRAAMS thermalised plasma.

Key deficiencies remain in the model, including absence of edge electric currents & plasma poloidal drifts, consistent impurity release & consequent strong radiation cooling. Real oblique target geometries are being incorporated by a LINDA staggered orthogonal grid, as illustrated in Fig.5. In any event, major levels of uncertainty remain in basic factors, such as transport coefficients, power distributions, radiation losses, and limitation of conductivity ($\hat{T}_e^{\text{TOL}} \approx 7.2$eV; $\hat{n}_e^{\text{TOL}} \approx 6.5 \times 10^{20}\text{m}^{-3}$ when $\alpha = 1$ with Hotston recycling). Precision of results clearly cannot exceed these governing errors.

4 Summary

The BRAAMS edge plasma and EIRENE recycled neutral gas transport models have been linked together in axisymmetric geometries defined by the LINDA orthogonal discretisation code. Trials for an illustrative ITER 22MA case with plausible pumping suggest a very cool ($\approx$ 3eV), dense ($\gtrsim 10^{21}\text{m}^{-3}$) plasma facing the adjacent target. Similar calculations with a simpler, analytical recycling model seem in agreement. Mesh resolutions are also in compliance with scale lengths both of recycling sources and the fluid plasma approximation. Major uncertainties in physical factors, however, imply results **cannot** be regarded as more precise than these supervening levels.

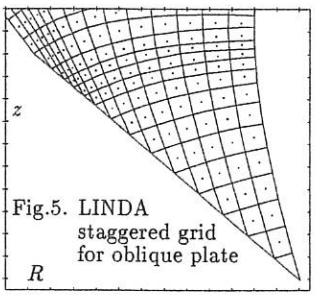

Fig.5. LINDA staggered grid for oblique plate

References

1. G P Maddison, NET rpt EUR-FU/XII-80/87/82
2. B J Braams, Culham Lab rpt CLM-P752
3. B J Braams, NET rpt EUR-FU/XII-80/87/68
4. D Reiter, KFA rpt JUL-1947
5. E Cupini et al, NET rpt EUR XII - 324/9, 1983
6. D Heifetz et al, J Comp Phys 46(1982)309
7. R Chodura, Phys Fluids 25(1982)1628
8. Culham rpt on NET contract 406/89-12, 1991

RETENTION OF GASEOUS IMPURITIES IN THE DIVERTOR OF DIII-D

S.Lippmann, A.Mahdavi, General Atomics, San Diego, California, USA
J.Roth, K.Krieger, G.Fußmann, Max-Planck-Institut für Plasmaphysik
EURATOM-Association, 8046 Garching, Germany
G.Janeschitz, JET Joint Undertaking, Abingdon, UK

Introduction:

The retention capability of a divertor configuration for recycling impurities, such as hydrocarbons produced at the divertor plate, but also of He ions originating from D,T-fusion processes in the main plasma, is one of the most important issues for future devices. This can be investigated by the injection of short gas puffs into the main plasma. The use of a heavy inert gas as a test impurity has the advantage that it can be spectroscopically investigated both in the plasma boundary and in the center without using charge exchange recombination lines, which are only available during neutral beam injection (NBI). Therefore, in the present study Ar was introduced in the main vessel of DIII-D, and its time dependent concentration balance between main plasma and divertor was studied by monitoring the Ar VII, VIII, XV, XVI lines. From this balance a divertor time constant, t_D, could be obtained and its variation during NBI studied.
Similar experiments have been previously performed in ASDEX /1,2/ and JET /3,4/ and allow a comparison of different divertor configurations.

Experimental:

The investigations were performed in standard deuterium discharges in DIII-D. During the stable ohmic phase of a 1.5MA single-null divertor discharge, B_t=2.11T, a=64.3cm, a 10ms pulse of a dilute Ar/D_2 mixture was injected near the midplane at 1800ms. The central Ar concentration reached equilibrium in just over 100ms in a trace amount which did not significantly affect T_e and n_e. The argon level was monitored using line emission of low and highly ionized Ar with a dual SPRED spectrometer. At 2500ms NBI was applied at a level of 2 MW and increased at 3100ms to 4 MW. The time dependence of the n_e and T_e profiles as measured in the plasma center by ECE emission and through the plasma boundary using multipulse Thomson scattering is shown in fig.1. These profiles were further used as input data for the time dependent code simulation of the Ar line signals.

Theoretical description:

A simple analytical model can be used to estimate the influence of various time constants on the impurity concentrations (fig. 2). A confined plasma with a total number of ions, N^+, loses ions into a divertor chamber according to a plasma confinement time constant t_p. The ions are neutralized at the divertor plates and a neutral flux returns to the main plasma with the divertor time constant t_D. Simultaneously, neutral atoms can be pumped by external pumps with a time constant t_{pump}. One gets thus a set of coupled equations fot the temporal behaviour after applying the impurity pulse

$$dN^+/dt + N^+/t_p = N^o/t_D \qquad (1a)$$

$$dN^o/dt + N^o(1/t_D+1/t_{pump}) = N^+/t_p \qquad (1b)$$

These equations for the number of ions in the plasma yield solutions in terms of a sum of two exponentials with a short and a long time constant according to

$$1/t_{short} = 1/2t + 1/2t\sqrt{1-4t^2/t_p t_{pump}}$$

and

$$1/t_{long} = 1/2t - 1/2t\sqrt{1-4t^2/t_p t_{pump}} \qquad (2)$$

where $1/t = 1/t_p + 1/t_D + 1/t_{pump}$

Simple solutions are only possible if the divertor retention time is much smaller than t_{pump}. Usually, the pumping time for inert gases is long compared to the plasma confinement or divertor retention time. For the condition of $t_{pump} >> t_D >> t_p$ it can be shown that t_{long} is dominated by t_{pump}, while t_{short} will essentially be given by t_p. If, however, all time constants are of the same magnitude, more complicated dependencies must be expected.

The above simplified analytic approximations give good insight in the asymptotic behaviour. For a more detailed simulation of the transport in the main plasma the one dimensional impurity transport code ZEDIFF /5/ was used in a modified version that allows to consider divertor recycling /1/. Consistent with eq. (1b) the ion flux out of the divertor is assumed to N^o/t_D. The background plasma is simulated using experimentally determined n_e and T_e profiles (fig 1).

Main input parameters into the transport code are the cross field diffusion coefficient, D, and an inward drift velocity, v. These quantities can be experimentally obtained from the simulations of laser blow-off experiments of non-recycling impurities. In the case of the present investigations a sudden Cu burst during the ohmic phase of a similar discharge was used to obtain the values for D and v (fig 3). Radially independent values of D = 7000cm^2/s were obtained, while for the NBI phase in the L-mode an enhanced diffusion was approximated by D = 14000cm^2/s, in general agreement with previous investigations at DIII-D /6/. For both regimes an inward drift velocity $v = -4D/a(r/a)^3$ was used, which fitted slightly better than a linear inward drift with a peaking factor of 2. Further input parameters into the code are the divertor retention time constant, t_D, and the pumping time constant, t_{pump}, which were used as fitting parameters to the Ar line signals. Main output parameters are the traces of selected line intensities that can be compared to experimental data, the impurity content in the main plasma and divertor and the global impurity confinement time.

Results and discussion:

The comparison of the code simulations to the experimental Ar XV and XVI line signals is shown in fig.4. As the absolute amount of injected Ar is not known, only the relative fitting of the initial peak to steady state behaviour was used to obtain t_D and t_{pump}. The long time decrease clearly indicated a divertor pumping time constant of about 1s, while the divertor retention time constant varied between ohmic and NBI phase. The best value for t_D in the ohmic phase was 130ms.

If t_D is not changed from ohmic to NBI phase, a decrease of the signal of the high charge states results due to an expulsion of the radiating shells to radial positions with smaller densities. In contrast, an strong increase of the line intensities is observed, which can only be simulated by a sudden decrease in t_D upon the onset of NBI to a value of 35ms. A similar, though much

stronger reduction has been reported from ASDEX /1/. However, in contrast to ASDEX, this reduction only applies for the first 150ms. After this period a recovery of t_D to a constant value of 70ms occurs.This indicates that with NBI the divertor temperature increases, which initially deteriorates the divertor retention. A subsequent increase of divertor density due to enhanced ionization improves the divertor retention again. The dependence of t_D on plasma density has been documented for ASDEX /1/. Upon the increase in NBI power at 3100ms the divertor retention time t_D decreases again to 25ms and does not recover within the investigated time interval.
A comparison of different divertor retention times for different machines is given in tab. 1

	DIII-D	ASDEX/1/	JET/3,4/
Ar ohmic	130	250	<400
NBI(L)	70	15	<400
He ohmic			300
NBI(L)			150

Ohmic divertor retention times are rather similar for all three machines. In relation to the much longer plasma confinement times in JET the same t_D results in a much higher impurity content in the main plasma. Consequently, the ratio of t_D/t_p determines the quality of the divertor configuration, while the ratio of t_{pump}/t_D is dominating the exhaust efficiency.
The above values can now be used for an estimate of the He concentration in the main plasma of an D-T burning fusion experiment. As an example, all parameters are taken from DIII-D and a He production rate is taken equivalent to a central plasma temperature of 15keV. The produced α-particles are added in the plasma center as an additional source term ϕ^+. With these assumptions the number of α-particles in the main plasma, in units of $\phi^+ t_p^\alpha$, is plotted in fig.5.
This can again be compared to the simplified analytic model. Therefore in eq.(1a) the source term ϕ^+ has to be added. Additionally, it has to be taken into account that the particle confinement time t_p^α for fusion α-particles is much longer, typically by a factor 100, than the global confinement time t_p for wall or divertor recycled impurities. In steady state the impurity content can then be written as

$$N^+ = \phi^+ t_p^\alpha \; (1 + t_{pump}/t_D \; t_p/t_p^\alpha) \qquad (3)$$

Curves for $N^+/\phi^+ t_p^\alpha$ are introduced in fig.5 for different values t_p^α/t_p. It can be seen that for DIII-D, as well as for ASDEX /2/, the values t_{pump}/t_D are of the order of 10. In this regime the central impurity content is of the order of $\phi^+ t_p^\alpha$ and cannot be reduced further by additional pumping. The resulting central He concentration is about 0.2% for DIII-D conditions.

References:

/1/ G.Janeschitz, G.Fußmann et al, Nuclear Fusion 26(1986)1725
/2/ J.Neuhauser, R.Aratari, M.Bessenrodt-Weberpals et al, IAEA-CN-53/A-5-52, Washington (1990)
/3/ G.Janeschitz, R.Giannella et al, 17th EPS, Amsterdam (1990)
/4/ G.Janeschitz, N.Gottardi, H.J.Jaeckel et al, these proc.
/5/ G.Janeschitz, L.B.Ran, G.Fußmann et al, IPP III/147 (1990)
/6/ M.Perry, GA-Report A19286 (1989)

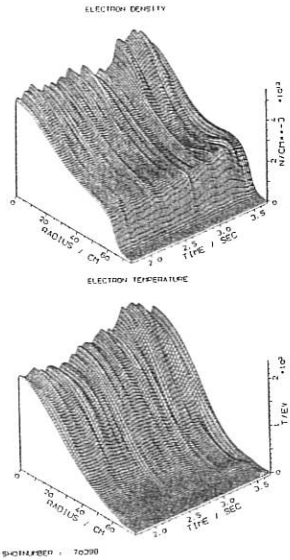

Fig.1: Time dependent electron density and temperature profiles

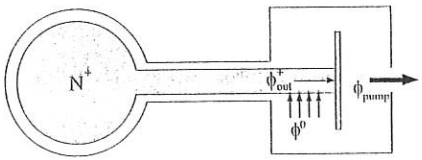

Fig.2: Simplified divertor model for analytical description

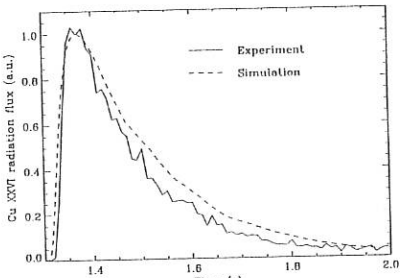

Fig.3: Fitting of Cu XXVI line calculation to copper-burst in ohmic phase

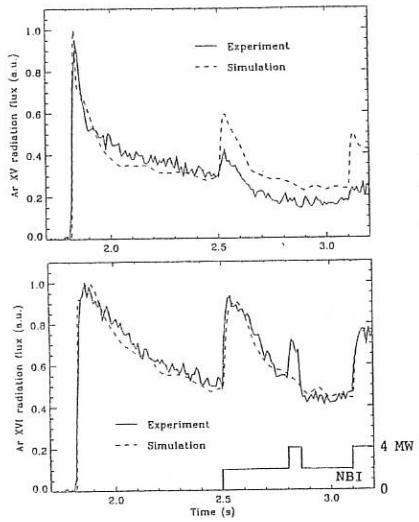

Fig.4: Comparison of Ar XV, XVI line intensities with code simulations.

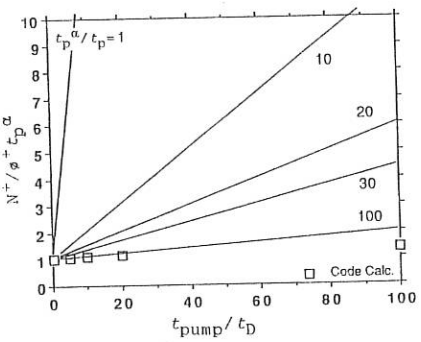

Fig.5: Dependence of the plasma He content on the ratio t_{pump}/t_D.

DIVERTOR PLATE BIASING EXPERIMENTS ON TdeV*

P. Couture, A. Boileau, R. Décoste, B. Gregory, C. Janicki, J.-L. Lachambre, D. Lafrance, D. Michaud, G.G. Ross, B. Stansfield, B. Terreault, C. Boucher, A. Hubbard, F. Martin, G. Abel, L. Gauthier, V. Glaude, E. Haddad, J. Kalnavarns, E. Knystautas, G. Le Clair, C. Liu-Hinz, H.H. Mai, R. Neufeld, D. Pinsonneault, N. Richard, A. Sarkissian, M. St-Onge, D. Whyte, W. Zuzak

Centre canadien de fusion magnétique, Varennes, Québec, Canada J3X 1S1

ABSTRACT

Divertor plate biasing on TdeV (Tokamak de Varennes) is used to affect the impurity influx and possibly influence the transport in the edge region [1]. Electrostatic microturbulence inside the separatrix is significantly reduced with either bias polarity in agreement with velocity shear stabilization. Biasing improves the divertor pumping efficiency for the top or bottom closed divertor chamber depending on the bias polarity, in agreement with the ExB/B^2 drift direction. Respectively, negative/positive biasing improves/degrades the plasma by reducing/increasing the carbon and CO fluxes, the loop voltage and the X-ray emissivity without noticable changes on the electron density or temperature profiles. The gradient density scale length near the separatrix, the poloidal rotation velocity near the edge, the heat pulse propagation speed and the sawtooth period and crash times are also affected by biasing.

INTRODUCTION

The electrostatic potential of the scrape-off layer is felt to play a role in determining both radial and poloidal particle flows in this region [1]. Plasma biasing can reduce sputtering or recycling at the walls, limiters [2] or divertor plates and, therefore, affect the impurity influx. Poloidal particle flows in the scrape-off layer, an important consideration for divertor efficiency, can also be strongly affected by local ExB drift or changes in scale length or other scrape-off variables. Finally, the electric field applied to the edge could positively influence the transport in the entire plasma region if the field modifies the structure or penetrates inside the separatrix.

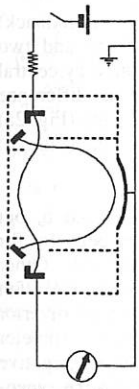

Figure 1

BIASING EXPERIMENT AND RESULTS

A schematic of the biasing experiment reported here is shown in Fig. 1. The neutralization plates of the double null poloidal divertor are electrically insulated on TdeV [3]. In the present case, the outer upper plates can be biased with either polarity, producing a radial electric field between the separatrix and the grounded walls. Other plates, left at a

* Supported by Atomic Energy of Canada Limited, Hydro-Québec and the Institut national de la recherche scientifique.

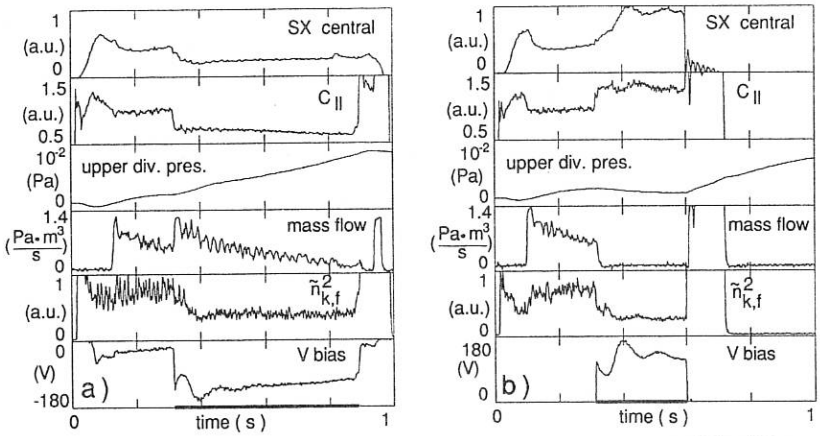

Figure 2 Soft X-ray (center), wall CII emission, upper divertor pressure, gas puffing rate, density fluctuations and measured bias versus time for (a) negative and (b) positive bias.

floating potential, are used to ascertain that the separatrix is indeed an equipotential and to measure the effective plasma bias voltage with respect to the wall. This plasma bias voltage is defined as the floating potential of other plates minus the potential without bias. The plasma bias voltage was varied from -200 to +150 V on the experiments reported below. On good discharges (without arcing), floating potential differences between these other plates do not exceed ±20 V, verifying that the plasma is an equipotential.

Biasing experiments were performed at a constant plasma density (with gas feedback) and plasma current (I_p= 210 kA, q_ψ(95%)=3.1 at B_ϕ=1.3 T and R_p= 0.87 m), and two differents toroidal field (1.3 and 1.5 T) [2]. The electron temperature, as measured by central and off-axis ECE, did not change significantly during biasing. Figure 2 shows the difference between negative and positive biasing on some reference signals. Negative biasing (Fig. 2a) was volontarily terminated before the end of the discharge, whereas positive biasing (Fig. 2b) ended on an arc near 600 ms.

The soft X-ray signal is shown for the central cord in both Figs. 2a and b, but detectors at other radial positions (5 complete arrays on TdeV) reveal a similar behavior for the entire profile. The CII signal represents the C influx from the inner graphite wall. Other components of the liner facing the plasma in the main chamber are made of Inconel with guard graphite limiters at critical locations. Pressures are measured in both closed divertor chambers and the main chamber by fast shielded gauges and a quadrupole mass spectrometer [4]. Figure 2a shows a significant increase of the upper divertor pressure during negative biasing only. When the negative bias is applied, the feedback system opens the piezo-electric valve (mass flow in Fig. 2a) to maintain the density at 2.2 x 10^{19}m^3 during all the discharge. This produces an increase of the pressure in the main chamber which later recovers to a lower value. Positive biasing is seen to close the feedback valve to maintain the same density in Fig. 2b. The turbulence level is obtained from coherent scattering on electron density fluctuations propagating in the poloidal direction with k=30 cm^{-1} and f=240

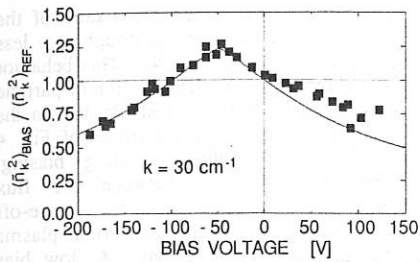

Figure 3 Variation of the turbulence level during biasing normalized to the level associated with a reference pulse as a function of the plasma bias voltage.

kHz in Fig. 2. Other frequencies and wave numbers probed show similar behavior, as discussed below. Finally, Fig. 2 shows the biasing voltage, measured on the bottom divertor plate. For this particular case, the nominal plasma biasing voltage corresponds to 130 V, as defined above.

Figures 3 and 4 show the variation of significant parameters as a function of the plasma bias voltage. The density gradient scale length just ouside the separatrix in Fig. 4 is inferred from profiles such as those of Fig. 5, obtained from Li laser ablation injection into the scrape-off layer. Profile deconvolution relies on a weak dependance on the electron temperature not known in this region. The poloidal velocity of Fig. 4 is deduced from the Doppler shift of a CIII line (6205.6Å). The deconvolution process averages over the biasing plateau and takes advantage of a complete poloidal view of the plasma, obtained through imaging onto the entrance slit of a spectrograph coupled to a camera. The plot of the rate of change of the divertor pressures in Fig.4 avoids the distortion of the pressure rise in the unpumped divertor chambers and is more representative of the net fluxes going into the divertors.

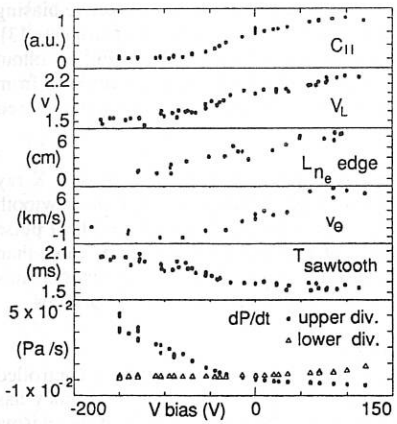

Figure 4 Wall CII emission, loop voltage, density gradient scale length at the separatrix, poloidal rotation speed, sawtooth period and rate of change of upper and lower divertor pressures versus plasma bias voltage.

DISCUSSION

A striking point of Fig. 2 is the strong reduction of the turbulence level for either polarity. The full line through the data points in Fig. 3 is a parameter fit based on the theory of velocity shear stabilisation [4]. Maximum turbulence does not correspond to $V_{bias}=0$ in Fig. 3. This is interpreted as inherent velocity shear stabilization, as suggested by poloidal velocity measurements, which confirms the finite rotation of the unbiased ohmic plasma (Fig. 4). The rotation velocity observed for positive and small negative biases is in the electron diamagnetic direction and opposed to the ExB/B^2 drift direction inferred below for the scrape-off layer. These measurements indicate that an electric field applied outside the plasma affects the rotation velocity inside the separatrix, suggesting that the electric field was able to penetrate or to modify gradients inside the plasma.

The pressure ratio between the upper divertor box and the main chamber increased from 10 without applied biasing, up to 90 during negative biasing; the lower divertor pressure barely changed during that time. The contrary is observed when the biasing polarity is

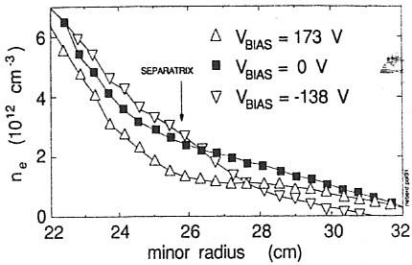

Figure 5 Electron density profiles for three biasing voltages values with B_ϕ=1.5 T.

reversed, i.e., the compression ratio of the lower divertor increases, although at a less pronounced rate (see Fig.4). This behavior is in agreement with the direction of particle flow expected from the ExB/B^2 drift in the scrape-off layer. The net fluxes of Fig. 4 (dP/dt), taken early on during biasing, represent differences between the flux recycling from the plate in the scrape-off layer and the gas flowing back to the plasma through the divertor throat. At low bias voltages, the compression ratio reaches an equilibrium during biasing (dP/dt=0), whereas this is not the case at higher voltages because of the finite biasing pulse duration, i.e., dP/dt remains >0 as shown in Fig.2 near the end of the biasing pulse.

Depending on the polarity, the impurity influx and content of the plasma appears to be improved or degraded by biasing, as suggested by the voltage loop and C influx, strongly correlated in Fig.4, and by the soft X-ray emission (Fig. 2). Improvement in the screening ability of the edge can explain the reduction: higher divertor pumping efficiency through ExB/B^2 flows, reduction in ion induced wall sputtering by an electrostatic barrier, and reduction in the scrape-off layer scalelength, increasing the distance to the walls. Alternatively, increased sputtering and gradient scalelength could explain the positive biasing results. An important point to be noted is that, contrary to limiter biasing experiments [3], where the density increased during biasing, the density would have decreased in Fig.2 without gas puffing compensation. This strongly suggests that recycling was indeed transfered from the limiter to the divertor plate, where it can be decoupled from the main plasma in a closed chamber geometry.

The center of the plasma was also affected by biasing, as evidenced by soft X-ray emissivity results. Over the positive to negative bias voltage variation of Fig.4, the sawtooth period (Fig.4) and crash time each increased by 20 % and the sawtooth induced heat pulse velocity was reduced by 40 %. Meanwhile, the inversion radius did not change by more than 0.5 cm, corresponding to the resolution of the diagnostic. It can not be determined at this point whether these changes are related to transport or modifications of the Z_{eff} profiles.

CONCLUSION

The electrostatic turbulence and the scrape-off layer scalelength have been controlled over a wide range by varying the plasma bias voltage. The divertor pumping efficiency has been improved several fold by the directional ExB/B^2 flow. Biasing also shifted the plasma erosion and recycling from the walls or limiters to the divertor plates, a region decoupled from the main plasma in a closed divertor configuration.

References:

[1] R.D. Stambaugh et al., Phys. Fluids B2 2941 (1990).
[2] P. Couture, B. Terreault et al. J. Nucl. Mater 176-177, 825 (1990)
[3] R. Décoste et al., this conference
[4] A. Boileau, P. Couture, D. Lafrance, J.L. Lachambre, B.L. Stansfield. 4th Transport Workshop, Austin, Texas, March 1991.

THE SIMULATION OF THE ITER DIVERTOR PLATES EROSION IN STATIONARY PLASMA

N.V.Antonov, A.M.Muksunov, V.A.Nikiforov, V.B.Petrov, V.I.Pistunovich, B.I.Khripunov, V.V.Shapkin

Kurchatov Institute of Atomic Energy, Moscow, USSR

1. Introduction. The problem of the divertor development for the ITER is put by very high heat loads (up to 15 MW/m^2) and high erosion rates of the plates structures. The plates are considered to be under floating potential (negative). Ions moving to the plates are accelerated by the potential difference $U=-3.5T_e$ thus causing destruction of the material if their energy is higher than the threshold value. One can reduce the energy of ions near the plates by lowering T_e. This is possible in particular conditions of particle recycling when the gas pressure near the plates is increased (gas divertor). In this report is considered the possibility to diminish erosion of the material by applying voltage between the reactor chamber and the plates [1] and some aspects of plasma flow interection with the wall.

2. Experimental technique. These experiments have been carried out in stationary plasma. The beam-plasma discharge in crossed electric and magnetic fields is used as plasma source [2,3]. Two devices have been used: SPRUT-4 and LENTA-M. The cylindrical electron beam of the SPRUT-4 device (fig.1) passes along the axis of the vacuum chamber in the magnetic field B= 0,1÷0,2 T. The electron beam energy is up to 10 keV, its power reached 25 kW. The chamber diameter was 16 cm, the beam diameter ~ 1cm. The chamber was separated in length by cross insulator walls. One of the sections (discharge zone)100 cm in length is filled with gas (deuterium) to pressures of $p< 10^{-3}$ Torr. When applying voltage ~100 V between electron beam and chamber one obtains in the discharge zone plasma filling the space between the beam and the chamber wall. The cross insulators of the discharge zone were perforated so that plasma annular flows 1÷3 cm thick passed to the neighbouring sections of the chamber. These sections could be fed by additional gas.

The LENTA-M device is 175 cm in length. Its other parameters are similar to those of SPRUT-4.

Plasma density and temperature measurements have been made in the discharge zone and in plasma flows by single and double Langmuir probes. Spectroscopy was developped for measurements of ionization conditions and plasma composition.

3.Results. 3.1. Target in plasma flow.

Probe measurements in the deuterium plasma of the SPRUT-4 device have given the following values for the discharge zone: $n<10^{13}$ cm^{-3}, T_e = 15÷30 eV. Tungsten and copper targets were exposed in plasma flows, the exposition time being t=0,5÷1,5 hours. The weight losses were determined after that. Measurements have been made for different values of the target potential. The dependence of the erosion rate δ of the target material (W,Cu) on target potential has been obtained. The erosion rate δ is given by [4]:

$$\delta = 0.6*10^{-20}\ A\ S_k\ \Sigma j_k \quad [g/h\ cm^2], \quad (1)$$

where A is atomic number, $\bar{S}_k$ is the average sputtering yield for the k-ion variety, j_k is the particle flow density in cm^{-2}s^{-1}. One obtains for tungsten (A=184) and for plasma flow parameters mentioned above $\Sigma_k j_k = 4*10^{18}$ cm^{-2}s^{-1}:

$$\delta_W = 0.6*10^{-20}\ 184\ 4*10^{18}\ \bar{S}_k^W \simeq 4.4\ \bar{S}_k^W ,$$

and for copper target (A=64), $\Sigma_k j_k = 5*10^{17}$ cm^{-2}s^{-1}:

$$\delta_{Cu} = 0.6*10^{-20}\ 64\ 5*10^{17}\ \bar{S}_k^{Cu} \simeq 0.2\ \bar{S}_k^{Cu} .$$

The $\delta(U)$ values are given in fig.2.3. One can see that when passing from floating potential point $U_t=U_{fl}<0$ to the point $U_t=0$ the erosion rates δ_W and δ_{Cu} (and the sputtering yield S_k according to (2),(3)) becomes a few times smaller. In the range of positive potentials the erosion rate is not changed practically, but electron current increases drastically.

3.2.Plasma flow interaction with the cross insulator wall and gas.

As mentioned above in recycling conditions and in increased gas pressures in the vicinity of the plates one can expect heat load on them to be reduced. This subject was searched on the Lenta-M device.

Plasma parameters (n_e, T_e) in the flow going from the discharge zone were measured, the annular flow having the width 5 cm. The axial length of the flow was Δ=35cm (from Z_0=35 to Z_0=0cm). Plasma parameters were obtained for three points Z_1= 5cm, Z_2= 35cm and Z_3= 65cm (the distance from the wall).

The values n_e and T_e in the points $Z_{1,2,3}$ are given in fig.4, deuterium was used as working gas. These measurements were made for r=5cm (distance from the chamber axis). For Z =65cm

(discharge zone) $n_e=4*10^{11}cm^{-3}$, $T_e=30$ eV. For $Z_1=5cm$ (near the wall) $n_e=1.4*10^{12}cm^{-3}$, $T_e=16$ eV. Simulteneous measurements show the increase of the gas pressure in the flow section(Z_1) with respect to the discharge zone (Z_3) approximately 6 times.

Also investigations were made with neon plasma. Neon neutral and ion lines intensities were measured optically in the discharge zone (Z_3)and near the cross wall (Z_1) It has been observed in particular that neutral line intensity ($\lambda=3520A^{O}$) in the wall region is higher (a few times) than that in the discharge zone that reveals the plasma flow neutralization on the wall. These measurements correspond to those in deuterium.

Some preliminary experiments on the annular plasma flow interaction (0.5cm width) with gas target were undertaken. The additional gas inlet was possible in the section where plasma flow entered without changes of plasma parameters in the discharge zone (plasma source). When changing deuterium pressure from 1mTorr to 10mTorr we observed simultaneous decrease of plasma density and temperature in this section (n_e:4 times, T_e:1.5 times).

4. Summary. These experiments show that grounding of the target reduces the erosion rate of the target material in plasma flow a few times, i.e. according to [1] the potential near the target is changed. The electron current to the target in this case is not high.

The investigations of plasma flow interaction with the cross wall show the increase of plasma density (3 times approximately) and electron temperature (2 times) for the distance Z<30 cm from it in the conditions of recycling.

References.

1.V.I.Pistunovich, "On the possibility to reduce erosion of divertor plates in ITER", ITER-IL-PM-13-0-S-4, Garching, FRG, Jan.,1990.

2.K.K.Gadeev, E.M.Erastov, A.A.Ivanov,A.M.Muksunov, V.A.Nikiforof, V.V.Severny, B.I.Khripunov, V.V.Shapkin,"The space beam-plasma discharge generation in crossed fields", Sov.Journ.Doclady AN USSR, v.256,n 4, p.834-837, 1981.

3. K.K.Gadeev, A.V.Denkevitz, A.A.Ivanov, V.A.Nikiforov, V.V.Shapkin,"Spatial characteristics of the beam-plasma discharge in crossed electric and magnetic fields." Beutrage aus der Plasma Physik, Band 24, Heft 3, 1984.

4.V.A.Abramov, Yu.L.Igithanov, V.I.Pistunovich, V.A.Pozharov, Preprint IAE-4463/8, Moscow, 1982.

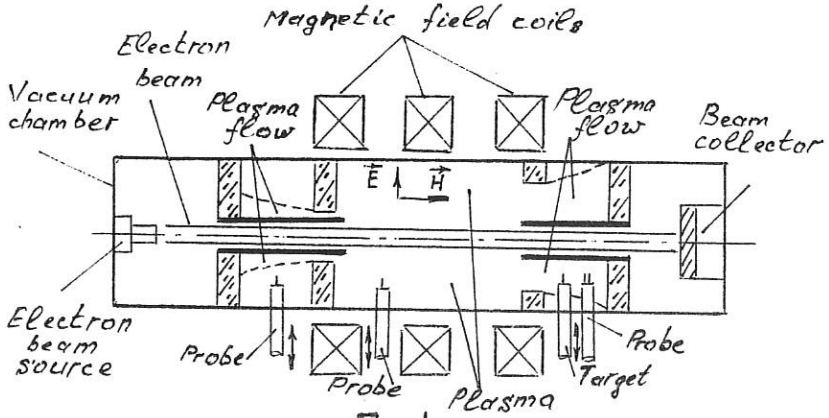

Fig.1

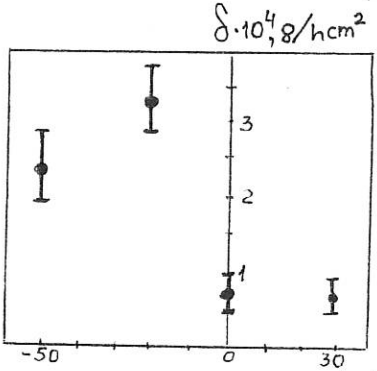

Fig.2

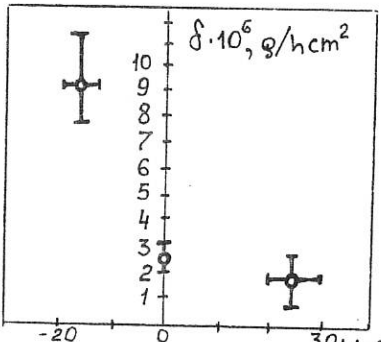

Fig.3

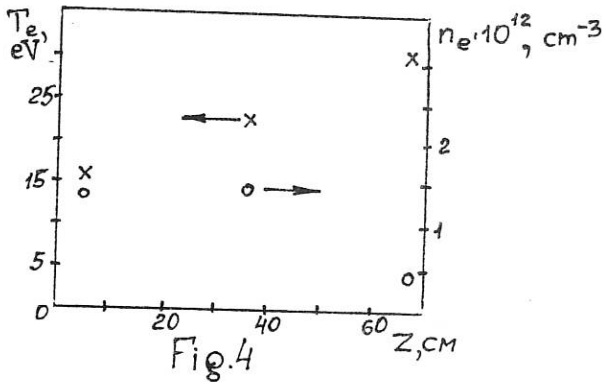

Fig.4

INFLUENCE OF KINETIC EFFECTS ON A SHEATH POTENTIAL AND DIVERTOR PLASMA PARAMETERS IN ITER

(A) S.I.Krasheninnikov, T.K.Soboleva

(B) Yu.L.Igitkhanov, A.M.Runov

Kurchatov Institute, Moscow, USSR

It was already noted *[1,3-5]* that strong inhomogenity of ITER divertor plasma parameters may be a reason of a pronounced deviation of a sheath potential U_d at a plasma-divertor plate contact from the local value $U_d \simeq 3.5T_d$ (T_d is an electron temperature in a vicinity of the divertor plate). This effect may badly influence the divertor plates sputtering resulting in a plasma contamination.

To obtain quantitatively an effect of superthermal electrons on a sheath potential kinetics of superthermal electrons in a divertor plasma was considered for the preset temperature $T_e(x)$ and density $n_e(x)$ profiles along the magnetic field lines (x-axis) *[2]*

$$v_x \frac{\partial f}{\partial x} - \frac{eE(x)}{m} \frac{\partial f}{\partial v_x} = St_e \qquad (1)$$

where: e,m are electron charge and mass respectively; St_e is a Coulomb integral; E(x) is an ambipolar electric field.

Equation *(1)* was solved numerically at length $x \in [0,L]$ for the following profiles $T(y)= T_e(y)/T_e(0)$ and $n(y)=n_e(y)/n_e(0)$:

$$T(y) = (1-(1-T_1^{7/2})y)^{2/7}, \quad n(y) = 1/T(y); \qquad (2)$$

where $T_1 = 0.1$.

A. Equation *(1)* was solved by means of stochastic differential equations method (by Artemjev method). Boundary conditions at both ends of the specified length were chosen from a condition of full reflection of an incident particle.

Solutions of Eq.*1* depends on plasma collisionality factor $G= \pi e^4 \Lambda n_e(0)L/(T_e(0)^2)$ (Λ is a Coulomb logarithm) and U_d value. Solving Eq.*1* we may obtain electron distribution function near the divertor plates ($y \equiv x/L = 1$) and then calculate heat (q_e) and particle (j_e) fluxes towards the divertor plates as functions of $U=U_d/T_e(0)$; $(j=j_e/n_e(0)(2T_e(0)/m)^{1/2}$,

$q=q_e/T_e(0)n_e(0)(2T_e(0)/m)^{1/2}$). It is to be noted that self-consistent U value is defined by ambipolarity condition for plasma flow toward the divertor plate ($j_e = j_i$). Eq.1 was solved for $Z_{eff} = 1,\ 1.5$; and for different collisionality factors $G \leq 15$ ($G \simeq 10^4 L_{[m]} n_{20}/T^2_{[ev]}$). For the chosen parameters dementionless ion flux towards the divertor plates in a local approximation was $3\ 10^{-2}$, and a sheath potential U= 0.35.

For the selfconsistent estimation of both U_d and $T_e(0)$ for preset q_e and $n_e(0)$ the following system of equations is to be solved:

$$F(G) \equiv \frac{q(G,U(G))}{G^{3/4}} = \frac{10^{-4} q_{e\,[MW/m^2]}}{(n_e(0)^7_{20}\, L^3_{[m]})^{1/4}}\ , \qquad (3)$$

$$T_e(0)_{[eV]} = 10^2 \left(\frac{L_{[m]} n_e(0)_{20}}{G} \right)^{1/2},\ j(G,U(G)) = 3\ 10^{-2}. \qquad (4)$$

Functions F(G) and U(G) are presented in Fig.1 ($Z_{eff}=1$). Substituting ITER divertor parameters ($n_e(0) \simeq 3.5\ 10^{13} cm^{-3}$; $q_e \simeq 400$ MW/m^2; $L \simeq 50$ m) in the rigtht-hand side of the relations (3,4) we obtain: $G \simeq 9$, $T_e(0) \simeq 150$eV, $U_d \simeq 70$eV (instead of $U_d \simeq 50$eV obtained in local approximation).

CONCLUSIONS (A). It is shown that for ITER relevant parameters kinetic consideration reveals strong influence of superthermal electrons on both divertor plasma parameters and sheath potential. The obtained sheath potential value is to be considered as lower estimation.

B. The same results can be readily obtained from the kinetic equation with the collision term in BGK approximation (see comparison with [6] in Fig.2). This approach gives the possibility also include the nonelastic collisions effect into the consideration by using the Born approximation:

$$St = \frac{n(x)\varphi_m - f}{\tau(x)} + \frac{I}{m_e} \frac{\partial}{\partial v} \left(\frac{\nu f}{v} \right),\ \nu = N(x) \frac{2\pi e^4}{m_e v} \frac{\zeta}{I} \ln\left(\frac{2\gamma}{m_e v^2} \right),$$

where $\zeta = 0.28$, $\gamma = 0.2$, $I = 13.6eV$ for hydrogen. The symmetric boundary conditions are set to each of the plates at the entry of sheath and have the form of mirror reflection for the electrons with the energy less than potential value. The main parameters are Knudsen's number for electrons $K = \lambda_s/L = 2/G$, and the average neutral density along the m. f. lines $\langle N \rangle$; n_s, T_s are plasma parameters at the separatrix, T_w-electron temperature at the plate. Selfconsistent potential drop value φ and T_s are defined by plasma flow ambipolarity at given electron energy flux to the plate.

As it follows from Fig.3 in the limit $K \ll 1$, $\langle N \rangle = 0$ the potential depends on the electron temperature at the plate and has its local value $\simeq 3.5T_w$. In the regimes with high K the suprathermal electrons from separatrix approach the plate, increasing the electron flux. The distribution functions turn out to be enriched with fast electrons in comparison with the equilibrium distribution. So in the range of changes in K from 0.1 to 1 (that corresponds to the increase in T_s from 100eV to 300eV at $n_s = 3.5\ 10^{13}\ cm^3$ for the ITER parameters the potential rises more than twice. A reduction in the potential with a rise in K is related with the absence of a source in a given statement of the problem. For the expected ITER parameters (at $K \leq 1$) it can be neglected. The potential drop with $\langle N \rangle$ related to the reduction of hot electrons. It is also to be noted that in the high recycling case the electron heat flux to the plate reduces to 200 MW/m^2. This corresponds $K \simeq 0.2$, $T_s \simeq 130$ eV, $e\varphi \simeq 5T_w$. At the expected range of electron heat flux $\simeq$ 200÷400 MW/m^2 the sheath potential turns out to be at the level 5÷7 T_w that corresponds T_s to ≃130÷180 eV (see Fig.4). In case $\langle N \rangle \simeq 50 n_s$ $e\varphi$ drops to $4 \div 5T_w$ (see Fig.5).

Conclusions (B). Our consideration shows that the kinetic effects on both divertor plasma parameters and sheath potential can rather precisely be obtained in the frame of BGK approximation. This effects are predominant in higher temperature regimes. Radiation and ionization decreases this deleterious effects.

References

1. Krasheninnikov S.I., "On the ITER divertor plasma parameters."; ITER report, ITER-IL-PH-13-9-S-14, June 1989.
2. Braginskij S.I.in: Review of Plasma Physics, V.1, 1963.
3. Takamura S., Physics Lett. A, 133, n 6, 1988, p 312.
4. Igitkhanov Yu.L.,in "Specialists working session on validation and development of edge plasma models",ITER-IL-PH-13-9-4, 1989.
5. Igitkhanov Yu.,Runov A.,Issues of Atomic Science and Technology,Series Thermonuclear Fusion, 1991,№.2,p.15
6. Krasheninnikov S.I., Soboleva T.K., "Influence of kinetic effect on a sheath potential and divertor parameters in ITER."; ITER report, ITER-IL-PH-13-0-S-14.

Figures captions

Fig.1 Functions F(G) and U(G).
Fig.2 Electron particle flux to the plate vs the potential drop; comparison between Fokker-Planck (dashed line[6]) and BGK (solid line) approximation, $T_s/T_w = 10$.
Fig.3 Potential drop vs Knudsen's number for a different $\langle N \rangle$.
Fig.4 Sheath potential and temperature at midplane selfconsistent with the electron heat and particle flux to the plate; $\langle N \rangle = 0$, $T_s/T_w = 10$.
Fig.5 The same as in Fig.4; $\langle N \rangle = 50 n_s$.

Fig.1

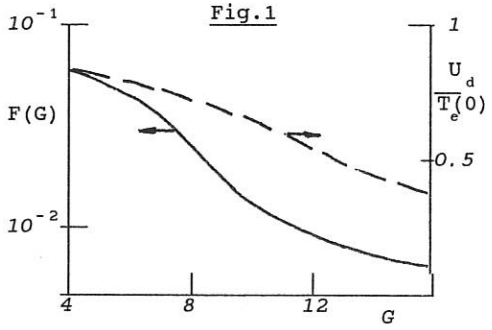

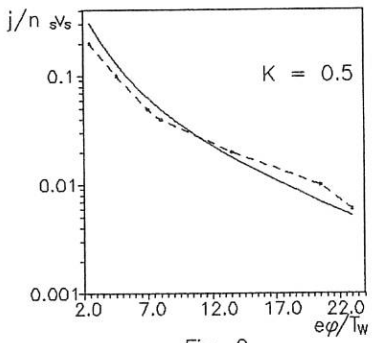

Fig. 2

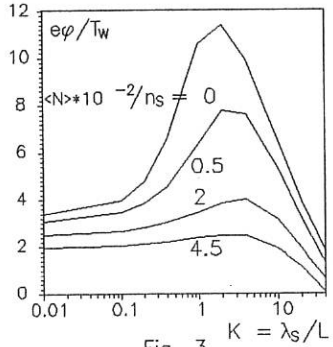

Fig. 3

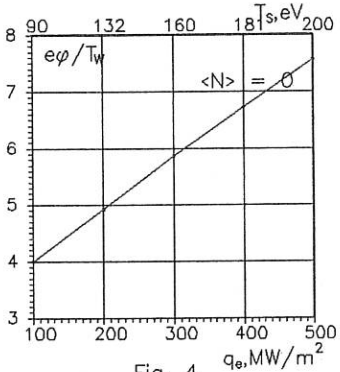

Fig. 4

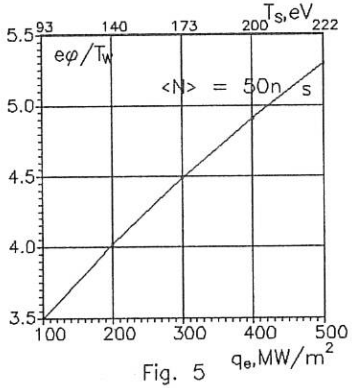

Fig. 5

CARBON RADIATION IN THE VICINITY TO THE NEUTRALISATION PLATES

V.A.Abramov, N.N.Brevnov, V.I.Pistunovich, S.B.Stepanov, L.N.Khimchenko

I.V.Kurchatov Institute of Atomic Energy, Moscow, USSR

As known, the reradiation of energy in the divertor volume is one of the possible ways of reducing the specific heat loading to the divertor plates of the ITER reactor.

The existing calculations of radiating power from a plasma with vareous impurities show, that the radiating power turns out to be insufficient for the complete reradiation of energy flux entering a divertor at the plasma parameters characteristic for the divertor zone, although the radiation loss power rises with a reduction in the electron temperature [1]. One should note, that practically all the calculations of radiating power loss are done in the corona approximation, when it is considered that the main role in the balance equation for ions of vareous multiplicity, as well as that in the balance equation of population levels, is played by atomic processes,the space and time effects are neglected. However, in the zone nearly the divertor plates the situation can be changed, since the escape of charged particles to the divertor plates and the emergece of neutral atoms from them play an important role. In this case, noticeable deviations from the corona model are possible that, in its turn, can result in a change in the calculated power reradiated in the divertor channel.

At present there are some models for calculating the radiating power loss, taking account of a deviation from a

corona state. A similar model is given in [2] in detail. The direct experimental verification of the mentioned model applicability to representation of plasma parameters in a divertor channel is of interest. Such studies were done at TVD tokamak [3].

These investigations were based on a temperature dependence of relative carbon line intensities CI, CII, CIII, in a plasma within the input channel of the TVD pump limiter, close to the neutralization plates. Channel was ≃ 6cm long, ≃ 1.5cm wide, the neutralization plates material - stainless steel. The plasma parameters in the input channel was: n_e = (0.5÷2.0)$10^{12}cm^{-3}$, T_e = 15 ÷ 45 eV, CO_2 gas was puffed into the pump limiter and an increase of optical lines was registrated.

The intensity of any spectral line I^z_{ik} is represented by the following expression:

$$I^z_{ik} = n_e n_{z,o} < \sigma v_{io} > \Delta E_{ik} \qquad (1)$$

where ΔE_{ik} is the transition energy for the corresponding spectral line, $< \sigma v_{io} >$ is the rate of excitation for the upper level i of the transition under consideration from the ground state, $n_{z,o}$ is the density of z-charged ions in the ground state.

The numerical calculations based on the model described in [2] allow one to obtain the temperature dependences of carbon ions density n_{c^+} and $n_{c^{++}}$ for various values of the $n_e\tau$ parameter; in this case, when $n_e\tau < 10^{12}$ $cm^{-3}s$, the results of calculations noticeably differ from the corona model predictions. Thus, substituting the calculated values of n_{c^+} and $n_{c^{++}}$ into (1) and calculating the values of $< \sigma v_{10} >$ for the spectral lines CII (λ = 4267Å) and CIII (λ = 4647Å) [4], one can obtain the parametric dependences of the I_{CII}/I_{CIII}

one can obtain the parametric dependences of the I_{CII}/I_{CIII} ratio on T_e for various $n_e\tau$ values.

For comparison of the I_{CII}/I_{CIII} ratio obtained from calculations with an experimental one one should estimate the value of $n_e\tau$ parameter, really observed in the experiment. One should note that in a given case the τ parameter has the meaning of an escape time for the corresponding carbonic ion from the zone, where a spectral lines emission is registered.

The C^+ ions departure time τ_{out} is found from the balance equations, taking account of atom ionization, $C^o \rightarrow C^+ + e$, C^+ ionization, $C^+ \rightarrow C^{++} + e$, C^+ escape from the radiative zone, and has the expression $\tau_{out} = n_{C^+} / n_e n_{C^0} \langle\sigma v\rangle_{ion}$. Recombination is negligible in a given case. The Fig.1 show the dependence of τ_{out} on plasma temperature.

Experimental values of the I_{CII}/I_{CIII} ratio as well as the theoretical parametric dependences of a given one on T_e are shown in Fig.2. The comparison between these values show that there is a good agreement between the theoretical snd experimental values of $n_e\tau$. This confirms the results, obtained on the basis of the model proposed for ITER [2].

1. R.V.Jensen, D.E.Post, W.N.Grasberger et al.
Nucl.Fusion 17, 1187(1977)
2. V.A.Abramov, V.I.Pistunovich
Contributions to plasma physics v.30, p.59 (1990), N1.
3. A.V.Bortnikov, et al., Preprint IAE-4554/8, Moscow, 1988.
4. L.A.Wainstein, V.P.Shevel'ko
"Struktura i characteristyki ionov v gorjachej plazme"
M., "Nauka", 1986. (in Russian)

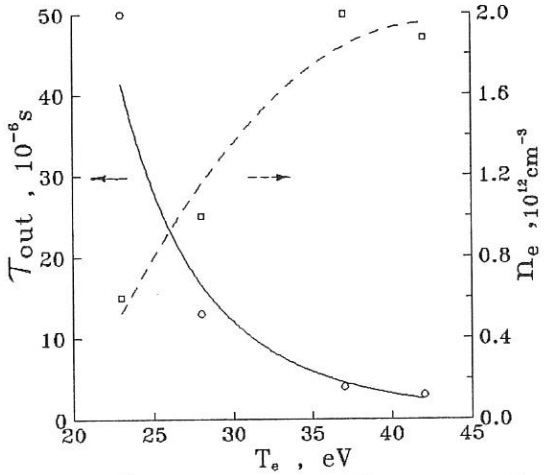

Fig.1. C^+ ions departure time τ_{out} and electron density n_e vs electron temperature inside the channel.

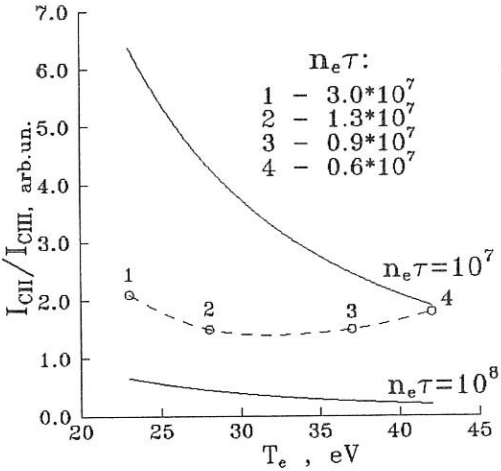

Fig.2. I_{CII}/I_{CIII} spectral line intensity ratio vs electron temperature inside the channel: (-) -model, (--) -exper.

AN ANALYTICAL MODEL FOR RETENTION OF DIVERTOR IMPURITIES BY FORCED FLOWS

G. C. Vlases and R. Simonini

JET Joint Undertaking, Abingdon, Oxon. OX14 3EA, U.K.

I. Introduction In this paper the retention of target produced impurities in a pumped divertor with "externally recirculated" or "forced flow" is studied using an analytical model. The results are compared with those from a detailed numerical study which has been previously reported [1,2]. The dominant forces acting on impurity ions in a scrape-off layer (SOL) are the ion thermal force, directed away from the divertor, and the ion friction force, directed towards the divertor. In steady state, an equilibrium is established in which the impurity pressure gradient balances the difference between these two forces, which is described by the equation for impurity density, n_z:

$$\ell n\left[\frac{n_z(s)}{n_z(o)}\right] = -\int_o^s F_{fi}\,ds + \int_o^s F_{T_i}\,ds \qquad (1)$$

where

$$F_{fi} = \frac{Z^2 C_f (1-f_v)\Gamma(s)}{T_i^{5/2}(s)} m^{-1} \quad , \quad F_{Ti} = \left(1.75\ Z^2 - 1\right)\frac{1}{T_i}\frac{dT_i}{ds} m^{-1} \qquad (2)$$

are the local inverse scale lengths associated with the friction and thermal forces. Here s is the distance along a flux tube, measured from the target plates, $f_v = v_z / v_i = o$ except in the impurity ionization region near the target, $\Gamma(s) = n_i(s)\, v_i(s)$ is the hydrogen flux, $T_i(s)$ is the hydrogen ion temperature, and $C_f = (1.2 \times 10^{20})$ for T_i in ev. Impurities will be said to be retained if $n_z(L)/n_z(0) = e^{-3}$, where L is the field line distance to the SOL stagnation point.

II.The Functions Γ and T_i. The integrals in eq. (1) can be evaluated provided the hydrogen source distribution, which determines Γ(s), is specified and the ion temperature $T_i(s)$ is known. In the code work, the sources are calculated from a 2D Monte Carlo package. In the analytical model, we represent Γ by the function, sketched in fig. 1,

$$\Gamma = \Gamma_t\left[(1-\varepsilon)e^{-s/s_i} + \varepsilon\right], \quad o < s < s_x \qquad (3)$$

where the exponential term arises from local (target) recycling of hydrogen over a distance s_i, and the second term is a constant flux which could be produced, for example, by withdrawal from the target region and reinjection, at a point s_x (e.g. the x-point), of a certain fraction ε of the target flux, Γ_t. Γ_t is determined primarily by the the SOL power flow and the stagnation SOL separatrix density,

n_b. We refer to the case $\varepsilon=0$ as "conventional" divertor operation, and the case $\varepsilon>0$ as that of "forced flow" or "external recirculation".

The ion temperature is calculated from a simple energy balance which incorporates conduction and convection, but neglects electron-ion transfer:

$$K_{oi}\, T_i^{5/2} \frac{dT_i}{ds} = q_i - \tfrac{5}{2}\, T_i(s)\, \Gamma(s) \qquad (4)$$

where q_i is the SOL ion power flux density and $K_{oi}T_i^{5/2}$ the ion parallel thermal conductivity. The solution to this equation for the assumed form of Γ given by Eq. (3) is sketched in fig. 2, where $T_d = T_i$ at s=o. $T_i^{7/2}$ vs. s is flattened near the origin and varies linearly with s to a distance of order $s_o/\varepsilon^{7/2}$, with $s_o = (2/7)\, K_{oi}\, T_d^{7/2}/q_i$, after which it approaches a constant value $(T_d/\varepsilon)^{7/2}$ asymptotically. For the linear portion, the slope is $(2/7)\,(q_i/K_{oi})\,(1-\varepsilon)$. I.e. the temperature profile, even in the presence of moderate convection, approximates a pure conduction profile with $q_{eff} = q_i\,(1-\varepsilon)$ over the range of s indicated.

III. Local Recycling Only, the "Conventional Divertor" Case. For the case where $\varepsilon=0$ and $\Gamma=\Gamma_t\, e^{-s/s_i}$, we take $T_i(s)$ = const. = T_d in the integral of F_{fi}, since the integrand goes to zero exponentially for $s>>s_i$, but we retain the spatial variation of $T_i(s)$ in evaluating the F_{Ti} integral. Equation 1 yields, for $n_z(L)/n_z(o) \le -3$,

$$\frac{C_f(1-f_v)Z^2\Gamma_t s_i}{T_d^{5/2}} \le \left(1.75\, Z^2 - 1\right) \ell n \frac{T_b}{T_d} + 3 \qquad (5)$$

where $T_b = T_i(L) \approx [(7/2)(q_i\, L/K_{oi})]^{2/7}$. Using $\Gamma_t = n_d\, C_o\, T_d^{1/2}$, with $C_o = 1.3 \times 10^4$ m/s.(ev)$^{1/2}$ (deuterium) and n_d the divertor ion density, and approximating s_i by $0.25/(n_d \times 10^{-20})$ m, equ. (5) can be rewritten

$$T_d^2 \le \frac{0.25\, C_o C_f Z^2 (1-f_v)}{14.8\, \ell n\,(T_b/T_d) + 3} \qquad (6)$$

This equation, which depends only weakly on q_i through the T_b term, gives the required divertor ion temperature for retention of impurities in the absence of forced flow; we find T_d < 20 ev for JET conditions (5MW<P_i<20 MW). This condition on T_d imposes a relationship between n_b and the SOL ion power, P_i. Using a simple SOL model similar to that proposed by Lackner [3] yields

$$n_{b,\min} = \frac{q_i}{\left(\frac{7}{2} q_i\, L/K_{oi}\right)^{2/7} C_o T_d^{1/2}} \qquad (7)$$

as the SOL density above which retention is obtained, where T_d given by eqn. (6) and ψ_{eff} is the effective hydrogen ionization energy. Since T_d from eqn. (6) varies only slightly over the range of q_i (and hence T_b) of interest, we find the

scaling law $n_b \alpha q_i^{5/7}$ for the required SOL density. Table I shows a comparison between the code results and the analytic model. The agreement is quite good at P_i equal 5 and 20 MW, but less satisfactory at 10 MW, for reasons not yet clear.

IV. The Forced Flow Case; Required Recirulation Flux. As n_b is reduced for a given P_i, Γ_t drops rapidly, and local recycling is insufficient. In this case $\int F_{fi}\, ds$ can be increased by "extending Γ" along the flux tube by injecting particles at some upstream location s_x to produce a constant flux $\varepsilon\Gamma_t$ between s_x and s_i. For values of $\varepsilon\Gamma_t > 0.1$, this term dominates local recycling in the integral, and (1) can be evaluated to give

$$\frac{\varepsilon}{(1-\varepsilon)^{5/7}} = \frac{\frac{2}{7}\left(\frac{7}{2}\frac{q_i}{K_{oi}}\right)^{5/7}}{C_f Z^2 \Gamma_t} = \frac{\left[\frac{2}{7}\left(1.75\, Z^{2-1}\right)\ell n\left(1+\frac{L}{s_o}\right)+3\right]}{\left[(s_x+s_o)\right]} \qquad (8)$$

as the required recirculation fraction. This can be written as an expression for the required injected flux itself, $\Gamma_x \equiv \varepsilon\Gamma_t \alpha\, q_{eff}^{5/7}\, f(q_{eff}, T_d, s_x, L)$ where the variation of f with its arguments is weak over the range of interest. Thus, $\Gamma_x \alpha\, q_{eff}^{5/7}$, independent of n_b, to first approximation. Figure 2 shows a set of code runs corresponding to a power scan at low to medium SOL densities [4]. The solid curve represents the dependence $\Gamma\alpha\, P_i^{5/7}$ normalized to the point at $P_i = 12$ MW. Actual evaluation of expression (9) gives a value for Γ_x about 10% higher than the normalized point. It can be seen that the scaling law describes these runs quite well.

V. Conclusions The analytical model indicates that there is a minimum SOL density, for a given SOL ion power flow, for which local recyling suffices to retain impurities. This density, $n_{b,min}$, scales as $P_i^{5/7}$, and corresponds to a divertor ion temperature, given by equ (7), of about 20 ev. For lower densities, the divertor ion temperature exceeds this value, and the friction force, confined to the local recycling region, is insufficient to overcome the integrated effect of the thermal force. An external recirculation can be imposed, which extends the friction force upstream, overcoming the thermal force, and insuring impurity retention. The required flow for the case of single-point (x-point) injection considered also scales as $P_i^{5/7}$, nearly independent of n_b, in the low to moderate SOL density regime. The predictions of the analytical model are in good agreement with the numerical results.

VI Acknowledgements. The authors wish to thank P. Harbour, M. Keilhacker, A. Taroni, D. Ward and M. Watkins for useful discussions.

References:

[1] M. Keilhacker, et al., Proc. IAEA Conf. on Controlled Thermonuclear Fusion, Wash. DC, Oct. 1990, paper CN53/A-5-1.
[2] M. Keilhacker et. al., Nuclear Fusion 31 535 (1991).
[3] K. Lackner, Plasma Physics and Controlled Fusion 26 105 (1984).
[4] A. Taroni, et al., Bull. A.P.S. (Oct. 1989)

P_i (MW)	n_b (10^{19})	
	Model	Code
20	12.3	11.8
10	7.5	9.7
5	4.5	4.1

Table 1. Value of n_b required for impurity retention without forced flow, as function of P_i.

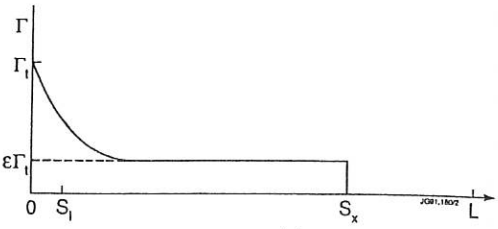

Fig. 1 Hydrogen flux Γ used in analytic model

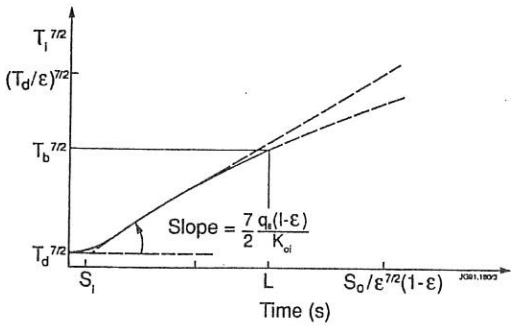

Fig. 2 Sketch of Soln. to equation (4)

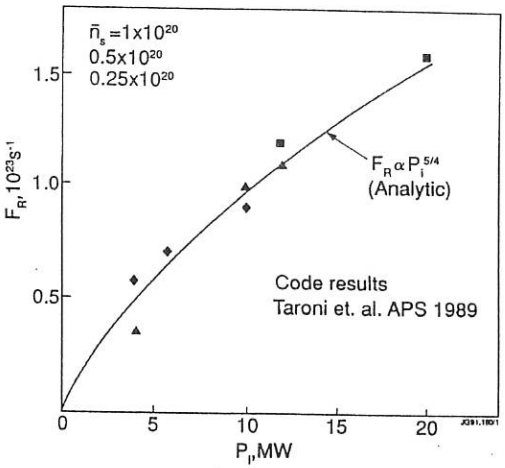

Fig. 3 Flow Required for Impurity Retention, X-Point Injection.

IMPURITY FLOW AT A DIVERTOR TARGET

R. Chodura, R. Zanino*
Max-Planck-Institut für Plasmaphysik
Euratom Association - D 8046 Garching - Fed. Rep. Germany
* Dipartimento di Energetica, Politecnico, I-10129, Torino

1. Introduction

The plasma in the scrape-off layer of a divertor fusion device in general is a mixture of several ion species, i.e. hydrogen isotopes and fusion produced helium provided by the bulk plasma, impurities of different masses and charge states produced at the divertor target plates and at the walls of the vessel. Only if one ion species, say hydrogen with density n_H, is dominant, such that

$$n_H >> \sum_i n_i Z_i^2 \tag{1}$$

where n_i and Z_i are the densities and charge states of the other ion species, these other ion components can be treated in the trace limit of only interacting with hydrogen and not among themselves and having no influence on the flow properties of the dominant hydrogen [1].

Another assumption frequently made for treating multi-component plasmas is the assumption of Maxwellian, fluid-like properties of all components. This assumption may not be justified for long mean free path lengths and steep gradients in particular near the target plates where hot ions from the bulk plasma penetrate through cold ions recycled from the target plates.

It is the purpose of this paper to study the 1D flow of a multi-component plasma near an emitting or recycling target plate without the above mentioned restrictions.

2. Fluid Considerations

Let us firstly assume that the plasma components may be treated as fluids with arbitrary densities. What are the flow velocities of these fluids at a neutralizing target? ("At the target" means about a mean free path length in front of the target sheath). It can be shown [2]that, similar to the case of only one ion component, the flow velocities V_i of the components i, i=1...N, at the target have lower bounds given by

$$V_i^2 \geq C_i^{*2} = (\gamma_i T_i + \frac{n_i}{n_e} Z_i^2 T_e)/m_i \tag{2}$$

where m_i and Z_i are mass and charge number of the i-th ion component, γ_i, n_i and T_i its adiabatic constant, density and temperature, $n_e = \Sigma_{i=1}^N n_i Z_i$ and T_e electron density and temperature at the target, respectively. As an example, Fig.2b shows the flow velocities of two ion components V_1 and V_2 together with their respective speeds C_1^* and C_2^* (from kinetic calculations of a highly collisional two-ion plasma).

From relation (2) follows the potential difference $\Delta\phi$ between plasma and target across the Debye sheath at a net current J

$$e\Delta\phi/T_e \leq -ln\{(\Sigma_i Z_i n_i C_i^* - J/e)/n_e(T_e/2\pi m_e)^{1/2}\} \quad (3)$$

. 3. Kinetic Approach

In order to model also multi-component plasmas with large mean free path lengths a collisional kinetic model [3]was extended to the case of a plasma consisting of electrons and two kinds of ions. No restriction on the relative concentrations of the plasma components are made. The model is 1D in space along the magnetic field (but 3D in velocity). It includes collisions between particles of all three plasma constituents as well as the electric field of the net charge distribution. It thus renders 1D transport and thermoelectric effects together with the electrostatic Debye sheath. The model is able to treat plasmas with arbitrary scale ratios of mean free path to gradient lengths. The Debye length scale is artificially enlarged.

Calculations were done for a case of two kinds of ambipolar particle sources, i.e. a primary source S_p localized around the symmetry midplane, representing particles coming from the bulk plasma or from the wall, and a source in front of the target plate S_r of particles recycled or created at the target plate as neutrals and ionized at some distance ahead of it (Fig.1). The target itself is assumed to neutralize all incoming charged particles.

The code has been run for the following tentative set of parameters:

ion mass: $m_1 = m_H$, $m_2/m_1 = 16$, ion charge: $Z_1 = 1, Z_2 = 4$,

ion flux density from recycling source $\Gamma_r = \int S_r dx$: $\Gamma_{r1} = 5.10^{23} m^{-2}s^{-1}$, $\Gamma_{r2} = 1.10^{23} m^{-2}s^{-1}$ (Fig.2) or $\Gamma_{r2} = 0$ (Fig.3),

temperature of recycled ions: $T_{r1} = 30eV$, $T_{r2} = 0$,

width of recycling region: $d_{r1} = 5m$, $d_{r2} = 2.5m$,

ion flux density from primary source $\Gamma_p = \int S_p dx$: $\Gamma_{p1} = \Gamma_{p2} = 0$ (Fig..2) or $\Gamma_{p2} = 1.10^{22} m^{-2}s^{-1}$, $\Gamma_{p1} = 0$ or $1.10^{23} m^{-2}s^{-1}$ (Fig.3a,b),

temperature of primary ions: $T_{p1} = 150eV$, $T_{p2} = 0$,

Width of the primary region: $d_p = 2.5m$.

Electrons are assumed to have a temperature $T_0 = 30eV$ at the midplane $x = 0$. The recycling width of species 1, d_{r1}, has been taken as the ionization length of hydrogen atoms of $4eV$ in electrons of density $n_e = 4.10^{19} m^{-3}$ and temperature $T_e = 10eV$ projected from target normal to the direction of the magnetic field at an angle of 89°. The mean free path lengths for collisions of ions 1 among themselves $\lambda_{11} = \tau_{11}(T_1/m_1)^{1/2}$ and of ions 2 with ions 1, $\lambda_{21} = \tau_{21}(T_2/m_2)^{1/2}$, with τ_{ab} the respective collision times [4] for $n = 1.10^{19} m^{-3}$ and $T_1 = T_2 = T_{r1} = 30eV$ are $1.3m$ and $0.24m$ respectively.

In Fig.2 ions of species 1 and 2 are created with different recycling widths d_{r1} and d_{r2} in front of the target, whereas the primary fluxes $\Gamma_p = 0$. Densities n_1, n_2 and mean velocities V_1, V_2 together with the velocities C_1^* and C_2^* of equ.(2)(with $\gamma_i = 3$) are shown for the two ion species. Cold ions of species 2 are heated up by collisions with warm ions of species 1 and tend to flow upstream away from the target due to their pressure gradient and thermal force. They are hold back by collisional drag of species 1. The mean velocities V_1 and V_2 of the two ion species are directed toward the target and increase within the recycling source. According to relation (2) they finally exceed the critical velocities C_1^* and C_2^* respectively. The velocity rise directly in front of the target is due to the (artificially extended) Debye sheath which is assumed source- and collision-free.

In Fig.3 ions of species 2 are created in a region remote from the target (between $x = 0$ and $2.5m$) with a primary flux $\Gamma_{p2} = 1.10^{22} m^{-2} s^{-1}$. They are absorbed at the target without recycling, $\Gamma_{r2} = 0$. Ions of species 1 recycle with a flux $\Gamma_{r1} = 5.10^{23} m^{-2} s^{-1}$ (Fig.3a). If, in addition, a flux $\Gamma_{p1} = 1.10^{23} m^{-2} s^{-1}$ of ions 1 are created near the midplane (Fig.3b) more ions of species 2 are swept to the target and their density at the midplane is reduced.

References

[1] J. Neuhauser et.al., Nuclear Fusion 24 (1984), 39

[2] R. Chodura, R. Zanino, in preparation

[3] R. Chodura, Proc. 12th Europ. Conf. on Controlled Fusion and Plasma Physics, Budapest, Europhysics Conf. Abstracts 9F-II (1985), 472

[4] F.L. Hinton in Handbook of Plasma Physics, (M.N. Rosenbluth, R.Z. Sagdeev eds.), Vol.1, North Holland Publ., 1983

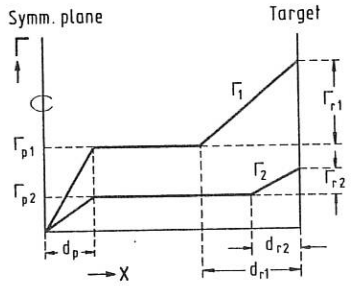

Fig.1 Flux distribution of primary and recycled ions of two species.

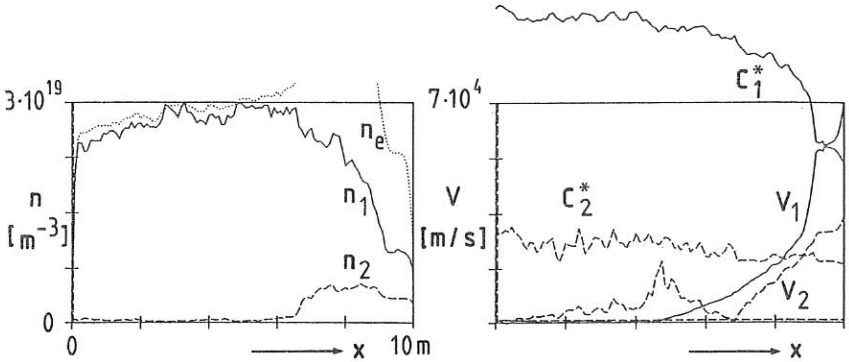

Fig.2 Densities n and mean velocities V of two recycling ion species for $\Gamma_{r1} = 5.10^{23} m^{-2} s^{-1}$ and $\Gamma_{r2} = 1.10^{23} m^{-2} s^{-1}, \Gamma_{p1} = \Gamma_{p2} = 0$.

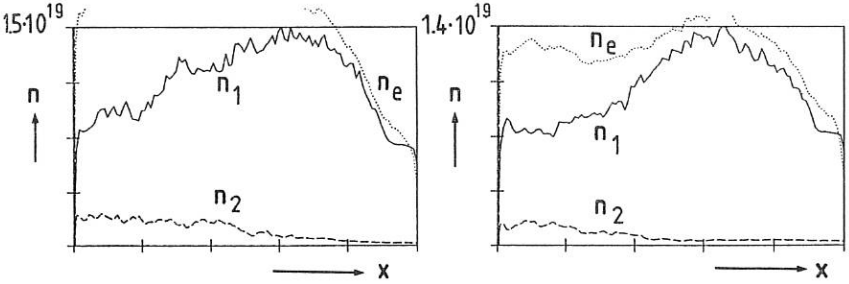

Fig.3 Densities of two ion species for $\Gamma_{r1} = 5.10^{23} m^{-2} s^{-1}$, $\Gamma_{r2} = 0$, $\Gamma_{p2} = 1.10^{22} m^{-2} s^{-1}$.
a) $\Gamma_{p1} = 0$ b) $\Gamma_{p1} = 1.10^{23} m^{-2} s^{-1}$.

IMPURITY TRANSPORT AT THE DIII–D DIVERTOR STRIKE POINTS*

G.F. MATTHEWS,† D.N. BUCHENAUER,‡ D.N. HILL,§ M.A. MAHDAVI, M. RENSINK,§ P.C. STANGEBY¶

General Atomics, San Diego, California

INTRODUCTION

Impurities are recognized as a serious problem for present and future high Q tokamak experiments. The study of the plasma boundary is therefore of increasing importance.[1]

In a tokamak fusion reactor the largest impurity source is expected at the divertor strike points. Design studies for machines, such as ITER, suggest that entrainment of these impurities in the hydrogenic flow close to the target plates will provide effective screening of the core. In this paper we discuss experiments on DIII–D which attempt to test the impurity transport predictions in the critical zone just in front of the divertor target plates.

EXPERIMENT

Deuterated methane gas (CD_4) was injected locally into the strike points of DIII–D discharges to study the transport of low charge state carbon ions in the vicinity of the divertor floor. Ohmic, H–mode and L–mode phases of the discharge were studied in the single-null configuration. Spatial distributions of C I (996–912 nm), C II (514.5 nm) light were recorded using a CCD camera and interference filters.

A highly localized source of carbon neutrals is required to enable measurements of the toroidal dispersal of carbon ions. This was produced using small bore tubes (0.68 mm i.d.) which were routed under the graphite floor tiles and terminated at tile joints near the outer and inner strike points, as indicated in Fig. 1. These are fed by Piezo valves and the system operates in the Poiseuille flow regime at 0.1 → 1 torr 1 s^{-1} with a rapid switch on and a 100 ms decay time.

RESULTS

The appearance of the C III light is always comet-like with the tail extending along the magnetic field in the direction of the divertor floor, as in the example of Fig. 2. The ionized plume has the same qualitative appearance at all radii inside and outside of the private flux region, during ohmic, L–mode and H–mode phases of the discharge.

* This work was sponsored by the U.S. Department of Energy under Contract Nos. W-7405-ENG-48, DE-AC03-89ER51114, and DE-AC03-76DP00789.

† Culham Laboratory, UKAEA/Euratom Fusion Association, U.K.

‡ Sandia National Laboratories Livermore.

§ Lawrence Livermore National Laboratory.

¶ Institute for Aerospace Studies University of Toronto, Canada.

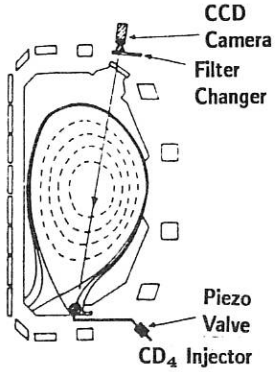

Fig. 1. Schematic of the gas injection and CCD systems plus the magnetic equilibrium for the same shot as Figs. 2 and 3.

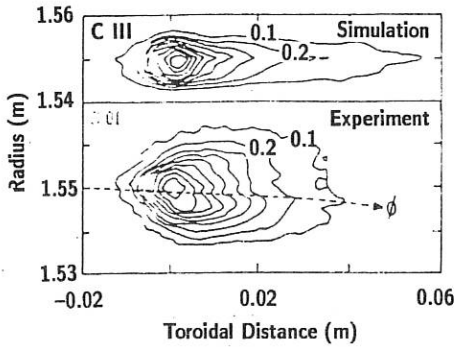

Fig. 2. Measured and simulated C III plumes at the outer strike point during the ohmic phase of a 1 MA discharge.

Results have been compared with a multi-dimensional Monte-Carlo impurity transport code based on LIM[2] using the plasma background measured by the divertor Langmuir probe array;[3] self-sputtering is included.[4] Figure 3 shows the plasma parameters, measured at the outer strike point during the ohmic phase of a 1 MA discharge with a line average density $n_e = 2.5 \times 10^{19}$ m^{-3}. The Braams B2 fluid code[5] was used to provide the poloidal variation in mach number and other key parameters, which are plotted in Fig. 4 along a flux surface at the gas-injection point. In Fig. 2 the simulated C III distribution is plotted above the experimental results.

Two effects may result in the flow of impurities away from the target plates. The most likely to cause a problem is the existence of recirculating layers[6] which may result when specific flux tubes have an excess ion source resulting from geometric effects in the recycling. These recirculating layers can potentially convect impurities out of the divertor. The second effect, which has similar consequences, is the ion temperature gradient (ITG) force[7] which forces impurities up the ion temperature gradient and therefore out of the divertor. Without any means of verification the ITG computed by B2 may be inaccurate, but it does allow us to estimate the magnitude of the ITG force. B2 predicts a peak ITG of about 35 eV m^{-1} along the field line which results in a force opposite to the direction of the usual plasma flow but one order of magnitude weaker than friction. This is a typical result and it is not thought that the ITG force plays an important role in regions of high flow.

Code results are in good qualitative agreement with experiment regarding the direction and magnitude of forces on injected impurity ions. Problems exist in modeling the spatial distribution of the C I emission which is of greater extent than expected and is skewed in the same direction as the C III. Figure 5 shows the measured C I, C II and C III toroidal distributions and Fig. 6, the code predictions. Although there is reasonable agreement between the predicted and measured C III, the observed C I and C II are broader than expected.

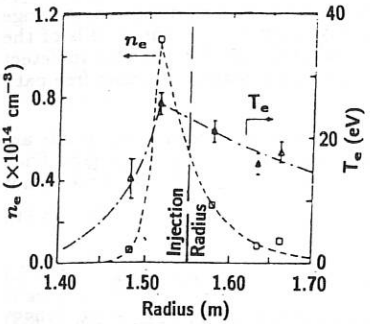

Fig. 3. Plasma parameters measured at the outer strike point using the Langmuir probe array.

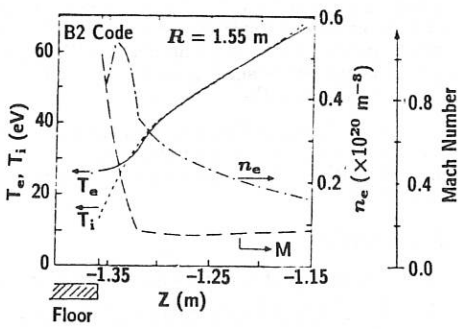

Fig. 4. Fluid code calculations of the plasma parameters as a function of height above the divertor floor.

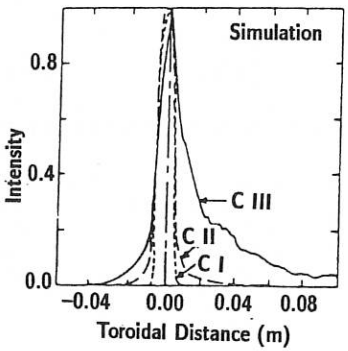

Fig. 5. Measured toroidal distributions of C I, C II, and C III light.

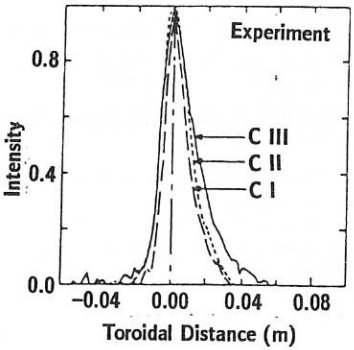

Fig. 6. Simulated toroidal distributions of C I, C II, and C III light.

DISCUSSION

One possible explanation of the behavior of the C I is that in the present model we treat the CD_4 puff as a jet of carbon neutrals with an energy of 0.1 eV.[8] Work by Langer[9] suggests that this may not be a good approximation since molecular ions may be entrained in the plasma flow and travel significant distances before disintegrating to produce neutral carbon atoms. Although the effect did not appear to be dependent on the flow rate of the CD_4, it is possible that local cooling of the flux tube might increase the range of the molecular ions.

To reproduce the observed spatial distribution of C III the model requires a high mach number $0.5 \rightarrow 1$ near the target. However, due to the relatively short range of the carbon neutrals, the distribution is relatively insensitive to the details of the mach profile further into the plasma. Hence we would not expect to be able to detect recirculating zones since they will be created one hydrogen ionization mean free path from the divertor floor.

Despite the difficulties in making a quantitative interpretation, these results are the first direct test of the physics of impurity transport near a divertor target. They also indicate that in this region, under normal circumstances, the ITG force is not dominant.

REFERENCES

1. Stangeby, P.C., and G.M. McCracken, Nucl. Fusion **30**, (1990) 1225.
2. Stangeby, P.C., C. Farrell, S. Hoskins, and L. Wood, Nucl. Fusion **28**, (1988) 2209.
3. Buchenauer, D., W.L. Hsu, J.P. Smith, D.N. Hill, Eighth Topical Conference on High Temperature Plasma Diagnostics, Hyannis, Massachusetts (1990), to appear in Rev. Sci. Instrum.
4. Roth, J., J. Nucl. Mater. **145-147**, (1987) 87-95.
5. Harrison, M.F.A., E.S. Hotston, A. DeMatteis, "Plasma Edge Physics for NET/INTOR," Report EUR-FU/XII-361/86/50, CEC, Brussels (1986).
6. Braams, B.J., NET Report No. 68, EUR-FU/XII-80/87/68, (1987).
7. Neuhauser, J., W. Schneider, R. Wunderlich, K. Lackner, Nucl. Fusion **24**, (1984) 39.
8. McCracken, G.M., U. Samm, S.J. Fielding, *et al.*, to be published in J. Nucl. Mater.
9. Langer, W.D., Nucl. Fusion **22**, (1982) 751-761.

OPERATING CONDITIONS OF THE BPX DIVERTOR*

D.N. Hill, B.J. Braams,[a] J.N. Brooks,[b] R. Campbell,[c] J. Haines,[d]
D. Knoll,[e] J. Milovich, A. Prinja,[e] T. Rognlien, D.P. Stotler,[f]
and M. Ulrickson[f]

Lawrence Livermore National Laboratory, Livermore, California 94550, USA

INTRODUCTION

In this paper we discuss the expected operating conditions at the divertor of the BPX tokamak (Burning Plasma Experiment), the next-step US tokamak proposed for the study of self-heated plasmas at $Q \simeq 5$ to ignition. In this double-null device ($\kappa \simeq 2$), the predicted first-wall loading is high because of its compact size ($R = 2.6\,m$, $a = 0.8\,m$, $I_p = 10.6\,MA$, and $B_T = 8.1\,T$) and its high projected fusion power output (100–500 MW with up to 20 MW of ICRH). Present designs call for inertially cooled carbon-based target plate materials and X–point sweeping to handle the divertor heat flux during the 3–5 s flat-top at full power. Figure 1 shows the cross section of the upper half of the tokamak, including the magnetic separatrix at the start and end of the single radial sweep. The X–point is maintained about 15–20 cm off the target plates (a distance of ~5 m along field lines), which represents a reasonable compromise between lowering the divertor electron temperature ($T_{e,d}$) by increasing the connection length, and lowering the peak divertor heat flux ($\hat{q}_d$) by increasing the magnetic flux expansion (which is about 15–20 in this case).

It is planned for the BPX device to operate with H–mode confinement; ELMs are expected because of the relatively high power flow through the edge plasma ($P_{sep} \simeq 0.6\,MW/m^2$ for $P_{fus} = 500\,MW$). The ELMs will help reduce the impurity concentration in the core plasma ($Z_{eff} \simeq 1.7$) and keep the density down, but should not add significantly to the divertor heat flux since their measured contribution to the global power balance drops with increasing input power.[1]

The global power balance and poloidal distribution of losses to the SOL plasma assumed for our modeling of the divertor plasma appear in Fig. 2. These assumptions are based on measurements from present day tokamaks operating with H–mode confinement, and are similar to those used in the ITER design study.[2] The total power flow to the SOL depends on the fusion power; for the worse-case divertor heat flux, we have examined the near-ignited situation with a total power deposition in the core of $P_\alpha + P_{ICH} = 100\,MW$. We assume that 40% of this power will be dissipated uniformly to the walls via radiative processes in the core, SOL, and divertor plasma, leaving 60% conducted through the SOL.

* Work performed under the auspices of the U.S. Department of Energy by the Lawrence Livermore National Laboratory under contract W-7405-ENG-48 and Princeton Plasma Physics Laboratory Contract No. DE–AC02–76–CHO–3073.

(a) New York University.
(b) Argonne National Laboratory.
(c) Sandia National Laboratories.
(d) McDonnell Douglas Corporation.
(e) University of New Mexico.
(f) Princeton Plasma Physics Laboratory.

NUMERICAL SIMULATION OF THE SOL PLASMA

The predicted operating conditions at the divertor are derived primarily from numerical simulations using the Braams B2 code.[3] Simulation is required because of the scarcity of systematic experimental studies[4] showing the scaling of key SOL plasma parameters with core parameters such as I_p, P_{heat}, B_T, or $\bar{n}_e$. The B2 code simulates the SOL plasma by solving the fluid equations for particle, energy, and momentum balance on a 2D mesh from the actual magnetic geometry of one quadrant of the SOL, extending from 1cm inside the separatrix to 4 cm outside the separatrix at the plasma midplane (the rf antenna limiter position).

The input parameters used for the P_{fus} =500 MW B2 run are listed in Table 1. These include the anomalous radial thermal conductivity ($\chi_{i,e}$), particle diffusion coefficient ($D_\perp$), and convective velocity (v_{conv}), all of which act uniformly in the SOL. The range of parameters which we have explored in the B2 runs is indicated parenthetically. We typically run the code with either fixed density on the separatrix and fixed power flow into the SOL ($T_{e,sep}$ calculated), or with fixed density and temperature (P_{sep} calculated). For the density on the separatrix, we use $n_{e,sep}/\bar{n}_e \simeq 0.25$ as the most likely for ELMing H–modes, but we note that most of the experimental database was obtained in quiescent H–modes; it may be higher with ELMs.

The results of the B2 simulations are as follows. For the near-ignited case with P_{fus} = 500 MW, the peak divertor heat flux is found to be in the range 20–30 MW/m^2 and the peak electron temperature below 50 eV. Profiles at the divertor are shown in Fig. 3. The width of the heat flux profile corresponds to λ_q = 4 mm at the midplane. The density e-folding length is 2–3 times larger, but the prediction is sensitive to the boundary conditions at the outer wall as well as the choice of v_{conv}. For the nominal operating point with Q$\simeq$ 10 and P_{fus} =200 MW, the peak heat flux is found to be about 10 MW/m^2.

PEAKING FACTORS AND UNCERTAINTIES

The nominal divertor parameters were obtained using our best present understanding of the physics of the SOL plasma, and do not include peaking or "safety factors" which arise because of uncertainties in the physics (e.g., choice of χ_e), unknown operational factors (e.g., locked modes), and engineering tolerances (e.g., misaligned tiles). Table 2 summarizes our estimates for these factors, which act as multipliers on the divertor heat flux calculated by the B2 code. Foremost among the various uncertainties is the choice of radial thermal diffusivity ($\chi_{e,i}$), the value of which has been inferred from measurements on lower field tokamaks. A Bohm-like scaling ($\chi \propto T/B$) would yield $\chi \simeq 1 m^2/s$ instead of 2 as used here and the calculated peak heat flux would increase by about 50%. Similar estimates are made for the effect of toroidal variations, other physics assumptions, and uncertainties in the poloidal distribution of power to the SOL (if 2:1 up/down asymmetric instead of 1.2:1). Note that the uncertainties which change the width of the SOL enter with an exponent of 0.5; this results from the combination of divertor sweeping and inertial cooling, which give a surface temperature rise proportional to $\sqrt{\lambda_q}$.

TARGET-PLATE SPUTTERING AND EROSION

We use the REDEP code[5] to calculate the expected net erosion of the graphite divertor targets, using a model background plasma from B2. The peak sputtered flux is highly temperature sensitive and ranges from 0.3 to 2.2×10^{24} cm^2/s for T_{surf} =400 to 1600°C, respectively. The peak electron temperatures at the divertor are predicted to be sufficiently low (about 30–60 eV) that runaway self-sputtering is not observed. Most of the sputtered carbon will be re-deposited in the gaps between divertor tiles and in regions shadowed from direct plasma bombardment due to the toroidal sawtooth alignment of the divertor tiles (designed to eliminate heat flux peaking at vertical edges). The peak net erosion due to steady plasma operation is expected to be about 0.2 μm per discharge at the highest power levels. This corresponds to less than 1 mm over the useful lifetime of the device. In contrast, graphite

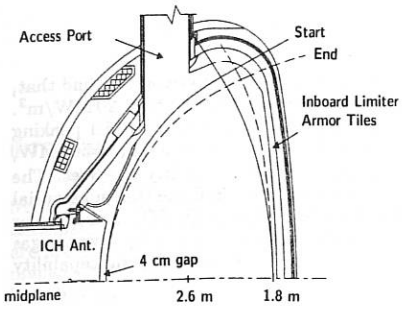

Fig. 2. Global power balance and distribution.

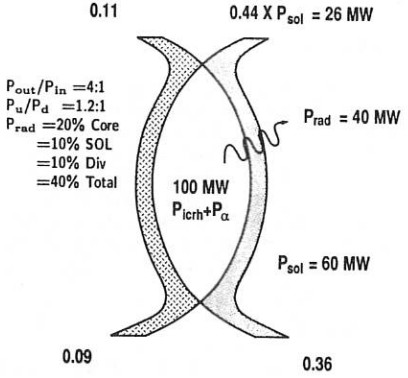

Fig. 1. Cross section of the upper divertor region.

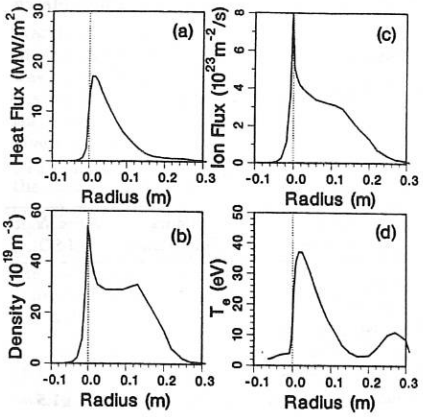

Fig. 3. Divertor profiles from B2 for (a) heat flux, (b) ion flux, (c) density, and (d) electron temperature.

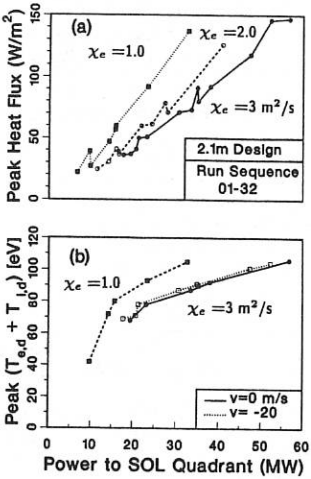

Fig. 4. Variation of peak divertor heat flux (a), and peak plasma temperature (b) with radial transport coefficient χ_e.

ablation during full-power disruptions could total as much as 1 cm over the same period of time.

SUMMARY

We have present the expected operating conditions for the BPX divertor. We find that, for the reference case operation at Q≃10, the peak divertor heat flux will be about 20 MW/m^2. The divertor design allows for a 10 sec flat top at this power level, including a 1.5:1 peaking factor due to toroidal asymmetries and tile misalignment. Near ignition, with P_{fus} =500 MW, the peak heat flux is about 20–30 MW/m^2, resulting in a full power capability of ≥3 sec. The large peaking factors due to uncertainties in the physics assumptions indicate that substantial benefits to the divertor design will result from better measurements in the SOL and divertor regions. In addition, recent experimental results showing heat flux reduction by divertor gas injection[6] suggest that will be possible to significantly increase the power handling capability of the divertor.

REFERENCES

1. D.N. Hill, T.W. Petrie, J.N. Brooks, *et al.*,, in *Proceedings of the Thirteenth International Conference on Plasma Physics and Controlled Nuclear Fusion Research*, (IAEA, Washington, D.C.), October 1990.
2. S.A. Cohen, M.F.A. Harrison, *et al.*, "Power and Particle Control," Section 3 of the ITER Physics Report (1991).
3. B.J. Braams, "A Multi-Fluid Code for Simulation of the Edge Plasma in Tokamaks," NET Report NR 68 (1987)
4. Y. Shimomura, M. Keilhacker, *et al.*, Nucl. Fusion **23**, 869 (1983), and I. Nakazawa, T. Shoji, H. Aikawa, *et al.*, in *Proceedings of the Sixteenth European Physical Society Conference on Plasma Physics and Controlled Nuclear Fusion*, (Venice, Italy, March 1989), p. 887.
5. J.N. Brooks, Nucl. Technol./Fusion 4, 33 (1983).
6. T.W. Petrie, D.N. Hill, D. Buchenauer, *et al.*, these proceedings.

Table 1

Quantity	Value (P_{loss} = 100 MW)	Range of Simulations
$n_{e,sep}$ (m^{-3})	10^{20}	0.4–1.5
$T_{e,sep}$ (eV)	350	300–700
Q_{sep} (MW) (1 quadrant)	26	7–57
χ_e (m^2/s)	2.0	1–3
χ_i (m^2/s)	0.6	0.3–1.0
$D_\perp$ (m^2/s)	0.6	0.3–1.0
V_{cov} (m/s)	–20	–20 to 0
R_{div}	0.97	0.90–1.0
Flus limiter	0.2	0.1–0.2

Table 2

Source of Uncertainty	Varies Total Power	Varies Width of SOL
Toroidal variations (physics)	1.2	
Toroidal variations (engineering)	1.3	
Up/down asymmetry	±1.2	
Scaling of transport coefficients		±1.5
Other physics scaling (e.g., n_{sep}		±1.3
Total multiplicative	1.9	±1.9 (1.4)
Resulting overall safety factor	2.7	

RECENT GASEOUS DIVERTOR EXPERIMENTS IN DIII–D*

T.W. Petrie, D.N. Hill,† D. Buchenauer,‡ A. Futch,†
C. Klepper,§ S. Lippmann, M.A. Mahdavi

General Atomics, San Diego, California

INTRODUCTION

The expected heat loads at the divertor plates for next generation tokamaks raise concern from the standpoints of both mechanical integrity and erosion rate. The peak heat flux anticipated for the present International Thermonuclear Experimental Reactor (ITER) design are predicted to be as high as $\sim 20\,\mathrm{MW/m^2}$. High peak heat fluxes can be reduced to more manageable levels by increasing the radiated power in the divertor, which has the additional benefit of reducing divertor plasma temperature and sheath potential, thereby lowering the ion impact energy. Neutral deuterium gas injection into or near the divertor has been suggested[1–4] as one means of reducing heat flux via radiation and/or momentum transfer and ionization collisions with the neutral gas; this method is often referred to as the "gaseous divertor." In this paper we report on experiments in which the gaseous divertor approach was used to reduce the heat flux on the divertor tiles of the DIII–D tokamak during ELMing H–mode discharges.

GENERAL FEATURES OF D_2 INJECTION

These plasmas were single-null divertors. D_2 gas was injected either from directly beneath the X–point (*i.e.*, between the inner and outer divertor strike points under the X–point) or from a location near the top of the DIII–D vessel. We begin with an example showing the general character of D_2 gas injection in DIII–D, and then move to a more detailed discussion.

Neutral gas injection could significantly affect global plasma properties. In the following example, 120 torr l/s of neutral D_2 gas was injected from a single location under the X–point; this injection rate was $\sim$10% of the "natural" particle recycling at the divertor plates and was $\sim$10x the NBI fueling. This shot (solid curves in Fig. 1) is compared with a control shot (dashed). Both discharges were characterized by rapid ELMing behavior ($\geq$100 Hz). After the first 800 ms of D_2 injection (*i.e.*, at $t = 2600$ ms), the total integrated heat flow onto the divertor tiles (P_{div}) fell by $\sim$10% relative to the control shot, although the peak heat flux ($Q_{\mathrm{div,peak}}$) to the divertor tiles fell to half that of the control shot. Further comparison with the control shot indicate that after 800 ms of D_2 injection (1) total measured radiated power (P_{rad}) was $\sim$50% higher, (2) plasma stored energy (W_T) was $\sim$7% lower, and (3) line-averaged electron density ($\bar{n}_e$) was $\sim$28% higher. While ELM activity continued throughout the control shot, ELM activity ceased in the D_2 injection shot after $t = 3100$ ms. Plasma stored energy for the D_2 injection shot continued to decrease after this time, as the plasma assumed L–mode characteristics. Further D_2 injection pushed the plasma to a disruptive density limit near $t = 4025$ ms.

Bolometrically-determined radiated power increased significantly during D_2 injection. Most of this increase was found in the divertor/X–point region of the plasma. The increase in radiation in the core plasma was entirely in the outer third of the plasma. Radiated power from

* This work was sponsored by the U.S. Department of Energy under Contract Nos. DE-AC03-89ER51114, W-7405-ENG-48, DE-AC03-76DP00789, and DE-AC05-84OR21400.

† Lawrence Livermore National Laboratory.

‡ Sandia National Laboratory, Livermore.

§ Oak Ridge National Laboratory.

the inner two thirds of the main plasma was typically somewhat lower for D_2 injection shots than for control shots. Radiation profiles for the two shots in Fig. 1 (t = 2600 ms) are shown in Fig. 2(a). In this example, we estimate that the radiated power from the divertor/X-point region has increased ~1.7 MW as a result of D_2 injection, while radiated power from the rest of the plasma core has increased only ~0.1 MW. Impurity content over most of the core plasma is also reduced during D_2 gas injection. In the example, we found that $Z_{eff} \sim 1.3$ in the injection case, compared to ~1.6 in the control case. Reductions in concentrations of low-Z impurities, carbon and oxygen, accounted for the drop in Z_{eff}. Spectroscopically-determined central nickel content was also reduced.

Electron density [Fig. 2(b)] was sharply reduced in the D_2 injection case for $\rho/a > 0.9$. Electron temperature [Fig. 2(c)] in the D_2 injection case was relatively low near the separatrix-defined flux surface (~50 eV),

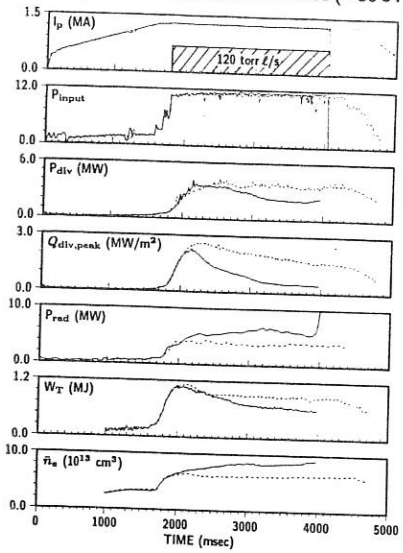

Fig. 1. A shot with D_2 injection during an ELMing H-mode (solid) is compared with a non-injection "control shot" (dashed). For both cases, I_p = 1.25 MA, B_T = 2.0 T, and P_{input} = 11.2 MW.

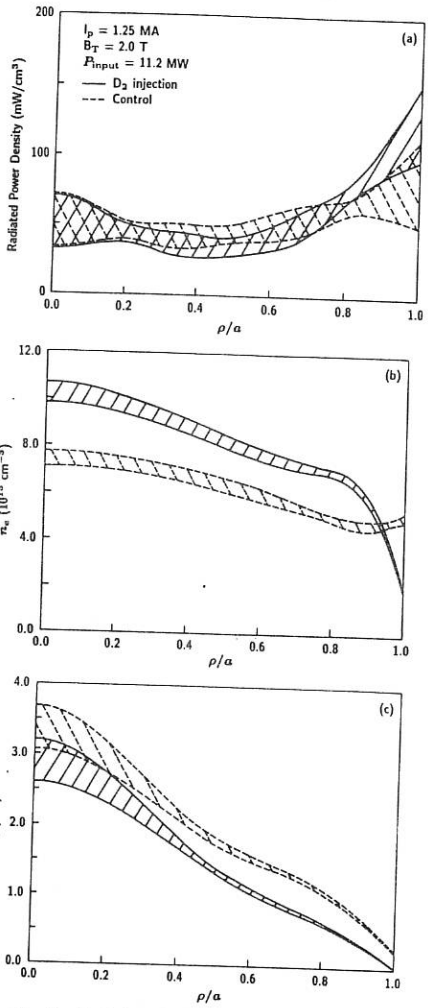

Fig. 2. Radial profiles of (a) radiative power density, (b) electron density, and (c) electron temperature for the injection and non-injection cases shown in Fig. 1 (t = 2600 ms). Each case is displayed as a band of one sigma deviation to the fitted data. The density and temperature data points used in the fitting near the edge are located poloidally opposite the X-point.

compared with the more typical values of 250–300 eV shown in the control shot. We think very strong radiation and density buildup at (or near) the X–point was responsible for this.

RADIAL DEPENDENCE OF Q_{div} AND $n_{e,div}$ ACROSS THE DIVERTOR TILES

Figure 3 shows the dependence of Q_{div} and $n_{e,div}$ on radial position across the divertor tiles for the two cases in Fig. 1 (t = 2600 ms). In the D_2 injection case, the peak heat flux along both inboard and outboard legs was reduced significantly. The heat flux along the inner leg was virtually eliminated. For the D_2 injection shot, the electron density at the strike point of the inboard divertor leg could not be detected by the Langmuir probes (sensitivity $\sim 1 \times 10^{12}$ cm^{-3}); the maximum $n_{e,div}$ for the control shot was $\sim 4 \times 10^{13}$ cm^{-3}. (The maximum electron temperature near the inboard strike point for the control shot ~8 eV.) Near the outer strike point, $\bar{n}_{e,div}$ for the D_2 injection case was considerably higher than that of the control shot. (The maximum electron temperature was ~9 eV for the D_2 injection shot, compared with ~30 eV for the control shot.) Thus, by t = 2600 ms, the plasma has detached from the tiles on the inboard side during D_2 injection, while becoming dense and cold near the outboard strike points.

PRESSURE AND LOCALIZED DENSITY BUILDUP IN THE DIVERTOR

After D_2 injection started, the neutral pressure measured under the X–point typically showed a slow buildup initially, followed by a more rapid increase, a peaking in pressure, and a return to much lower pressure. This is shown in Fig. 4, where we again use the shots from Fig. 1. After the divertor pressure peaked ($t \sim$ 2240 ms), the non-divertor pressure increased at a faster rate. (This behavior was also observed when D_2 gas was injected from a non-divertor location.) As this was occurring, density appeared to be building up in the vicinity of the X–point. This is suggested by the increasing fractional difference in line-averaged density chords ($\Delta \bar{n}_e/\bar{n}_e$), where $\Delta \bar{n}_e$ is the difference in the line-averaged density of a CO_2 interferometer chord that passed near the X–point and a chord that did not. This density "asymmetry" showed more rapid growth at about the time that divertor pressure began to show accelerated growth, and exhibited a jump in growth shortly before divertor pressure peaked. In previous work with ohmic– and L–mode plasmas, we determined that at least part of this density growth could overlap the X–point during high density operation.[6]

Unlike the rapid fueling of the plasma core that occurs during ELM-free H–modes, ELMs appear to inhibit fueling. In the above example, after 800 ms of heavy D_2 injection, <5% of the deuterium has gone to fuel the core. The inhibiting effect of ELMs on fueling likely triggers the apparent accumulation in density in the X–point/divertor during D_2 injection. The abrupt rise in $\Delta \bar{n}_e/\bar{n}_e$ at $t \sim$ 2240 ms may indicate the onset of a MARFE-like process[7] near the X–point. Near this time, n_e and T_e measured inside the edge of the main plasma dropped (Fig. 4), as did the ion saturation current near the strike point of the inboard divertor leg. This detachment of the inboard leg from the divertor probably facilitated the escape of neutrals from the private region. Based on Langmuir probe data measured at t = 2050 ms, the ionization mean free path of a 5 eV Franck Condon neutral in the inner divertor leg was comparable to the distance of escape through that leg whereas its mean free path in the outer divertor leg wass much less than the distance of escape. Thus, the outboard leg acted as a "barrier" to neutrals, while the inboard leg offered much less resistance to the escape of the neutrals. Further reduction in n_e and T_e on the inboard leg, which occured near t = 2240 ms, would make the inboard leg fairly transparent to the trapped neutrals. The removal of the inboard divertor leg "barrier" for the neutrals likely would account for the observed similarity in discharge evolution for divertor and non-divertor gas injection cases following detachment.

SUMMARY AND CONCLUSION

We have found that D_2 gas injected into an ELMing DIII–D H–mode discharge can reduce total integrated heat flux at the divertor tiles up to ~2x and peak heat flux at the

divertor tiles more than 2x, with modest degradation to plasma stored energy. Steady gas injection with no pumping leads to eventual degradation in stored energy and ultimately to L–mode plasma conditions. Measured increased radiated power is comparable to the observed reduction in the total divertor heat load. Since the bolometer does not detect charge-exchange particles originating from the divertor, line radiation is primarily responsible for this heat load reduction and D_2 ionization and charge exchange play a secondary role. Nevertheless, charge exchange with neutrals may still play an important role in reducing *peak* heat load at the divertor plates by making the heat flux profile more diffuse.

REFERENCES

1. Mills, R.G., "A Fusion Power Plant," Princeton Plasma Physics Laboratory report MATT-1050, (1974).
2. Hsu, W.L., Yamada, M., Barrett, P., Phys. Rev. Lett. **49**, (1982) 1001.
3. Lackner, K., Keilhacker, M., J. Nucl. Mater. **128**, (1984) 368.
4. Barr, W.L., Logan, B.G., Fusion Technol. **18**, (1990) 251.
5. Lao, L.L., St John, H., Stambaugh, R.D., Kellman, A.G., Pfeiffer, W., Nucl. Fusion **25**, (1985) 1611.
6. Petrie, T.W., Kellman, A.G., Mahdavi, M.A., "Plasma Density Limits During Ohmic– and L–Mode Operation in DIII–D," submitted to Nucl. Fusion.
7. Drake, J., Phys. Fluids **30**, (1987) 8.

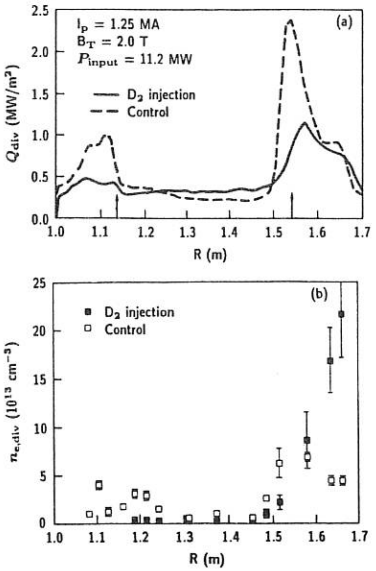

Fig. 3. (a) Heat flux and (b) electron density are displayed as a function of radial location on the divertor tiles for the injection and non-injection cases shown in Fig. 1 ($t = 2600$ ms). The locations of the inner and outer separatrix strike points, as predicted by the EFITD magnetics code,[5] are denoted by the arrows in (a).

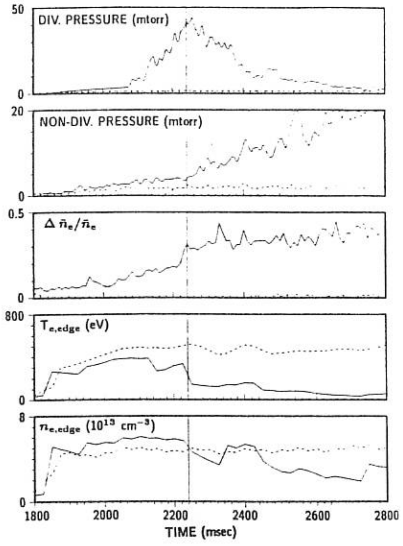

Fig. 4. Behavior of neutral pressure, line-averaged density "asymmetry", edge electron density, and edge electron temperature for the injection and non-injection cases described in Fig. 1. $T_{e,edge}$ and $n_{e,edge}$ are measured 1–2 cm inside the separatrix-defined flux surface from a poloidal location opposite the X–point.

ADVANCED DIVERTOR EXPERIMENTS ON DIII–D*

M.J. SCHAFFER, D. BUCHENAUER,† D.N. HILL,‡ C.C. KLEPPER,§
M.A. MAHDAVI, T. OSBORNE, T.W. PETRIE, AND R.D. STAMBAUGH

General Atomics, San Diego, California

INTRODUCTION

The poloidal divertor is presently favored for next-step, high-power tokamaks. The DIII–D Advanced Divertor Program (ADP) aims to gain increased control over the divertor plasma and tokamak boundary conditions. This paper reports experiments done in the first phase of the ADP. The DIII–D lower divertor was modified by the addition of a toroidally symmetric, graphite-armoured, water-cooled divertor-biasing ring electrode at the entrance to a gas plenum.[1] See Fig. 1. (In the past DIII–D operated with an open divertor.) The plenum will eventually contain a He cryogenic loop for active divertor pumping. The separatrix "strike" position is controlled by the lower poloidal field shaping coils and can be varied smoothly from the ring electrode upper surface to the divertor floor far from the entrance aperture. External power, at up to 550 V and 8 kA separately, has been applied to the electrode to date.

SOL CURRENT FLOW

It was anticipated that the injected current would flow in a nearly force-free manner in the scrapeoff layer (SOL) magnetic surfaces contacting the ring electrode. This was checked by an expanded version of the original "tile current array",[2] an array of floor, inner wall and ceiling graphite armour tiles equipped with current-sensing resistors, to measure where the electrode current appeared. Current does not cross flux surfaces near either the inner wall nor the ceiling, unless the respective gaps are made very small. Current along the open magnetic lines in the "private" region below the divertor X–point has not yet been measured accurately under diverse conditions, but such current is not large. Electrical power supplied to the electrode ranges typically from several 10^5 to $>10^6$ W. This large power significantly perturbs the SOL plasma, increasing divertor heat flux and/or radiation; it can also "reattach" detached divertor plasmas. The SOL current during quiet H–mode is limited to ~1 kA, presumably by low ion saturation current at the divertor sheath, but larger currents flow in Ohmic, L–mode and steadily ELMing H–mode plasmas. There has been no appreciable impurity accumulation in the confined plasma during divertor bias.

PLENUM GAS PRESSURE

Without bias, neutral gas pressure in the plenum is maximized when the divertor separatrix is near grazing just under the ring electrode. The exact position is uncertain because of the accuracy limits of the EFITD magnetic fitting code. Plenum pressure at the optimum position increases approximately linearly with neutral beam heating power during ELMing H–mode.

Application of a bias potential to the SOL drives radial and poloidal $\vec{E} \times \vec{B_T}$ plasma flows.[3,4] For toroidal magnetic field directed clockwise when viewed from above the tokamak (standard direction in DIII–D), positive bias drives plasma away from the plenum entrance,

* This work was sponsored by the U.S. Department of Energy under Contract Nos. DE-AC03-89ER51114, DE-AC03-76DP00789, W-7405-ENG-48, and DE-AC05-84OR21400.

† Sandia National Laboratory, Livermore.

‡ Lawrence Livermore National Laboratory.

§ Oak Ridge National Laboratory.

lowers gas plenum pressure, and increases recycling at the inner divertor and inner wall. Negative bias drives plasma toward the entrance, increases plenum pressure, and recycling at the inner wall and divertor virtually disappears. Plenum pressure, at the maximum pressure position, varies with bias by about 2 mtorr/100 V, whether the plasma is Ohmic, L–mode or ELMing H–mode. See Fig. 2. Plenum pressure with negative bias is a much less sensitive function of separatrix position than without, to such a degree that almost the maximum pressure is still obtained in ELMing H–mode when the separatrix is about half way up the electrode inner face. This seemingly incongruous result might be explained by the qualitative electric potential surfaces and $\vec{E}\times\vec{B}$ directions illustrated in Fig. 3. Here $\vec{E}_{Pol}\times\vec{B}$ drifts plasma across flux surfaces and down into the private region, where electric field between surfaces then drifts it grazingly under the ring electrode and into the entrance aperture.

All the experiments have shown that the DIII–D semi-closed divertor geometry traps sufficient gas pressure in the plenum to allow good pumping.

DIVERTOR HEAT FLUX SHIFT

Divertor bias shifts the separatrix position; this is because the plasma response to the external shaping magnetic field is a function of the different plasma edge and SOL current distributions. Furthermore, the inner divertor heat flux is seen to shift *relative* to the separatrix. See Fig. 4. The divertor heat flux is calculated from the floor tile surface temperature, measured by a vertically viewing IR TV camera. The vertical face of the electrode cannot be seen by this system. The heat flux shift is in the same direction as $\vec{E_{Pol}}\times\vec{B}$. Consider the ratio between $\vec{E_{Pol}}\times\vec{B_T}/B^2$ convection and thermal diffusion, $(5/2)nT(E_{Pol}/B_T)/(\chi n\nabla T)\approx(5/2)E_P\lambda/\chi B_T$, where λ is the SOL temperature gradient length. Representative numbers yield a ratio of

$$(5/2)(120\text{ volt}/6\text{ m})(0.02\text{ m})/(1\text{ m}^2/\text{s})(2\text{ T})=0.5\quad.$$

Therefore, the two processes can be of comparable magnitude.

If electric heat flux shift proves robust, an alternating divertor bias voltage might offer an easier means of sweeping divertor strike points in fusion reactors, to reduce the time-average divertor power, than by the presently envisioned modulated currents in distant superconducting coils.

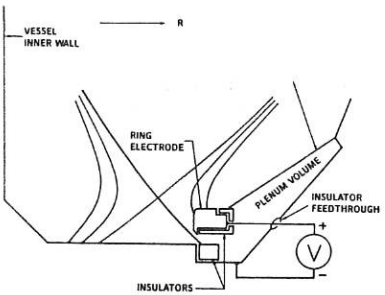

Fig. 1. DIII–D divertor ring electrode and pumping plenum, shown with representative magnetic surfaces.

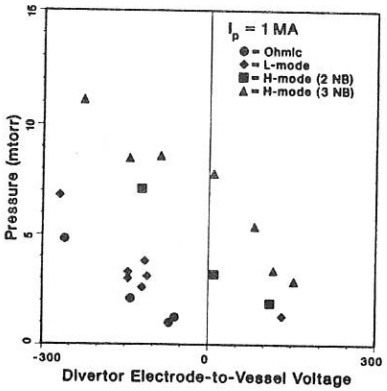

Fig. 2. Maximum plenum gas pressure versus divertor bias voltage at $I_p = 1$ MA.

H-MODE POWER THRESHOLD

Divertor bias changes the L- to H-mode transition power threshold. This effect was studied quantitatively while holding the strike point on the vertical electrode face (Fig. 5). Moderate negative bias raises the threshold by about 1 MW per 100 volt of bias. The minimum threshold power is found at about +80 V in 1 MA plasmas with the standard toroidal field direction.[5] In H-mode near the transition boundary, bias reduces the ELM frequency. These observations might constrain H-mode theoretical models.

CONCLUSIONS

The new DIII-D semi-closed divertor traps sufficient gas pressure in the plenum to allow good pumping. SOL current driven by a single-ring electrode bias mostly encircles the tokamak plasma poloidally; much less current flows in the "private" region below the X-point. Bias shifts the separatrix strike point locations, probably because it changes the boundary current profile. Bias shifts divertor and edge recycling strongly, apparently by $\vec{E}\times\vec{B}$ drifts, and this effect can be used to augment flow into the pumping plenum. Bias also shifts divertor heat flux, which might be useful to sweep the heat flux across reactor divertor plates. Bias changes the H-mode power threshold and ELM frequency, an effect that might constrain H-modetheoretical models. Divertor bias has little effect on impurity content.

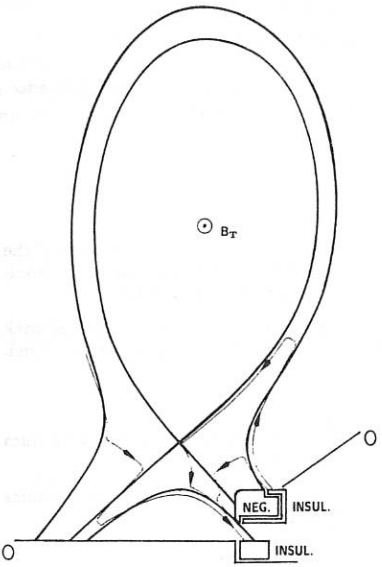

Fig. 3. Qualitative illustration of proposed $\vec{E}\times\vec{B}$ SOL drifts (arrows) and equipotentials (thin lines) for negative bias.

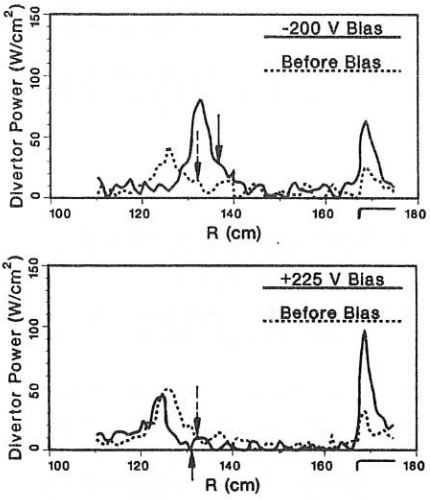

Fig. 4. Divertor heat flux before ($t = 3.4$ s) and during ($t = 4.0$ s) positive and negative bias. Bias began at $t = 3.5$ s. Arrows show approximate inner separatrix locations. Ring electrode spans, $R = 167 \sim 175$ cm, is also indicated. $I_p = 1.2$ MA, heating $\approx$ 13 MW.

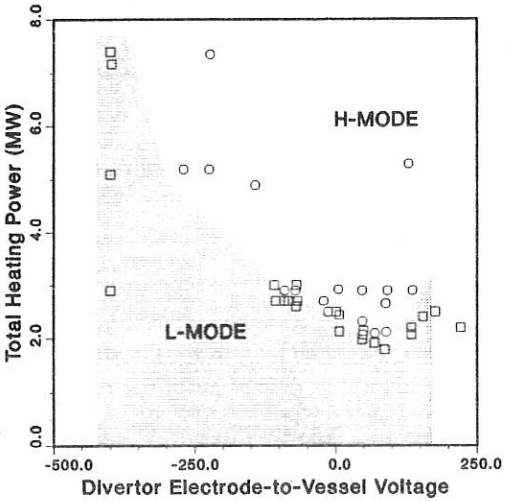

Fig. 5. H–mode (circles) and L–mode (squares) discharges versus total heating power and divertor bias voltage, stroke point on vertical electrode face, in 1 MA plasmas.

REFERENCES

1. Anderson, P.M., *et al.*, "Engineering, Installation, Testing and Initial Operation of the DIII–D Advanced Divertor," presented at the Sixteenth Symposium on Fusion Technology, (London, United Kingdom, 1990), to be published in the Proceedings.

2. Schaffer, M.J., and B.J. Leikind, "Observation of Electric Currents in Diverted Tokamak Scrape-off Layers," General Atomics Report GA-A20128 (1991), submitted to Nucl. Fusion.

3. Strait, E.J., Nucl. Fusion **21**, (1981) 943.

4. Schaffer, M.J., *et al.*, "Electric Field Convection of Plasma and Heat," General Atomics Report GA-A20474 (1991), to be submitted to Phys. Rev. Lett.

5. Mahdavi, M.A., "Effect of Divertor Bias on H–mode Power Threshold," General Atomics Report GA-A20475 (1991), to be submitted to Phys. Rev. Lett.

Dynamic Measurements of the Hydrogen Inventory in Graphite exposed to a RF Discharge

C. Jandl, W. Möller, B. Scherzer

Max-Planck-Institut für Plasmaphysik
D-8046 Garching, Germany

Introduction

The hydrogen inventory in the first wall of fusion devices is being discussed controversially. In the major tokamaks ([1,2,3] and others) graphite limiters and tiles show a large pumping capability for hydrogen plasma particles. Especially after helium discharge conditioning this 'wall pumping' led to an improvement of plasma parameters in confinement experiments.

In laboratory experiments with monoenergetic keV ion beams [8] dynamic wall pumping of hydrogen could not be observed. Therefore, we designed a RF plasma experiment (Figure 1).

In a closed SS304 cylinder graphite targets (Ringsdorff EK98, 1 mm thick, 28 mm diameter) are exposed to a hydrogen gas discharge ignited between the bottom (1) of the cylinder (the "grounded" electrode) and a pot-shaped, isolated SS304 electrode (2) connected to a commercial RF transmitter via a tuning matchbox.

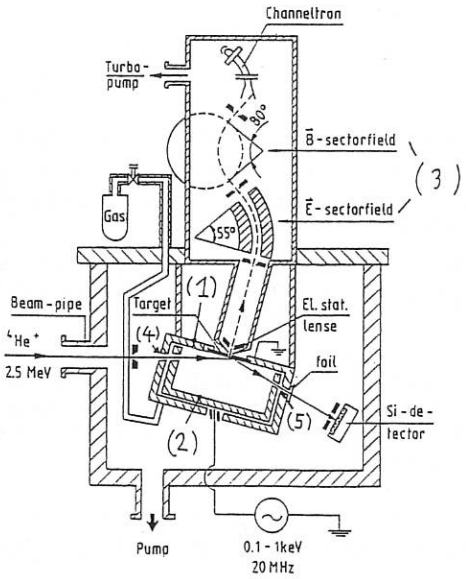

Figure 1: The RF plasma experiment as described in the text: the differentially pumped mass-energy analyzer (3), the plasma chamber with the inner RF electrode (1,2) and target, the path of the $^4He^+$ beam for ERD depth profiling and the beamline-connection to the 2.6 MV Van-der-Graf-accelerator.

The mass-energy distribution of the discharge ions can be analyzed through a 0.1 mm hole in the center of target by electric and magnetic sector fields (3). An entrance hole (4) of 1 mm diameter and escape windows (5) (shielded by a 5 μm SS304 foil to stop the reflected $^4He^+$ beam-ions) in the electrode allow for in situ depth profiling of H and D by ERD analysis at 2.6 MeV.

As the target is under direct plasma ion bombardment no target current can be measured. Therefore a moveable faraday cup in front of the entrance hole (4) monitors the beam current; during ERD analysis it can be moved out and back in. The pressure in the chamber is fixed by an automatic UHV leak valve. Transmitter powers up to 100 Watt are adjustable. The target temperature is measured by a Pt-100 sensor. The ion flux onto the target can be determined by measuring the current of a faraday cup mounted directly into the 'grounded' electrode.

Experiment

To investigate a probable dynamic inventory, three experimental steps were performed:

1. The energy distribution of the plasma ions was measured to determine the mean kinetic energy of the impinging hydrogen atoms.
2. After plasma ignition the amount of implanted hydrogen in the target was measured by periodic depth profiling. After attaining a steady-state inventory the discharge was switched off.
3. Finally the inventory was measured during and after plasma implantation by single channel counting only the peak integral part of the depth profiles in several subsequent periods (figure 2). These plasma "ON/OFF" cycles were repeated several times to reduce statistical fluctuations.

Results and Discussion

Four of such experimental runs were performed at 20 to 80 W transmitter powers.

The mass distribution is dominated by H_3^+-ions (H_2^+, H^+ just make less then 10% of the total ion intensity). The energy distribution has an almost symmetric double-peaked shape which can be explained by the theory of RF plasma sheath [11].

Hydrogen ion energies were measured from 0 up to 200 eV resulting in corresponding mean kinetic energies per hydrogen atom from 18 to 70 eV at target temperatures from 300 K to 370 K and hydrogen fluxes from 1.5 to $2.2 \cdot 10^{15}$ atoms/cm^2.

The results are shown in figure 3: The dynamic hydrogen inventory ranges from $5.1 \cdot 10^{15}$ atoms/cm^2 at 18 eV to $8.4 \cdot 10^{15}$ atoms/cm^2. It decays after plasma switch off with a time constant of about 100 s (e.g., as can be seen from figure 3). The steady-state background of hydrogen inventory was found to be $\sim 3.2 \cdot 10^{16}$ atoms/cm^{2}for all runs and differed less than 10% for all measurements.

The dynamic inventory of hydrogen observed in the present experiment amounts to a coverage of a few monolayers. Its quantity as well as the time constant of its decay are

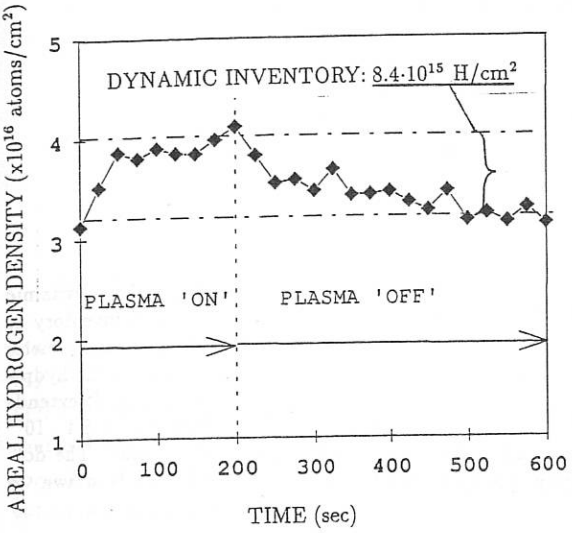

Figure 2: The figure shows a typical experimental run. Every point in this diagram is the integral of 10 s ERD depth profiling after a 15 s beam interruption by the moveable faraday cup. The gas discharge is ignited at 0 s and switched off at 200 s, the total time for one cycle is 600 s. To reduce statistical errors, this integral is normalized to the averaged beam. The cycle was repeated 15 times at a pressure of 20 Pa at 350 K and 70 eV mean kinetic energy/H).

in reasonable agreement with the results obtained in fusion machines during after-pulse outgassing [1,2,3].

We regard the present findings as the first unambiguos proof of the formation of a dynamic hydrogen inventory during plasma exposure of graphite above room temperature. Scherzer et al. [9] had observed a total mobile hydrogen inventory of 3.0–5.5·10^{16} D/cm^2 at temperatures between 116 K to 223 K, but failed to do so at room temperature [10]. Experiments by Morita et al. [6] which seemed to indicate a mobile inventory around 10^{17} H/cm^2 during 3 keV H_2^+ bombardment of isotropic graphite, possibly suffered from problems with the ERD analysis technique [12].

It is also evident that any dynamic inventory could not be found in former experiments using keV ion beam experiments: The amount of trapped hydrogen at saturation during 1 keV bombardment at room temperature is well above 10^{17} atoms/c^2 [7]. Thus, a detection of a dynamic fraction would require a precision in the order of 10^{-2} which is beyond the capabilities of high-energy ion beam analysis techniques.

The physical mechanisms which are responsible for the formation of a near-surface dynamic hydrogen inventory are still unknown. Recent plasma simulating experiments led to the assumption that hydrocarbon films, being co-deposited from impinging hydrogen and sputtered carbon atoms, are responsible for the dynamic inventory: Hsu et al. [4] found 7.2·10^{17} D/cm^2 at plasma ion energies between 300 eV and 500 eV at 540 K. In addition, Hirooka et al. [5] observed a delayed emission of CH_4 after plasma bombardment.

The co-deposited hydrocarbon layers exhibit much larger hydrogen coverages than observed in the present experiments. Furthermore, a formation of a co-deposited layer appears unlikely in our setup as the walls of the discharge chamber are made of stainless

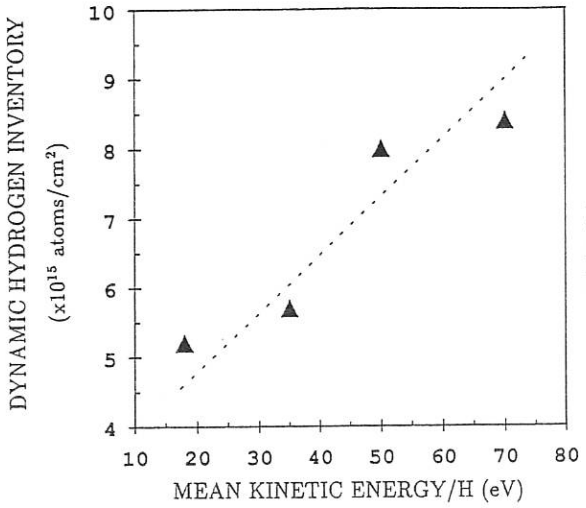

Figure 3: Dynamic hydrogen inventory at different mean kinetic energies of the hydrogen atoms. It extends from 5.1 to 8.4 · 10^{16} atoms/cm^2. The dotted line is drawn to guide the eye.

steel with only a small inserted graphite target.

Thus, we propose two possible mechanisms: (i) The dynamic inventory might be formed by adsorption of hydorgen or some hydrocarbon species at the surface or in near-surface pores. (ii) It might be dissolved in metallic or carbidic impurities which are formed by sputtered metal atoms. In metals, a dynamic inventory due to diffusing hydrogen is well knwon [13]. Indeed, a small coverage of metallic impurities has been found in recent RBS analysis of the exposed graphite samples. Further experiments are in progress to clarify these proposed mechanisms.

References

[1] L. de Kock, J. Nucl. Mater. **145/147** (1987) 26.
[2] Y. G. Wang, W. Poschenrieder, G. Venus, J. Vac. Sci. Technol. **A4**(6) (1986) 2520.
[3] H. F. Dylla and TFTR Team, J. Nucl. Mater. bf 145/147 (1987) 48.
[4] W. L. Hsu, R. A. Causey, J. Vac. Sci. Technol. **A5**(4) (1986) 2768.
[5] Y. Hirooka, W. K. Leung, R. W. Conn, D. M. Goebel, B. Labombard, R. Nygren, K. L. Wilson, J. Vac. Sci. Technol. **A6**(5) (1988) 2965
[6] K. Morita, K. Ohtsuka, Y. Hasebe, J. Nucl. Mater. **162-164** (1989) 990
[7] G. Staudenmaier, J. Roth, R. Behrisch, J. Bohdansky, W. Eckstein, P. Staib, S. Matteson, S. K. Erents, J. Nucl. Mater. **149-156** (1979) 149
[8] B. M. U. Scherzer, P. Børgesen, W. Möller, IPP-JET-Report No. 32 (1986)
[9] B. M. U. Scherzer, J. Wang, W. Möller, Nucl. Meth. and Instr. **B45** (1990)
[10] B. M. U. Scherzer, J. Nucl. Mater. **168** (1989) 121
[11] F. Chapman, Glow discharge processes (Wiley, Chichester 1980)
[12] K. Morita, private communication
[13] W. Möller and J. Roth in: Physics of Plasma-Wall Interaction in Controlled Fusion, by D. Post, R. Behrisch, Nato ASI Services **B**, Vol. 131 (Plenum Press, N. Y. 1986)

NUMERICAL ANALYSIS ON NEUTRAL BEAM CURRENT DRIVE WITH AN ENERGY SPREAD OF THE NEUTRAL BEAM

Takashi Okazaki and Michio Ohtsuka

Energy Research Laboratory, Hitachi, Ltd.,
1168 Moriyama-cho, Hitachi-shi, Ibaraki-ken, 316 Japan

I. Introduction

Neutral beam current drive is a good candidate for realizing the steady-state tokamak reactor. However the current drive efficiency of the neutral beam may be one order smaller than that of the lower-hybrid wave in recent experiments [1]. It is of primary importance to enhance the current drive efficiency of the neutral beam for its application to the reactor. The neutral beam with an energy spread is studied to obtain a large current drive efficiency. Since the ion velocity component perpendicular to the toroidal magnetic field increases with the energy spread, the trapped ion effect may become important. The trapped ion effect has been studied for the neutral beam with the mono-energy [2]. In the paper, the two-dimensional Fokker-Planck equation is solved for the neutral beam with energy spread and the current drive efficiency of the neutral beam is obtained under the trapped ion effect.

II. Analytical Model

The fast ion Fokker-Planck equation, which includes the average drag on electrons and ions as well as pitch-angle diffusion, is described as [3],

$$\frac{1}{\tau_s u^3}\left[u\frac{\partial}{\partial u}(u^3+u_c^3)f + \frac{Z_2 u_c^3}{2}\frac{1}{\sin\theta}\frac{\partial}{\partial\theta}\sin\theta\frac{\partial f}{\partial\theta} \right] + S(u,\theta) = 0, \qquad (1)$$

where the ion velocity u is normalized by the electron thermal velcity v_e, τ_s is the slowing down time, f is the fast ion distribution function, Z_z is the effective charges of the background ions, u_c is the crossover velocity, and $S(u, \theta)$ is the fast ion source. Gaussian beam is used as the source term in order to take into account the energy spread of the neutral beam, although a delta function is usually used for simplicity.

Using the conservation of the magnetic moment $b \sin^2\hat{\theta} = b_m \sin^2\theta$, the coordinate system (u, θ), is transformed to the system $(u, \hat{\theta})$, where b is the

normalized toroidal magnetic field of the tokamak defined by $b = (1-\varepsilon\cos\psi)/(1+\varepsilon)$, ε is the inverse aspect ratio, ψ is the poloidal angle and $b_m = (1-\varepsilon)/(1+\varepsilon)$. By dividing Eq. (1) by $\cos\theta/b$ and averaging with the magnetic field direction, Eq. (1) becomes

$$\frac{1}{u^2}\frac{\partial}{\partial u}u^2\Gamma_u + \left\langle\frac{b}{\cos\theta}\right\rangle^{-1}\frac{1}{\cos\hat{\theta}}\frac{1}{u\sin\hat{\theta}}\frac{\partial}{\partial\hat{\theta}}\sin\hat{\theta}\Gamma_\theta + S(u,\hat{\theta}) = 0, \qquad (2)$$

where

$$\Gamma_u = \frac{u^3+u_c^3}{\tau_s u^2}f, \quad \Gamma_\theta = \frac{Z_2 u_c^3 b_m}{2\tau_s u^2}\frac{\langle\cos\theta\rangle}{\cos\hat{\theta}}\frac{\partial f}{\partial\hat{\theta}},$$

and brackets mean the bounce average. Detailed formulations are shown in Ref. [4].

The fast ion distribution function can be obtained by solving Eq. (2) with the BCG (bi-conjugate gradient) scheme. Total current can be obtained by $I_t = I_i F$, where I_i is the ion current driven by the neutral beam, which is obtained from the fast ion distribution function, and F is the correction factor due to the electron current induced by the beam [5]. To clarify the trapped ion effect on the neutral beam with energy spread, the ion current drive efficiency is defined as,

$$\eta_i = \frac{nI_iR}{P}, \qquad (3)$$

where n is the plasma density, R is the major radius and P is the beam power injected into the plasma.

III. Numerical Results

Behavior of the ion current drive efficiency has been studied for the ITER. Figure 1 shows the dependence of the ion current drive efficiency on the beam energy V_b. The following parameters were used: major radius R = 6.0 m; minor radius a = 2.15 m; elongation κ = 1.98; plasma density $n = 10^{20}$ m^{-3}; plasma temperature T = 10 keV; effective charge Z_{eff} = 2.0; beam power P =75 MW; energy spread $V_{bt}/V_b = 10^{-3}$; inverse aspect ratio ε = 0; and D° -beam. The figure indicates that the ion current drive efficiency increases with the beam energy.

Figure 2 shows the dependence of the ion current drive efficiency on the energy spread of the neutral beam. Parameters taken were the beam energy V_b = 1.5 MeV or 2.0 MeV, with others being the same as those of Fig. 1. The ion current drive efficiencies increase with the energy spread V_{bt}/V_b and saturate at some

value of V_{bt}/V_b. The reason for this is shown in Fig. 3, which indicates the contour of the function $g = u^2 f(u, \hat{\theta})$. Parameters taken in Fig. 3 were $V_b = 1.5$ MeV and $V_{bt}/V_b = 10^{-3}$, $\varepsilon = 0$ in (a); $V_{bt}/V_b = 10^{-2}$, $\varepsilon = 0$ in (b); $V_{bt}/V_b = 2\times10^{-2}$, $\varepsilon = 0$ in(c); $V_{bt}/V_b = 10^{-3}$, $\varepsilon = 0.1$ in (d). First, the reason why the function g spreads to a low energy region in Fig. 3 (a) is that low energy ions are easily decreased, as seen in the first term of Eq. (2), compared with high energy ions. As the energy spread is increased, the decrement of the energy for high energy ions becomes smaller than that for low energy ions in Fig. 3 (b). So the energy spread means an increase in the number of high energy ions so that the ion current drive efficiency becomes large. Saturation of the efficiency is due to the small contribution of low energy ions to the ion current, since the energy of the ions is decreased as the energy spread is increased in Fig. 3 (c).

Figure 4 shows the dependence of the ion current drive efficiency on the inverse aspect ratio. Parameters used here were $V_b = 1.5$ MeV, $V_{bt}/V_b = 10^{-3}$ or 10^{-2}, with the others being the same as those of Fig. 1. The ion current drive efficiency decreases as the inverse aspect ratio increases. The decrement of the efficiency at $\varepsilon = 0.1$ can be 10 - 20 % of the efficiency at $\varepsilon = 0$ for the neutral beam with mono-energy [5]. In Fig. 4, the decrement becomes 20 % for $V_{bt}/V_b = 10^{-3}$ and 30 % for $V_{bt}/V_b = 10^{-2}$. The decrement for the neutral beam with the energy spread is larger than that for the beam with the mono-energy. This is due to the fact that ions with a large $u_\perp$ for the beam with the energy spread approach the trapped ion region and they are dragged to a low energy region as shown in Fig. 3(d). Such decrement is increased with the energy spread in Fig. 4, as mentioned above.

IV. Conclusions

The neutral beam with energy spread has been studied to enhance the ion current drive efficiency. The bounce-averaged, two-dimensional Fokker-Planck equation was solved for the fast ion distribution function. The ion current drive efficiency for the beam with the energy spread is decreased due to the trapped ion effect, compared with that for the mono-energy beam. However, the efficiency can be increased by using the energy spread and the increment overwhelms the decrement due to the trapped ion effect.

Acknowledgements

The authors thank Drs. A. Doi, K. Inoue and T. Ohmae for their encouragements.

References

[1] C.D Challis, etal., Nucl. Fusion 29, 563 (1989).

[2] J.G. Cordey, Nucl Fusion 16, 499 (1976).

[3] J.D. Gaffey, Jr., J. Plasma Phys. 16, 149 (1976).

[4] T. Okazaki, et al., Plasma Phys. and Controlled Fusion 33, 61 (1991).

[5] D.F.H. Start and J.G. Cordey, Phys. Fluids, 23, 1477 (1980)

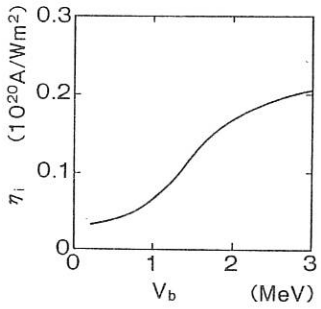

Fig.1 Ion current drive efficiency vs. beam energy. Here ITER parameters are used, the energy spread is $V_{bt}/V_b = 10^{-3}$ and the inverse aspect ratio is $\varepsilon = 0$.

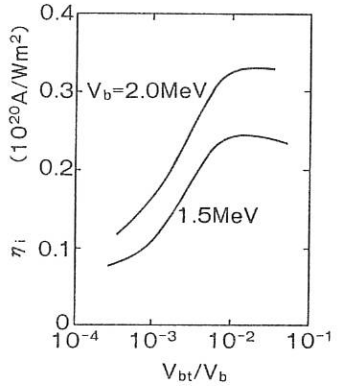

Fig.2 Ion current drive efficiency vs. energy spread. Parameters used here are the same as those of Fig. 1. The beam energy is V_b = 1.5 MeV or 2.0 MeV.

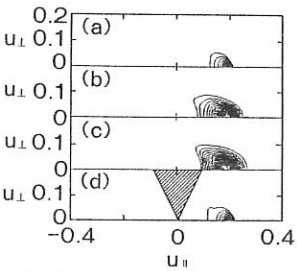

Fig.3 Contour plot of the function $g = u^2 f(u, \hat{\theta})$. Diagonal lines mark the trapped ion region. Here V_b = 1.5 MeV;
(a) $V_{bt}/V_b = 10^{-3}$, $\varepsilon = 0$;
(b) $V_{bt}/V_b = 10^{-2}$, $\varepsilon = 0$;
(c) $V_{bt}/V_b = 2\times10^{-2}$, $\varepsilon = 0$;
(d) $V_{bt}/V_b = 10^{-3}$, $\varepsilon = 0.1$.

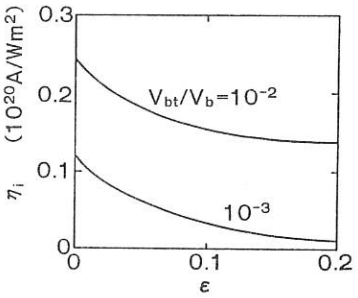

Fig.4 Ion current drive efficiency vs. inverse aspect ratio. Parameters are V_b = 1.5 MeV and $V_{bt}/V_b = 10^{-3}$, 10^{-2}.

EFFICIENCY STUDIES OF HIGH FREQUENCY CURRENT DRIVE

S.J. Karttunen[1], T.J.H. Pättikangas[2] and R.R.E. Salomaa[2]

[1]Technical Research Centre of Finland, Nuclear Engineering Laboratory
P.O. Box 169, SF-00181 Helsinki, Finland
[2]Helsinki University of Technology, Department of Technical Physics,
SF-02150 Espoo, Finland

1. Introduction: Pulsed high power free-electron-lasers (FELs) offer new possibilities for the current drive in tokamaks. High intensity FELs apply to the excitation of nonlinear wave-wave processes, such as beat-waves (BW) and stimulated Raman scattering (SRS), in which large phase velocity ($v_{ph} \gg v_e$) electrostatic modes are generated [1–5]. These can accelerate resonant electrons to high parallel velocities $v_{\parallel} \simeq v_{ph}$, which produces a slowly decaying current. Furthermore, the fast electrons with $v_{\parallel} \gg v_{\perp}$ are not toroidally trapped into banana orbits. The operation at high frequencies provides for the FEL beam an easy access into the plasma centre. This makes possible to suppress sawtooth activity by profile control and to expand the operational limits in parameter space. Raman and beat-wave methods apply particularly well to bootstrap current seeding, which may considerably enhance the overall current drive efficiency [2,4,6].

Both Raman forward (SRS-F) and backward (SRS-B) scattering can be applied to current drive. At high, reactor relevant temperatures SRS-F is the dominant process, because SRS-B is suppressed due to heavy damping of the plasma wave. At temperatures of a few keV, SRS-B dominates because of its short gain length. In this report we shall estimate the current drive efficiency at temperatures relevant for MTX and for a tokamak reactor. We shall also consider the dependence of the efficiency on the peak intensity of FEL in these two cases.

2. Current drive efficiency: In Raman current drive there are three important parameters: (i) phase velocity of the plasma wave, (ii) quantum efficiency Q_e of SRS and (iii) relative action transfer R_c. The product $Q_e R_c$ determines the conversion efficiency from the electromagnetic energy to the energy of the electron plasma wave. The phase velocity determines the collision rate of the fast electrons ($v \simeq v_{ph}$) with bulk electrons and ions and thus the power dissipated in collisions.

The two dimensional slowing down of fast electrons has been studied in detail by Karney and Fisch [7]. In the following we shall assume that the power absorbed by the plasma wave is $Q_e R_c P$, where P is the power of the FEL beams. We shall also assume that all the energy of the plasma wave is transferred to the resonant electrons. If we consider a narrow spectrum of fast, Landau damped waves in the limit of small background temperature, we find for the current drive efficiency with $Z = 1$ [4,7]

$$\frac{n_e R J}{P} = Q_e R_c \frac{2\epsilon_0^2 m_e c^2}{e^3 \ln \Lambda} \left[(\frac{v}{c})^2 - 2 \frac{\gamma (v/c)^2 - 2 \ln \gamma}{(\gamma - 1)^2} \right], \qquad (1)$$

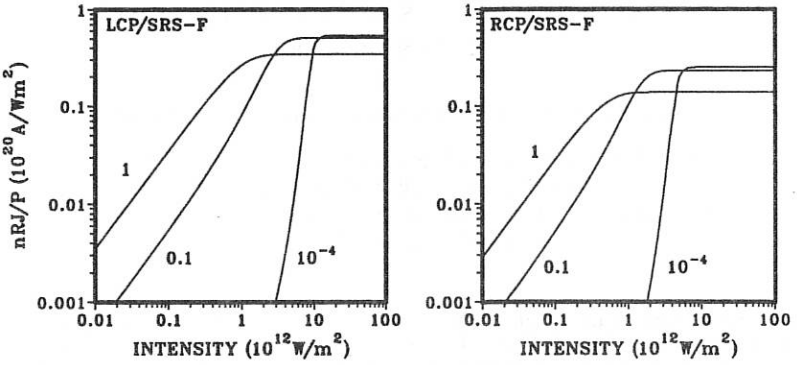

Figure 1: *CD-efficiency vs FEL pulse intensity and ϵ_N in the reactor case.*

where n_e is the electron density, R is the major radius of the tokamak and γ is the Lorentz factor.

3. Quantum efficiency: The quantum efficiency Q_e in Eq. (1) depends on the details of the stimulated Raman process. SRS is a parametric instability in which an intense electromagnetic pump wave $(\mathbf{k}_0, \omega_0)$ decays into a scattered wave $(\mathbf{k}_-, \omega_-)$ and a longitudinal plasma wave $(\mathbf{k}, \omega)$. The phase matching conditions for the wave vectors and frequencies are $\mathbf{k}_0 = \mathbf{k}_- + \mathbf{k}$ and $\omega_0 = \omega_- + \omega$.

We shall assume a homogeneous plasma of length L and a simple geometry in which all the waves propagate parallel to the external magnetic field. This assumption is expected to be fairly well valid when the FEL beam meets the magnetic axis tangentially. The dispersion relations of the electromagnetic waves are $k_j^2 c^2/\omega_j^2 = 1 - \omega_p^2/\omega_j^2(1 \pm |\Omega_e|/\omega_j)^{-1}$, where Ω_e is the electron gyrofrequency and $j = 0, -$. The lower sign must be chosen for right circularly polarized (RCP) waves and the upper one for left circularly polarized (LCP) waves. The electron plasma wave propagating along the magnetic field obeys the Bohm-Gross dispersion relation.

The phase matching conditions together with dispersion relations can be easily solved to obtain the wave numbers and frequencies of the waves involved. Thus the phase velocity $v_{ph} = \omega/k$ and the quantum efficiency $Q_e = \omega/(\omega_0 + \epsilon_N \omega_-)$ are readily obtained [4]. The ratio of the action flux densities of the incoming waves is $\epsilon_N = |\Psi_-(0)/\Psi_0(0)|$, where $\Psi_j = v_{gj} W_j/\omega_j$, v_{gj} is the group velocity and W_j is the energy density. In the beat-wave case $\epsilon_N \simeq 1$ and in the Raman case $\epsilon_N \ll 1$.

4. Relative action transfer: The relative action transfer R_c of SRS in magnetized plasma can be solved from the coupled mode equations for the two electromagnetic waves and the plasma wave [1,4]. In most cases ($T_e > 10$ keV) SRS-F dominates over SRS-B due to the weaker Landau damping. For weakly damped Raman forward process the relative action transfer, $R_c = \Delta\Psi_0/\Psi_0(0)$, where $\Delta\Psi_0 = \Psi_0(0) - \Psi_0(L)$, is given in terms of Jacobian elliptic functions [4].

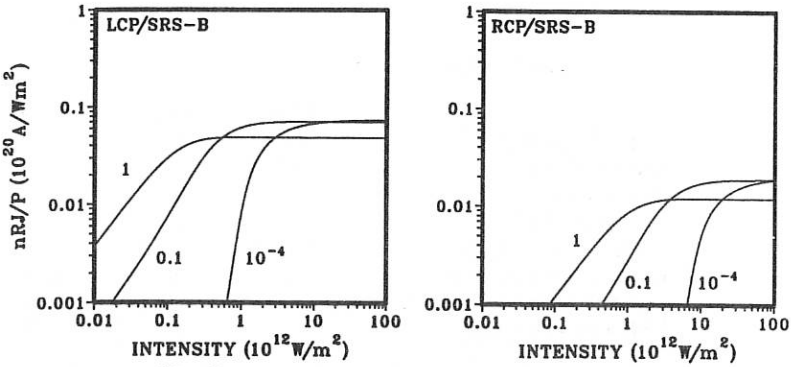

Figure 2: *CD-efficiency vs FEL pulse intensity and ϵ_N in the MTX case.*

When the linear damping starts to limit the growth of the Raman forward scattering, the steady-state action transfer R_c in SRS-F can be estimated from [1,4]

$$R_c + \epsilon_N = (1 - R_c)\epsilon_N \exp[(2L_aL/L_g^2)(1 + \epsilon_N)]\,, \tag{2}$$

where L_g is the gain length in magnetized plasma [4] and L_a is the linear absorption length. The intensity dependence of R_c is in the gain length, i.e., $L_g \sim 1/\sqrt{I_0}$, where I_0 is the peak intensity of the FEL pulse (cf. Figs 1–2). The solution (2) requires $L_g/L_a > 1$.

At low temperatures the electron plasma wave in Raman backscattering is weakly damped and the steady-state solution with $\epsilon_N = 0$ gives $\mathrm{K}(\sqrt{R_c}) = L/L_g$. The function K is the complete elliptic integral of the first kind. At moderate temperatures of a few keV, adiabatic approximation in SRS-B leads to the well known solution [1,4]: $(R_c + \epsilon_N)(1 - R_c) = \epsilon_N \exp[(2LL_a/L_g^2)(1 - R_c - \epsilon_N)]$. Now the relative noise level is defined by $\epsilon_N = |\Psi_-(L)/\Psi_0(0)|$.

5. FEL current drive: We consider the FEL current drive in two different cases: (i) in a full scale reactor in which the Raman current drive can seed a large bootstrap current and (ii) in a small scale MTX-type demonstration experiment [8]. The parameters are given in Table 1. In both cases the bootstrap current is maximized by high plasma pressure.

Bootstrap reactor: Fig. 1 shows the current drive efficiency (1) as a function of FEL pulse intensity I_0 for various ϵ_N–values for a reactor (see Table 1). Nearly ten times higher intensities are required to obtain the maximum efficiency in the SRS-F case ($\epsilon_N = 10^{-4}$) than in the BW case ($\epsilon_N = 1$), but the maximum current drive efficiency is about two times better for SRS-F. Low intensity beat-wave system, however, suffers from the density detuning which should stay well below 1 % [4].

For the LCP pump, the peak intensity $I_0 = 10^{13}$ W/m^2 leads to an average FEL power $P = 28$ MW and beam radius 0.19 m, if the pulse length is 50 ns and the repetition

Table 1: *Reactor and MTX-parameters*

	MTX [8]	Reactor
major radius R [m]	0.64	7.0
minor radius a [m]	0.17	2.5
elongation κ	1.0	2.2
magnetic field B [T]	6.8	4.81
electron density $n_e(0)$ [m^{-3}]	2×10^{20}	10^{20}
electron temperature $T_e(0)$ [keV]	3.0	30
FEL wavelength LCP/RCP [mm]	1.06/0.63	1.29/0.58
FEL interaction length L [m]	0.1	2.0

rate is 0.1 kHz. This is enough to drive a seed current of 2 MA, which is amplified to 15 MA by the neoclassical bootstrap effect, if the reactor parameters are as in Table 1 and the temperature and density profiles are parabolic [6]. Smaller seed currents would lead to unstable safety factor profiles [6]. The efficiency is $J/P = 0.54$ A/W, when the bootstrap effect is taken into account.

MTX-type experiment: The situation in MTX is different from the reactor case (see Table 1). Since the temperature is lower, the SRS-B plasma wave is weakly damped and the backscattering dominates over SRS-F. This implies that the current drive efficiencies are lower, because the resonant electrons are less energetic in SRS-B than in SRS-F. According to Fig. 2 the CD-efficiency in the LCP case exceeds 5×10^{18} A/Wm^2, when the FEL intensity is 5×10^{12} W/m^2. If the beam radius is 1.6 cm, this corresponds to an average FEL power of 1 MW assuming that the pulse length is 50 ns and the pulse repetition rate is 5 kHz. The FEL driven current is 40 kA and the total bootstrap amplified current may exceed 250 kA assuming that the profiles are parabolic and the MTX parameters are as in Table 1 [6]. Thus the current/power ratio $J/P = 0.25$ A/W is now somewhat lower than in the reactor case.

REFERENCES

1. Cohen, B.I. et al., Nucl. Fusion **28** (1988) 1519.
2. Heikkinen, J.A. et al., Nucl. Fusion **28** (1988) 1845.
3. Amin, M.R., Cairns, R.A., Nucl. Fusion **30** (1990) 327.
4. Karttunen, S.J. et al., Nucl. Fusion 1991 (to be published).
5. Ghizzo, A. et al., Europhys. Conf. Abstr. **14 B** (1990) 1299.
6. Alava, M.J., Karttunen, S.J., Plasma Phys. Contr. Fusion **32** (1990) 1135.
7. Karney, C.F.F., Fisch, N.J., Phys. Fluids **28** (1985) 116.
8. Thomassen, K.I., Plasma Phys. Contr. Fusion **30** (1988) 57.

RELATIVISTIC ELECTRON CYCLOTRON ABSORPTION FOR PERPENDICULAR PROPAGATION IN AN INHOMOGENEOUS MAGNETIC FIELD

M. BORNATICI

Physics Department, University of Ferrara, Ferrara, Italy
Physics Department "A. Volta", University of Pavia, Pavia, Italy

The electron cyclotron absorption profile of the fundamental ordinary-mode is evaluated by accounting for both relativistic and girokinetic effects. The range of validity of the standard, locally uniform analysis is assessed and it is shown that, for perpendicular propagation, the absorption profile has to do with relativistic effects. The independence of the optical thikness on the pole in velocity space is discussed.

Introduction. As is known, the standard analysis of electron cyclotron (EC) absorption in weakly inhomogeneous magnetized plasmas is carried out whithin the framework of the geometrical optics approximation, which is applicable as long as wave absorption is weak and the wavelenght is short compared to the spatial width of the cyclotron resonance /1,2/. Recently, however, it has been argued that such a locally uniform approach may be questionable as regards the EC absorption profiles since it neglects the effects of magnetic field variation across the (electron) Larmor orbit /3/. More specifically, using a nonrelativistic gyrokinetic theory, EC absorption profiles are obtained /3/ for both the fundamental ordinary (O)-mode and second harmonic extraordinary-mode for perpendicular propagation in a Maxwellian plasma, which are in marked contrast with the standard relativistic profiles /2,4/. The corresponding optical thicknesses, though, are the same as the ones obtained by means of a relativistic calculation /2/.

Here we evaluate the EC absorption profile (and the optical thickness) of the perpendicular O-mode by accounting for both the relativistic mass variation and the self-consistent magnetic field variation. By determining the range of validity of the standard, locally uniform approach, we show, in particular, that for perpendicular propagation the EC absorption profile has to do with relativistic effects in all relevant cases.

EC absorption of the fundamental O-mode. For propagation perpendicular to the magnetic field $\mathbf{B} = B\,(1+x/L_B)\,\hat{\mathbf{z}}$ and into the field gradient, the (resonant) contribution from the lth-harmonic to the anti-Hermitian part of the dielectric tensor of a Maxwellian plasma is

$$\varepsilon^{(1)}_{a,zz} = \frac{2}{\sqrt{\pi}} \left(\frac{\omega_p}{\omega}\right)^2 \frac{\omega L_B}{v_T\, l!} \left(\frac{k_x \rho}{2}\right)^l \cdot$$

$$\cdot \mathrm{Re}\left\{ \int d^3V\, V_z^2 \left(V_x - iV_y\right)^l e^{-v^2 + ik_x \rho V_y} \delta\left(a_l(x, V_y, V^2)\right) \right\} \qquad (1a)$$

$$a_l(x,V_y,V^2) = \zeta_l(x) - V_y + \frac{l}{\mu}\frac{L_B}{\rho}V^2 \qquad (1b)$$

with $\zeta_l(x) \equiv (L_B/lv_T)(\omega - l\omega_c(x))$, $l(\geq 1)$ is the harmonic number; $\rho = v_T/\omega_c$ is the electron Larmor radius, $\mu \equiv 2(c/v_T)^2 = mc^2/T$, and $Re\{a\}$ denotes the real part of a. Expression (1a) is obtained from Eq.(53) of Ref.3 by accounting for the (weakly) relativistic mass variation (the last term on the r.h.s. of (1b)) in the resonant denominator in the kinetic integral. Also, finite Larmor radius effects are kept to the lowest order.

Of pratical relevance is the evaluation of both the absorption coefficient, $\alpha^{(0)} = (\omega/cN_\perp^{(0)})\,\varepsilon_{a,zz}$, with $N_\perp^{(0)}$ the (perpendicular) refractive index of the O-mode, and the optical thickness, $\tau = \int_{-\infty}^{\infty}\alpha\,dx$. As for the evaluation of the latter, one can carry out the x-integration before the integration over velocity space, appearing in (1a), thus requiring explicitly only the x-dependent part of the argument (1b) of the δ-function in (1a), i.e. the optical thickness has to do with (the pole connected with) the inhomogeneity of the magnetic field, no matter what is the pole in velocity space, if any. Explicitly, noting that $dx = -(v_T/\omega_c)d\zeta_l$ for a linear field profile and using (1a), one has

$$Re\left\{\int d^3V\, V_z^2\left(V_x - iV_y\right)^l e^{-V^2 + lk_x\rho V_y}\int dx\,\delta\left(a_l(x,V_y,V^2)\right)\right\} =$$

$$= \frac{v_T}{\omega_c}\,Re\left\{\int d^3V\, V_z^2\left(V_x - iV_y\right)^l e^{-V^2 + lk_x\rho V_y}\right\} = \frac{\pi^{3/2}}{2}\frac{v_T}{\omega_c}\left(\frac{k_x\rho}{2}\right)^l \qquad (2a)$$

so that

$$\tau_l^{(0)} = \frac{\pi\, l^{2l-1}}{2^l l!}\left(\frac{\omega_p}{\omega_c}\right)^2 (N_\perp^{(0)})^{2l-1}\left(\frac{T}{mc^2}\right)^l \frac{\omega_c L_B}{c} \qquad (2b)$$

which is just the standard expression of the optical thickness for perpendicular propagation /2/.

In contrast to the optical thickness, the absorption coefficient and, hence, the absorption profile depend explicitly on the pole in velocity space which governs the corresponding integration in (1a). Let us consider explicitly the first harmonic (l=1) O-mode. The velocity integration in (1) can be carried out by using the δ-function for the integration over V_z, the V_x-integration being then straightforward, and making the change of variable $V_y = (\mu/2)(\rho/L_B) + (z/\mu\rho/L_B)\tau$, so that the τ-integration can be expressed in terms of the modified Bessel functions $I_\nu(z)$ of half-integer index ν and (real) argument

$$z \equiv \mu \frac{\rho}{L_B}\left[\mu \frac{\omega_c - \omega}{\omega_c} + \left(\frac{\mu}{2}\frac{\rho}{L_B}\right)^2\right]^{1/2}, \quad \frac{\omega}{\omega_c} \leq 1 + \frac{\mu}{4}\left(\frac{\rho}{L_B}\right)^2 \equiv \frac{\omega_{max}}{\omega_c} \qquad (3a)$$

Explicitly one obtains

$$\alpha_1^{(0)} = \sqrt{\pi}\left(\frac{\omega_p}{\omega_c}\right)^2 N_\perp^{(0)} \frac{\omega_c}{c} P\left(z, \mu\frac{\rho}{L_B}\right) e^{-\mu\frac{\omega_c - \omega}{\omega_c}} \qquad (3b)$$

with the profile-function

$$P\left(z,\mu\frac{\rho}{L_B}\right) \equiv \frac{2\sqrt{2\pi}\, z^{3/2}}{(\mu\rho/L_B)^3}\left\{\left[\left(\frac{\mu}{2}\frac{\rho}{L_B}\right)^2 + \left(\frac{z}{\mu\rho/L_B}\right)^2\right] I_{3/2}(z) - \left[1 + \left(\frac{2}{\mu}\frac{L_B}{\rho}\right)^2\right] z\, I_{5/2}(z)\right\} e^{-\frac{1}{2}\left(\mu\frac{\rho}{L_B}\right)^2} \qquad (3c)$$

Discussion of the absorption profile. Let us consider first the limit in which gyrokinetic effects are negligible w.r.t. relativistic effects, i.e.,

$$\left(\frac{\mu}{2}\frac{\rho}{L_B}\right)^2 \ll \text{Min}\left\{1, \mu\frac{|\omega_c - \omega|}{\omega_c}\right\} \qquad (4a)$$

so that $z \ll 1$, and the series expansion of $I_\nu(z)$ can be used. The profile function (3c) then reduces to

$$P\left(z,\mu\frac{\rho}{L_B}\right) = \frac{4}{15}\left(\mu\frac{\omega_c - \omega}{\omega_c}\right)^{5/2}, \quad \omega < \omega_c \qquad (4b)$$

to lowest order with regard to condition (4a). Such a result, which follows directly from (1) by neglecting the V_y-term in the δ-function, is just the standard relativistic expression of the EC absorption of the fundamental O-mode for perpendicular propagation /2/. On the other hand, for $\omega = \omega_c$, one obtains $P(\omega = \omega_c) = \frac{8}{5}\left(\frac{\mu\rho}{2L_B}\right)^5 (\ll 1)$. Condition (4a) appears to be easily satisfied due to the smallness of the electron Larmor radius ρ w.r.t. the scale lenght L_B ($\simeq$ the major radius in a tokamak) ; in fact, $\frac{\mu}{2}\frac{\rho}{L_B} = 2.7\left[T^{1/2}(\text{keV})\ B\ (10^4\text{G})\ L_B(\text{cm})\right]^{-1} (< 10^{-1}$, typically).

When condition (4a) is reversed, so that $z \simeq (1/2)(\mu\rho/L_B)^2 \gg 1$, by using the asymptotic expansion of the Bessel functions in (3c) one gets

$$P\left(z,\mu\frac{\rho}{L_B}\right) e^{-\mu\frac{\omega_c-\omega}{\omega_c}} = \frac{L_B}{\rho}\frac{T}{mc^2}\zeta_1^2 e^{-\zeta_1^2} \qquad (5a)$$

to lowest order with regard to the condition

$$\left(\frac{\mu}{2}\frac{\rho}{L_B}\right)^2 \gg \text{Max}\left\{1,\mu\frac{|\omega_c-\omega|}{\omega_c},\zeta_1^{-2}=\left(\frac{L_B}{v_T}|\omega-\omega_c|\right)^{-2}\right\} \qquad (5b)$$

Result (5a), which follows straightforward from (1) by neglecting the V^2-term in the δ-function, has to do with gyrokinetic effects only and is just the results obtained in Ref.3. Such an absorption profile, with features noticeably different from those of the relativistic profile (4b), is, however, subject to condition (5b) which is hardly ever satisfied.

In conclusion, we have shown that, for perpendicular propagation, the EC absorption profile has to do with relativistic effects in all relevant cases.

Acknowledgement. This work was supported by the Ministero della Pubblica Istruzione of Italy.

References

/1/M.Bornatici and F.Engelmann, Commments Plasma Phys. Contr. Fusion **8**, 57 (1983).

/2/M.Bornatici, R.Cano, O.De Barbieri and F.Engelmann, Nucl. Fusion **23**, 1153 (1983).

/3/C.N.Lashmore-Davies and R.O.Dendy, Phys. Fluids **B1**, 1565 (1989).

/4/M.Bornatici , U.Ruffina and E.Westerhof, Comments Plasma Phys. Contr. Fusion 9, 73 (1985).

3D TREATMENT OF THE EFFECTS OF RADIAL TRANSPORT ON RF CURRENT DRIVE IN TOKAMAKS

M R O'Brien, M Cox, J S McKenzie and C D Warrick

UKAEA/EURATOM Fusion Association, Culham Laboratory
Abingdon, OX14 3DB, UK.

1 Introduction

A 3D Fokker-Planck code, BANDIT3D, has been written to study combined kinetic and transport effects in tokamaks. In ECRH current drive (ECCD) experiments on CLEO [1], in which the driven current was a third of the theoretically predicted value and the energy confinement time (τ_E) was comparable with the collision time of the heated electrons (τ_C), radial transport processes were thought to account for the reduced current drive efficiency [2,3]. In larger tokamaks with $\tau_E \gg \tau_C$ the radial transport, while not reducing the current drive efficiency, is predicted to broaden the RF driven profile [3,4], with consequences for the use of localised RF current drive to stabilise MHD activity in tokamaks [5]. Unlike analytic techniques [2,4] or 2D codes [3], a 3D code allows the treatment of nonlinear problems (e.g. quasilinear flattening) and trapped particle effects. In this paper, we discuss the physics modelled by the code and describe its use to model the ECCD experiments on CLEO and DITE [6], and to study LHCD in JET- and ITER-sized tokamaks.

2 3D Fokker-Planck Equation

The code solves for the electron distribution function $f(v,\theta,r,t)$ as a function of momentum (v), pitch-angle (θ), flux surface radius (r), and time (t). The bounce-averaged Fokker-Planck equation may be written schematically as:

$$\frac{\partial f}{\partial t} = \left(\frac{\partial f}{\partial t}\right)_{coll} + \left(\frac{\partial f}{\partial t}\right)_{ECRH} + \left(\frac{\partial f}{\partial t}\right)_{LH} + \left(\frac{\partial f}{\partial t}\right)_{\Omega} + \left(\frac{\partial f}{\partial t}\right)_{tran} \qquad (1)$$

Here the terms due to collisions (with electrons and ions), Electron Cyclotron, Lower Hybrid and Ohmic heating are those used in 2-D (in velocity space) Fokker-Planck codes [7]. The radial transport term is of the form:

$$\left(\frac{\partial f}{\partial t}\right)_{tran} = \frac{1}{g(1+\epsilon)r}\frac{\partial}{\partial r}\left[\, r\,\left(\, D_{tr}\frac{\partial(g(1+\epsilon)f)}{\partial r} + V_{tr}g(1+\epsilon)f\,\right)\right] \qquad (2)$$

In equation (2) ϵ ($= r/R_o$, with R_o the major radius) and g (proportional to the bounce/circulation time for trapped/passing electrons) arise from the bounce-averaging. The radial diffusivity and inward pinch, D_{tr} and V_{tr}, may be functions of v, θ and r: in this paper we take D_{tr} independent of v and θ and $\sim \chi_E$, the thermal diffusivity, and adjust V_{tr} to maintain $n_e(r)$. The code treats non-circular equilibria and time dependent problems although only circles and steady state solutions are discussed here. Details of the method used to solve this equation are given elsewhere [8].

3 Modelling of ECCD Experiments

In the CLEO 2nd harmonic ECCD experiments [1], the rf power drove $\sim \pm$4-5kA (about a third of that predicted theoretically) out of a total plasma current of 10kA. The remaining plasma current was driven by the loop Voltage, 0.15V (0.5V) for co (counter) ECCD. The code was used to simulate these experiments using experimental parameters namely $R_o = 0.94$m, $a = 0.13$m, $n_e(r) = (0.06+0.54(1-(r/a)^2)) \times 10^{19}\mathrm{m}^{-3}$, $V_L = 0.15$V, magnetic field at $R_o = 1.026$T ($\omega = \omega_{ce}$ at $R = 0.9$m, i.e. $r = 0.04$m) and $Z_{eff} = 2$. The ECRH parameters were chosen to match the launch conditions (60GHz radiation launched in the X mode at 15 degrees to the major radius vector with total absorbed power 155kW) and gave an absorption profile that agreed with ray tracing [1]. In the simulation the radial diffusivity D_{tr} was taken to be independent of θ and v. Its radial dependence and magnitude ($n_e(r)D_{tr}(\theta, v, r) = 1.5 \times 10^{19}(1+3(r/a)^3)$ m^{2}s^{-1}, i.e. $D_{tr} \sim \chi_E$, and V_{tr} chosen to maintain $n_e(r)$) gave the increased transport observed in the outer regions of tokamaks.

Figure 1 shows the temperature, current and power deposition profiles predicted by the code, together with the (input) density profile. The level of transport chosen gave good agreement with both the soft X-ray temperature profile ($T_e(r) \sim 1.3(1-(r/a)^2)^3$ keV) and the correct total current (10kA). This result shows that the same level of transport can account for both the reduced current drive efficiency and the observed $T_e(r)$. Figure 2 shows contours of f as a function of $v_\parallel$ and $v_\perp$ (evaluated on the outside of the flux surface) for $r = 0.0325$m, showing that f is close to Maxwellian at low speeds, but that there is an enhanced population of fast trapped electrons: evidence for these in CLEO ECRH experiments has been reported elsewhere [9]. This simulation was for the experiment in which the Ohmic and ECCD currents were in the same direction. A simulation for the counter ECCD gave a hollow $j(r)$ (with $j(r = a/4) \sim 2j(r = 0)$) and, for the correct $T_e(r)$, too low a plasma current (5.7kA). This may be due to the absence from the code of processes that resist such a non-monotonic $j(r)$.

The DITE ECCD experiments [6], in which $\sim$ 8kA out of 37kA were driven, have also been simulated by the code. Agreement was found for both co and counter ECCD if the bootstrap currents predicted from the plasma profiles were allowed for, and the broadening of $j(r)$ due to radial transport processes agreed with l_i measurements. The reason for the need to include I_{BS} for DITE but not for CLEO ($\sim$ 4kA from profiles) is unclear: investigation awaits the inclusion of the terms giving I_{BS} in BANDIT3D.

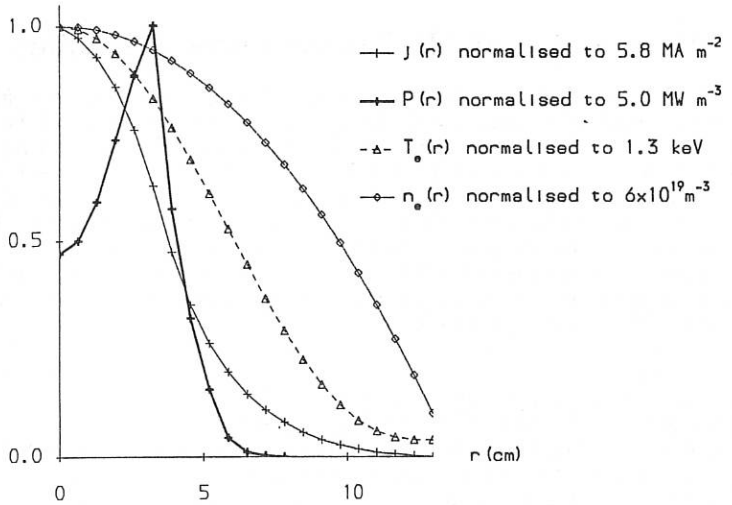

Figure 1 Plasma profiles for the CLEO ECCD experiment.

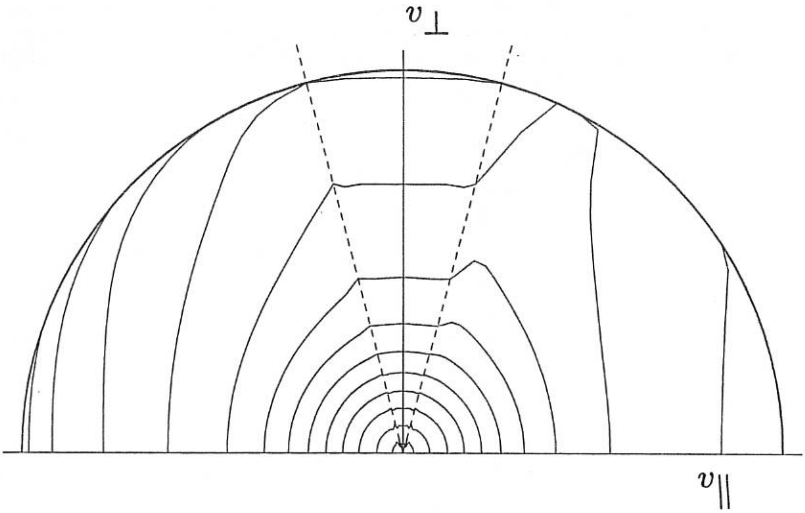

Figure 2 Contours of f in velocity space at $r = 3.25$cm for CLEO ECCD. The maximum speed is $5(2T_e/m_e)^{\frac{1}{2}}$. The dashed lines are the trapped passing boundaries.

4 Broadening of LH Driven Current Profiles

In tokamaks with $\tau_E \gg \tau_C$, the transport will not reduce the current drive efficiency. However it may still broaden $j_{RF}(r)$, particularly if the density is low and the heated electrons fast. Figure 3 shows $j_{LH}(r)$ with and without radial transport for a JET-sized tokamak (R_o = 3m, a = 1.2m) for LHCD at $r = a/2$ with a radial spread $\sim a/10$, $n_{\|} = 2$, $\Delta n_{\|} = 0.2$, $T_e(0)$ = 15keV, $n_e(0) = 3 \times 10^{19}$ m^{-3}, $Z_{eff} = 2$. The diffusivity, which satisifes $n_e(r)D_{tr} = 3 \times 10^{19}\ m^2 s^{-1}$, is comparable to typical tokamak values for χ_E, with V_{tr} maintaining parabolic $n_e(r)$. There is some experimental evidence that D_{tr} drops at high energies and so these values may be over-estimates. Figure 3 shows that for these conditions the radial transport broadens $j_{LH}(r)$ by a factor ~ 2. However for larger ITER-like devices the effect is smaller.

References

[1] Lloyd, B, et al, Nucl. Fus. 28 (1988) 1013.
[2] Dendy, R O, and O'Brien, M R, Nucl. Fus. 29 (1989) 480.
[3] O'Brien, M R, Cox, M and McKenzie, J S, to be published as a letter in Nucl. Fus.
[4] Rax, J M, and Moreau, D, Nucl. Fus. 29 (1989) 1751.
[5] O'Brien, M R, et al, Proc 13th EPS Conference, Schliersee 1986, Vol 2 p270.
[6] Arshad, S, et al, Proc 17th EPS Conference, Amsterdam 1990, Vol 3 p1267.
[7] O'Brien, M R, Cox, M and Start, D F H, Nucl. Fus. 26 (1986) 1625, and references therein.
[8] McKenzie, J S, O'Brien, M R, and Cox M, to be published in Comp Phys Commun.
[9] Robinson, D C, in Turbulence and Transport (Proc. Int. Workshop on Small Scale Turbulence and Anomalous Transport in Magnetized Plasmas, Cargese, 1986), Editions de Physique, Orsay (1987) 21.

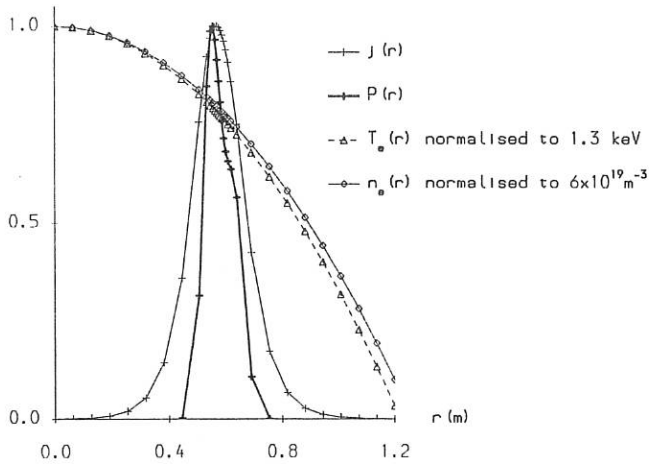

Figure 3 Plasma profiles for the simulation of LHCD in a JET-sized tokamak.

THREE-DIMENSIONAL SIMULATION OF ELECTRON CYCLOTRON CURRENT DRIVE IN TOKAMAK PLASMA

Yu.N.Dnestrovskij*, D.P.Kostomarov, A.G.Shishkin, A.P.Smirnov

*I.V.Kurchatov Institute of Atomic Energy, Moscow, USSR
Moscow State University, Moscow, USSR

Abstract

The trajectories of electron cyclotron (EC) waves and the absorption of RF power on different magnetic surfaces in tokamak plasma are determined within the framework of geometric optics. The wave induced current is calculated on each magnetic surface by the solution of 2D bounce-averaged Fokker-Planck equation with the quasilinear diffusion term. The radial profiles of the current and absorbed RF power density for the tokamak with parameters of T-10 Tokamak are presented.

Model

The model developed consists of three basic parts:
- the determination of trajectories and absorption of EC waves;
- the determination of quasilinear diffusion coefficient;
- the solution of 2D bounce-averaged kinetic equation.

1) The propagation and the absorption of EC waves in plasma are described by the following geometric optics equations:

$$\frac{d\vec{r}}{d\tau} = \frac{\partial H}{\partial \vec{p}}, \qquad \frac{d\vec{p}}{d\tau} = -\frac{\partial H}{\partial \vec{r}}, \tag{1}$$

where $\vec{r}:\{\rho,\theta,\varphi\}$ are the toroidal coordinates, $\vec{p}:\{k_\rho, \rho k_\theta, (R_o+\rho\cos\theta)k_\varphi\}$ are the components of wave vector $\vec{k}$ as conjugate momenta [1], τ is the arc length along the ray. The left hand side of dispersion relation with dielectric tensor for cold plasma is used as Hamiltonian of (1). To calculate wave absorption the non-relativistic dispersion relation for Maxwellian plasma is used. The fraction of RF power, $\Delta(\tau)$, absorbed by the plasma is given by

$$\Delta(\tau)=1-\exp\left(-2\int_0^{\tau} \mathrm{Im}\,\vec{K}\cdot d\vec{r}\right) \qquad (2)$$

where the integral is along the ray path.

2) The wave-particle interaction is described within the framework of quasilinear theory by the solution of 2D bounce-averaged Fokker-Planck equation. The integrals of motion - the module of velocity v and the normalized magnetic moment $s=v_1^2 B_0/v^2 B$ - are chosen as independent variables in velocity space. The time evolution of the electron distribution function is evaluated by means of the following equation [2,3]:

$$J_1 \cdot \frac{\partial f_e^{\circ\mp}}{\partial t} = \left\langle \left[\frac{\partial f_e^{\circ\mp}}{\partial t} \right]_{coll} \right\rangle + \left\langle \left[\frac{\partial f_e^{\circ\mp}}{\partial t} \right]_{ec} \right\rangle \qquad (3)$$

where "o", "+" and "-" correspond to trapped and to passing particles moving along the magnetic field and in opposite direction respectively. $\left\langle \left[\frac{\partial f_e^{\circ\mp}}{\partial t} \right]_{coll} \right\rangle$ is the linearized Fokker-Planck operator of Coulomb collisions of suprathermal electrons with Maxwewllian background,

$$\left\langle \left[\frac{\partial f_e^{\circ\mp}}{\partial t} \right]_{ec} \right\rangle = \frac{1}{v^2}\frac{\partial}{\partial v}\cdot\left[v^2 s\cdot \hat{J}_1^{\circ\mp}\cdot\frac{\partial \hat{f}_e^{\circ\mp}}{\partial v} + 2vs\cdot\hat{J}_2^{\circ\mp}\cdot\frac{\partial \hat{f}_e^{\circ\mp}}{\partial s}\right] +$$

$$\frac{1}{v^2}\frac{\partial}{\partial s}\cdot\left[4s\cdot\hat{J}_3^{\circ\mp}\cdot\frac{\partial \hat{f}_e^{\circ\mp}}{\partial s} + 2sv\hat{J}_2^{\circ\mp}\cdot\frac{\partial \hat{f}_e^{\circ\mp}}{\partial v}\right] \qquad (4)$$

is the quasilinear diffusion operator for electron cyclotron waves,

$$\hat{J}_n(\rho,s)=\frac{1}{2\pi}\int \hat{D}^{\circ\mp}(1+\varepsilon\cdot\cos\theta-s)^{n-3/2}\,d\theta, \quad n=1,2,3.$$

3) The value of the quasilinear diffusion coefficient $\hat{D}(\rho,\theta,v,s)$ is determined by the absorbed power, its poloidal localization on magnetic surface and the resonance region in velocity space. The following representation for the diffusion coefficient is used:

$$\hat{D}(\rho,\theta,v,s)=D(\rho,\theta)\cdot\delta(v-v_1(\rho,\theta,v,s)). \qquad (5)$$

The resonance velocity v_1 is defined by the equation $k_\parallel v_\parallel = \omega - \omega_{ce}$, i.e. $k_\parallel(\rho,\theta)v_1\left(1 - \frac{sB(\rho,\theta)}{B_0}\right)^{1/2} = \omega - \Omega_e(1 - v^2/c^2)$, where $\Omega_e = eB(\rho,\theta)/m_e c$.

To determine the coefficient D the radiation pattern was divided into M rays. We consider that RF power is absorbed at a volume localized around i ray trajectory and this power $P(\rho,\theta_i)$ is poloidally localized on given magnetic surface near the point of intersection θ_i of the ray with the surface. The value of $D(\rho, \theta_i)$ is defined by the following balance equation

$$P(\rho,\theta_i) = \int_{\theta_i-\delta}^{\theta_i+\delta} \sum_{o,+,-} \left\langle \left(\frac{\partial f_e^{o}}{\partial t} \right)_{ec} \right\rangle \frac{m_e v^2}{2} d^3v \, \rho d\theta \, \Delta\rho \, 2\pi R_o. \quad (6)$$

Numerical results

Numerical calculations were performed for the parameters of T-10 Tokamak. The radial profiles of the absorbed EC power density and the current density for the following parameters:

the major radius R=150cm; the minor radius a=30cm;

the toroidal magnetic field on the axis B_o=27.3kG;

the density and temperature profiles:

$n_e(\rho)=[1.3(1-\rho^2/a^2)+0.5]\cdot 10^{13}cm^{-3}$;

$T_e(\rho)=[5.5(1-\rho^2/a^2)+0.5]keV$

are shown in Fig.1 and 2. Here waves with the ordinary mode are launched from the external side of tokamak at an angle of 60° to the magnetic field. The total input power P_{ec}=1MW. Two different cases are considered:

1) the wave frequency f=78.21GHz (the resonance surface is in the centre of plasma torus $r_{res}=R_o$);

2) f=81.75GHz (the resonance surface is displaced on 6.5cm from plasma centre to the high field side of tokamak $r_{res}=R_o$-6.5 cm).

In the former case the total generated current I=0.167MA and in the latter case I=0.224MA. The high level of launched power resulted in the considerable deviation of the electron distribution function from Maxwellian one.

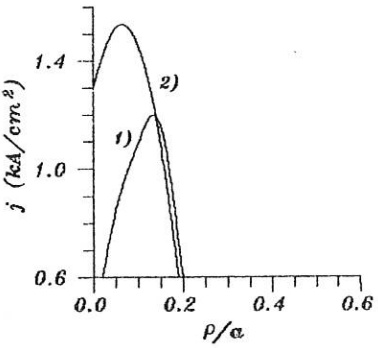

Fig.1

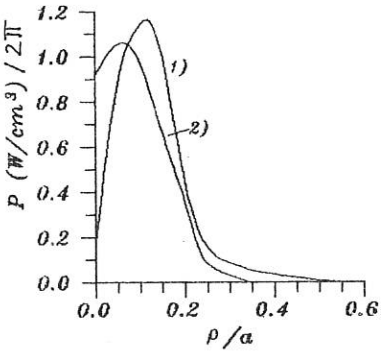

Fig.2

Fig.1 The radial profiles of current density for cases 1) and 2).

Fig.2 The radial profiles of absorbed RF power density for cases 1) and 2).

For the parameters of case 1) the computations have been done also for low level P_{ec}=1W of input RF power (I=0.11A). Now the distortions of distribution function were small. From the results obtained one can conclude that the electron cyclotron current drive efficiency $\eta=I/P_{ec}$ is power dependent and increases above the linear values for P_{ec}=1W. These results are in a good agreement with the results of Ref.4.

References

1. Smirnov A.P., Shishkin A.G. Fiz.Plazmy, 1991, v.17, №2, p.260.
2. Dnestrovskij Yu.N., Smirnov A.P., Shishkin A.G. Fiz.Plazmy, 1990, v.16, №11, p.1286-1292.
3. Dnestrovskij Yu.N., Kostomarov D.P., Shishkin A.G., Smirnov A.P. In: Proc. of 17th EPS Conf. on Controlled Fusion and Plasma Heating, Amsterdam, 1990, v.14B, Part III, p.1239-1242.
4. Lohr J., James R.A., Giruzzi G. et al. In: Proc. of Int. Conf. on Theory of Nonlinear Waves in Plasmas, Suzdal, 1990.

SPECTRAL PROPERTIES AND ABSORPTION OF ALFVEN WAVES IN TOROIDAL PLASMAS

Elfimov A.G.*, Medvedev S.Yu., Pestryakova G.A.

Keldysh Institute of Applied Mathematics
USSR Academy of Sciences, Moscow, USSR
*I.N.Vekua Institute of Physics and Technology,
Sukhumi, USSR

Alfvén wave heating has been simulated in the frame of linear Hall MHD (HMHD) for low pressure (cold) plasma. Infinitely thin antenna was placed into vacuum region between plasma surface and perfectly conducting shell. Variational formulation of equations in straight field lines flux coordinates (ψ,θ,ζ) was used for numerical calculations. Finite element (f.e.) technique [1] employing Fourier series in θ,ζ and hybrid f.e. in ψ was chosen.

Analytic [2] and numerical [3] investigations of toroidal plasma continuous spectrum revealed the existence of gaps in continuum and global eigenmodes in the gaps (TAE) due to poloidal nonuniformity of magnetic field.

The ideal HMHD equations can be written in the form analogous to [2]:

$$\nabla\psi\cdot\nabla\begin{pmatrix}\xi\\ B_{\parallel}\end{pmatrix} = C\begin{pmatrix}\xi\\ B_{\parallel}\end{pmatrix} + D\begin{pmatrix}\lambda\\ B_{\perp}\end{pmatrix},\quad F\begin{pmatrix}\xi\\ B_{\parallel}\end{pmatrix} + G\begin{pmatrix}\lambda\\ B_{\perp}\end{pmatrix} = 0, \qquad (1)$$

ψ – magnetic surface label, $\nabla\psi\cdot\mathbf{B}_0=0$; $\xi=\mathbf{x}\cdot\nabla\psi$, $\lambda=\mathbf{x}\cdot\mathbf{B}_0\times\nabla\psi/|\nabla\psi|^2$ – displacement components; $B_{\parallel}=\mathbf{B}\cdot\mathbf{B}_0/B_0^2$, $B_{\perp}=\mathbf{B}\cdot\mathbf{B}_0\times\nabla\psi/B_0^2$ – perturbed magnetic field components; C, D, F, G – matrix operators 2×2 including $\mathbf{B}_0\cdot\nabla$ and $\mathbf{B}_0\times\nabla\psi\cdot\nabla$ only. The solution singularities locate at the magnetic surfaces where

$$G\begin{pmatrix}\lambda\\ B_{\perp}\end{pmatrix} = 0 \quad\text{or}\quad \frac{\omega^2}{\gamma v_A^2}|\nabla\psi|^2\lambda + \mathbf{B}_0\cdot\nabla\left(\frac{|\nabla\psi|^2}{B_0^2}\mathbf{B}_0\cdot\nabla\lambda\right) = 0, \qquad (2)$$

$\gamma = 1 - \omega^2/\omega_{CI}^2$, $v_A^2 = B_0^2/4\pi\rho_0$.

The set of eigenvalues of (2) for all magnetic surfaces is HMHD continuous spectrum.

Fig.1 shows noncircular plasma continuous spectrum. Plasma boundary was given by

$$r/R = 1 + \varepsilon\cos(\theta + \delta\sin\theta),\quad z/R = \kappa\,\varepsilon\sin\theta,$$

$$A=1/\varepsilon=4.5,\qquad \kappa=1.25,\qquad \delta=0.25,$$

(r,z,φ) – cylindrical coordinates, R – torus major radius, A – aspect ratio, θ – poloidal angle, κ – elongation, δ – triangularity. Force-free equilibrium was computed for given toroidal current density $rj_t(\bar{\psi})=(1-\bar{\psi}^{\alpha})^{\nu}$, $\alpha=0.7$, $\nu=0.5$ ($\bar{\psi}$ – normalized

poloidal flux) and safety factor at the magnetic axis q_0=1.1 corresponding to q_s=2.16 at the plasma surface. Density distribution over magnetic surfaces was chosen to be $\rho_0(\bar{\psi})=\rho_0(0)(1-\beta\bar{\psi})$, β = 0.6; toroidal wave number N = 1.

The results of computations show that plasma cross-section elongation and triangularity being the source of additional magnetic field poloidal nonuniformity give rise to continuum gaps and specific "2D" global eigenmodes (Fig.2b, 2c). Poloidal nonuniformity couples poloidal modes with poloidal wave numbers l_1 and $l_2=l_1+l$, where l=2 for elongate, l=3 for triangular plasma cross-section. The number of gaps is proportional to N and depends on profile of $q(\bar{\psi})$. Fig.2 presents Fourier harmonics of normal to magnetic surfaces electric field component $E_N=E\cdot\nabla\psi/|\nabla\psi|$ corresponding to the global eigenmodes induced by plasma cross-section geometry. The l_1, l_2 harmonics dominate reaching their maxima near the surfaces of continuum branches reconnection. The number of induced global modes coincides with the number of continuum gaps.

The 2D HMHD code was employed to investigate Alfvén wave heating of low pressure toroidal plasma using helical antennae. Circular cross-section deuterium plasma with minor radius ρ_p=12cm was considered. The equilibrium parameters were A=4.5, κ=1, δ=0, α=1, ν=1, q_0=1.1, q_s=2.68, β=0.97. The magnetic field at the magnetic axis, antenna and shell radii were B_0=2T, ρ_A=13cm, ρ_s=16.5cm. The antenna current density was given by $j_A=j_0\delta(\rho-\rho_A)e^{i(M\theta+N\varphi-\omega t)}$, M,N – poloidal and toroidal wave numbers, ρ – the distance from magnetic axis. The computations shows the behavior of surface (S) and global (G) modes frequencies far from continuum gaps to be in accordance to 1D computations. Like in 1D case the dispersion depends strongly on the profile and value of toroidal current as well as the signs of M and N [4]. While the signs are negative the S mode frequency approaches the threshold frequency ω_{th} with increasing |N|. For some values of q and ν there exists the N_{cr} corresponding to combined resonance [5] at the frequency close to that of global mode frequency (Fig.3).

Under such conditions high energy absorption near the plasma center takes place. The value of antenna loading reaches maximum while the plasma reactance is not higher than resistance (Fig.4). The profiles over magnetic surfaces of absorbed power and harmonics of binormal electric field component $E_\perp=\mathbf{E}\cdot\mathbf{B}_0\times\nabla\psi/(B_0|\nabla\psi|)$ are shown in Fig.5,6 (ω/ω_{CI}=0.471, $N=N_{cr}$=–4).

1. L.M.Degtyarev , S.Yu.Medvedev, Comput. Phys. Commun. 43, 29, (1986)

2. C.E.Kieras, Y.A.Tataronis, J.Plasma Phys., 28, 395, (1982).
3. C.Z.Cheng, M.S.Chance, Phys. Fluids, 29, 3695, (1986).
4. A.G.Elfimov, K.G.Komoshvili, V.P.Sidorov, S.Yu.Medvedev, G.A.Pestryakova, Proc. Contrib. Papers 16th Europ. Conf. Contr. Fusion and Plasma Phys., Venice, v.1, p.423, 1989
5. A.G.Elfimov, K.G.Komoshvili, V.P.Sidorov, Proc. Contrib. Papers Intern. Conf. Plasma Phys., Kiev, v.1, p.22, 1987

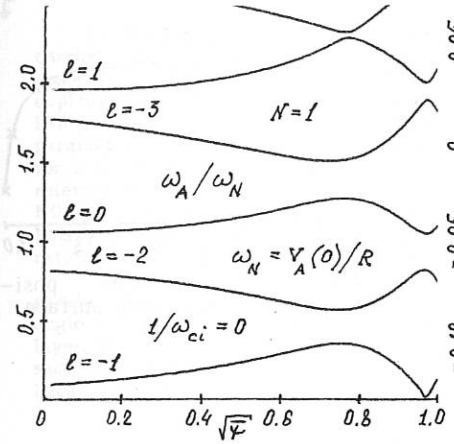

Fig.1 Alfvén continuous spectrum

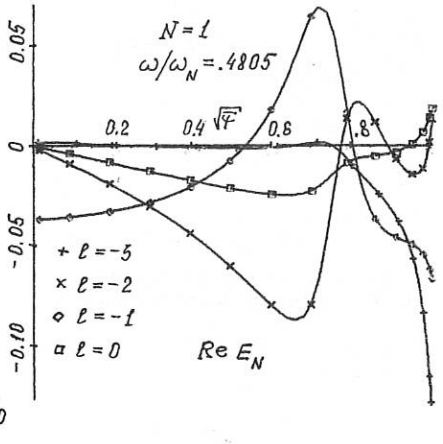

Fig.2a

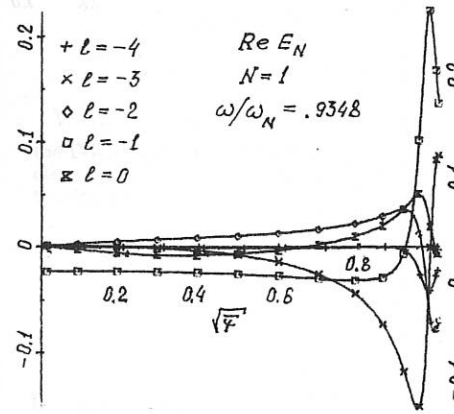

Fig.2b

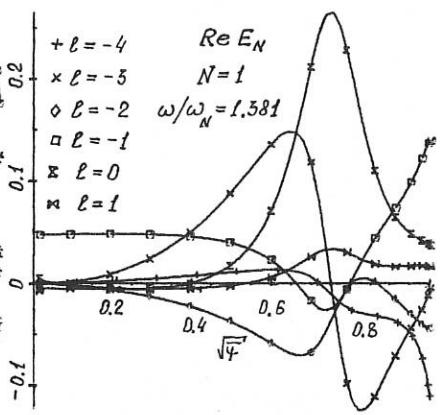

Fig.2c

Fig.2 Poloidal harmonics of normal electric field for a) TAE; b),c) Alfvén eigenmodes induced by elongation and triangularity

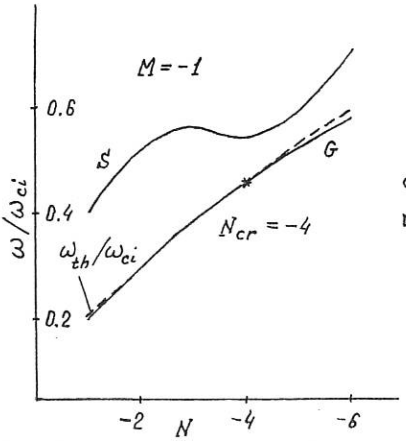

Fig.3 Low-frequency spectrum vs the toroidal wave number N

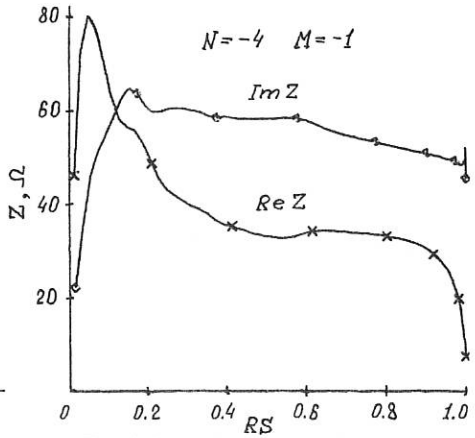

Fig.4 Impedance vs the position of main resonance surface

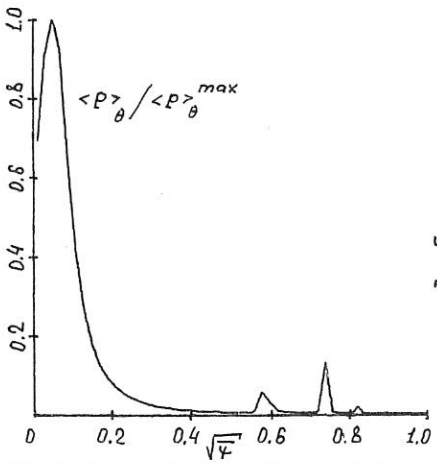

Fig.5 Averaged absorption profile; $N=N_{cr}=-4, M=-1, RS=0.515, \omega/\omega_{CI}=0.471$

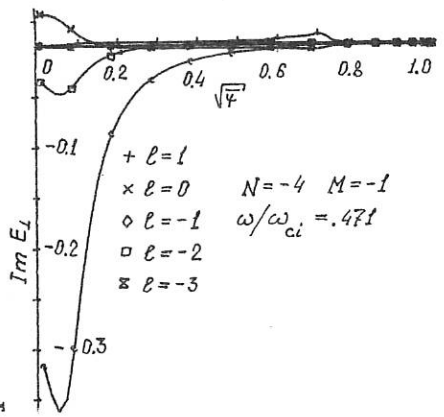

Fig.6 Poloidal harmonics of binormal electric field

THEORY OF LINEAR PROPAGATION AND ABSORPTION OF ION BERNSTEIN WAVES IN TOROIDAL GEOMETRY

A. Cardinali and F. Romanelli

Associazione EURATOM-ENEA sulla Fusione, C. R. E. Frascati,
C.P. 65 - 00044 - Frascati, Rome, Italy

I. INTRODUCTION

Ion Bernstein Waves (IBW) injection experiments at high power level (1 MW) carried out on DIII-D tokamak machine [1] have shown a very peripherical wave absorption and no significant central ion heating. In this paper we attempt to find an explanation of this unsuccessful result within the framework of the linear theory of IBW propagation and absorption without invoking non-linear theories as the onset of parametric decay instability [1]. The ray tracing equations for IBW propagation in toroidal geometry can be solved by choosing an appropriate ordering scheme for the relevant parameters $k_\perp\rho_i$ and ω. To be specific we assume $k_\perp\rho_i \approx 0(\varepsilon^{-1})$ and $(\omega - N\Omega_{ci})/\omega \approx 0(\varepsilon)$, where $k_\perp$ is the perpendicular wavenumber ρ_i is the ion Larmor radius, N is the harmonic number of the ion cyclotron resonance and ε is the inverse aspect ratio. Details of the calculation are given elsewhere [2].

The solution of the ray tracing equations shows an oscillating behaviour of the parallel refractive index and a strong dependence of its amplitude on the poloidal angle at the antenna or alternatively on the value of θ_0 at the lower hybrid conversion layer. The calculation of the absorption along the trajectory has been also obtained, showing that rays launched at angles $\theta_0 > 5°$ are absorbed at the plasma periphery because of the strong increase of $n_\parallel$.

RAY TRACING EQUATIONS AND ABSORPTION

The simplified Hamiltonian (hermitean part of the electrostatic dispersion relation) obtained using the above defined ordering can be written as

$$1 - \frac{m_i}{m_e}\frac{k_\parallel^2\rho_i^2}{2N^2} - \frac{\omega}{\pi^{1/2}k_\perp\rho_i(\omega - N\Omega_{ci})} = 0 \qquad (1)$$

This expression of the Hamiltonian is valid for $k_\perp\rho_i \gg 1$ and breaks down only in the extreeme periphery of the plasma where $k_\perp\rho_i \leq 1$. In such region the cold electrostatic dispersion relation can be retained. Using Eq. (1) we can write the ray tracing equations in toroidal geometry as follows:

$$\frac{d\theta}{dx} = \frac{\partial H/\partial m_\theta}{\partial H/\partial k_r} = -\frac{\rho_i}{\pi^{1/2}R_0}\frac{m_i}{m_e}\frac{1}{q^2N^2}\frac{m_\theta}{x}$$

$$\frac{d\phi}{dx} = \frac{\partial H/\partial n_\theta}{\partial H/\partial k_r} = -\frac{\rho_i}{\pi^{1/2}R_0}\frac{m_i}{m_e}\frac{1}{qN^2}\frac{m_\theta}{x} \qquad (2)$$

$$\frac{dm_\theta}{dx} = -\frac{\partial H/\partial\theta}{\partial H/\partial k_r} = \frac{R_0}{\pi^{1/2}\rho_i}\frac{\theta}{x}$$

where x is the distance in the major radius from the resonance layer normalised to the plasma radius, q is the safety factor, R_0 is the major radius of the torus, N is the harmonic resonance number, ρ_i is the ion Larmor radius, θ and ϕ are respectively the poloidal and toroidal angles and m_θ is the poloidal wavenumber.

In writing Eqs. (2) we have used the approximation $\theta \ll 1$ and $m_\theta \gg qn_\phi$ (with n_ϕ being the toroidal wavenumber) which can be a posteriori justified. The second approximation yields $k_\parallel \approx m_\theta/R_0q$, and $k_\chi \approx m_\theta/r$, which is valid everywhere far from the external layer of the plasma.

As the x variation of q and m_θ is faster than the equilibrium profile variation Eqs. (2) can be analitically solved yielding [2]:

$$k_\parallel(x) = \frac{m_\theta(0)}{R_0 q} + \left(\frac{m_e}{m_i}\right)^{1/2} \frac{\theta_0 N}{\rho_i} \sin(\nu \ln x) + k_{\parallel 0} \cos(\nu \ln x) \qquad (3)$$

where $k_{\parallel 0} = n_\phi/R_0(1 + \varepsilon x_0 \cos\theta_0)$, x_0 is the normalized plasma radius and it is taken to be 1, θ_0 and $m_\theta(0)$ are the values of the poloidal angle and wavenumber at the edge and the constant ν is

$$\nu = \frac{1}{\pi^{1/2}} \left(\frac{m_i}{m_e}\right)^{1/2} \frac{1}{Nq} \gg 1 \qquad (4)$$

For equatorial launching $\theta_0 = 0°$, the behaviour of $k_\parallel$ is dominated by the "cos" function of Eq. (3) whose amplitude (the constant $k_{\parallel 0}$) is the launched parallel wavenumber. However, for $\theta_0 \gg (m_i/m_e)^{1/2} k_{\parallel 0}(\rho_i/N)$ the $k_\parallel$ behaviour is dominated by the "sin" function in Eq. (4).

At the points where $\nu \ln x = \pi/2 + k\pi$, $|k_\parallel|$ is determined by $(m_e/m_i)^{1/2}(\theta_0 N/\rho_i) \gg 1$ and the wave can be absorbed by Electron Landau damping.

III-NUMERICAL RESULTS

The numerical solution of the ray tracing equations applied to DIII-D tokamak has confirmed the analytical behaviour of the parallel wavenumber which strongly depends on the starting poloidal angle. In our simulation we have calculated the ray trajectories and the related absorbed power for rays starting at different poloidal angle and $n_\parallel$. The spatial extension of the antenna corresponds to $|\theta_0| \leq 20$ and the power spectrum is mainly centred on $n_\parallel = 0$. The plasma parameters used in the calculation are f = 38 MHz, $n_e(0) = 4.5\times10^{13}$ cm^{-3}, $T_e(0) = 1.5$ keV, $T_i(0) = 800$ eV, $n_e(a) = 3\times10^{10}$ cm^{-3}, $T_e(a) = T_i(a) = 7$ eV with $n_e(0)$ ($n_e(a)$), $T_e(0)$ ($T_e(a)$) and $T_i(0)$ ($T_i(a)$) being the central (edge) density and electron and ion temperatures. The temperatures and density profiles are given by generalized parabola with exponent 0.5 and 5 respectively. Moreover $\varepsilon = a/R_0 = 0.38$, $I_p = 854$ kA, $B_0 = 1.8$ T, and the second harmonic of the hydrogen occurs behind the antenna while the 3 $\Omega_{cH}/2$ occurs at the centre where the non-linear ion absorption is expected to take place. The main results are summarized in Fig. 1 where a plot is shown of the absorbed power P/P_0 vs x, the radial variable normalized to the plasma radius. Several poloidal launching angles θ_0 have been considered ($\theta_0 = 0°, \pm5°, \pm10°, \pm15°, \pm20°$) and $n_{\parallel 0} = 0$ (solid line) and 3 (dashed line). For poloidal angles very close to $\theta_0 \approx 0°$ the power can reach the plasma core while for $\theta_0 > 5°$ it possible to notice a strong Electron Landau Damping (ELD) of the ray at radial position which increases as the angle is increased. For $\theta_0 = 20°$ the Landau damping occurs in the very edge of the plasma ($x \approx 0.85$). Note that the results is not sensitive to the choice of the launched $n_\parallel$ for $n_\parallel \leq 3$. We can deduce that only a small fraction of the total launched spectrum can reach the plasma core

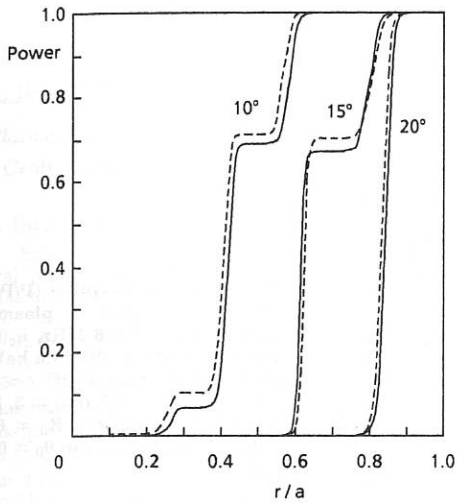

Fig. 1 - Power absorption (P/P_0) vs r/a for DIII-D plasma parameters: f=38 MHz, $n_e(0)=4.5\times10^{13}$ cm^{-3}, $T_e(0)=1.5$ keV, $T_i(0)=800$ eV, $n_e(a)=3\times10^{10}$ cm^{-3}, $T_e(a)=T_i(a)=7$ eV, $\varepsilon=a/R_0=0.38$, $I_p=854$ kA, $B_0=1.8$ T, $\omega=3\Omega_{cH}/2$, and for $\theta_0=0°, \pm5°, \pm10°, \pm15°, \pm20°$, and $n_{\|0}=0$ (solid line) $n_{\|0}=3$ (dashed line)

the remainder is lost in the plasma periphery. This results seems to agree with the experimental observations of DIII-D tokamak.

Other IBW heating experiments as Alcator C[3], PLT[4] tokamaks have shown a central power absorption. Alcator C for example, has exhibited a strong increase of the central ion temperature ($\Delta T_i \approx 200$ eV) due to non linear ion heating for $\omega = 3\,\Omega_{cH}/2$ near the plasma centre and no peripherical electron heating was observed. In Fig. 2 we show P/P_0 vs x for the following plasma parameters typical of Alcator C machine: central density and temperatures $n_e(0) = 1.5\times10^{14}$ cm^{-3}, $T_e(0) = 1.8$ keV, $T_i(0) = 1$ keV, edge density and temperatures $n_e(a) = 10^{10}$ cm^{-3}, $T_e(a) = T_i(a) = 50$ eV with parabolic profiles, $q(a) = 3$, $I_p = 300$ kA, the minor radius $a = 12.5$ cm, the major radius $R_0 = 64$ cm, the toroidal magnetic field $B_0 = 7.6$ T. The toroidal loop antenna which couples 100 kW to the plasma is 25 cm long and 4 cm wide and the power spectrum is centered around $n_\| = 5$. From Fig. 2 we can deduce that owing to the small poloidal extension of the antenna, rays which start at angles included between ±5° can reach without peripherical absorption the plasma centre where the non linear heating would act. A small amount of the power goes also to the electrons via ELD owing to the high value of $n_\|$. This result seems to confirm the successful IBW heating experiment of Alcator C.

Similar results have been obtained for PLT IBW heating at $\omega = 3\,\Omega_{cD}/2$. The rays which start from the PLT loop antenna at angles included between ±3° go to the centre without ELD at the plasma edge. The JFT-2M[5] experiment shows a behaviour similar to DIII-D. The IBW power is launched by a loop antenna installed at the oblique port of the tokamak with angle $\theta_0 = 43°$ to the horizontal plane, a strong ELD is observed in the very edge of the plasma. This result confirms the experimental observation obtained by a Langmuir probe which observes a sudden increase of the edge temperature at the onset of IBW pulse.

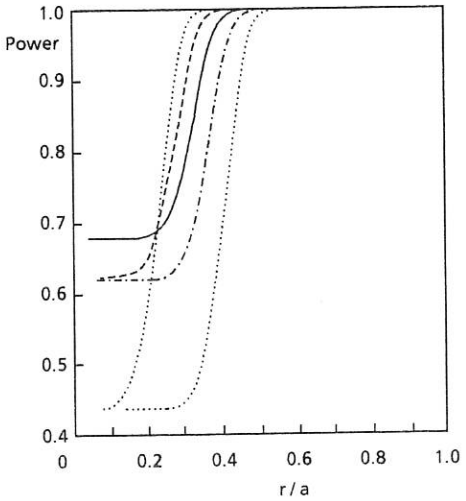

Fig. 2 - Power absorption (P/P_0) vs r/a for Alcator C plasma parameters: f = 183.6 MHz, $n_e(0) = 1.5\times10^{13}$ cm^{-3}, $T_e(0)$ = 1.8 keV, $T_i(0)$ = 1 keV, $n_e(a)=10^{10}$ cm^{-3}, $T_e(a) = T_i(a)$ = 50 eV, q(a) = 3, I_p = 300 kA, a = 12.5 cm, R_0 = 64 cm, B_0 = 7.6 T, $n_\parallel$ = 5, and θ_0 = 0°, ±2.5°, ±5°,

CONCLUSIONS

The numerical as well as the analytical analysis of the wave propagation and absorption of the Ion Bernstein frequency in tokamak plasmas has shown a strong dependence of the absorption on the poloidal angle of injection. Poloidally wide antennas (DIII-D) or antennas placed at the oblique port of the tokamak with high poloidal angle (JFT-2M) have shown a peripherical heating of the electron population, while compact toroidal loop antennas (Alcator C or PLT) whose injection angles is included between ±5° are indicated to allow the propagation of the wave up to the plasma centre.

REFERENCES

[1] R. I. Pinsker, M. J. Mayberry, M. Porkolab, and R. Prater; Proceedings of the 8th AIP Topical Conference on Radio-Frequency Power in Plasmas, (Roger McWilliams editor), Irvine, CA 1989, p. 314.

[2] A. Cardinali and F. Romanelli, submitted to Phys. of Fluids B.

[3] J. D. Moody, M. Porkolab, C. L. Fiore, F. S. McDermott, Y. Takase, J. Terry, and G. M. Wolfe; Phys. Rev. Lett. **60**, 298 (1988).

[4] M. Ono, P. Beiersdorfer, R. Bell, S. Bernabei, A. Cavallo, A. Chmyga, S. A. Cohen, P. Colestok, G. Gammel, G. J. Greene, J. Hosea, R. Kaita, I. Lehrman, G. Mazzitelli, E. Mazzucato, D. McNeill, K. Sato, J. Stevens, J. Timberlake, J. R. Wilson, and A. Wouters; Phys. Rev. Lett. **60**, 294 (1988)

[5] H. Tamai, T. Ogawa, H. Matsumoto, K. Odajima; Proceedings of the 8th AIP Topical Conference on Radio-Frequency Power in Plasmas, (Roger McWilliams editor), Irvine, CA 1989, p. 350.

MAXIMIZING ABSORPTION IN ION-CYCLOTRON HEATING OF TOKAMAK PLASMAS

A. Bers, V. Fuchs,† and C. C. Chow

Plasma Fusion Center, M.I.T., Cambridge, MA 02139 U.S.A.

† *Centre Canadien de Fusion Magnetique, Varennes, Québec, Canada*

I. Introduction

Efficient ion-cyclotron heating in tokamak plasmas is effectively localized in the central region of the plasma, near the ion second-harmonic layer in a single ion species plasma, or near the ion-ion hybrid layer in a plasma containing a minority ion species. The fast Alfvén wave (FAW), which carries the incident rf power, from the low magnetic field side, is generally focused in (by antenna design and propagation) toward this central region on the equatorial plane of the tokamak plasma. There the FAW encounters a "coupling" region and may undergo reflection (R), transmission(T)—to the high magnetic field side, mode conversion (C)—to an ion-Bernstein wave (IBW), and kinetic dissipation (D)—due to Doppler-shifted ion-cyclotron damping. (Here we ignore electron TTMP and/or Landau damping; these can be readily included by expanding on our formalism.) To determine these power transfer coefficients (R, T, C and D) the problem is in general formulated as an integro-partial-differential equation based upon the linearized Vlasov-Maxwell equations for an inhomogenous plasma. This is however difficult to solve, even numerically, and has been usually approximated by a fourth or sixth-order o.d.e. description which is amenable to numerical integration.

We have attempted to formulate reduced order analyses that can give approximate, closed form analytic results for these coefficients [1]. We have recently completed this and here we only summarize the results. From these we show the regime of parameters that gives maximum energy deposition on the ions in the central plasma region of interest.

II. Results of Reduced-Order Analyses

Our analytic model describes the central plasma region of interest in slab geometry and neglects the effects of poloidal magnetic fields. Away from the coupling regions we use the Vlasov-Maxwell local dispersion relation expanded to second-order in $(k_\perp \rho_i)^2$ [1]. This gives an eikonal description of the FAW's [2] and IBW's [3].

(a) Transmission. The power transmission coefficient T for the FAW can be obtained from perturbation of modes that entails the solution of only a first-order o.d.e. [4].

(b) Reflection. Both the power transmission and reflection coefficients (T and R) for the FAW can be obtained from a second-order o.d.e. that describes the modified FAW due to its coupling to the IBW [2]. From this we have recently obtained an approximate analytic description of the power reflection coefficient [5].

(c) Conversion. The power conversion coefficient C gives the amount of incident FAW power converted to the IBW. We have shown that it can be obtained from an approximate coupled mode formulation that entails solving two, coupled, first o.d.e.'s [6].

(d) Dissipation. The kinetic power dissipation coefficient D follows from the global power conservation, i.e. integrating the energy flow over a volume containing the coupling, central plasma region. For the FAW incident from the low-field side of the toroidal magnetic field we then have

$$T + R + C + D = 1 \tag{1}$$

With T, R, and C known, (1) then gives D. When kinetic dissipation is dominant, D

can also be obtained approximately from a local, kinetic WKB propagation analysis [7].

III. Maximizing Single-Pass Absorption

Here we focus our discussion to $D(H)$ plasmas with the FAW incident from the low-field side. From [6] we find that, for small parallel Alfvén indices $N_\parallel = k_\parallel c_A/\omega$, C is proportional to T, as might be expected. Furthermore, from [4] and [5] we have approximately

$$T = e^{-a}\ ;\quad a \approx \frac{\pi}{4} R_A(\eta + \beta_D N_c^2) \tag{2}$$

$$R = (1-T)^2 e^{-b}\ ;\quad b \approx \frac{4\pi}{9} R_A N_\parallel^2 \frac{\beta_H^*}{(\beta_H^* N_c^2 + \eta)} + 3\sqrt{\pi} R_A \eta \delta e^{-\delta^2} \tag{3}$$

where $R_A = (R_0\omega/c_A)$, $\eta = n_H/n_D$, $\beta_D = (2T_D/m_D c_A^2)$, $\beta_H^* = 2\beta_D T_H/T_D$, $\delta = [(3/4)(\eta + \beta_D N_c^2)/N_\parallel(\beta_H^*)^{1/2}] > 1$, N_c^2 is of order unity (weakly dependent on η and $N_\parallel$), and other such terms of order unity multiplying a and b have been omitted.

From (2) we note that for $a > 1$, we have $T \approx 0$ essentially independent of $N_\parallel$. It then follows from [6] that $C \approx TR\exp(-2D_c)$ will become vanishingly small; D_c is defined in [6] and does not play an important role in our considerations of low-field incident FAW's. Hence (1) becomes approximately

$$R + D \approx 1 \tag{4}$$

Since R is a strong function of $N_\parallel^2$, complete absorption (i.e., $D \approx 1$) is then obtained for $N_\parallel$ in a range exceeding (by about a factor of two or four) the $N_\parallel$ that makes $R \approx (1/2) \approx D$; we call the latter the "crossover-$N_\parallel$." As can be seen from (2) and (3), the ion minority species fraction η and its temperature T_H will also affect the above considerations for making $D \approx 1$. Clearly, high-density and large R_0 plasmas are amenable to this optimization.

The results can be conveniently illustrated in a plot of the crossover-$k_\parallel$ as a function of η for various values of T_H. Since this entails calculating only R, we have used the approximate fast-wave equation [2] to solve numerically for these parameters when $R \approx (1-T)/2$ (this allows for nonzero T when $\eta \to 0$ and β_D is not sufficiently large). The approximate analytic calculations in [4-6], viz. (2) and (3) can be used to understand the numerical results. Figure 1 shows such results for parameters relevant to forthcoming ICH in Alcator C-Mod: $R_0 = 0.67m$, $B_0 = 5.33T$, $D(H)$ plasma, $n_{e0} = 5 \times 10^{20}/m^3$, $T_D = 2keV$. Figure 2 shows the results for parameters relevant to plans for CIT/BPX: $R_0 = 2.8m$, $B_0 = 5.66T$, $DT(H)$ plasma, $n_{e0} = 2.5 \times 10^{20}/m^3$, $T_D = 3keV$. In each case: Figure (a) shows a calculation of R, D, T, and C (not visible since it is zero) for a given η and T_H; Figure (b) gives the crossover-$k_\parallel$ as a function of η with T_H as a parameter.

IV. Acknowledgements

This work was supported in part by U. S. Department of Energy Grant No. DE-FG02-91ER-54109 and in part by National Science Foundation Grant No. ECS-88-22475.

V. References

[1] A. Bers et al., 14th EPS-Fusion, Madrid, Vol 11 D, part III, p. 995 (1987).
[2] C. N. Lashmore-Davies et al., Phys. Fluids **31**, 1614 (1988).
[3] R. A. Cairns and V. Fuchs, Phys. Fluids **B1**, 350 (1989).
[4] G. Francis et al., A.I.P. Conf. Proc. **159**, pp. 370-373 (1987).
[5] C. C. Chow, V. Fuchs, and A. Bers, Phys. Fluids **B2**, 2185 (1990).
[6] V. Fuchs and A. Bers, Phys. Fluids **31**, (1988).
[7] C. C. Chow, A. K. Ram, and A. Bers, Phys. Fluids **B1**, 2018 (1989).

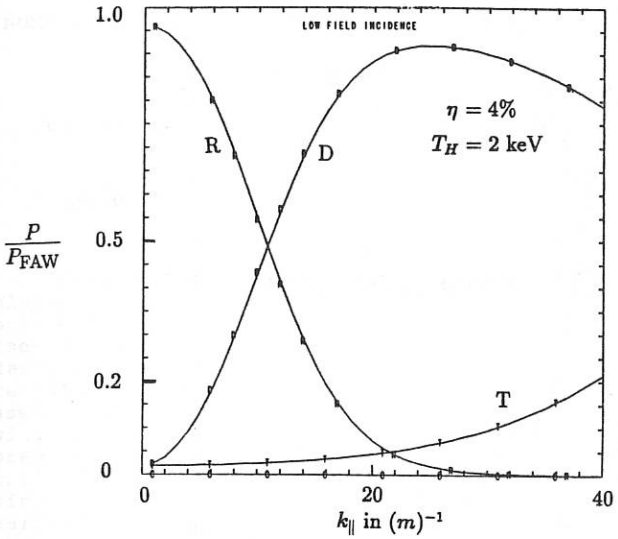

Figure 1a

ALCATOR C-MOD TYPE PLASMA

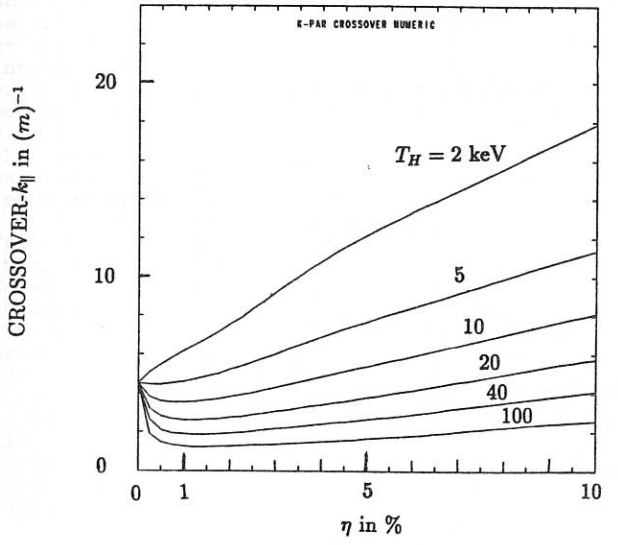

Figure 1b

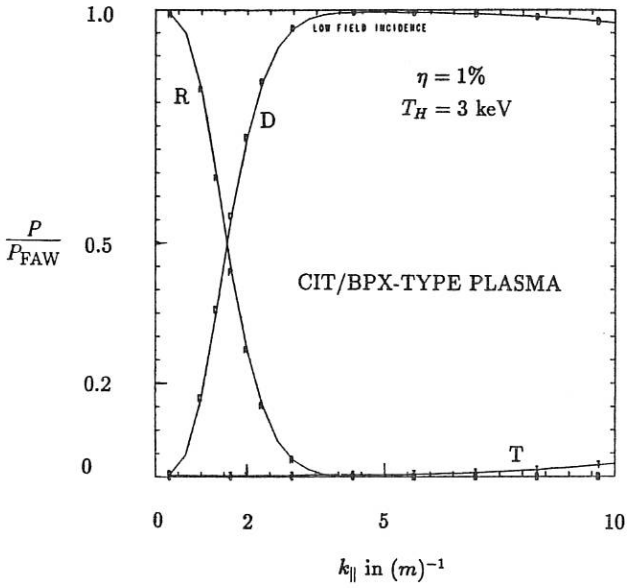

Figure 2a

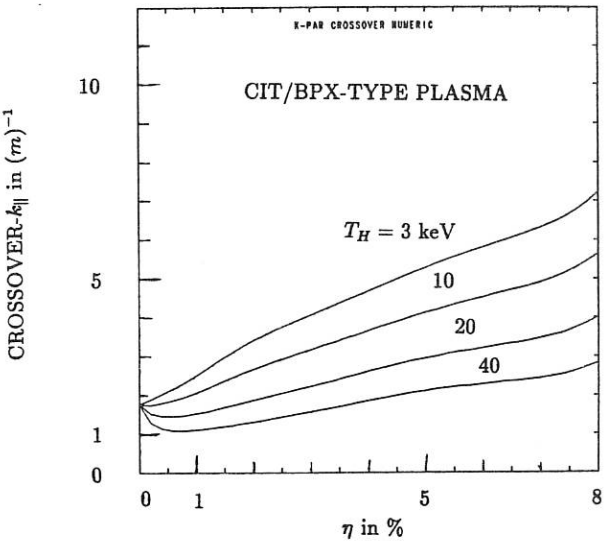

Figure 2b

NUMERICAL MODELING, ANALYSIS, AND EVALUATION OF ICRH ANTENNAE

W.Grossmann, S. Riyopoulos, K.Ko+, M.Kress++, A.T.Drobot

Science Applications International Corporation
1710 Goodridge Drive, McLean,VA 22102

Introduction. Most analyses of ICRH antennae and rf plasma heating studies are carried out using combinations of one- and two-dimensional plasma-antenna models. These studies (see e.g. ret. 1) have provided valuable insights to antennae designers and have also been successful in analyzing the results of current ICRH experiments. In spite of the usefulness of today's simulation capabilities, reactor antennae will require more robustness and fidelity in the model predictions if survivable antennae are to be designed and built. To this end, SAIC is developing a three-dimensional simulation capability of rf antennae that will allow rf performance (with and without plasma) and structural and thermal analyses to be carried out on the same common geometrical representation.

Simulation Codes. SAIC's MASK (2-D) and ARGUS (3-D) system of codes is fully electromagnetic and consists of modules that couple fluid and PIC solvers to treat complex geometrical situations involving variable media. External boundary conditions ranging from simple metallic walls or periodic boundaries to boundary conditions describing ingoing or outgoing radiation can be imposed on the simulation. Internal material regions (structures) can be specified on the grid, either as perfect conductors or as regions of specified complex tensor material properties. The two codes can treat a wide range of complex geometry and plasma/beam interactions. The results of ARGUS ICRH benchmark comparisons with experimental data from vacuum antenna measurements have been reported earlier[2-3].

3-D Antenna Simulation. The numerical grid resulting from application of the ARGUS geometry package on the double strap TFTR Bay M antenna is shown in Figure 1. Dimensions and details of the antenna were obtained from engineering drawings supplied by the Princeton Plasma Physics Laboratory. The figure shows a cutaway of a quadrant of the antenna (symmetry used to reduce computing requirements) with current straps, Faraday rods, end plates and center septum. Power leads to the antenna are simulated through a gap in the back plate fed with an applied voltage at the actual frequency. ARGUS calculates all rf electric and magnetic field components, current distribution in straps, Faraday rods and walls. Derived quantities such as strap current phase velocity and mutual inductances (multiple straps) can be calculated from the ARGUS

output. In this paper, we present results from an analysis of the near field power radiated away in vacuum from the antenna in the radial direction. Figure 2a shows the Poynting flux and 2b the poloidal electric field component (in arbitrary units) for the Pi phasing of the current straps. Figures 2c and 2d show the results for the in phase case. The figure shows the full antenna radiation pattern obtained by applying appropriate phase boundary conditions across the symmetry planes. Since the toroidal rf magnetic field is roughly uniform along the poloidal direction, the Poynting flux distribution is similar to the poloidal electric field. The peaks or lobes in the electric field distribution are due to the spatial gaps between the last Faraday rod and the antenna end plane. Simulations of other antennae lacking the large gap show significantly reduced lobes. A Fourier analysis of the poloidal electric field in Figure 2 shows that most of the radiated power is in the main toroidal wave numbers with a small amount of energy spread over poloidal wave numbers.

2-D rf-Sheath Formation. Sheath formation around the Faraday screen bars during intense rf heating is a well known effect. Analytical and numerical efforts to model rf sheaths in magnetized plasmas have, to date, been focused on one-dimensional models.[3] The rf-driven sheath theory in unmagnetized plasmas leads to a result similar to Langmuir-Childs law for dc discharge sheaths. The sheath width is $\Delta_s = C\lambda_D(e\langle V\rangle/kT))^{3/4}$, replacing the dc potential with the time-averaged, rectified rf potential $\langle v\rangle$. The theory,[4] valid for $\lambda_D << \Delta_s$, assumes an electron density boundary, oscillating with the rf and ions responding to the averaged sheath potential. It has been argued[5,6] that the model remains valid in magnetized plasmas with magnetic field lines intercepting the conducting surface.

The main limitation of 1-D models in magnetized plasmas is that transport occurs only parallel to the magnetic field. If the plasma-boundary interface is along the X-direction, with the sheath across the Y-direction, no electrostatic perturbations with finite k_y can exist in 1-D. The canonical momentum P_y and consequently the Y_{GC} position of the guiding center are exact invariants, prohibiting cross-field transport. In reality, however, the opposite $E_y \times B_z$ drifts among electrons and ions excite strong electrostatic perturbation of finite E_y, k_y. This destroys the Y_{GC} invariance and introduces considerable cross-field transport.

A two dimensional simulation of rf sheath formation in a magnetized plasma has been undertaken, using the PIC module in the SAIC MASK code. The simulation plane xy is a cross-section of one screen bar, x corresponding to the radial and y to the poloidal direction. The fields are purely electrostatic. Presently, the driving rf field is modeled by an alternating voltage between the top and the bottom metal plates. In a new code version, the capacitor field with the rod inside is stored as the externally applied field, while the plasma sees only the metal bar boundaries in the center, and periodic boundary conditions in both x and y.

Plots of equipotential surfaces for typical runs A and B are shown in Figure 3a and 3b respectively. In both cases we use $m_i/m_e = 180$ with real electron mass, and $T_e = T_i = 16$ eV. Case A corresponds to high density $n_o = 3.75\times10^{10}cm^{-3}$, $B_{zo} = 0.5$ T, and magnetic field lines tilted 15° relative to the toroidal direction, $B_{yo}/B_{zo} \simeq 0.25$. Case B corresponds to low density $n_o = 1.60\times10^{9}$ cm^{-3}, $B_{zo} = 0.3$ T, and $B_{yo}/B_{zo} = 0.25$. The applied external voltage amplitude is 500 V in both cases. The parameters chosen mimic well the experimental situation. Thus we have in both cases $\Delta_s > \rho_i \gtrsim \lambda_D$ and $\Omega_i < \omega_{rf} < \omega_{LH}$ with $\Omega_i \sim \omega_{pc}$.

A sheath with strong potential gradients localized near the bar surface, as well as at the top and bottom boundaries, is formed in Case A. In contrast, no strong sheath formation can be seen in Case B, although the plasma thickness should be enough, according to the 1-D result[4], to rectify the applied potential. Instead, a potential "cell" with dimension $\Delta_x \sim \Delta_y$ is formed in the presheath area.

We speculate from the results in A and B that when the predicted 1-D thickness of the sheath becomes comparable to the bar cross-section, anomalous ion transport becomes important. This is consistent with the scaling $E_x/E_y \sim \Delta_y/\Delta_x$ and the fact that cross-transport is induced by E_y. Thus 2-D effects dominate when the sheath thickness is comparable to its length. Ion transport is enhanced to the point where the steady state condition $J_e \simeq J_i$ is maintained without a strong potential barrier to slow down electrons, i.e. without electron depletion. In the high density Case A, however, $\Delta_y \ll \Delta_x$ and the simulation results seem to be in agreement with the 1-D theory.

In cases of strong sheath formation, strong ion energization localized inside the sheath has been observed. The ion energies exceeded the sheath averaged potential $< V >$ by a factor of 3. A stochastic acceleration theory for magnetized ions has been proposed to account for the effect.[7] Additionally, considerable electron heating is observed to be uniform throughout the simulation area.

Conclusions. The utility of ARGUS for modeling future reactor configurations lies in the ability to use a common geometry data base for rf performance, and for structural and thermal analyses. A plasma module has recently been added to the ARGUS antenna simulator, allowing antenna plasma loading to be evaluated. The antenna simulations will be applied to the PBX experiment and other future devices such as ITER. The 2-D rf sheath formation simulations will continue to examine different Faraday rod cross-sections, allowing optimum Faraday rod designs to be evaluated under realistic operating conditions.

+ Permanently at Stanford Linear Accelerator Center, CA
++ Permanently at the College of Staten Island, NYC, NY

1. D.B.Batchelor, Presented at the "Workshop on ICRF Physics and Design", Boulder,CO, (1991).

2. Grossmann, W.,et.al, 16th Eur. Conf.on Contr. Fusion and Plasma Physics, Venice, Italy (1989).
3. D'Ippolito,D.A.,et.al.,Proc.of 13th Intl. Conf.on Plasma Physics and Controlled Nuclear Fusion Research, Paper IAEA-CN-53/E-3-1,Washington, D.C.(1990)
4. M.A. Lieberman, IEEE Trans. on Plasma Science **16**, 638 (1988).
5. F.W. Perkins, Nucl. Fusion **29**, 583 (1989).
6. J.R. Myra, D.A. D'Ippolito, M.J. Gerver, Nucl. Fusion **30**, 845 (1990).
7. S. Riyopoulos, W. Grossmann, A. Drobot, and M. Kress, Proc. 1991 Sherwood Conference, Seattle, WA.

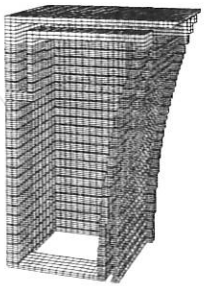

Figure 1.

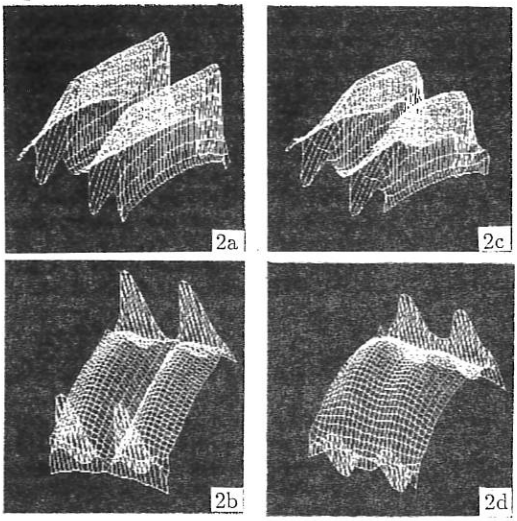

Figure 2.

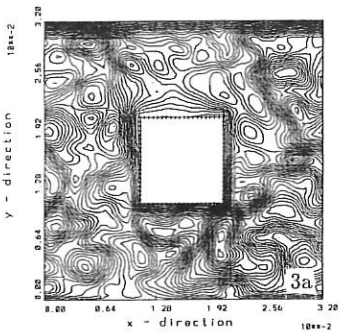

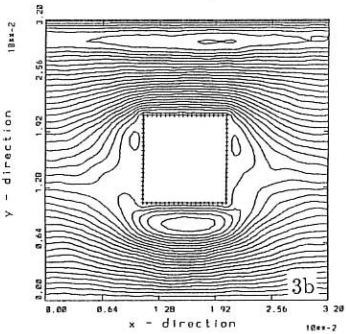

Figure 3.

FAST ELECTRON TRANSPORT DURING LOWER-HYBRID CURRENT DRIVE

K. Kupfer, A. Bers, and A. K. Ram

Plasma Fusion Center, M.I.T., Cambridge, MA 02139 U.S.A.

I. Introduction

In steady state lower-hybrid current drive (LHCD), the toroidal current in tokamaks is sustained by fast electrons which absorb energy and momentum from externally injected waves. The dynamics of the fast electron population is well described by balancing wave induced quasilinear diffusion with collisional slowing down and pitch angle scattering off of fixed Maxwellian field particles. Here we consider a quasilinear-Fokker-Planck formulation which includes the wave induced radial transport of fast electrons, thus generalizing the radially local, velocity space treatments of LHCD [1,2,3].

The best current drive efficiencies for LHCD experiments are achieved when the wave spectrum launched into the plasma is narrow and close to the accessibility limit. For central electron temperatures up to a few kev, waves launched near the accessibility limit are very weakly damped and there results a significant "spectral gap" which must be filled before the waves can Landau damp on electrons. Because of the weak dissipation, the ray trajectories of the waves can make several toroidal transits and suffer numerous radial reflections. It has been shown that by including toroidal effects in the ray dynamics, the poloidal mode numbers of the rays can upshift [4] and thus fill the spectral gap [5]. The fields required to bridge the spectral gap thus have a significant poloidal component, which will contribute to the radial $E \times B$ drift of resonant electrons.

II. The Fokker-Planck Equation

In the absence of the RF fields, the electron orbits are assumed to follow the magnetic field lines with a constant parallel velocity, u. We consider the evolution of the electron distribution function, $f(u, v_\perp, \rho, t)$, where $\frac{1}{2}v_\perp^2$ is the perpendicular energy and ρ is a radial variable which labels the magnetic flux surfaces. For a small inverse aspect ratio tokamak with circular flux surfaces, we take $\rho = r + \Delta(r)\cos\theta$, where $\Delta(r)$ is the Shafranov shift. The evolution of f is given by

$$\frac{\partial}{\partial t} f = (\frac{\partial}{\partial t})_{ql} f + (\frac{\partial}{\partial t})_c f \quad , \tag{1}$$

which represents a balance between RF quasilinear diffusion and collisional pitch angle scattering and slowing down. Here, $(\partial/\partial t)_c$ is the linearized collision operator for fast electrons slowing down and pitch angle scattering in $(u, v_\perp)$ space, as given in various references (see e.g. [3]). The collisional contribution to radial transport has a negligible effect on the confinement of fast electrons and can be ignored; hence the collision operator does not act on the ρ dependence of f. The quasilinear operator is

$$\begin{aligned}(\frac{\partial}{\partial t})_{ql} f &= \frac{1}{\rho}\frac{\partial}{\partial \rho}\rho[D_{\rho\rho}\frac{\partial}{\partial \rho} + D_{\rho u}\frac{\partial}{\partial u}]f \\ &\quad + \frac{\partial}{\partial u}[D_{uu}\frac{\partial}{\partial u} + D_{u\rho}\frac{\partial}{\partial \rho}]f \quad .\end{aligned} \tag{2}$$

Assuming that the RF fields remain in the slow wave (electrostatic) polarization, the quasilinear diffusion coefficients are:

$$D_{uu} = \frac{\pi e^2}{2m_e^2}\langle \sum_s |\Phi_s|^2 \delta(u k_\parallel^s - \omega)(k_\parallel^s)^2 \rangle$$

$$D_{pu} = \frac{\pi e}{2m_e B_o} \langle \sum_s |\Phi_s|^2 \delta(uk_\parallel^s - \omega) k_\parallel^s k_p^s \rangle$$
$$D_{pp} = \frac{\pi}{2B_o^2} \langle \sum_s |\Phi_s|^2 \delta(uk_\parallel^s - \omega)(k_p^s)^2 \rangle \quad , \tag{3}$$

where $D_{up} = D_{pu}$ and B_o is the toroidal field on axis. The angular brackets in (3) represent a flux surface average. The RF scalar potential, $\Phi_{rf}(\mathbf{x}, t)$, is represented in eikonal form,

$$\Phi_{rf} = \frac{1}{2} \sum_s \Phi_s(\mathbf{x}) \exp i \left(\int^{\mathbf{x}} dx' \cdot \mathbf{k}_s(\mathbf{x}') - \omega t \right) \quad + \text{c.c.} \quad , \tag{4}$$

where Φ_s and $\mathbf{k}_s$ are assumed to be slowly varying. We have also defined $k_\parallel^s = \mathbf{k}_s \cdot \mathbf{b}$ and $k_p^s = \mathbf{b} \times \mathbf{k}_s \cdot \nabla\rho$, where $\mathbf{b}$ is the spatially varying unit vector along the equilibrium magnetic field. The basic physics of (2) is simple; resonant electrons experience a diffusion in u, due to the wave's parallel field, as well as a diffusion in ρ, due to the radial component of the $E_{rf} \times B$ drift. Because these two processes are coupled, the quasilinear operator also includes cross flows that are proportional to D_{pu} and D_{up}. We use the previously developed ray-tracing model of Bonoli and Englade [5], to determine the fields inside the plasma, thereby allowing us to evaluate the radial flow of fast electrons.

III. The Radial Flux

The radial flux of fast electrons, Γ_{rf}, is obtained by integrating (1) over the velocity space coordinates,

$$\Gamma_{rf} = -\int 2\pi v_\perp dv_\perp du \, (D_{pp} \frac{\partial}{\partial \rho} + D_{pu} \frac{\partial}{\partial u}) f \quad . \tag{5}$$

To calculate Γ_{rf} we ignore the enhancement of the perpendicular energy of f due to the pitch angle scattering of resonant electrons with large parallel energy [2,3]. One then finds that

$$\Gamma_{rf} = \int du [V_\rho F(u,\rho) - D_\rho \frac{\partial}{\partial \rho} F(u,\rho)] \quad , \tag{6}$$

where

$$V_\rho(u,\rho) = \frac{u D_c D_{pu}}{v_e^2 (D_c + D_{uu})} \tag{7}$$

$$D_\rho(u,\rho) = D_{pp} - \frac{D_{pu}^2}{D_{uu} + D_c} \quad . \tag{8}$$

Here $D_c = (Z_i + 2)\nu_o v_e^5 / u^3$, $\nu_o = \omega_{pe}^4 \ln\Lambda / (4\pi n_e v_e^3)$, Z_i is the ion charge state, $v_e = \sqrt{T_e(\rho)/m}$

$$F(u,\rho) = N \exp \left(\int^u \frac{-D_c u du}{v_e^2 (D_c + D_{uu})} \right) \quad . \tag{9}$$

Since there are relatively few electrons in the tail, we may take $N = n_e / (v_e \sqrt{2\pi})$, where n_e is the local electron density. Because D_{uu} is so large, electrons are diffused rapidly in the resonant region, where $F(u,\rho)$ develops a tail. It is therefore appropriate to consider the following velocity averages of V_ρ and D_ρ:

$$\bar{V}_\rho(\rho) = N_T^{-1} \int du V_\rho(u,\rho) F_T(u,\rho) \tag{10}$$

$$\bar{D}_\rho(\rho) = N_T^{-1} \int du D_\rho(u,\rho) F_T(u,\rho) \tag{11}$$

where $F_T(u,\rho) = F(u,\rho) - (n_e / v_e \sqrt{2\pi}) \exp(-u^2/2v_e^2)$ and $N_T(\rho) = \int du F_T(u,\rho)$.

The quantity $\bar{V}_\rho$ is the average convection velocity of resonant electrons and, similarly, $\bar{D}_\rho$ is their average radial diffusion coefficient. The radial convection depends on the amount of momentum absorbed from the waves and the ratio of $k_p/k_\parallel$ at resonance; since the momentum absorbed from the waves is balanced by the momentum destroyed in collisions with the bulk plasma, the radial convection is proportional to D_c and independent of the wave amplitude. There is generally a large asymmetry in the k_p spectrum, because toroidal effects on the wave propagation tend to fill in the spectral gap. In general, the upshifted spectrum, which fills the spectral gap, drives an outward radial convection.

IV. Numerical Results

Let us consider the Alcator C experiment, previously simulated by [5]. The parameters are $n_{eo} = 7.5 \times 10^{13}$ cm^{-3}, $T_{eo} = 1.5$ kev, $T_{io} = 0.7$ kev, $a = 16.5$ cm, $R_o = 64$ cm, $I_p = 170$ kA, and $B_o = 10$T. Here n_{eo}, T_{eo}, and T_{io} are the peak values of the electron density, electron temperature, and ion temperature, I_p is the toroidal plasma current, and a is the minor radius of the plasma. The assumed profiles are described in [5]. The RF frequency is 4.6 GHz (i.e. $\omega/2\pi$). The Brambilla power spectrum is modeled by

$$S(n_\parallel) = \begin{cases} S_a & \text{if } n_a < n_\parallel < n_b \\ S_b & \text{if } n_b < n_\parallel < n_c \\ 0 & \text{otherwise} \end{cases} , \tag{12}$$

where $n_\parallel \equiv ck_\parallel/\omega$. For Alcator C, we take $n_a = 1.25$, $n_b = 2.0$, and $n_c = 7.0$; S_a and S_b are determined so that 70 percent of P_{in} is launched between n_a and n_b. (Note, we have ignored any power which couples into the plasma at negative $n_\parallel$.) For $P_{in} = 440$ kW, we found that the total power resonantly absorbed by electrons was $P_{rf} = 390$ kW, with the remaining 50 kW being damped non-resonantly through electron-ion collisions in the plasma periphery.

The parameters for the JT60 current drive experiments are [6]: $n_{eo} = 3.0 \times 10^{13}$ cm^{-3}, $T_{eo} = 3.0$ kev, $T_{io} = 3.0$ kev, $a = 70$ cm, $R_o = 310$ cm, $I_p = 1.5$ MA, and $B_o = 4.5$T. The RF frequency is 2 GHz. The power spectrum of the multi-junction waveguide array is very narrow and is modeled by (12), where $n_a = 1.25$, $n_b = 1.75$, and $n_c = 4.75$; S_a and S_b are determined so that 80 percent of P_{in} is launched between n_a and n_b. For $P_{in} = 4.6$ MW, the total power resonantly absorbed by electrons was $P_{rf} = 4.2$ MW, the remainder being absorbed non-resonantly through collisions.

The results of our numerical simulations are given in Figures 1 and 2. For both Alcator C and JT60 the radial convection velocity is outward across most of the plasma and has a broad maximum of nearly 1 m/sec. In both cases, the radial diffusion is found to be highly localized near the magnetic axis. For JT60, the peak of the diffusion profile can be quite large, nearly 1 m^2/sec.

V. Acknowledgements

We wish to acknowledge fruitful discussions with Dr. Paul Bonoli, and to thank him for the use of his ray tracing code. This work was supported in part by National Science Foundation Grant No. ECS-88-22475 and in part by U. S. Department of Energy Grant No. DE-FG02-91ER-54109.

VI. References

[1] N. J. Fisch, Phys. Rev. Lett. **41**, 873 (1978).
[2] C. F. F. Karney and N. J. Fisch, Phys. Fluids **22**, 1817 (1979).
[3] V. Fuchs et al., Phys. Fluids **28**, 3619 (1985).
[4] P. L. Colestock and J. L. Kulp, IEEE Trans. Plasma Sci. PS-8, 71 (1980).
[5] P. T. Bonoli and R. C. Englade, Phys. Fluids **29**, 2937 (1986).
[6] Y. Ikeda et al., Nucl. Fusion **29**, 1815 (1989).

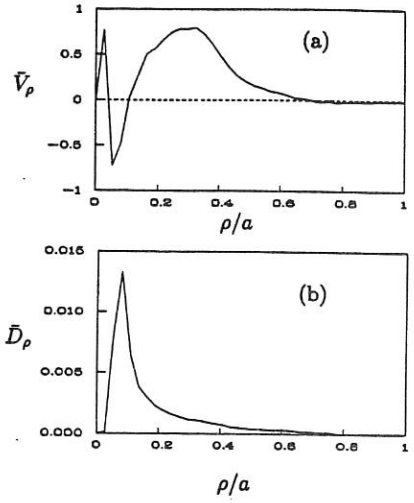

Figure 1: Model results for Alcator C; radial profiles of (a) average radial convection velocity, $\bar{V}_\rho$ (m/sec) and (b) average radial diffusion coefficient, $\bar{D}_\rho$ (m^2/sec).

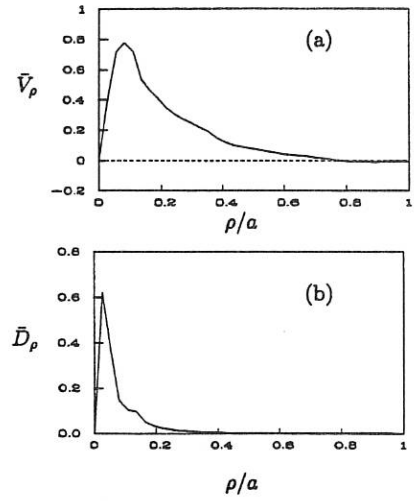

Figure 2: Model results for JT60; radial profiles of (a) average radial convection velocity, $\bar{V}_\rho$ (m/sec) and (b) average radial diffusion coefficient, $\bar{D}_\rho$ (m^2/sec).

FAST WAVE HELICITY CURRENT DRIVE IN TOKAMAKS

J. A. Tataronis, P. E. Moroz and N. Hershkowitz

University of Wisconsin - Madison
Madison, WI 53706 USA

1. INTRODUCTION

Several recent studies[1-4] have suggested that plasma waves with intrinsic magnetic helicity, and therefore nonlinear polarization, may be effective in driving steady current in magnetized plasmas. Current appears as wave helicity is transferred to the background plasma in response to effects of wave dissipation and spatial inhomogeneities in the plasma. In this paper, we report on a study of helicity wave current drive (HWCD) over a broad frequency range that extends below and above the ion cyclotron frequency. The parameters of the Phaedrus-T tokamak at the University of Wisconsin-Madison are assumed in our calculations. Numerical calculations of the wave electric and magnetic fields, and the resulting steady current, have been carried out with the global 3-D code, FASTWAC, which is a version of FASTWA,[5,6] modified to treat current drive resulting from wave helicity and momentum transfer. FASTWAC is based on the hot plasma dielectric tensor with small electron and ion gyro-radii. It includes particle trapping effects, and a variety of wave absorption processes, such as Landau damping, TTMP, ion cyclotron absorption, and collisions.

2. GOVERNING EQUATIONS OF HWCD

Steady-state current resulting from wave helicity transfer to the plasma requires nonlinear wave polarization and wave damping. For low frequencies, much less than the ion cyclotron frequency, the circularly polarized Alfvén wave, described by magnetohydrodynamics (MHD) with resistivity, produces HWCD[1-3]. In the MHD frequency limit, the steady-state current is computed by averaging Ohm's law over the the wave period, resulting in the expression,

$$\eta \mathbf{j}_0 = \langle \tilde{\mathbf{V}} \times \tilde{\mathbf{B}} \rangle \tag{1}$$

where η is the plasma resistivity, $\mathbf{j}_0$ is the driven current density, $\tilde{\mathbf{V}}$ and $\tilde{\mathbf{B}}$ are the fluid velocity and magnetic field of the wave, and the brackets <...> denote an average over the wave period. Only in the presence of nonlinear wave polarization and wave damping does $\tilde{\mathbf{V}} \times \tilde{\mathbf{B}}$ have a nonzero average value. In the higher frequency range, the electron force equation with inertia effects neglected gives the time-averaged current density, $\mathbf{j}_0$,

$$n_0 q \eta \mathbf{j}_0 = q\langle \tilde{n}_e \tilde{\mathbf{E}} \rangle - \langle \tilde{\mathbf{j}}_e \times \tilde{\mathbf{B}} \rangle + \nabla \cdot \langle \mathbf{P}_e \rangle \tag{2}$$

where n_0 and q designate respectively the equilibrium number density and the magnitude of the charge of the electron fluid, $\tilde{\mathbf{E}}$ is the wave electric field, and

$[\tilde{n}_e, \tilde{\mathbf{j}}_e, \mathbf{P}_e]$ represent respectively the fluctuating electron number density, the fluctuating electron current density and the electron pressure tensor. Equation (2) contains contributions both from momentum transfer and helicity wave transfer. The helicity component originates from $\langle \tilde{\mathbf{j}}_e \times \tilde{\mathbf{B}} \rangle$. To compute the wave variables, we use the collisional Vlasov equation and Maxwell's equations, linearized about an equilibrium plasma state. The resulting driven current is then quadratic in the wave amplitudes.

3. HWCD IN CYLINDRICAL GEOMETRY

In the higher frequency range intermediate between the ion and electron cyclotron frequencies, HWCD in axisymmetric cylindrical geometry is a problem that can be treated by purely analytic means. In this case, ion motion and electron density fluctuations are negligible, and Ohm's law, in the absence of electron pressure, reduces to the expression,[7,8]

$$\mathbf{E} = \eta \mathbf{J} + \frac{1}{q n_0} \mathbf{J} \times \mathbf{B} \tag{3}$$

where $\mathbf{E}$ is plasma electric field. Equation (3) is used in Ref. (7) to model numerically current drive by an applied travelling wave. After combining Eq. (3) with Maxwell's equations, and linearizing about a uniform equilibrium with magnetic field, $\mathbf{B}_0 = \hat{\mathbf{z}}\, B_0$, tractable equations result. Introducing cylindrical coordinates $[r,\theta,z]$ with propagation of the form, $\exp[i(\omega t - m\theta - kz)]$, the fluctuating magnetic field satisifes the equation,[8]

$$\nabla \times \tilde{\mathbf{B}}(r) = \beta \tilde{\mathbf{B}}(r) \qquad \beta \equiv -k\omega_{ce} \frac{1 - \sqrt{1 + 4i\nu_{ei}\,\omega \left(\frac{\omega_{pe}}{\omega_{ce} kc}\right)^2}}{2i\nu_{ei}} \tag{4}$$

where ω_{ce} and ω_{pe} are respectively the electron cyclotron and plasma frequencies, c is the vacuum speed of light, and ν_{ei} is the electron-ion collision frequency. The wave frequency and axial wavenumber are determined by an external antenna. Expressing $\tilde{\mathbf{B}}(r)$ in terms of cylindrical components, $[b_r(r), b_\theta(r), b_z(r)]$, it is found that $\tilde{B}_z(r)$ satisfies Bessel's equation: $\tilde{B}_z(r) = H(\omega,m,k)\, J_m(\alpha r)$, where α is an effective radial wavenumber, $\alpha^2 = \beta^2 - k^2$, and $H(\omega,m,k)$ is a constant determined by the antenna and boundary conditions at the plasma-vacuum interface. The radial and azimuthal components of $\tilde{\mathbf{B}}(r)$ are expressed in terms of $\tilde{B}_z(r)$ and its first derivative. After averaging Eq. (3) over the wave period, the following expression for the z-component of the steady state current results,

$$j_{oz} = \frac{1}{\mu_0 q n_0} \left| \frac{H(\omega,m,k)}{2\alpha} \right|^2 \beta_i \left(\left| (\beta+k) J_{m-1}(\alpha r) \right|^2 - \left| (\beta-k) J_{m+1}(\alpha r) \right|^2 \right) \tag{5}$$

where μ_0 is the vacuum permeability and β_i is the imaginary part of β. Equation (5) expresses the current in terms of the wave polarization, a signature of helicity transfer. In the absence of collisions, β_i and therefore j_{oz}

would be zero. If the frequency is near an eigenfrequency of the configuration, $H(\omega,m,k)$ can become large, suggesting a possible increase in the current.

4. CURRENT DRIVE IN TOROIDAL KINETIC MODEL

Our numerical study of HWCD is based on a kinetic plasma model in axisymmetric toroidal geometry. Spatial inhomogeneities of the equilibrium magnetic field and plasma density in the perpendicular direction are incorporated in calculations, as well as the effects of the ion-ion hybrid and Alfvén resonances. The code, FASTWAC, has the following organization. It first calculates a 3-D picture of the wave electric and magnetic fields for a given external antenna structure using the algorithm of FASTWA[5]. Particular attention is given to the correct inclusion of the electron absorption processes[6]. Electrons gain energy from the wave through three processes: TTMP, Landau damping and cross-term absorption with respective energy absorption rates $[P_{mp},P_{ld},P_{cr}]$ defined in terms of $\tilde{B}_{\|}$ and $\tilde{E}_{\|}$, the toroidal components of the wave electric and magnetic field, respectively:

$$\left.\begin{aligned} P_{mp} = 2\,\gamma\,G\,|\tilde{B}_{\|}|^2, \quad P_{ld} = G\frac{|\tilde{E}_{\|}|^2}{\gamma n_{\|}^2 c^2}, \quad P_{cr} = 2\,G\frac{\mathrm{Im}(\tilde{B}_{\|}^{*}\tilde{E}_{\|})}{n_{\|}c} \\ \gamma \equiv \frac{1}{2}\frac{\omega}{\omega_{ce}}\frac{v_e^2}{c^2}, \qquad G \equiv \frac{1}{2\mu_0}\frac{\omega_{pe}^2}{\omega_{ce}}\frac{\omega}{k_{\|}v_e}\,\mathrm{Im}\left[Z_p\left(\frac{\omega}{k_{\|}v_e}\right)\right] \end{aligned}\right\} \tag{6}$$

In Eq. (6), $Z_p(...)$ is the plasma dispersion function, v_e is the electron thermal speed, and $k_{\|}$ and $n_{\|}$ are respectively the wavenumber and the index of refraction in the toroidal direction. The total rate of energy absorption by the electrons, P_e, is the sum, $P_{mp} + P_{ld} + P_{cr}$.

We use Eq. (2), averaged over the equilibrium magnetic surfaces, to compute $j_{\|}$, the toroidal component of the driven current, where $\tilde{j}_e$ is calculated in terms of the wave electric field via the hot plasma mobility tensor of the electron fluid. The steady driven current is composed of two parts: $j_{\|} = j_m + j_h$, where j_m and j_h designate respectively current resulting from momentum and helicity transfer. The total electron energy absorption rate, P_e, determines j_m,

$$\frac{j_m}{P_e} = \frac{k_{\|}}{\omega}\frac{q}{m v_{ei}} \tag{7}$$

Since the helicity current j_h does not include electron absorption or any other particle resonant effects, we incorporate trapped electron effects only in the evaluation of j_m. When trapped particle effects are included, Eq. (7) is replaced by the expression[9,10],

$$\frac{j_m}{P_e} = \frac{19.2\cdot10^{18}}{\ln\Lambda}\frac{T_e}{N}\left\{\left(\frac{8u^2}{5+Z} + 2 + 12\frac{6+Z}{(5+Z)(3+Z)} + 2\frac{D}{Zu}\right)F(u,\varepsilon,\theta,Z)\right\} \tag{8}$$

where the curly brackets, {...}, denotes a magnetic surface average of the enclosed quantity. The variables and units of Eq. (8) are defined in Refs. (9) and (10). Electron detrapping due to collisions has also been included in FASTWAC. Detrapping has been found important for the high $k_{\|}$ part of the antenna spectrum under Phaedrus-T conditions. Also included in our calculations is the bootstrap current. In the code, the bootstrap current and the poloidal magnetic field have been computed self-consistently. Since the total

driven current is critically dependent on asymmetries in the wave excitation, wave penetration and absorption, we have explored several antenna systems for current drive. In this paper, we show the results for a 2-strap antenna with the phasing, $\pi/2$. This antenna is now installed in Phaedrus-T tokamak.

Figures (1) and (2) illustrate our numerical results for a pure hydrogen plasma. The frequency is slightly higher than ω_{ci}. Figure (1) shows the wave polarization, $S \equiv |E_-|^2 - |E_+|^2$, where E_- and E_+ designate respectively right and left circularly polarized components of the electric field. It is seen that the excited wave is essentially right circularly polarized ($S > 0$), which is important for HWCD. Figure (2) shows spatial profiles of the bootstrap and wave-driven currents as functions of magnetic surface. The curves B, H and M show respectively the bootstrap current and the noninductive currents due to helicity and momentum transfer. In this case, the helicity current is opposite to the current produced by momentum transfer. We plan to explore the influence of the ion-ion hybrid and Alfvén resonances on HWCD for lower frequencies.

Work supported by U.S. DOE grant DE-FG02-88ER53264 and NSF grant PHY-8921300.

[1]R. R. Mett and J. A. Tataronis, Phys. Rev. Lett. **63**, 1380 (1989).
[2]J. B. Taylor, Phys. Rev. Lett. **63**, 1384 (1989).
[3]R. R. Mett and J. A. Tataronis, Phys. Fluids B **2**, 2334 (1990).
[4]V. S. Chan, R. L. Miller, and T. Ohkawa, Phys. Fluids B **2**, 944 and 1442 (1990).
[5]P. E. Moroz , R. Majeski and N. Hershkowitz, Sherwood Int. Conf. (1990).
[6]P. E. Moroz and P. L. Colestock, Plasma Phys. Contr. Fusion **33**, No. 5 (1991).
[7]R. G. Storer and J. A. Staines, **Theory of Fusion Plasmas** (Proc. Varenna-Lausanne Workshop, Varenna, 1990).
[8]F. F. Chen, UCLA, Inst. Plasma anf Fusion Research Report PPG-1317 (1990).
[9]D. A. Ehst and K. Evans, Nucl. Fusion **27**, 1267 (1987).
[10]D. A. Ehst and C. F. F. Karney, Argonne National Laboratory Report ANL/FPP/TM-247 (1987).

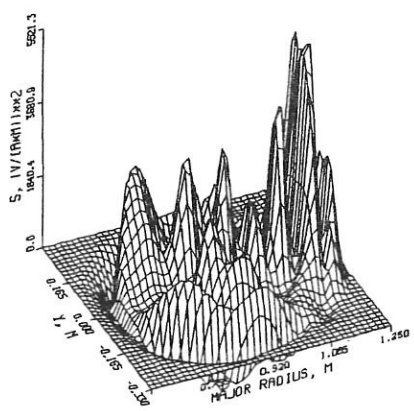

Fig. 1. Wave Polarization

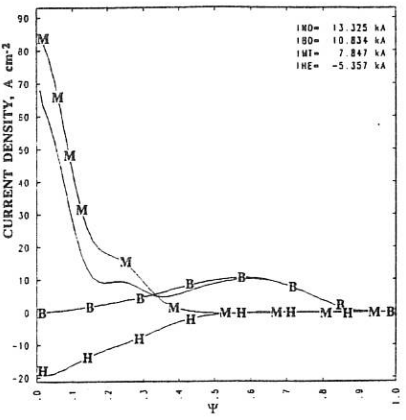

Fig. 2. Noninductive Current

NUMERICAL SIMULATION OF CURRENT DRIVE BY RF FIELDS AND HELICITY INJECTION

Elfimov A.

I.N.Vekua Institute of Physics and Technology, Sukhumi, USSR

Churkina G., Dmitrieva M., Potapenko I.

Keldysh Institute of Applied Mathematics USSR Academy of Sciences, Moscow, USSR

Theoretical and experimental investigations [1-2] demonstrated the possibility to generate steady-state current by RF helicity injection additional to drag current in inhomogeneous plasmas due to gradient forces. In the first part of this paper the results of numerical simulation of propagation, absorption and generation of drag and additional current due to helicity injection are treated by the help of 1-D full-wave code ICCYL for hot tokamak plasmas taking account finite Larmor radius effects for ITER parameters. The fast magneto sonic waves (FMSW) are investigated. Due to the helicity injection current it is possible to generate a current in tokamaks which may be comparable with the drag one for effective sustainment the stationary current in reactor.

In the second part of the report we analize current drive generation by kinetic Alfven wave using the 2-D space velocity Fokker-Planck code taking into account untrapped electrons Landau dumping.

I. In [2] it was presented the derivation of the stationary current from the analysis of averaged RF forces using the kinetic equation with the collision integral in Landau form. We use the model of cylindrical, radially inhomogeneous plasma column. After averaging kinetic equation for electrons and ions over the time and space period of RF field and integrating over velocity space averaged parallel current $\langle j_\parallel \rangle$ was obtained in form :

$$\langle j_\parallel \rangle = - \frac{|e|\, k_\parallel}{m\ \nu_e\ \Omega_{ei}} \left[P + \frac{1}{2} \frac{1}{e\, k_\parallel} \frac{d}{dr} \langle \mathrm{Im}(E_\parallel^* j_r^{(e)}) \rangle \right] \qquad (1)$$

Where Ω -RF frequency, $P = 0.5\ \mathrm{Re}\ (\vec{j}^{(e)} \vec{E})$ - the power density absorbed by electrons, $j_{\alpha\beta}^{(e)} = -\ (i\Omega/4\pi)\varepsilon_{\alpha\beta}^{(e)} E$ - the oscillating current, $\varepsilon_{\alpha\beta}^{(e)}$ - local tensor for hot, magnetized plasma reduced to the sixth order with respect to Larmor radius . The first term in brackets corresponds to the drag current, the second one - to the helicity injection current.

The scenarios proposed in [3] for generation current by FMSW at low frequencies have shown that the influence of trapped particles leads to the peaked profiles for current in spite of the rather expended profiles of absorption. In this situation the current generation by means of RF helicity injection may be more efficient. We treated the 1-st FMS resonance for ITER parameters (T_e= 36 kev, n_e= 1.4 10^{20} m^{-3}, B=5 T, Ω=1.6 Mhz, poloidal antennae number M=-1, toroidal number N=-1). Fig.1 shows a radial distribution of the RF electric field, power absorption, helicity and drag current densities and total current $I(r)=\int j_r\, r\, dr$. The profile of the current due to the helicity injection is rather smooth and expanded and the amplitude value is comparable with the drag current.

II. The kinetic - Alfven-wave current drive generation for the tokamak with circle magnetic surfaces is studied. The treatment is based on the numerical calculations of the Fokker - Planck collision integral $\hat{C}f$ (in the neoclassical approximation). The electron distribution function $f(v,\mu)$ evolves according to

$$I\,\partial f/\partial t = \hat{C}f + \hat{Z}f + \hat{D}f + \hat{E}f \qquad (2)$$

where $I= 4\,K(\varkappa)/(\mu^2+\varepsilon)^{1/2}$, $\varkappa^2= 2\varepsilon/(\mu^2+\varepsilon)$, $K(\varkappa)$ - being the complete elliptical integral of the first kind, μ - is connected with the dimensionless magnetic moment. The emphasis is made on the correct averaging of the equation over the magnetic surfaces ($0 < \phi < 2\pi$), it was assumed that the inverse aspect ratio is small - $\varepsilon = r/R << 1$. To describe the RF field effect on the circulating electrons the quasi - linear operator $\hat{D}f$ is used. The resonant region $v \simeq 2/\pi C_A\, K(\varkappa)/(\mu^2+\varepsilon)^{1/2}$ differs from that one in [4,5]. The influence of trapped particles may be modeled by the "impulsive mixing" operator $\hat{Z}f$ within the phase space region $\mu^2 < \varepsilon$. The presence of the quasistationary electrical field E small to that of Dreiser E_{Dr} is included.

The evolution of the average current for C_A=0.4 V_{Te} with jont and disjoint action of the operators $\hat{D}f$ and $\hat{E}f$ is shown on Fig.2. The deviation of the electron distribution function from Maxwellian for C_A = 0.6 V_{Te} and diffusion coefficient D= 1.5 is performed (Fig.3). During the particle motion along the magnetic field the significant increase (as compared with neoclassical calculations [5]) of the current drive is obtained because of the velocity modulation and stimulated plasma conductivity effect [4]. The efficiencies are: j/P = 2.25, 2.45, 2.46 for C_A= 0.4, 0.6, 1.0 V_{Te}. In the presence of the electrical field E = 0.005 E_{Dr} the generation efficiencies have increased : $(j-j_E)/(P-P_E)$=2.4, 2.54, 2.6.

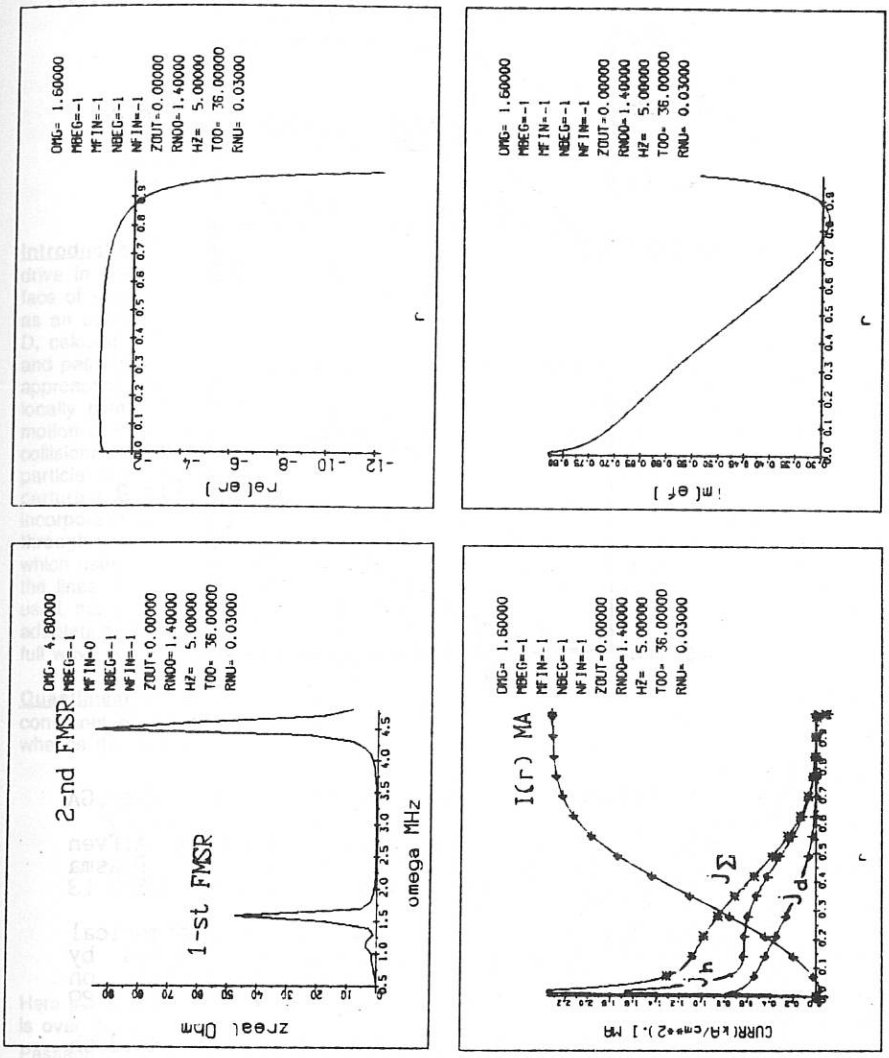
2-nd FMSR
1-st FMSR
zreal Ohm
omega MHz
OMG= 4.80000
MBEG=-1
MFIN=0
NBEG=-1
NFIN=-1
ZOUT=0.00000
RNOO=1.40000
Hz= 5.00000
TOO= 36.00000
RNU= 0.03000
Re(Ωr)
OMG= 1.60000
MBEG=-1
MFIN=-1
NBEG=-1
NFIN=-1
ZOUT=0.00000
RNOO=1.40000
Hz= 5.00000
TOO= 36.00000
RNU= 0.03000
Im(Ωr)
I(r) MA
CURR(kA/cm**2), MA
OMG= 1.60000
MBEG=-1
MFIN=-1
NBEG=-1
NFIN=-1
ZOUT=0.00000
RNOO=1.40000
Hz= 5.00000
TOO= 36.00000
RNU= 0.03000

Fig.1

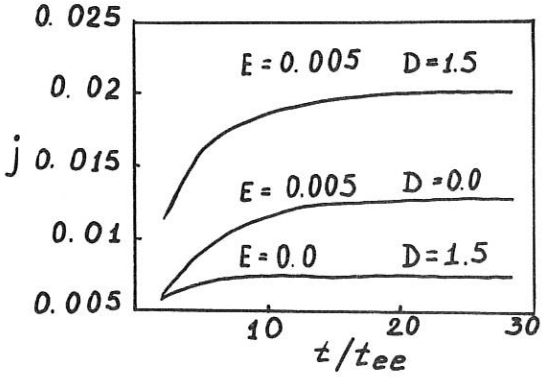

Fig. 2

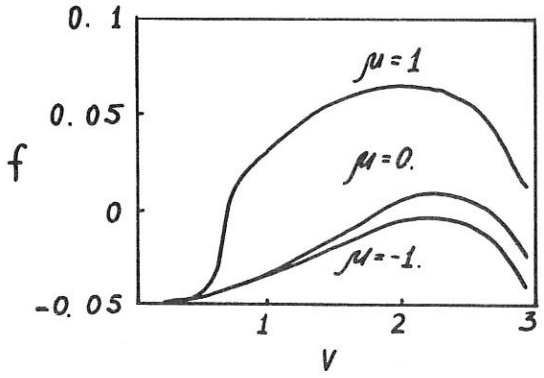

Fig. 3

REFERENCES:

1. Chan V.S., Miller K.L., Ohkava T., Gen. Atomic Rep., GA 19585 1989

2. Kirov A.G., Elfimov A.G. et al., Current drive by Alfven waves (Helicity injection), 13 Int. Conference on Plasma Physics and Controlled Nuclear Fusion, IAEA-AN-53/E-3-13 Washington, USA, 1-6 October 1990

3. Dmitrieva M.V., Vdovin V.L., Fedorov S.V., Numerical simulation of current drive by fastmagneto sonic waves by multi-loop antennas in ITER, 17 Europe Conference on Controlled Fusion and Plasma Heating, Amsterdam, 25-29 June, 1990

4. Elfimov A.G., Potapenko I.F., Preprint N 197 Keldysh Appl. Institute Ac. of Sciences URRS, Moscow, 1988.

5. Ehst D.A., Karney C.F., Preprint ANL/FDP/TM-247, Argonne Nat. Lab. Aprile 1990.

Quasilinear Description of Heating and Current Drive in Tokamaks by Means of Test Particle Fokker-Planck Equation

D.W. FAULCONER and M.P. EVRARD

Laboratoire de Physique des Plasmas - Laboratorium voor Plasmafysica
Association "Euratom-Etat belge" - Associatie "Euratom-Belgische Staat"
Ecole Royale Militaire - B 1040 Brussels - Koninklijke Militaire School

Introduction The Fokker-Planck equation is employed to describe wave heating and current drive in fields which are strong enough to distort the zero-order velocity distribution in the face of Maxwellianization by collisions. The effect of the imposed HF wave enters this equation as an additional diffusive term alongside the usual collision term, with a diffusion coefficient, D, calculated from quasilinear theory. In order to account for the irregular motion of trapped and passing particles in a tokamak, this equation is "bounce averaged" over this motion. Such approaches employ either of two general procedures: 1) averaging of the D which follows from locally homogeneous theory or 2) deriving D from a quasilinear theory which employs the motion of individual particles in the inhomogeneous tokamak magnetic field. Considering low collisionality, we adopt the latter approach as more fundamental in allowing retention of wave-particle phase effects which can limit heating and current drive due to the coherent HF perturbation (see section on stochasticity). An earlier model of the second type which incorporates this limitation has adopted a Hamiltonian formalism, deriving D by proceeding through the Vlasov equation written in action-angle variables [1]. In contrast to this work which uses the kinetic equation, we derive D directly, employing a test particle approach along the lines of work on electron cyclotron resonance [2,3]. The full Hamiltonian formalism is not used, nor is modal decomposition of poloidal spatial dependence imposed, these points favoring adaptation to diverse field geometries and wave codes (e.g. the SPRUCE 2-D finite difference full wave code which uses Fourier analysis only in toroidal angle).

Quasilinear Analysis We consider the zero-order velocity distribution as a function of drift constants of motion μ and J (magnetic moment and longitudinal invariant, respectively), whence the quasilinear contribution to the Fokker-Planck equation in μ-J space (αth species):

$$\left\langle\left(\frac{\partial f_\alpha}{\partial t}\right)_w\right\rangle = \frac{\partial}{\partial\mu}\left[\left\langle\frac{\Delta\mu\,\Delta\mu}{2\Delta t}\right\rangle\frac{\partial f_\alpha}{\partial\mu} + \left\langle\frac{\Delta\mu\,\Delta J}{2\Delta t}\right\rangle\frac{\partial f_\alpha}{\partial J}\right] + \frac{\partial}{\partial J}\left[\left\langle\frac{\Delta\mu\,\Delta J}{2\Delta t}\right\rangle\frac{\partial f_\alpha}{\partial\mu} + \left\langle\frac{\Delta J\,\Delta J}{2\Delta t}\right\rangle\frac{\partial f_\alpha}{\partial J}\right]$$

$$= \vec{\nabla}_{\mu,J}\cdot\left(\vec{\vec{D}}\cdot\vec{\nabla}_{\mu,J} f_\alpha\right) \qquad (1)$$

$$J = \oint p_{//}\,ds\ ,\quad \mu = u_\perp^2/B_0\ ,\quad p_{//} = m_0\gamma v_{//} = m_0\,u_{//}\ ,\quad \gamma = \left(1-\frac{v^2}{c^2}\right)^{-1/2}$$

Here μ, J change by $\Delta\mu$, ΔJ in time interval Δt with the limit $\Delta t\to\infty$ taken, and the average $\langle\ \rangle$ is over the initial values θ_{μ_0}, θ_{J_0}, of the angles θ_μ, θ_J, canonically conjugate to μ, J [2,3]. Passage to the more commonly employed coordinates u, $\varnothing_0$ in place of μ, J is made with the transition $\mathbf{D}\to\mathbf{VDV}^\dagger$ ($\vec{u}=\gamma\vec{v}$, $\varnothing_0$=pitch angle at outer equatorial plane) [2]; since **V** is independent of HF field quantities, we limit consideration to **D** as being the quantity of essential interest. Recalling the definition of **D** in Eqn.(1), we restrict the following discussion to one of its elements, $\langle\Delta\mu\Delta\mu/\Delta t\rangle$, the remaining elements following by direct analogy.

In calculating $\Delta\mu$ we assume a given particle's guiding center to stay on a given magnetic line. Variables ψ (parametrizing magnetic surface), and χ (parametrizing poloidal position on magnetic surface) are introduced in the poloidal cross-section of the tokamak. Noting that the arclength s along $\vec{B}_o$ traversed by a particle can be parametrized in terms of χ, $s(\chi)$, one has as equation of motion of the particle along $\vec{B}_o$ following from the drift approximation: $d\chi/dt=(d\chi/ds)(ds/dt)=v_{/\!/}(\chi)/(ds/d\chi)=\pm\sqrt{[(2/m_o)(\in -m_o\mu B_o(\chi)/\gamma^2)]}/(ds/d\chi)$, $\in =m_o v^2/2$, giving: $t(\chi)=\int(ds(\chi)/d\chi)/v_{/\!/}(\chi)d\chi$. Analogous explicit integration to find $\chi(t)$ being impossible, we adopt χ as independent variable, this giving after Fourier transforming in toroidal angle φ, (details at end of section): $\Delta\mu = \int_0^{\Delta t} dt(d\mu/dt)|_{trajectory} = \int_{\chi_o}^{\chi} d\chi(d\mu/d\chi)|_{trajectory}$ or

$$\Delta\mu = \frac{1}{2}\sum_{n,p}\int_{\chi_o}^{\chi}\frac{d\mu_{n,p}}{d\chi}(\chi)\, e^{i[n\varphi(\chi) + p\theta(\chi) - \omega t(\chi)]}\, d\chi + c.c. \qquad (2)$$

where the cyclotron motion enters via the harmonics in θ (θ=cyclotron angle, $d\theta/dt=\omega_c(\chi)$=relativistic cyclotron frequency, ω_{co}/γ).

Restricting attention to the case of a passing particle we write: $d\varphi/d\chi=<d\varphi/d\chi>_\chi+d\tilde{\varphi}/d\chi$, $d\theta/d\chi=<d\theta/d\chi>_\chi+d\tilde{\theta}/d\chi$, $[d\theta/d\chi=\omega_c(ds/d\chi)/v_{/\!/}]$, $dt/d\chi=<dt/d\chi>_\chi+d\tilde{t}/d\chi$, or integrating: $\varphi(\chi)=q(\chi-\chi_o)+\tilde{\varphi}(\chi)-\tilde{\varphi}(\chi_o)+\varphi_o$, $\theta(\chi)=<d\theta/d\chi>_\chi(\chi-\chi_o)+\tilde{\theta}(\chi)-\tilde{\theta}(\chi_o)+\theta_o$, $t(\chi)=(\chi-\chi_o)/\Omega_b+\tilde{t}(\chi)-\tilde{t}(\chi_o)$, $[\Omega_b^{-1}=(2\pi)^{-1}\int_0^{2\pi}(ds(\chi)/d\chi)/v_{/\!/}(\chi)d\chi]$, where χ dependence has been split into linear and 2π-periodic ($\tilde{}$) contributions with the introduction of particle bounce frequency Ω_b and safety factor q. Substitution of these expressions in Eqn.(2) yields:

$$\Delta\mu = \frac{1}{2}\sum_{n,p}\int_{\chi_o}^{\chi}\frac{d\mu_{n,p}}{d\chi}(\chi)\, e^{i\left[\Delta_{n,p}\chi + \tilde{f}_{n,p}(\chi) - \Delta_{n,p}\chi_o - \tilde{f}_{n,p}(\chi_o) + n\varphi_o + p\theta_o\right]} d\chi + c.c. \qquad (3)$$

$$\Delta_{n,p} = nq + p\left\langle\frac{d\theta}{d\chi}\right\rangle_\chi - \frac{\omega}{\Omega_b}$$

where $\tilde{f}(=n\tilde{\varphi}+p\tilde{\theta}-\omega\tilde{t})$ regroups periodic contributions. Exploiting toroidal invariance, one can show the average $<\ >$ to be equivalent to an average $<\ >_{\varphi_o,\theta_o}$. One thus has:

$$\left\langle\frac{\Delta\mu\Delta\mu}{\Delta t}\right\rangle = \lim_{\Delta t\to\infty}\left\langle\frac{\Delta\mu\Delta\mu}{\Delta t}\right\rangle_{\varphi_0,\theta_0} = \lim_{\Delta\chi\to\infty}\Omega_b\left\langle\frac{\Delta\mu\Delta\mu}{\Delta\chi}\right\rangle_{\varphi_0,\theta_0} = \lim_{N\to\infty}\frac{\Omega_b}{2\pi N}\langle\Delta\mu\Delta\mu\rangle_{\varphi_0,\theta_0} \qquad (4)$$

$$= \frac{\Omega_b}{4\pi}\sum_{n,p,j}\delta(\Delta_{n,p}-j)\left|\int_0^{2\pi}\frac{d\mu_{n,p}}{d\chi}(\chi)\, e^{i\left[j\chi + \tilde{f}_{n,p}(\chi)\right]} d\chi\right|^2$$

where the angular averages remove nondiagonal contributions in (n,n'),(p,p') in the limit shown (N=number of bounces) and we have exploited the periodicity of $\tilde{f}$. If the absolute value of the integral is a slowly varying function of j and the Chirikov overlap criterion is satisfied, one can invoke stochasticity to substitute $\Sigma_j \to \int dj$ finding:

$$\left\langle \frac{\Delta\mu\Delta\mu}{\Delta t} \right\rangle = \frac{\Omega_b}{4\pi} \sum_{n,p} \left| \int_0^{2\pi} \frac{d\mu_{n,p}}{d\chi}(\chi)\, e^{i[n\varphi(\chi) + p\theta(\chi) - \omega t(\chi)]}\, d\chi \right|^2 \qquad (5)$$

Cyclotron resonance is notably manifest in the points of stationary phase of the integrand where $d/d\chi[n\varphi(\chi)+p\theta(\chi)-\omega t(\chi)]=0$.

As regards trapped particles, the previous analysis goes through essentially unchanged if, in place of χ, one introduces the new variable χ' defined such that $d\chi'=|d\chi|$. Denoting by χ_t the amplitude of particle guiding center oscillation in χ ($\chi=0$ on outboard equatorial plane), the foregoing formulae remain valid with the substitutions $\int_0^{2\pi} \to \oint_{-\chi_t}^{\chi_t}$, $\Delta n,p \to \Delta o,p$.

In order to make the expression for $\langle \Delta\mu\Delta\mu/\Delta t \rangle$ in Eqn.(5) more concrete it is worthwhile to indicate how the quantity $d\mu_{n,p}/d\chi$ appearing in it is written in terms of HF field quantities $\vec{E}$, $\vec{B}_1$. One has:

$$\frac{d\mu}{d\chi} = \frac{\frac{ds}{d\chi}}{v_{//} B_0} \left\{ \frac{e_\alpha}{m_0} \left[\vec{E}(\vec{r}_{g.c.}+\vec{r}_L, t) + \vec{v} \times \vec{B}_1(\vec{r}_{g.c.}+\vec{r}_L, t) \right] . \vec{u}_\perp \right\} \qquad (6)$$

Local Cartesian coordinates are introduced with $\vec{e}_z$ and $\vec{B}_0$ directions coincident, giving: $\vec{u}=u_\perp(\vec{e}_x\cos\theta - \vec{e}_y\sin\theta)+u_{//}\vec{e}_z$, $\vec{r}_L = \vec{e}_z \times \vec{v}\,(\theta)/\omega_c$. The φ dependence of the HF fields is developed in Fourier series and the dependence on $\vec{r}_L$ expanded in a Taylor series in $\vec{r}_L \cdot \nabla$ about guiding center $\vec{r}_{g.c.}$. The quantity $d\mu_{n,p}/d\chi$ follows from the coefficient of exp $i(n\varphi+p\theta-\omega t)$.

Stochasticity In deriving the expression for $\langle \Delta\mu\Delta\mu/\Delta t \rangle$ appeal was made to the Chirikov overlap criterion in effecting the transition $\Sigma_j \to \int dj$ (when the criterion is not fulfilled, quasilinear diffusion becomes negligible). We now make this criterion explicit in the context of the present formalism. An electron TTMP-Landau damping scenario is adopted by way of example where $\omega << \omega_{ce}$, this implying $p=0$ and allowing the HF electron dynamics to be treated in the drift approximation, whence $\Delta n,p \to \Delta n = nq - \omega/\Omega_b$ and **D** has $\langle \Delta J \Delta J/\Delta t \rangle$ as sole nonzero element. The relation for the increment in longitudinal invariant ΔJ follows from replacement of μ by J in Eqn.(3) where we develop the integral as a sum over the contributions from each of N successive bounces:

$$\Delta J = \frac{1}{2} \sum_n e^{i(n\varphi_0 + \ldots)} \left[1 + e^{i2\pi\Delta n} + \ldots + e^{i2\pi(N-1)\Delta n} \right] \int_{\chi_o}^{\chi_o + 2\pi} \frac{dJ_n(\chi)}{d\chi} e^{i[\Delta n\, \chi + \tilde{f}_n(\chi)]} d\chi + c.c \qquad (7)$$

When the resonance value $J \equiv J_{n,j} \Rightarrow \Delta_n \equiv j$ (j=integer) is assumed, one finds the changes over the (N+1)st particle bounce to be:

$$J(N+1) - J(N) = \frac{1}{2} e^{i(n\varphi_0 + \ldots)} e^{iN2\pi\Delta_n} \int_{\chi_o}^{\chi_o + 2\pi} \ldots + c.c. \approx \sin\left(\Theta(N) + \Theta_0\right) \left| \int \ldots \right|$$

$$\Theta(N+1) - \Theta(N) = 2\pi\,(\Delta_n - j) \qquad (8)$$

where the new angular variable $\Theta(N)=2\pi N(\Delta_n - j)$ gives the phase modulo 2π and is hence slowly varying. One can thus pass from finite differences to differentials on the left sides of these equations and linearize about the value $J_{n,j}$ ($J=J_{n,j}+\delta J$):

$$\frac{d\delta J}{dN} = \left| \int \ldots \right| \sin\left(\Theta - \Theta_0\right), \quad \frac{d\Theta}{dN} = 2\pi \frac{\partial \Delta_n}{\partial J}(J_{n,j})\,\delta J \Rightarrow \frac{d^2\Theta}{dN^2} = 2\pi \frac{\partial \Delta_n}{\partial J} \left| \int \ldots \right| \sin\left(\Theta - \Theta_0\right) \qquad (9)$$

the last equation describing motion in Θ in a potential~$\cos(\Theta - \Theta_0)$ with N as a time-like variable. In Θ,J space a particle can thus exhibit either trapped (island) or passing behavior with J localized about $J_{n,j}$. Note that the trapping is not to be identified with any zero-order effect taking place in the absence of the HF fields, but is driven by the latter (the fields appear in $\int\cdots$). The localization of J, which precludes current drive, will break down at field amplitudes large enough for the onset of stochasticity; this occurs when trajectories from neighboring resonances begin to overlap as was pointed out by Chirikov. The resulting stochastic behavior of J then admits a diffusive Fokker-Planck description. One can estimate the threshhold amplitude of the δJ variation, $\delta\hat{J}$, by putting $\delta J \to \delta\hat{J}$ in the expression for $d\Theta/dN$ in Eqns.(9) and using the result as an effective frequency, Ω_{eff}, for Θ in reading $\delta\hat{J}$ from the first of Eqns.(9): $\delta\hat{J} \sim |\int\cdots/\Omega_{eff}| = |\int\cdots/(2\pi\delta\hat{J}\,\partial\Delta_n/\partial J)|$ or $\delta\hat{J} \sim |\int\cdots/(2\pi\partial\Delta_n/\partial J)|^{1/2}$. Equating this amplitude to the distance to the nearest neighboring resonance value, $J_{n',j'}$, gives a criterion for the onset of stochasticity. As $\int\cdots$ is a function of the HF fields, this criterion defines threshholds for the latter also:

$$\left| \frac{\int \ldots}{2\pi \frac{\partial \Delta_n}{\partial J}} \right|^{\frac{1}{2}} \geq \min_{n',j'} \left| J_{n,j} - J_{n',j'} \right| \qquad (10)$$

Conclusion A non-Hamiltonian quasilinear heating/current drive formalism has been presented (see Eqn.(5)) which adapts to diverse plasma geometries and wave descriptions. A simple prototype evaluation of the criterion for the onset of the stochasticity necessary to heating and current drive has been made (Eqn.(10)).

Acknowledgements The authors are grateful for helpful discussions with Dr A. Bécoulet, Professor B.D. Fried, Professor A.N. Kaufman and Dr D. Moreau.

References

[1] A. Bécoulet, D.J. Gambier, A. Samain, Phys. Fluids **3** 137 (1991); A. Bécoulet, Thèse de Doctorat, Juin 1990, Université de Paris-Sud, Centre d'Orsay.

[2] M.R. O'brien, M. Cox, D.F.H. Start, Nucl. Fusion **26** 1625 (1986).

[3] G. Laval, R. Pellat, in Plasma Physics, Les Houches, C. DeWitt and J. Peyraud Eds., Gordon and Breach , 217 (1985).

EXPERIMENTAL STUDIES ON RF CURRENT DRIVE BY A STANDING ALFVEN WAVE

A.G.Kirov , D.A.Voytenko, A.V.Sukachëv, L.F.Ruchko

I.N.Vekua Institute of Physics and Technology, Sukhumi, USSR

The experiments on current drive by Alfven waves via RF helicity injection are continued in the R-O device. A radial profile of the current generated by a standing Alfven wave and the effect of resonant minority heavy ion species on the current generation are studied.

1. At present, a possibility of current drive via RF helicity injection is widely discussed; that is, averaged RF forces complementary to those of RF dragging may be used. This method of current generation using RF waves with $\omega<\omega_{Bi}$ was proposed by Ohkawa et al. [1]. DC current up to *0,6 kA* generated by a standing Alfven wave (AW) has been observed in the R-O device [2]. The current scaling law and, also the change in sign in the DC current generated by a travelling AW, with an increasing in plasma density [2,3], indicate that the current is due to RF helicity injection.

2. The R-O device is a $l=3$ stellarator with a quartz discharge chamber ($R=50$ *cm*, $b=5$ *cm*, $a=3.5-4$ *cm*, $B_o<8$ *kG*, $\bar{n}_{13}=0.5-8$, $\bar{T}<100$ *eV*, $J_{ohm}=0$, H_2). A RF antenna of the device consists of *8* helical winds enclo sing chamber and allows to excite travelling and standing AWs with $m/n=\pm1/\pm1$, $\pm2/\pm2$, $\pm4/\pm4$ ($k_\Theta=m/r$, $k_z=-n/R$). The RF field frequencies in the present experiments are *0,8 MHz* and *1,2 MHz*. Radial profiles of the current have been reproduced by measuring poloidal fields of the current using magnetic probes.

3. Measurements of radial distributions of the RF driven current generated by a travelling AW [4] have shown that the current has a hollow profile typical for the dragging current generated by an AW exciting at the steep gradient of the plasma density. The DC current generated by a standing AW has a hollow profile as well (Fig.1). A distribution of a dipolar harmonic of the Pfirsch-Schlüter equilibrium current shown in the same figure. The unidirectional current profile, $J_0(r)$, is broadened relative to the dipole harmonic, $J_1(r)$, and shifted towards to the plasma column centre. This fact indicates that the DC current is not result from Pfirsch-Shlüter current (J_1^{PS}) or diffusion bootstrap current (J_0^B): $J_0^B \propto J_1^{PS} \propto P'(r)/\iota(r)$.

4. Effect of minority ions (He) in a hydrogen plasma on generation of a DC current by a standing AW are studied. DC current amplitudes de creased resonantly when the pumping RF field frequency is close to the cyclotron one of He^+- minority (Fig.2). The above effect is observed when the minority concentration exceeded some critical value. This value depends upon the toroidal magnetic field B_0 and increases with growth in B_0 (Fig.3). When the critical value is exceeded there is an increase in plasma density and the active impedance of the antenna becomes smaller (by ~10%), the RF power input being approximately the same. Apparently, extra amounts of minority result in the AW dispersion alteration and, hence, the power input grows at the plasma column periphery.

REFERENCES

1. Chan V.S., Miller R.L., Ohkawa T. General Atomics Report, GA-A19585, 1989.

2. Kirov A.G. et al. 17th Europ. Conf. Contr. Fusion and Plasma Heat., Amsterdam 1990, v.14B, part 3, p.1319.

3. Kirov A.G. et al. 13th Int. Conf. on Pl.Phys. and Contr. Nucl. Fus. Res., Washington, 1990, IAEA-CN-53/E-3-13.

4. Demirkhanov R.A. et al. 10th Europ. Conf. on Contr. Fus. and Plasma Phys., Moscow, 1981, v.1, E-7.

CAPTIONS

Fig.1. Zero and dipolar harmonics of the poloidal magnetic field of plasma current ($B_{\theta o}$,$B_{\theta 1}$) vs radius and current components profiles ($j_o(r)$,$j_1^{PS}(r)$). Dashed lines are dipolar harmonics profiles for model of plasma pressure $P(r) = P_o\cdot[1-(r/a)^6]^2$ and stellarator transform angle $\iota(r)=\iota_a(r/a)^2$.

B_o=3,1 kG, the standing AW $m=\pm2/n=\pm2$, f=0,8 MHz, J_{pl}=0,25 kA

Fig.2. The plasma current generated by a standing AW vs the toroidal magnetic field in the presence of heavy minority. The standing mode $m=\pm2/n=\pm2$, f=1,2MHz, $P_{RF}\simeq$200kW, H_2+2,3% He.

Fig.3. The current generated by a standing AW in the plasma vs the amount of He-minority.

The standing mode $m=\pm2/n=\pm2$, f=1,2 MHz, $P_{RF}\simeq$ 280 kW.

1) B_o= 2,6 kG; 2) $B_o\simeq B_i(He^+)$ = 3,15 kG; 3) B_o= 3,75 kG.

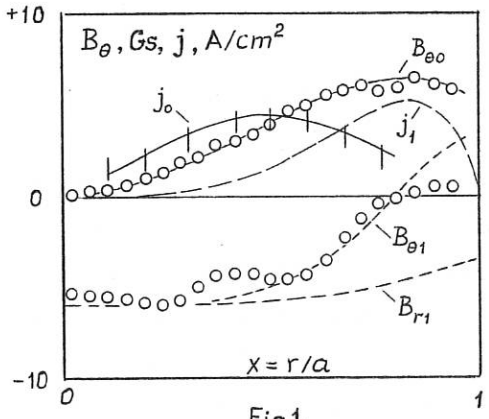

Fig.1.

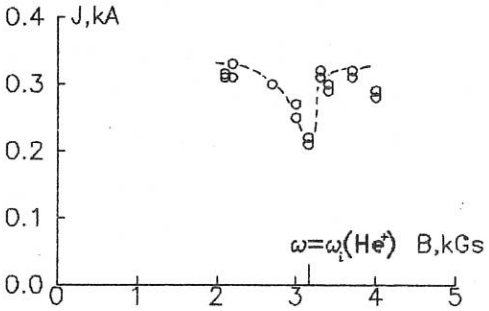

Fig.2.

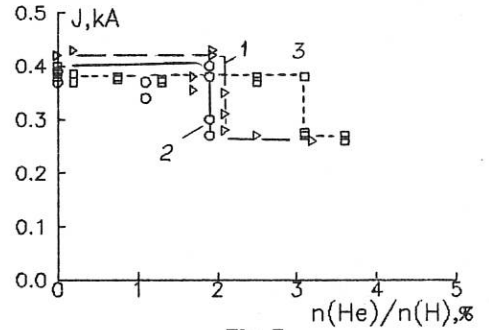

Fig.3.

THE EFFECT OF POLOIDAL PHASING OF ICRF ANTENNAE ON WAVE EXCITATION

M.J. Alava and J.A. Heikkinen

Helsinki University of Technology, Department of Technical Physics,
SF-02150 Espoo, Finland

1. Introduction

The recent success of ion cyclotron resonance heating (ICRH) has stimulated interest in reliable theoretical models for calculating the coupling between various antennae and the plasma. While the experimental differences between various toroidal phasing alternatives are by now well understood, the corresponding consequences of different poloidal excitation scenarios remain little studied. Of interest are the questions of optimizing the coupling resistance and estimating the parasitic electrostatic wave coupling.

2. The Coupling Resistance

We estimate the coupled power for given toroidal and poloidal refractive indices n_z and n_y according to a standard 3–D coupling geometry [1,2]. The power spectrum $P(n_z, n_y)$ is given by $P = P_a \,\mathrm{Re}[\Gamma]/|\Gamma|^2$, where P_a scales as

$$P_a(n_z, n_y) \sim \frac{\sinh(\nu_x(w-a))^2}{\sinh(\nu_x w)^2} |j_y - i\frac{n_y}{\nu_x^2} j_x|^2. \tag{1}$$

Here w and a are the Faraday–screen to wall and screen to antenna –distances, respectively, ν_x is defined by $\nu_x^2 = n_z^2 + n_y^2 - 1$, Γ is determined by the plasma response to the antenna fields and j_x and j_y are the Fourier transforms of the antenna current distribution in the radial and poloidal directions. For simplicity, it is assumed that the antenna and the screen are ideally aligned along the magnetic field lines.

Our model antenna consists of two adjacent current straps in the poloidal direction. We have $j_x = -in_y j_y$ [1] and the Fourier transform, j_y, is

$$j_y = \frac{1}{4\pi^2}\frac{1}{w_z w_y}\int_{-w_x/2}^{w_x/2}\int_{-w_y/2}^{w_y/2} dz\, dy\, e^{-in_z z - in_y y} J_y(e^{i\Theta_1} + e^{i\Theta_2} e^{-in_y w_y}), \tag{2}$$

where w_z and w_y are the toroidal and poloidal widths of the straps and J_y is the constant current density in each strap in the antenna housing. Θ_i ($= 0$ or π) define the direction of the current in each strap ($i = 1, 2$). Note that all the spatial lengths are normalized by c/ω where c is the light speed and ω is the angular frequency of the radiation.

The plasma response is estimated by solving the wave fields in front of antenna numerically. This is accomplished by applying finite element techniques to appropriate 1-D

wave equations including finite electron inertia and corrections to second order in ion Larmor radius [2]. As boundary conditions at the high density point, $x = L$, we demand that the electric fields can be decomposed into three independent wave branches, i.e. the fast, slow and ion Bernstein modes which are described in the WKB limit. At the antenna, we set the condition that the kinetic energy flux vanishes. The plasma response can then be determined from the numerical solution of E_y/B_z at $x = 0$.

The coupling for given n_z, n_y is determined by the antenna spectrum and plasma response. In Fig. 1a we show the antenna dependent part, $P_a(n_z, n_y)$, for an antenna consisting of two straps in monopole phasing ($\Theta_1 = \Theta_2 = 0$, see Table for the other parameters). The coupling is in this case strongest at low n_z. Changing the phasing to a dipole one (straps in opposite phase) removes the region of strong response centered around $n_z = 0$, $n_y = 0$. Because of the feeder effect [1], the relative coupling strength is rather low for large $|n_y|$. Fig. 1a demonstrates the suppression of high n_y values in the spectrum. This should be compared to Fig. 1b where the feeders are neglected by setting $j_x = 0$ in (1). The latter figure demonstrates a very smooth dependence of the antenna spectrum on n_y together with the disappearance of the fine structure around $n_z^2 + n_y^2 = 1$. The omission of the feeder effect and the resulting enhancement in coupling for large $|n_y|$ [3] has further consequences on parasitic electrostatic wave coupling.

3. Results

In addition to fast wave coupling, mode conversion of the heating power may take place due to the strongly inhomogeneous density profile in the vicinity of the antenna [4]. Given a low enough density at the antenna, the lower hybrid (LH) resonance couples some part of the power directly into the electrostatic mode. Another, competing mechanism exists due to the gradient of the polarization of the fast wave, which works even at somewhat higher edge densities. The relative conversion grows in optimal conditions very rapidly as a function of $|n_y|$. This is demonstrated in Fig. 2a, where we show the fraction of the total coupled power converted to the electrostatic mode for $n_z = 0$.

To discuss the effects of different n_y–spectra we solve for the total power integrated over n_y for a given n_z. The plasma and antenna parameters are typical of the JET–tokamak (see Table). In Figure 2b the mode converted power is shown integrated from $n_y = -5$ to $n_y = 5$ as a function of n_z. The antenna characteristics dominate the coupling process and suppress the conversion of the coupled wave power at high n_y. However, because of the large coupling to electrostatic waves at high $|n_y|$, the total coupling remains substantial. Neglecting the feeder effects leads to a much higher, upto fivefold, coupling resistance for small $n_z \leq 4$ and the corresponding converted power is also substantial at low n_z ($C \simeq 50$ %).

4. Discussion

In order to overcome the feeder effect and achieve good coupling for moderate to large values of the poloidal refractive index the antenna dimensions and geometry play the major role. For the current antenna and plasma parameters, typical of a large JET–type tokamak, the maximum coupling region is located around the $n_y = 0$–axis. However, there is experimental evidence that if the antenna poloidal dimension is comparable to

the size of the plasma, poloidal phasing can enhance the total coupling [5]. This may be due to simultaneous slow and fast wave excitation by an optimal choice of phasing. Generally, an increase in coupling could be obtained with an antenna geometry, which does not suppress the high n_y–modes like in the current slab antenna model with feeders.

For a high plasma edge density and an antenna with feeders the relative converted power remains low. This may be typical of large tokamaks with low magnetic fields. On the other hand, the mechanisms responsible for the coupling, i.e. the LH resonance and the polarization gradient, are expected to be of more importance in small, low aspect ratio, high field and high density devices such as the Compact Ignition Tokamak.

References

1. Bhatnagar, V.P., Koch, R., Messiaen, A.M. and Weynants, R.R., Nucl. Fusion **22** (1982) 280.
2. Brambilla, M., Nucl. Fusion **28** (1988) 549.
3. Ram, A. and Bers, A., Nucl. Fusion **24** (1984) 679.
4. Alava, M.J. and Heikkinen, J.A., submitted for publication.
5. Takeno, H., Inoue, S., Yasaka, Y. and Itatani R., Nucl. Fusion **30**, (1990) 925.

Ion densities at screen n $[10^{16}m^{-3}]$	1. (D), 0.05 (^{3}He), 0.05 (H)
Temperature at screen T $[eV]$	30
Major radius R $[m]$	4.15
Wave frequency ω $[1/s]$	2.11×10^8
Toroidal field at screen B_T $[T]$	2.34
Slab length L $[m]$	0.02
Density gradient length L_n $[m]$	0.0037
Temperature gradient length L_T $[m]$	0.029
Screen to wall –distance w $[m]$	0.11
Antenna to wall –distance a $[m]$	0.0975
Antenna toroidal width w_z $[m]$	0.14
Antenna poloidal width w_y $[m]$	$0.70 = 2\times\ 0.35$

Table 1: Antenna coupling parameters

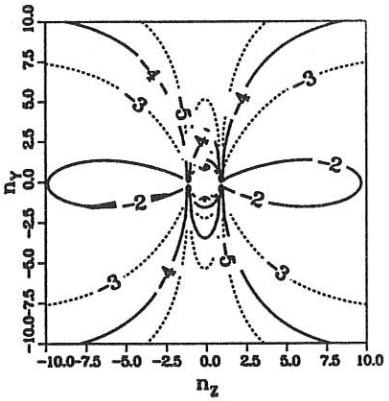

Figure 1a. The logarithm of the antenna spectrum for a poloidally monopole phased, two–strap antenna with the feeders. Units are arbitrary.

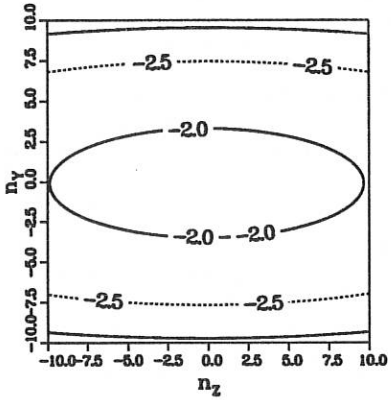

Figure 1b. The same antenna without the feeder contribution.

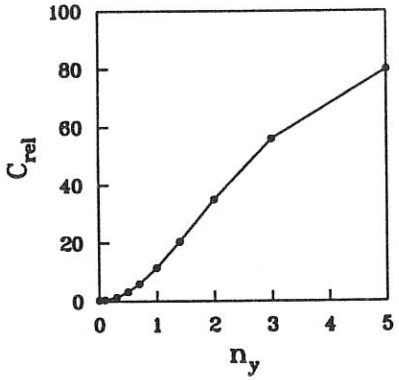

Figure 2a. The fraction of the coupled power converted into the ion Bernstein mode as a function of n_y for $n_z = 0$.

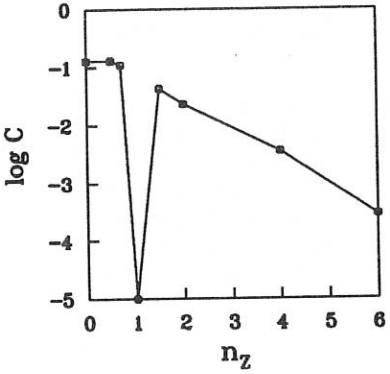

Figure 2b. The logarithm of the fraction of power coupled in the electrostatic mode as a function of n_z, integrated over n_y.

THE EFFECT OF REALISTIC ANTENNA GEOMETRIES ON PLASMA LOADING PREDICTIONS*

P.M. Ryan, F.W. Baity, D.B. Batchelor, R.H. Goulding, D.J. Hoffman, J.S. Tolliver

Oak Ridge National Laboratory, Oak Ridge, TN 37831-8071, USA

Introduction

Plasma loading resistances for Ion Cyclotron Resonance Heating (ICRH) antennas are often calculated with sophisticated plasma models and only rudimentary antenna geometries. This paper presents techniques for modifying loading calculations for cavity antennas to account for such realities as return currents in the antenna sidewalls and backplane, the transmission and reflection properties of the Faraday shield, the end effects due to a finite length antenna, the reduction in phase velocity due to strap interaction with the Faraday shield, and the effect of slots in the cavity sidewalls and dividing septa.

Loading Calculations

Plasma loading calculations are made with RANT[1] , a two-dimensional (2D) code with provisions for arrays of arbitrarily-phased current straps in recessed cavities. The source current's toroidal distribution on the antenna strap (infinitely thin in the radial or x-direction) can be specified arbitrarily, either from measurements or from a self-consistent 2D magnetostatic calculation, while the return current distribution along the recessed, perfectly conducting cavity walls is determined self-consistently. A diffuse-boundary magnetized plasma, uniform in z, extends to infinity in the radial direction, with its density profile an arbitrary input. The system is assumed uniform in the poloidal direction and the plasma loading for these TE modes is expressed in ohms per meter of strap length. Figure 1 shows a typical plasma profile and regions in which the wave fields are represented.

The plasma loading is greatly affected by the sidewalls of the cavity recess and the septa that separate the current straps. Loading for an early BPX antenna design was reduced by a factor of two when sidewalls were added to the conducting backplane, which constrains the flux to the vicinity of the strap. This code does not model the Faraday shield, which has the effect of redistributing the strap current, decreasing the flux transmission to the plasma, decreasing the strap inductance by flux reflection, and decreasing the phase velocity along the strap. Methods of compensation for these effects are presented in this paper.

Effect of the Faraday Shield

The Faraday shield affects the plasma coupling properties of ICRH antennas in many ways. It necessarily reflects some of the magnetic flux produced by the current strap, thus lowering the strap inductance as well as the flux transmission to the plasma. It also terminates the electrostatic component of the electric field by presenting a ground plane in close proximity to the current strap, greatly increasing the strap capacitance and hence lowering the phase velocity along the current strap. The transmission/reflection coefficients of the Faraday shield and the strap inductance per unit length are calculated with a 3D magnetostatic code that has been described in detail elsewhere[2]. Figure 2 shows the geometry and the boundary conditions for the calculation. Laplace's equation for the magnetic scalar potential is solved over one poloidal period of the shield, with Dirichlet boundary conditions on the midstrap symmetry planes corresponding to the total strap current, and Neumann conditions on all other

*Research sponsored by the Office of Fusion Energy, U.S. Department of Energy, under contract DE-AC05-84OR21400 with Martin Marietta Energy Systems

surfaces corresponding to a vanishing normal component of the magnetic field. This code is used to calculate the flux and power transmission coefficients (T_ψ and T_p) and the strap inductance per unit length (L'), while the strap capacitance per unit length (C') is obtained from a complementary 3D electrostatic calculation using the same geometry. The phase velocity along the strap is obtained by representing the current strap as a lossy two-conductor transmission line with $v_p = (L'C')^{-1/2}$.

While the reflection coefficient of the Faraday shield is essentially independent of the strap-to-shield gap, L' is dependent on the magnitude of the reflected field and hence decreases as the gap decreases. A T_ψ of 85% can decrease L' by 10% for a 1.5 cm gap and by 20% for a 0.7 cm gap. However, the increase in C' is greater than the decrease in L', and v_p decreases to values around $0.67c$ for a 1.5 cm gap and $0.5c$ for a 0.7 cm gap. The increase in C' with strap width is roughly proportional to the decrease in L', so that v_p is nearly independent of strap width, although the characteristic impedance decreases with increasing width.

Effective Length of Antenna

Most two-dimensional plasma coupling codes such as RANT calculate antenna loading in terms of ohms per unit poloidal length; the net loading is determined by the length of the antenna. However, the effective length of the current strap is dependent both on the finite wavelength along the antenna and its poloidal geometry. The 3D magnetostatic analysis[3] is used to calculate the decrease in the toroidal field component due to poloidal end effects and return currents in the antenna cavity. The loading from fast wave coupling is proportional to the toroidally-integrated square of the toroidal component of the antenna's magnetic field. The length attenuation factor due to geometric effects is α, calculated at the Faraday shield,

$$\alpha = \frac{\int_0^L dy \int_0^{2\pi R} dz\, B_z^2(y,z)}{\int_0^{2\pi R} dz\, max\, B_z^2}$$

where $max\ B_z$ is the maximum value of the toroidal component and corresponds to the value encountered in 2D calculations. Figure 3 shows an example of this falloff in the toroidal component for the DIII-D FWCD end-grounded antenna[4]($\alpha = 0.87$). Typical antennas have α in the range of 0.87 to 0.93; the shorter the antenna, the greater the end effect influence, and the smaller α. The length reduction factor k due to finite wavelength effects is

$$k = \frac{1}{h}\int_0^h dy \cos^2(\beta y),$$

where $h = L$ for end-grounded straps, $h = L/2$ for center-grounded straps, and $\beta = \omega/v_p$ uses the previously calculated phase velocity (for $v_p = 0.55c$, $k = 0.71$ at 60 MHz).

Effects of Slots in the Cavity Sidewalls and Septa

Providing slots in the side walls of ICRH antennas is a method of allowing expansion of the current strap's magnetic field pattern, thus downshifting the toroidal wave spectral peaks and increasing the plasma loading. Placing slots in the septa that separate current straps in multiple strap arrays also changes the wave spectrum by redistributing the return currents, at the expense of increasing the interstrap coupling. The effectiveness of such slots is determined by their transparency to magnetic flux, which is a function of slot shape, area, position, thickness, and poloidal periodicity. More care must be taken when slotting septa for arbitrarily phased arrays for current drive than for arrays which are driven with adjacent strap phase shifts of either 0 or π. While slotting septa generally increases the array directivity, which is desirable for current drive applications, the increase in mutual coupling can exacerbate the phase stability of the matching system and make phase control more difficult[4] .

If the cavity side wall in Figure 2 were extended to meet the "plasma" surface to form a septum, this would be equivalent to a symmetric pair of current straps being driven out of phase. Symmetry demands a Neumann boundary for the potential, that is, the normal component of the magnetic field should vanish along the plane that includes the septum. However, if the straps are driven in phase, then symmetry demands that the tangential component of the magnetic field vanish along the plane of the septum; that is, the nonmetallic part of the symmetry plane, including the slots, becomes an equipotential (Dirichlet) surface, while the conducting walls of the septum remain Neumann surfaces. The magnitude of the scalar potential applied to this symmetry surface is determined by the constraint of global flux conservation: there can be no net flux crossing any constant z surface. In practice, the potential applied to the septum midplane is iterated in a converging fashion until the total magnetic flux passing behind the current strap equals the flux passing in front of the strap.

Once the in-phase and the out-of-phase inductances are known, the mutual inductance or the mutual coupling coefficient can be calculated. The comparison of this coupling coefficient to values obtained from a fully open septum (i.e., slot height extends to full poloidal period) and a fully closed septum (slot height vanishes) gives a indication of the transparency of the slotted septum to magnetic flux. The interstrap coupling coefficient for the DIII-D fast wave current drive array was calculated to be 6.3% and measured to be 6.8%; these slots in the 2 cm thick septum are 5.3 cm deep and 0.32 cm high, spaced every 5 cm. When these slots are extended to the rear of the cavity (i.e., 15 cm deep), the calculated interstrap coupling coefficient increases to 20.1%. The coupling coefficient with no septum at all is 32.6%, indicating that narrow slots can be quite transparent to flux (-4.2 dB) provided they extend far enough behind the current strap to pass the flux generated between the strap and the rear wall.

The mutual coupling coefficient can be calculated in 2D geometry by the same (0,0), $(0,\pi)$ phasing techniques outlined above. We have obtained good agreement between the measured fields and the calculated fields, both 2D and 3D, when the length of the solid septa in the 2D calculations is adjusted until the coupling coefficients agree with measurements and 3D calculations. This is shown in Fig. 4, where B_z of a test antenna is plotted vs z at 2 cm from the shield, both with and without slots in the septum and sidewalls (mutual coupling is 1.8% or -35 dB for the solid septum, and 4.9% or -26 dB for the slotted septum).

Conclusions

The RANT code calculates plasma loading per poloidal length for recessed cavity geometry, arbitrary strap phasing, and quite flexible plasma profiles; the toroidal distribution and radial location of the strap sheet current may be specified by calculations from a 2D magnetostatic code. Combining results of 2D and 3D magnetostatic codes can give effective septa lengths to be used in RANT. For example, the 18.8 cm long septa of the DIII-D array with the 5.3 cm deep, 6.3% transparent slots can be represented by a solid septum 16.5 cm long. To continue with this particular example (Fig. 3), the length attenuation factor α due to end effects is 0.88, the phase velocity due to the Faraday screen is $0.55c$, giving a length reduction factor k of 0.71 at 60 MHz, and the power transmission coefficient is 0.72. The actual length of the current strap is 45 cm, but the overall effective length for obtaining the loading in ohms from the output of RANT is the product of the above factors

$$R_L = \alpha k L\, T_p R_L' = L_{eff} R_L',$$

or 20.2 cm, which is only 45% of the actual strap length.

References

[1] J.S. Tolliver and D.B. Batchelor, Bull. Amer. Phys. Soc. **35** (Nov. 1990), 2047
[2] P.M. Ryan *et al*, Fusion Engineering and Design **12** (April 1990), 37
[3] P.M. Ryan *et al*, AIP Conf. Proc. **190** (1989), 322
[4] R.H. Goulding et al, 17th EPS Conf. on Controlled Fusion and Plasma Heating 14B,v. III, (Amsterdam, June 1990), 1311

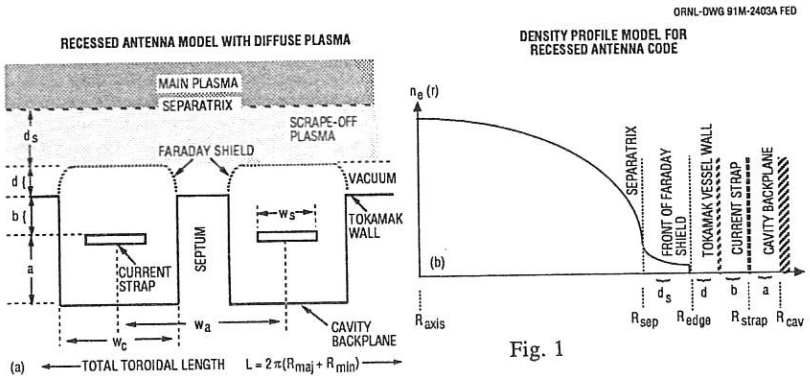

Fig. 1

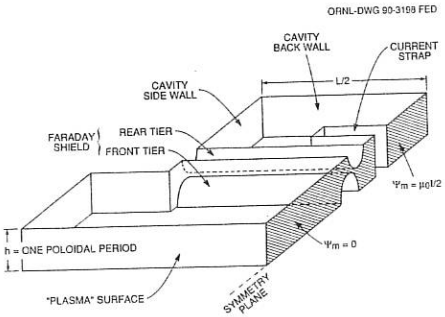

Fig. 2

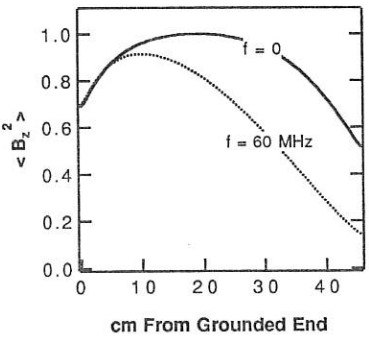

Fig. 3

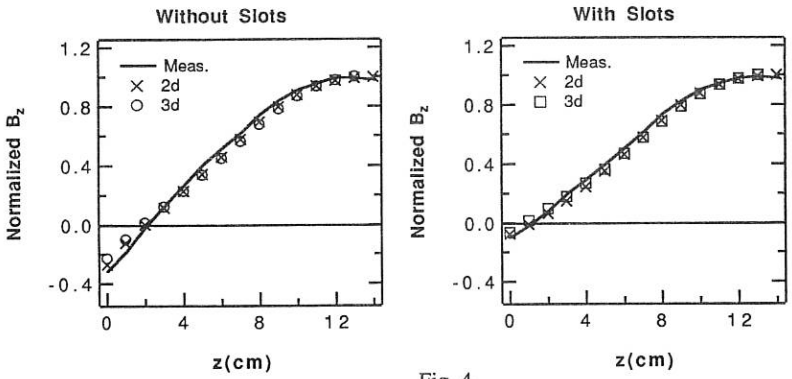

Fig. 4

CURRENT DRIVE BY EC-WAVES IN STELLARATORS

F. Castejón, J. A. Coarasa and C. Alejaldre

Ascociación EURATOM/CIEMAT
Av. Complutense, 22. 28040-Madrid (Spain)

Linear evaluation of current drive is a fast method to compute the induced current. This fact allows the inclusion of the efficiency function in a ray tracing code, which calculates the absorbed power density and, from that, the induced current in a complex magnetic configuration can be computed. Furthermore, we must assume that the distribution function is nearly a Maxwellian and that the absorbed power density is low.

The induced current density parallel to the magnetic field can be written in terms of the absorbed power density as follows :

$$J_{\parallel}(\vec{r}) = A\int d\vec{v}\,\frac{\delta J}{\delta P}\sum_s W_s(\vec{v}) \tag{1}$$

The efficiency is obtained from the Langevin equations and averaged for a Maxwellian distribution function. For the relativistic case this function is (see [1]):

$$\eta(\vec{v}) = \frac{\delta J_{\parallel}}{\delta P_d} = G(v)\left[N_{\parallel} - \frac{v_{\parallel}}{v^2}(\gamma + 1 + Z)\right] + \frac{2vv_{\parallel}}{\gamma^2} \tag{2}$$

$$G(v) = \frac{2}{v}\left[\frac{\gamma(v)+1}{\gamma(v)-1}\right]^{\frac{1+Z}{2}} \int_0^v dx \left[\frac{x}{\gamma(x)}\right]^3 \left[\frac{\gamma(x)-1}{\gamma(x)+1}\right]^{\frac{1+Z}{2}} \tag{3}$$

$$\vec{v} = \frac{\vec{p}}{mc} \quad ; \quad \gamma = \left(1+v^2\right)^{1/2}$$

For Z_{eff}=1 the efficiency can be computed analytically, but for arbitrary values of Z_{eff} the intregration must be performed numerically. In figure 1 the efficiency is presented for some values of Z_{eff}. It is shown that the efficiency decreases with Z_{eff}, which means that the impurities have a negative influence on the current drive efficiency.

On the other hand we consider the absorbed density power in the phase space, W_s, which is different from zero only for the resonant electrons. This fact ensures that we obtain zero current for $N_{\parallel}$=0, since W_s is an even function and the efficiency an odd one. The current density can be written as follows:

$$J_{\parallel} = \sum_{s=1}^{\infty} \int_{v_-}^{v_+} dv_{\parallel}\, \eta(v_{\parallel})\, W_s(v_{\parallel}) \tag{4}$$

The absorbed power density for a Maxwellian is given by [3]:

$$W_s(v_{\parallel}) = \frac{\omega_p^2 \mu^2}{16\omega K_2(\mu)} v_{\perp}^2 \left|\vec{E}\cdot\vec{\Pi}_s\right|^2 \exp(-\mu\gamma_s) \tag{5}$$

As far as the deformation of the distribution function can be considered a perturbation of the Maxwellian, we can assume that it is well localized in the momentum space. The position of the deformation will be near the so called collective resonant momentum. The induced current density parallel to the magnetic field at a point in the plasma can be approximated by this expression [3], [4]:

$$j_{\parallel}(<r>) \approx \eta(\vec{p}_R) < P_{cy} >, \qquad (6)$$

where the efficiency is calculated at the collective resonant momentum. This approximation can be avoided calculating numerically the momentum integral (4). In figure 2 the current density obtained by both methods at the second harmonic is shown. The collective resonant momentum approximation (curve 1) is accurate at downshifted frequencies. However such an approximation is not appropriate in the presence of trapped particles.

Numerical application to the heliac TJ-II

The following step is to adapt the expression (4) to the ray tracing code RAYS. The parameters needed to calculate the efficiency are given by the code. The volume and the area of the given magnetic surface are calculated in terms of the mean radius, which is obtained from the magnetic flux. The total intensity is estimated integrating the current density perpendicular to a toroidal surface. We assume that the power density is uniform at every magnetic surface [4], so we must calculate the average power density absorbed inside a given magnetic surface.

The microwave beam structure must be taken into account, because its width is 5 cm, which is not negligible respect to the plasma dimensions. We take a gaussian beam simulated by 16 rays and we disregard the four corner rays. This will make the absorption area more unlocalized in the plasma than when considered only one ray, so the current profiles we obtain are wider.

A case is shown in figures 3a and 3b for 2nd harmonic microwave injection in the vertical direction, out of axis. The density on axis is 1.2×10^{13} cm^{-3} and the temperature is 0.8 keV. The total induced current is I=0.79 kA and the current density maximum 4.5 A/m^2.

Trapped particles

The magnetic configuration of stellarators allows a great variety of trapping mechanisms. So the trapped particle effects are very important in Electron Cyclotron Current Drive and their influence on the efficiency must be taken into account.

To do that we consider how trapped particles modify the response function [5]. Trapped particles do not contribute to the current in the average, so the efficiency is zero in the trapped region:

$$\eta_T(v_{\parallel}) = 0 \quad ; \quad v_1 \le v_{\parallel} \le v_2 \quad ,$$

where

$$v_{1,2} = \frac{Y_s N_{\parallel} \mu_t^2 \pm \mu_t \left[Y_s^2 - 1 + \mu_t^2 N_{\parallel}^2 \right]}{1 - \mu_t^2 N_{\parallel}^2} \qquad (7)$$

On the other hand, circulating particles can become trapped. The contribution of this kind of particles modify the response function:

$$\chi_T(\vec{v}) = \chi(\vec{v}) - \frac{v_{||}}{|v_{||}|}\chi(\vec{v}_T) \tag{8}$$

where the response function is defined as:

$$\chi(\vec{v}) = \int_0^{\infty} j_{||}(t,\vec{v})dt \tag{9}$$

A particle starting with momentum v becomes trapped when its momentum takes the value:

$$\frac{v_{||}}{v}(t) \le \mu_t \equiv \left(1 - \frac{B}{B_{max}}\right)^{1/2}, \tag{10}$$

where B is the local magnetic field and B_{max} is the maximun magnetic field on a field line. Taking into account the Langevin equations, averaged over an ensemble of particles, one obtains the particle momentum when it becomes trapped:

$$v_T = \frac{2\sqrt{f}}{1-f} \quad ; \quad f(\vec{v}) = \left(\frac{\mu_t v}{|v_{||}|}\right)^{\frac{2}{Z+1}} \frac{\gamma - 1}{\gamma + 1} \tag{11}$$

By using equation (8) we obtain the efficiency:

$$\eta_T(\vec{v}) = \eta(\vec{v}) - \frac{v_{||}}{|v_{||}|}\frac{1+2f}{(1-f)^2\sqrt{f}}\left(\frac{\mu_t v}{|v_{||}|}\right)^{\frac{2}{Z+1}} \frac{\partial \chi(\vec{v}_T)}{\partial v_T} \times$$

$$\times \left\{ Y_s \left(\frac{\gamma - 1}{\gamma + 1}\right) \frac{1}{v_{||}^2} + \frac{2}{(\gamma+1)^2}\left[1 + \frac{1}{1+Z}(Y_s - \gamma)\left(\frac{v_\perp}{v_{||}}\right)^2\right]\right\}, \tag{12}$$

where the derivative of the response function is:

$$\frac{\partial \chi(\vec{v}_T)}{\partial v_T} = \frac{\mu_t}{2}\left[\left(\frac{v_T}{\gamma_T}\right)^3 - (Z+1)\left(\frac{\gamma+1}{\gamma-1}\right)^{\frac{Z-1}{2}} \frac{v_T}{\gamma_T(\gamma_T - 1)^2} \int_0^{v_T} dv \left(\frac{v}{\gamma}\right)^3 \left(\frac{\gamma - 1}{\gamma + 1}\right)^{\frac{Z+1}{2}}\right] \tag{13}$$

Then we calculate the integral (4) introducing the efficiency (12). In figure 4 the influence of trapped particles on EC current drive efficiency is shown. The nature of the EC diffusion in the momentum space, which is mainly in the perpendicular direction, makes the effect of trapped particles deleterious.

References

[1] N. J. Fisch. Physical Review A 24, 3245 (1980)

[2] I. Fidone, G. Granata and J. Johner. Physics of Fluids 31, 2300 (1988)

[3] V. Krivenski, I. Fidone, G. Giruzzi, G. Granata, R. L. Meyer and E. Mazzucato. Nuclear Fusion 25, 127 (1985)

[4] F. Castejón and C. Alejaldre. Proceedings of the 17th European Conference on Controlled Fusion and Plasma Physics. EPS, part III, 1255. Amsterdam (1990)

[5] G. Giruzzi. Nuclear Fusion **27**, 1933 (1987)

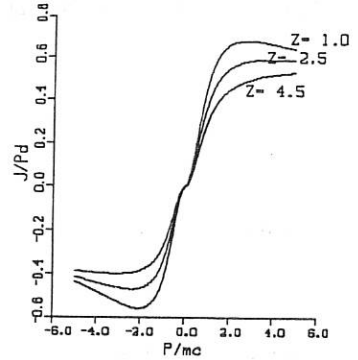

Fig. 1 Efficiency versus parallel momentum for Npar=0.1, for several values of Z.

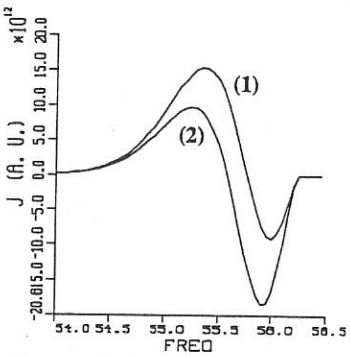

Fig. 2 Current density vs. frequency for n=1, Npar=0.1, B=1, T=1. Resonant momentum approximation (1) and numerical integration (2).

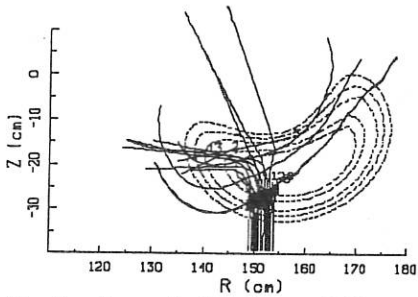

Fig. 3a Ray paths for a beam of 16 rays. The absorption happens out of axis, mostly at upshifted frequencies.

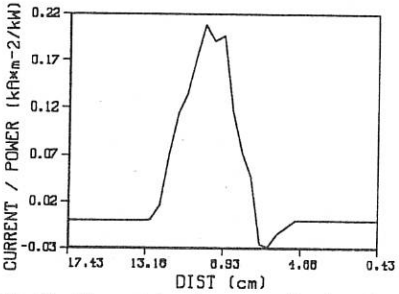

Fig. 3b Current density, normalized to the injected power, vs. distance to magnetic axis in TJ-II. The total current in this case is I=0.79 kA. The total injected power is 200 kw.

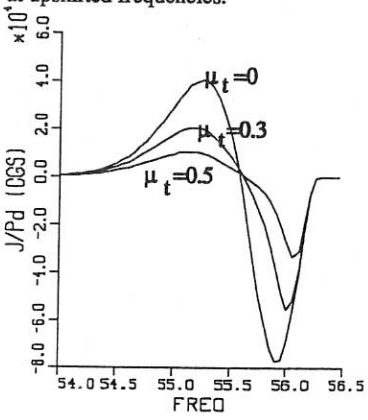

Fig. 4 Current drive efficiency (in cgs units) versus frequency (in GHz) in presence of trapped particles, for the same plasma parameters as in fig. 2.

ECRH PRODUCED START-UP PLASMAS IN RTP

R.W. Polman, A.C.A.P. van Lammeren, J. Lok, F.C. Schüller, F.M.A. Smits, and RTP-Team

FOM-Instituut voor Plasmafysica Rijnhuizen, Association EURATOM-FOM,
P.O. Box 1207, 3430 BE Nieuwegein, The Netherlands.

Abstract

Experiments on plasma build-up have been performed in RTP using 60 GHz ECRH in 1st harmonic O-mode and 2nd harmonic X-mode irradiation. Second harmonic irradiation seems less effective.

Introduction

The future research programme of the Rijnhuizen Tokamak Project RTP is concentrated on the study of transport mechanisms in strongly auxiliary heated tokamak plasmas [1,2]. The additional heating power for RTP is supplied by an Electron Cyclotron Resonance Heating (ECRH) system.

ECRH is also attractive for tokamak start-up because a reduction of the necessary voltage reduces the Vs-consumption and can lead to a decrease of the initial runaway electron population in the plasma. ECRH-assisted start-up, which has already been studied in a number of machines, further permits control over the localization of the initial breakdown, thereby reducing plasma-wall interaction and the losses arising from impurity line radiation. This start-up technique has proven to be essential to RTP since, up to now, reproducible operation of the machine could only be obtained by using a short (typically 10ms) ECH pulse. The best scenario for low-voltage start-up and current ramp-up is now searched for via studies on plasma breakdown and start-up optimization.

This paper will restrict to plasmas produced and sustained by sole ECRH power, thus to plasmas in the phase prior to the switch-on of the toroidal electric field which produces and drives the eventual tokamak current. The preionization plasma is produced by 60 GHz irradiation.

Experimental set-up

The experiments have been carried out on the Rijnhuizen tokamak device RTP. The vacuum chamber has a major radius of 0.72 m, and a minor radius of 0.24 m. The minor radius of the plasma has been set to 0.164 m.

The RF power is generated by one 60 GHz, 200 kW, 100 ms gyrotron and is fed to the plasma via an oversized waveguide containing various mode convertors, and a launcher mounted in the midplane at the lower field side of the torus. The power is irradiated perpendicular to the magnetic field in the nearly linearly polarized TE_{11}-mode. It has been launched into the torus with polarizations to couple to the 1st harmonic O- mode and to the 2nd harmonic X-mode. The power not absorbed in single pass is reflected at the opposite wall by a roof-top mirror that is composed of two smooth cylindrical mirrors [3]. This mirror reflects under angles $\pm 8^0$ with the radial direction to prevent reflection back into the launcher. The toroidal magnetic field, B_T, can be varied in 10 steps and ranges up to $B_T = 2.4$ T. For the present studies $B_T(R_0)$ has mostly been chosen to be 1.95 T. This corresponds to 1st harmonic 60 GHz resonance at the higher field side, 6 cm from the centre.

The torus is continuously pumped. In advance of the ECR pulse, hydrogen gas is supplied at the proper rate to get the desired pressure, p_{fill}. After that the toroidal field B_T is applied. Then, by injecting the 60 GHz microwave power during 100 ms a plasma is produced. The electron density is controlled by gas puffing. Before or during the ECH pulse a vertical (B_v) and a radial magnetic field (B_h) can be superposed on B_T. It is possible to choose B_v and B_h stationary as well as time dependent. There are strong indications that the toroidal field coil system also produces stray fields in the poloidal plane. This has been checked by inversing the polarity of the the toriadal field. No primary voltage is yet applied to induce the toroidal electric field. Nevertheless currents up to more than 3 kA are initiated and sustained by the RF power.

The RTP diagnostics has been extended [1]. A high-resolution, high-sensitivity multi-chord interferometer [4] with 8 to 12 channels operational delivers every 20 μs a profile of the line integrated electron density during 160 ms to visualize the plasma formation and evolution in an easy way. A diagnostic called TraP [3] measures the fraction of the irradiated power not absorbed in single pass. Its nine horns, placed in a cross and embedded in the roof-top mirror mentioned above, face the ECH launcher and measure the power incident on the mirror at five locations in the poloidal and in the toroidal plane. The overall absorption of the plasma is measured with a sniffer probe placed at a different toroidal position. Electron temperature data are obtained from Thomson-scattering.

Results

In earlier, exploring, studies emphasis was laid on the ECH induced current I_p [5]. The data were obtained with a simple flat mirror that reflected the ECH power under 8^0 with the radial direction. This mirror has been replaced by the roof-top mirror of the TraP system. Further, RTP became boronized in the course of the present experiments. It was checked whether these alterations, for which the ECH induced current was supposed to be sensitive, did lead to different experimental results. For 1st harmonic O-mode launch the dependence of I_p on the applied magnetic fields and on the filling pressure appeared to be the same for all three experimental conditions. This suggests that single pass absorption plays a minor role in the plasma formation phase and that the plasma behaviour is governed by a multiple reflection process. In line with this TraP measurements show for low densities a low single pass absorption while the sniffer probe indicates that the total absorption is very high. Both observations support the view that though only the X-mode incident from the higher magnetic field side is expected to be absorbed effectively enough for plasma formation and heating through the radiation barrier it might be possible as well to inject an O-mode, or even non-polarized waves, from the lower field side and rely on polarization scrambling [6]. In contrast: when using 2nd harmonic X-mode launch a current was hardly detectable, if present.

The dependence of the plasma formation on various experimental parameters - i.e. the resonant magnetic field location, the filling pressure, the ECRH power level, the direction of B_T and the gas-puff rate - has been studied for 1st harmonic O-mode irradiation while for 2nd harmonic X-mode the dependence on the resonance location and on the filling pressure was observed.

In all cases the birth of the plasma takes place very close to the resonance layer position, from where it fills out the torus in outward direction. The time evolution and the shape of the n_e-profiles, however, are different for various experimental conditions. With no external B_v and B_h applied the stray fields in RTP are such that the density centre moves to the inner wall in a few milliseconds (p_{fill} = 0.15 mTorr). Then the density sharply decreases and the line-integrated density profiles become very broad, suggesting extremely hollow electron density profiles. To find a better initiation scans of B_v and B_h were made at fixed values of B_T (1.95 T) and p_{fill} (0.15 mTorr). ECRH was applied from t = 0 to 100ms, B_h was switched on at t = 30 ms and B_v at t = 60 ms; the first 30 ms are a check of the reproducibility, while the effect of the fields is seen thereafter. The plasma formation starts after a delay of about 0.3 ms and the total number of

electrons grows to 0.36 10^{19} at 1.1 ms. (The volume of the RTP vacuum vessel is about 1.0 m^3. The usual plasma volume is 0.39 m^3; such volume filled with 0.15 mTorr H_2 gas of room temperature contains about 0.4 10^{19} electrons. It would require about 75 kW to ionize this gas if each ionization event counts for 100 eV). The number of electrons then decreases and amounts to 0.02 - 0.1 10^{19} at 8.5 ms, depending on memory effects (strong gas puffing or unfavourable choice of B_v and B_h). Thomson temperatures in the center of the torus at 25 ms are typically in the range 50 - 100 eV, densities are 0.2 - 0.5 10^{19} m^{-3}. After switch-on of the additional fields (mostly as a step function) the chord-integrated electron density profile, the electron contents, and the ECH induced current react. As a selection criterium for the best fields the highest number of electrons produced in the tokamak or the highest value of the ECH induced I_p can be chosen. Though one could argue that these are counterly tending, it surprisingly appeared that both criteria go hand in hand at the assumed best choice for B_v and B_h. It should be noted that part of this best choice is needed to compensate the erroneous poloidal poloidal stray field induced by the toroidal field system. After switch-on of a good B_h field, the Thomson data indicate at 55 ms temperatures above 100 eV and densities of about 0.25 10^{19} m^{-3}. At 6 cm above the torus centre temperaures range from 60 to 100 eV and densities from 0.3 to 0.45 10^{19} m^{-3}.

A filling-pressure scan (p_{fill} = 0.06 - 1 mTorr) has been done with the best fields already switched on at the start of the ECH pulse. Again, after some delay, the total number of electrons grows to a maximum and then steadily decreases at a rate depending on p_{fill}. The plasma stays in the centre of the vacuum vessel during the full 100 ms of the ECH pulse. The time delay is 0.65 ms at 0.06 mTorr and decreases via 0.13 ms at 0.5 mTorr, to 0.10 ms with 1.0 mTorr filling pressure. The time interval between the delayed start and the occurrence of the maximum electron number increases with pressure: from 0.8-ms (0.06 mTorr), via 2 ms (0.5 mTorr), to about 6 ms with p_{fill} = 1 mTorr; the values appear sensible to memory effects. The maximum electron contents increases from 0.2 10^{19} (0.06 mTorr) to 0.6 10^{19} at p_{fill} = 0.4 - 0.5 mTorr, and stabilizes around that value for the higher filling pressures. By gas puffing the electron number can be kept constant or be made to increase. However, with p_{fill} = 1 mTorr combined with heavy gas puffing from the beginning on $n_{e,total}$ was constant during the whole pulse but did not exceed 0.6 10^{19} (i.e. a volume averaged density of 1.5 10^{19} m^{-3}).

Second harmonic X-mode irradiation in a non-boronized RTP showed a much longer time delay after switch on of ECRH. Plasma build-up now became detectable after typically 5 to 11 ms, depending on memory effects. Further the density buildup to the maximum value happened much slower as compared with 1st harmonic: 4 ms with p_{fill} = 0.2 mTorr, and 11 ms with p_{fill} = 0.5 mTorr. Also the maximum electron contents was lower: 0.12 10^{19} and 0.25 10^{19} with p_{fill} = 0.2 and 0.5 mTorr, respectively. The density profiles were much more peaked than with 1st harmonic O-mode. This probably indicates a more localized electron production.

For 1st harmonic O-mode and a non-boronized torus we compared 50 kW and 200 kW irradiation. The delay with 50 kW is increased a few ten percents when compared with 200 kW, the time necessary to build up the maximum increased with 50% or more. The maximum electron contents with 50 kW is half the value of the 200 kW case.

The decay of the afterglow discharge, with no power input, shows an effective particle containment time of about 3 ms.

Acknowledgement

This work was performed under the Euratom-FOM association agreement with financial support from NWO and Euratom.

References

[1] F.C. Schüller et al., this conference.
[2] R.W. Polman et al., Proc. 16th Eur. Conf. on Controlled Fusion and Plasma Phys., Venice (1989) Vol.III, 1139.
[3] F.M.A. Smits et al, this conference.
[4] A.C.A.P. van Lammeren et al, this conference.
[5] R.W. Polman et al., Proc. 17th EPS Conf. on Controlled Fusion and Plasma Heating, Amsterdam (1990) Vol.III, 1121.
[6] M. Bornatici et al., Nucl. Fusion 23 (1983) 1153.

Examples of plasma production by ECRH. The figures show the time evolution of the plasma build-up during the first 2 ms for four resonance locations (B_T between 1.75 and 2.35 T; p_{fill} = 0.35 mTorr). The horizontal axes indicate the radial position (0.59 - 0.86 m), the vertical axes apply to the line integral of the electron density (a.u.). The plasmas are born at the location where B_T = 2.14 T, i.e. the resonant field value for 60 GHz. The stray fields were not eliminated here.

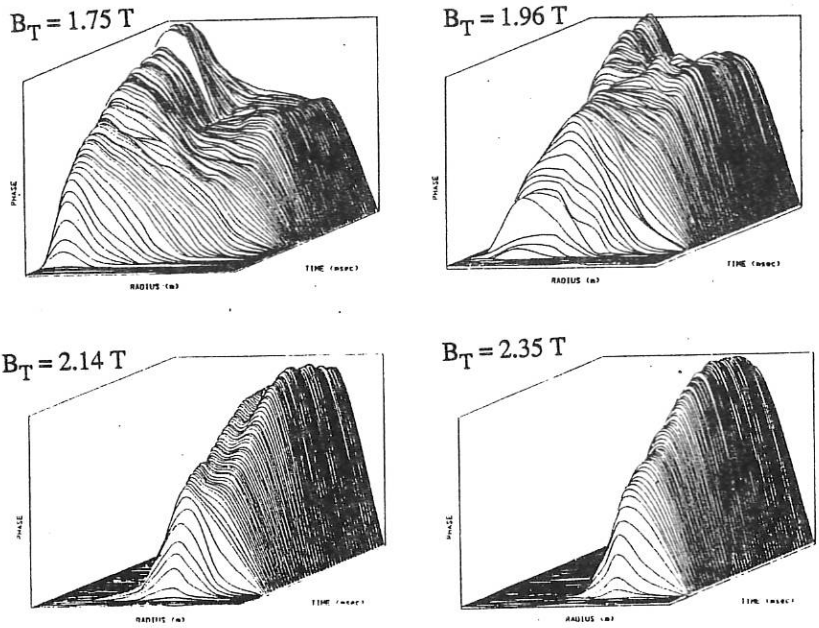

SAWTOOTH STABILIZATION BY ELECTRON CYCLOTRON HEATING NEAR q=1 SURFACE IN THE WT-3 TOKAMAK

S. Tanaka, K. Hanada, H. Tanaka, M. Iida, S. Ide, T. Minami
M. Nakamura, T. Maekawa, and Y. Terumichi
Department of Physics, Faculty of Science
Kyoto University, Kyoto 606, JAPAN
and
M. Yamada, J. Manickam and R. B. White
Plasma Physics Laboratory, Princeton University,
P.O.Box 451, Princeton, N J 08543 USA

1. INTRODUCTION

Sawtooth oscillations (STO) in the ohmically heated (OH) WT-3 tokamak are strongly modified or suppressed by localized electron cyclotron resonance heating (ECH) near the q=1 surface, where q refers to the safety factor. The effect of ECH is much stronger when it is applied on the high field side, as compared to the low field side. Complete suppression of the STO is achieved for the duration of the ECH when it is applied on the high field side, in a low density plasma, provided the ECH power exceeds a threshold value. This threshold decreases with the increasing safety factor at the limiter q_L. The STO stabilization is attributed to a modification of the current density profile by high energy electrons generated by ECH, which reduces the shear in the q=1 region [1].

2. EXPERIMENTAL RESULTS

The experiments were carried out in the WT-3 tokamak [2], with major and minor radii R=65 and a=20cm, respectively. The toroidal field was 1.75T, and the plasma current $I_p \leq 150$kA. Microwaves from a gyrotron ($\omega/2\pi$=56GHz, $P_{ECH} \leq 200$kW, T<100ms) were transferred through circular waveguides to a Vlasov antenna with an elliptic reflector placed along the major radius and injected into the plasma from the low-field side. This sharply focused wave, propagating as the X mode with an angle of θ=84° to the toroidal field, is absorbed at the second harmonic ECH resonance layer.

Sawtooth oscillations were observed when the current was such that the safety factor at the limiter was in the range q_L=2.2 ~ 6.0 . The sawtooth period τ_s, as well as the amplitude, increase when the ECH power, P_{ECH}, is applied. At the same time, the electron density decreases slightly, $n_e = (7 \rightarrow 6) \times 10^{12}$cm^{-3}, and the temperature as measured by Thomson scattering increases, $T_{e\perp}(0) = 510 \rightarrow 670$ eV, resulting in a decrease of loop voltage, V_L=1.5 → 0.8V, while the plasma current was held constant at I_p=80kA (q_L=4.3). There appears a hard x-ray signal I_{HX} (35keV), suggesting generations of the energetic electrons, while there is no change in the OV impurity line emission. Here ECH is applied near the q=1 surface on the low field side. The above-mentioned modifications of STO are very sensitive to the field B_T which determines the location where the ECH is localized. The ECH power is held constant and B_T is adjusted so that the resonance occurs at different layer; the geometric configuration is shown in Fig. 1(a),

while the changes in the soft X-ray (SXR) signal, I_{SX} due to the ECH are shown in Figs.1(b)-(d). When the ECH is at the q=1 surface on the high field side, (HFS), Fig. 1(b), the sawtooth oscillation are completely stabilized. When the heating occurs on the low field side (LFS) of the same q=1 surface, τ_s increases enormously, and is greater than the energy confinement time, τ_E, (τ_s=3ms, τ_E=1ms), and the amplitude saturates, Fig. 1(d). In contrast, when the heating occurs away from the q=1 surface, at the magnetic axis, I_{SX} ramps up sharply and drops deeply during the crash phase, Fig. 1(c). These observations clearly indicate the critical importance of the location of the application of ECH. Other effects can be easily excluded, since the plasmas in the ohmically heated phase are essentially similar.

These results are shown in greater detail in Fig. 2. Fig. 2(a) shows the dependence of τ_s on the radial position of ECH resonance layer r(2Ωe), which is varied by changing B_T, without and with ECH. In the former case we observe that there is no significant variation at all. On the other hand τ_s has two resonance values when B_T is such that the ECH occurs at $r_{q=1}$, where τ_s increases significantly. When $r_{ECH}=r_{q=1}$ on the HFS, τ_s is increased up to the entire duration of ECH power and complete stabilization is observed. On the hand when the heating is on the LFS, τ_s is increased substantially but stabilization is not observed. These results are complemented by the corresponding variation in the amplitude, Fig. 2(b), which shows the peaking of the amplitude when the ECH is on axis and at $r_{q=1}$.

In addition to the influence of B_T, which determines the location of the ECH, other plasma parameters play an important role as well. These include the power of the ECH, P_{ECH}, and the electron density, n_e. The dependence on P_{ECH} is shown in Fig. 3, where we have plotted τ_s as a function of P_{ECH}/P_{OH}. We observe that there is an initial linear phase where τ_s increases lineally, and at large value of P_{ECH}/P_{OH} there is a rapid non-linear increase, resulting in complete stabilization. This threshold occurs at P_{ECH}/P_{OH}=3.5 for the particular set of plasma conditions of q_L=3.4, n_e=5x10^{12}cm^{-3} when the ECH is at $r_{q=1}$ on the HFS. In contrast, τ_s just increases lineally with P_{ECH} when the ECH is on the LFS or at the magnetic axis.

Further, the period τ_s increases abruptly when n_e decreases below n_e=6x10^{12}cm^{-3}, a complete suppression is obtained when n_e ~ 5x10^{12}cm^{-3}, and the ECH is at $r_{q=1}$ on the HFS. Concomitantly the X-ray energy spectra show a high energy tail indicating the presence of a hot electron population with T_{eh}=60keV extending up to 300keV, in these low density plasmas. In the absence of ECH, (T_e= ~0.5keV), hot electron tails are not observed. These observations suggest that the high energy tail electrons generated by ECH in the low density regime, may be responsible for the stabilization of the STO by the enhancement of two effects which will be described in 3.

As q_L increases, the q=1 surface shrinks and the radius $r_{q=1}$ decrease. In the high q_L discharge, the sawtooth can be stabilized easily and the threshold decreases with the increasing q_L and is P_{ECH}/P_{OH}~1 for q_L~4.7, as shown in Fig. 4. It is interesting to note that in such high q_L region as q_L=4.7~6, the complete stabilization of STO is possible even when ECH is applied on the LFS of q=1 surface, though the threshold value for the LFS is large than the HFS. Both

values might be coincident with each other in the high q_L limit (q_L=6), above which there is no sawtooth in the OH discharge.

In very high q_L region (q_L=6~7), the sawtooth are excited, in contrast with the suppression, when ECH is applied in the vicinity of the magnetic axis. It is noticeable that the sawtooth can not be excited when ECH is applied just at the magnetic axis.

It was necessary to generate a narrow wave beam in order to stabilize STO by the localized ECH. We use the Vlasov antenna with the elliptic reflector, where the wave beam is narrow (35 mm in width for 1/e power at the position of plasma center) compared with the other parabolic antenna (64mm). Their wave trajectories and single-pass absorption rates(~60%) are calculated for various ECH resonance positions. The experiments showed that the complete suppression of STO is achieved by using the elliptic antenna when ECH is applied on the HFS of q=1 surface, but it is never obtained by the parabolic one.

3 THEORETICAL CONSIDERATIONS

The explanations on the above-mentioned experimental results of sawtooth stabilization can be described as follows: The sawtooth stabilization is due to a modification of the current profile in such a manner as to lower the shear at the q=1 surface, thus stabilizing the resistive m/n=1/1 mode [1]. In fact, the experiments showed that the electron temperature profile has the smaller peaks, ($\Delta T_e/T_e$=0.2-0.3) near the ECH resonance layer and a weak hollow profile is formed when ECH is applied on the HFS or LFS of q=1 surface. Therefore we suggest that when ECH is applied, $T_{e\perp}$ increases, ($\delta T_{e\perp}/T_{e\perp}$=0.3),and the electron collisionality and hence the plasma resistivity is reduced, driving more current in this region. This incremental change of the current density would result in a local reduction of the shear, $s=(2/q)(dq/d\psi)(V/dV/d\psi)$, where ψ refers to the poloidal flux, and V refers to the plasma volume enclosed by the surface. If this reduction in s occurs at the q=1 surface it will have a stabilization effect on the m/n=1/1 resistive mode which plays an important role in STO.

We have modelled this, using the PEST code. We start with a current profile that smoothly vanishes at the plasma edge with q_{axis}=0.83, and q_L=3.37, and has the q=1 surface at an average radius of 0.35 of the plasma minor radius, a parabolic pressure profile is chosen. We determine the stability of this model equilibrium to the ideal and resistive m/n=1/1 modes. The q-profile is modified locally near the q=1 surface in a manner which reduces the shear at that surface, and a new equilibrium is computed.

The stability limits of such a sequence of equilibria at different values of β_{pol} are calculated. In the initial OH phase the plasma is unstable to the resistive mode, and as the ECH is applied the shear is reduced and the plasma is at marginal stability , further heating reduces the shear further and stabilizes the mode completely. The current profile at this point shows a local peak near the q=1 surface and is associated with a reduction of the local shear. Thus we attribute the suppression of the sawtooth to a stabilization of the m/n=1/1 mode by profile modification.

To explain the differences when heating on the HFS and LFS, the following considerations are suggested. When ECH is applied on the HFS,

the high energy electrons can traverse most of the surface enhancing a locally peaked current profile on the entire surface. In contrast when the ECH is applied on the LFS, many of the high energy electrons are easily trapped in the banana region and do not contribute to an enhancement of the current density. As a result there is a smaller influence on the shear and hence the stability when heating on the LFS.

REFERENCES

[1] K. Hanada and WT-3 group, Phys. Rev. Lett. (to be published).
[2] H. Tanaka and WT-3 Group, Phys. Rev. Lett. 60, 1033(1988).

Fig. 1.

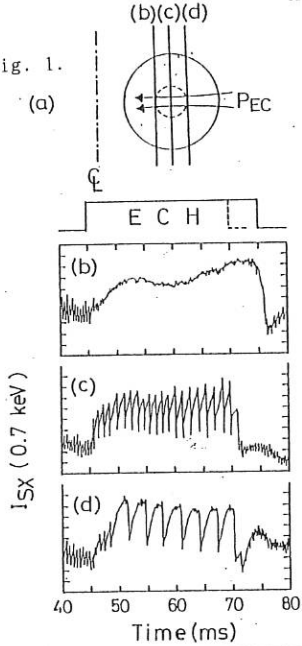

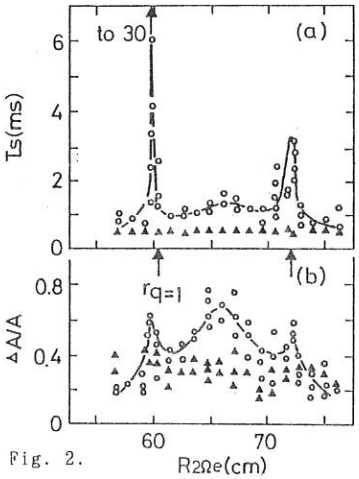

Fig. 2.

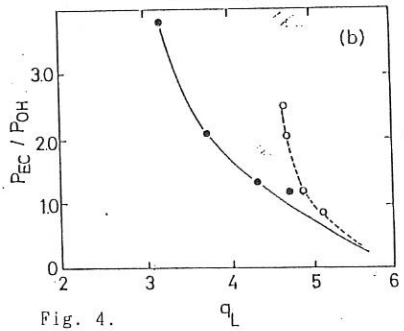

Fig. 4.

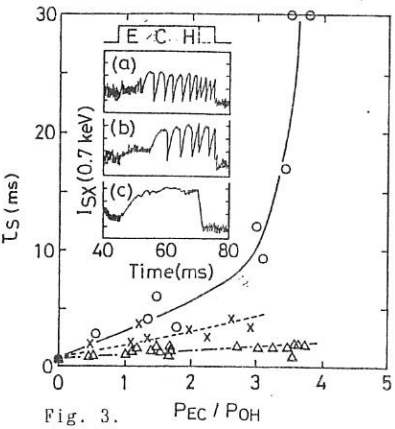

Fig. 3.

HIGH FREQUENCY ION BERNSTEIN WAVE HEATING EXPERIMENTS WITH MINORITY AND NEUTRAL BEAM HEATING ON THE JIPP T-Ⅱ U TOKAMAK

R.Kumazawa, M.Ono*, T.Seki, Y.Yasaka+, T.Watari, F.Shinbo, A.Ando, Y.Oka, O.Kaneko, K.Adati, R.Akiyama, Y.Hamada, S.Hidekuma, S.Hirokura, K.Ida, A.Karita, K.Kawahata, T.Kawamoto, Y.Kawasumi, Y.Kitoh, M.Kojima, T.Kuroda, K.Masai, S.Morita, K.Narihara, Y.Ogawa, K.Ohkubo, S.Okajima#, T.Ozaki, M.Sakamoto, M.Sasao, K.Sato, K.N.Sato, H.Takahashi, S.Tanahashi, Y.Taniguchi, K.Toi, T.Tsuzuki

National Institute for Fusion Science, Nagoya, 464-01 Japan
*PPPL, Princeton University, Princeton New Jersey, 08543 U.S.A.
+Dep. of Engineering, Kyoto Univ., Kyoto, 606 Japan
#Dep. of Applied Physics, Chubu Univ., Kasugai, 487 Japan

Abstract. An ion Bernstein Wave(IBW) Heating experiment has been carried out on the JIPP T-Ⅱ U Tokamak in combination with NBI and fast wave heating, where an IBW branch between the 4th and 3rd harmonics of the hydrogen ion cyclotron frequency was used, the frequency being 130MHz. Parallel refractive index can be chosen to be $N_{//}$=4 or 8. RF power up to 400kW has been injected so far, which is about 4 times the previous experimental level at 40MHz. Core plasma heating has been observed as well as an electron density increase near the plasma axis. The heating efficiency is improved with simultaneous fast wave heating.

Introduction. Ion Bernstein Wave Heating(IBWH) experiments began in 1983 on the JIPP T-Ⅱ U tokamak/1/. This was the first demonstration of IBWH as a heating tool on a middle-size tokamak, followed by PLT/2,3/, Alcator C/4/, and TNT/5/. In another experiment, refered to Mode-Ⅱ/6/, electron heating was observed and the importance of the paralell refractive index was demonstrated.

At this time we have constructed an oscillator with a higher frequency, f=130MHz, and with RF power ranging up to 700kW. The equivalent ion energy and the excursion length under the influence

of RF field near the antenna are reduced by one order at this higher frequency, 130MHz, compared with the previous IBWH experiments(f=40MHz). The decrease in the impurity influx to the plasma makes the high power IBW heating possible without plasma disruption.

Experimental set-up. A T-shaped antenna was designed for RF power to be fed into the center. The three T-shaped antennas are aligned along the toroidal direction on the low field side of the JIPP T-ⅡU tokamak(circular cross-section plasma bounded by carbon limiters, R=91cm, a=23cm, B_t=3T). The refractive index parallel to the magnetic field line is determined to be $N_{//}$=4 and 8 obtained by choosing adjacent antenna phase differences, (0 , π , 0) and (0 , 0 , 0), respectively. In addition, JIPP T-ⅡU is equipped with five RF antennas in the high field side, by which fast wave heating(FWH) can be achieved up to 2MW(f=40MHz), as well as a neutral beam injection system(NBI, P_{NBI} up to 700kW) injecting parallel to the magnetic field lines.

Experimental results. We have tried three different experimental modes, refered to as IBWH alone, IBWH+ NBI(parallel injection) and IBWH+ FWH.

For the IBWH alone mode, the effectiveness of the IBW heating is clearly observed as shown in Fig.1. This figure shows the time evolutions of the average electron density and the stored energy measured by a diamagnetic loop. The IBWH power was also applied to an ohmic plasma, I_p=190kA, n_e=1.4× $10^{19}m^{-3}$ for B_t=3.0T and P_{IBW}=190kW for $N_{//}$=4. The density increases during IBWH up to about 3 times the value prior to IBWH because of the improvement of the particle confinement time, as has already been demonstrated in PLT and other experiments. The increment of the stored energy exceeds that of the electron density, suggesting ion or electron heating. The radial profile of the electron temperature is shown in Fig.2, measured at about 20 ms after the start-up of IBWH, a time when the electron density is 50 % larger than in the ohmic plasma. The central electron temperature increases from 0.77keV to 1.02keV, and the temperature increases over half a minor radius.

For the IBWH+ NBI mode, IBW heating power is applied during

NBI heating(P_{NBI} = 0.5MW). $N_{//}$ is selected to be 4, a value that is favorable for the ion heating. The ion temperature increases near the plasma center as shown in Fig.3, where the ion temperature is measured by charge-exchange recombination spectroscopy(CXRS)/7/, possible only during NBI. The increase in the ion temperature agrees with that measured by the fast neutral particle analyzer. This similarly peaked profile is also obtained for the electron temperature(in Fig.2). In this experiment, a density profile was also observed using 6 channels of the HCN laser interferometer method. The electron density radial profile shows a peaked profile during IBWH.

For the IBWH+ FWH mode, IBWH was applied during FWH, where FWH power(P_{FWH}) is varied from 0 to 330kW at n_e=4× $10^{19}m^{-3}$. Figure 4 shows the increment of the stored energy($\delta W_{dia.}$) obtained by IBWH, with P_{IBWH} kept constant (P_{IBWH}=200kW). $\delta W_{dia.}$ increases almost linearly with P_{FWH}. This increment of the plasma stored energy should be attributed to the increased power absorption that is assocated with the population of high energy hydrogen ions. A small amount of high energy ions, less than 1%, is sufficient to interpret a 40% increase in the stored energy. The plasma loading resistance(R_p) also increases by 20% as shown in Fig.4, and is explained by the edge plasma modification.

Acknowledgement. One of the authors(R.Kumazawa) would like to express thanks to Dr.J.R.Hiskes(LLNL) for careful reading of the manuscript.

References

/1/ Ono,M.,Watari,T.,Ando,R.,et al.,Phys. Rev. Lett.54(1985)2339.

/2/ Ono,M.,Colestock,P.,Wilson,J.R.,et al.,in Radiofrequency Plasma Heating(Proc. 6th Top. Conf. Callaway Gardens, GA, 1985) American Institute of Physics, New York(1985)83.

/3/ Ono,M.,Beiersdorfer,P.,Bell,R.,et al., in Plasma Physics and Controlled Nuclear Fusion Research 1986(Proc. 11th Int. Conf. Kyoto,1986), Vol.1, IAEA, Vienna(1987)477.

/4/ Porkolab,M.,Bonoli,P.,Chen,Kuion, et al., ibid.,p.509.

/5/ Shinohara, S., Naito, O., Ueda, Y., Toyama, H., Miyamoto, K., J. Phys. Soc. Jpn. 55(1986)2684.
/6/ Ogawa, Y., Kawahata, K., Ando, R., et al., Nucl. Fusion 27(1987)1379.
/7/ Ida, K., Hidekuma, S., Rev. Sci. Instrum. 60(1989)867.

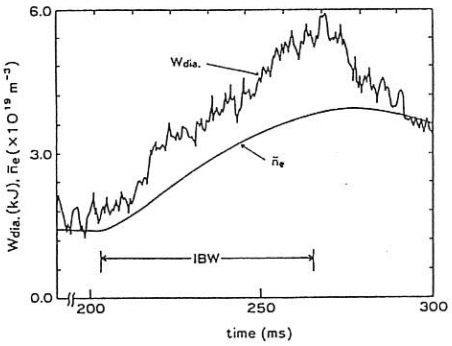

Fig.1 Time evolution of average density and stored energy during IBWH.

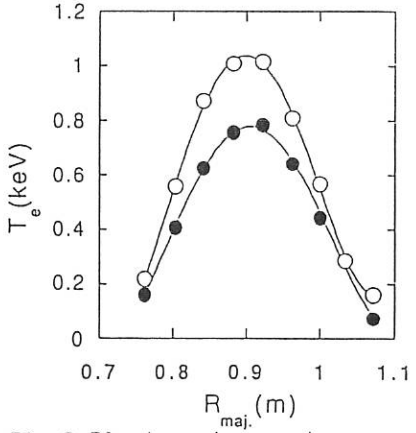

Fig.2 Electron temperature profile with(open circles) and without(solid circles) IBWH.

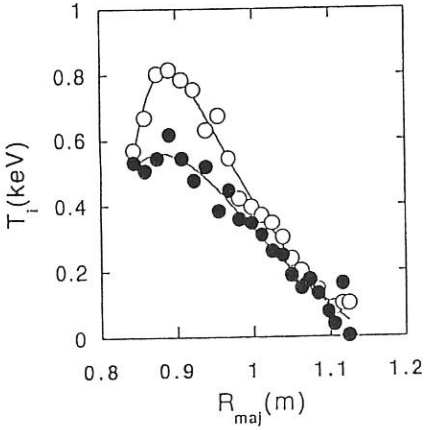

Fig.3 Ion temperature profile with(open circles) and without (solid circles) IBWH during NBI.

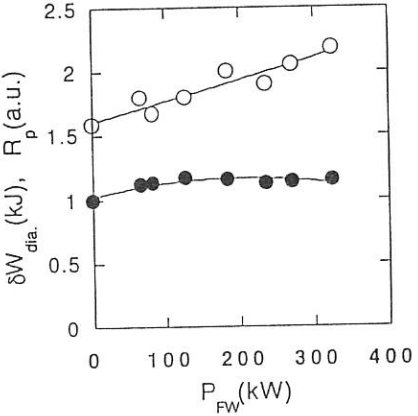

Fig.4 Dependence of stored energy increment(open circles) and plasma loading resistance (solid circles) by IBWH on P_{FW}.

TUNING METHOD FOR MULTIPLE TRANSMISSION LINES WITH MUTUALLY COUPLED FAST WAVE ANTENNAS IN JFT-2M

H. Kazumi, K. Yoshioka, S. Kinoshita, T. Yamamoto*, C. C. Petty* and M. Saigusa*

Energy Research Laboratory, Hitachi, Ltd.
1168 Moriyama-cho, Hitachi-shi, Ibaraki-ken, 316 Japan
*Department of Thermonuclear Fusion Research,
Japan Atomic Energy Research Institute

1. Introduction

Phased-array loop antennas are used for fast wave current drive and recent ICRF heating applications. The coupling characteristics between RF waves and plasma depend on the refractive index parallel to the toroidal magnetic field $n_{//}$. The index $n_{//}$ is controlled by adjusting the output phase of each transmission line. But strong interactions between loop antennas often cause difficulties in obtaining simultanenous matching for every transmission line while keeping the phase angle as well as the amplitude of each antenna current within the required values. To overcome this problem a computer-aided tuning procedure is developed. This procedure is based on a numerical model for transmission lines and mutually interacting arrayed antennas. The effectiveness of this procedure is confirmed by applying it to the JFT-2M fast wave current drive experiment.

2. Tuning procedure for mutually coupled loop antennas

On the basis of our previous 3D analysis on the phased array antenna [1], the array antennas are modelled as a mutually interacting lumped parameter circuit presented by impedance matrix Z_A :

$$\begin{pmatrix} V_1 \\ \cdot \\ \cdot \\ V_m \end{pmatrix} = Z_A \begin{pmatrix} I_1 \\ \cdot \\ \cdot \\ I_m \end{pmatrix}, \quad Z_A = \begin{pmatrix} Z_{11} & \cdots & Z_{1m} \\ \cdot & & Z_{2m} \\ \cdot & Z_{ii}\ Z_{ij} & \cdot \\ Z_{m1} & \cdots & Z_{mm} \end{pmatrix},$$

where V_i, I_i are the voltage and current on each antenna strap. In the impedance matrix Z_A, the diagonal elements Z_{ii} present the self-impedance of each antenna, whereas the off-diagonal elements Z_{ij} $(i \neq j)$ present the reactive power flow from neighboring antennas. It

is found [1] that the value of each element Z_{ij} is dependent on the antenna spectrum, i.e. dependent on the phase angles $\Delta\phi_i$ as well as the amplitude I_i of each antenna current.

At first, Z_{ij} would seem to be presented by a pure imaginary number i.e. mutual inductance [2], since the origin of Z_{ij} is reactive power. However, according to our 3D study [1], the off-diagonal element Z_{ij} must be treated as a general complex number. Physically this means that the reactive waves, having started from one antenna, travel according to $e^{i(\omega t - kz)}$ and when they arrive at the neighboring antenna the phase of waves is rotated as $e^{ik\Delta z}$, where Δz is the distance between antennas and k is the wave number. Transmission lines are modelled using standard transmission line theory.

The tuning process consists of two steps as shown in Fig.1. The first identifies the impedance Z_A from the measured signals on the transmission lines sampled from preceding several shots. The second step searches for operating parameters for the RF system which offer minimum power reflection on every transmission line, while keeping the phase and amplitude of the antenna current within required values. The predicted operating parameters are tested in the next shot. If performance is unsatisfactory, all the steps are repeated again.

Figure 2 shows the transmission line of the JFT-2M system, where powers of forward and reflective waves P_f, P_r, phase differences between them ψ and phase differences between antenna currents $\Delta\phi$ (called antennaphasings in the following) are measured. The impedance Z_A is identified by nonlinear programing in which Z_A is searched for such that the norm between the calculated values A_{cal} and the corresponding measured values A_{mes} is minimized. Optimum operating conditions are searched in the same manner; changing tunable parameters such as ψ, P_f and lengths of stub tuners l_{s1}, l_{s2}, the objective function f, which consists of the power reflection coefficients as well as mismatch of antenna phasings $\Delta\phi$ and antenna current I_i from desired values, is minimized.

The prediction accuracy of this procedure depends greatly on the accuracy of the Z_A identification. The following two points are considered to influence the identification. The first is the change of the loading impedance caused by the fluctuation in plasma density at the data-sampling. The second arises from the deviation of Z_A according to the change of antenna phasing $\Delta\phi$. The impedance Z_A at the data-sampling differs from that at the predicted tunable parameters. The former is expected to be improved by collecting enough data for Z_A identification. The inaccuracy arising from the second factor can be removed if data are re-sampled around the newly predicted operating condition and Z_A is re-identified using these sampled data. Thus, all tuning procedures of steps 1 and 2 are repeated to obtain more accurate Z_A identification and a more satisfactory tuning prediction.

3. Application to the JFT-2M RF system

The above tuning procedure has been applied to JFT-2M with 4 phased array loop antennas. To identify Z_A, data for about five shots were taken, which differed in stub tuners positions l_{s1}, l_{s2} and antenna phasings $\Delta\phi$. Fig.3 shows the errors between measured values and calculated ones using the identified Z_A, where the symbols I - IV denote the number of the transmission line. Although it represented a non-negligible deviation which arose from the Z_A changes, the average errors totaled 20%. After searching for the operating parameters for $\Delta\phi = \pi/2$ antenna phasing, these parameters were applied to JFT-2M. As shown in Fig.4 (open symbols), the obtained operating conditions were not so satisfactory, since the power reflection coefficients were above 50% and deviations of measured phases from expected values were 20%. This could be attributed to inaccuracy of the identified Z_A appropriate for $\Delta\phi = \pi/2$ as mentioned above.

Data for three additional shots were obtained around the predicted parameters and operating parameters were searched again. Closed symbols in Fig.4 show the performance results using the parameters repredicted by this. The power reflection coefficients were within 25% and phase deviations within 20%. Nearly satisfactory performance for JFT-2M fast wave current drive experiment could be realized by repeating the tuning process twice. The same results were obtained in the heating mode $\Delta\phi = \pi$. The tuning procedure could realize satisfactory performance within 10 shots in both cases. It could reduce shot numbers to obtain satisfactory performance to one-third compared to the conventional method which decides the parameters from experience.

4. Summary

We have developed a tuning procedure for multiple transmission lines including mutually coupled antennas. This procedure at first identifies the antenna impedance using measured data and second searches for the optimum operating conditions. The whole process is repeated so that predicted operating parameters realize good performance. The usefulness of this procedure has been confirmed by applying to the JFT-2M fast wave current drive antenna. Nearly satisfactory performances for $\Delta\phi = \pi/2, \pi$ corresponding to current drive and heating modes, were realized by repeating the whole tuning process twice, which was got within 10 shots.

[1] S.Kinoshita, K.Yoshioka, in Proc.IEEE 12th Symposium on Fusion Engineering (Monterey,1987),vol. II 1374
[2] M.J.Mayberry, GA report (to be published)

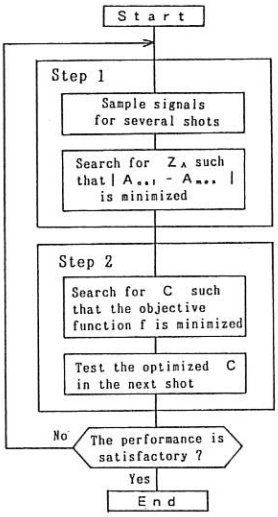

Fig.1 Algorithm of fast wave transmission line tuning procedure

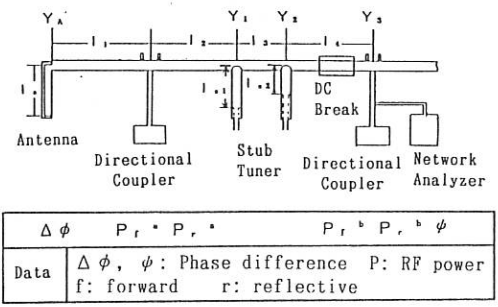

Fig.2 Fast wave transmission line with phased array antenna in JFT-2M

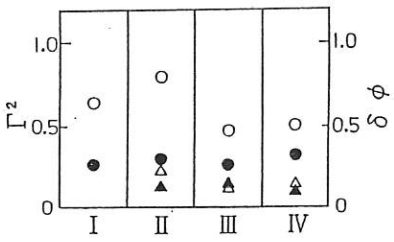

Fig.4 Optimization results for $\Delta\phi = \pi/2$ in JFT-2M.
Symbols I – IV denotes the number of the transmission line.
$\Gamma^2 = P_f / P_r$
$\delta\phi \equiv (\Delta\phi_{cal} - \pi/2)/(\pi/2)$
open symbols: result obtained by repeating the whole steps once
closed symbols: result obtained by repeating the whole steps twice

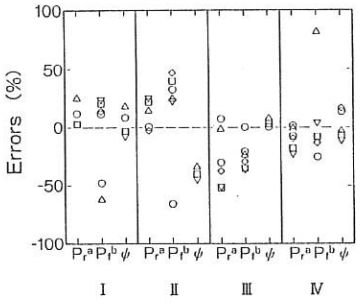

Fig.3 Errors between the measured and calculated values at first iteration. Errors denotes $|A_{cal} - A_{meas}| / A_{meas}$. $P_r{}^a$, $P_f{}^b$ and ψ are the reflective power, forward power and the phase difference between forward and reflective waves. Symbols I – IV denotes the number of the transmission line. Symbols show the results of different shots with different tuning parameters.

THE GENERATION OF HARMONICS AND THE COUPLING BETWEEN MHD ACTIVITY AND THE FUNDAMENTAL FREQUENCY DURING ALFVEN WAVE HEATING IN TCA

G.G.BORG P.A. DUPERREX and J.B. LISTER

Centre de Recherches en Physique des plasmas
Ecole Polytechnique fédérale de Lausanne
21 Av. des Bains, Ch-1007, Lausanne, Switzerland

1. Harmonic Generation During Alfvén Wave Heating

During Alfvén Wave Heating (AWH) at 2.5 MHz in TCA (ω_{ci} = 11.5 MHz), harmonics are observed on the wavefields in the plasma scrapeoff layer (SOL). The spectrum of harmonics consists predominantly of signals at frequencies that are integer multiples of the fundamental. No evidence for half-odd integral harmonics has been observed and harmonics are not observed at very low power. It is generally believed that the harmonics observed in the SOL during ICRH are due to a sheath effect at the antenna [1]. In our experiments, the possibilities of wave excitation by shielded and unshielded antennas [2] and the measurement of the rf Langmuir current (fault current) [3] flowing between an unshielded antenna and the plasma, permit us to provide a definite conclusion about the relevance of this mechanism in AWH.

In TCA there are four pairs of top and bottom antennas equally spaced toroidally. These permit antenna phasings with toroidal mode numbers N = 1, 2 and 4 and poloidal mode numbers M = 0 and 1. In Fig. 1 we show magnetic wavefield traces of the fundamental (f_0) and first harmonic (f_1 = 4.98 MHz) for four phasings (N,M) of the antennas. The peaks are resonances of the discrete Alfvén wave (DAW) [4]. We note that the DAW spectrum versus density is remarkably similar for f_0 as for f_1. The amplitude of f_1 is generally between 2 and 10 times lower than f_0. All harmonic spectra show resonances of the DAW. Experiments in which the toroidal field was lowered showed that the resonance densities of f_0 and f_1 were always the same; in the case of (2,1) excitation, the f_1 peak was present above the ion cyclotron frequency. In addition, although there is some evidence of DAWs excited directly at the harmonic in these traces, DAWs at f_1 were generally not observed. From this we conclude that the peaks in the harmonic traces are plasma responses to the DAW peak in the fundamental.

Finally we note that similar traces are observed even if only one antenna pair is excited, whether or not the antennas are screened.

The fault current driven from an excited antenna to the SOL, which is totally eliminated by screens, tends to follow the antenna voltage and does not have the detailed DAW structure evident in Fig. 1. Its amplitude is typically about 5% of the circulating current ($\approx$ 1000 A) although as previously noted [3] it is difficult to measure when the antenna is excited symmetrically. The power structure in the f_0 trace arises from the change in the angle between a structureless circulating antenna current and antenna voltage. In an earlier paper [3] however, it was shown that the fault current is in phase with the driving voltage so that power dissipation by the fault current must also be structureless. We conclude that the fault current and hence a sheath effect at the antenna is not the source of the harmonics.

The fault current driven passively in the matching circuitry of an unexcited antenna, just like the rf component of the Langmuir probe saturation current (I_{sat}) and floating potential, does have the DAW structure whether or not waves are excited by shielded or unshielded antennas. It is possible that harmonics are generated by the passive fault current driven at the fundamental in unexcited antennas, limiters and perhaps even at the vessel wall by fluctuations in the SOL potential. This is a difficult hypothesis to check and it is difficult to imagine that it would compete with the active fault current. The current flowing to the vessel wall was measured to be negligible compared to that flowing to an unshielded antenna; typically a few amperes. An experiment with excitation of the earthed shielded antenna pair in which two pairs of unshielded antennas were disconnected showed that, despite a reduction in the total passive fault current by a factor of two, there was no observable change in the amplitude of f_1 with respect to f_0 measured on the edge wavefields. In this experiment though one is never certain that a non-negligible part of the passive fault current has been eliminated.

We have given strong evidence against a sheath effect at the antenna (and perhaps anywhere) being responsible for the production of harmonics in AWH. The relative amplitude of the fundamental and harmonics appears to suggest that MHD nonlinear effects are not possible. Further studies are being made to investigate the possibility of electrostatic effects in the SOL during AWH.

2. Coupling Between MHD Activity And Alfvén Waves.

It has been observed that frequency spectra of the RF field associated with the Alfvén waves exhibit side-bands around the fundamental frequency (2.5MHz). Analysis of magnetic pick-up coil signals was undertaken to understand their origin and what information could be extracted concerning, for instance, MHD activity and turbulence.

For the broadband magnetic turbulence, test of 3-wave coupling between the side-bands and the low frequency signals has been performed using the bicoherence analysis on fast digitized data (sampl.f≤32MHZ). No positive results have been obtained. A new function t was calculated to test if the side-bands were due to an pure amplitude modulation: $t(f,\Delta f)=\frac{E(X_-(f,\Delta f)\cdot X_+(f,\Delta f))}{E(|X_-(f,\Delta f)|^2)^{0.5}\cdot E(|X_+(f,\Delta f)|^2)^{0.5}}$ where $X_\pm(f,\Delta f) = Y(f\pm\Delta f)\cdot Y^*(f)$, Y(f) is the Fourier spectrum and E(Z) denotes an ensemble average over several spectra. The results indicate that the sidebands cannot be simply explained by an amplitude modulation. Demodulation experiments show that Mirnov activity is also visible on the demodulated sine and cosine signals, indicative of a coupling between the Alfvén waves and the MHD activity. In the Fourier spectrum of the demodulated signal, the Mirnov peak location varies with the Alfvén resonance conditions as shown in Fig.2. The peak (at f≈15kHz) is in the upper sideband before the (2,1)DAW. At and after the (2,1)DAW, this peak is located in the lower sideband. At the (2,1)DAW, an additional peak at lower frequency compared to Mirnov is always observed (f≈9kHz in Fig.2), probably due to coupling with MHD activity in the plasma centre. Correlation between the sidebands and the directly measured low-frequency (f<500kHz) magnetic broadband fluctuations has only been observed in a few cases.

These results indicate that Alfvén sidebands contain information (by frequency modulation) about internal MHD activity and fluctuations, the nature of this information depends on the excited Alfvén mode. Such activity in the plasma centre is not always detectable by direct low frequency magnetic probe measurements in the plasma edge. If the coupling surface can be selected by launching an appropriate Alfvén mode and the combined measurements of several magnetic probes, it appears that the analysis of the sidebands should provide a measurement of internally located magnetic fluctuations.

Acknowledgements: We wish to thank the whole TCA team for its support. This work was partially supported by the Fonds National Suisse de la Recherche Scientifique

References.

[1] R. Van Nieuwenhove et al., IAEA Technical Committe Meeting on ICRH/Edge Physics, Garching bei München, October 1989, Fusion Engineering and Design.
[2] G.G. Borg and B. Joye, 17th European Conference on Controlled Fusion and Plasma Heating, Amsterdam, vol.13B part III, p.1179 (1990).
[3] G.G. Borg et al., 16th European Conference on Controlled Fusion and Plasma Heating, Venice, vol.13B part III, p.1199 (1989).
[4] G.A. Collins et al., Phys. Fluids 29(1986)2260.

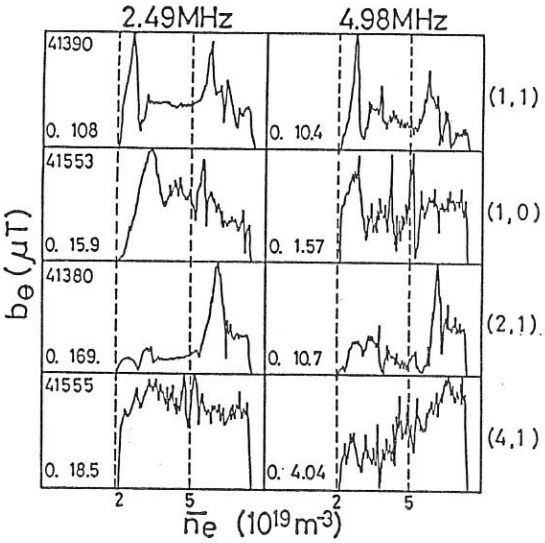

Fig.1:
RF magnetic field traces showing the DAW peaks in the fundamental and the corresponding peaks in the harmonic for various mode numbers (N,M). The scales are in μT.

Fig.2:
Time evolution of the Mirnov coil and demodulated signals.

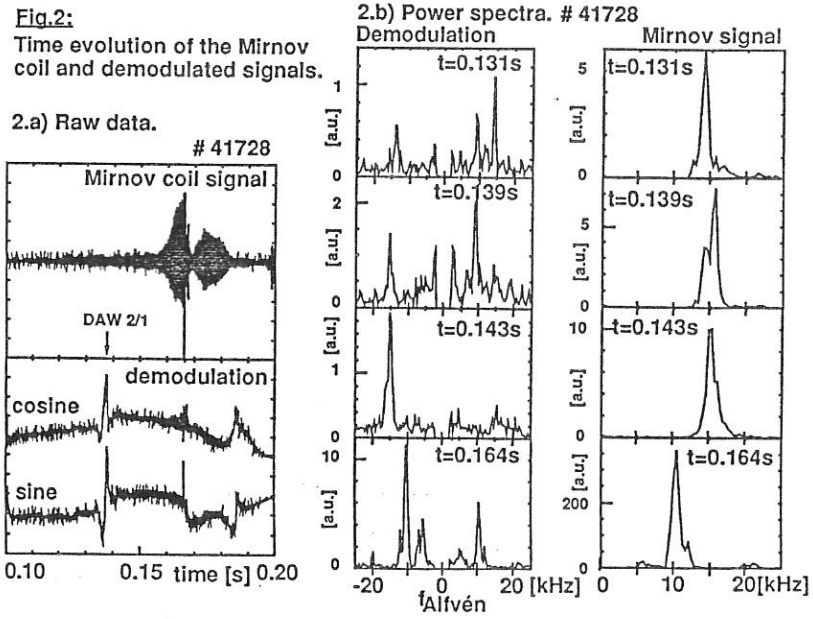

EFFECTIVENESS OF X- AND O-MODE ECRH BREAKDOWN AND STARTUP IN TCA

A. Pochelon, D. R. Whaley, T. P. Goodman, B. P. Duval, M. Q. Tran, R. Behn, G. Besson, A. Cardinali†, B. Joye, A. J. Knight

Centre de Recherches en Physique des Plasmas
Association Euratom - Confédération Suisse
Ecole Polytechnique Fédérale de Lausanne
21, Av. des Bains, CH-1007 Lausanne, Switzerland
†ENEA, Frascati, I-00044 Frascati, Italy

Introduction

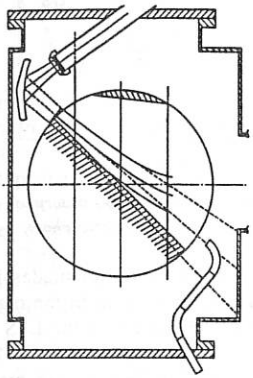

Fig. 1. Poloidal cross section of TCA.

Comparative studies of X- and O-mode launch for ECH-assisted, low loop voltage startup have been performed on the TCA tokamak. The $39GHz$ TE_{02} cylindrical cavity gyrotron and microwave line, presently used on TCA[1], are planned for daily ECH startup in the upcoming TCV continuous vessel tokamak. To investigate the respective merits of X- and O-mode launch, high field side (HFS) linearly polarised HE_{11} injection has been chosen, with a steering mirror movable poloidally and toroidally ($\pm 25^\circ$ to the radial), shown in Fig. 1. In TCA ($R/a = .615m/.18m$, $B\varphi \leq 1.6T$), the ω_{ce} resonance position can be varied between $-0.5 \leq x=r/a \leq 0.5$, limited by an ω_{ce} resonance on the window for low B_φ and the maximum B_φ available for TCA. Other parameters are varied in the following ranges: $P_{ECH} < 125kW$; $10ms < \Delta t_{ECH} < 80ms$; $0.6V < V_L < 2.1V$.

Absorption characteristics in startup plasmas

As a specific microwave absorption diagnostic, two receiving horns placed opposite the steering mirror in the same poloidal plane, measure microwave transmission in both X- and O-mode polarisations. The line-integrated H_α emission is recorded by a 128-pixel camera[2], temporally resolving horizontal spatial power deposition structures. A 10-channel horizontal camera measuring visible Bremsstrahlung radiation complements the vertical H_α camera. A four-channel interferometer measures horizontal electron density profiles.

The average electron density in breakdown plasmas is typically $n_e=0.2 \cdot 10^{19} m^{-3}$. Hot plasma code calculations predict much higher X-mode, first-pass absorption at these low startup densities. Experimentally, X-mode launch is characterised by high first-pass absorption with a prompt density rise. Transmission measurements indicate near 100% first-pass X-mode absorption for all startup conditions. First-pass O-mode absorption, however, is much lower and can vary from 50% at high ECH power to near zero at low ECH power. This leads to wall reflections and mode mixing for O-mode launch.

Horizontal H_α camera profiles for X- and O-mode startup are shown in Figs. 2. For O-mode launch a narrow emission peak is seen at the ω_{ce} resonance, which is virtually

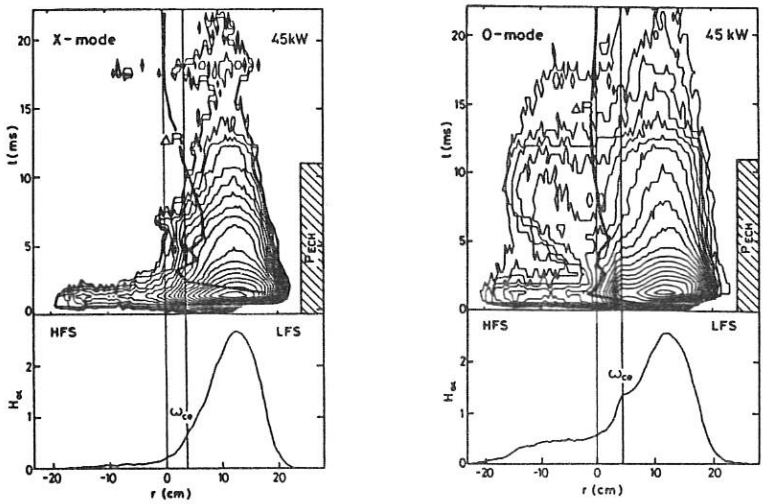

Fig. 2. $H\alpha$ profiles and contours for (a) X-mode and (b) O-mode launch. Evidence of ω_{ce} absorption and current broadening is visible with O-mode launch. ΔR indicates current position during startup phase.

undetectable for X-mode launch. However, the dominant feature for both modes is a more intense broader peak on the low field side (LFS) of the ω_{ce} resonance in the region of the upper hybrid resonance (UHR)[3], which is seen to move further to the LFS for higher n_e. The presence of this peak, expected to exist only for X-mode launch, further indicates incomplete first-pass O-mode absorption followed by wall reflections and mode-mixing. In addition, X-mode startup vertical Bremsstrahlung profiles show a clear initial emission peak while O-mode startup shows a broad emission profile. This localised X-mode peak moves with magnetic field and mirror position as expected.

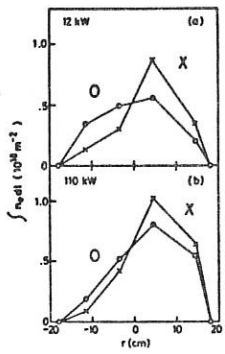

Fig. 3. Density profiles for (a) low power and (b) high power X- and O-mode launch. Density profiles are more peaked in X-mode and displaced further to the LFS with increased power.

Density profiles of Figs. 3 show that X-mode profiles are more peaked and further displaced to the outside. High-power X- and O-mode profiles show a significantly larger fraction of density to the LFS than low-power profiles as the absorption location moves with the UHR. O-mode density profiles, however, always remain broader and more centrally located as the ω_{ce} resonance remains fixed and the density rises more slowly.

Carbon-IV line burnthrough times indicate an initial heating rate twice as high in X-mode, as shown later in Fig. 5(c). A further indication that higher electron temperatures are produced during X-mode launch is given by the systematic need for higher gas injection for X-mode to maintain low runaway populations.

Startup characteristics

The different spatial absorption characteristics of X- and O-mode launch influence startup current position. Figure 4(a) shows that strongly localised LFS-UHR X-mode

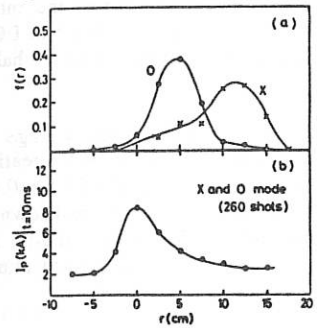

Fig. 4. (a) Distribution of startup current position for X- and O-mode showing a more central startup for O-mode. (b) Startup current vs. current position showing advantage of centrally started current. Tokamak feedback control is set for central current positioning. This curve is independent of X- or O-mode launch.

absorption initially creates a highly non-centered plasma. O-mode launch, however, by creating more centrally located absorption profiles allows the current to start near the center. Figure 4(b) shows the advantage of a centrally located startup current. Independent of the mode launched, currents starting nearer the center of the poloidal cross section (result of O-mode injection) experience significantly higher current ramp rates than those starting nearer the LFS (result of X-mode injection).

The dependence of startup on plasma current location is reflected in the current ramp rates for a series of X- and O-mode startup shots at varying ECH powers (*5-110kW*). In this series the ω_{ce} resonance is close to axis. Figures 5(a-b) show the

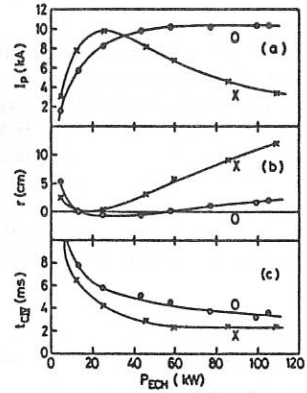

Fig. 5. X/O-mode, ECH-assisted startup power series showing (a) plasma current at end of ECH pulse, (b) corresponding radial plasma position, (c) carbon-IV burnthrough times.

plasma current attained by the end of the ECH pulse and the corresponding current center. The degraded startup performance of X-mode launch at high ECH power can be attributed to the movement of the current center to large r as power is increased. This displacement is consistent with the density profile changes caused by strong X-mode absorption near the UHR layer which moves to large r as ECH power, and thus electron density, increases. The current center for O-mode launch also moves to larger r with increasing power but the broader absorption profile allows it to remain near the axis over

the entire power range. At constant power, the average current ramp rate is independent of r_{res} for $-9cm < r_{res} < 4cm$[4].

Well-sustained discharges are characterised by a spreading of the H_α emission from the center to the HFS attesting to the formation of a hot plasma across the entire cross section. Discharges which do not develop this feature are not sustained at ECH turn off. The H_α emission of sustained discharges develops into the usual radiative halo.

Loop voltage and volt-second saving

These ECH-assisted startup studies generally use a constant loop voltage of $1.2V < V_L < 2.1V$ chosen to minimise volt-second consumption while still creating acceptable current ramp rates. Minimum startup loop voltage values reached $V_L = 0.6V$ ($E=0.15V/m$), compared to the minimum required 8V for purely inductive breakdown in TCA. Figure 6 shows significant volt-second saving over standard ohmic startup for $\Delta t_{ECH} > 20ms$. At $\Delta t_{ECH} = 40ms$, volt-second saving reaches 35% of that of ohmic startup.

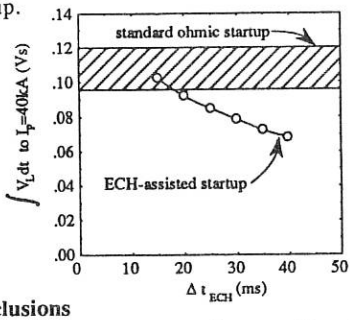

Fig. 6. Volt-second consumption for ECH-assisted and ohmic startup to 40kA. ECH startup values are shown for varying ECH pulse lengths for 60kW, O-mode launch. Total available flux on TCA is .48Vs.

Conclusions

In these startup experiments, X-mode launch has never exhibited better current rampup properties than O-mode, although its absorption properties are seen to be far better. X-mode experiences highly localised first pass absorption near the UHR layer, creating a peaked absorption profile at large r. O-mode launch, on the contrary, is less efficiently absorbed and creates a broader absorption profile after wall reflections and mode mixing. The practical superiority of O-mode launch is attributable to the more uniformly spread power deposition which allows rapid current rampup over a much wider range of operating conditions. Low loop voltage startup has been achieved for $V_L = 0.6V$ and significant volt-second saving over standard ohmic startup is seen for ECH pulse lengths of $\Delta t_{ECH} > 20ms$.

Acknowledgements

The authors acknowledge the support of the TCA and gyrotron teams. This work was partially supported by the Fonds National Suisse de la Recherche Scientifique.

References

1 A. Pochelon, T. Goodman, D. Whaley, M.Q. Tran, et al.16th. Symp. on Fusion Technology, London (1990).

2 B. P. Duval, to be published.

3 R. M. Gilgenbach et al., Nucl. Fus. 21 (1981) 319.

4 B. Lloyd, T. Edlington et al., 13th EPS on Contr. Fus. and Plasma Heating, Schliersee, Vol. 10C, PartII (1986) 266.

DENSITY FLUCTUATIONS AND PARTICLE CONFINEMENT DURING OH/LHCD ON TOKAMAK CASTOR

Žáček F., Stöckel J., Badalec J., Dvořáček L., Jakubka K., Kletečka P., Kryška L., Magula P.

Institute of Plasma Physics, Czechoslovak Academy of Sciences
Pod vodárenskou věží 4, 182 11 Prague 8, Czechoslovakia

ABSTRACT

An effect of lower hybrid current drive on the turbulent parameters of the tokamak CASTOR periphery is reported. Suppression of the density fluctuations is correlated with the changes of the radial electric field, an increase of poloidal rotation velocity and the improvement of the global particle confinement time.

INTRODUCTION

A direct link between the level of electrostatic edge plasma turbulence and particle confinement time has been proved in many tokamaks. It was also shown that under certain conditions the fluctuations can be significantly suppressed and so called regimes with improvement confinement can be reached /1 - 5/. A similar situation has been found in tokamak CASTOR during the combined OH/LHCD regimes as well /6/. The mechanism of such lower hybrid wave effect is not clear, however. As it was suggested in /7 - 9/ and experimentally observed in /1-5/, a crucial role can play a rearrangement of radial electric field at the plasma edge and an increase of poloidal rotation velocity. This contribution gives some experimental information about the behaviour of these quantities in tokamak CASTOR during the LH wave application.

ARRANGEMENT

The experiment was carried out on the CASTOR tokamak (R/a= =0.4/0.085 m, B_T = 1 T, I_P = 12 kA, $\tau \lesssim 50$ ms) in the density range 4 - 8 x 10^{18} m^{-3}. The plasma position is feed-back stabilized. For combined OH/LHCD operation at frequency 1.25GHz, a multijunction waveguide grill with a broad power spectrum N_z = 1 - 4 was used. The lower hybrid power was below the initial OH power input ($P_{OH} \simeq 24$ kW).

Several Langmuir probes, located in the equatorial plane, have been used for measurement of the edge plasma:

1) A rotation single probe to determine radial profiles of the floating potential and ion saturation current during a single shot (135° toroidally away from the grill).
2) A double probe with poloidally separated tips (d = 7 mm)

for determination of rotational velocity of density fluctuations; the fluctuating signals from the negatively biased tips are processed in the frequency range 0.1 - 300 kHz by means of A/D convertors with sampling rate 0.5 μs.

3) A triple probe for determination of the electron temperature.

The last two probes were located 180° toroidally away from the grill and their position could be changed from shot to shot to obtain radial profiles.

EXPERIMENTAL RESULTS

Some typical features, rutinely observed during the LHCD shots on CASTOR tokamak /6/, are demonstrated in Fig. 1. It may be seen that the decay of the line average density is stopped and afterwards an increase is measured. A certain broadenning of the radial density profile is observed. The H_α radiation from limiter and lower hybrid antenna regions remains close to its OH value. It indicates an improvement of the global particle confinement by a factor of about 2 during the LHCD phase of the discharge. Simultaneously, the rms value $\tilde{n}_e$ of density fluctuations decreases significantly.

Main aim of the experiment was to investigate the rotation of the plasma in these regimes with an improved particle confinement and the reduced edge electrostatic turbulence. Due to experimental limitations, the poloidal rotation of density fluctuations has been studied by means of the cross-correlation technique. Fig. 2 presents cross-correlation functions of fluctuating signals from the double probe during OH and LHCD periods of the discharge. From the shift of the maximum of correlation function the poloidal velocity v_p of density fluctuations can be derived. Fig. 3 gives temporal variations of v_p for three different probe radial positions. For comparison two variations in pure OH shots are shown as well. It may be concluded from these measurements:

(i) In the limiter shadow, the fluctuations rotate in direction of the ion diamagnetic drift, while inside the plasma column the rotation has direction of the electron diamagnetic drift. The narrow transition layer between this two regions (a velocity "shear layer" /10/) is formed in the vicinity of the last closed

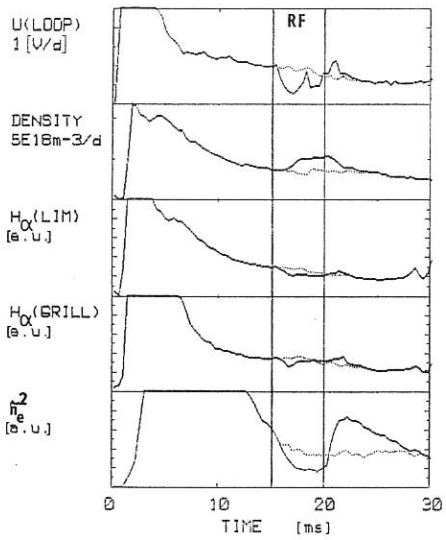

Fig. 1

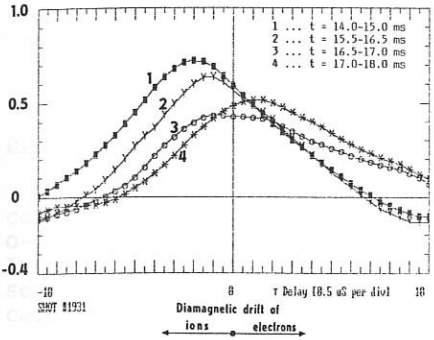

Fig. 2

magnetic surface.

(ii) A certain decorrelation between the density fluctuations appears, when the probe is inside the shear layer.

(iii) The "shear layer" stays around the radius r_s = 84 mm in the OH phase. During LHCD, it starts to move outwards, despite of the fact that the magnetic measurements do not show any change in the plasma position.

(iv) The poloidal velocity of density fluctuations increases by a factor of 1.5 - 2 during LHCD on the both sides of the

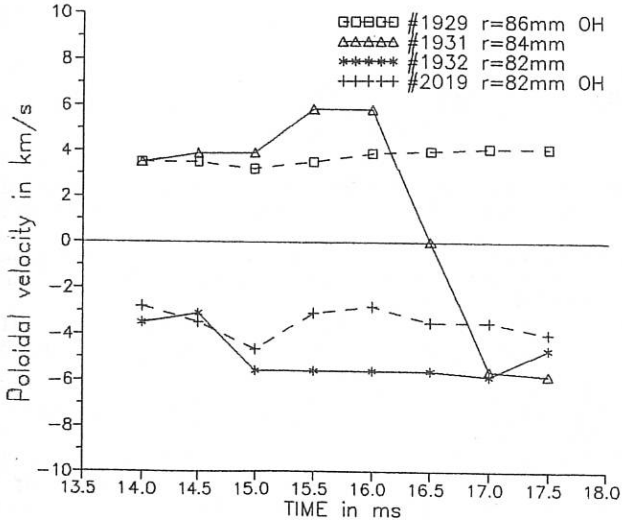

Fig. 3

"shear layer", which may be related to the observed reduction of electrostatic fluctuations at the plasma edge /8/.

Observed changes in the poloidal rotation can be understood from behaviour of the radial electric field during LHCD. Fig. 4 brings a comparison of radial profiles of plasma floating potential for both OH and LHCD phase. The triple probe data show that the electron temperature is nearly constant in the limiter region (around r = 85 mm). Therefore, the profiles of the plasma space potential $U_S = U_F + 3\ T_e/e$ and consequently the radial electric field E_r are determined predominantly by the profile of the floating potential $U_F(r)$ in this region of radii.

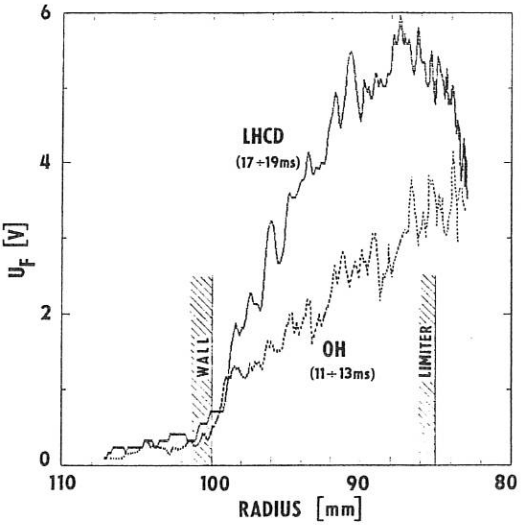

Fig. 4

A very close relation between the poloidal rotation v_P and the radial electric field E_r can be drawn comparing Figs. 3 and 4:

(i) a monotonous profile of $U_F(r)$ during the OH discharge period is changed by the profile with a maximum in the "shear layer" during the LHCD period;

(ii) taking into account this profile of electron temperature, an increase of absolute value of radial electric field E_r by factor 2 is deduced during the LHCD;

(iii) this increase of E_r is in accordance with increase of poloidal rotation velocity $v_P = E_r/B_T$ measured during LHCD on the corresponding radius, see Fig. 3;

(iv) if "shear layer" appears somewhere in the limiter region ($r = 85$ mm), the inner probe measures an opposite sense of poloidal rotation, in concordance with this fact.

REFERENCES

/1/ Taylor R. J. et al.: Phys. Rev. Lett. 63 (1989) 2365
/2/ Weynants R. R. et al.: Nucl. Fus. 30 (1990) 945
/3/ Groebner R. J. et al.: Phys. Rev. Lett. 64 (1990) 3015
/4/ Taylor R. J. et al.: IAEA-CN-53/A-6-5, Washington 1990
/5/ Weynants R. R. et al.: IAEA-CN-53/A-6-6, Washington 1990
/6/ Stöckel J. et al.: IAEA-CN-53/A-7-2, Washington 1990
/7/ Itoh S. I. et al.: Phys. Rev. Lett. 60 (1988) 2276
/8/ Shaing K. C. et al.: Phys. Fluids B, 2 (1990) 1492
/9/ Rozhanskij V. A. et al.: Sov. PZhETP 53 (1991) 80
/10/ Ritz C. P. et al.: Nucl. Fus. 27 (1987) 1125

THE EFFECT OF LOWER HYBRID CURRENT DRIVE ON THE PENETRATION BEHAVIOUR OF TEST IMPURITIES

D. Hildebrandt, H. Pursch, L. Weixelbaum, K. Jakubka[x]

Central Institute of Electron Physics, Hausvogteiplatz 5-7, O-1086 Berlin, FRG
[x]Institute of Plasma Physics, Czechoslovak Academy of Sciences,Pod vodarenskou vezi 4, CS 18069 Prague 8, Cechoslovakia

Introduction

The radial penetration of small droplets (diameter about 1μm) into the plasma of the tokamak CASTOR was studied using a CCD-line imaging for spatial recording of impurity line radiation. The test particles were injected by controlled arc ignition during ohmic discharges (OH) and during discharges with application of the lower hybrid current drive (LHCD). It was found that the application of LHCD reduced the penetration depth of injected impurities considerably. At transitions from OH- to LHCD-regimes both, the droplet ablation and the ioniza- tion of the ablated atoms shifted from the boundary plasma into the SOL-region.

Experiment

CASTOR is a small sized tokamak with minor and major radii of 105mm and 400mm, respectively. The last closed flux surface (LCFS) was determined by a sector limiter with a poloidal extension of about 60° located at a minor radius of r_s = 78mm on the torus topside. Moreover an aperture limiter was installed at r_a = 85mm. The discharge parameters were as follows: plasma current I_p = 12 kA, line averaged density $n_e = 4.10^{18}m^{-3}$, toroidal magnetic field B_T = 1.3 T. The RF-power (frequency - 1.25 GHz, power 40 kW) was launched into the plasma via a grill located at the torus outside. The test particles were injected radially from outside, toroidally opposite to the RF-grill using a special arc source described elsewhere [1]. The divergence of the injected material beam was ±10°. The impurity amount injected into one discharge was about 10^{16} atoms which was less than 5% of the number of the background ions. With these conditions there was no observable effect of the impurity injection on the recorded plasma parameters.

An AlLi-alloy (2.5% Li) was choosen as cathode material. The arc source emits vaporized atoms and droplets (ions are rejected by the magnetic field). Due to their different velocities the erosion components entered the plasma at different times. This allowed to observe the penetration behaviour of the vapour (Al and Li) and the droplets, separatively. It was found that droplets started to appear in the plasma with a temporal delay of 6-8ms after arc ignition while signals from the vapour could be observed immediately. This corresponds to droplet velocities of the order of 10m/s. The duration of the emission of both components, the vapour and the droplets was serveral ms. This paper concentrates on the droplet behaviour. A CCD-camera was used to observe light emission in the radial intervall from r = 100mm to r = 40mm in front of the source entrance. Interference filters were used to select the radiation lines of Li I (671 nm), Li II (548 nm), Al I (875 nm) and Al II (466 nm and 620 nm). The data were recorded repitively at a frequency between 20 and 1000 Hz, depending on the intensity of the lines.

Results

The measurements were made during ohmic heated discharges and at additional lower hybrid current drive. For investigating the penetration behaviour of the droplet material during the RF-phase the arc source was ignited 5ms before the RF-power was started to launch. Fig. 1 demonstrates typical signals of the light emission from the droplet material during phases with OH only and with additional LHCD. Because excitation and ionization of lithium is not very sensitive to the plasma temperature, the Li- line emission may here serve as indication of the radial dependence of the ablation rate.

From fig. 1a it is seen that the ablation of the droplets was localized in a radial intervall of about 10mm in both regimes. With the known velocity of the droplets (about 10m/s) it can be concluded that the droplets were ablated in a time less than 1ms. In OH-regimes the ablation took place inside the LCFS at a minor radius of about 72mm. A similar observation had been already made with injection of Ta-droplets [1]. During application of LHCD the ablation zone shifted radially outwards into the SOL-region to a minor radius of 87mm. Even the line emission of Li- and Al-ions shifted continuously from r = 57mm in the ohmic phase to r = 82mm during application of LHCD.

The results indicate a change of the particle and heat fluxes in the plasma edge at a transition from the ohmic to the RF-phase. Using the signals of the Li-line radiation from the vapour component emitted from the arc source we obtained at a minor radius of 85mm a value of the plasma density of $1.10^{18}m^{-3}$ during the ohmic phase and of $2.10^{18}m^{-3}$ during the RF-phase [2]. An increase of the plasma density was also measured by a Langmuir

probe installed in the grill at a minor radius of 87mm (see fig.2). Naturally this density increase affects the ionization of impurities penetrating into the plasma as observed.

However these values of the plasma density and the measured electron temperature of 20 eV [3] are too low to explain the observed ablation of the droplets.

Treating a droplet as a floating probe [4] which is negatively charged in a thermal plasma the heat flux to the droplet can be estimated to be about 10^{19} eV/s.mm^2. Simple evaporation of a μm-sized Al-droplet (sublimation energy 3 eV) in a time smaller than 1ms as observed needs a heat flux in the order of 10^{20} eV/s.mm^2. As already shown the heat flux in ohmic discharges is mainly carried by suprathermal or run-away electrons [1]. The existence of the latter ones is evidenced by hard X- ray emission observed at the limiter. The decrease of the HXR- signal at application of the RF-power shows that due to the lower loop voltage the production of run-away electrons is suppressed during the RF-phase (see fig. 2). Nevertheless, photographs show bended droplet pathes with a deflection in counterdirection of the plasma current during the RF-phase demonstrating that the droplet ablation is caused by an anisotropic heat flux. In contrast to ohmic discharges this (anisotropic) component of the heat flux is large enough in the SOL-region to ablate the droplet.

Summary

There is experimental evidence of the existence of an anisotropic suprathermal component of the electron flux outside the LCFS during LHCD. The heat flux carried by these suprathermal electrons which is one order of magnitude larger than that carried by the thermal electrons to a floating probe reduces the penetration of macroparticles into the plasma compared to ohmic discharges where suprathermal electron fluxes were observed inside the LCFS. LHCD affected also the ionization of the impurities by an increase of the plasma density in the SOL-region.

References

[1] D. Hildebrandt et al, Nucl. Fusion 29 (1989) 305
[2] D. Hildebrandt et al, to be published
[3] D. Hildebrandt et al, Contrib. PLasma Phys. 27 (1987) 455
[4] D.M. Manos, G.M. McCracken in Physics of Plasma Wall Interactions inControlled Fusion, Edited by D.E. Post and R. Behrisch, NATO ASI Series B: Physics, Vol.131, Plenum Press, New York, 1984

An AlLi-alloy (2.5% Li) was choosen as cathode material. The arc source emits vaporized atoms and droplets (ions are rejected by the magnetic field). Due to their different velocities the erosion components entered the plasma at different times. This allowed to observe the penetration behaviour of the vapour (Al and Li) and the droplets, separatively. It was found that droplets started to appear in the plasma with a temporal delay of 6-8ms after arc ignition while signals from the vapour could be observed immediately. This corresponds to droplet velocities of the order of 10m/s. The duration of the emission of both components, the vapour and the droplets was serveral ms. This paper concentrates on the droplet behaviour. A CCD-camera was used to observe light emission in the radial intervall from r = 100mm to r = 40mm in front of the source entrance. Interference filters were used to select the radiation lines of Li I (671 nm), Li II (548 nm), Al I (875 nm) and Al II (466 nm and 620 nm). The data were recorded repitively at a frequency between 20 and 1000 Hz, depending on the intensity of the lines.

Results

The measurements were made during ohmic heated discharges and at additional lower hybrid current drive. For investigating the penetration behaviour of the droplet material during the RF-phase the arc source was ignited 5ms before the RF-power was started to launch. Fig. 1 demonstrates typical signals of the light emission from the droplet material during phases with OH only and with additional LHCD. Because excitation and ionization of lithium is not very sensitive to the plasma temperature, the Li- line emission may here serve as indication of the radial dependence of the ablation rate.

From fig. 1a it is seen that the ablation of the droplets was localized in a radial intervall of about 10mm in both regimes. With the known velocity of the droplets (about 10m/s) it can be concluded that the droplets were ablated in a time less than 1ms. In OH-regimes the ablation took place inside the LCFS at a minor radius of about 72mm. A similar observation had been already made with injection of Ta-droplets [1]. During application of LHCD the ablation zone shifted radially outwards into the SOL-region to a minor radius of 87mm. Even the line emission of Li- and Al-ions shifted continuously from r = 57mm in the ohmic phase to r = 82mm during application of LHCD.

The results indicate a change of the particle and heat fluxes in the plasma edge at a transition from the ohmic to the RF-phase. Using the signals of the Li-line radiation from the vapour component emitted from the arc source we obtained at a minor radius of 85mm a value of the plasma density of $1.10^{18}m^{-3}$ during the ohmic phase and of $2.10^{18}m^{-3}$ during the RF-phase [2]. An increase of the plasma density was also measured by a Langmuir

probe installed in the grill at a minor radius of 87mm (see fig.2). Naturally this density increase affects the ionization of impurities penetrating into the plasma as observed.

However these values of the plasma density and the measured electron temperature of 20 eV [3] are too low to explain the observed ablation of the droplets.

Treating a droplet as a floating probe [4] which is negatively charged in a thermal plasma the heat flux to the droplet can be estimated to be about 10^{19} eV/s.mm^2. Simple evaporation of a μm-sized Al-droplet (sublimation energy 3 eV) in a time smaller than 1ms as observed needs a heat flux in the order of 10^{20} eV/s.mm^2. As already shown the heat flux in ohmic discharges is mainly carried by suprathermal or run-away electrons [1]. The existence of the latter ones is evidenced by hard X- ray emission observed at the limiter. The decrease of the HXR- signal at application of the RF-power shows that due to the lower loop voltage the production of run-away electrons is suppressed during the RF-phase (see fig. 2). Nevertheless, photographs show bended droplet pathes with a deflection in counterdirection of the plasma current during the RF-phase demonstrating that the droplet ablation is caused by an anisotropic heat flux. In contrast to ohmic discharges this (anisotropic) component of the heat flux is large enough in the SOL-region to ablate the droplet.

Summary

There is experimental evidence of the existence of an anisotropic suprathermal component of the electron flux outside the LCFS during LHCD. The heat flux carried by these suprathermal electrons which is one order of magnitude larger than that carried by the thermal electrons to a floating probe reduces the penetration of macroparticles into the plasma compared to ohmic discharges where suprathermal electron fluxes were observed inside the LCFS. LHCD affected also the ionization of the impurities by an increase of the plasma density in the SOL-region.

References

[1] D. Hildebrandt et al, Nucl. Fusion 29 (1989) 305
[2] D. Hildebrandt et al, to be published
[3] D. Hildebrandt et al, Contrib. PLasma Phys. 27 (1987) 455
[4] D.M. Manos, G.M. McCracken in Physics of Plasma Wall Interactions inControlled Fusion, Edited by D.E. Post and R. Behrisch, NATO ASI Series B: Physics, Vol.131, Plenum Press, New York, 1984

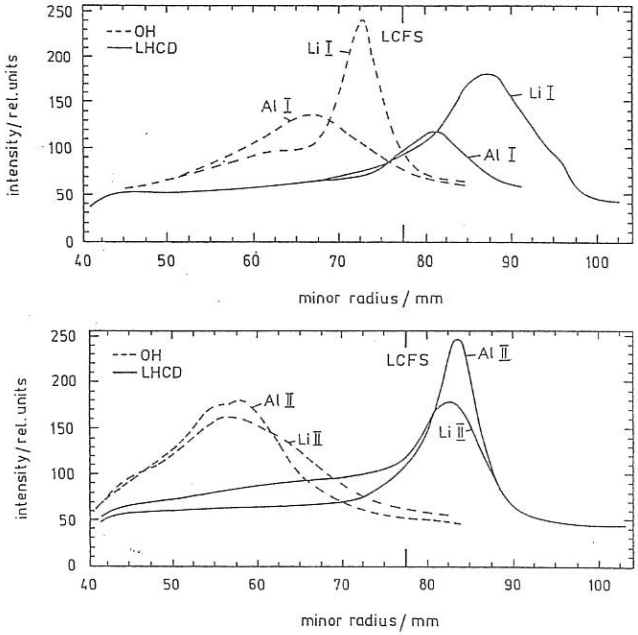

Fig.1: Intensities of lithium and aluminium line emission in dependence on the minor radius.
a) for atom lines b) for ion lines

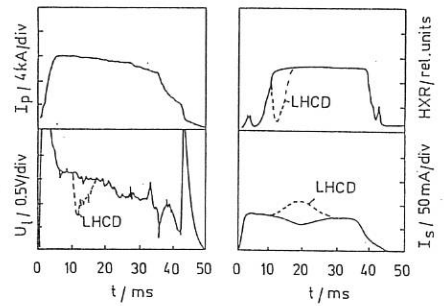

Fig.2: Diagnostic traces of plasma current I_p, loopvoltage U_l, hard x-ray emission at the limiter HXR, and plasma density at r = 87mm.
Dashed curves: at application of LHCD.

POWER DEPOSITION PROFILE DURING LOWER HYBRID CURRENT DRIVE IN TORE SUPRA

A-L.Pecquet, A. Hubbard*, D. Moreau, J. M. Moret+, T. Fall, J. Lasalle, P. Lecoustey, M. Mattioli, Y. Peysson, N. Augé, L. Rodriguez, M. Talvard

Association Euratom-CEA
Centre d' Etudes Nucléaires de Cadarache
Département de Recherches sur la Fusion Contrôlée
F-13108 Saint -Paul -Lez-Durance FRANCE
*Centre canadien de fusion magnétique, Varennes, Québec, Canada
+Centre de Recherches en Physique des Plasmas, Lausanne, Switzerland

Introduction:

Lower hybrid current drive (LHCD) experiments have been performed in Tore Supra in various density regimes. The total power coupled to the plasma reached 4MW and a strong electron heating has been observed.To investigate the power deposition mechanism on the electrons, r.f power modulation experiments have been performed.These experiments allow us to estimate the power deposition profiles on both thermal and non-thermal electrons and also to study their respective time responses. From these studies it is possible to deduce a thermal heating scenario which agrees with the experimental results.

Experimental conditions

The LHCD modulation experiments have been performed in helium discharges, at a toroidal field of 4 Teslas, with a plasma current of 1.6MA and at relatively high volume averaged densities up to $\langle ne \rangle = 5\ 10^{19} m^{-3}$, kept constant over the rf pulse (Fig 1). The thermal and fast electron responses are analysed using in particular the following diagnostics.

A soft X-ray pinhole camera views the plasma along 43 vertical chords (Δr=3cm,Δt=500μs) and measures the photon emission in the 2-15 keV energy range.The signal delivered by a detector can be written as:

$$i(r) = G\ ne(r)^2\ Te(r)^{\alpha}\ f(Zeff)$$

where G is a constant, generally α=2 because of the 125μm beryllium filter in front of the detectors, and f(Zeff) represents the impurity contribution which can be evaluated quantitatively from VUV spectroscopy and visible bremsstrahlung data.

A set of 6 Fabry Perot and one Michelson interferometers measure both the thermal and non-thermal responses of the electron distribution function by analysing the E.C.E spectrum. The Fabry Perots, looking in an equatorial plane (Δr=10cm,Δt=1ms) are tuned to the second harmonic, 5 of them in the optically thick region (signal mostly proportional to Te) and the last one at the edge where the plasma is optically thin and therefore sensitive to the non-thermal electrons. In the latter case,we made sure that the second order transmission corresponding to the ECE third harmonic has been properly filtered.

A hard X-ray (30-700keV) spectrometer views the plasma along 5 chords (Δr=5cm, Δt=1s).

A Thomson scattering system measures the electron temperature (Te) profile (Δr= 6cm , Δt= 1ns with a time repetition of 37ms).

The soft X-ray signal modulations are thought to be caused only by the temperature modulation as numerical simulations using spectroscopy, Thomson scattering and Fabry Perot data have shown no significant impurity variation during the r.f. modulations.

Power deposition profiles

For the measurements of power deposition, r.f. power was modulated during 2 seconds, between 1.6 and 2.4 MW, with a 200 ms period square wave. Figure 1 shows the modulations induced on the soft X-rays, Te and on the non-thermal ECE.

To analyse the power deposition profiles on the bulk electrons, a number of terms have to be included in the power balance equation, namely the ohmic power source which varies during the modulation ($\tilde{P}_{oh}$), the radial heat diffusion and the power flux arising from the thermalisation of the fast electrons ($\tilde{P}_{LHCD}$).This can be written for the perturbed quantities as:

$$\frac{3}{2} ne(r) \frac{d\tilde{Te}(r)}{dt} = \frac{1}{r} \frac{d}{dr} ne(r) r \chi e \frac{d}{dr} \tilde{Te}(r) + \tilde{P}_{oh} + \tilde{P}_{LHCD} \qquad (1)$$

Fig. 2 (bottom) shows the experimental power deposition profile on the thermal electrons deduced from the slope variation of the soft X-ray signals at the switching on and off of the r.f. modulations. It represents the l.h.s term of the above equation. For comparison fig2 (top) shows the hard X-ray profiles measured at four different energies (50-100-150-200 keV). We observe that, at these high densities, the obtained bulk power deposition is quite uniform over the plasma cross section (r<50cm),whereas the high energy electrons are produced off-axis consistently with the accessibility criterion [1].

Time responses

To study the time responses of the thermal and non-thermal electrons, further modulation experiments have been carried out in which the r.f. power was square modulated from 1.2 to 2.3 MW with the waveform shown on fig.3. This waveform is repeated successively 6 times during the same shot and has a large frequency spectrum. The sampling period of the soft X-ray and non-thermal ECE data was T=1ms. The line-averaged density (4 x 10^{19} m^{-3}) was kept perfectly constant over all measurement chords and corresponds to the above situation where the high energy X-ray profiles are hollow. Fig. 3 (top) also shows the non-thermal ECE together with a central chord soft X-ray signal. The following observations can be made from the respective time evolution of these signals :

- the ECE trace varies on a much shorter time scale than the soft X-ray one, thus showing a direct response to the fast electron population whereas the soft X-rays do not have any rapidly varying component (cf. short modulations) ;
- this ECE signal does not in turn contain any slowly varying component. This is not the case for the other five ECE channels which view optically thick regions and are clearly influenced by both thermal and non-thermal electron populations.
- although there is a change in the general slope of all the soft X-ray traces when the r.f. modulation is turned on and off (long modulations), this response establishes itself more rapidly on the off-axis chords than on the central ones. This indicates that a significant part of the central heating source is somewhat delayed in time with respect to the off-axis one.

In order to analyse this delay quantitatively we have numerically processed the various signals [2] assuming that the responses are linear, and obtained approximate z-transfer functions between the r.f. excitation and the measured data. Simulated data obtained with these transfer functions and the real r.f. input data are displayed on fig. 3 (bottom) for the non-thermal ECE, a central soft X-ray chord and an off-axis one.

The slow time response of the soft X-rays is assumed to be related to the first eigenmode of the heat diffusion operator and shows up as a pole in the corresponding transfer functions (the related time constant, common to all chords, is found to be 125 ms). It was not possible to find other realistic poles (higher eigenmodes) and the delayed part of the

transfer function, after the pole has been removed, is assumed to represent the response $H_S(z)$ of the heat source to the r.f. excitation. In the low frequency domain (0-10 Hz) we can plot the phase of $H_S(z=\exp(j\omega T))$ versus frequency for various chords (fig.4 top) and versus radius for a set of different frequencies (fig.4 bottom).

For each chord the phase shift increases linearly with frequency at a rate which is identified as the local build-up time of the fast electron distribution, either from local or non-local (spatial transport) power absorption. This is supported by the fact that the non-thermal ECE response (not shown on fig.4) coincides with the r = 35cm line in fig.4 (top), i.e. with a characteristic time of 8 ms corresponding to the slowing down time of ≈ 250 keV electrons or to a radial diffusion time.

Furthermore, for modulation frequencies lower than 10 Hz, i.e. much slower than the fast electron build-up time, the phase delay between the heat source and the r.f. power is increasing when one moves towards the plasma center and reaches 50 degrees on axis for 10 Hz. This can be interpreted as caused by the radial transport of fast electrons towards the center, on a time scale τ which is of the order of 14 ms as found from the slope of the central chord curves in fig.4 (top). This diffusion time is of the order of the slowing down time of the fast electrons which makes difficult the distinction between the two effects.

Conclusion

Although X-ray measurements, accessibility considerations and ray-tracing simulations [3] indicate that coupling to high energy electrons occurs at half plasma radius at relatively high densities, thermal power deposition profiles show that fairly uniform bulk heating takes place across the profile. A detailed analysis of the time response at different radii exhibits a phase delay at the centre corresponding to a characteristic time of ≈ 14 ms. This could be explained by a model in which fast electrons diffuse towards the centre during their thermalisation process. With more precise knowledge of the r.f. deposition profiles, their diffusion coefficient could then be estimated. For example, assuming that the r.f. power is deposited with an off-axis Bessel-like profile, e.g. $J_0(k_0 r)$-$J_0(k_1 r)$ with $k_0 = 2.4$ and k_1=5.5, one would find a characteristic diffusion coefficient, $D \approx a^2/(k_1^2 \tau) \approx 1.4\ m^2/s$.

These results have important implications for a reactor-like scenario in which LH waves will generally not be accessible to the centre. Further experiments are in progress to study the dependence of the fast electron creation and diffusion on the plasma density and on the launched LH power spectrum.

Ackowledgements

The authors are grateful to the whole LH and TORE SUPRA team for the experiments.

References

[1] Y. Peysson, et al., this conference.
[2] J. M. Moret, EUR-CEA-FC-1409 (1990), submitted to Journal of Comp. Phys.
[3] J. P. Bizarro, et al., this conference.

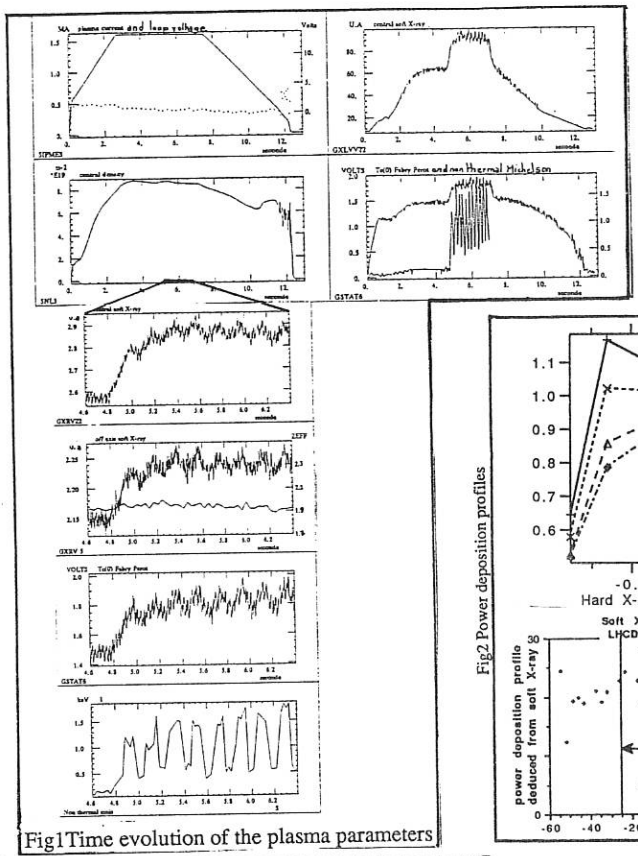

Fig1Time evolution of the plasma parameters

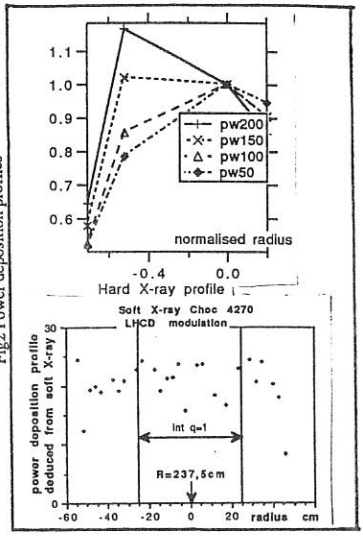

Fig2 Power deposition profiles

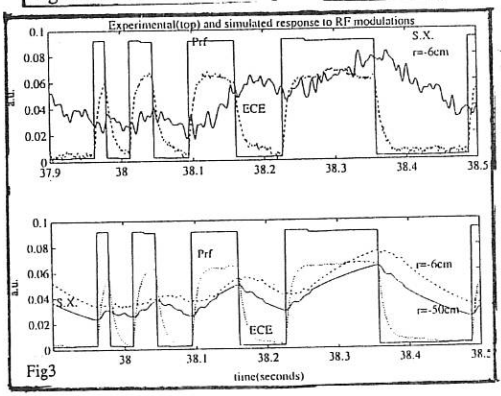

Fig3

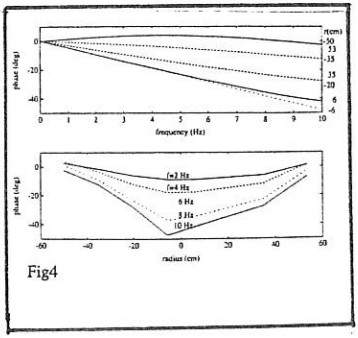

Fig4

LOWER HYBRID WAVE COUPLING IN TORE SUPRA THROUGH MULTIJUNCTION LAUNCHERS

X. Litaudon, P. Bibet, M. Goniche, G. Berger By, J. P. Bizarro, J. J. Capitain, G. T. Hoang, R. Magne, D. Moreau, Y. Peysson, J. M. Rax, G. Rey, G. Tonon

Association Euratom-CEA sur la Fusion Contrôlée
Centre d'Etudes Nucléaires de Cadarache. F-13108 Saint-Paul-Lez-Durance, France

1. INTRODUCTION

The TORE SUPRA Lower Hybrid Current Drive experiments (8 MW/ 3.7GHz) use large phased waveguide arrays (4 rows of 32 waveguides for each of the two "grills") to couple the waves to the plasma [1].These launchers are based on the "Multijunction" principle which allows them to be quite compact but needs to be fully assessed for the design of efficient multi-megawatt antennas in NET/ITER.

2.METHOD OF ANALYSIS

A detailed experimental study of LH wave coupling to the TORE SUPRA plasma has been carried out from the analysis of the RF measurements available at the input of each module. The power in each module is first divided poloidally through a vacuum hybrid junction and two 4-waveguide E-plane junctions. Two rows of 8 modules are juxtaposed toroidally to form one launcher. The power and phase in each module can be varied independently thus allowing the launched spectrum to peak between $n_{//} \approx 1.5$ and $n_{//} \approx 2.3$.

Instead of comparing the power reflection coefficient in the individual modules for various phasing conditions, we have measured the plasma loaded scattering matrices S which, by definition, link together the incident and reflected fields. The scattering matrices contain the intrinsic features of the plasma loaded antenna, independently of the feeding conditions.To determine the 8*8 elements of the complex matrix $\mathbf{S}$, it suffices to consider 8 independent arrangements of incident electric field phases, at stationary and reproductible plasma conditions, and to measure the corresponding reflected field.

In the framework of the 2-D linear coupling theory of the "grill" [2] and using the SWAN code [3], S has been numerically calculated in various edge plasma conditions (edge electron density and edge density gradient). Comparison with experimental results has been made possible since the internal power splitting of each module and the gaps (1mm) between adjacent modules have been fully modelled. The internal power splitting model has been successfully compared to the measurements performed on a test module [4].

3.EXPERIMENTAL RESULTS

3.1 Coupling results

The dominant scattering coefficients of the waveguide arrays have been obtained in various edge plasma conditions. The electron temperature and density of the plasma facing the LH antenna have been investigated by means of 3 Langmuir probes toroidally spaced in the equatorial plane. Figure 1 depicts the case where the measured edge plasma density was kept constant well above the LH cut-off density , i.e $n_e \approx 1.4 \times 10^{18}$ $m^{-3} \pm 20\%$. An excellent agreement has been obtained between all these measured scattering coefficients, including their phases, and those deduced from the linear coupling theory. The symmetry of the scattering matrix ($S(i+1,i) = S(i,i+1)$), which is an implication of the field reciprocity theorem, is verified. Moreover, the dispersion (if any) enables us to estimate the relative errors of the electric field measurement, which in the worst cases are $\pm$ 10% and $\pm$ 20° respectively on the amplitude and phase.

Such agreement gives us strong confidence in the determination of the power spectra radiated by the multijunction antennas. Figure 2 shows the deduced experimental asymmetric

power spectra obtained with phase shift, $\delta\Phi$, between the juxtaposed modules of -90°,0°,+90°.

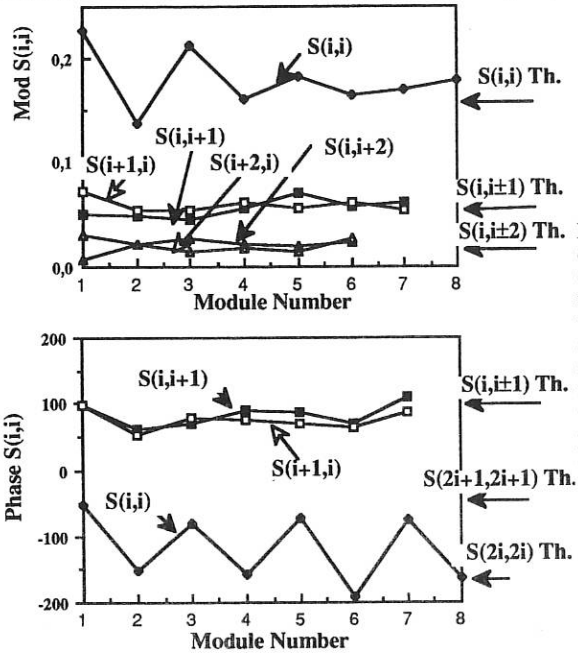

Fig. 1: Amplitude and Phase of the experimental S(i,j) coefficients versus the module number i . The theoretical calculations assumed an edge electron density of $n_e = 1.4 \times 10^{18}$ m^{-3} ($n_e \approx 7 \times n_{co}$) and an electron density decay length of 2cm according to the Langmuir probe measurements.

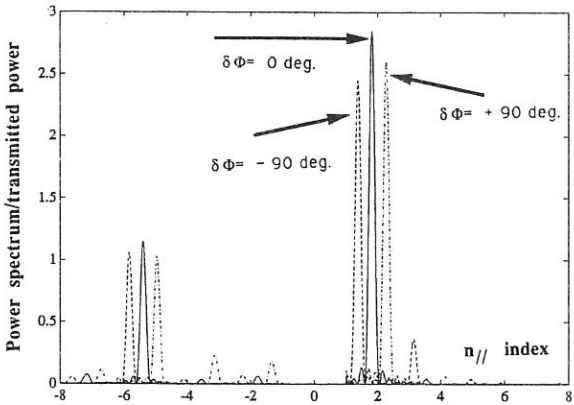

Fig.2:"Experimental" radiated spectra. $\delta\Phi$= -90°, 0°, +90° respectively $n_{//peak}$=1.4, 1.8, 2.3.

Figure 3 shows that average power reflection coefficients of a few percent (2 to 4 %) have been obtained in a large range of edge plasma densities (0.3×10^{18} $m^{-3} \leq n_e \leq 1.4 \times 10^{18}$ m^{-3}) and phasing between modules ($\delta\Phi$= -90° to +90°). The experimental data are in good agreement with the theoretical simulations performed with the measured edge plasma density.

To conclude, it should be emphasized that figures 2 and 3 illustrate that flexibility in $n_{//}$ is obtained in a large range of edge plasma densities (or antenna positions) while preserving an optimum behaviour of the antenna [5].

Fig. 3

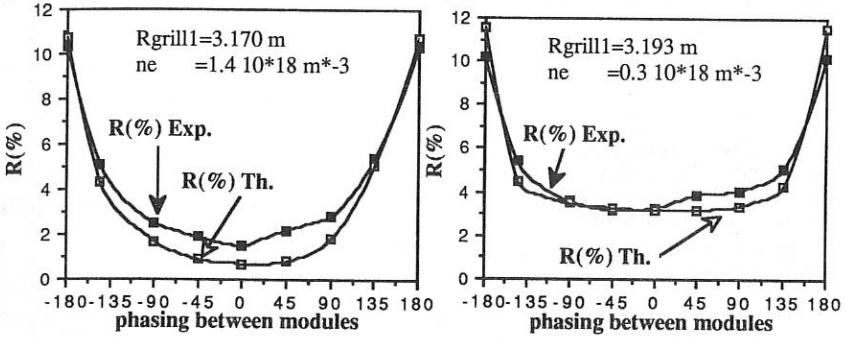

3.2 Density and temperature modification of the scrape-off-layer

During current drive experiments at high RF power, strong outgassing of the antenna (up to 2 x 10^{20} particles/second -fig. 4-a) may occur in not fully conditioned operations. Consequently an increase of the electron density, up to 50 %, was measured at the grill aperture (fig. 4-b). This is consistent with a flattening of the electron density profile measured with the I. R interferometer. By ramping the RF power launched by one antenna between 0 to 2.8 MW, the scrape-off layer facing the antenna is significantly heated at a rate, normalized to the edge electron density, of 5 eV / MW / 10 ^{18} m^{-3} (fig. 5). Anyway, we have confirmed that in the presence of LH power the observed edge density and temperature perturbation do not modify the good coupling characteristics of the antennas.

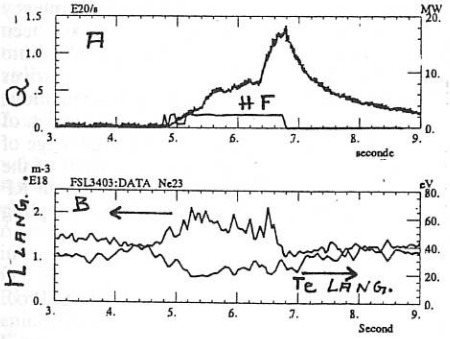

Fig. 4:Gas injection from LH antenna

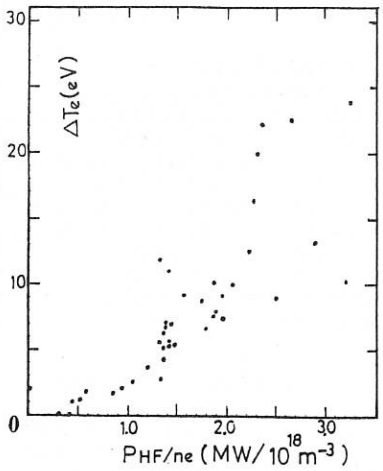

Fig. 5: S.O.L. heating by LH power

3.3 High power experiments

The good behaviour of the TORE SUPRA antennas observed at low transmitted power ($\leq 5MW/m^2$) is still obtained at higher power levels. More than 3 MW have been transmitted separately by each antenna. Fig 6 confirms that the power reflection coefficient and its phase measured in the central modules are kept constant ($R \leq 3\%$) at power densities up to $45MW/m^2$.

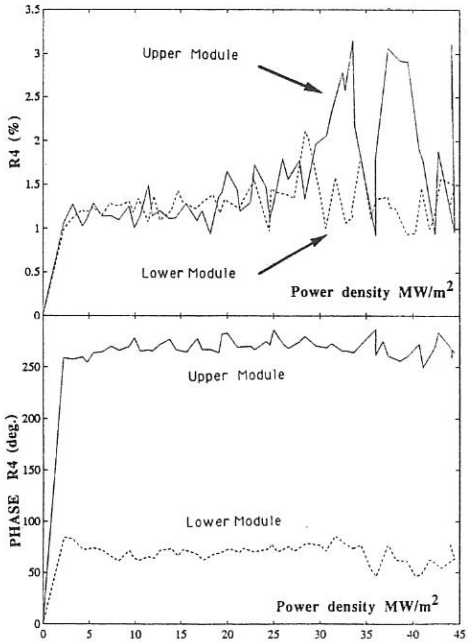

Fig.6: Power reflection coefficients and phases - central modules- versus the injected power density (MW/m^2). The phases remain constant indicating that RF breakdown in the modules have not occured.

4. CONCLUSION

Extensive coupling measurements have been performed to study the Radio-Frequency characteristics of the plasma loaded multijunction antennas.The experimental data have been related to the output of the linear coupling theory which, in its advanced stage, takes into account the specific features of the compact launchers. The measurements, scattering matrices and power reflection coefficients, are in perfect agreement with the theoretical simulations performed with the measured edge plasma density. Our analysis leads to the determination of the $n_{//}$ radiated spectra. We demonstrate that the $n_{//}$ flexibility is obtained in a large range of edge plasma densities (or antenna positions) while preserving an optimum behaviour of the antenna. Finally, the "Multijunction" launcher has proved to be able to transmit high RF powers since power densities up to $45MW/m^2$ have been reached with good linear coupling characteristics and spectrum control.

REFERENCES

[1] Goniche M., Moreau M., Tonon G., et al in Controlled Fusion and plasma Heating (Proc. 17th Eur. Conf. Amsterdam 1990) PART III, EPS (1990) 1231
[2] Brambilla M., Nucl. Fusion 16 (1976) 47
[3] Moreau D. , Nguyen T. K., Rep EUR-CEA-FC-1246, C.E.N. / Grenoble (1984)
[4] Bibet Ph., et al , Rep EUR-CEA-FC-1390, C.E.N./ Cadarache (1990)
[5] Litaudon X., Moreau D., Nucl. Fusion 30 (1990) 471

Analysis and Simulations of Lower Hybrid Current Drive in Mixed OH-LH Discharges in TORE SUPRA

J.P. Bizarro, G.T. Hoang, G. Berger By, Ph. Bibet, J.J. Capitain, V. Fuchs*, M. Goniche, A. Hubbard*, X. Litaudon, R. Magne, D. Moreau, Y. Peysson, J.M. Rax, G. Rey, G. Tonon

Département de Recherches sur la Fusion Contrôlée, Association Euratom-CEA
Centre d'Etudes Nucléaires de Cadarache F-13108 Saint-Paul-Lez-Durance - FRANCE
* Centre Canadien de Fusion Magnétique, Varennes, Québec, Canada J0L 2P0

Introduction

The quasi continuous f=3.7 GHz Lower Hybrid system installed in Tore Supra (B=4 T, R=2.34 m, a=0.78 m) consists of two multijunction launchers fed by 16 klystrons having a total power capability of 8 MW. Up to now, the RF power coupled to the 1.6 MA / 3.85T Helium plasma at a line average density of $\bar{n}=3.8\times10^{19}m^{-3}$ has reached 4.5 MW, which was not sufficient to replace completely the OH current by the LH driven current.

The experimental results have been simulated by an upgraded version of the Bonoli-Englade- Fuchs code [1,2,3]. Its main features are: a toroidal ray-tracing module; a transport module in which the electron thermal diffusivity varies with minor radius as $\chi_e(r) \alpha F(r)/n(r).r^2$, with F(r) a monotonic increasing function of r; a 1D Fokker-Planck calculation, where two-dimensional effects are included by increasing the perpendicular temperature ,$T_\perp$, of fast electrons in the tail generated by the LH waves; a global model for the radial diffusion of the RF current in which the current diffusion coefficient is found as an eigenvalue of a boundary value problem consistent with the conservation laws predicted by the Fokker-Planck equation.

Experimental results

Current drive experiments have been performed in two density regimes, namely $\bar{n}=1.5\times10^{19}m^{-3}$ and $\bar{n}=3.8\times10^{19}m^{-3}$, and in 1.6MA / 3.85T Helium discharges. In both regimes, the best loop voltage drop occurs with a phasing between modules of -60° which corresponds to a wave parallel index $N_{//peak}$ = 1.6 and a power directivity of 68% [4]. A significant loop voltage drop (20%) and a fast electron population were still observed up to central densities of $9.7\times10^{19}m^{-3}$, with 1.4MW RF power, indicating that the LHCD density threshold (αf^2) above which damping occurs on fast ions was not yet attained. Zero loop voltage has been obtained in a 1.6 MA, $\bar{n}=1.5\times10^{19}m^{-3}$ Helium discharge with a short RF pulse -0.5s, 3.2 MW- with the corresponding efficiency, defined as nRI_{RF}/P_{RF}, of 1.75×10^{19} A m^{-2}/W.

In the 1.6MA / $3.8\times10^{19}m^{-3}$ regime, the relative loop voltage drop, $\Delta V/V$, attains a value of 57% with 4 MW RF power . As shown in figure 1, the RF current, I_{HF}, increases with the RF power up to 0.84MA for P_{RF} = 4MW, where I_{HF} is calculated by taking into account the change of plasma resistivity due to the electron heating and the enhancement of Zeff (typically $\Delta Zeff$ / Zeff≈40%), and the corresponding efficiency reaches 1.87×10^{19} A m^{-2}/W. However, in these mixed OH-LH discharges, the RF current is defined as the current which is carried by fast electrons produced by LH waves and given by Fisch [5]: $j_{HF}=j_0(1+\mu E+...)$, where j_0 is the RF current in the absence of electric field and μ is proportional to $1/n^2.R.N_{//}^2$. Therefore, the enhancement of current drive efficiency due to the residual electric field can be important. Figure 2, in which j_{HF} decreases when the RF power increases, illustrates the RF power dependence of the electric field effect. It should be noted that the determination of the RF current is very delicate when the residual electric field is not negligible, due to a change in plasma resistivity. As shown in figure 2, for low RF power ≈1.5MW (during RF V≈0.7Volts, DV/V=0.3), the current drive efficiency, without plasma resistivity correction, attains the value

of $3x10^{19}$ A m^{-2}/W instead of $2x10^{19}$ A m^{-2}/W. The power taken by the fast electron population from the OH transformer, $P_{el}=j_{HF}$ E, can be evaluated from the Fisch-Karney theory [6].The ratio P_{el}/P_{abs}, where P_{abs} is the RF power absorbed by the fast electrons, is a function of the wave phase velocity, and depends only on Zeff when the phase velocity is normalized to the critical runaway velocity (figure 3). The fit of the experimental data, in which we assume 70% of the RF power absorbed by resonant electrons and an upshift of wave parallel index by a factor 1.3 ($\approx R_{ant}/R_0$), shows good agreement between the experimental points and the theoretical curves for Zeff≈3-4 . In the $\bar{n}=1.5x10^{19}m^{-3}$ regime,the ratio P_{el}/P_{abs} can reach 60% . In the high density regime, the residual electric field effect is much smaller: P_{el}/P_{abs} = 10-20%, and the zero loop voltage efficiency can be found to be around $1.6x10^{19}$ A m^{-2}/W by extrapolating the results on the basis of LHCD theory ($\eta \propto n_{//}^{-2}$).

During LHCD experiments, bulk electron heating by slowing down of fast electrons is also observed (figure 4). At high densities, the temperature peaking, defined as Te(0)/<Te>, is unchanged indicating that all of the plasma volume is heated, whereas at low densities ($\bar{n}=1.5x10^{19}m^{-3}$) the electron heating occurs preferentially in the center of the plasma: Te on axis increases from 3 to 6.3 keV for 4MW RF power. The global energy confinement time deduced from diamagnetic measurements (the contribution of the fast electrons is neglected) is plotted versus the total power in figure 5, by taking into account the injected RF power. The degradation of the confinement time seems more pessimistic than L-mode scaling law for high power. This may be explained by a decrease of the absorbed power.

Simulations

The OH plasma is simulated by adjusting the electron thermal diffusivity (through a mutiplicative constant) so that a good fit is obtained for the loop voltage and the electron temperature. The full launched LH spectrum, as given by the SWAN code[4], is taken into account by distributing 50 rays on each side of it (positive and negative). The confinement time of fast electrons is assumed to have the form [1] $\tau = \tau_0\gamma^\beta$, where γ is the relativistic factor and τ_0 is taken to be the energy confinement time deduced from diamagnetic measurements. The RF plasma is fitted by varying the ratio of $T_\perp$ to the bulk electron temperature ,Te.

Figure 7 shows the results for shot 5319- B=3.85T, Ip=1.6MA, $\bar{n}=3.8x10^{19}m^{-3}$, Zeff=2.8, P_{RF}=2.4 MW, τ_o=160 ms. By taking $T_\perp/Te=20$ for fast electrons good agreement was obtained with the experiments, both for bulk plasma parameters (loop voltage drop and increase in central electron temperature) and for local properties (profiles). The fit of the OH plasma gave $\chi_e\approx 0.94$ m^2/s at half radius (corresponding to an electron heat loss time of $\tau_e\approx(a/2)^2/\chi_e\approx 160$ ms) and the RF current diffusion calculation gave a momentum loss time of 1 ms and a global RF current diffusion coefficient of $\chi_e\approx 3.6$ m^2/s. These results confirm what was expected in high density plasmas: wave absorption in the outer half of the plasma column, due to accessibility constraints, and negligible RF current diffusion.

At lower densities ($\bar{n}=1.5x10^{19}m^{-3}$) the plasma response time for the loop voltage and for the self-inductance seem more difficult to simulate, giving the feeling that the wave absorption and the resulting current density profile given by the code are more centrally peaked than they really are. Nevertheless, the steady-state loop voltage and electron temperature are well simulated both in OH and RF plasma.

Conclusions:

Lower hybrid current drive in Tore Supra has been performed in typical discharges, Ip=1.6MA/$\bar{n}=3.8x10^{19}m^{-3}$. A maximum LH driven current of 0.84MA is achieved in a mixed OH-LH discharge with 4MW RF power, of which 15% is estimated to be due to the residual electric field. The corresponding current drive efficiency, $n RI_{HF}/P_{RF}$, is $1.87x10^{19}$ A m^{-2}/W. During LHCD the central electron temperature increases from 3 to 6.3 keV with 4MW RF power at $\bar{n}=1.5x10^{19}m^{-3}$.

Ray-tracing simulations prove to be a good tool to simulate these experiments. It should be pointed out that only two free parameters were allowed for in these simulations: a scale factor in χ_e for the OH plasma and the ratio $T_\perp/T_e$ for the RF plasma.

References
[1] Bonoli, P.T., Englade, R.C., Phys. Fluids 29 (1986) 2937
[2] Bonoli, P.T., Porkolab, M., et al., Nucl. Fusion 28 (1988) 991
[3] Fuchs, V.,Shkarofsky, R.A., et al., Nucl. Fusion 29 (1989) 1479
[4] Litaudon, X., Bibet, P., et al., this conference
[5] Fisch, N.J., Phys. Fluids 28 (1985) 245
[6] Karney, C.F.F., Fisch, N.J., Phys. Fluids 29 (1986) 180

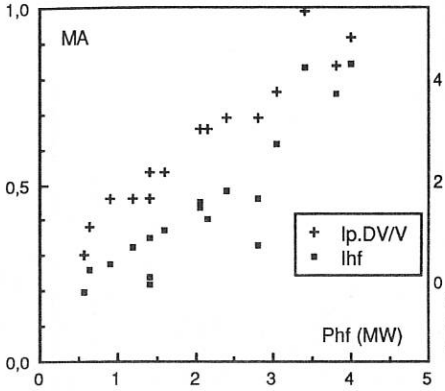

Figure 1: LH driven current versus RF injected power (Ip=1.6MA, $n=3.810^{19}$ m^{-3})

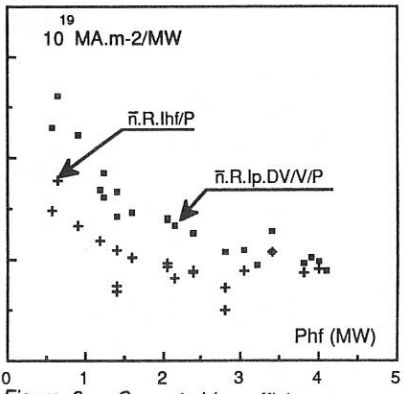

Figure 2: Current drive efficiency versus RF injected power (Ip=1.6MA, $n=3.810^{19}$ m^{-3})

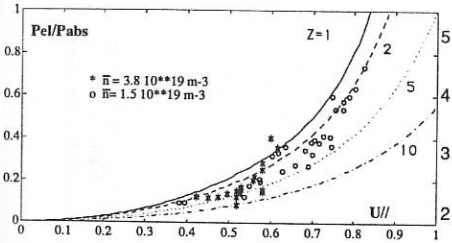

Figure 3: Pel / Pabs versus wave phase velocity normalized to runaway velocity

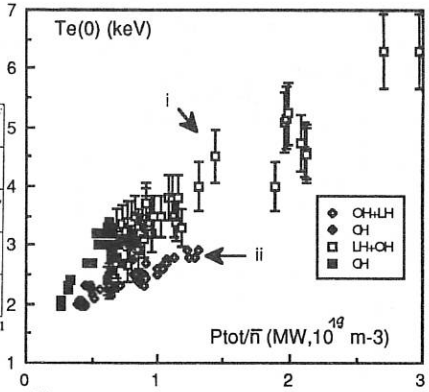

Figure 4: Central electron temperature versus total power normalized to line average density
i: Ip=1-1.6MA, $\bar{n}=1.510^{19}m^{-3}$
ii: Ip= 1.6MA, $\bar{n}=3.810^{19}m^{-3}$

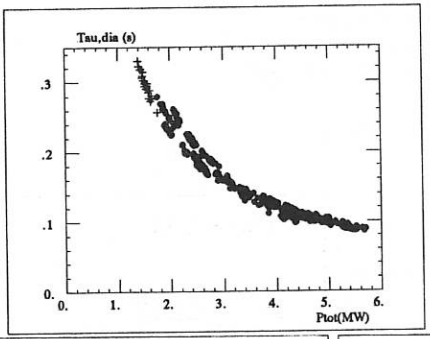

Figure 5: Energy confinement time deduced from diamagnetic measurement versus total power (I_p=1.6MA, $\bar{n}$=3.810^{19}m^{-3})

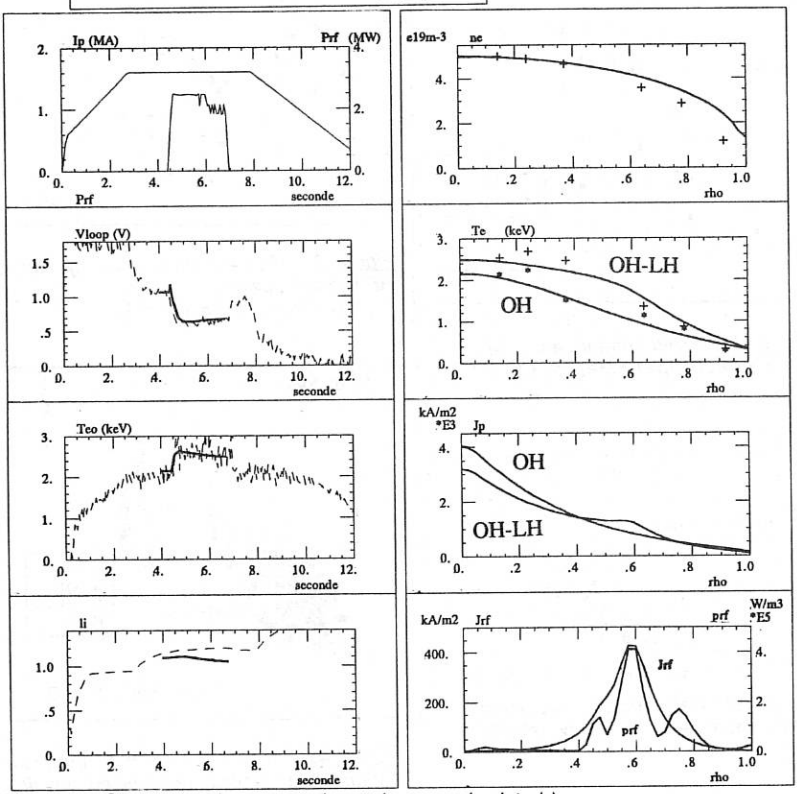

Figure 6: Shot 5319 (..... experimental ; ___ simulated)
Time evolution: a) plasma current and RF pulse, b) loop voltage, c) central electron temperature, d)plasma self-inductance
Radial profiles: e)electron density, f) electron temperature, g) plasma current density, h)RF power density deposition and RF current density

ECCD EXPERIMENTS ON T-10

V.V.Alikaev, A.A.Bagdasarov, A.A.Borschegovskij, N.L.Vasin, V.V.Volkov, Yu.A.Gorelov, A.V.Gorshkov, S.A.Grashin, Yu.N.Dnestrovskij, M.M.Dremin, D.Yu.Elizavetin, Yu.V.Esipchuk, N.V.Ivanov, D.V.Kachalin, Yu.N.Kilpio, A.Ya.Kislov, D.A.Kislov, P.E.Kovrov, L.K.Kuznetsova, S.E.Lysenko, D.A.Martynov, Yu.S.Maximov, A.A.Medvedev, V.Yu.Mirenskij, G.E.Notkin, Yu.D.Pavlov, V.V.Parail, G.V.Pereverzev, A.B.Pimenov, K.A.Razumova, I.N.Roy, V.V.Sannikov, A.V.Sushkov, K.B.Titishov, V.M.Trukhin, P.N.Yushmanov, G.S.Yaramyshev

I.V.Kurchatov Institute of Atomic Energy, 123182, Moscow, USSR.

G.G.Denisov, M.I.Petelin, V.A.Flyagin

Institute of Applied Physics, 603600, N.Novgorod, USSR.

J.Lohr, R.Harvey

General Atomics, San Diego, Cal., USA.

R.A.James

Los Alamos National Laboratory, Los Alamos, N.M., USA.

ABSTRACT. *The current is shown to be driven in ECH on T-10.*

1. The experiments are in progress on T-10 to investigate the possibility of EC current drive and to determine its efficiency.

The EC waves are launched from the low field side. The EC set consists of two gyrotron groups: i) the main group with λ = 3.69 mm, total power $P_{HF} \leq 2.2$ MW, launched by reflection from a mirror at an angle $\alpha = 21^{o}$ to the major radius in the injection point; ii) the additional group with λ = 4.0 mm, $P_{HF} \leq 0.64$ MW, injected perpendicular to the toroidal field B. The first group was used for current drive and the second one for plasma heating only.

The EC pulse duration was $\Delta t \leq 0.25$ s. To extend Δt up to 0.5 s, consequent turn-on of gyrotrons was used at P_{HF} = 0.7 MW. Experiments were conducted in regimes with the plasma current I_p = 75 to 180 kA and the density $\bar{n}_e = (0.5 \text{ to } 1.4)\times10^{19}$ m^{-3} normalized to the chamber radius a_{ch} = 0.39 m, (a_{lim} = 0.28 m). The resonance position was changed by variation in B from 2.6 to 2.8 T. The optimal field B = 2.77 T corresponds to 8 cm shift of the resonance inside the machine center (for λ = 3.69 mm gyrotrons).

2. The most desirable demonstration and the best conditions for measurements of the driven current I_{CD} would be in the achievement of operation with zero or negative loop voltage U_o. It was one of the main goal of the ECCD experiments on T-10. The U_o value as low as 40 mV was achieved in the regime: I_p = 75 kA, $\bar{n}_e = 1\times10^{19}$ m^{-3}, B = 2.7 T with $P_{HF} \simeq 1.0$ MW (λ=3.69) + 0.64 MW (λ=4.0). But this result seems to be not a proof of the complete replacement of the OH current by ECCD because of the bootstrap current was about 0.5 I_p.

The main experiments on measurements of I_{CD} are those with change of the

OH electric field direction (co- and counter- generation). The discharge parameters, such as T_e profile, Z_{eff}, radiative losses P_{rad}, and others were nearly unchanged. The feedback control for $\bar{n}_e$ was used.

The I_{CD} value was determined from simulation of U_o temporal behaviour. The neoclassical conductivity and bootstrap current was taken into account in simulations, as well as the experimental profiles of T_e and n_e, that were in agreement with the diamagnetic measurements. We tried to reach the best fit with the experimental value of U_o for co- and counter- cases simultaneously, all during the ECH pulse except an initial stage (~ 50 ms). In accordance with the experiment, Z_{eff} was believed constant along the plasma radius. We also supposed $I_{CD,co} = I_{CD,count}$.

The above mentioned method allows us to limit the estimation error in I_{CD} by 15%, but gives no possibility to find out the dependence of I_{CD} on the residual electric field $E = U_o/2\pi R$. Values of I_{CD} such estimated correspond to $E = 0$.

3. Fig. 1 shows the SXR spectra, registered by PHA with the Ge detector along the central chords. In the OH regime, as well as in the ECH regime with perpendicular launch, the spectra are maxwellian. With the oblique injection of HF power, suprathermal electrons with energy $\mathcal{E} \geq 25$ keV are produced. Spectra are practically identical in the co- and counter- cases. Appearance of the suprathermal electrons is indicative of existence of the prerequisite conditions for the I_{CD} generation.

Traces of the fundamental parameters are displayed in Figs. 2 and 3 for discharge with I_p= 100 kA, B= 2.77 T, $\bar{n}_e = 0.5\times10^{19}$ m^{-3}, P_{HF} = 0.71 MW. The temporal variation in U_o indicates the current generation in a narrow filament in the center ($r/a \leq 0.3$); the reorganization of the current profile takes a time of order of the skin time. The difference $\Delta U_o = U_{co} - U_{count}$ increases in time up to saturation more rapidly for lower I_p, i.e. for more narrow T_e profile. At $I_p \leq 100$ kA, when the current reorganization is shown by the simulation to be the strongest, the sawteeth appear ~ 50 ms after the ECH start in co-case and they do not appear in the counter-case, as well as at the OH stage (Fig.2,c). The internal inductance increases in time in the co-case and it drops in the counter- case (Fig.2, e).

These results give the evidence of the EC current drive.

4. In the ECCD experiments on T-10, the current I_{CD} = 110±15 kA has been generated in plasma with I_p = 175 kA, B = 2.77 T, $\bar{n}_e = 1.0\times10^{19}$ m^{-3}, and P_{HF} = 1.45 MW (λ = 3.69) + 0.63 MW (λ = 4.0). The I_{CD} value increased with the P_{HF} and T_e rise. The simulation shows that central current density $j_{CD}(0)$ exceeds $j_{OH}(0)$ and reachs 400 A/cm^2 or more.

The efficiency of the current drive $\eta_{exp} = I_{CD}/P_{ab}$ is displayed on Fig. 4, a as a function of $T_e(0)/[n_e(0)(Z_{eff} + 5)]$. The P_{ab} value, as determined from the diamagnetic measurements, is $0.85 \cdot P_{HF}$. In the above mentioned regime, η_{exp} was about 0.09 ($T_e(0)$ = 7 keV, $n_e(0) = 2.2\times10^{19}$ m^{-3}, and $\langle Z_{eff}\rangle$= 1.7). The theoretical values η_{th} shown in Fig.4 were calculated by the codes [1, 2]. In those codes, propagation and resonance absorption of the EC waves are calculated from the set of the Gamilton equations, and the CD efficiency is determined from kinetic equation with a quasilinear operator which includes the relativistic and toroidal effects.

The comparison of the experimental data with the theory shows that the achieved efficiency η_{exp} is less than the predicted one, η_{th}, by factor 0.6

to 1 for the regime I_p = 175 kA; the factor is less for lower I_p. The peculiarity of the ECCD experiments on T-10 is that the energy confinement time, τ_E, is of order of the collisional time, τ_{col}, for the resonance electrons ($v_{e,res}/v_{e,th} \simeq 2$) at $\bar{n}_e \simeq 1\times10^{19}$ m^{-3}. The e-folding time of the X-rays intensity with $\mathcal{E} \geq 25$ keV is equal to that for the thermal component. The η_{exp} value appears to be close to the predicted one, η_{th}, if the factor $G = (1 + \tau_{col}/\tau_E)$ is taken into account.

One more reason low η_{exp} could be connected with the low value (70 to 80%) of one-pass absorption due to narrow profiles of T_e and n_e, especially in the low current regimes ($I_p \leq 100$ kA).

The difference in the U_o values ($U_{count} < U_{co}$) at the initial stage of ECH, $\Delta t \leq 100$ ms can be explained by the existence of the reversed current (up to 25 kA in the regime I_p=75 kA) because a part of HF power is absorbed on inner side of the plasma column, $R < R_{res}$, and it is able to drive reverse current.

5. In low density plasmas a threshold exists $(P_{HF}/n_e)_{thr}$ beyond which the plasma-wall interaction as well as, possibly, the plasma-limiter interaction becomes more intensive (Fig.5). One can see the P_{rad} and Z_{eff} rise, which follows by an increase in U_o. Appearance of an instability, caused by the runaway electrons (produced by the EC waves), is a possible explanation of those phenomena.

In conclusion, the decrease of efficiency of the current drive at lower I_p as well as with existence of the $P_{HF}/\bar{n}_e$ - threshold did not allow us to realize the regime with $U_o \leq 0$.

REFERENCES

[1]. L.K. Kuznetsova et al. Proc. of 17th EPS Conf. on Contr. Fusion and Plasma Heating, Amsterdam, 1990, v. 3, p. 1247.

[2]. G. Giruzzi. Phys. Fluids, 31 (1988) 3305

Figure captions

Fig.1. X-ray spectra registered along the central chords.

Fig.2. Traces of the major parameters in discharges with co- and counter-generation: (a,b) - loop voltage; (c) - central T_e; (d) - mean density; (e) - internal inductance. Regime: I_p = 100 kA, $\bar{n}_e = 0.5\times10^{19}$ m^{-3}, B = 2.77 T. The results of simulation of $U_o(t)$ are also shown in (a, b).

Fig.3. Profiles of T_e and n_e in the same regime as for Fig.2.

Fig.4. a) Efficiency of the ECCD $\eta = I_{CD}/P_{ab}$, comparison of experiment with theory;
b) The same, but finite τ_E is taken into account.

Fig.5. a) Typical traces of the plasma parameters at $P_{HF}/\bar{n}_e$ beyond the threshold. Regime: I_p = 150 kA, $\bar{n}_e = 0.55\times10^{19}$ m^{-3}, B = 2.78 T;
b) U_o as a function of $\bar{n}_e$; the threshold of $P_{HF}/\bar{n}_e$ is demonstrated.

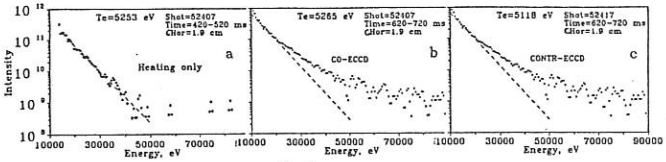

Fig.1

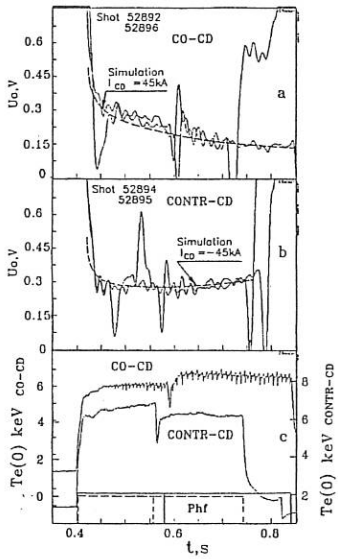

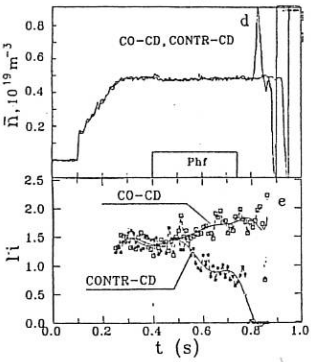

Fig.2

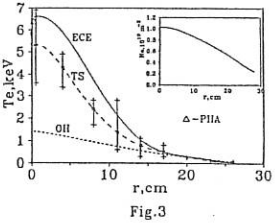

Fig.3

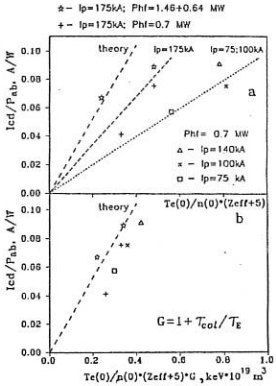

Fig.4

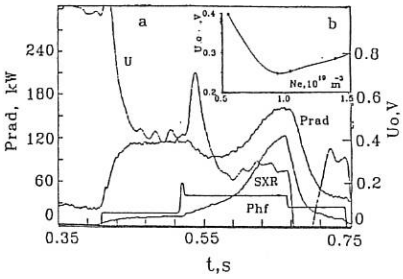

Fig.5

FOKKER-PLANCK ANALYSIS OF ECCD EXPERIMENTS IN DIII-D

G. Giruzzi

ASSOCIATION EURATOM-CEA SUR LA FUSION
DRFC - C.E.N. de Cadarache
Saint-Paul-lez-Durance (FRANCE)

R.A. James

LAWRENCE LIVERMORE NATIONAL LABORATORY
Livermore, California (U.S.A.)

John Lohr

GENERAL ATOMICS
San Diego, California (U.S.A.)

Introduction. Electron cyclotron current drive experiments (ECCD) have been performed using 60 GHz waves launched from the high field side of the torus and have produced rf driven currents up to 100 kA [1]. These are the first ECCD experiments to be performed with plasma conditions relevant to the future application of this method to a tokamak reactor, i.e., i) the waves are totally absorbed in a single transit; ii) the rf power deposition is localized in space; iii) the energy confinment time is much longer than the slowing-down time of the rf generated current carriers. Since the dynamics of the current-carrying superthermal electrons is essentially determined by the local values of the absorbed rf power, the dc electric field and the Coulomb collisions, these unique experimental conditions permit a comparison with the kinetic theory of ECCD [2].

Such a comparison is a challenging task, since the available rf power (1 MW) is not sufficient to drive all the current necessary for plasma confinment. Thus, a residual Ohmic electric field is always present, resulting in a significant enhancement of the rf-driven current (up to 150 percent). Under such conditions, no simple analytical formulae for the ECCD efficiency are available and a perturbation analysis [3] is not applicable. Thus, the comparison has to be made by solving the appropriate kinetic equation numerically. This approach has an important advantageous by-product: a very detailed description of the velocity-space electron distribution function on several flux surfaces. In addition to yielding the driven current, this detailed information can be used to predict the output of diagnostics which are sensitive to the superthermal electron distribution, such as non-thermal Electron Cyclotron Emission spectra (ECE). Satisfactory agreement in the simulation of such diagnostics thus serves as a good check of the validity of the theoretical model.

The DIII-D ECCD experiments were systematically modeled by means of a 3-D bounce-averaged Fokker-Planck code [4-6]. The experimental CD efficiency was determined from the drop in the measured loop voltage, corrected for the change in the plasma resistivity and bootstrap current. Density and plasma current scans were performed, including a reversal of the toroidal current I_p. The experimental rf-driven current was found to be in excellent agreement with the theoretical simulations for a large number of discharges. The residual Ohmic electric field

and electron trapping strongly influence both the experimental and theoretical results. These results will be extensively reported elsewhere. Here we want to present the model used in the computation and discuss the simulation of the non-thermal ECE spectra.

Theoretical model. The process of ECCD is governed by the kinetic equation for the electron distribution function $f(u_{\parallel},u_{\perp},r,t)$,

$$\frac{\partial f}{\partial t} = \left\langle \left(\frac{\partial f}{\partial t}\right)_{EC} \right\rangle + \left\langle \left(\frac{\partial f}{\partial t}\right)_{coll} \right\rangle + \left\langle \left(\frac{\partial f}{\partial t}\right)_{dc} \right\rangle \quad , \tag{1}$$

where u is the electron momentum normalized to $(mT_e)^{\frac{1}{2}}$. The three terms on the right hand side of Eq. (1) describe respectively: quasilinear diffusion , Coulomb collisions and parallel acceleration due to the dc electric field. The rf power spectrum inside the plasma is evaluated by splitting the injected spectrum of angular spread ± 10° into 45 elementary rays and following their trajectories by means of a toroidal ray-tracing code. The absorption along each ray is evaluated self-consistently by solving the appropriate fully relativistic dispersion relation. The brackets in Eq. (1) denote flux-surface averaging in toroidal geometry, thus accounting for electron trapping effects [6]. For the collision term, the high-energy expansion of the Landau collision operator is used, which is adequate for most current drive problems [2]. The experimentally measured loop voltage, as well as density, temperature and Z_{eff} profiles are used in the computation. Equation (1) is solved by means of a time-dependent finite difference scheme [5] on 11 flux surfaces, using a 128 x 64 grid in u,θ_0 space, where $\cos\theta_0 = u_{\parallel}/u$ at the low field side in the equatorial plane. Steady state is attained in 5 ms typically, which is much shorter than the experimental energy confinement time of about 35 ms. This proves that kinetic theory without losses is adequate to model ECCD in these experimental conditions. The steady-state distribution function can be inserted into a radiation code [7] which evaluates the ECE spectra for arbitrary angle and harmonics, taking wall reflections into account.

Simulation of experimental results. We now discuss a typical ECCD discharge (65218), characterized in a stationary state during 0.9 MW of rf heating by the following plasma parameters: R = 1.6 m, a = 0.6 m, elongation = 1.2, B = 2.14 Tesla, $T_e(0)$ = 3.2 keV, $n_e(0) = 1.35 \times 10^{19}$ m^{-3}, V_ℓ = 0.33 Volts, $Z_{eff} \simeq 4$, I_p = 400 kA. The waves were launched at an angle of ~15° with respect to the normal to the toroidal direction, co-aligned with I_p. The time history of this discharge is presented in Ref. 1. The experimentally determined rf-driven current is I_{rf} = 63 ± 15 kA. Fokker-Planck simulations with E_{dc} = 0 yield I_{rf} = 39 kA; including the dc field but neglecting electron trapping effects yields I_{rf} = 93 kA, whereas including both trapping and finite E_{dc} we get I_{rf} = 62 kA, in very good agreement with the experimental value. This example shows the importance of both the Ohmic field and trapping effects in the simulation of the experiments. The steady-state distribution function at $r/a \simeq 0.28$ is shown in Fig. 1. Since wave absorption takes place at $\omega < \omega_c$, the resonance curve crosses the $u_{\parallel} = 0$ axis and the level curves (a) display large deformations for both $u_{\parallel} > 0$ (the direction of the electron drift due to the Ohmic field) and $u_{\parallel} < 0$. The asymmetry related to the rf current is more evident in the plot of the parallel distribution (b). The dashed curve is the parallel distribution for $P_{rf} = 0$ and is slightly asymmetric because of the dc electric field. The dashed line shows that the target plasma is practically Maxwellian. Figure 1

(c) shows the perpendicular temperature as a function of $u_{\parallel}$. It appears that at this space location the combined effects of the rf and the dc fields drive an energetic electron tail for $2 < u_{\parallel} < 6$, whereas a less dense tail is created for $u_{\parallel} < 0$, mostly because of collisional pitch-angle scattering. The power absorbed per unit volume (computed by the Fokker-Planck code) is shown in Fig. 2 versus r/a. On the same figure, the parallel resonant velocity $u_{\parallel}$ along three rays is plotted for different poloidal injection angles (0° and $\pm$10°) and the same toroidal angle (-15°). As mentioned earlier, the steady-state electron distribution function can be used to predict the radial non-thermal ECE spectra. In Figure 3, the computed radial spectrum (solid line) is compared to the experimental data (points). The experimental data is obtained by means of a 10-channel grating polichromator, used to detect 2nd harmonic ECE. The intensity of the non-thermal peak (at $r/a \simeq 0.8$) is strongly dependent on the wall reflection coefficient. The value used in the computation (0.85) was measured by comparison of the intensities of different harmonics in thermal discharges. It is important to note that the power deposition profile, and thus the detailed shape of the electron distribution function in 3-D phase space ($u_{\parallel}$, $u_{\perp}$ and r) is very sensitive to the local values of ω/ω_c and the wave vector. Thus the excellent agreement between the theoretical and the experimental spectra helps to corroborate the systematic agreement obtained between the predicted and measured rf-driven current and thus strenghtens our confidence in the theoretical model. As is well known, a notorious difficulty in the interpretation of non-thermal spectra is that the spatial location and the energy of the emitting electrons are inextricably coupled by the resonance condition. Using our computed electron distribution function, we can now investigate from where the non-thermal ECE spectrum originates in 3-D phase space. This is accomplished by simply excluding parts of the 3-D distribution function and assessing the resulting change in intensity of the 2nd harmonic, non-thermal ECE signal. As a result of this analysis we find that: i) most of the non-thermal emission comes from a narrow radial region around $r/a \simeq 0.25$, where the rf power deposition peaks (Fig. 2); ii) the non-thermal ECE is due to electrons with energies in the range of 55 - 140 keV, the peak corresponding to an energy of 80 keV, i.e., $u \simeq 8.4$; iii) all the non-thermal ECE is due to electrons having $v_{\perp} > v_{\parallel}$, and 70 percent of it is due to trapped electrons. We conclude that non-thermal emission at the 2nd harmonic is dominated by high-$v_{\perp}$ electrons, driven by the rf but carrying little or no current. Therefore, the 2nd harmonic ECE spectrum during ECCD yields information on a radially well-localized hot spot, but it is only indirectly related to the current-carrying electrons.

References

[1] JAMES R., et al., *Contr. Fusion and Plasma Heating* (EPS, Amsterdam, 1990) **14B**, III, 1259.
[2] FISCH N.J., Rev. Mod. Phys., **59** (1987) 175.
[3] FISCH N.J., Phys. Fluids **28** (1985) 245.
[4] FIDONE I., et al., Phys. Fluids **26** (1983) 3292.
[5] MEYER R.L., et al., Comp. Phys. Comm. **40** (1986) 153.
[6] GIRUZZI G., Phys. Fluids **31** (1988) 3305.
[7] GIRUZZI G., Nucl. Fusion **28** (1988) 1413.

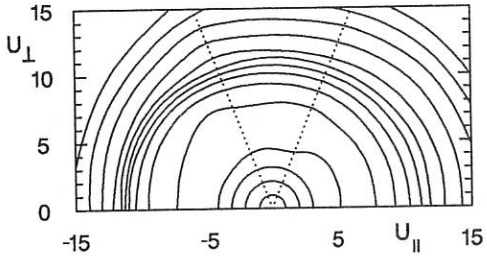

Fig 1a

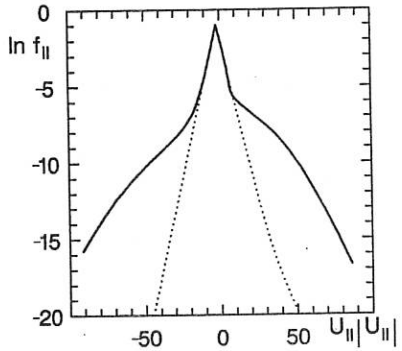

Fig 1b

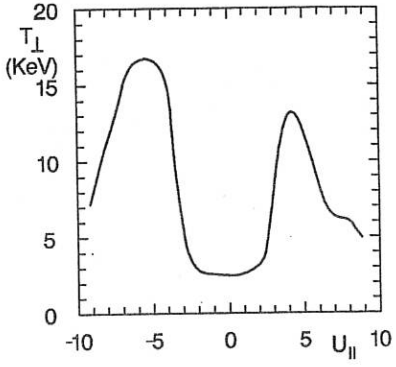

Fig 1c

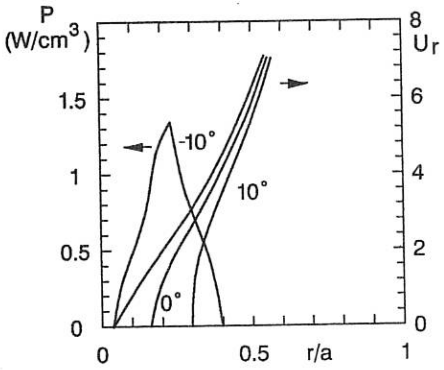

Fig 2

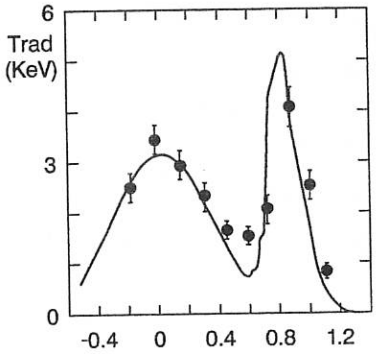

Fig 3

110 GHz ECH SYSTEM FOR DIII-D*

C. Moeller, R. Callis, W. DeHope, J. Doane, R. Freeman,
R. Prater, D. Remsen, and L. Sevier

General Atomics, San Diego, California

INTRODUCTION

Electron cyclotron heating (ECH) has proven effective for localized heating and current drive applications in tokamaks. This ECH system is designed to support experiments on H-mode physics, noninductively ECH driven plasma current (≈500 kA), and localized heating for plasma stabilization in the presence of substantial neutral beam power. The second harmonic X-mode will be launched from the outside using a mirror that can be rotated in the poloidal and toroidal directions.

In order to satisfy the physics objectives, it is necessary not only that the microwave power be transmitted from the gyrotron to the plasma efficiently and reliably for pulses as long as 10 seconds, but that the power be transmitted in a single mode, so that the radiation pattern is narrow and independent of small changes in gyrotron operating conditions.

Noteworthy features of the transmission system, shown schematically in Fig. 1, are:

- A novel mode converter from the gyrotron $TE_{15,2}$ mode to the HE_{11} mode in which the power is contained entirely in waveguide.
- A relatively small waveguide diameter (1.25 in.) for transmission of the low-loss HE_{11} mode.
- An all-vacuum system to ensure reliability at high power.
- A windowless system using differential pumping together with a fast shutter to avoid contaminating the tokamak vacuum.
- A quasi-optical launcher using a steerable mirror.

$TE_{15,2}$ to HE_{11} Mode Converter. This converter[1] has some similarity to quasi-optical Vlasov converters in that the radiation initially travels helically after leaving the input circular waveguide. However, as shown in the right half of Fig. 2, the radiation propagates in a coaxial waveguide that is unfolded into rectangular waveguide. In order to avoid diffraction and mode conversion, it is necessary that the local fields correspond to a single normal mode of the local cross section. That implies that the large dimension of the output rectangular guide, along which the field has a uniform amplitude, must be the direction of the electric field to satisfy the metallic boundary conditions, while the small dimension of the guide must then be the direction of the transverse component of the magnetic field. This polarization is orthogonal to the output polarization of the usual Vlasov converter.

In order to excite what is basically the fundamental mode in the rectangular waveguide, the required field pattern in the coaxial guide must correspond to a combination of the coaxial $TE_{15,2}$ and $TM_{15,1}$ modes so that the radial component of the electric field is cancelled. These modes are not quite degenerate in smooth wall coaxial guide for a finite radius, but the combination is a normal mode of helically grooved coaxial guide. This combination also has the advantage of lower ohmic losses than the coaxial $TE_{15,2}$ mode alone.

The incident $TE_{15,2}$ radiation in hollow waveguide is transferred to the helically grooved coaxial waveguide region by a large number of axial slots equally spaced around the circumference of the common wall of the circular and coaxial waveguides. The design ensures that the desired low loss hybrid mode is preferentially coupled.

* This work was sponsored by the U.S. Department of Energy under Contract No. DE-AC03-89ER51114.

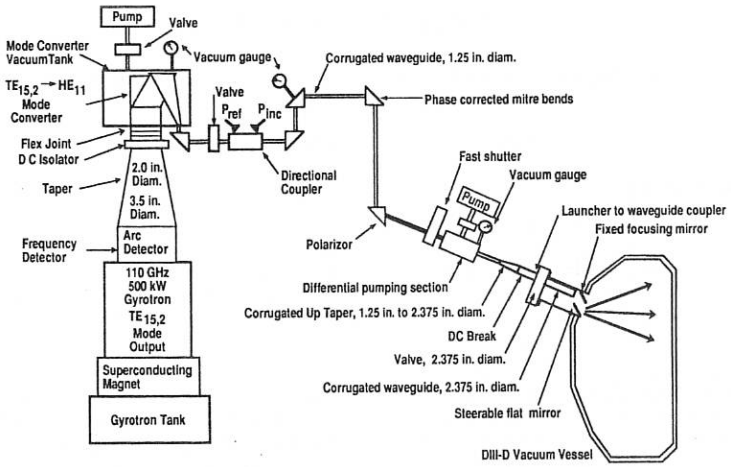

Fig. 1. 110 GHz waveguide transmission system.

After the coaxial region is unfolded into the large rectangular waveguide, the grooves in the outer conductor are removed. A combined 180-deg. H–plane bend and E–plane mirror allow a subsequent compact E–plane taper to rectangular waveguide of more normal aspect ratio. Corrugations introduced in the broad wall and tapered gradually from one-half to one-quarter wavelength in depth convert the TE_{10} mode to a rectangular waveguide HE_{11} mode. A corrugated E–plane taper then brings this mode to square waveguide with dimensions suitable for direct coupling to the HE_{11} mode in corrugated circular waveguide.

This converter has been built and tested at low power using a coupled cavity converter from the TE_{11} mode to the $TE_{15,2}$ mode having more than 98% output mode purity. A transmission measurement through the central waveguide, using a rotatable waveguide probe, shows that at least 95% of the input power is extracted through the prototype slot coupler, with further improvement expected in subsequent versions. Combining the coupler with the unfolding section, a near field scan at the tall rectangular output shows that the required polarization and uniformity in the E plane is indeed obtained, with cross polarization more than 20 dB down. A similar scan at the folded mirror, with an HE_{11} mode input at what would normally be the output of the TE_{01} to HE_{11} converter, shows a high uniformity in the E plane and cross polarization more than 30 dB down. With the entire unit assembled, we have also made a far field scan at the HE_{11} output in our standard 31.8 mm corrugated waveguide, a preliminary example of which is shown in Fig. 3 for E and H plane scans. The cross polarization in both scans is at least 30 dB below the HE_{11} peak. The power in the side lobes is estimated to be less than 5% of the total.

Corrugated 1.25-in. HE_{11} Waveguide. Corrugated waveguide can propagate the HE_{11} mode with very low loss even in moderately small diameters. For example, in 1.25-in. (31.8-mm) diameter at 110 GHz, the predicted loss in aluminum is only about 2% in 40 meters.

One advantage of the relatively small diameter is its insensitivity to misalignments. Similarly, it is possible to negotiate small angle bends in reasonable lengths. For example, a 22-deg. bend with a hyperbolic secant curvature variation[2] can be made with negligible mode conversion in an arc length of 65 in.

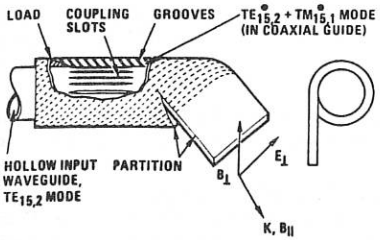

Fig. 2. The slotted coupling and unwrapping sections of the $TE_{15,2}$ to HE_{11} mode converter that convert a circular $TE_{15,2}$ input to an oversized rectangular TE_{01} output.

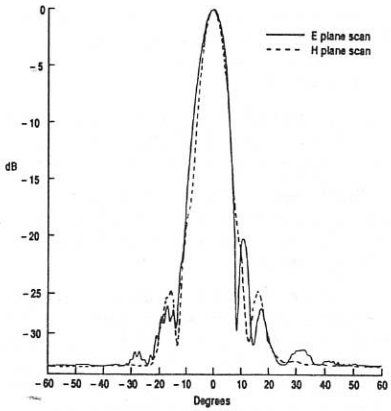

Fig. 3. A far field scan in the E and H planes at the 31.8 mm corrugated output of the converter.

Phase correcting mirrors[3] have been designed to allow the use of 90-deg. miter bends with low loss in this 1.25-in. size. The relatively small size also provides relatively large losses for the high order modes that typically are generated and reflected from miter bends.

A machine has been constructed for direct machining of 2 m long corrugated aluminum waveguide sections. A vacuum seal and waveguide coupling has been designed with a simple sleeve, snap rings, and a helicoflex seal on the faces of the waveguides. This design eliminates any welding or brazing of flanges, and waveguide sections can be inserted or removed without shifting adjacent sections.

We have performed low power transmission tests on these components using corrugated tapers from fundamental rectangular waveguide to the 31.8 mm diameter followed by sections of 31.8 mm diameter dielectric waveguide. The latter provide preferential attenuation of higher order modes to attenuate trapped mode resonances and fundamental mode reflections at the tapers. Transmission measurements of a 10 m assembly of straight sections show a loss consistent with the predicted value ($\leq 0.5\%$). We have also found, as expected, that the transmission is insensitive to gentle deflections of such an assembly. The mitre bends were tested by placing six in series, with a group of two separated by a group of four by 2 m of straight waveguide. The measured transmission loss was $<6\%$, consistent with the expected loss of 1% per bend. Furthermore, over a 500 MHz sweep(occurring over 5 minutes to reveal very sharp resonances), there was no evidence of any trapped modes between the groups of bends, showing that the higher order modes generated at the mitre bends are effectively damped in the 31.8 mm corrugated waveguide.

Vacuum System. The requirement of operating up to 10-second pulses at 0.5 MW (and 1 MW in the future) make a window design difficult, especially for the HE_{11} mode, for which the power is concentrated near the waveguide center. Face-cooled windows with fluorocarbon liquid are unacceptable near the tokamak. Therefore, we have designed an evacuated waveguide system without a window on the tokamak end.

We originally planned to bake the waveguide to 100°C, but we found in a test of 30 meters of the cleaned but unbaked corrugated that after 50 hours the pressure 30 meters from the pump reached 5×10^{-6} torr, which is entirely acceptable with regard to breakdown as discussed below. The relatively high pumping resistance of the small waveguide diameter helps to reduce the impurity influx into the tokamak to an acceptable level with a windowless transmission line

with differential pumping. With an outgassing rate of 3×10^{-12} torr-liters/(s-cm^2) measured after 24 hours in the same experiment, the flow into DIII–D is only 2×10^{-9} torr-liters/sec with 40 meters of waveguide, assuming only the section between the differential pump and the vessel is baked.

To protect the tokamak vacuum from a catastrophic leak, a fast shutter is located on the gyrotron side of the downstream pump. A better but slower seal is provided by the conventional isolation valve next to the tokamak.

Breakdown. The improved power handling capability of the waveguide under vacuum is a direct consequence of the very high frequency, which at low pressures is much larger than the collision frequency. Correspondingly, the power absorbed by electrons from the microwave field is very small.[4]

The rate of electron population increase due to ionization is offset by the rate of diffusion to the waveguide walls. At low pressures, breakdown occurs when these rates are equal. For example, at 10^{-2} torr in our 31.8 mm/diameter waveguide, the field at breakdown calculated from simple theory[4] is over 50 kV/cm. (The peak HE_{11} field at 1 MW is 23.7 kV/cm.) Consideration of other electron loss mechanisms, imperfect ionization efficiency, and the nonuniform microwave field distribution leads to much higher values of breakdown fields.[5]

We conclude that the present system, with pressures below 10^{-6} torr and fields under 25 kV/cm, has a large safety margin.

Tapers. A 60 cm long parabolic taper[6] in HE_{11} corrugated waveguide connects the 31.8 mm waveguide to 60.3 mm corrugated waveguide near DIII–D. The larger size is more convenient for the vacuum valve and dc break, and it gives a narrower beam width from the quasi-optical launcher.

Quasi-Optical Launcher. Radiation from the end of the HE_{11} corrugated waveguide is focused and rotated by two mirrors. The fixed mirror at the end of the waveguide is a paraboloid of revolution, and slightly focuses the free space gaussian beam generated by the radiating HE_{11} mode. At the power deposition region in the plasma, approximately 1 meter from the radiating waveguide, 98% of the power is contained in a beam diameter of 13 cm. Rotation of the flat mirror provides broad poloidal coverage of the DIII–D plasma. This mirror will also be rotatable toroidally, but in its initial construction this will require a machine vent.

REFERENCES

1. Moeller, C.P., "Compact Waveguide Converter Apparatus," U.S. Patent Application filed January 9, 1990.
2. Doane, J.L., IEEE Trans. Microwave Theory Tech. MTT-32 (1984) 1362.
3. Vaganov, R.B., Radio Eng. Electr. Phys. 18, (1973) 170.
4. Brown, S.C., Introduction to Electrical Discharges in Gases (Wiley, New York, 1966).
5. MacDonald, A.D., and S.J. Tetenbaum, High Frequency and Microwave Discharges, in: Gaseous Electronics, Vol. 1, eds. M.N. Hirsh and H.J. Oskam (Academic Press, New York, 1978).
6. Doane, J.L., Int'l J. Infrared and Millimeter Waves 5, (1984) 737.

Measurement of the ICRH power absorption from modulation experiments in TEXTOR

Lebeau D., Koch R., Messiaen A.M., Vandenplas P.E.

Laboratoire de Physique des Plasmas - Laboratorium voor Plasmafysica
Association "Euratom-Etat belge" - Associatie "Euratom-Belgische Staat"
Ecole Royale Militaire - B1040 Brussels- Koninklijke Militaire School

Introduction

By modulating the radio-frequency (RF) power amplitude in TEXTOR, we examine some important aspects of ion cyclotron resonance heating experiments: the energy confinement time, the deposition profile and the fraction of the RF power absorbed by the plasma. The modulation creates a moderate perturbation (e.g. 15 % of the average power) of the RF power amplitude at a frequency $\Omega/2\pi$. We detect this modulation on the diamagnetic energy (W_{dia}) and the equilibrium energy (W_{equ}). Defining the RF excitation $P_{RF} = P_{RF,o} + Re\,[\tilde{P}_{RF}\ exp(j\Omega t)]$ and the energy response $W = W_0 + Re[\tilde{W}\ exp(j\Omega t)]$, the complex transfer function is $\tilde{W}/\tilde{P}_{RF}$. From repetitive discharges in which Ω is varied, we build the experimental transfer function and compare it to models allowing us to draw interesting conclusions concerning which fraction of the RF power is well confined and which is poorly confined.

Diamagnetic energy measurement

In TEXTOR, the diamagnetic flux measurement has two important features: (i) the loops are located between the liner - a thin metallic shell - and the vessel and (ii) the flux variation is the difference of potential between the diamagnetic loop and a compensated loop. The diamagnetic loop measures the variation of the plasma poloïdal currents and therefore of the perpendicular pressure. The compensated loop suppress the effect due to driven or eddy poloïdal currents circulating in and outside the vessel [1].

The time response of the loops is computed by solving Maxwell's equations in cylindrical geometry with a plasma of constant conductivity and a surface modulated current in $exp(j\Omega t)$. The wall time constant τ_W is found to be $\approx 50\ \mu s$ for perfectly compensated loop. Taking into account $o(10^{-2})$ errors in the compensation, τ_W can reach a fraction of ms, a value which is small compared to the confinement time (20-50ms) and to the $2\pi/\Omega$ range (30ms-1s).

Equilibrium energy measurement

The non-stationary equation of motion of a plasma column (thin casing case [2]) states that the equilibrium field (proportional to W_{equ}) is the sum of the external applied vertical field and of the casing self-stabilizing field induced by plasma motion. Fourier analysis of this equation shows that, at low Ω, the casing is transparent to the external field and W_{equ} is proportional to the control field whereas, at high Ω, the casing is opaque to the external field and W_{equ} is proportional to the plasma velocity. The difficulty to estimate correctly the plasma velocity and the resistive time makes the determination of $\tilde{W}_{equ}$ not feasible at high Ω.

Theoretical transfer function

In the particular ICRH scenario considered here (minority H in D), we call α_{min}, α_{di}, α_{de} the fractions of P_{RF}, the total RF power, directly going to minority ions, majority ions and electrons (due to mode conversion) respectively. Defining W and $W_\perp$ the total energy of the plasma and its perpendicular part, $W \le W_{dia} \le W + W_\perp/2$. Depending if the plasma is purely isotropic or not, lower and upper limit of W_{dia} are respectively reached. Since, in presence of ICRH, electrons and majority ions remain isotropic, $W_\perp$ refers only to minority ions whose distribution function f presents a perpendicular tail. When the average RF power given to minority ions ($\alpha_{min}\ P_{RF}$) is low, f is quasi-

isotropic and $W_\perp = 0$ (lower limit). In this case, the frequency dependence of W_{dia} is described by the model $\partial W/\partial t = \alpha P_{RF} - W/\tau$ where τ is the incremental confinement time (close to the auxiliary confinement time defined in [4]) and $\alpha = \alpha_{de} + \alpha_{di} + \alpha_{min} \leq 1$ is the fraction of the power absorbed by the plasma. Linearisation around the modulated component gives: $\tilde{W}/\tilde{P}_{RF} = \alpha/(j\Omega+1/\tau)$ (1). When $\alpha_{min} P_{RF}$ is large, f displays a perpendicular velocity tail. $W_\perp$ is described by the equation: $\partial W_\perp/\partial t = \alpha_{min} P_{RF} - 2W_\perp/t^*_{se}$. $2/t^*_{se} = 2/t_{se} + 1/\tau_{min}$. t_{se} and τ_{min} are the slowing down time on electrons and the confinement time of the minority ions. The slow minority ions exchange their energy with the majority ions and have an isotropic f whereas the fast ones exchange their energy with the electrons and have a purely perpendicular f. The upper limit is: $\tilde{W}_\perp/\tilde{P}_{RF} = 0.5\ \alpha_{min}/\ (j\Omega+2/t^*_{se})$. Therefore:

$$\frac{\alpha}{\tau^{-1}+j\Omega} < \frac{\tilde{W}_{dia}}{\tilde{P}_{RF}} < \frac{\alpha}{\tau^{-1}+j\Omega} + \frac{\alpha_{min}/2}{j\Omega+2/t^*_{se}} \qquad (2)$$

Figure 1 illustrates schematically this relation. The middle line plots the amplitude of $\tilde{W}_{dia}$ For large Ω, the phase shift between W_{dia} and P_{RF} is -90° and the amplitude is in $1/\Omega$. This experimental diamagnetic curve can be fitted with the transfer function $\alpha_{dia}/(j\Omega + \tau_{dia})$ and is bounded by the lower limit (isotropic f) and by the upper limit (purely perpendicular f). α_{dia} and τ_{dia} obey the following conditions obtained from the low Ω and the high Ω limits:

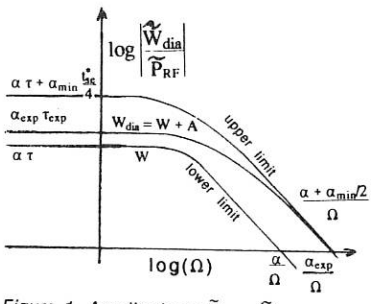

Figure 1. Amplitude of $\tilde{W}_{dia}/\tilde{P}_{RF}$ versus Ω Schematic evolution.

$$\alpha\tau < \alpha_{dia}\tau_{dia} \leq \alpha\tau + \frac{1}{4}\alpha_{min} t^*_{se}$$
$$\alpha < \alpha_{dia} \leq \alpha + \frac{1}{2}\alpha_{min} \qquad (3)$$

A non-stationary anisotropic quasilinear Fokker-Planck code [3] tells that, at high Ω, only the perpendicular part of the tail is modulated and, therefore, $\tilde{W}_{dia}/\tilde{P}_{RF}$ reaches the upper limit. Such a result favours high Ω experiments.

HFS antennae experiments

With the HFS antenna set-up [5], theoretical calculations [6] suggest that 80 % of the power is coupled directly to electrons via the mode conversion mechanism. Assuming $\alpha_{min}=0$, equation (2) becomes: $\tilde{W}_{DIA}/\tilde{P}_{RF} = \alpha/(j\Omega+1/\tau)$. In the discharges 24446-56 (fig 2a), a fit with the model of equation (1) gives: $\alpha = 0.5$ and $\tau = 54$ ms. In [4], a first analysis of this series has used $\tau_W = 12$ ms and provided $\alpha = 1$ able to satisfy low Ω simulations. The difference between the two analysis arises because the modulated pulse length was small leading to large error bars and because, for this limited series of discharges, $\Omega/2\pi$ was only varied from 2.5 to 22 Hz. Indeed, the experimental choice of Ω has a large incidence on the estimate of α and τ. Depending whether $\Omega << \tau^{-1}$ or $\Omega >> \tau^{-1}$ or $\Omega \approx \tau^{-1}$, $\alpha\tau$, α or τ can be accurately determined. Thus the above low Ω analysis could not accurately determine α. We therefore now analyse (fig 2b) a previously non-analysed series over which $\Omega/2\pi$ is varied in a much wider domain (8-480Hz). Because of the 1 kHz acquisition frequency, the point at 480 Hz close to the Shanon frequency is neglected. The error bars on the amplitude are small for high frequency modulated discharges because of the $1/\Omega$ dependence observed for the noise. The amplitude displays also a clear $1/\Omega$ behaviour which confirms the absence of a significative τ_W in the diamagnetic measurement in agreement with the τ_W obtained above from theory. A small time delay τ_{acq} introduced by the acquisition system explains the rising phase. Such a numerical delay affects only the phase and is modelled by $\tilde{W}_{DIA}/\tilde{P}_{RF} = \alpha\ \exp(j\Omega\tau_{acq})/(j\Omega+1/\tau)$. From the fit, we get: $\alpha = 0.4$, $\tau = 33$ ms, $\tau_{acq} \approx 0.4$ ms.

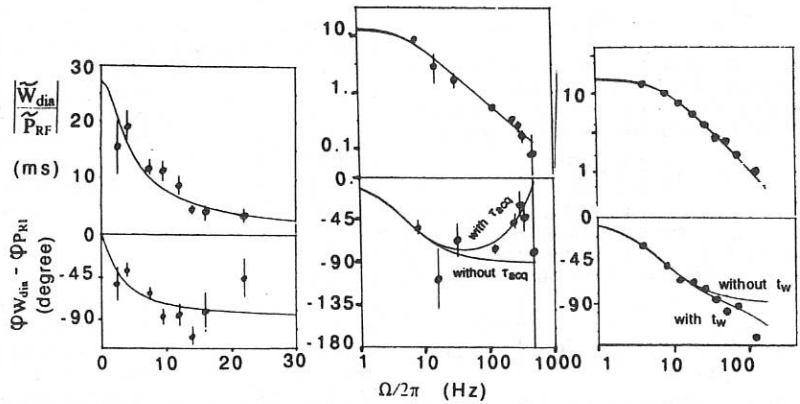

Figure 2. Experimental (amplitude and phase) transfer function of $\tilde{W}_{dia}/\tilde{P}_{RF}$ versus Ω. a) #24446-56, LFS antennae; b) #22780-7, LFS antennae, with and without τ_{acq} (0.4 ms); c) #40209-18, HFS antennae, with and without a τ_w (0.4 ms).

LFS antennae experiments

With the new low field side (LFS) antenna system [7], α_{de} [8] and α_{di} [6] are small. Therefore, the RF power is mainly absorbed by the minority ions ($\alpha \approx \alpha_{min}$). The stationary analysis of the difference between W_{equ} and W_{dia} shows that a perpendicular tail exists [9]. This anisotropy increases with Ω because only fast perpendicular particles are affected by the modulation. Therefore, experimental parameters of the fit are close to the right-hand limits of equation (3): $\alpha_{dia} = 3\alpha/2$. The following table gives α_{dia} and τ_{dia} for 3 series of modulated discharges.

#	α_{dia}	2/3 α_{dia}	τ_{dia}	
32450-56	0.70	0.47	15	
38544-52	0.54	0.36	28	antennae 1
	0.45	0.30	26	antennae 2
40209-18	0.70	0.47	21	fig 2c

If $1/\tau < \Omega < 1/\tau_W$, one modulated discharge is sufficient to determine $\alpha_{dia} \approx \Omega\ |\tilde{W}_{DIA}/\tilde{P}_{RF}|$. The influence on α_{dia} of the toroïdal field and the radial antennae position is studied hereafter with $\Omega/2\pi$ = 60 and/or 120 Hz (#44072-84).

antennae position	47 cm	51 cm
B_t = 2.25 T	α_{dia} = 0.63	α_{dia} = 0.57
B_t = 2.1 T	α_{dia} = 0.54	

In a pure H plasma (low absorption regime), we get α_{dia} = 0.1 for an ohmic target and α_{dia} = 0.25 with NBI. These low values, in agreement with theoretical predictions, confirm the validity of the method.

Experimental result summary

With HFS antennae, we measure $0.4 < \alpha < 0.5$ and with LFS antennae, $\alpha_{dia} < 0.7$ ($2\alpha_{dia}/3 < \alpha < \alpha_{dia}$). The two antennae configurations are similar with respect to the RF absorption mechanisms. Where is the remaining ICRH power going to? The answer is obtained from the careful study of the transport equation.

Transport equation

The non-stationary evaluation of W (equation 1) is an approximation of the following simplified transport equation:

$$\frac{\partial E}{\partial t} = \frac{1}{r}\frac{d}{dr}\left(r\,\chi\,\frac{dE}{dr}\right) + p_{RF} + p_{OH}$$

E, χ, p_{RF} and p_{OH} are the energy, the diffusivity, the RF heating and the ohmic heating deposition profiles. Linearising around the modulated perturbation, one gets:

$$j\Omega\tilde{E} = \frac{1}{r}\frac{d}{dr}\left(r\,\chi\,\frac{d\tilde{E}}{dr}\right) + \tilde{p}_{RF} \qquad (4)$$

The modulation of p_{OH} and χ are neglected. Inserting, in equation (4), an eigenfunction expansion $\tilde{E} = \Sigma\,\tilde{\alpha}_i\,E_i$ and projecting the resulting operation on the eigenfunction set, we get:

$$\tilde{a}_i = \frac{\langle E_i\,p_{RF}\rangle}{\langle E_i^2\rangle\,(j\Omega + 1/\tau_i)} \quad \text{with} \quad \langle\blacklozenge\rangle = \int_0^{\text{plasma radius}} \blacklozenge\; 2\pi r\,dr$$

τ_i is the confinement time of the i-th mode equal to the inverse of the i-th eigenvalue. Using $\tilde{W}=\langle\tilde{E}\rangle$, the transfer function becomes:

$$\frac{\tilde{W}}{\tilde{P}_{RF}} = \sum_{i=1} \frac{\alpha_i}{j\Omega + 1/\tau_i} \quad \text{with} \quad \alpha_i = \frac{\langle E_i\,p_{RF}\rangle\,\langle E_i\rangle}{\langle E_i^2\,p_{RF}\rangle\,\langle p_{RF}\rangle}$$

α_i is the fraction of the RF power absorbed in the plasma and coupled to the i-th mode. This transfer function shows that $\alpha(\Omega)$ defined as equal to $\Omega\,|\tilde{W}_{DIA}/\tilde{P}_{RF}|$ increases from 0 to $\Sigma\alpha_i = \alpha$ with Ω. Experimental confirmation of such an evolution of $\alpha(\Omega)$ is plotted on figure 3 (#40209-18, data of figure 2c). When $10 < \Omega/2\pi < 30$ Hz, $\alpha(\Omega) \approx 0.6$. This corresponds qualitatively to the RF power fraction coupled to the fundamental mode and absorbed by the plasma with the best confinement time. The remainder of the power goes to other modes with decreasing confinement times. Such a precise time-dependent analysis allows to distinguish qualitatively between the fraction of the power absorbed by the central core of the plasma (good confinement) and the fraction absorbed by the edge (poor confinement).

Conclusions

By analysing a great number of discharges with RF amplitude modulation at frequencies varying from 2 to 500 Hz, we have found that the RF power fraction absorbed by the plasma is roughly 50% whatever the antenna configuration (HFS or LFS) being used. A good estimate of this fraction can be obtained using only one discharge with high frequency modulation. From the transport equation, we have shown that an infinite series of decreasing confinement times is needed to correctly describe the energy transfer function. Each of them corresponds to a mode differently excited depending on the RF deposition profile. From this analysis, it was concluded that half of the power is coupled to the central core of the plasma with a good confinement time and that the remaining part is coupled to the edge with very low confinement time.

References

[1] G. Fuchs et al., internal report, KFA-IPP-1B-1/84. *[2]* V.S. Mukhovatov et V.D. Shafranov (1971) Nuclear Fusion 11 605 *[3]* D. Lebeau et al. (1990) Proceedings of the 17th Eur. Conf. on Plasma Physics and Control. Fusion, Amsterdam, Vol 14B 1044. *[4]* P.E. Vandenplas et al. (1986) 11th Int. Conf. on Plasma Physics and Controlled Fusion Research, IAEA, Kyoto, Vol 1 485 *[5]* A.M. Messiaen et al. (1986) Plasma Phys. Contr. Fusion 28 71 *[6]* D. Van Eester (1990) PhD thesis, KUL Leuven *[7]* G. Van Ooost et al. (1987) Fusion Technology 12 449 *[8]* D. Lebeau et al. (1990) Plasma Phys. Contr. Fusion 32 249 *[9]* A.M. Messiaen (1990) Invited paper. 17th EPS conf. on Controlled Fusion and Plasma Heating. Amsterdam.

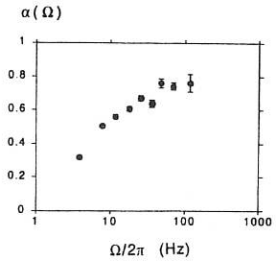

Figure 3. $\alpha(\Omega) = \Omega\,|\tilde{W}_{dia}/\tilde{P}_{RF}|$ versus Ω. #40209-18, HFS antennae

Neutron yield during ICRH and NBI modulation experiments in TEXTOR

Lebeau D., Van Wassenhove G., Delvigne T., Hoenen F.*, Sauer M.*

Laboratoire de Physique des Plasmas - Laboratorium voor Plasmafysica
Association "Euratom-Etat belge" - Associatie "Euratom-Belgische Staat"
Ecole Royale Militaire - B1040 Brussels- Koninklijke Militaire School

* Institut für Plasmaphysik, Forschungszentrum Jülich GmbH
Association "Euratom-KFA", D5170 Jülich, FRG

Introduction

In TEXTOR, the time evolution of the neutron emission is measured during discharges where the power amplitude of ICRH or NBI is modulated. By varying the modulation frequency of the additional power in a series of reproducible discharges, we construct the experimental transfer function (i.e. amplitude and phase versus the frequency) of the neutron yield versus the additional heating power. From the measured transfer function, we determine the different characteristic times: 16 ms and 1 ms during ICRH and 60 ms during NBI modulation. In section 1, the neutron production mechanisms relevant to our experiments are recalled. In section 2 and 3, the relations between the measured characteristic times and the slowing down and confinement times are explained.

1 Neutron production and detection

The neutron production reaction rate between ions of type i and j is given by:

$$R = \iint f_i(\mathbf{v})\, f_j(\mathbf{u})\, \sigma(|\mathbf{v}-\mathbf{u}|)\, |\mathbf{v}-\mathbf{u}|\, d^3\mathbf{v}\, d^3\mathbf{u} \qquad (1)$$

where f_i and f_j are the distribution function and σ is the cross-section of the reaction. In present TEXTOR conditions, the ions i and j are deuterium. When the neutrons are produced by collisions of maxwellian deuterium ions, equation (1) reduces to:

$$R = \frac{1}{2} n_D^2 \langle \sigma v \rangle$$

The reactivity $\langle \sigma v \rangle$ is a function of the ion temperature T_i of the plasma. n_D is the deuterium ion density. Therefore during ICRH modulation experiments, the modulation of the neutrons is mainly driven by the modulation of the majority ion temperature through the modulation of $\langle \sigma v \rangle$. In our analyses, we neglect the influence of a small density modulation.

During injection of a deuterium beam in a deuterium plasma in TEXTOR, neutrons are mainly produced by beam plasma interaction (95% in the analysed discharges). To calculate the beam plasma production rate, R, in equation (1), is evaluated considering a maxwellian distribution of the deuterium ions of the target plasma. The beam distribution function is classically developed in the quasi-spherical coordinates system (v,ξ). This leads to a Legendre polynomial expansion in ξ, the cosine of the pitch angle. Following Core [2], the integration on ξ is performed, showing that only the isotropic part of the beam distribution function g_b - first term in the Legendre polynomial expansion - plays a role:

$$R = 4\pi n_D \int [\sigma v]\, g_b\, v^2\, dv \qquad (2)$$

$[\sigma v](v,T_i)$ is the mean value of σv for monoenergetic ions of velocity v interacting with a maxwellian target plasma of temperature T_i. g_b is the isotropic part of the velocity distribution function of the beam.

The neutron detector [1] is a liquid scintillator not collimated and surrounded by a lead protection. The time resolution of the detection system is of the order of 1 ms. The neutron yield measured is proportional to the total emission. To calculate the total neutron emission an integration over the total plasma

volume is required. But, as the neutrons are coming principally from the central core of the plasma, local parameters are sufficient in a first order analysis.

2 ICRH modulation experiments

In the particular scenario of ICRH heating considered here, the absorption mechanisms are mainly the fundamental cyclotron heating of the minority ions (dominant mechanism) and, to a lesser degree, direct heating of electrons due to mode conversion and subsequent Landau or TTMP damping. The direct heating of majority ions due to second harmonic heating is found to be small according to ray-tracing calculations [3] and is neglected in the model. The power balance of the central energy density E_i of the majority ions (D) is used to explain the time evolution of T_i deduced from the neutron yield:

$$\partial E_i/\partial t = q_{e,i} + p_{min,i} - E_i/\tau_i \qquad (3)$$

q_{ei} and $p_{min,i}$ are the central power densities provided respectively by the electrons (equipartition) and by the minority ions (slowing down) through collisions and τ_i is the central energy confinement time of the majority ions.

Equation (3) is linearized assuming that the modulated quantities (~) have an $\exp(j\Omega t)$ dependence, Ω being the modulation frequency. Neglecting the modulation of the ion density (n_D) and of the equipartition power (q_{ei}) which are of the T_i and $p_{min,i}$ modulation, the transfer function of the ion energy becomes:

$$\frac{3}{2} n_D k \tilde{T}_i = \tilde{p}_{min,i} (j\Omega + 1/\tau_i)^{-1} \qquad (4)$$

In this equation, τ_i is the incremental value of the majority ion confinement time estimated around the mean parameters. The transfer function between the power transferred from minority ions to majority ions ($p_{min,i}$) and the RF power directly given to minority ions (p_{min}) has been studied in [4, equation 30]. Many characteristic times appear in this transfer function including those of the order of the slowing down time on majority ions $t_{s,i} = t_{s,e} \sqrt{m_e/m_i}$ [5]. $t_{s,e}$ is the slowing down time on electrons and m_α the mass of particles α. As an approximate result, one can consider:

$$\tilde{p}_{min,i} / \tilde{p}_{min} \approx (1 + j\Omega t_{s,i}/2)^{-1} \qquad (5)$$

Therefore, the transfer function of the ion temperature becomes:

$$\tilde{T}_i / \tilde{p}_{min} \approx (j\Omega + 1/\tau_i)^{-1} (1 + j\Omega\, t_{s,i}/2)^{-1} \qquad (6)$$

Figure 1 gives the experimental amplitude and phase of the ratio of the neutron yield to the RF power versus the modulation frequency (#38544-53; antenna 2). In the determination of $\tilde{T}_i$, the influence of the sawtooth period modulation [4] is neglected. The data are measured in a series of repetitive ICRH modulated discharges (Ω varying from 5 to 45Hz). By adjusting a model similar to equation (6) to this data, we identify experimentally two characteristic times: 16 ms and 1 ms. The first is related to τ_i and the second to $t_{s,i}/2$.

The incremental confinement time of the majority ions can be, therefore, measured in the central core of the plasma by the analyses of the neutron yield during ICRH modulation. The value, estimated to 16 ms, is smaller but close to the incremental energy confinement time measured from the diamagnetic energy response to ICRH modulation [6]. A second characteristic time of 1 ms confirms the theoretical prediction proposed in [4] which states that $t_{s,i}/2$ is the characteristic time of the power transfer between minority ions and majority ions.

3 NBI modulation experiments

In the case of NBI heating (D beam in D plasma) the power modulation is obtained by varying the beam current of the co-injected beam [7]. The analysed discharges are sawtooth-free during beam injection (#41362-8). The modulation frequency $\Omega/2\pi$ is varied from 2.5 to 20 Hz. The measured transfer function between neutron rate and beam intensity is presented in figure 2. Observing that the phase delay tends to reach -90° and that the amplitude has a $1/\Omega$ asymptotic behaviour, we first fit the experimental data with the model:

$$\frac{\tilde{R}/R_o}{\tilde{I}/I_o} = (1 + j\Omega t_R)^{-1} \qquad (7)$$

and determine a characteristic time t_R of 60 ms. Subscript o makes reference to stationary values. This characteristic time t_R is 7 times smaller than the slowing down time on electrons ($t_{se} \approx 400$ ms). To understand the relation between t_R and t_{se}, a calculation of R taking into account the time dependent velocity distribution function of the beam is developed. This distribution function satisfies the Fokker-Plank equation:

$$\frac{\partial g_b}{\partial t} = \mathcal{C}(g_b) + S(v,t) \qquad (8)$$

S is the isotropic part of the source term directly connected to the modulated beam intensity I(t) through:

$$S(v,t) = \frac{I(t)}{4\pi v^2}\,\delta(v-v_b) \qquad (9)$$

and $\mathcal{C}$ is a simplified collision operator:

$$\mathcal{C} = \frac{1}{t_{se}v^2}\frac{\partial}{\partial v}(v^3+v_c^3)g_b \qquad (10)$$

The Fokker-Plank equation is solved following the method of Gaffey [8]:

$$g_b(v,t) = \frac{t_{se}}{v^3+v_c^3}\,I(t-\tau(v))\,U(v_b-v) \qquad (11)$$

$$\text{with} \quad \tau(v) = \frac{t_{se}}{3}\ln\left(\frac{v_b^3+v_c^3}{v^3+v_c^3}\right)$$

U is the step function, v_b is the beam velocity and v_c is the beam critical velocity defined in [8]. Introducing eq. (11) in eq. (2) gives:

$$R = t_{se}\,n_D\int_0^{v_b}[\sigma v]\,I(t-\tau(v))\,\frac{v^2\,dv}{v^3+v_c^3} \qquad (12)$$

At first order, R is insensitive to the modulation of n_D because of the $1/n_D$ dependence of t_{se}. The modulation of I is developed around the perturbation as in the previous section. The modulated reaction rate becomes:

$$\tilde{R} = \tilde{I}\,t_{se}\,n_D\int_0^{v_b}[\sigma v]\,e^{-j\,\Omega\,\tau(v)}\,\frac{v^2\,dv}{v^3+v_c^3} \qquad (13)$$

To compare the experimental data with a model based on equation (13), we neglect the plasma volume integration. As 90 % of the neutrons are produced by the full energy component of the beam, the two other components are neglected. The theoretical evolution of the phase and of the amplitude of $\tilde{R}$ versus Ω is calculated using a good fit of the reaction rate in the vicinity of v_b: $[\sigma v] = A\,v^B$; B = 5.2. An important point is that the best agreement between the data and the model is obtained just by using a t_{se} of 0.4 s and v_c/v_b of 0.8, values deduced from experimental measurements at r = 10 cm, the radius of the maximum neutron production. In some sense, NBI modulation allows us to measure t_{se} in this region..

Our model explains correctly the time response of the neutron yield during NBI modulation and, particularly, the presence of such a small characteristic time. To give an intuitive idea of the origin of such characteristic time, eq. (13) is solved analytically in the limit $v_c/v_b \rightarrow 0$. The calculation gives a transfer function with one characteristic time $t_{se}/B \approx 77$ ms. As a general rule, any moment of order α of the distribution function g_b will give the characteristic time t_{se}/α if collisions with majority ions are neglected with respect to collisions with electrons. Collisions with majority ions will further reduce the observed characteristic time.

Another mechanism which tends to diminish the characteristic time is the presence of charge exchange losses. These are studied by adding a term $-g_b/t_{cx}$ (t_{cx} being the mean charge exchange lifetime of a particle) in equation (8). A rough estimation based on the neutral particle confinement time gives t_{cx} = 90 ms which influence on $\tilde{R}$ is shown in figure 2. In the intuitive model obtained taking $v_c/v_b \rightarrow 0$, the presence of charge exchange losses decreases the characteristic time which becomes $(B/t_{se}+1/t_{cx})^{-1}$.

We finally point out the parasitic effects associated with the unavoidable modulation of T_e and v_b. These modulations can lead, at the lowest frequencies, to rather large correc-

tions explaining, partly, the discrepancies remaining between the experiment and the theoretical model.

Conclusion

We measure the time dependent evolution of the neutrons yield during ICRH and NBI modulation and observe completely different behaviours. During ICRH, this evolution reflects the time evolution of the ion temperature. From the majority ion energy balance in the case of minority heating, transfer function of the ion temperature is modelled with 2 characteristic times. By fitting the experimental points with the model, a method is proposed to measure the ion confinement time of the central part of the plasma and the mean ion slowing down time. During NBI, the neutron yield evolution is governed by the time evolution of the beam distribution function. A theoretical study allows us to understand why the characteristic time measured from experimental points is 7 times smaller than the slowing down time on the electrons.

Acknowledgements

The authors thank Drs. Messiaen and Koch for helpful discussions and Dr. Conrads for his support of NBI modulation experiments.

References

[1] Th. Delvigne et al. (1990) Proceedings of the 16th Symposium on Fusion Technology SOFT, London, to be published.

[2] W.G.F. Core, JET report, IR(87)11

[3] D. Van Eester (1990) Ph.D. Thesis, K.U.L. Leuven

[4] D. Lebeau et al. (1990) Plasma Phys. Contr. Fusion **32** 249

[5] D. Anderson et al. (1987) Nucl. Fusion **27** 911

[6] D. Lebeau et al. (1991) this conference F-56.

[7] H. Conrads et al. (1990) Proceedings of the 16th Symposium on Fusion Technology SOFT, London, to be published.

[8] J.D. Gaffey (1976) J. Plasma Physics **16**, part 2, 149.

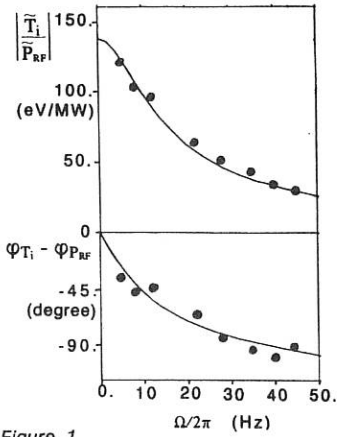

Figure 1
Evolution of $\tilde{R}/\tilde{P}_{RF}$ versus $\Omega/2\pi$.
Amplitude and phase delay.
Circles: experimental data
Line: theoritical model
ICRH modulated discharges.

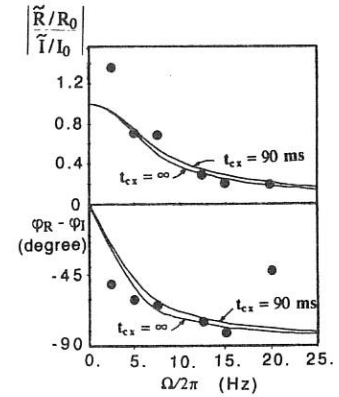

Figure 2
Evolution of $(\tilde{R}/R_o)/(\tilde{I}/I_o)$ versus $\Omega/2\pi$.
Amplitude and phase delay.
Circles: experimental data
Lines: theoretical model with t_{se} = 400ms and v_c/v_b = 0.8.
NBI modulated discharges.

ICRF H-mode Coupling and Heating in BPX and JET*

J.E. Scharer, N.T. Lam and M. Bettenhausen
Electrical and Computer Engineering Department

University of Wisconsin, Madison, WI 53706-1687, USA

ABSTRACT

ICRF coil launcher coupling to BPX density and temperature profiles is considered. The dependence of the ICRF launcher radiation resistance on the density profile and its gradient is studied. Our ANTIMP cavity code as well as a modified Brambilla code are used to examine the coupling. For BPX, we find that the radiation resistance decreases by a factor of about two during the L- to H-mode transition. The use of four coax end-feeds to drive each coil for H-mode coupling is found to increase the radiation resistance as compared to a two-feed case. The problems of fundamental minority ^{3}He and D heating scenarios are addressed for BPX utilizing XWAVE, a code which treats full wave effects including reflection, mode conversion and absorption. The power conservation relation follows from a definition of local power absorption and a companion general expression for kinetic flux based on fundamental principles. Wave absorption, reflection and mode conversion for possible scenarios including fundamental deuterium or ^{3}He are presented.

I. Calculation of Plasma Coupling - We consider the effects of the L- to H-mode transition on launchers designed for fast wave heating of tokamaks, specifically BPX [1]. The launcher configuration is a recessed cavity. For the fast wave, we may assume $E_z = 0$ everywhere. Between the antenna and the Faraday shield, the transverse components E_y and B_z can be decomposed in terms of the cavity eigenfunctions $F_{mn}(y,z)$. At the antenna, we have explicitly :

$$E_y = \sum_{mn} A_{mn}F_{mn}(y,z) \text{ and } H_z = \sum_{mn} D_{mn}B_{mn}F_{mn}(y,z) \text{ , where } D_{mn} = \text{mode admittance.}$$

Continuity of E_y and H_z at the launcher-plasma interface yields a system of linear equations for A_{mn} and B_{mn}. The coefficients of this system involve a matrix element $L_{mn;m'n'}$ which can be expressed as an integral over k-space :

$L_{mn;m'n'} = \frac{1}{4\pi^2}\int Y_{zy}(k_y,k_z)F^{*}_{mn}(k_y,k_z)\,F_{m'n'}(k_y,k_z)\;\; dk_y dk_z$, where $F_{mn}(k_y,k_z)$ is the Fourier transform of $F_{mn}(y,z)$ and Y_{zy} = plasma surface admittance = H_z/E_y at the plasma-launcher interface. The calculation of Y_{zy} for a cold plasma has been discussed in [2]. Further, we impose the discontinuity condition at the antenna : $D_{mn}[B_{mn} - A_{mn}] = J_{mn}$ with $J_{mn} \propto$ Fourier component of the antenna current density. With an antenna oriented along the y-direction, the power radiated by the antenna is given by $1/2\Re e\,[\int J^{*}_{y}E_y dy] \propto \Re e\,[\sum_{mn} J^{*}_{mn}A_{mn}]$. Thus, given the antenna current density and plasma density profiles, we can calculate the coefficients A_{mn} and the radiation resistance of the antenna. We have implemented these calculations with our code ANTIMP, which has been benchmarked against a finite element code developed by M. Brambilla [3].

II. Power Conservation and Wave Heating in the Plasma Core -- Our work is distinct in providing fundamental definitions of local power absorption and kinetic flux. The total power absorbed by all the particles passing through $\bar{r}$ is obtained [4] by an integration over v.

$$P(\bar{r}) = \int d^3v \; < q\bar{E}(\bar{r}',t') \cdot \bar{v}' \, f^{*}_{1}(\bar{r}',\bar{v}',t') > \qquad (1)$$

where < > denotes the time-average over t' and the star indicates the complex conjugate. Kinetic flux is the flux of energy carried by the coherent oscillation of plasma particles. The amount of energy being transferred between the particles and the wave at time t' is given by

$$\Phi = \Re e\,[E(r', t') \cdot v']\,\Re e\,[f_1(r', v', t')] \qquad (2)$$

The total energy gained or lost by the particles since a time τ seconds before t until t is $\int_0^t \Phi(\tau')\,d\tau'$. Φ contains a **secular** part which we designate as $< \Phi >_\tau$. The total kinetic flux is identified as

$$S_k = \int d^3v\, v \left\langle \int_0^{\infty} (\Phi - <\Phi>_\tau)\, d\tau \right\rangle_t \quad . \qquad (3)$$

The evaluation of the kinetic flux terms in Eq. (3) to third order is carried out in the same manner as that for local power absorption. A computer code, XWAVE, has been written which solves the wave equation for a fast wave incident from either the high or low magnetic field side of the mode conversion zone or for a Bernstein

wave incident from the high-field side. It also computes the local power absorption profile for each particle species and the power flux.

III. Results -- We consider coupling for a BPX-like plasma with the following parameters: major radius R = 259 cm; minor radius a = 79 cm; B_0 = 9.0 T; 1-1 D-T plasma with central electron density $n_e = 4.0 \times 10^{14}$ cm^{-3} ; percentage of ^{3}He = 2% of the total electron density; heating frequency f = 85 MHz. For our calculations, we examine piece-wise linear and parabolic density profiles , i.e. $n = [n_0 - n_{sep}][1 - (x/r_{sep})^2]^{\alpha} + n_{sep}$ with $n_{sep} = 10\%\ n_0$ and $\alpha = 1.0\ (0.25)$ for the L (H) -mode. Figure 1 shows the variation of R_{rad} vs. Δ (a parameter inversely proportional to the density profile gradient at the separatrix) for the semi-infinite and finite cavities. The antenna consists of two uniform current straps, driven in the $(0,\pi)$ mode. The cavity width is set at 59.8 cm and we have chosen the cavity height as 10 m and 1.1 m for the semi-infinite cavity and infinite cavity, respectively. For BPX parameters, the effect of finite cavity height is seen to reduce R_{rad} by 20%. Figure 2 shows R_{rad} vs. the effective antenna propagation constant for the 2-feeder and 4-feeder shemes. Both the L- and H- modes are also shown. These results have been obtained using a modified version of the Brambilla code. Note that R_{rad} drops by a factor of 2 to 3 during the L- to H-mode transition. The effect of the 4-feeder scheme is to make the antenna current more uniform, thereby increasing R_{rad} by 34%, as compared to a 2-feeder scheme.

We next consider the field solutions, power absorption and power conservation for low-field fast wave incidence for BPX ohmic conditions, where $n_e = 2.5 \times 10^{14}$ cm^{-3}, $n(^3\text{He}) = 1.5\%\ n_e$ with $n_D = n_T = 43.5\%\ n_e$, T = 3 keV, and B_0 = 8.48 T. The region of the plasma that is examined is the ±15 cm core around the axis at R_0 = 2.79 m. Figure 3 illustrates the resulting absorption, reflection, mode conversion and transmission for the case when the wave frequency is equal to the the fundamental ^{3}He cyclotron resonance on the axis. At low $k_{\|}$, reflections from the absorption zone with significant mode conversion exist. At higher $k_{\|} \approx 15$ m^{-1}, the ^{3}He absorption dominates (63%), with some second harmonic tritium and electron absorption in the core.

Figure 4 illustrates the results for ^{3}He minority heating in a burning BPX case with $n_e = 5.0 \times 10^{14}$ cm^{-3}, $n(^3\text{He}) = 2\%\ n_e$, $n_D = n_T = 43\%\ n_e$, T = 20 keV, B_0 = 9.0 T. In this case, the core is defined as the central ±20 cm region around R_0 = 2.79 m. Note that the absorption is almost complete over the 6 m^{-1} < $k_{\|}$ < 20 m^{-1} region.

Electron and second harmonic tritium heating are strong (≅ 20% each) over a wide part of the spectrum. Other heating scenarios for BPX and JET have also been examined.

IV. ACKNOWLEDGEMENTS

Research supported by U.S. DOE grant No. DE-FG02-86ER53218 and Princeton Contract S-3204G.

[1] CIT Physics Design Description, PPPL, Jan. 1990.
[2] N.T. Lam and J.E. Scharer, Fus. Eng. and Design **12**, 1 (1990).
[3] M. Brambilla, Nucl. Fus. **28**, 549 (1988).
[4] R.S. Sund and J.E. Scharer, Physics of Fluids, May, 1991.

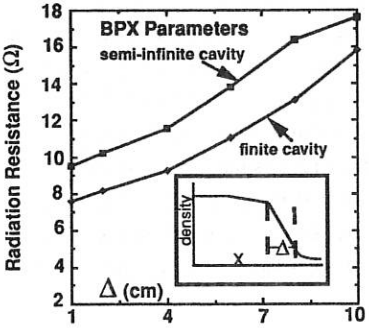

Figure 1

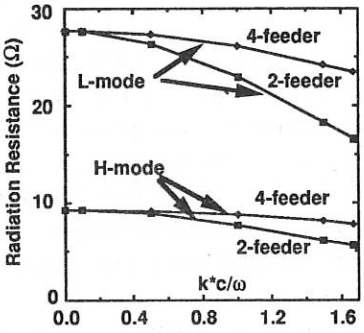

Figure 2

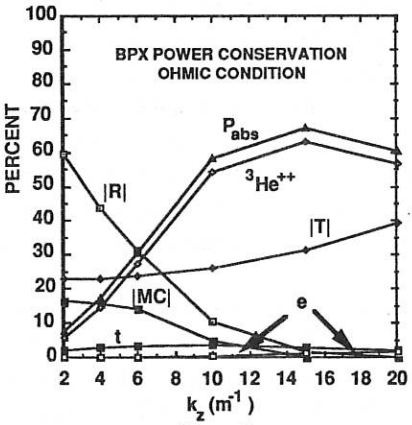

Figure 3

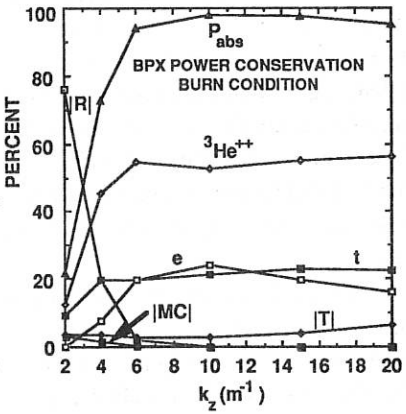

Figure 4

ELECTRON HEATING IN JET BY ICRH

J.G. Cordey, J.P. Christiansen, W.G.F. Core, G.A. Cottrell, L-G. Eriksson, M.A. Kovanen, P. Lomas, D.F.H. Start, A. Taroni and F. Tibone.

JET Joint Undertaking, Abingdon, Oxon, OX14 3EA, U.K.

I Introduction

Several ICRH experiments carried out on JET during the period 1988-90 have been directed specifically at raising the electron temperature to a high value by maximising the total input power per particle (P_{tot}/n). It has been found [1] that the electron temperature saturates around 12-14 keV in sharp contrast to NBI ion heating experiments in which ion temperatures exceed 25 keV.

Initial calculations [2] suggested that this saturation was due to strongly enhanced transport in the central region. It is shown in this paper that the saturation is due to a lack of heating in the plasma centre. The power input to electrons in an ICRF minority heating scheme is mainly via collisional transfer from the minority fast ions and a main problem is to maintain a peaked profile of fast ions. In the present experiments the highest fast ion energy content 4 MJ has been achieved with a He^3 minority scheme, the equivalent fast ion toroidal β is 8%; electron temperatures in the range 11-14 keV are attained in these pulses.

There are several possible physical effects that can give rise to the broadening of the fast ion radial profile: sawteeth, fishbones, fast ion finite orbit effects and Alfvén or drift wave turbulence driven by the large gradients of fast ion pressure (discussed in section IV). The existence of such phenomena in many JET pulses means that the calculation of the power input profile by codes which contain purely classical collisional processes can be misleading. Hence an alternative approach is developed in section II; the measured fast ion energy is used directly to evaluate the power input to the central region; the scaling of the electron temperature with the actual power per particle can therefore be determined (section III).

II Direct calculation of power input to the electrons from measured fast ion content

The power transferred to the electrons from fast ions inside a normalised radius ρ (= r/a) is

$$P(\rho) = \pi a^2 \int_o^\rho \frac{w_{fast}}{\tau_s} d\rho^2$$

where w_{fast} is the *local* flux surface averaged fast ion energy density and τ_s ($\sim T_e^{3/2}/n$) is the local fast ion slowing down time. To relate the power $P(\rho)$ to the total fast ion energy content W_{fast} we assume gaussian spatial profiles for

W_{fast}, T_e, n_e (half widths a_f, a_T, a_n). The power deposited inside the half width of the temperature profile is given by

$$P(a_T) = \frac{W_{fast}}{\tau_s(o)}\, g \qquad (1)$$

where $g = \left[1 - \exp\left(\frac{3}{2} - a_T^2/a_f^2 - a_T^2/a_n^2\right)\right] / \left[1 - \frac{3}{2} a_f^2/a_T^2 + a_f^2/a_n^2\right]$

Over the region of interest $0.2 < a_f < a_T$ the function g is almost constant ($1<g<1.3$). Thus in the following use will be made of equation (1) to estimate the power deposited in the central region. W_{fast} in Eq. (1) is obtained from the difference between diamagnetic and MHD measurement of the total stored energy: $\frac{4}{3}$ (W_{dia} - W_{MHD}) ≡ W_{fast} -3 $W_{fast||}$ ~ 0.7 W_{fast}.

The main advantage of using equation (1) is that it gives a simple direct measure of the central input power and takes into account any broadening of the heating profile due to sawteeth, fishbones, FLR effects etc.

III Scaling of the central electron temperature with power per particle

In Fig. 1 the scaling of the central electron temperature (ECE) versus the total ICRH power per particle is shown for a representative data set. This data shows the saturation of the electron temperature with the applied power per particle at around $P_{tot}/n \sim 4$. The contours of Fig. 1 refer to the fast ion energy content that would be required to provide the central heating power/particle and temperature given by Eq. 1. If all those data points of Fig. 1, for which the 'measured' power using Eg. (1) is at least 30% less than the applied power, are omitted, then the saturation of temperature with power/particle is no longer apparent; those data points are marked in Fig. 1 by open circles. In fact an offset linear scaling ($T_e \sim 3.5 + 2.1\ P/n$) is a reasonable fit to the data. Such a scaling is similar to that obtained for ions in L-mode plasma (see Fig. 2) confirming the result originally obtained by P. Thomas et al [3] that the central electron and ion confinement properties in L-mode are very similar.

An alternative data representation, shown in Figure 3, is to plot T_e against W_{fast}. From equation (1) we can relate any scaling of $T_e(o)$ with $P(a_T)/n(o)$ to a scaling of T_e with W_{fast}. Two scalings are also shown in Fig. 3: curve (1) is the offset linear scaling of Fig. 1 and curve (2) is a pure gyro-Bohm scaling, $T_e(o) \sim [P(a_T)/n(o)]^{2/5}$. The significance of the data representation in Fig. 3 is that *all* data points (both open and closed circles in Fig. 1) now follow the same scaling. Extrapolations show that to obtain T_e (o) ~ 20 keV requires the confinement in JET of a fast ion energy content in excess of 12 MJ, equivalent to a $\beta_{fast} \sim 24\%$!

IV Mechanisms which broaden the fast ion profile

A study has been made of those pulses (marked by open circles in Fig. 1) for which there is a discrepancy between the fast ion energy content and that expected from classical coulomb processes. It appears that no single phenomena is wholly responsible for the discrepancy. There is clear evidence that both

sawteeth and fishbones expel fast ions from the central region. We therefore investigate if fast ion finite orbit effects can explain the remaining discrepancy.

In the example shown in Fig. 4 the fast ion energy content is shown versus time for a typical high P/n pulse with a hydrogen minority. The top curve is a calculation using the PIONT [5] code in which the fast ions are described by a zero banana width Fokker Planck solver. The result can be seen to be somewhat larger than the measured fast ion energy.

Several approaches have been used to estimate the fast ion finite orbit effects on the broadening of the heating profile. The curve labelled PIONTO in Fig. 4 is from a code with an approximate orbit model. The single point D is the modified Stix model of Cottrell and Start [5] and the point H is the full Monte Carlo treatment of ICRH [6]. Figure 4 shows that a significant part of the discrepancy between measured and theoretical value of W_{fast} is accounted for by finite orbit effects. The residual discrepancy is within experimental error bars, but additional non-classical processes cannot be excluded. The effect of finite orbit effects on the heating power profile is shown in Fig. 5 [6].

V Conclusion The "apparent" saturation of the electron temperature with ICRF power is caused by a saturation of the central heating power density and is not a transport phenomena. Several effects which broaden the heating profile have been studied; fast ion FLR effects account for a significant part of the broadening.

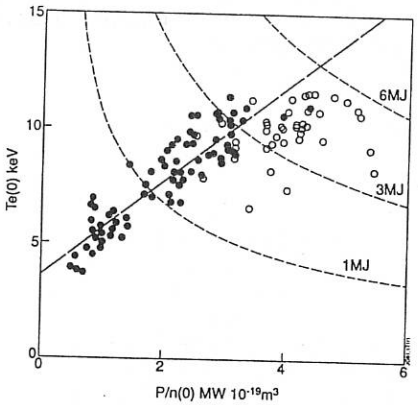

Fig. 1. T_e (o) versus ICRH power per particle P_{RF}/n (o). The 'measured' power deposited in the centre is within 30% of the applied power for the solid points and outside this range for the open points.

[1] S. Attenberger, et al., 17th EPS Conf. Amsterdam, Vol 1 (1991) 5.
[2] P.H. Rebut, et al., 13th IAEA Conf. Washington, IAEA-CN-531A-1-2 (1990).
[3] P. Thomas, et al., 12th IAEA Conf. Washington, IAEA-CN-531A-1-2 (1990).
[4] L.G. Eriksson, U. Willén and T. Hellsten, Proceedings of the Joint Varenna-Laussanne International Workshop on "Theory of Fusion Plasmas", Varenna, Italy, August 27-31, 1990, p 421.
[5] G. Cottrell, D.F.H. Start, Nucl. Fusion, 31 (1991) 61
[6] M.A. Kovanen, W.G.F. Core, JET Preprint JET-P (90) 40.

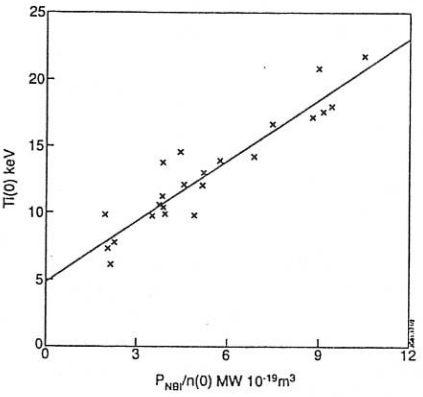

Fig. 2. Central ion temperature versus NBI power per particle.

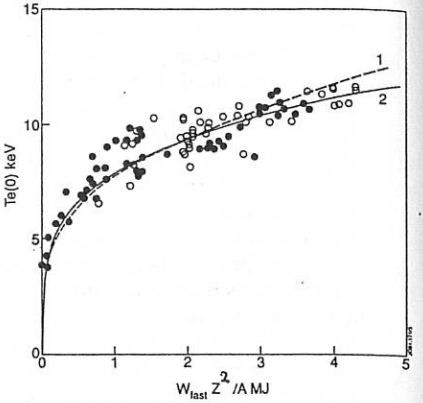

Fig. 3. T_e (o) versus the measured fast ion energy $\frac{4}{3}$ (W_{dia} - W_{MHD}) Z^2/A. Curve (1) is an offset linear form $T_e(o) = 3.5 + 2.1\ P(a_T)/$ and curve (2) is a pure gyro - Bohm form $T_e(o) \alpha [P(a_T)/n(o)]^{2/5}$. The solid and open points have the same meaning as in Fig. 1.

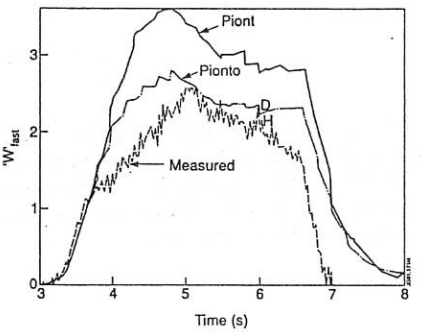

Fig. 4. Fast ion energy versus time: measured and two simulations.

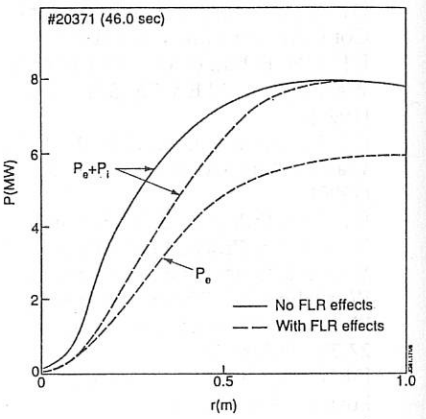

Fig. 5. Integrated power within radius r versus radius r with and without finite orbit (FLR) effects.

FAST ELECTRON DYNAMICS DURING LHCD ON JET

P.Froissard, M.Brusati, J.M.Adams#, A.Ekedahl, C.Gormezano, O.N.Jarvis, D.Pasini, Y.Peysson*, M.C.Ramos de Andrade, F.Rimini, G.Sadler

JET Joint Undertaking, Abingdon, Oxon OX14 3EA, UK
#AEA Industrial Technology, Harwell Laboratory, Didcot, OX11 0RA, UK
*CEN Cadarache, 13108 St Paul lez Durance, France

INDTRODUCTION

Lower Hybrid driven currents in tokamaks are carried by suprathermal electrons created via Landau Damping of a high directivity spectrum of Lower Hybrid waves.

In the initial phase of the JET LHCD experiments (1), up to 1.6 MW of LH power was coupled to a variety of plasmas, with a 70% directivity narrow spectrum peaking at $N_{//} = 1.8$, corresponding to a resonant parallel electron energy of 100 keV. These fast electrons emit a continuum spectrum of bremsstrahlung when colliding with the ions and thermal electrons in the plasma (fig 1).

The Fast Electron Bremsstrahlung (FEB) diagnostic is a multichord detection system designed to detect hard X-ray emission in the range 100 keV upwards. It has been developed on JET to provide information on the energy, location and density of fast electrons in order to assess the LHCD performance.

DIAGNOSTIC HARDWARE

The FEB diagnostic comprises two cameras of 9 and 10 detectors looking at a poloidal cross section of the plasma. It is located in the same concrete shielding and with the same viewing geometry as the JET Neutron Emission Profile Monitor (2).

For the first experiments only the vertical camera was in use (figure 2). The lines of sight are viewing the plasma through a 1.5 mm Inconel port window. The radial resolution in the mid plane of the vessel is around 12 cm for the central lines and 15 cm for outer lines.

The detectors used are 10 x 10 x 15 mm^3 CsI (Tl) crystals coupled to Si photodiodes. The low energy limit of analysis is 100 keV dictated by detector noise and signal absorption in the window.

The data acquisition system recorded signals corresponding to 4 equal energy intervals in the range 100 to 300 keV for each detector. With the present electronic setting, a count rate up to 20 kHz could be achieved without significant pile-up effects.

EXPERIMENTAL RESULTS

Results (3) have been obtained for different deuterium plasmas at 2.8 T, 2 and 3 MA, with line average density ranging from 1.5 10^{19} to 4. 10^{19} m^{-3}, central

electron temperature from 3 up to 10 keV and different levels of ICRH and NBI injected power.

The time evolution of the measured signal for a central line of sight is shown in figure 3. A 100% signal modulation is observed during 100% LH power modulation. When NBI or ICRH is employed, a background of high energy gamma ray and neutron signal is detected. However analysis of LH X-ray emission is possible for moderate levels of ICRH.

In low density plasmas, the fast electron energy spectrum extends up to 500 keV while at high density the upper limit is reduced to 300 keV, showing that the fast electron energy content scales inversely with the plasma density.

DYNAMICS OF FAST ELECTRONS

The behaviour of fast electrons in the plasma has been studied using the 100% LH power modulation at 2 Hz (figure 4).

The characteristic rise time τ_R and decay time τ_D of the detected signal are functions of Landau damping rate, the fast electron slowing down time and diffusion in phase space. Figure 5 shows the variation of τ_R and τ_D with Bremsstrahlung energy (E) and compares it with the fast electron classical slowing down time on the bulk.

The $E^{3/2}$ dependence of the slowing down time is in very good agreement with the measurement of τ_R in the 4 energy windows. τ_D on the other hand, decreases with increasing energy. A model is being developed to investigate the energy dependence of the diffusion process.

PROFILE EFFECTS

Seven out of the possible nine lines of sight were used for profile analysis, as the innermost line was not operational and the signal measured on the outermost line included a contribution of thick target bremsstrahlung due to fast electrons striking the bottom belt limiter.

Most of the results have been obtained for limiter plasmas with the plasma centre located between channel 15 and 16, as indicated in figure 6. A misalignment between the detector box and the collimator array resulted in some uncertainty concerning the detector areas exposed to X-rays, leading to large error bars on the profile data. The preliminary results indicate hollow line integrated emission profiles, with hollowness increasing with energy and electron density. While the density dependence could be explained in the framework of LH current drive theory, the energy dependence of the profile is currently being investigated. A fit of the profile can be achieved using a strongly hollow local emissivity profile peaked at 50 cm from the plasma centre. Assuming a smooth variation of the fast electron distribution function with plasma radius, this profile is a good representation of the fast electron density profile.

CONCLUSION

First results obtained by the FEB diagnostic have shown:

- A large hard X-ray signal is observed during LH power on JET.
- The characteristic rise time of the signal obtained during LH power modulation is comparable with the fast electron slowing down time, while the decay time seems strongly influenced by diffusion.
- Hollow emissivity profiles have been measured with profile hollowness increasing with electron density and fast electron energy.

The next experiments will be done using the two cameras, which will allow local analysis of the X-ray emission to be performed.

REFERENCES

1. M Pain et al., 13th Symposium on fusion engineering, Knoxville '89
2. J.M.Adams et al., 14th Eur. Conf. Ctr. Fusion & Plasma Physics Madrid '87
3. C.Gormezano et al., this proc.

Fig. 1

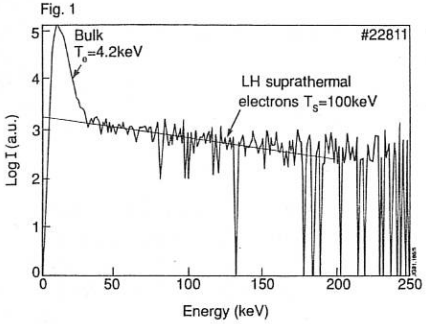

Hard X-ray energy spectrum obtained by X-ray PHA using a Ge diode detector.

Fig. 2

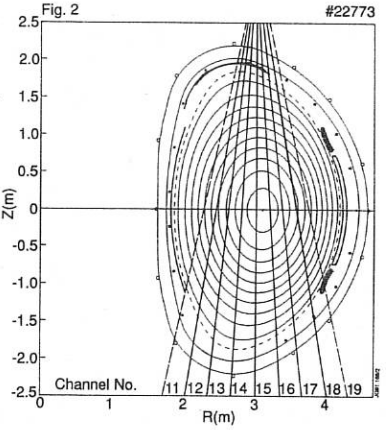

FEB viewing lines for the vertical camera.

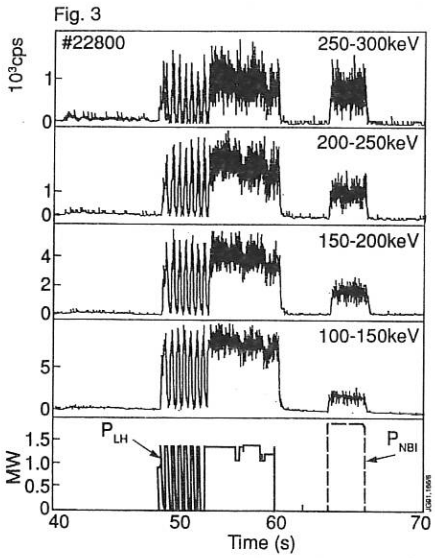

Time evolution of measured signal for ch# 16 and the applied LH power.

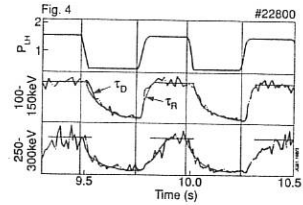

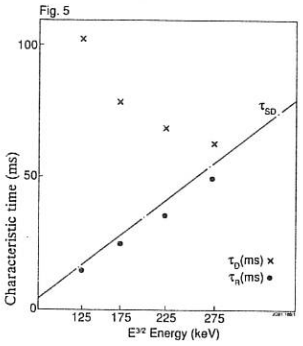

Modulation experiment.
τ_R and τ_D evolution with $E^{3/2}$

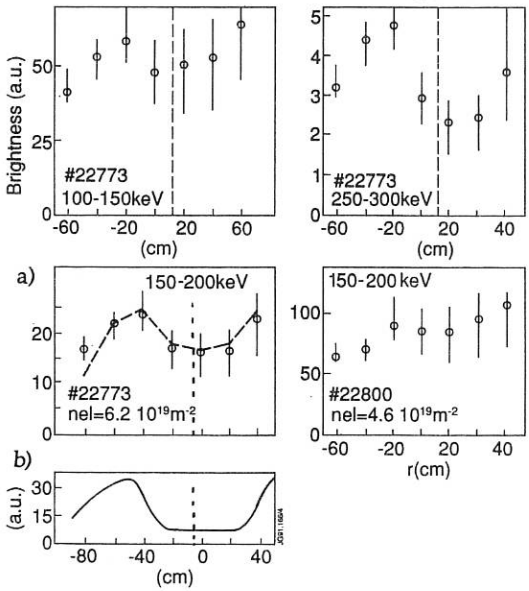

Profile evolution with energy and plasma density. The vertical dashed line indicates the plasma centre. The experimental profile a) can be fitted by the local emissivity profile b).

LOWER HYBRID CURRENT DRIVE EXPERIMENTS ON JET

C.Gormezano, G.Bosia, M.Brusati, J.Dobbing, A.Ekedahl, P.Froissard, J.Jacquinot, A.Kaye, M.Lennholm, O.Naito*, M.Pain, F.Paoletti, D.Pasini, C.Ramos de Andrade, G.Rey#, F.Rimini, P.Schild.

JET Joint Undertaking, Abingdon, Oxon, OX14 3EA, UK

* On leave from JAERI # On leave from CEN Cadarache

SUMMARY

Current density profile control in JET can be achieved by using Lower Hybrid Current Drive. In the JET LHCD system the narrow parallel wave spectrum, at a frequency of 3.7 GHz, can be adjusted from $N_{//} = 1.4$ to $N_{//} = 2.4$ /1/. While the full system, capable of launching 10 MW of power, is being prepared, initial experiments have been carried out with a prototype launcher, allowing up to 1.6 MW of LH power to be coupled to the plasma for up to 20 sec /2/ in the following experimental conditions:

- Limiter or double null (L mode) plasma configurations
- Plasma current: 2 to 3 MA - toroidal field Bt = 2.8 to 3 Tesla
- central density: 1 to 3 10^{19} m^{-3} - Zeff : 1.6 to 2.2

The electron temperature was varied from 3 to 9 keV by combined operation of LH and Ion Cyclotron Resonance Heating at power level up to 4.5 MW (H minority in D plasmas, in monopole antenna configuration at 42 MHz). The following main results have been achieved.

- Significant loop voltage drop (50%) for densities up to $n_{eo} = 3\ 10^{19}$ m^{-3}, corresponding to LH non inductive current up to 1 MA.
- Broadening of the current profile which increases with plasma density.
- Sawtooth free period up to 2.9 sec in ICRF heated plasmas.
- Improved current drive efficiency up to $nRI/P = 0.4\ 10^{20}$ m^{-2} when the volume averaged electron temperature increases up to 1.9 keV due to ICRH and LH application.
- Increase of the central electron temperature.

CURRENT PROFILE CONTROL

The behaviour of the current profile is monitored by the time evolution of the internal inductance l_i and of the second Shafranov moment as obtained from the magnetic equilibrium reconstruction code IDENTC.

Typical time variation of l_i with and without ICRH is shown in fig 1. During the ohmic phase, the inductance decreases and eventually reaches a steady state after a duration time of about 8 sec, close to the current diffusion time. When ICRH is applied, the peaking of the current leads to an initial rise of

the inductance. After 0.5 sec, the inductance saturates and remains constant throughout the rest of the ICRH pulse, indicating that the current broadening due to LHCD compensates current peaking caused by electron heating. It is to be noted that Z_{eff} remains constant for the entire pulse.

The current broadening is also evident in fig 2, where radial profiles of the safety factor q (from magnetic analysis) are given for plasma shots with and without LHCD and are compared with the sawtooth inversion radius determined from soft x-ray emission measurements. Central q rises from 0.8 to 0.9. Current broadening appears to increase with density up to 3 10^{19} m^{-3}, above which value higher power would be required to achieve further flattening.

The current profile effects and their density dependence are confirmed by radial profiles of X-ray emission induced by the LH generated fast electron population /3/. The hollowness measured in the X-ray emission agrees with the observed broadening of the current profile.

Long sawtooth free period of the "monster" type have been achieved in ICRF heated plasmas, up to 2.9 sec at Ip = 2 MA and up to 2.3 sec at Ip = 3 MA. Fig 3 shows the time evolution of the central electron temperature from ECE measurements. When a significant amount of LH power is applied, long sawtooth free periods are obtained. In the particular case of fig 3b, the "monster" terminates due to a continuous increase of density throughout the pulse. This behaviour could be explained by a combination of stabilization effects by the fast ions accelerated by ICRH and reduction of the volume of the q = 1 surface due to off-axis LHCD.

CURRENT DRIVE EFFICIENCY

The estimation of current drive efficiency is based on the analysis of the time behaviour of the surface loop voltage. Up to 50% drop in loop voltage is observed (fig 1) which increases linearly with the power per particle and has no apparent dependence on the plasma current /2/.

Current drive efficiency depends upon the launched parallel wave spectrum, as suggested by theory /4/ and observed in many experiments. In JET, phasing between klystrons is optimised by monitoring the cross-talk between adjacent multijunctions and the coupling to the plasma. In most of the experimental campaign a zero phasing spectrum with a 70% directivity corresponding to $N_{//} = 1.8$ has been used. Experiments carried out with $N_{//} = 2.4$ have shown a reduced current drive efficiency /2/.

As in JT-60, current drive efficiency appears to be sensitive to Z_{eff} and to the volume averaged electron temperature (fig 4). The amount of LH driven current is estimated, by taking into account corrections due to time variation of the plasma inductance, by comparing the loop voltage obtained with LH power to the one which would correspond to resistivity changes, i.e. by taking into account changes in Z_{eff} and in electron temperature. The effect of the remaining electric field is estimated via the so called HF resistivity /5/. Such an effect is rather small at high electron temperature when the remaining loop voltage is in the order of 0.25 V /6/.

Non inductive currents up to 1.2 MA are estimated to be driven at <Te> = 1.9 keV with corresponding efficiencies (n R I/P) up to 0.4 $10^{20} m^{-2}$ A/W. These results are in qualitative agreement with a spectral gap model where the energy needed to fill in the gap in velocity space is reduced when the electron temperature increases. The efficiency follows approximately the dependence given by JT-60 /5/ and reaches the maximum values which can be estimated from Fish /2/. It is not clear if a saturation is already observed in the experimental efficiencies.

Another interesting result is the observed central electron heating during the LH pulse. The electron temperature on axis as measured by the LIDAR diagnostic, shows an increase of 0.5 - 1 keV with LH alone and of up to 2.-3 keV during combined LH and ICRH. It is possible to estimate the local power deposition on the bulk electrons by using the change of slope of the electron temperature during LH power modulation. For this purpose, ECE measurements at different radial locations, and in a frequency range where non-thermal emission can be considered negligible, have been used. The computed power deposition profile, for cases with and without ICRH, is shown in fig 5; the central deposition seems to be in contradiction with the observed hollow electron emissivity profiles /3/ and possible explanations, such as synergistic effects between ICRH and LHCD, are under investigation.

REFERENCES

1) M.Pain et al., Proceedings of 13th Symp. on Fus. Eng. (Knoxville, 1989).
2) C.Gormezano et al, 32nd APS meeting, Cincinati, Nov 1990 (JET-IR (90)07).
3) P.Froissard et al, these proceedings.
4) N.Fish, Phys. Rev. Lett. 41 (1978) 873.
5) K.Ushigusa, Proceedings Con. Fus. and Plasma Heating, 17th EPS.
6) N.Fish Phys. Fluids 28 (1985) 245.

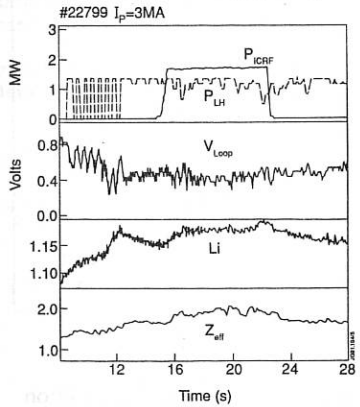

Fig 1: Lower Hybrid Current Drive on JET.

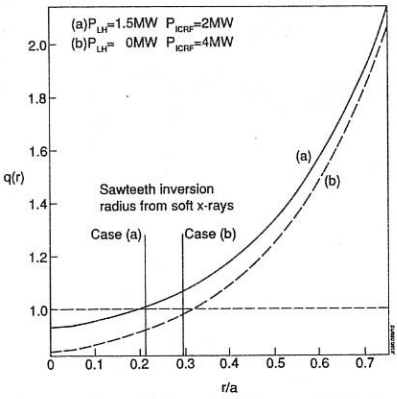

Fig 2: Radial profile of the safety factor with and without LHCD.

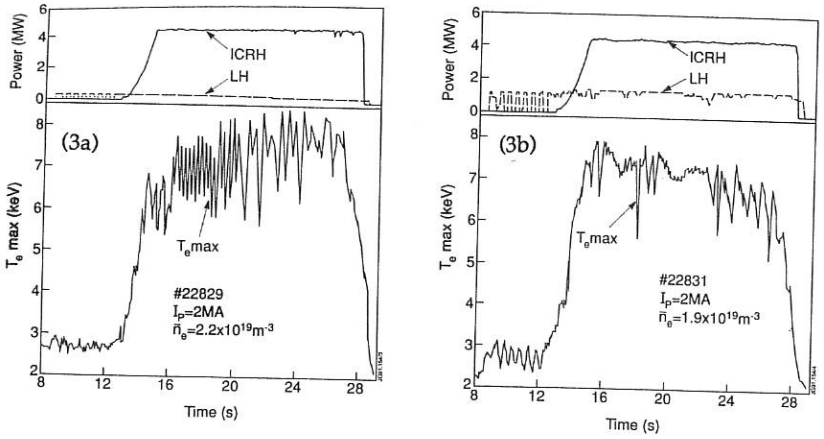

Fig 3: Time evolution of the central electron temperature from ECE without (3a) and with (3b) LHCD.

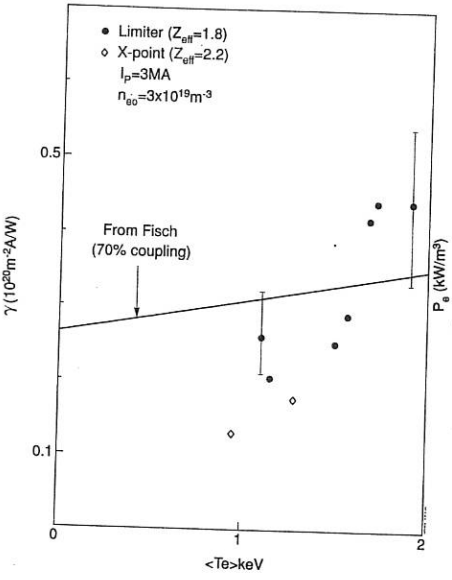

Fig 4: LH Current drive efficiency versus volume averaged electron temperature.

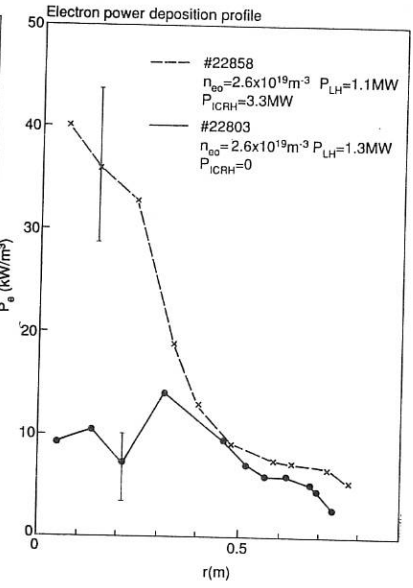

Fig 5: Electron heating power deposition profile during LHCD in OH and ICRH heated plasmas

ROLE OF PARAMETRIC DECAY INSTABILITIES AND EDGE PLASMA FLUCTUATIONS ON CURRENT DRIVE EFFICIENCY OF LOWER HYBRID WAVES

V. Pericoli-Ridolfini, R. Cesario

Associazione EURATOM-ENEA sulla Fusione, C. R. E. Frascati,
C.P. 65 - 00044 - Frascati, Rome, Italy

Experimental current drive (CD) efficiency of lower hybrid (LH) frequency waves at 2.45 GHz was found to vary more than 50% down its maximum in Asdex if some plasma parameters and/or vessel conditions are changed [1].

The available theories and numerical simulations of LHCD fail in explaining this observation since all the main quantities there considered were taken into account also in [1] when processing experimental data. The decrease of LHCD efficiency is, instead, very wall correlated to the spectral braodening of the frequency spectrum of the launched LH pump, as detected by a RF probe just outside the plasma column, and it is possibly due to a modification of its $n_\parallel$ spectrum ($n_\parallel$ = parallel index of refraction). This paper analyzes the causes of this broadening and searches for possible similar effects due to the other main feature of the frequency spectrum, namely the ion cyclotron satellites.

This last point was investigated comparing the decrease of the loop voltage, V_{loop}, when the ion cyclotron sidebands were either present or absent, maintaining unchanged all the other parameters. For the LH power this was achieved exciting respectively only one or both grills of the launcher and exploiting the different convective losses of the instabilities originating the sidebands and the different electric fields in the two cases [2]. The results obtained for two plasma densities are shown in Fig. 1. The shaded ranges of LH power are those where ion cyclotron satellites are well developed for one grill case and almost negligible for the two grill case. No difference is visible between the V_{loop} within the experimental errors.

The causes of the spectral broadening can be either parametric decay instabilities (PDI) involving low frequency ion sound quasi modes or scattering by density fluctuations. This point was investigated experimentally and theoretically.

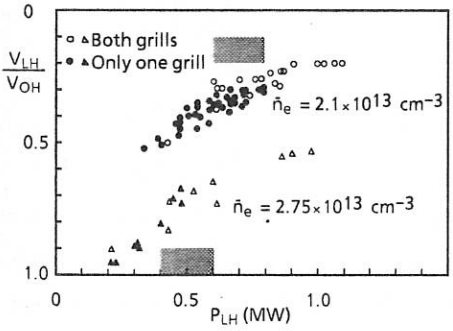

Fig. 1 - Ratio of loop voltages in LH and OH phase vs coupled LH power, for two different plasma densities. Full symbols: only one grill excited: Open symbols: both grill excited. Shaded ranges of power: high ion cyclotron sideband for one grill case; negligible for two grills case

The experiment was aimed to search for the main features of PDI, namely threshold powers and convective losses, and to look at possible correlations with edge density fluctuations, measured with either Langmuir probes or microwave reflectometer. The theoretical work was instead limited up to now to evaluate the power threshold for the instability with the highest growth rate in the desired frequency range, namely within about 2 MHz from the pump.

The results, shown in Fig. 2, where the pump spectral width Δf_p is plotted vs the coupled LH power for different grill configurations, demonstrate that the only important parameter is the total power, while convective losses are not influent. Indeed according to the usual models the spatial extension of the grill should strongly affect the growth of PDI. That it is not so is particularly evident comparing configurations E and F, simulating two independent grills, with B and C: they have same total power and LH electric field, different convective losses, but same Δf_p.

Power scans extended down to 1 kW for plasma conditions similar to those of Fig. 2 did not show the existence of any threshold even though this behaviour can change at lower plasma densities. Together with no threshold neither any saturation is observed, very differently from the ion cyclotron sidebands case [2]. Langmuir probes and a X-mode microwave reflectometer, tuned in order to have the reflecting layer slightly outside the separatrix radius studied the correlation of Δf_p with edge fluctuations. Both techniques show an increase of the global fluctuation level and an enhancement of their frequency power spectrum above 100 kHz. In Fig. 3 Δf_p is plotted vs the relative fluctuation level of the ion saturation current on a Langmuir probe placed 4 cm outside the separatrix radius for three different densities. A good degree of correlation exists despite the scattering of the data. Even clearer evidence of such correlation was found several times when, during a single LH pulse, fluctuations happen to increase suddenly.

Figure 4 shows the increase of the reflectometer signal above the ohmic level, measured at 0.5 MHz, and the increase of the RF probe signal 0.5 MHz from the

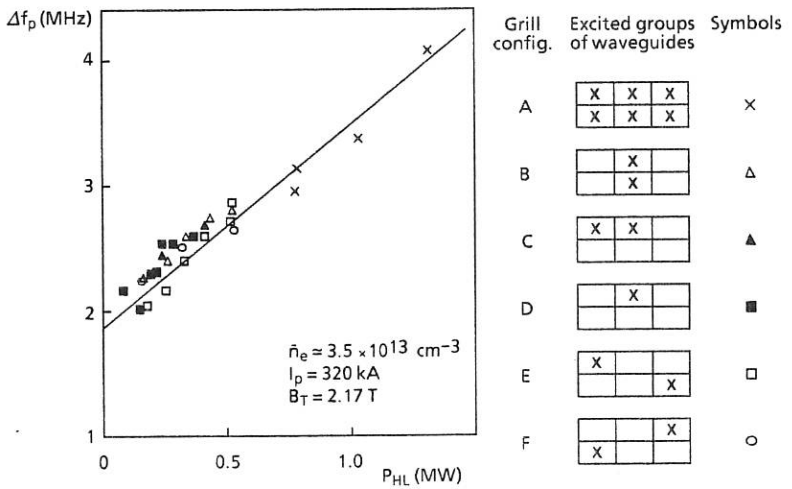

Fig. 2 - Frequency width of the LH pump vs coupled LH power for different configurations of the launching grill

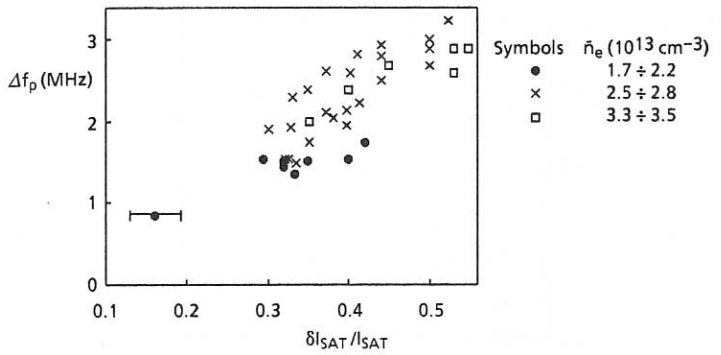

Fig. 3 - Pump frequency width vs relative fluctuation of the ion saturation current on a Langmuir probe, 4 cm outside the separatrix radius

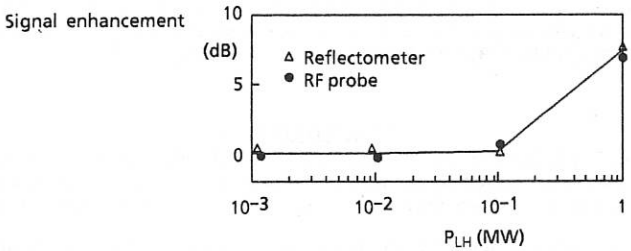

Fig. 4 - Enhancement of the signals from the reflectometer looking in the scrape off layer at 500 kHz, and from the RF probe at 500 kHz far from the pump frequency and relative to the peak level, vs the injected power in a single shot, $\tilde{n}_e = 3.4 \times 10^{13}$ cm^{-3}, $B_T = 2.8$ T, $I_p = 420$ kA

pump frequency, relative to P_{LH} = 1 kW case, plotted vs the injected power. This figure is a clear evidence how the spectrum of the pump is linked to that of the fluctuations and both to LH power.

On the theoretical side the equation governing the parametric dispersion relation, derived from a linear model was solved numerically [3,4]. The highest grow rates in the frequency range relevant to the pump spectral broadening ($f \leq 2$ MHz) were found for ion sound quasi modes. Then the power thresholds were calculated for the specific case of Asdex considering the convective losses due to the finite extent of the LH grill in two dimensions, and the typical edge plasma. The parameter space of all the quantities appearing in this model was extensively explored but a power threshold lower than 10 MW, a value all above the capability of the LH system, was never found. As an example Fig. 5 gives the behaviour of the calculated power threshold along the normalized radius.

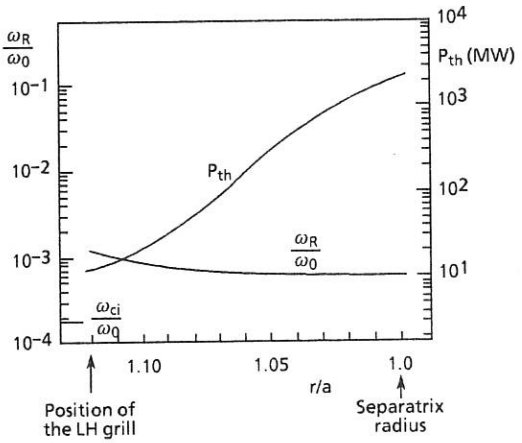

Fig. 5 - Calculated power thresholds P_{th}, and real frequency, ω_R, of the ion sound quasi mode vs normalized radius in Asdex. Parameters assumed in calculation are: $\tilde{n}_e = 3 \times 10^{13}$ cm^{-3}, $T_{e,pK} = Ti_{,pK} = 1$ keV; $B_T = 2.2$ T; $n_{\|,0} = 2$; $\omega_0/2\pi = 2.45$ GHz; $\delta = 90°$

CONCLUSIONS

PDI are irrelevant for LHCD: Ion cyclotron sidebands probably because they are always too poorly developed in the plasma regimes where CD is significant, and low frequency sidebands because they are not excited at all, as experiment and theory show.

On the contrary, edge fluctuations are responsible for the pump spectral broadening and the related degradation of CD efficiency. However a simple multiple scattering model as in Ref. [5] does not seem sufficient to describe them since LH waves in turn broaden their spectrum and enhance the turbulent state of the edge plasma.

REFERENCES

[1] A. Cardinali et al.: Proc. 17th Europ. Conf. on Contr. Fusion and Plasma Heating (Amsterdam 1990) vol. 14B, part. III, p. 1203 (1990)

[2] V. Pericoli-Ridolfini: Proc. 8th Top. Conf. on Radiofrequency Power in Plasmas, Irvine, CA, USA, 1989, p. 166

[3] J.F. Drake, P.K. Kaw, Y. Lee et al.: Phys. Fluids **20**, 2058 (1977)

[4] R. Cesario et al.: "Turbulence Induced by the RF Power and Frequency Spectral Broadening During the Lower Hybrid Current Drive Experiment on Asdex" (in preparation)

[5] P.L. Andrews, F.W. Perkins, Phys. Fluids **26**, 2546 (1983)

TRANSPORT ANALYSIS OF LHCD DRIVEN PLASMAS IN ASDEX

V.V. Parail, G.V. Pereverzev.
I.V. Kurchatov Institute of Atomic Energy, Moscow, USSR.

F.X. Söldner,
Max-Planck-Inst.f.Plasmaphysik, D-8046 Garching, Germany, EURATOM Association

This paper is devoted to a theoretical analysis of a transport properties of ASDEX plasmas in the regimes with LH waves used for heating and current drive. Discharges with LH wave sawteeth suppression and consequent sharp peaking of electron temperature profile were analyzed (the main discharge characteristics of two typical discharges are shown in Table 1). 1.5D transport code ASTRA was used for numerical modeling of the energy balance in ASDEX. The code was supplemented by the system of equations for LH waves propagation and for their interaction with suprathermal electrons:

$$\frac{eE_{\parallel}}{m}\frac{\partial f}{\partial v_{\parallel}} = St(f) + Q_{LH}(f), \qquad (1)$$

$$\mathrm{div}\,(v_{gr}W_k) = -2\gamma_k W_k . \qquad (2)$$

First term in right hand side of equation (1) describes relaxation of the electron distribution function f_e due to the Coulomb collisions. The second one - due to quasilinear interaction with LH waves. The linearized 1D collisional operator was used; influence of 2D effects on current drive efficiency was taken into account by the corresponding renormalization of the collisional operator. W_k is spectral density of waves's energy, v_{gr} is their group velocity and γ_k is quasilinear damping rate. The empirical diffusive model for spectral broadening of LH waves on $N_{\parallel}$ was used:

$$\frac{d}{dN_{\parallel}} D(N_{\parallel}) \frac{dW_k}{dN_{\parallel}} - W_k = W^{in}_{N\parallel} \qquad (3)$$

where $W^{in}_{N\parallel}$ is the input spectral density of LH waves near plasma surface. The diffusion coefficient was chosen in the form:

$$D(N_{\parallel}) = D_0(N_{\parallel}^3 - 1). \qquad (4)$$

Eq. (3) with the diffusion coefficient (4) approximately describes transformation of LH waves spectrum due to diffraction [1], specifically for ASDEX conditions $D_0 \simeq 1$.

We did not take into account all other mechanisms of spectrum broadening (in particular toroidal effects); it was shown by numerical simulation that diffraction broadening adequately describes experimental results.

The equations for electron and ion temperatures, density of a plasma and poloidal magnetic field distribution constitute system of transport equation. It should be noticed that equation for density was not solved - both density profile and its time evolution were prescribed in accordance with experimental data. Heat flow both in electron and ion channels was chosen in the simplest form $q_{e,i} = \kappa_{e,i}\nabla T_{e,i}$ which does not include heat pinch. It should be mentioned also that ion heat flow was small enough in the experiments under

consideration and does not require any anomalous thermal diffusivity. The expression for anomalous electron thermal diffusivity will be discussed below.

It was mentioned above that main peculiarities of the analyzed experiments were simultaneous stabilization of sawtooth oscillations and sharp rise of the central electron temperature. At a first glance, these two facts are in a contradiction because sawtooth suppression is usually concerned with current flattening which in turn requires broad enough LH power distribution. And in the contrary, very peaked temperature profile is usually associated either with peaked power deposition profile or with an assumption that $\chi_e(0) \ll \chi_e(a)$. Thus the experimental confirmation of the concept of current profile broadening by LHCD (by means of Li^+ beam) allows one to reduce considerably class of possible functions for the electron thermal diffusivity description. As an analysis shows the best coincidence between experimental data and numerical simulation is achieved if the electron thermal diffusivity has the following form

$$\chi_e(r) = \chi_e^{Al}(r) + C_{FIT}\frac{a^2}{\tau_{E\,ITER}}(r/a)^4 + C_{MHD}\chi_e^{MHD}(r) + \chi_e^{nc}(r). \qquad (5)$$

First term in the right hand side of Eq.(5) corresponds to well known Alcator scaling [2,3] which has certain theoretical approvement [4,5] and describes T_e evolution in Ohmic discharges fairly well. Namely this term is responsible for electron transport in the central part of the plasma column during the sawtooth free period. Second term in the right hand side of Eq. (5) is a 1D analog of ITER power law scaling for energy confinement time [6], being expressed in term of energy content. This term is dominant during additional heating and controls the volume average electron temperature because of strong radial dependence. It is worthwhile to notice that an attempt to describe anomalous electron transport by using different models of drift instabilities for which $\chi_e \simeq T_e^{3/2}$ leads to much greater divergence with experimental data. Third term in the right hand side of Eq.(5) also empirically describes enhanced transport (both electron and ion) in the sawtooth dominated region.

The comparative characteristics of the main measured and calculated plasma parameters are given in the Table 1 and in the Fig.1,2 and demonstrate reasonably good coincidence. After the LH power is turned on, the current profile is flattened and sawtooth oscillations disappear if plasma density is rather low and the LH power is high enough. It is seen from the Fig. 1 that as a consequence the anomalous transport drops in the central region and sharp increase of central electron temperature occurs. And finally it's possible to estimate the central electron thermal diffusivity in the regime when sawtooth oscillations are suppressed. Really it follows from electron energy balance equation

$$6.4\cdot10^{-3}\frac{T_e(0)}{a_{T_2}^2}\chi_e(0) = \frac{P_{LH}(0)}{n_{e19}(0)} = 0.16\cdot j_{LH}(0)\,. \qquad (6)$$

where keV, m, m^2/s and MW/m^3 are used and $P_{LH}(0)$ is LH specific power which is released in the central part of plasma column. The second equality in Eq.(6) follows from experimentally measured LHCD efficiency and corresponds to theoretical expectation. Taking into account that following inequality should be fulfilled during sawtooth free period q(0) > 1, i.e. $j_{LH}(0) < 2.5MA/m^2$, one

can obtain from Eq.(6) $\chi_e(0) \leq 0.25\ m^2/s$. It is interesting to mention that obtained estimation for $\chi_e(0)$ coincides with neoclassical value of electron thermal diffusivity by the order of magnitude.

In conclusion, the possibility of sawteeth suppression by LHCD and consequent sharp increase in the central electron temperature was confirmed by numerical simulation. Comparison of the calculated and measured plasma parameters allows us to choose the model for electron thermal diffusivity and its dependence on absorbed power and plasma density.

References.

1. G.V.Pereverzev, JETP Lett. 44, No.9, 426 (1986).
2. A.Goldhalekar et al. in Proc. 7th Int. Conf. on Plasma Phys. and Contr. Nucl. Fus. Res., Vol.1. IAEA, Vienna (1979), 211.
3. V.M.Leonov et al. in Proc. 8th Int. Conf. on Plasma Phys. and Contr. Nucl. Fus. Res., Vol.1. IAEA, Vienna (1981), 393.
4. T.Ohkawa. Gen. Atom. Rep. N JA-AI-4433, May, 1977.
5. V.V.Parail and P.N.Yushmanov, JETP Lett. 42, 343 (1985).

Table 1. Experimental/calculated data for two ASDEX shots.

Shot No	$\bar{n}_e$ ($10^{19} m^{-3}$)	t (sec)	$P_{OH}+P_{LH}$ (kW)	τ_E (ms)	W_e (kJ)	$T_e(0)$ (keV)	$\langle T_e \rangle$ (keV)
30833	1.4	1.1	366/448	61/40	11.8/12	1.64/1.64	0.69/0.72
		1.6	672/642	56/59	15.4/15	2.55/2.56	0.96/0.99
		2.1	1060/1050	42/55	19.6/23	4.57/4.58	1.16/1.56
30839	4.0	1.1	447/562	87/65	20.6/19	1.03/0.96	0.44/0.42
		1.6	910/945	59/53	28/25	1.45/1.46	0.56/0.52
		2.1	1304/1301	43/48	30/31	1.56/1.66	0.60/0.63

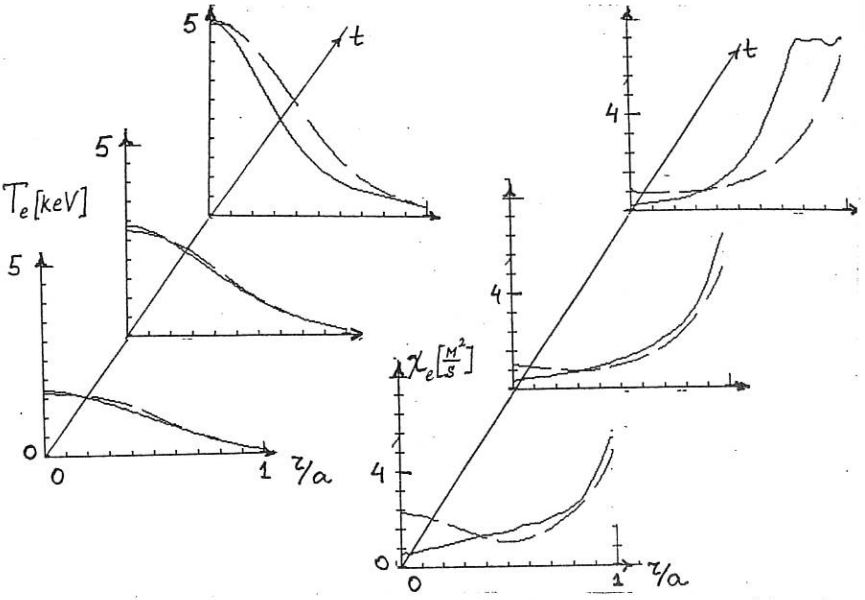

Fig. 1. Shot # 30833. Time evolution of the electron temperature (a) and electron thermal diffusivity (b). Solid line - experiment, dashed line - calculation.

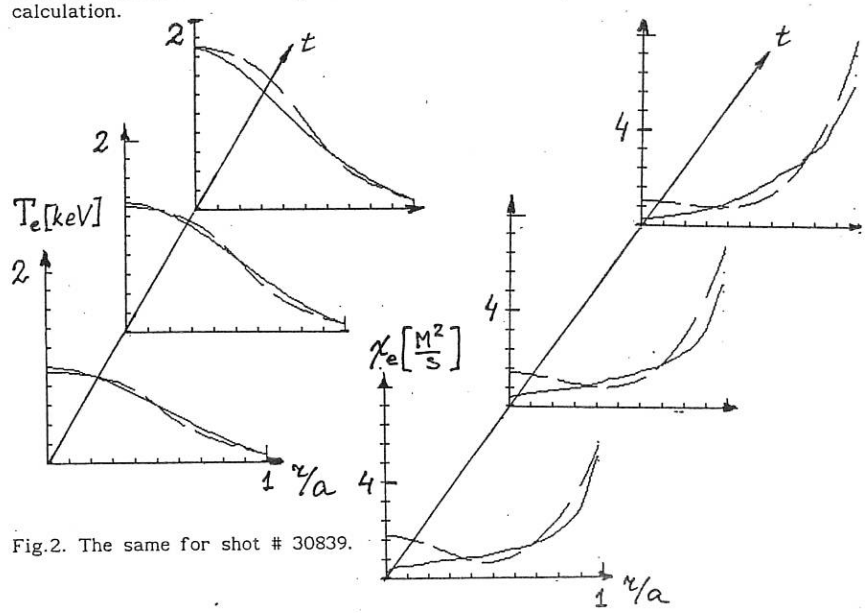

Fig.2. The same for shot # 30839.

COMBINED OPERATION OF LOWER HYBRID AND NEUTRAL BEAM INJECTION ON ASDEX

F.X.Söldner, R.Bartiromo[1], F.Leuterer, M.C.Zarnstorff[2]
and LH-team, NI-team, ASDEX-team

Max-Planck-Institut für Plasmaphysik, D-8046 Garching, Germany,
EURATOM Association
[1] ENEA , Frascati, Italy, [2] Princeton Plasma Physics Laboratory, Princeton, USA

Current drive and heating with Lower Hybrid (LH) waves were combined with heating by neutral beam injection (NBI) on ASDEX up to total powers of 4 MW. LH waves are launched from two antennae allowing superposition of different wave spectra /1/. Absorption of LH power results in preferential electron heating for $\bar{n}_e < 5 \times 10^{13}$ cm^{-3}. NBI, on the other hand, leads at low density mainly to ion heating. For combined operation of LH and NBI, the current drive efficiency and the confinement behaviour were investigated. Profile control by LH-current drive was applied during NBI heating in order to study the potential for confinement improvements.

Current Drive Efficiency

LH-current drive (LHCD) has been studied extensively in Ohmic target plasmas. The experimental current drive efficiency agrees well with theory. In combination with medium power NBI the same efficiency was found as for LHCD alone /2/. In this paper power scans with both, LHCD and NBI are analyzed and the results of combined operation in L- and H-mode are compared. The powers vary in the range P_{NI} = 1 - 2.25 MW, P_{LH} = 0.6 - 1.65 MW with $\bar{N}_{||} = 2.2$ ($\Delta\phi = 90°$). The plasma parameters with B_t = 2.8 T, I_p = 420 kA, $\bar{n}_e \approx 3 \times 10^{13}$ cm^{-3} should allow full accessibility for LH to the plasma center. With constant feedback-controlled plasma current I_p , the LH-driven current is given by the drop in Ohmic power input ΔP_{OH} / P_{OH} (OH). During the different phases of the discharge the density may vary due to changes in recycling and confinement. As the LH-driven current is inversely proportional to the density, the drop in OH power is normalized with:

$$\Delta P_{OH} / P_{OH}\,(OH) \times \bar{n}_e\,(cm\text{-}3) / 3 \times 10^{13}$$

The Ohmic power input decreases also with NBI alone due to the reduced resistivity with higher electron temperatures. A variation of the electrical resistivity leads to a nonlinear dependence of the LH-driven current on power /3/. The results from the different scenarios with LHCD, NBI and LHCD + NBI are therefore presented with a unified power scale:

$$P_{eff} = P_{LH,net} + P_{add}$$

An effective power P_{eff} is determined by adding to the LH power $P_{LH,net}$ for NBI and LHCD+NBI a power which gives the NBI-produced drop in OH power with LHCD:

$$P_{add} = P_{LH}^{fit} (\Delta P_{OH} (NI) = \Delta P_{OH} (LH)) \text{ for LHCD+NBI, NBI;} \quad P_{add} = 0 \text{ for LHCD}$$

The normalized drop in OH power is plotted versus effective power in Fig. 1. The same power dependence is obtained for LHCD alone and in combination with NBI, both in L- and H-mode. The electron temperature varies by more than a factor of 2 in these experiments: T_{eo} = 1.1 - 2.7 keV, $\langle T_e \rangle$ = 0.6 - 1.3 keV. The profile factor $Q_{Te} = T_{eo} / \langle T_e \rangle$ varies in the range Q_{Te} =1.6 - 2.8. The current drive efficiency therefore seems not very sensitive to the electron temperature and its profile form. It is also not affected by the presence of fast beam ions. Charge exchange measurements with a neutral particle analyzer confirmed that no fast ions were accelerated by the LH in this regime /4/.

Confinement

Improvement of the energy confinement above Ohmic values was found with LHCD at low density /5/. With increasing power, however, the confinement time degrades. The results from combined operation of LHCD + NBI are compared in Fig.2 with LHCD and NBI, each alone. The same power dependence for the global energy confinement time τ_E is found in all operation scenarios. Electrons and ions are largely decoupled for the plasma conditions studied here. This is seen from Fig.3 where the temporal evolution of beta values, central electron temperature, the profile factor and the electron density is shown for the different stages of LHCD, NBI and the combined operation. LHCD leads mainly to electron heating with a strong increase of the central temperature and a peaking of the profile. With additional NBI T_{eo} does not change and the increase in the electron beta results only from a broadening of the profile with volume heating. The large rise in total beta values originates from dominant ion heating. In both cases the same global confinement time is obtained. The same incremental energy confinement times were also found in a wider density range for LHCD and NBI /6/. The dominant energy transport mechanism therefore does not depend on the heating method and seems therefore not linked with a particular particle species but rather with the total energy content of both, electrons and ions.

H-modes could be obtained routinely in the combined operation of NBI + LH, with LH waves injected either with symmetric spectra or in current drive phasing. With LH switched on during NBI, transitions from L- to H-mode were triggered and a variation of the ELM frequency was achieved in grassy H-modes. Least efficient are symmetric spectra with low $\bar{N}_{||}$. Nearly no influence also is seen with off-axis counter-current drive by injection of compound spectra with -90°+180°. The most efficient scheme for decreasing the ELM frequency and triggering H-modes from an L-mode is off-axis current drive and heating with compound LH wave spectra at 90°+180°. The triggering of an ELM-free H-mode by LHCD is shown in Fig.4. After 500 ms steady-state L-mode with NBI alone, LH is switched on with a compound spectrum 90°+180°. The H-transition is triggered immediately with a few ELM´s first, as seen on the D_α emission. After a short delay then an ELM-free phase is

established with a strong continuous rise in density. The power flow in the Ohmic transformer in this phase is reversed. The rise in density and impurity accumulation lead to a decrease of the LH-driven current. A large ELM finally causes the transition back to an H-phase with frequent ELM´s.

Profile Control

The electron temperature profile and the current profile can be varied with LHCD to a large extent /7/. Peaking of $T_e(r)$ is achieved after stabilization of sawteeth and the m=1 mode. This could be obtained also in combination of LHCD + NBI. At low density, however, the density often rises during the combined operation, probably due to enhanced plasma wall interaction. The LH-driven current then decreases and the m=1 mode is reexcited. The peaking of $T_e(r)$ is then lost and the central temperature drops to values as obtained with LH in symmetric phasing. At higher target density the variations are small and m=1 modes remain stabilized by LHCD during NBI. T_{eo} is then kept high and $T_e(r)$ stays peaked as seen in Fig.3.

Control of the current profile with LHCD was combined with high power NBI. In Fig.5 two discharges with different LH spectra are compared. Off- axis current drive with the compound spectrum 90°+180° leads to a broadening of the current profile, as inferred from the slow decay of the signal $l_i/2 + (\beta_{II}-\beta_{\perp})/2$ during the phase with LH alone. With off-axis counter-current drive in the phasing -90°+180°, on the other hand, j(r) peaks slightly. Sawteeth are suppressed with normal current drive but not in the discharge with counter-current drive. Nevertheless a larger increase in the diamagnetic beta is obtained with NBI + counter-LHCD than in the case with broad j(r) from normal LHCD. Also the neutron flux is larger and the ion temperatures are higher. After switching off LH, the form of the current profile returns slowly to the original form as seen from the signal in the upper part of Fig.5.

The enhancements in β_p^{dia}, neutron flux and T_i then disappear. We have to conclude therefore that the energy confinement is higher with peaked than with broad current density profiles.

The Lower Hybrid experiments are performed in collaboration between IPP Garching, ENEA Frascati and PPPL Princeton.

REFERENCES

/ 1/ Leuterer, F., et al., 16th Europ. Conf. on Contr. Fusion and Plasma Physics, Venice 1989, Vol. IV, 1287.
/2/ Leuterer, F., et al., 17th Europ. Conf. on Contr. Fusion and Plasma Physics, Amsterdam 1990, Vol. III, 1291.
/3/ N. Fisch, Review of Modern Physics 59, 175,(1987)
/4/ Fahrbach, H.-U., et al., 17th Europ. Conf. on Contr. Fusion and Plasma Physics, Amsterdam 1990, Vol. III, 1171.
/5/ Söldner, F.X, et al., 13th Int. Conf. on Plasma Physics and Controlled Nuclear Fusion Research, IAEA-CN-53 / E-1-1, Washington (1990).
/6/ Bartiromo, R., et al., 17th Europ. Conf. on Contr. Fusion and Plasma Physics, Amsterdam 1990, Vol. III, 1092.
/7/ Söldner, F.X., et al., 17th Europ. Conf. on Contr. Fusion and Plasma Physics, Amsterdam 1990, Vol. III, 1323.

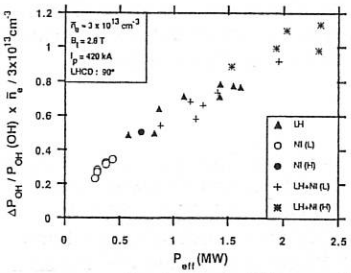

Fig.1: Normalized drop in OH power input versus effective current drive power.

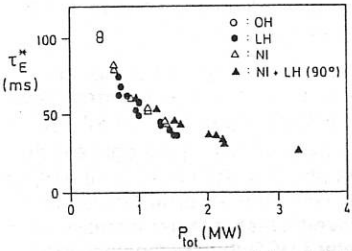

Fig.2: Power dependence of the global energy confinement time.
B_t=2.8 T,I_p=420 kA,$\bar{n}_e$=3 x 10^{13} cm^{-3}

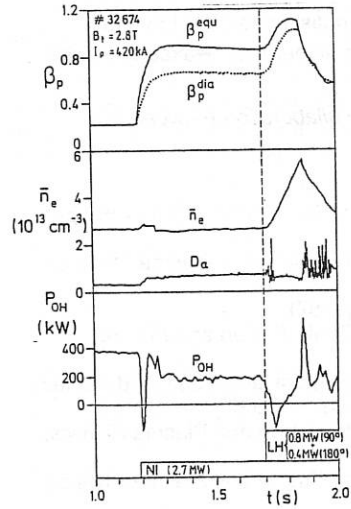

Fig.4: L-H-transition triggered by LHCD.

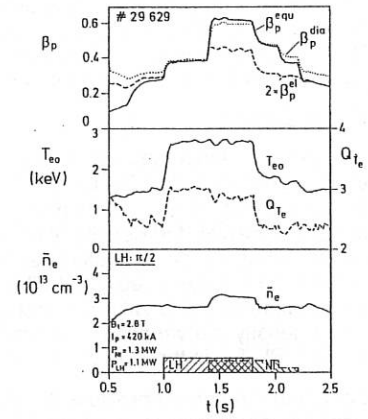

Fig.3: Temporal evolution of β_p values, central electron temperature, profile factor $Q_{Te} = T_{eo} / \langle T_e \rangle$ and density with combination of LHCD and NBI.

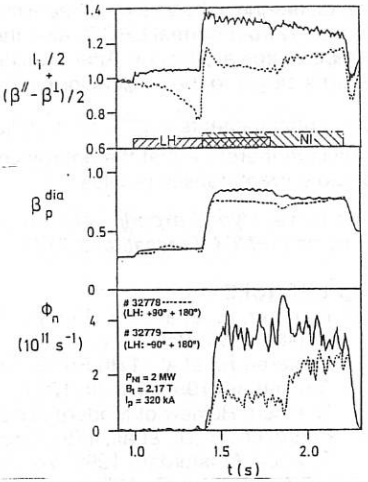

Fig.5: Internal inductance and anisotropy $l_i/2 + (\beta_{||} - \beta_\perp)/2$, β_p^{dia} and the neutron flux with j(r) control by LHCD during NBI.

EVIDENCE FOR NONLINEAR COUPLING OF THE LOWER HYBRID GRILL IN ASDEX

F. Leuterer, F.X. Söldner, L. Giannone, R. Schubert

Max Planck Institut für Plasmaphysik, D-8046 Garching, Germany, EURATOM Ass.

V. Petrzilka

Institute of Plasmaphysics, Czechoslovak Academy of Sciences, Prague, CSFR

The grill in ASDEX consists of two stacked arrays of 24 waveguides each (upper and lower grill) with inner dimensions of 10 X 109 mm and 4 mm walls inbetween. A phasing of $\Delta\varphi = 180°$ generates a symmetric spectrum with $N_{||} = \pm 4.4$, while $\Delta\varphi = 90°$ generates an asymmetric spectrum with $N_{||} = 2.2$. The grill (i.e. its metallic surface) was usually at a radial position of $R_g = 212.5$ cm, the major radius of the plasma was $R_p = 168$ cm, the positions of separatrix and protection limiters were $R_s = 208$ cm and $R_l = 212$ cm. In a first campaign the grill was surrounded by protection tiles which protruded beyond the waveguides by 3 mm. In these conditions the average reflection coefficient R was between 10 % and 50 % depending on the phasing and power / 1 /. Later these tiles had been cut back to be flush with the waveguides. This improved the coupling considerably as seen in fig. 1. The difference can be understood on the basis of the linear coupling theory with a step and ramp electron density profile, if a vacuum gap $X_p \leq 2$ mm is, or is not, allowed between the grill and the plasma / 1,2,3 /, as seen in fig. 2 in the phase dependence of calculated and measured average reflection coefficients. However, in both cases <R> increased with power with a tendency to saturate (fig. 1).

Power densities up to 4 kW/cm^2 have been transmitted to the plasma. At this power level the electromagnetic energy density is much larger than the electron pressure in front of the grill in ohmic discharges / 4 /. The ponderomotive force should thus lead to a decrease of the plasma density in front of the grill with a corresponding variation of the reflection / 5 /.

We have applied a simple model to estimate this variation of <R>. A step and ramp profile is assumed for the unperturbed edge electron density and temperature

$$(1) \qquad n_0(x) = n_b + n_c\, x / L_n$$

$$(2) \qquad T(x) = T_0\,(1+g)(1 + x / L_T),$$

where n_c is the cutoff density. The temperature is modelled to increase proportional to the Poynting flux by taking $g = S/S_0$. With LH power the density $n_0(x)$ in eq. (1) changes according to the following equations / 5 /,

$$(3) \qquad n(x,z) = n_0\, e^{-\delta(x,z)},$$

$$(4) \qquad \delta = \varepsilon_0\, |E_z(x,z)|^2 / 4\, n_c\, T(x).$$

The density is modified only where $E_z \neq 0$, i.e. within the resonance cone.

We consider in the model only waves with one $N_{||}$. Higher harmonics are neglected. Thus the ansatz for the electric fields is

$$(5) \qquad E_z(x,z) = E_1^{(+)}(x)\exp(ik_z z) + E_1^{(-)}(x)\exp(-ik_z z).$$

The basic equations then are / 5 /

$$(6) \qquad \frac{d^2E_1^{(\pm)}}{dx^2} + (k_0^2 - k_z^2)E_1^{(\pm)} = \frac{n_0(x)}{\lambda n_c}(k_0^2 - k_z^2)\int_0^{\lambda} \exp(\mp ik_z z - \delta(x,z))E_z(x,z)dz$$

where $\lambda = 2\pi/k_z$, $k_0 = \omega/c$. These equations for $E_1^{(+)}$ and $E_1^{(-)}$ are solved numerically with boundary conditions chosen deep enough inside the plasma, where the ponderomotive force effects are negligible. The RF electromagnetic fields computed in this way imply the values of the wave reflection coefficient $R_w(z)$ at the grill mouth. The power reflection coefficient, averaged over z, then is

$$(7) \qquad R = \int_0^{\lambda} S(z)\frac{|R_w^2(z)|}{1-|R_w^2(z)|}dz \left(\int_0^{\lambda} \frac{S(z)}{1-|R_w^2(z)|}dz\right)^{-1}$$

where S (z) is the x-component of the Poynting vector of the LH waves transmitted into the plasma.

In fig. 3 we show calculated reflection coefficients at different edge densities n_b. The dashed lines are calculated with g = 0, i.e. without power dependent heating. Due to the ponderomotive force the density is reduced in front of the grill leading to a continuous rise of <R> which finally would reach 1. With $g \neq 0$, however, <R> does not rise as strongly, as shown in the solid lines in fig.3, rather the reflection tends to saturate as observed in the experiments. This is due to the increasing electron pressure which opposes the radiation pressure. In our calculations we have varied the parameters n_b, T_0, L_n, L_T and S_0, and verified that a higher pressure in the edge plasma leads to weaker drop in the edge density.

Besides the variation of <R> with power there is more experimental evidence to support this picture. The distribution of the reflection coefficients in each waveguide along the grill shows characteristic changes, as shown in fig. 4 for a shot, where the power was ramped up in steps. This confirms a decreasing edge electron density in front of the grill when the power is increased, as also observed when the plasma is withdrawn from the grill at constant injected power, / 1 /. By comparison with linear coupling calculations we estimate from fig. 4 a drop in the edge density of about 25% within the power range of 150 to 600 kW. However, an X-mode reflectometer installed near to the grill, / 6 /, but outside of the area through which the rf-power is transmitted, indicates no essential change of the density at the grill radius. But the ion saturation current to a Langmuir probe at R = 211 cm, shown in fig. 5, shows a strong increase with power, indicating an appreciable heating of the electrons in this

region. The electron temperature was estimated to rise by about a factor of 1.5 with a power of 500 kW launched with both grills. This corresponds to a power density of 1 kW/cm^2 and is of the order as used in the computations presented in fig.3.

We observed also a luminous glow in front of the lower parts of the two grills and along the outer side wall at the ion diamagnetic drift side. In previous experiments at 1.3 GHz we found that the glow is due to D_α light. Its structure is independent of the phasing and appears in the whole range of densities explored. Reversing magnetic field and plasma current the glow occurs at the upper sides of the active grills and again at their ion diamagnetic drift side. The reason is the formation of a vortex, as studied in a linear discharge / 7 /, which is a consequence of electron heating in front of the grill and leads to a poloidal inhomogeneity. We see its influence also on the X-mode reflectometer profiles and the ion saturation current which are different if only the upper or the lower grill are active. Such a vortex will also have an impact on the grill coupling through generation of higher order evanescent modes in the waveguides. To estimate this one needs a coupling theory which treats a two dimensional inhomogeneous plasma, which however is not available.

The experiments have been performed in cooperation with ENEA-Frascati and PPPL-Princeton.

/ 1 / Leuterer F. et al., 17th EPS Conf. Amsterdam 1990, Europhys. Conf. Abstr. Vol. 14B, III, 1287, to be publ. in Pl. Phys. and Contr.Fus.

/ 2 / Brambilla M., Nucl. Fusion 16 (1976), 47

/ 3 / Stevens J., Ono M., Horton R., et al., Nucl. Fusion 21 (1981), 1259

/ 4 / Tsois N., et al., 16th EPS Conf. , Venice 1989, Euro. Conf. Abstr. 13B, III, 907

/ 5 / Petrzilka V., Klima R., Pavlo P., J. Plasma Physics 30 (1983), 211

/ 6 / Schubert R. et al.,17th EPS Conf. Amsterdam 1990, Euro.Conf.Abs.14B,1525

/ 7 / Motley R., Phys. Fluids 23 (1980), 2050

Fig.1 Reflection coefficient R of the upper grill as a function of incident rf-power for grills with protruding and nonprotruding graphite tiles. $\Delta\phi = 90°$.

Fig.2 Calculated and measured reflection coefficient as a function of phase $\Delta\phi$. Calculation: $\nabla n = 5\cdot10^{11}$ cm^{-4}, $n_{edge} = 5\cdot10^{11}$ cm^{-3}, $X_p = 0$, 1, and 2 mm. Expt.: $P_{lh} = 300$ - 600 kW; open dots: protruding tiles; full dots: flush tiles

Fig.3 Nonlinear reflection coefficient R vs. transmitted rf-power density S. Dashed lines: $g = 0$. Solid lines : with heating of the edge plasma, $g \neq 0$. $L_n = 0.3$ cm ($\nabla n \approx 2.5\cdot10^{11}$ cm^{-4}), $T_0 = 5$ eV, $L_T = 3$ cm, $S_0 = 2$ kW/cm^2, $X_p = 0$, a) $n_b/n_c = 2$ ($n_{edge} = 1.5\cdot10^{11}$ cm^{-3}), b) $n_b/n_c = 4$ ($n_{edge} = 3\cdot10^{11}$ cm^{-3}).

Fig.4 Reflection coefficients in each waveguide, at different powers

Fig.5 Ion saturation current to a probe at R = 211 cm, as a function of rf-power.

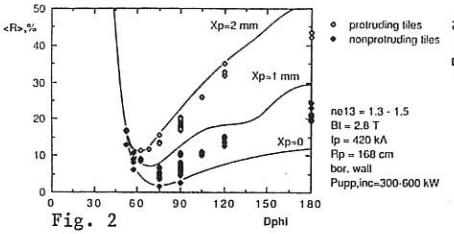

Fig. 2

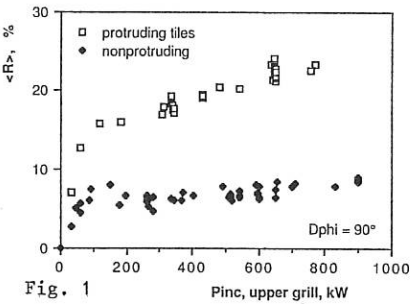

Fig. 1

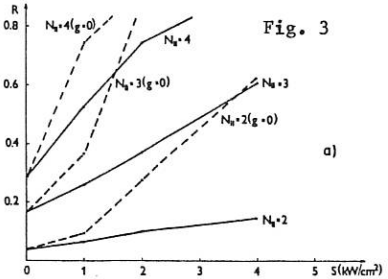

Fig. 3

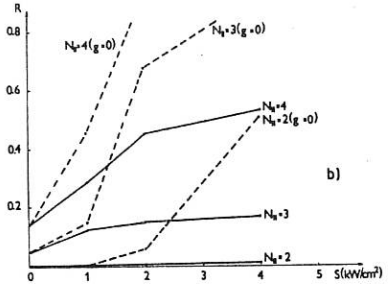

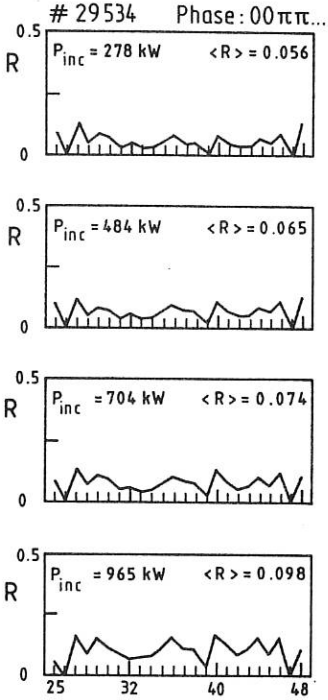

Fig. 4

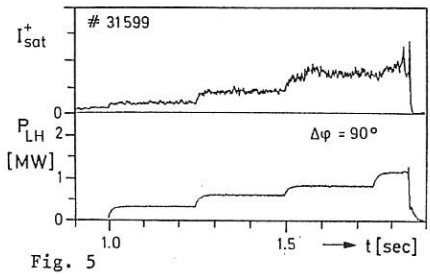

Fig. 5

ICRF POWER DEPOSITION AND CONFINEMENT SCALING IN ASDEX

F. Ryter, U. Stroth, M. Brambilla, ICRH-Team, ASDEX-Team, NI-Team

Max-Planck-Institut für Plasmaphysik, EURATOM-IPP Association
D-8046 Garching, FRG

Introduction

In ASDEX, ICRF and NI heated plasmas obey very similar L-scaling laws /1/. This suggests that the plasma energy transport does not depend on the heating method. Whether this is true can only be decided in transport studies of ICRF and NBI heated plasmas which require quantitative power deposition profile. In this paper, we present a new approach to obtain, from experimental data, a quantitative estimate for the ICRF power deposition profiles and compare the results with theoretical profiles.

1. ICRF power deposition profiles

1.a. Deposition profiles from the energy balance method:

Starting from the observation that the L-mode confinement only slowly emerges from OH plasmas with increasing heating power, we use the transport coefficients (χ) calculated for the OH phase to describe moderately ICRF heated plasmas. The transport in the OH phase has been studied in detail under numerous different conditions with complete sets of experimental profiles /2/.

For the energy balance of electrons and ions, the standard equations for the volume integrated stationary energy fluxes are used:

$$\Gamma_e(r) = 4\pi^2 R_0 \int_0^r (Q_{OH}(r') + Q_{ICRF}(r') - Q_{rad}(r') - Q_{ei}(r') - Q_{ion}(r'))r'dr' \qquad (1)$$

$$\Gamma_i(r) = 4\pi^2 R_0 \int_0^r (Q_{CX}(r') + Q_{ei}(r') - Q_{ion}(r'))r'dr' \qquad (2)$$

The energies transported by electrons (Γ_e) and ions (Γ_i) across a flux surface are given by integrals over the sources and sinks inside the flux surface. Ohmic heating (Q_{OH}), charge exchange (Q_{CX}), neutral ionization (Q_{ion}), impurity radiation profiles from Abel-inverted bolometer measurements (Q_{rad}) and electron-ion coupling ($Q_{ei} \sim (T_e - T_i)/T_e^{3/2}$) are taken into account. The electron temperature and density are taken from the the Thomson scattering system. The neutral particle density is calculated using a Monte Carlo code. The unknown function is the ICRF power deposition profile Q_{ICRF} which is supposed to appear only in the electron energy balance (justified for minority heating with low ion absorption considered in this work). The fluxes through the surface S(r) are then interpreted by an ansatz for diffusive transport which includes the convective losses Γ_n known from the continuity equation.

$$\Gamma_e(r) = 5/2\Gamma_n(r)T_e(r) - \chi_e \mathrm{grad}T_e(r)S(r) \qquad (3)$$

$$\Gamma_i(r) = 5/2\Gamma_n(r)T_i(r) - \chi_i \mathrm{grad}T_i(r)S(r) \qquad (4)$$

If the electron and ion transport coefficients χ_e and χ_i are taken from an OH plasma, T_i can be calculated by equating eqs. (2) and (4). From eqs. (1) and (3) and the measured T_e profiles, the deposition profile can be calculated.

The enhanced transport in the centre due to the sawtooth activity is taken into account based on experimental T_e and n_e data and is found to be negligible for the discharges considered here.

1.b. Deposition profiles from the wave absorption calculations:
The theoretical ICRH deposition profiles are calculated with a code which solves the finite Larmor radius wave equations for a slab plasma between two metallic walls and with a realistic antenna. The experimental density and temperature profiles are used. The absorption by the walls is negligible and no extra absorption or losses are introduced. Typical results are given in Fig.1 for the minority scenario with an H-concentration of 7%. This high value of the concentration is typical for ASDEX discharges during the recent experiments.

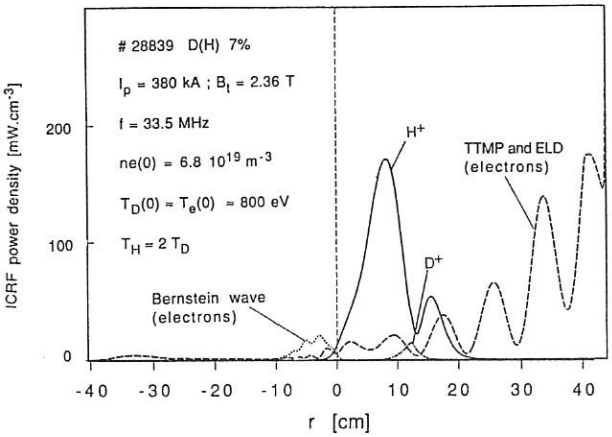

Fig.1 ICRF power density deposition profile from wave calculation in slab geometry.

The powers absorbed by ions and electrons are indicated. The power density deposited to the electrons in the outer part of the plasma, due to TTMP and electron Landau damping, increases with the H-concentration. The radial modulation of this curve is due to standing waves. The collisions, also included in the calculation and only effective at the edge, play a minor role. For the applications, the slab geometry profiles are smoothed and transformed into a cylindrical one by dividing by r.

2. Results and discussion

Fig.2 and Fig.3 compare the profiles obtained from the energy balance approach and from the wave code for the conditions indicated in the figures. The machine was boronized. The large errors (3%) on the minority concentration measurements are taken into account in the wave calculations, as indicated by the shaded area.

The profiles given by both methods have the following main features. They both show a central deposition, but also a non-negligible (30%) deposition in the edge region ($0.6 < r/a < 1$; a = 40 cm). The volume integrated ICRF power from the energy balance method is also plotted for two assumptions: without changes in χ with the total heating power (P_{tot}) and with a χ enhancement by $(P_{tot}/P_{OH})^{0.6}$, according to the L-scaling. Both values for r/a = 1 do not differ much and are in very good agreement with the launched ICRF power. This is a surprise, considering the low experimental global absorption efficiency (0.6±0.1) measured from the plasma energy time derivative at the ICRF turn-on /3/. This experimental value corresponds to the integrated power calculated for $0 < r/a < 0.7$ in Fig.2 and Fig.3. The power deposited in the outer region ($r/a > 0.7$) is probably rapidly lost due to the usual L-mode transport increase

with radius in this part of the plasma. This might explain the experimentally measured low absorption efficiency.

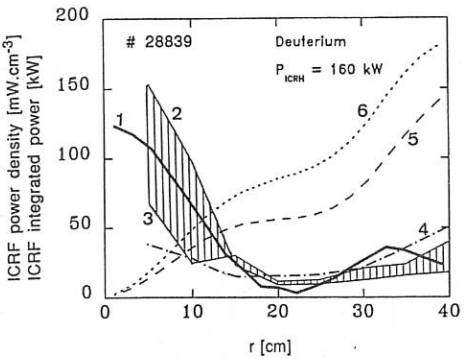

Fig.2

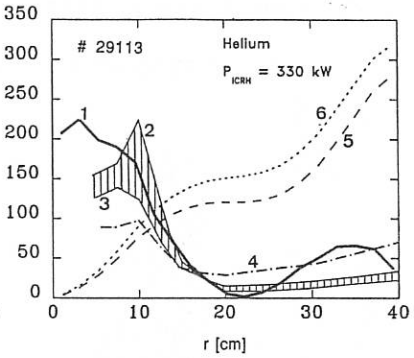

Fig.3

ICRF power density profiles from both methods for H-minority heating:
Fig.2 deuterium plasma; I_p = 380 kA ; B_t = 2.36 T ; f = 35.5 MHz
Fig.3 helium plasma; I_p = 460 kA ; B_t = 2.8 T ; f = 39.7 MHz
curves 1: from the power balance method.
curves 2 and 3: from the wave calculations for H-temperature twice the bulk ion temperature and for lower and higher H-concentration respectively; Fig.2: 7% and 10%; Fig.3: 5% and 8%.
curves 4 : from the wave calculations for H-temperature equal to the bulk ion temperature and for H-concentration of 8%
curves 5 and 6: volume integrated ICRF power from the power balance method for χ_{OH} and χ_{OH} enhanced with $(P_{tot}/P_{OH})^{0.6}$ respectively.

The uncertainties for the energy balance method are due to the errors on the experimental T_e and radiation profiles. The T_e errors act trough the profile gradients and are smoothed over the 16 radial points of the scattering system. They are not expected to influence dramatically the shape of the results. The impurity radiation power has an important contribution to the energy balance in the outer part of the profile where the second maximum is found. The increase of the radiation power density measured by the bolometer from the OH phase to the ICRF phase corresponds to half the ICRF power density found for this discharge. Thus, even large errors on the measured radiation power cannot artificially create the outer maximum. Looking for another confirmation, we applied the energy balance method to a NBI heated case: no NBI deposited power was found outside r/a = 0.7, confirming that the outer deposition is an ICRF feature and is not introduced by the method.

Uncertainties are also linked to the wave calculation. The actual geometry is not taken into account but no important changes are expected from that. The ratio between the central and the outer absorption depends sensitively on the temperature of the H-tail. As an example, we indicate, with curve (4) in Fig.2 and Fig.3, a case of very low ion absorption and high outer electron absorption occurring at high H concentration and low H temperature equal to the bulk temperature.

In summary, this study suggests that, in the frame of the uncertainties, the outer ICRF deposition might be an actual feature of the RF deposition in these discharges.

3. ICRF L-mode confinement

After the ASDEX shut-down, we started a statistical analysis of the confinement with ICRH. The data set built so far contains 200 discharges with hydrogen second harmonic heating, covering the parameter ranges accessible in ASDEX. In Fig.4 and Fig.5, these data are compared with two existing scaling laws.

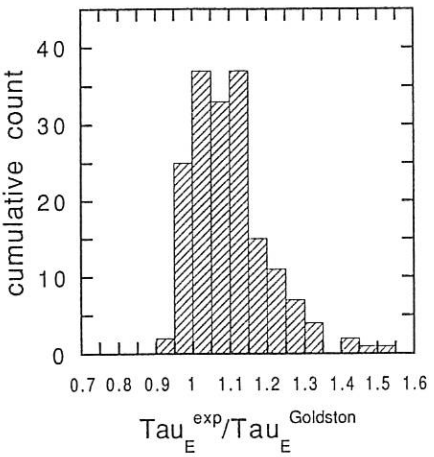

Fig.4 Statistical distribution of the experimental confinement time normalised to the Goldston mass-corrected L-scaling.

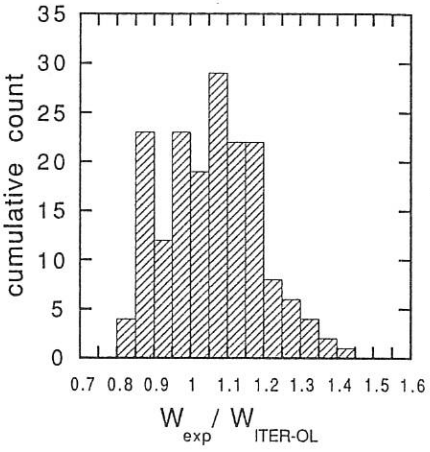

Fig.5 Statistical distribution of the experimental plasma energy normalised to the ITER89-OL off-set linear scaling law.

The ICRF results are in better agreement with the Goldston power law than with the ITER89-OL off-set linear scaling. For the power law, the high values of the ratio correspond to the high power discharges. In fact, all the power scans, at fixed current, nicely follow an off-set linear relation. The poor agreement with the ITER89-OL is attributed to its low current dependence

Conclusion

The ICRF power deposition profiles were extracted from experimental data with an energy balance method and compared with the theoretical wave absorption profiles. A reasonable agreement is found between both methods, particularly concerning a clear indication of ICRF power deposition in the outer plasma region. Further work along these lines (high ICRF power, combination with NBI, second harmonic heating) could eventually give enough confidence to introduce these profiles into transport calculations and compare the ICRF and NBI local confinement. The statistical analysis of the global L-confinement for ICRF in ASDEX shows a better agreement with the Goldston power law although all the single power scans at fixed current nicely follow an off-set linear relation.

References

/1/ J.-M. Noterdaeme at al. 12th IAEA Conf. Plasma Phys. Contr. Fus., Nice 1988.
/2/ E. Simmet at al., This conference.
/3/ K. Steinmetz at al. Nucl. Fus. Vol 29. (1989) 277-293.

SPATIAL DIFFUSION OF FAST ELECTRONS DURING THE 2.45 GHz EXPERIMENT ON ASDEX

E. Barbato, R. Bartiromo, L. Gabellieri, A.A. Tuccillo

Associazione EURATOM-ENEA sulla Fusione
CRE Frascati, C.P. 65
I-00044 Frascati, Rome (Italy)

Modulation of the RF power is a well known technique [1] to study the power deposition profile and transport processes in plasmas. In this paper we report on modulation experiments of Lower Hybrid (LH) power into ASDEX plasmas and we investigate the spatial diffusion of LH generated fast electrons by comparing the experimental results with a simulation model.

The plasma response is studied by measuring bremsstrahlung emission from fast electrons in the photon energy range from 40 keV to 500 keV with two systems : the first one records simultaneously the emission from three radial chords (0, 13, 27 cm), the second looks tangentially on the equatorial plane with a tangency point variable from 40 cm on the inner side to 20 cm on the outer side of the magnetic axis on a shot by shot basis. Both systems use three inches NaI detectors with standard electronics and data acquisition.

The tangential detector has been used to record the Hard X Ray (HXR) forward emission when the LH power is injected into the plasma with a 10 Hz square wave modulation. The emission in this condition is directly related to the LH generated fast electrons. Its time evolution is studied, on a fast time scale to get information on the LH power deposition profile and on a slower time scale to infer information on the spatial diffusion of fast electrons. For this purpose also the radial emission is used assuming that its time behaviour is mainly determined by the fast particle density evolution.

In Fig. 1 are shown radial HXR signals, for a discharge with I_p = 420 kA, B_t = 2.8 T, $\bar{n}_e = 1.5 \times 10^{13}$ cm^{-3}, P_{LH} = 0.9 MW, after the application of a box car technique to improve the statistic by averaging ten periods of the modulation. Only the peripheral radial signal shows a slow rise time suggesting that this line of sight is situated outside of the deposition zone. Information on the power deposition can be obtained from the derivative of the HXR signal in the forward direction at the onset of the radiofrequency pulse; in fact this derivative is higher when the line of sight is closer to the deposition region. In Fig. 2 its experimental values are plotted as a function of the tangency radius of the tangential system when looking at the outer part of the plasma. An outward shift of the power deposition can be observed when the electron density and $n_{||}$ are increased.

To study the electron response to the LH waves and the spatial diffusion of fast electrons, the following equation for the electron distribution function should be solved:

$$\frac{\partial f}{\partial t} = \nabla_v (S_W + S_c + S_E) + \nabla_r S_r + N(r) \qquad (1)$$

where S_W, S_c, S_E are the fluxes in the velocity space due to LH waves, collisions, and electric field, S_r is the flux in the real space connected

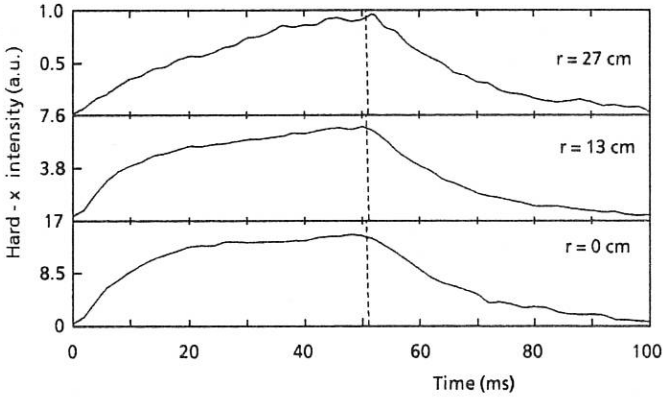

Fig. 1 - Radial HXR signals, normalized to r=27 cm ,after a ten pulses box car averaging in a discharge with I_p = 420 kA, B_t = 2.8 T, $\bar{n}_e = 1.5 \times 10^{13}$ cm^{-3}, P_{LH} = 0.9 MW, $\Delta\phi = 90°$

to spatial diffusion processes and N(r) a particle source at low energy.

Instead of solving Eq. (1), we approach the problem in an approximate way, dividing the plasma into different parts: the wave power deposition region ($R_1 < r < R_2$) and the external regions ($r < R_1$, $r > R_2$). In the deposition region we neglect the spatial diffusion and assume that the electron tail formation due to the wave occurs on a time scale shorter than the spatial diffusion time. In such region we solve, at each radial position, the time dependent model [2] for the electron distribution function. From this solution we get the fast electron population $\tilde{n}_F(r) = \int_{v1}^{\infty} dv_{||}\, f(v_{||})$. Outside the deposition region we solve the spatial diffusion equation for n_F:

$$\frac{\partial n_F}{\partial t} = \frac{\partial}{r\partial r}\, r\, D_s \frac{\partial}{\partial r}\, n_F \qquad (2)$$

with the initial condition $n_F(r, 0) = 0$ and the boundary conditions $n_F(R_2, t) = \tilde{n}_F(R_2, t)$, $n_F(R_1, t) = \tilde{n}_F(R_1, t)$, $n_F(a, t) = 0$.

In the latter equation, where integration has been performed on the velocity space with respect to Eq (1), only electrons which diffuse over the plasma radius in a time longer than the slowing down time are considered.

We assume steady state temperature profiles according to the experimental ones. Furthermore the HRX signal levels collected at different radial positions are assumed to be proportional to the fast electron population $n_F(r)$ at the same radial position.

The other parameters to be fixed in the simulations are R_1 and R_2, $n_{||min}(r)$, $n_{||max}(r)$ (the minimum and maximum $n_{||}$ at a given radius), the LH wave quasilinear diffusion coefficient D_{LH} and the spatial diffusion coefficient D_s. R_1 and R_2 are deduced from the time derivative of the HXR signal at the beginning of each modulation pulse. The normalized D_{LH} is assumed equal to 0.5, $n_{||min}(r)$ is set equal to the local accessible value

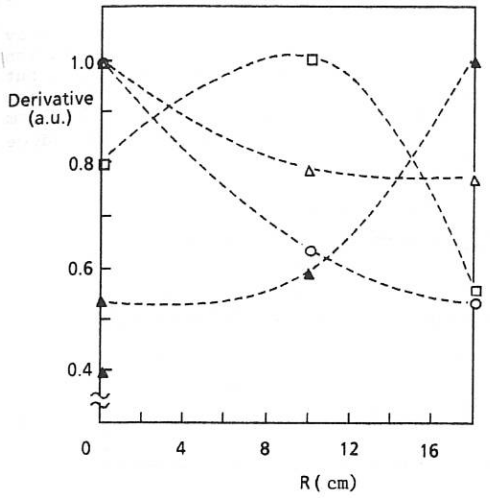

Fig.2 - Value of tangential HXR signal derivatives at the onset of RF pulses (I_p = 420 kA, B_t = 2.8 T, P_{LH} = 0.9 MW).

$n_{acc}(r)$ while $n||_{max}(r)$ is chosen in such a way to fit the total LH power absorbed in the experiment according to a deposition profile able to give $n_F(r)$ values proportional to the experimental HXR signal levels. Finally D_s, which is assumed to be constant on r, is deduced by fitting the time behaviour of the HXR signal in the diffusion region.

Two shots have been simulated, one at low density ($\hat{n}_e$ = 2 10^{13} cm^{-3}) and high temperature ($\hat{T}_e$ = 2.4 keV) and the other at higher density ($\hat{n}_e$ = 5 10^{13} cm^{-3}) and low temperature ($\hat{T}_e$ = 1.5 keV).

In the first case R_1 = 0, R_2 = 20 cm were assumed according to the deposition inferred from Fig. 2. The values of $n||_{max}$ were 4.8, 5.1, 5.6 at r = 0, 13, 20 cm respectively giving a total absorbed power of 600 kW. The deposition profile was peaked at the centre with such a choice of $n||_{max}$. A DC electric field corresponding to a V_{loop} = 1 V was considered in the Fokker-Planck equation, with an oscillating part of 30% in phase opposition with the modulated power.

Fig. 3 shows the time behaviour of $n_F(r)$ at r = 0 cm, r = 13 cm (inside the deposition region) and r = 27 cm (in the diffusion region). The three curves at r = 27 cm correspond to three different values of D_s, namely D_s = 1500, 3000, 5000 cm^2/sec. Fig. 3 has to be compared with Fig. 1 where the experimental HXR signal are shown. As already pointed out the $n||_{max}$ values were chosen in such a way to give a suprathermal population in the three different radial positions proportional to the intensity of the corresponding HXR signal. A value of $D_s \cong 3000$, 5000 cm^2/sec seems to be adequate to describe the experimental time behaviour in the diffusion region (r = 27 cm). This value is 10 time smaller than the bulk particle diffusion coefficient found in ASDEX during LH power injection, at the same density [3]. It is worth noting that the time behaviour coming from the solution of the quasilinear Fokker-Planck equation in the presence of an electric field is in fair good agreement

with the experimental time behaviour as it results from the comparison of Figs 1 and 3

Going to higher density and lower temperature the rise and decay time of the HRX signals at the beginning and at the end of the modulation pulses become shorter. This tendency is reproduced in the simulation but such times are slightly shorter than the experimental ones. The simulation was done assuming R_1=5 cm, R_2=25 cm, $n_{||max}$=5,5.5,6.5 at r=5,13,25 cm respectively. A value of $D_s \cong 5000\text{-}7000$ cm^2/sec was required to reproduce the time behaviour of the HRX signal in the diffusion region (r=27 cm).

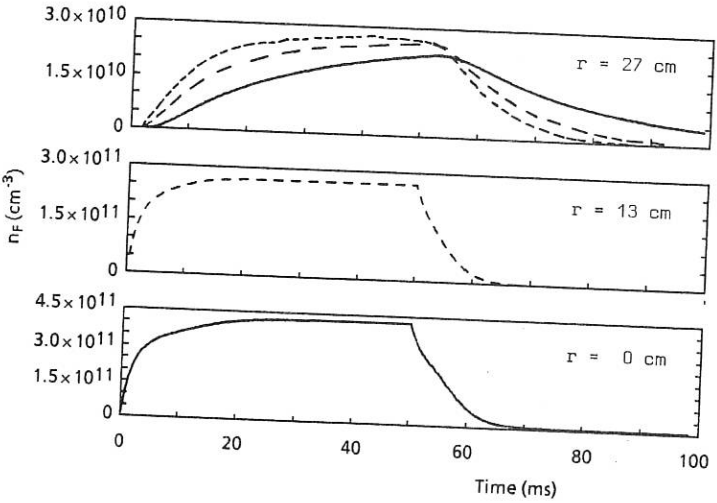

Fig. 3 - Computed fast electron density n_F as a function of time at the same radial position of Fig.1.

REFERENCES

[1] E. Barbato, R. Giannella, Phys. Lett. A 110 (1985), 309

[2] C.F.F. Karney, N.J. Fisch, Phys.Fluids 22 (1979), 716

[3] O. Gehre et al, Proc. of 17th EPS Conference on Controlled Fusion and Plasma Heating, Amsterdam (1990), Vol. I, p.70

INDEX OF AUTHORS